

Molecular mechanisms of RASopathy-associated hypertrophic cardiomyopathy

Dissertation

This dissertation is submitted
for the degree of the Doctor of Philosophy
to the Faculty of Mathematics and Natural Sciences
at the Heinrich-Heine-University Düsseldorf

Presented by

Farhad Bazgir

from Khorram abad, Iran

Düsseldorf, February 2023

Molekulare Mechanismen der RASopathie- assoziierten hypertrophen Kardiomyopathie

Inaugural-Dissertation

zur Erlangung des Doktorgrades
der Mathematisch-Naturwissenschaftlichen Fakultät
der Heinrich-Heine-Universität Düsseldorf

vorgelegt von

Farhad Bazgir

aus Khorram abad, Iran

Düsseldorf, February 2023

From the Institute of Biochemistry and Molecular Biology II
At the Heinrich Heine University Düsseldorf

Published by permission of the
Faculty of Mathematics and Natural Sciences
At Heinrich Heine University Düsseldorf

1st Supervisor: Prof. Dr. Reza Ahmadian

2nd Supervisor: Prof. Dr. Vlada Urlacher

Date of the oral examination: 27.10.2023

Table of contents

Summary	6
List of abbreviation.....	7
Amino acid abbreviation.....	9
 Chapter 1	 10
General introduction.....	
Human heart	10
Hypertrophic cardiomyopathy.....	10
Stem cells	10
Induced pluripotent stem cells (iPSCs).....	11
RAS superfamily of GTPases and their regulation	11
RAF1 kinase	12
RASopathies	13
Noonan syndrome.....	13
RIT1 (Ras like without CAAX 1)	15
Costello syndrome and epidermal homeostasis	16
HRAS (Harvey Rat sarcoma virus).....	16
RIN1 (RAS and RAB interactor)	17
RAB5	17
RHO family GTPases.....	18
ARF GTPases.....	19
 Chapter 2	 20
Alteration of myocardial structure and function in RAF1-associated Noonan syndrome: Insights from cardiac disease modeling based on patient-derived iPSCs	
 Chapter 3	 43
Cutaneous manifestations in Costello syndrome: HRAS p.Gly12Ser affects RIN1-mediated integrin trafficking in immortalized epidermal keratinocytes	
 Chapter 4	 59
The microenvironment of hypertrophic cardiomyopathy	
 Chapter 5	 98
A comprehensive analysis of RAS-effector interactions reveals interaction hotspots and new binding partners	
 Chapter 6	 112

Functional Testing of Novel Mosaic RIT1 Mutations Identified in Patients with Arteriovenous Malformations Paves the Way for Targeted Therapy

Chapter 7 135

Accessory proteins of the RAS-MAPK pathway: moving from the side line to the front line

Chapter 8 146

CDC42-IQGAP Interactions Scrutinized: New Insights into the Binding Properties of the GAP-Related Domain

Chapter 9 162

Dominant ARF3 variants disrupt Golgi integrity and cause a neurodevelopmental disorder recapitulated in zebrafish

Chapter 10 192

General discussion

iPSC modeling of the RAF1-associated Noonan syndrome's altered myocardial structure and function 193

HRAS p.Gly12Ser affects RIN1-mediated integrin trafficking in epidermal keratinocytes 197

Characterization of RIT1 indels in Arteriovenous Malformations Enables Targeted Therapy..... 198

References 199

Acknowledgements 206

EIDESSTÄTTLICHE ERKLÄRUNG 207

Summary

The RAS family of GTPases (Guanosine triphosphatases) act as molecular switches to control several key processes in all eukaryotic cells, existing in an active (GTP-bound) or inactive (GDP-bound) state with Guanine nucleotide exchange factors (GEFs) enabling the release of GDP leading to the activation of the protein and GTPase activating proteins (GAPs) facilitating the return to the inactive state by accelerating the intrinsic GTPase activity. RAS proteins link modifications in the surrounding environment of the cell to internal signal transduction pathways by interacting with a wide range of target proteins controlling many cellular processes, including proliferation, differentiation, survival, and migration. The most prevalent among RASopathies, Noonan syndrome (NS), is brought on by germline mutations in genes that encode RAS-MAPK pathway elements. Some variations, such as the frequent Ser257Leu substitution in RAF1, are connected to severe hypertrophic cardiomyopathy (HCM). In a relevant study, I used three-dimensional cardiac bodies and bioartificial cardiac tissues made from patient-derived induced pluripotent stem cells (iPSCs) with the aforementioned pathogenic RAF1 mutation to evaluate the molecular relationship between NS-associated RAF1^{S257L} and HCM. Vastly elevated levels of the heart failure marker BNP and an ultrastructural shortening of the I-bands along the Z-line region of sarcomere in both patient specific iPSC-derived RAF1^{S257L} cardiomyocytes were found upon molecular, structural, and functional evaluation of the differentiated cardiac models. These modifications coincided with titin's isoform shift from a longer (N2BA) to a shorter (N2B) variant, which also had an impact on the active force generation and contractile tensions. In this model, hyperactivation of the ERK, p38, and YAP signaling pathways were observed as contributing factors in the development of the HCM phenotypes. By employing both MEK inhibition and a CRISPR-Cas9 gene-corrected isogenic cell line, the disease phenotype was largely reversed, adding important and novel mechanistic insights into the disorder's pathophysiology. RIT1, another member of the RAS-MAPK pathway, is highly associated with development of HCM upon germline mutations in NS patients and Arteriovenous malformation syndrome (AVM) upon somatic alterations. Molecular evaluation of three novel RIT1 indels in patients with AVM indicated a massive hyperactivation status of ERK which was shown to be rescued upon MEK inhibition but not SHP2 inhibition, providing critical insights into available clinical options of the subject patients. The complex developmental condition Costello syndrome is mainly linked to HRAS germline mutations, namely the Gly12Ser substitution, which is a frequently mutated residue in several cancer types, locking HRAS in a constitutively active state. HRAS has been known to interact with RIN1 and boosts the activation of RAB5 GTPases and ABL1/2 tyrosine kinases affecting endosomal sorting and cytoskeletal dynamics. Investigating into this, I contributed to find that the HRAS^{G12S} boosts the RIN1-dependent RAB5A activation and subsequently disrupts the membrane availability and trafficking of integrins in keratinocytes, which highlights critical molecular events in etiology of the dermatological symptoms in Costello syndrome. Patients with various degrees of neurodegeneration events were found to have novel ARF3 GTPase mutations. Our structural-functional investigations of ARF3 mutations revealed a significant increase in their nucleotide exchange rates. The study was able to demonstrate that the identified variations are sited in the nucleotide-binding pocket, interfering with the protein's ability to function by maintaining the protein in GTP-bound state and ultimately disrupting the integrity of the Golgi. These findings collectively provide critical mechanistic understanding into the pathogenesis and treatment options of several patient-specific MAPK-associated disorders in various proteins and mutation profiles.

List of abbreviations

Abbreviation	Full form
Aa	Amino acid
ACK	Activated CDC42 kinase
AKT	Proteinkinase B
ARF	ADP ribosylation factor
AVM	Arteriovenous malformation syndrome
BNP	B-type natriuretic peptide
CDC42	Cell division control protein 42 homolog
CRD	Cysteine rich domain
CR	Costello syndrome
e.g.	Exempli gratia, for example
ERK	Extracellular-signal regulated kinase
ESC	Embryonic stem cell
GAP	GTPase activating protein
GDI	Guanine nucleotide dissociation inhibitor
GDP	Guanosin-di-phosphate
GEF	Guanine-nucleotide exchange factor
GPCR	G-protein coupled receptors
GTP	Guanosine-Tri-phosphate
GTPases	Guanosine triphosphatases
HRAS	Harvey Rat sarcoma virus
IQGAP	IQ motif containing GTPase activating protein
iPSC	Induced pluripotent stem cell
kDa	Kilo dalton
KRAS	Kirsten rat sarcoma virus

MAPK	Mitogen-activated protein kinase
MEK	MAPK/ERK kinase
MEKi	MEK inhibitor
NF1	Neurofibromatosis type 1
NFAT	Nuclear factor of activated T-cells
NS	Noonan syndrome
PAK	P21 activated kinase
PI3K	Phosphoinositide 3-kinases
PLN	Phospholamban
RAB	Ras related in brain
RAC	Ras-related C3 botulinum toxin substrate
RAF	Rapidly growing fibrosarcoma
RAL GDS	Ral guanine nucleotide dissociation stimulator
RAS	Rat sarcoma
RBD	RAS binding domain
RHO	Ras Homolog
RIN	RAS and RAB interactor
ROCK	RHO associated protein kinase
RTK	Receptor tyrosine kinase
SERCA	Sarcoplasmic/endoplasmic reticulum calcium ATPase
SH	Src homology
SOS	Son of Sevenless

Amino acid abbreviations

Amino Acid	Three letter code	Letter code
Alanine	Ala	A
Arginine	Arg	R
Asparagine	Asn	N
Aspartic acid	Asp	D
Cysteine	Cys	C
Glutamine	Gln	Q
Glutamic acid	Glu	E
Glycine	Gly	G
Histidine	His	H
Isoleucine	Ile	I
Leucine	Leu	L
Lysine	Lys	K
Methionine	Met	M
Phenylalanine	Phe	F
Proline	Pro	P
Serine	Ser	S
Threonine	Thr	T
Tryptophan	Trp	W
Tyrosine	Tyr	Y
Valine	Val	V

Chapter 1 – General introduction

Human heart

Four functionally and physically diverse chambers make up the heart as a complex organ. To permit continuous contraction and relaxation across various pressures, stresses, and biophysical inputs in each chamber, cardiac anatomical and functional complexity needs perfect orchestration of disparate cell populations (Litviňuková *et al.*, 2020). Two heart fields, which are made up of multipotent progenitor cells, give rise to the heart. The left ventricle is largely populated by cells from the first heart field, the right ventricle by cells from the second heart field, and the atria are populated by cells from both heart fields. During cardiogenesis, gene regulatory networks that are regulated by transcription factors, cofactors, and chromatin modifications—in which non-coding RNAs also take part—control the distribution of cardiac progenitor cells. (Meilhac and Buckingham, 2018).

Hypertrophic cardiomyopathy

One in 500 people in the general population have the genetic cardiovascular condition known as hypertrophic cardiomyopathy. More than 1400 mutations in 11 or more genes, which code for proteins in the cardiac sarcomere, have been reported to be the cause of this disorder (Maron and Maron, 2013). It is most frequently characterized by left ventricular (LV) hypertrophy, with a variety of possible consequences including heart failure and sudden cardiac death, but also the possibility of surviving to a normal life expectancy (Semsarian *et al.*, 2015). The main characteristic associated with HCM is an increase in the left ventricular wall thickness, which can very commonly cause a diastolic dysfunction that can be driver for the above mentioned complications at the organ level. Recently, it has also been discovered that the development of HCM is also influenced by mutations in genes that do not directly encode sarcomeric proteins, such as several members of the RAS-MAPK pathway related proteins. Although HCM is infrequently seen in RASopathies (20–30%), it is more often seen in those who have pathogenic mutations of the genes RAF1 and RIT1 (Gelb *et al.*, 2015; Aoki *et al.*, 2013).

Stem cells

In 1998, two articles detailing the in vitro development of human embryonic stem (ES) cells from either the early blastocyst's inner cell mass (ICM) or the primitive gonadal regions of early aborted fetuses were published. Many years of research on mouse ES cells have previously demonstrated their remarkable flexibility, basically being able to develop into practically any cells that emerge from the three germ layers (Alison *et al.*, 2002). While stem cells may be found in both adult and embryonic cells, there are numerous stages of specialization with each one resulting in a reduction in developmental potential. As a result, a unipotent stem cell cannot differentiate into as many distinct types of cells as a pluripotent one. As a totipotent cell, the zygote has the highest capacity for differentiation, enabling cells to develop into both embryos and extra-embryonic structures. In contrast, pluripotent stem cells (PSCs), such as embryonic stem cells (ESCs), can develop into cells of all germ layers but not extraembryonic structures like

the placenta. Compared to PSCs, multipotent stem cells have a smaller range of differentiation, that can specialize in distinct cells from certain cell lineages with haematopoietic stem cell as an example which may give rise to many blood cell types. (Zakrzewski *et al.*, 2019).

Induced pluripotent stem cells (iPSCs)

In 2006 in Shinya Yamanaka's group, by ectopic expression of four genes using murine fibroblasts, and in 2007 from human fibroblasts, stem cells with properties similar to ESCs could be generated, named iPSCs (Takahashi and Yamanaka, 2006; Takahashi *et al.*, 2007). The astounding advancement of reprogramming technology has propelled the science of stem-cell biology ahead. Through this ectopic co-expression of reprogramming factors, somatic cells can regain their pluripotency, opening up new and exciting options for disease modeling and tailored regenerative cell treatments (Robinton and Daley, 2012). Several of the preexisting concerns, including efficiency, ethical, and immunological challenges, were resolved with the advent of iPSCs. They have the traits of self-renewal and pluripotency as well as the morphological and physiological qualities of ESCs, although yet showing some variances to ESCs in their expression and epigenetics profile (Chin *et al.*, 2009). The ability to simulate human disorders in a culture plate has become possible because to iPSC technology. An endless source of human tissues containing the genetic variants that triggered or aided in the development of the disorder may be produced by reprogramming somatic cells from patients into an embryonic stem cell-like state and differentiation into disease-relevant cell types (Soldner and Jaenisch, 2012). A potential new paradigm in drug development that places human disease pathophysiology at the center of preclinical drug discovery has been offered thanks to an increasingly sophisticated ability to differentiate these iPSCs into disease-relevant cell types. Many monogenic disorders have disease models created from iPSCs that exhibit cellular disease phenotypes, but more importantly iPSCs can also be employed for phenotype-based drug screening in complicated diseases for which the underlying genetic mechanism is unclear (Grskovic *et al.*, 2011).

RAS superfamily of GTPases and their regulation

RAS superfamily GTPases function as molecular switches to regulate a variety of crucial processes in all eukaryotic cells. The RAS and RHO families are of particular relevance among the roughly 60 members that have been discovered so far in mammalian cells because they link internal signal transduction pathways to alterations in the outside environment. Similar to other GTPases, they can exist in both active (GTP-bound) and inactive (GDP-bound) conformations (Bar-Sagi and Hall, 2000). Guanine nucleotide exchange factors (GEFs) facilitate the release of GDP leading to activation of the protein considering higher cellular concentration of GTP (Schmidt and Hall, 2002), while on the other hand, RAS and RHO GTPases return to their inactive state through the intrinsic GTPase activity, further accelerated by GTPase activating proteins (GAPs). Ras and Rho GTPases interact with their target proteins in the GTP-bound state promoting a cellular

response (Bernards and Settleman, 2004; Wennerberg *et al.*, 2005). RAS proteins generally respond to a wide variety of extracellular inputs and are among the signaling molecules that are indirectly related to several distinct cell surface receptors. They regulate a variety of signaling pathways and, as a result, a wide range of cellular functions, such as migration, adhesion, proliferation, and differentiation. Cancer, developmental problems, metabolic, and cardiovascular illnesses are consequently caused by any imbalance of these pathways (Nakhaei-Rad *et al.*, 2018).

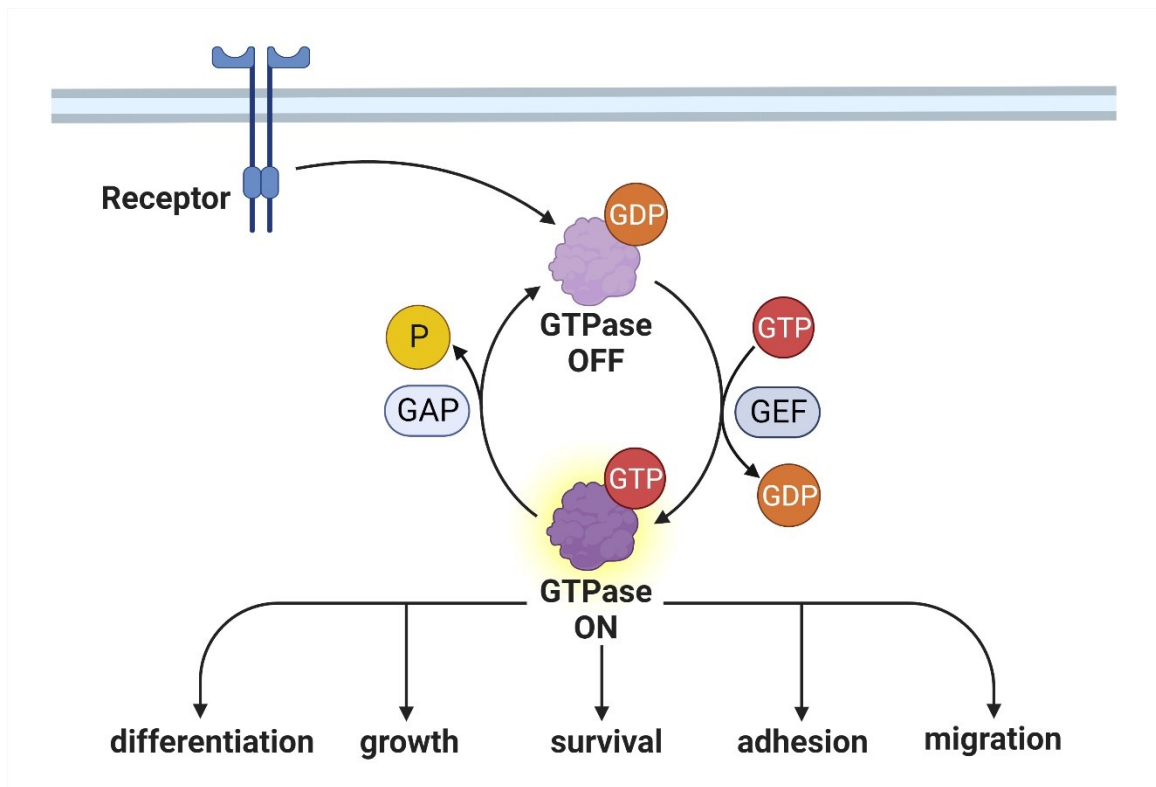


Figure 1. Schematic overview of RAS proteins' downstream signaling pathways and their GTP/GDP cycle. Through the activities of two key regulatory proteins, GEF and GAP, RAS proteins cycle between GDP/GTP bound forms. GAPs increase their intrinsic GTPase activity, whereas GEFs accelerate the conversion of GDP to GTP. GTPases can only transduce a signal when they are GTP-bound and at the membrane as a result of post-translational modifications. The biological activities of RAS proteins are transmitted through interactions with effectors and activation of the downstream pathways. RAS, rat sarcoma; GEF, guanine nucleotide exchange factor; GAP, GTPase-activating protein.

RAF1 kinase

The MEK/ERK pathway and the RAS family proteins are connected via the RAF Ser/Thr kinases, which regulate a variety of biochemical activities including proliferation, differentiation, and survival (Yoon and Seger, 2006). By identifying the viral oncogene v-raf from the transforming murine retrovirus 3611-MSV, the first RAF member was identified in 1983 (Rapp *et al.*, 1983). Its first cellular homologue CRAF was found shortly

after (Bonner *et al.*, 1985), and then its paralogs ARAF (Huleihel *et al.*, 1986) and BRAF (Ikawa *et al.*, 1988) were identified.

There are three conserved regions (CR) that are present in all three human RAF paralogues. CR1 is made up of a RAS-binding domain (RBD) and a cysteine-rich domain (CRD), both of which are necessary for interacting with plasma membranes and active RAS proteins (Desideri *et al.*, 2015; Mott and Owen, 2015). The N-terminal of RAF kinases in an inhibited state suppresses the kinase domain resulting a form of cytosolic auto-inhibited RAF kinases. 14-3-3 proteins attach to two CRAF phosphorylation sites, the first of which is in CR2 (pS259 of CRAF), while the other is behind CR3 (pS621 of CRAF), facilitating the maintenance of RAF in this auto-inhibited state (Freed *et al.*, 1994; Fischer *et al.*, 2009).

The first step in RAF activation is its interaction with GTP-bound RAS, which is followed by its translocation to the plasma membrane, 14-3-3 dissociation, and dephosphorylation of the CR2 negative regulatory site (pS259) (Ghosh *et al.*, 1994; Kubicek *et al.*, 2002). Activated RAF dimers send the signal to MEK1/2, which then phosphorylates ERK1/2 (Cseh *et al.*, 2014). In a negative feedback regulation, ERK phosphorylates RAF and then through re-phosphorylation at S259, the protein returns again to the inhibited state (Dougherty *et al.*, 2005).

RASopathies

A clinically recognized class of medical genetic diseases known as the RASopathies is brought on by germline mutations in genes that encode either regulators or components of the RAS/mitogen-activated protein kinase (MAPK) pathway. The RASopathies have many overlapping phenotypic characteristics because of the same underlying RAS/MAPK pathway dysfunction (Rauen, 2013). Numerous unique syndromes, such as Noonan syndrome, Costello syndrome, and neurofibromatosis type 1 can be brought on by these germline abnormalities (Jafry and Sidbury, 2020). Recognizing these germline derived and linked syndromes is crucial for effective care, even if activating RAS somatic mutations can be discovered in up to 30% of human malignancies. Over 1 in 1000 people worldwide are affected by the RASopathies, which collectively make up the prevalent group of developmental malformation syndromes (Tidyman and Rauen, 2016).

Noonan syndrome

A hereditary multisystem condition called Noonan syndrome is distinguished by unusual facial traits, developmental delays, learning challenges, small height, congenital heart problems, renal abnormalities, lymphatic malformations, and bleeding issues. Dysregulations in the RAS-MAPK pathway lead to development of Noonan syndrome, affecting the gene encoding proteins involved in the signaling events (Roberts *et al.*, 2013). The frequency of this autosomal dominant, variable expression, multisystem disease is estimated to be 1 in 1000–2500 people (Mendez *et al.*, 1985). Jacqueline Noonan described nine individuals with pulmonary valve stenosis, short height, hypertelorism, minor intellectual impairment, ptosis, undescended testes, and skeletal

deformities as the condition's first case study (Noonan, 1963). Since high throughput sequencing methods have become more widely available over the past years, mutations in several genes have been found to be the primary factor contributing to the emergence of the disorder. There have been reports of germline mutations in the genes PTPN11, KRAS, SOS1, RAF1, RIT1, NRAS and KRAS in people with Noonan syndrome (Schubbert *et al.*, 2006; Roberts *et al.*, 2007; Aoki *et al.*, 2013; Pandit *et al.*, 2007; Cirstea *et al.*, 2010).

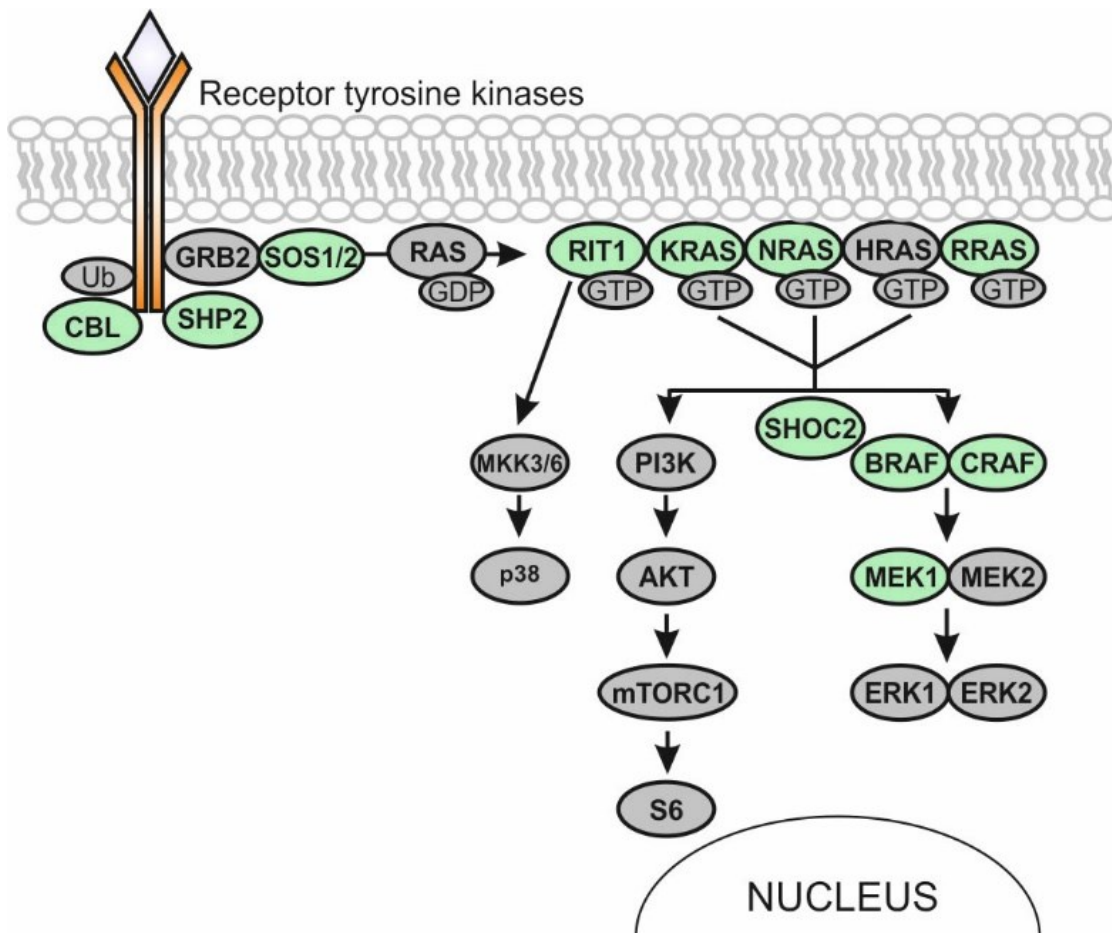


Figure 2. Schematic overview depicting the RAS-MAPK pathway and the genes involved in the development of Noonan syndrome. When a ligand interacts with receptor tyrosine kinases, SOS1 is drawn to the membrane where it functions as a RAS GEF and activates RAS. The RAF family is targeted by the signal that active RAS transmits. Then, RAF phosphorylates MEK1/2, which phosphorylates ERK1/2 in turn. An autosomal dominant condition called Noonan syndrome is characterized by germline mutations in the genes that produce proteins that are connected to the RAS-MAPK pathway (affected genes associated with NS are highlighted in green).

RIT1 (Ras like without CAAX 1)

RIT1 is a member of the RAS superfamily of low-molecular-weight GTP-binding proteins that cycle between an active GTP-bound and an inactive GDP-bound state in response

to cellular signaling events (Shi *et al.*, 2013). Similar to several RAS GTPases, RIT1 has five well-conserved amino acid motifs: G1, G3, G2, and G4 and G5, which are used for phosphate binding, effector binding, and GTP binding and hydrolysis, respectively (Colicelli, 2004). RIT1 is expressed in many tissues at different stages of development as well as conferring functional roles in neuronal morphogenesis, neural differentiation, and cellular stress resistance in a number of studies using different cell lines (Shi *et al.*, 2006; Lein *et al.*, 2007; Cai *et al.*, 2011; Spencer *et al.*, 2002).

In addition to initial reports for a number of somatic cancer mutations (Gomez-Segui *et al.*, 2013; Berger *et al.*, 2014), the importance for a developmental role of RIT1 was highlighted upon detection of germline mutations in families with Noonan syndrome (NS), a developmental RASopathy marked by cardiac abnormalities, growth retardation and affected craniofacial morphology (Aoki *et al.*, 2013; Kouz *et al.*, 2016; Yaoita *et al.*, 2016). The frequency of RIT1 mutations in NS is at least 5%. Comparatively to other NS subtypes affected by mutations in several proteins involved in regulation of RAS-MAPK pathway such as SOS1, SOS2, SHP2, LZTR1, and SHOC2 (Roberts *et al.*, 2007; Yamamoto *et al.*, 2015; Bentires-Alj *et al.*, 2004; Young *et al.*, 2018), those with RIT1 mutations have a higher prevalence of cardiovascular symptoms and lymphatic abnormalities (Cavé *et al.*, 2016; Calcagni *et al.*, 2016).

Unlike canonical RAS GTPases (NRAS, HRAS, and KRAS) having mutational hotspots around Glycine 12 and 13 residues, RIT1 mutations mostly occur proximal to the switch II domain. Despite no GAPs been identified for RIT1 so far, it is possible that the differences in mutational profile of RIT1 in comparison to other canonical RAS proteins could confer functional variations in regard to GTPase activity of RIT1.

RAS GTPases share several effector molecules, including RAF1 and the PI3K p110 catalytic subunit towards downstream signaling regulation. In spite of previous efforts for identification of candidate direct effectors for RIT1 GTPase activity (Shao and Andres, 2000; Shi and Andres, 2005; Castel *et al.*, 2019), there is the lack of a multidirectional comprehensive proteome approach in literature for identification of novel signaling nodes mediating downstream pathway activations influenced by RIT1.

The recent disclosures of the involvement of RIT1 in several cancer implications and developmental disorders brings to light the crucial importance of molecular characterization of different identified pathogenic RIT1 mutations in regards to molecular switch properties as well as a crack-down of potential downstream targets, mediating cellular signaling stimulations via RIT1, exposing the pathogenic states open for molecular targeting and therapy.

Costello syndrome and epidermal homeostasis

The numerous congenital abnormality and mental retardation condition known as Costello syndrome is characterized by a coarse face, loose skin, cardiomyopathy, and a

propensity for malignancies. Cases of the Costello syndrome have frequently been linked to germline changes in the HRAS Glycine 12 and 13 residues (Aoki *et al.*, 2005).

Four layers of keratinocytes that engage in both programmed differentiation and proliferation make up the skin's epithelium, or epidermis. The precondition for a functioning and healthy skin is a process known as epidermal stratification, and previous reports have demonstrated that HRAS is a key regulator of keratinocyte stratification (Drosten *et al.*, 2013; Drosten *et al.*, 2014). Basal keratinocytes have a high rate of proliferation and use hemidesmosomes and focal adhesions to link the dermis and extracellular matrix (ECM) of the epidermis. In addition, cell-cell interactions such as adherens junctions, tight junctions, desmosomes, and gap junctions keep nearby keratinocytes in close proximity (Simpson *et al.*, 2011; Hegde and Raghavan, 2013). A variety of transmembrane and cell adhesion proteins, including cadherins, claudins, and integrins, promote each of these cell-cell and cell-ECM connections. Transmembrane integrins transmit signals in both ways and link the cell's actin cytoskeleton to the ECM. Alpha and beta subunits make up integrin receptors, and the majority of these heterodimers include the $\beta 1$ subunit, which is crucial for maintaining epidermal stratification and adherence to the basement membrane (Moreno-Layseca *et al.*, 2019; Rippa *et al.*, 2013). In order to maintain the dynamic physiology of the epidermis and epidermal homeostasis in Keratinocytes, a well regulated mechanism is needed for contact and adhesion proteins that must be internalized, recycled back to the plasma membrane, and/or degraded (De Franceschi *et al.*, 2015).

Different studies have looked at the molecular pathophysiology brought on by disease-associated HRAS mutations in a variety of cell types, including fibroblasts, heart muscle cells, and neuronal cells (Rosenberger *et al.*, 2009; Krencik *et al.*, 2015a; Hinek *et al.*, 2005). It remained largely unknown, nevertheless, what was causing the dermatological and epidermal symptoms in RASopathies like Costello Syndrome.

HRAS (Harvey Rat sarcoma virus)

By switching between an active guanosine triphosphate (GTP)-bound and an inactive guanosine diphosphate (GDP)-bound state, HRAS functions as a molecular switch. By binding to a range of effectors, active HRAS regulates a number of cellular signaling pathways. The serine/threonine RAF kinases, catalytic subunits of phosphoinositide 3-kinases (PIK3CA), phospholipase C1 (PLCE1), and RAL guanine nucleotide dissociation stimulator (RALGDS) are the best known among different HRAS effectors (Simanshu *et al.*, 2017). Since the discovery of an oncogenic HRAS mutation in bladder cancer (Land *et al.*, 1983), mutations of KRAS, HRAS, and NRAS have been discovered in around 30% of human malignancies. These RAS GTPases generally become active oncogenes when they have mutations at codons 12, 13, or 61 (Bos, 1989).

RIN1 (RAS and RAB interactor)

The human RIN1 gene was initially discovered as a cDNA fragment that prevented the yeast *Saccharomyces cerevisiae* from exhibiting RAS-induced phenotypes (Colicelli *et al.*, 1991). Following study of full-length RIN1 clones revealed that the protein produced by this gene binds to activated RAS with great affinity and specificity (Wang *et al.*, 2002). RIN1 has been found to promote endocytosis mediated by Rab5 guanine nucleotide exchange, and Rab5A-dependent endosome fusion. Activated HRAS enhanced the stimulatory effects of RIN1 on these processes (Tall *et al.*, 2001). Based on functional research and sequence alignment, the RIN1 protein includes four distinct domains. A SRC homology 2 (SH2) domain is present in the amino terminal half of RIN1 and interacts to the cytoplasmic portions of several receptor tyrosine kinases (Barbieri *et al.*, 2003). Tyrosine phosphorylation substrates and proline-rich domains are also found in the amino terminus of RIN1, which combined enable persistent binding to the SH2 and SH3 domains of tyrosine kinases from the ABL family (Hu *et al.*, 2005). A RAS association (RA) domain and a guanine nucleotide exchange factor (GEF) domain are located in the carboxy terminal region of RIN1 (Bliss *et al.*, 2006). Endosomal sorting activities and cytoskeletal dynamics are coordinated through the activation of RAB5 GTPases and ABL1/2 tyrosine kinases, which are activated in response to the binding of active HRAS to RIN1 (Tall *et al.*, 2001; Balaji and Colicelli, 2013). Ser351 phosphorylation dependent binding to 14-3-3 proteins regulates RIN1's translocation between cytoplasmic and membrane compartments (Wang *et al.*, 2002).

RAB5

The RAB family of GTPases, in particular the RIN1 effector RAB5, governs the distribution of integrins within vesicles, which in turn modulates cell adhesion and adhesion-dependent activities including cell spreading and migration (Yuan and Song, 2020). Integrins are imported and go through the endocytic-exocytic pathway before being recycled back to the plasma membrane in order to facilitate cell attachment to extracellular matrix. The activity of integrins in the cell is modulated by a variety of context-dependent controls on this protein family's trafficking (Moreno-Layseca *et al.*, 2019). Both integrin-dependent cell adhesion and motility depend on spatiotemporal remodeling of the actin cytoskeleton, and these processes can be aided by the tyrosine kinases ABL1/2 downstream of RIN1 (Woodring *et al.*, 2003; Khatri *et al.*, 2016).

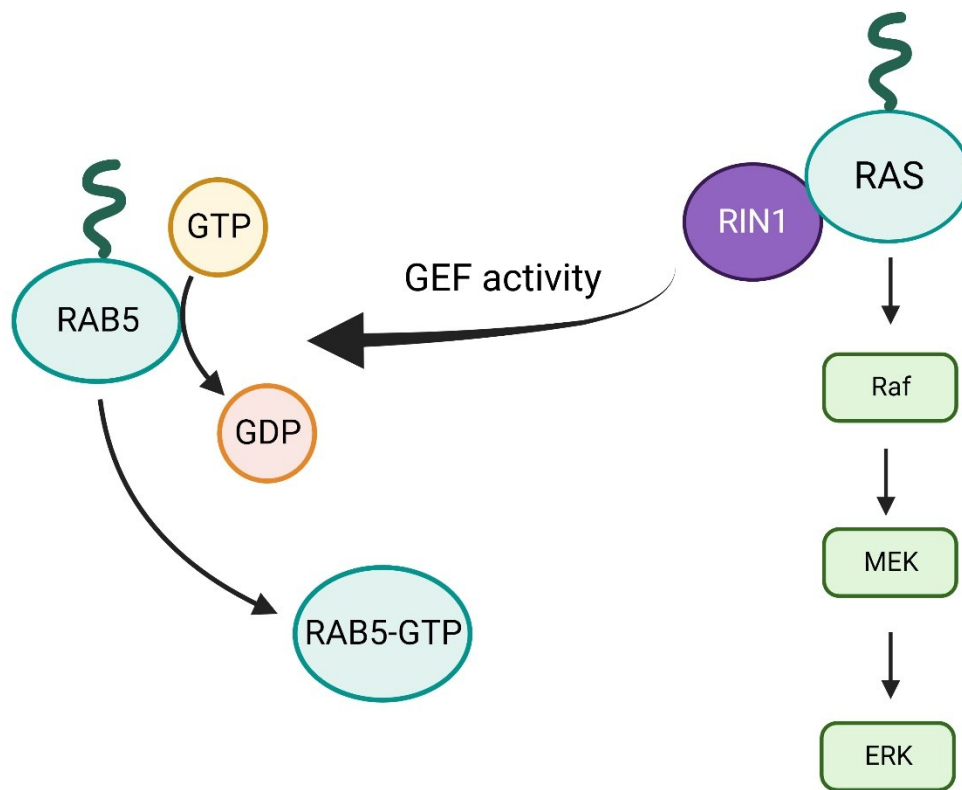


Figure 3. Overview of the role of RAS proteins in the RIN1-mediated regulation of the RAB5 GTPase. The RAB5 guanine nucleotide exchange and RAB5A-dependent endosome fusion processes that increase endocytosis is mediated by RIN1. RIN1's stimulatory effects on these activities are enhanced by activated HRAS. The activation of RAB5 GTPases, which occurs in response to the binding of active HRAS to RIN1, allows endosomal sorting activities and cytoskeletal dynamics to be coordinated. RIN1 is one of the high affinity effector binders for HRAS that can compete with RAF kinases for HRAS binding.

RHO family GTPases

RHO GTPases cycle between an active (GTP-bound) and an inactive (GDP-bound) state while acting as molecular switches, with a few exceptions. Guanine nucleotide dissociation inhibitors (GDIs), guanine nucleotide exchange factors (GEFs), and GTPases activating proteins are typically three types of regulatory proteins that regulate their actions at the plasma membrane (GAPs) (Dvorsky and Ahmadian, 2004; Cherfils and Zeghouf, 2013). RHO GTPases, like CDC42, undergo a conformational shift in two locations known as switch I and switch II when they transition from the inactive GDP-bound state to the active GTP-bound state eventually leading to association with downstream effectors, e.g., PAK1, WASP, IQGAP1, ROCK1 and ACK (Nouri *et al.*, 2020; Morreale *et al.*, 2000; Mott *et al.*, 1999; Dvorsky *et al.*, 2004; Bishop and Hall, 2000).

The presence of a 12 amino acid insertion (aa 124–135 in CDC42) that extends from the G domain structure and forms a short helix, the so-called insert helix (IH), which is highly charged and varies among members of the RHO family, is one distinctive characteristic that sets the RHO family apart from other small GTPase families (Thapar *et al.*, 2002). Membrane attachment, a requirement for RHO protein function, is accomplished by the post-translational alteration of isoprenylation. In this way, a third regulation mechanism that guides the membrane targeting of RHO proteins to certain subcellular locations regulates their activity. In particular, guanine nucleotide dissociation inhibitors (GDIs) limit the cycling of prenylated RHO proteins between the cytosol and membrane by preferentially binding to these proteins (Etienne-Manneville and Hall, 2002).

In addition to acting as a molecular switch for actin cytoskeleton remodeling (Paterson *et al.*, 1990), RHO signaling also promotes the creation of focal adhesions, which make it easier for cells to adhere to ECM by raising integrin avidity amongst other well-known instances of Rho-controlled cell processes such as neurite retraction and cytokinesis. (Morii *et al.*, 1992; Jalink *et al.*, 1994; Narumiya and Thumkeo, 2018).

ARF GTPases

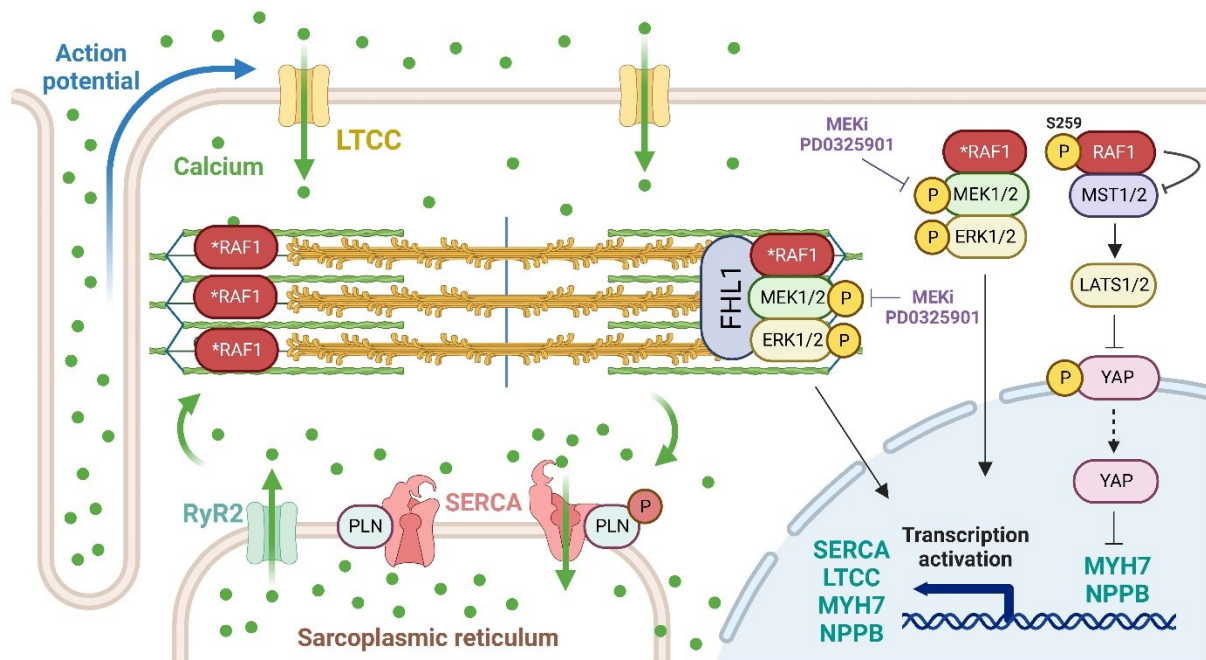
The phosphatidylinositol (PtdIns) kinases (PIK), which may alter the lipid content of membranes, are recruited and activated by ARF GTPases, which are widely expressed and mediate important processes such as bidirectional membrane trafficking, known as endocytosis and exocytosis (Cherfils, 2014; Donaldson and Jackson, 2011).

The ADP-ribosylation factors (ARF) family of small GTPases, which consists of six members (ARF1, ARF3-6, and ARF2, absent in primates), controls important processes related to Golgi structure and function, vesicular biogenesis, and cargo transport (Volpicelli-Daley *et al.*, 2005). The role of ARFs in cells is mostly redundant and overlapping; they take part in the bidirectional membrane trafficking necessary for endocytosis, anterograde/retrograde transport, and protein recycling to the membranes or their destruction (Donaldson and Jackson, 2011; Khan and Ménétrey, 2013).

Similar to other RAS proteins, ARF GTPases cycle between an active GTP bound and an inactive GDP bound state and the cycling between the two steps is facilitated by ARFGAPs and ARFGEFs (Donaldson and Jackson, 2011; Helms and Rothman, 1992). For cell division and cytokinesis, mitotic ARF-regulated Golgi dynamics are essential. Ultimately, ARFs actively contribute to the fine regulation of significant events throughout embryogenesis by managing Golgi structure, function, cargo sorting, and trafficking (Hanai *et al.*, 2016; Nakayama, 2016; Rodrigues and Harris, 2019).

Chapter 2

Alteration of myocardial structure and function in RAF1-associated Noonan syndrome: Insights from cardiac disease modeling based on patient-derived iPSCs



Status: Under revision at Nature-Communications Biology (online at BioRxiv)

Impact factor: 6.54

Contribution: 25 %

iPSC culture and propagation, cardiac differentiation, western blotting, RT-PCR, Immunohistochemistry and Confocal microscopy, ELISA, Flow cytometry, preparation and illustration of the figures, writing and drafting of the manuscript and discussion.

Alteration of myocardial structure and function in RAF1-associated Noonan syndrome: Insights from cardiac disease modeling based on patient-derived iPSCs

Saeideh Nakhaei-Rad^{1,16,†}, Farhad Bazgir^{1,†}, Julia Dahlmann^{2,3,16,‡}, Alexandra Viktoria Busley^{4,5,6,‡}, Marcel Buchholzer^{1,16,‡}, Fereshteh Haghighi^{1,3,5,‡}, Anne Schänzer⁷, Andreas Hahn⁸, Sebastian Kötter⁹, Denny Schanze², Ruchika Anand¹⁰, Florian Funk¹¹, Andrea Borchardt¹⁰, Annette Vera Kronenbitter¹¹, Jürgen Scheller¹, Roland P. Piekorz¹, Andreas S. Reichert¹⁰, Marianne Volleth², Matthew J. Wolf¹², Ion Cristian Cirstea¹³, Bruce D. Gelb¹⁴, Marco Tartaglia¹⁵, Joachim Schmitt¹¹, Martina Krüger⁹, Ingo Kutschka^{3,5}, Lukas Cyganek^{4,5,6}, Martin Zenker^{2,*}, George Kensah^{3,5,*}, Mohammad R. Ahmadian^{1,*}

¹Institute of Biochemistry and Molecular Biology II, Medical Faculty and University Hospital Düsseldorf, Heinrich Heine University Düsseldorf, Düsseldorf, Germany

²Institute of Human Genetics, University Hospital, Otto von Guericke-University, Magdeburg, Germany

³Clinic for Cardiothoracic and Vascular Surgery, University Medical Center, Göttingen, Germany

⁴Stem Cell Unit, Clinic for Cardiology and Pneumology, University Medical Center Göttingen, Göttingen, Germany

⁵German Center for Cardiovascular Research (DZHK), partner site Göttingen, Germany

⁶Cluster of Excellence "Multiscale Bioimaging: from Molecular Machines to Networks of Excitable Cells", University of Göttingen, Germany

⁷Institute of Neuropathology, Justus Liebig University Giessen, Giessen, Germany

⁸Department of Child Neurology, Justus Liebig University Giessen, 35392 Giessen, Germany

⁹Institute of Cardiovascular Physiology, Medical Faculty and University Hospital Düsseldorf, Heinrich Heine University Düsseldorf, Düsseldorf, Germany

¹⁰Institute of Biochemistry and Molecular Biology I, Medical Faculty and University Hospital Düsseldorf, Heinrich Heine University Düsseldorf, Düsseldorf, Germany

¹¹Institute of Pharmacology and Clinical Pharmacology, Medical Faculty and University Hospital Düsseldorf, Heinrich Heine University Düsseldorf, Düsseldorf, Germany

¹²Department of Medicine and Robert M. Berne Cardiovascular Research Center, University of Virginia, USA

¹³Institute of Comparative Molecular Endocrinology, University of Ulm, Helmholtzstrasse 8/1, 89081 Ulm, Germany

¹⁴Mindich Child Health and Development Institute and Departments of Pediatrics and Genetics and Genomic Sciences, Icahn School of Medicine at Mount Sinai, New York, NY 10029, USA

¹⁵Genetics and Rare Diseases Research Division, Ospedale Pediatrico Bambino Gesù, IRCCS, 00146 Rome, Italy

¹⁶Current address: Saeideh Nakhaei-Rad, Stem Cell Biology and Regenerative Medicine Research Group, Institute of Biotechnology, Ferdowsi University of Mashhad, Mashhad, Iran; Julia Dahlmann, Leibniz Research Laboratories for Biotechnology and Artificial Organs (LEBAO), Department of Cardiac, Thoracic-, Transplantation and Vascular Surgery, REBIRTH-Research Center for Translational and Regenerative Medicine, Biomedical Research in Endstage and Obstructive Lung Disease (BREATH), German Center for Lung Research (DZL), Hannover Medical School, 30625 Hannover, Germany; Marcel Buchholzer, Institute for Molecular Physiology, Heinrich Heine University Düsseldorf, Düsseldorf 40225, Germany;

[†]These authors contributed equally: Saeideh Nakhaei-Rad, Farhad Bazgir

[‡]These authors contributed equally: Julia Dahlmann, Alexandra Viktoria Busley, Marcel Buchholzer, Fereshteh Haghighi

*Corresponding authors: reza.ahmadian@uni-duesseldorf.de;

george.kensah@med.uni-goettingen.de; martin.zenker@med.ovgu.de.

Abstract

Noonan syndrome (NS), the most common among the RASopathies, is caused by germline variants in genes encoding components of the RAS-MAPK pathway. Distinct variants, including the recurrent Ser257Leu substitution in RAF1, are associated with severe hypertrophic cardiomyopathy (HCM). Here, we investigated the elusive mechanistic link between NS-associated RAF1S257L and HCM using three-dimensional cardiac bodies and bioartificial cardiac tissues generated from patient-derived induced pluripotent stem cells (iPSCs) harboring the pathogenic RAF1 c.770C>T missense change. We characterize the

molecular, structural and functional consequences of aberrant RAF1 –associated signaling on the cardiac models. Ultrastructural assessment of the sarcomere revealed a shortening of the I-bands along the Z disc area in both iPSC-derived RAF1S257L cardiomyocytes, and myocardial tissue biopsies. The disease phenotype was partly reverted by using both MEK inhibition, and a gene-corrected isogenic RAF1L257S cell line. Collectively, our findings uncovered a direct link between a RASopathy gene variant and the abnormal sarcomere structure resulting in a cardiac dysfunction that remarkably recapitulates the human disease. These insights represent a basis to develop future targeted therapeutic approaches.

Keywords: Cardiac bodies, hypertrophic cardiomyopathy, iPSC, MAPK pathway, Noonan syndrome, RAF kinase, RASopathy, sarcomere

Introduction

Germline variants of genes encoding RAS-mitogen-activated protein kinase (MAPK) signaling components result in a set of developmental disorders collectively referred to as RASopathies. They are characterized by craniofacial dysmorphism, delayed growth, variable neurocognitive impairment, and cardiac defects, including hypertrophic cardiomyopathy (HCM). HCM is known to vary in prevalence and severity depending on the genotype [3, 19, 52, 55]. At the organ level, HCM is manifested as an increase in the left ventricular wall thickness that may result in diastolic dysfunction, outflow obstruction, increased risk of heart failure, stroke and cardiac arrhythmia [38].

In Noonan syndrome (NS), the most prevalent disease entity among the RASopathies, development of HCM is associated with significant morbidity and risk of cardiac death. Notably, more than 90% of NS individuals with a *RAF1* variant are affected by HCM, whereas the overall frequency of HCM in NS is only about 20% [47, 53]. One variant, c.770C>T (p.Ser257Leu), accounts for more than 50% of cases with *RAF1*-associated NS (NSEuroNet database). Similar to other variants affecting transducers and positive modulatory proteins with role in the MAPK signaling cascade, the Ser257Leu amino acid substitution confers a functional enhancement (gain-of-function) to RAF1 kinase activity [38, 54]. Functional studies on RAF1 activity have mainly been focused on its role in activation of the MAPK pathway in cancer [8]. Recently, new paths of RAF1 cardiac-specific signaling towards ERK5 and calcineurin-NFAT have been discovered [9, 29, 59]. However, how coaction of RAF1-specific signaling pathways in cardiomyocytes (CMs) results in the phenotypical changes that lead to the development of HCM remains an open question. At the cellular level, HCM is characterized by an increase in CM size, re-activation of the fetal gene program, change in the amplitudes of calcium (Ca²⁺) transients, increased protein synthesis, and changes in the organization of the sarcomere structure and dysfunctional contractility

[46]. Therefore, there is a critical need to combine signaling, phenotypical, and functional studies to dissect and understand the pathogenesis of HCM driven by RAF1^{S257L} gain-of-function (GoF).

To analyze the cardiac-specific function of RAF1 signaling, pure populations of human CMs are required to establish informative *in vitro* HCM disease models, where CMs should be able to respond to external stimuli and stress conditions as well as increase cell size rather than cell number. CMs generated from patient-specific induced pluripotent stem cells (iPSCs) have been used as human HCM models of several genetic etiologies as well as for drug screening [34, 40, 42, 66, 67]. Such *in vitro* models may recapitulate several HCM features at the cellular level, including the increase in cell size, aberrant calcium handling, reactivation of the fetal gene programs, and arrhythmia [13, 26, 29, 34, 59].

In this study, we generated and used two different three-dimensional (3D) human cardiac cell models, cardiac bodies (CBs) and bioartificial cardiac tissues (BCTs) to elucidate the molecular and cellular mechanism of RAF1-induced HCM. To this end, two iPSC lines derived from two different individuals carrying the recurrent *RAF1* c.770C>T (p.Ser257Leu) variant and three independent control iPSC lines were used (Fig. 1A). In iPSC-derived cardiomyocytes, we elucidated the effects of heterozygous RAF1^{S257L} on sarcomere structure, contractile behavior, Ca²⁺ handling, and intracellular signaling. Treatment with a MEK inhibitor (PD0325901) rescued the observed HCM phenotype caused by RAF1 GoF, which was validated using a gene-corrected isogenic iPSC line. Importantly, critical structural findings of the *in vitro* models matched the findings of a myocardial biopsy of one of the patients.

Results

Generation of patient-specific iPSCs

To model the RAF1-induced HCM based on patient-derived iPSCs, two NS individuals with severe HCM,

heterozygous for the pathogenic *RAF1* c.770C>T variant (p.Ser257Leu; *RAF1*^{S257L} hereafter), were recruited for this study (Fig. 1A). From both individuals, patient-specific iPSC lines were generated by integration-free methods (Fig. S1 and S2). Reprogramming of fibroblasts to iPSC was performed using a cocktail of transcription factors *OCT3/4*, *SOX2*, *L-MYC*, *TRP53*, and *EBNA-1* as previously described [44]. Furthermore, an isogenic iPSC line from one of these individuals was generated via CRISPR/Cas9 technology (Fig. S2H). In parallel, control iPSC lines from three healthy individuals (iPSC-WT1,2,3) were used and characterized (Fig. S3)[58]. The iPSC-WT and iPSC-*RAF1*^{S257L} lines were positive for different pluripotency markers, including alkaline phosphatase (Fig. S1B and S3B), OCT4, TRA-1-60, and SSEA4 (Fig. S1C, S2A-C and S3C). Sequencing verified the presence of the heterozygous *RAF1* c.770C>T variant in the iPSC-*RAF1*^{S257L} lines (Fig. S1D and S2D), and karyotyping confirmed the stable chromosomal integrity of the iPSC lines (Fig. S1E and S2E). Spontaneous embryoid body (EB) formation and spontaneous undirected differentiation confirmed the tri-lineage differentiation potential of each line (Fig. S1F-G, S2F-G and S3F-G).

Cardiac differentiation of patient-specific iPSCs

Human iPSC lines were differentiated into cardiomyocytes in 3D aggregates by temporal modulation of canonical WNT signaling as described previously [5, 35]. After EB formation (Fig. 1B), differentiation was initiated with GSK3 β -inhibitor CHIR-99021 for 24h followed by WNT pathway inhibitor IWR-1 for 48h (Fig. 1C). Five to seven days after induction of cardiac differentiation, CBs started to contract spontaneously. At d10 of differentiation, metabolic selection was performed by replacing glucose with lactate in the medium, leading to a purified population of CBs taking advantage of the unique metabolic pathways and energy sources characterizing CM (Fig. 1C). Analyses showed that the cells were negative for the presence of pluripotency markers at mRNA and protein levels (data are not shown) and positive for cardiac markers (Figs. 1D,E and S5A). At d40 of differentiation, CBs were more than 96% cTNT-positive and 96% MLC2v-positive, as analyzed by flow cytometry (Fig. 1D). Immunofluorescence of cryosections of CBs revealed homogenous populations of cTNT- and α -actinin-positive cells in the center as well as in the periphery of the CBs (Fig. 1E).

Cardiac hypertrophy is defined as enlargement of the cardiomyocytes. iPSC-derived CMs were tested for their inability to proliferate in response to external stimuli. To this goal, d40 CBs were dissociated, and single CMs were seeded on coverslips. Thereafter, CMs were fixed and assessed for the presence of the mitotic marker phospho-Ser10-histone 3 (p-H3), confirming their negative p-H3 staining at d47 (Fig. 1F). As a positive control, proliferative human iPSCs were

treated for 12 h with 100 nM nocodazole (NC) to be arrested in mitosis (Fig. 1F and S4A,B). Cell cycle analysis indicated that NC-treated human iPSCs were mainly captured at the G₂/M phase and stained positive for p-H3 (Fig. S4B,C). Moreover, dissociated CMs at d40 were treated with 100 μ M L-phenylephrine (PE), an α -adrenergic agonist, for 7 days. These cells remained p-H3 negative, but increased in size (Fig. S4D-F), which is consistent with PE's pro-hypertrophic activity. Collectively, these data indicate that in our experimental system employed iPSC-derived CMs had the ability to increase in size in response to hypertrophic stimuli, but did not undergo proliferation (hyperplasia), providing a suitable *in vitro* model to study the molecular mechanism implicated in *RAF1*-driven HCM.

Signaling events in *RAF1*^{S257L} CBs

Serine²⁵⁷ (S257) is located in close proximity to the negative regulatory phosphorylation site S259 within the conserved region 2 (CR2) of *RAF1* (Fig. 2A). The latter provides a docking site for 14-3-3 proteins, thereby stabilizing *RAF1* in its auto-inhibited state [14, 54]. To determine the impact of the S257L substitution on the S259 phosphorylation status in cells with endogenous expression of the kinase, we immunoprecipitated total *RAF1* protein with an anti-*RAF1* antibody from lysates of undifferentiated iPSCs-WT and iPSCs-*RAF1*^{S257L}(line1). Immunoblot analysis with anti-*RAF1* and anti-p-*RAF1*^{S259} revealed up to 44% reduction in the levels of *RAF1*^{S257L} phosphorylated protein, compared to WT *RAF1* at S259 (Fig. 2B). Therefore, due to the heterozygous status of the mutation in the model system, it can be assumed that the majority of the mutant *RAF1* protein remains unphosphorylated, accounting for almost 50% of total *RAF1*. This observation demonstrates a reduced ability of *RAF1*^{S257L} to be subjected to the 14-3-3 inhibitory control at physiological conditions.

Next, we investigated the activity of selected RAS/*RAF*-dependent signaling in WT and *RAF1*^{S257L} CBs in the presence and absence of the MEK inhibitor PD0325901 (MEKi; Fig. 2C). In untreated CBs, the PI3K-AKT-S6K-mTORC-AKT and *RAF1*-ASK1-JNK signaling axes did not show remarkable differences between *RAF1*^{S257L} and control CBs (Fig. 2D,E). However, increased levels of p-ERK1/2 and p-p38, and decreased levels of p-YAP in *RAF1*^{S257L} CBs were documented. The p-ERK1/2 and p-p38 levels were significantly reduced upon treatment with MEKi, while a significant increase in the level of p-YAP was observed (Fig. 2D,E and S5B,C). Furthermore, we examined the impact of the signaling signature of CRISPR-corrected *RAF1*^{iso} CBs (*RAF1*^{L257S}) vs. its mother clone (*RAF1*^{S257L} CBs) and found the opposing pattern of phosphorylation of the former pathways (Fig. 2F), which highlights the explicit impact of the *RAF1* point mutation at Serine257 on the observed signaling patterns.

Quantitative real-time PCR (qPCR) analysis showed significant upregulation of *NPPB* in $RAF1^{S257L}$ CBs, which was partially reverted in the presence of MEKi (Fig. 2G and S5D). The gene *NPPB* encodes for BNP (brain natriuretic peptide), a well-known clinical biomarker for heart failure and is upregulated during hypertrophy due to a return to a fetal-like gene expression program. Next, we examined the levels of secreted pro-BNP in medium of the cultured CB variants. Interestingly, the results indicated that $RAF1^{S257L}$ CBs secrete more than 12 and 30-fold amounts of BNP in their medium compared to MEKi-treated and isogenic control CBs, respectively (Fig. 2H). Notably, the isogenic control elucidated even lower amount of BNP than MEKi treated cells, which may indicate for activity of the parallel pathways beside $RAF1$ -MAPK in regulation of BNP levels, e.g., p- $RAF1$ -MST2-YAP (Fig. 7).

RAF1^{S257L} alters stretch-shortening of sarcomere

Familial non-syndromic HCM caused by mutations in sarcomeric proteins is known to affect sarcomere architecture [45]. To address the question of whether the sarcomeric architecture is also altered in $RAF1^{S257L}$ -associated HCM, CBs at d40 were dissociated and single CMs were cultured for 7 d on coverslips. $RAF1^{S257L}$ CMs showed less oriented and more disarrayed myofilaments as compared to WT CMs (Fig. 3A), which was confirmed by immunohistochemistry (IHC) and electron microscopy (EM). In particular, $RAF1^{S257L}$ CBs revealed shortened or more contracted I-band regions and thickened Z-line pattern (Fig. 3B). Left ventricular cardiac tissue (CT) was available for one of the NS individuals with $RAF1^{S257L}$, and staining of desmin and cardiac troponin I confirmed a disorganized sarcomeric structure with shortened I-bands, as seen on iPSC-derived CMs and CBs along with a thickened Z-line (Figs. 3C,D). Notably, $RAF1$ was localized and condensed near the sarcomeric structures in $RAF1^{S257L}$ CMs, while in WT CMs $RAF1$ expression was more cytoplasmic (Fig. 3E).

To examine the influence of the dysregulated MAPK signaling on the observed phenotype, we treated the $RAF1^{S257L}$ CBs with PD0325901 (0.2 μ M) at early stages of development (d12) until d40. Remarkably, ultrastructure analysis revealed that MEKi treatment restored the I-band width around the Z-line in the $RAF1^{S257L}$ CBs (Fig. 3F and S5H). To confirm the observed I-band shortening, we prepared cryosections of $RAF1^{S257L}$ and WT BCTs and dissected a part of giant sarcomeric protein titin by immunostaining the PEVK domain of titin to mark the I-band region and α -actinin staining to indicate Z-lines (Fig. 4A). PEVK domains of titin and α -actinin were strikingly colocalized in $RAF1^{S257L}$ BCTs, while clearly separated from each other in WT BCTs (Fig. 4A and B), suggesting a major shortening of the I-band region with dislocation of the titin PEVK region in the $RAF1^{S257L}$ BCTs. Area histograms of the

selected sub-images (Fig. 4B; boxed and magnified) were created to determine the distance between the two PEVK segments and quantify the average distances of more than 50 different Z-lines per sample. These abnormalities of the overlapped peaks corresponding to the two PEVK domains relative to α -actinin were remarkably restored and comparable to WT BCTs when $RAF1^{S257L}$ BCTs were treated with MEKi (Fig. 4C). The significant separation of the distance between the two adjacent PEVK segments upon MEKi treatment strongly suggests a functional normalization of the sarcomeric structures in $RAF1^{S257L}$ BCTs (Fig. 4D). Moreover, by measuring the average distance between α -actinin signals as the Z-line marker, a decrease in the sarcomere lengths was observed for the $RAF1^{S257L}$ BCTs compared to WT BCTs (Fig. 4E). We further determined a significant increase in the mRNA levels of the predominant longer and more compliant (*N2BA*) titin isoform towards the shorter and stiffer isoform (*N2B*) in $RAF1^{S257L}$ BCTs (Fig. 4F).

Collectively, the data demonstrate that $RAF1$ GoF promotes I-band shortening and reduces the flexibility of the spring elements of the titin I-band region.

Aberrant expression of sarcomeric regulatory proteins

The impaired sarcomere organization of $RAF1^{S257L}$ CMs prompted us to quantitatively analyze the expression of key sarcomeric components, including troponins, myosins, and actin-related proteins. In comparison to WT CBs at d24, $RAF1^{S257L}$ CBs strikingly exhibited higher levels of *MYH7* and *MYL2*, but lower levels of *TTN*, *MYH6*, *MYL7*, and α -*SMA* (Fig. 5A). We analyzed the *MYH7*-to-*MYH6* ratio in CBs at two different maturation stages (d24 and d47). Both, immature (d24) and more mature (d47) CBs displayed a significant increase in the *MYH7*-to-*MYH6* ratio (Fig. 5B and S5E). Notably, MEKi treatment partially reversed the *MYH7*-to-*MYH6* ratio in d47, but not d24, $RAF1^{S257L}$ CBs.

Reduced Ca²⁺ transients RAF1^{S257L} CMs

Next, we investigated a possible dysfunctional calcium handling of $RAF1^{S257L}$ CBs, which is a central feature of HCM [34]. We first analyzed the expression of the components that regulate intracellular calcium cycling in WT and $RAF1^{S257L}$ CBs at d24 and d47. These components include ryanodine receptor type-2 (RyR2), sarco/endoplasmic reticulum Ca²⁺-ATPase (SERCA2A), phospholamban (PLN), and the calcium voltage-gated channel α (CACNA) subunits 1C and 1D (L-type calcium channels (LTCCs)). At d24, *PLN*, *SERCA2A*, *RyR*, and *CACNA1C* mRNA expression was downregulated in $RAF1^{S257L}$ CBs (Fig. 5C). Furthermore, *SERCA2A* and *CACNA1D* expression was significantly reduced in $RAF1^{S257L}$ CBs at d47 (Fig. 5C). Remarkably, the decrease of the

SERCA2-to-PLN ratio in RAF1^{S257L} CBs was reversed to WT levels upon MEKi treatment in d47 CBs (Fig. 5D and S5F).

Phosphorylation of PLN at Ser¹⁶ inhibits PLN activity. SERCA2a, PLN, and p-PLN^{Ser16} were reduced in RAF1^{S257L} compared to WT, CBs (Fig. 5E). The SERCA2/active PLN ratio, which was calculated at protein levels by measuring the ratio of SERCA2 to PLN/p-PLN^{Ser16}, was also significantly reduced in RAF1^{S257L} CBs (Fig. 5F). The changes in SERCA2a and PLN expression and the ratio of PLN to p-PLN^{Ser16} were consistent with aberrant calcium handling properties, a characteristic of maladaptive hypertrophy [11, 34]. Therefore, we measured intracellular calcium transients by seeding CMs (d47) on Geltrex-coated coverslips and loaded the cells with the calcium indicator Fura-2. The calcium release was significantly decreased in RAF1^{S257L} CMs as compared to WT CMs (Fig. 5G). Despite reduced transients, the kinetics of cytosolic calcium rise and decrease in RAF1^{S257L} CBs were not different from WT CBs (Fig. 5H and I). Collectively, these data suggest that the RAF1^{S257L} variant modulates the contractile cardiac function by impairing cellular calcium cycling.

Negative impact of RAF1^{S257L} on the contractile apparatus

Next, we analyzed the effect of RAF1^{S257L} on cellular contractility using a multimodal bioreactor system to generate, cultivate, stimulate, and characterize BCTs non-invasively [32]. RAF1^{S257L} BCTs showed a significantly higher spontaneous contraction frequency as compared to WT BCTs, which was significantly reduced by 0.1 and 0.2 μ M MEKi (Fig. 6A). Quantification of cross-sectional areas, which is a measure of myocardial thickening, showed no significant difference between WT and RAF1^{S257L} BCT samples (Fig. 6B). However, RAF1^{S257L} BCTs treated with MEKi had a reduced cross-sectional area. Active force and tension measurements revealed a significantly lower contractile force and contractile tensions for RAF1^{S257L} BCTs compared to WT BCTs (Fig. 6C,D). RAF1^{S257L} BCTs treated with 0.1 μ M MEKi had improved contractile force and re-established contractile tensions (Fig. 6C,D). Moreover, analysis of morphology of contraction peaks revealed a longer time to peak and shorter time to 80% relaxation of RAF1^{S257L} BCTs compared to WT BCTs (Fig. 6E,F). Again, the latter was increased upon MEKi treatment. Notably, BCTs showed a much better rescue response to 0.1 μ M MEKi treatment as compared 0.2 μ M MEKi. In summary, RAF1^{S257L} BCT have higher contraction frequencies, less contractile force and tension, impaired contractile kinetics, and accelerated relaxation kinetics. Most of the observed effects were reversed by application of the MEKi, in a dose dependent manner.

Discussion

The *in vitro* cellular reprogramming, differentiation, and tissue engineering of patient-derived samples reproducibly generated CBs and BCTs as human 3D disease models to investigate the molecular events contributing to HCM in RAF1-related Noonan syndrome. This genetically determined human disorder is caused by aberrantly enhanced function of the RAF1 kinase. We characterized the CBs' and BCTs' cytoskeletal and sarcomeric ultra-structures by super-resolution and EM imaging, to assess their calcium handling and contractility, and intracellular signal transduction. These complementary approaches identified reduced *MYH6* abundance over *MYH7*, elevated expression of *NPPB* and secretion of pro-BNP, decreased *SERCA2/PLN* ratio, sarcomeric fibril disarray, reduced force generation accompanied by a reduced rate of intracellular calcium transients, increased levels of p-ERK1/2, p-p38, and attenuation of p-YAP, as signatures of RAF1^{S257L} CMs. Most remarkably, RAF1^{S257L} CBs and BCTs as well as heart biopsy samples from the RAF1^{S257L} individuals revealed common ultrastructural features, namely shortened I-bands. The alterations in titin and shortened I-bands of RAF1^{S257L} CBs/BCTs were attenuated by treatment with the MEK inhibitor PD0325901. Collectively, our results suggest RAF1^{S257L}-mediated activation of the MAPK pathway produces an abnormal cardiac phenotype involving structural and physiological aspects, that can be in part rescued with MEKi.

RAF1^{S257L} signaling in human cardiomyocytes

CMs with heterozygous RAF1^{S257L} exhibited an approximately 50% reduced inhibitory phosphorylation of RAF1 at S259, which is consistent with previous reports [29, 47, 53]. The best studied RAF1 function is activation of the MEK1/2-ERK1/2 pathway, which regulates the activity of a wide range of signaling molecules in the cytoplasm and nucleus. Accordingly, higher p-ERK1/2 levels were detected in RAF1^{S257L} CMs compared to control CMs, also consistent with previous studies [9, 29] and, p-ERK1/2 levels were remarkably reduced in CBs upon MEKi treatment (Fig. 2D,E and S5B-C). In addition to its crucial role in normal heart development, the MAPK pathway may also act as central signaling node for many factors stimulating adaptive and maladaptive hypertrophy [18, 57]. However, the detailed mechanisms involving aberrant RAF1^{S257L}-MEK1/2-ERK1/2 signal transduction to induce hypertrophy remain unclear. This phenomenon may be rooted in the regulation of cardiac specific-transcription activators or/and direct/indirect transcriptional modulations of cardiac components (Fig. 4F) via ERK1/2 regulation (nuclear substrates) as well as direct modulation of cardiac function by affecting contractile

machinery (cytoplasmic/sarcomeric substrates; Fig. 7). Accordingly, we detected a differential expression of a fetal-like gene program, proteins of the contractile machinery, *MYH7* and, calcium transient regulators, in *RAF1*^{S257L} CBs as compared to WT and MEKi-treated CBs. The observed changes in the expression for these genes likely results from transcriptional activation of the hypertrophic-responsive gene promoters by GATA4, AP1, MEF2, NFAT, and NFκB, as described by previous studies [10, 25, 27]. Future investigations employing chromatin immunoprecipitation of these transcription factors from isolated nuclei of *RAF1*^{S257L} CBs combined with proteomic approaches may clarify the transcriptional regulation by MAPK pathway.

Activated *RAF1* binds to *MST2* (also called *STK3*) and inhibits the *MST1/2-LATS1/2* pathway (Romano et al., 2010; Romano et al., 2014). As a consequence, *YAP* translocates into the nucleus, associates with *TEAD* to serve as a transcriptional co-activator, and regulates transcription of the mitogenic factors, including *CTGF*, *NOTCH2* and *c-MYC* as well as *miR-206*. The *MST1/2-LATS1/2-YAP* axis is critical for heart development, growth, regeneration, and physiology [69]. It regulates proliferation in neonatal heart and growth and survival in adult heart [7, 65, 73]. The *YAP-miR206-FOXPI* axis regulates hypertrophy and survival of CMs through upregulation of fetal genes, e.g., *MYH7* and *NPPB* [68]. We demonstrate here that the reduced inactivating phosphorylation of *YAP* in *RAF1*^{S257L} was restored upon MEKi treatment (Fig. 2D-F), which is likely explained by the enhanced *RAF1*^{S257L} kinase activity along with a switch of *RAF1* binding from *MST1/2* to *MEK1/2* (Fig. 2C) [56]. We also observed increased expression of *YAP* targets, such as *MYH7* and *NPPB* in *RAF1*^{S257L} CBs. Highly elevated levels of the *NPPB* gene product pro-BNP were detected in the supernatant of *RAF1*^{S257L} CBs, considerably above the critical clinical thresholds defined for likelihood of a heart failure state in patients (Fig. 2H) [63]. This validates the observed signaling impact of hyperactive *RAF1*^{S257L} signaling on the fetal gene expression programs, directing the cells towards a heart failure condition. Considerably, we inhibited the MEK-MAPK axis in cardiac cells without targeting *RAF1* directly, therefore we expected that only the MAPK-dependent phenotype is rescued upon MEKi treatment. However, we observed that parallel pathways downstream of *RAF1* is also reverted by MEKi treatments such as *MST2/YAP*.

We propose that MEK inhibition abrogates the negative feedback phosphorylation of *RAF1* by ERK, and thus restores *RAF1* membrane localization and activity [12].

Other MAPKs besides ERK1/2, such as p38, JNK, and ERK5, appear to be involved in cardiac development, function, and also progression of myocardial disease (Jaffre

et al., 2019a; Rose et al., 2010). Our data indicated an increase in p38 phosphorylation, but not JNK, in *RAF1*^{S257L} CBs. Aberrant p38 phosphorylation was reverted to (near) normal upon MEKi treatment. The molecular mechanism that underlies p38 activation *via* *RAF1*^{S257L} in cardiac cells is unclear. We propose that elevated levels of p-p38 in *RAF1*^{S257L} cells may be a compensatory response of cells to reduce the effects of the sustained ERK activity towards an unknown ERK-dependent or ERK-independent positive feedback regulation of p38. One possible mechanism would be the positive regulation of the HDAC class I by ERK1/2, which deacetylates and inhibits the dual-specificity phosphatase 1 (*DUSP1*; Fig. 7). Acetylated *DUSP1* binds with greater affinity to p38, resulting in p38 dephosphorylation. Therefore, the inhibition of *DUSP1* by the ERK1/2-HDAC-*DUSP1* axis could result in accumulation of more p-p38 in mutant cells (Fig. 7). Our results are consistent with this mechanism, because MEKi reduces p-p38 levels possibly by inhibiting the ERK1/2-HDAC axis and increasing acetylated *DUSP1* to target phospho-p38 [17, 21]. Based on previous studies, ERK1/2 was introduced as a negative regulator of p38 *via* inhibition of ASK1-p38 axis (Fig. 2C), however, our data indicate a novel crosstalk between ERK1/2 and p38 in CMs with hyperactive *RAF1*^{S257L}. The precise mechanism of the MAPK crosstalk in cardiac myocytes needs further investigation.

Altered cardiac calcium handling in *RAF1*^{S257L} cardiomyocytes

One characteristic of maladaptive hypertrophy is an abnormal calcium handling that affects myocardial contractility [11, 34]. In the myocardium, calcium-induced calcium release is essential for excitation-contraction coupling [16]. Depolarization of the plasma membrane through action potential results in L-type calcium channels activation (LTCC) and calcium influx. RYR2 is highly sensitive to small changes in calcium concentration and becomes activated upon local calcium influx, which then facilitates the releases of Ca²⁺ from the sarcoplasmic reticulum into the cytosol. Binding of Ca²⁺ to troponin C causes tropomyosin translocation, which exposes actin filaments for binding to myosin heads, cross-bridge formation and triggers contraction (systole). During diastole, Ca²⁺ is transported into the SR by sarcoplasmic reticulum Ca²⁺-ATPase (*SERCA2A*).

At the transcriptional level in *RAF1*^{S257L} CMs, we observed the downregulation of two main regulators of intracellular calcium transients, *SERCA2a* and *LTCC*, as well as changes in the *SERCA2/PLN* ratio. MEKi treatment of *RAF1*^{S257L} CMs restored the *SERCA2/PLN* ratio and significantly downregulated *NPPB* to levels similar to that of WT CMs. This suggests that *SERCA2/PLN* ratio and

NPPB expression may be under direct or indirect transcriptional control of ERK1/2 (Fig. 7). Previous studies have shown that the RAS-MAPK pathway regulates *SERCA2A*, *PLN*, and *LTCC* expression that is downregulated during hypertrophy and heart failure [6, 27, 28]. Consistently, an increase in BNP, which is known as a HCM biomarker, leads to a decrease in *SERCA2A* expression [70].

In addition to the observed transcriptional alterations of calcium regulators, *RAF1*^{S257L} CMs also had reduced intracellular Ca²⁺ transients. The influence of hyperactivation of RAS signaling on expression and regulation of *SERCA2* and *PLN* mediated calcium handling and its role in diastolic dysfunction in HCM has been previously reported in mouse models [72]. A lower *SERCA2/PLN* ratio in *RAF1*^{S257L} CMs may thereby cause a delay in Ca²⁺ re-entry to the SR via inhibition of *SERCA* by *PLN* and thus changes the kinetics of calcium transients and consequently decreases the capacity of cardiac contractility [37]. Therefore, a decreased *SERCA2a/PLN* ratio could be considered as stressor to induce the HCM phenotype [28, 48]. In a similar manner, iPSC-derived CMs with GoF variants in *BRAF* and *MRAS* displayed changes in intracellular Ca²⁺ transient [26, 30]. In contrast, a recent study that compared the idiopathic HCM and *RAF1*^{S257L}-associated HCM has shown that CMs from idiopathic cases, but not *RAF1*^{S257L} CMs, exhibit significant alterations in calcium handling [59].

Sarcomere disorganization in RAF1^{S257L} *cardiomyocytes*

RAF1^{S257L} CMs revealed a disorganized sarcomeric structure (Fig. 3A-D). A remarkable and unprecedented finding in the present study is the atypical I-bands, in both *RAF1*^{S257L} CMs as well as the heart biopsy samples from the corresponding individual with the heterozygous *RAF1*^{S257L} variant. We observed this phenotype in several independent experiments, and it was completely re-established upon MEK inhibition.

Immunohistochemistry of the selected region of I-band, the PEVK domains of titin, and Z-line (α -actinin) indicated that two adjacent PEVK regions in *RAF1*^{S257L} BCTs overlapped (in green) on the Z-line (in red), whereas in WT, the Z-line was clearly surrounded by two distinct and well separated PEVK regions (Fig. 4B). Treatment of BCTs with 0.1 μ M MEKi resolved these abnormalities (Fig. 4B and 4C). The I-band segment of titin acts as a molecular spring that develops tension when sarcomeres are stretched, representing a regulatory node that integrates and perhaps coordinates diverse signaling events [33]. The four-and-a-half LIM domain 1 protein (FHL-1) has been shown to bind to titin at the elastic N2B region and to enhance cardiac MAPK signaling by directly interacting as a scaffold protein with *RAF1*, *MEK2*, and *ERK2* [61]. In our experiments, *FHL1* mRNA expression was up-regulated in *RAF1*^{S257L} CMs (Fig.

S5G). Additionally, we observed that *RAF1* was predominantly localized alongside the sarcomeres in *RAF1*^{S257L} CMs (Fig. 3E). Interestingly, the N2B region of titin has been identified as a substrate of *ERK2*, and phosphorylation by *ERK2* reduces the stiffness of titin [49, 51]. We propose that *RAF1*^{S257L} hyperactivates the *MEK1/2-ERK1/2* pathway, which is most likely localized alongside the sarcomeres, via *FHL1*, and enhances titin phosphorylation at its N2B region. To what extent these events may result in altered sarcomere distensibility and contributes to the cardiac abnormalities observed with *RAF1*^{S257L} remains to be determined (Fig. 7, right side).

RAF1^{S257L} effects on cardiac excitation-contraction coupling

The molecular alterations, structural abnormalities and reduced intracellular Ca²⁺ transients in *RAF1*^{S257L} CMs expectedly affected contractile behavior of cardiac tissue [15]. Physiological analysis of *RAF1*^{S257L} BCTs revealed a 1.3-fold higher beating frequency compared to WT BCTs. Treatment of *RAF1*^{S257L} BCTs with 0.1 and 0.2 μ M MEKi decreased the contraction frequency to 0.8- and 0.7-fold of WT BCTs, respectively. The maximum force generation by *RAF1*^{S257L} BCTs was significantly lower than WT BCTs and inhibiting *RAF-MAPK* pathway by 0.1 μ M MEKi partially restored this value. The *RAF1*^{S257L} BCTs exhibited reduced contractile tension and 0.1 μ M MEKi significantly increased these values to the normal level. Slower contraction might correspond with the reduced Ca²⁺ release shown in Fig. 6F. Furthermore, relaxation would be faster in *RAF1*^{S257L} than in WT BCTs (Fig. 6F) despite unchanged rates of cytosolic calcium elimination (Fig. 5I).

The link between the *RAF1*-MAPK signaling pathway and contractile behavior in the myocardium is unclear. One explanation for the altered contractile behavior of *RAF1*^{S257L} CMs may be the perturbed *MYH6* (α -MYH)-to-*MYH7* (β -MYH) switch due to the aberrantly activated MAPK signaling (Fig. 5B, 7 and S5E). *ERK1/2* is known to phosphorylate the cardiac-specific transcription factor *GATA4* at S105 and enhances its transcriptional DNA-binding activity. *GATA4* is critical for the expression of structural and cardiac hypertrophy response genes, such as *NPPB*, *MYH7*, *TNNI3* (troponin I), and *ACTA1* (α -skeletal Actin) [2, 4, 10, 25, 36]. We assume that cardiac-specific transcription factors mediate upregulation of myosin heavy chain isoforms by *RAF-MAPK*. The ATP hydrolyzing capacity of the two myosin heavy chain paralogs are dissimilar; α -MYH has a 3-fold higher ATPase activity and generates more force than β -MYH, which affects the velocity of myofibril shortening and, consequently, contraction [39]. Reduced *MYH6* levels have also been reported in human heart failure [41]. Therefore, we propose that *RAF1*^{S257L} CMs exhibited higher levels of

MYH7, leading to less absolute force generation and contractile tension. Additionally, *RAF1*^{S257L} BCTs need longer time to reach the peak of contraction (Fig. 6E). β -MYH is known as the slower and α -MYH as the faster paralog [20], therefore, *RAF1*^{S257L} BCTs may need more time to reach the peak of contraction. Alternatively, increased PLN-to-SERCA2 ratio and reduced intracellular calcium transients that may affect intracellular calcium concentrations and cross-bridge cycling kinetics. In addition to the *MYH6*-to-*MYH7* switch, further factors including SERCA2/PLN ratio, titin phosphorylation by ERK1/2, disorganized sarcomeric structures, and changes in length/shape of the flexible I-band region of titin, might also affect force generation and elastic properties of the myocardium. These changes in the spring elements of titin altering its flexibility may influence timing of contraction and relaxation, where *RAF1*^{S257L} BCTs need more time for contraction and less time for relaxation (Fig 6E and F). Cardiac contraction-relaxation processes are multifactorial and complementary analysis are required for more clear-cut conclusions.

Collectively, we demonstrated new aspects of *RAF1* function in human iPSC-derived CMs, which resemble the observed *in vivo* phenotype from the corresponding individuals, especially changes in the ultra-structure of the sarcomeres. The S257L variant in *RAF1* CMs modulates *RAF1*-dependent signaling networking, fetal gene program, contraction, calcium transients, and the sarcomeric structures. Here, we did not assess the behaviors of all known *RAF1* binding partners that may also be critical for cardiac function and contraction, including troponin T, DMPK, ROCK, MYPT, and calcineurin [1, 8, 9, 29, 31, 50, 62, 71]. Therefore, further studies would be supportive to uncover how altered *RAF1* signaling impacts these components. We believe future studies with further advanced models of myocardium will uncover more precisely the physiological output of hypertrophic *RAF1* variant(s).

Materials and methods

Generation, cultivation, and gene-correction of induced pluripotent stem cells

Blood samples and dermal fibroblasts were obtained with the institutional ethics approvals (Justus-Liebig-University Giessen, Germany: AZ258/16, Otto von Guericke University Medical Center Magdeburg: 173/14; University Medical Center Göttingen: 10/9/15) and under informed consent of the parents from two unrelated individuals with Noonan syndrome carrying the heterozygous substitution c.770C>T in exon 7 of *RAF1*.

Primary cells were reprogrammed using either episomal reprogramming vectors Epi5TM [44] (Thermo Scientific #15960) or Sendai virus system Cytotune 2.0 (Thermo

Scientific #A16517). Resulting iPSCs were clonally picked and expanded in mTESR (Stemcell Technologies) or StemMACS iPS-Brew (Miltenyi Biotech) to UMGi164-A clone 1 (7B10, here referred to as *RAF1*^{S257L} line 1) from patient 1 and UMGi102-A clone 17 (isRASb1.17, here referred to as *RAF1*^{S257L} line 2) from patient 2, respectively, and passaged using Versene (STEMCELL Technologies) at a ratio of 1:3 to 1:6, depending on cell density. Prior to their utilization for experiments, clonal iPSCs were subjected to detailed characterization including Sanger sequencing to confirm the presence of the variant, iPSC morphology, assessment of expression of pluripotency markers by RT-PCR, immunofluorescence staining and flow cytometry, and chromosomal integrity. Furthermore, elimination of persisting reprogramming factors was confirmed by PCR and RT-PCR, respectively. Three unrelated wild-type (WT) iPSC lines, UMGi163-A clone 1 (ipWT16.1, here referred to as WT1) [22], UMGi014-C clone 14 (isWT1.14, here referred to as WT2) and UMGi020-B clone 22 (isWT7.22, here referred to as WT3) [58]. A CRISPR-corrected isogenic iPSC line was used as control. Genetic correction of the *RAF1*^{S257L} variant (c.770 C>T, heterozygous) in the iPSCs from patient 2 was performed using ribonucleoprotein (RNP)-based CRISPR/Cas9 by targeting exon 7 of the *RAF1* gene, as previously described [24]. The guide RNA target sequence was (PAM in bold): 5'-TGGATGTCAACCTCTGCCTC **TGG** -3'. For homology-directed repair, a single-stranded oligonucleotide with 45-bp homology arms was used. After picking clones, successful gene-editing was identified by Sanger sequencing and the CRISPR-corrected isogenic cell line UMGi102-A-1 clone 9 (isRASb1-corr.9) underwent the same detailed characterization as mentioned above.

Human iPSC culture

Before initiation of cardiomyogenic differentiation, undifferentiated iPSCs were cultured as feeder-free monolayers for up to 15 passages in murine embryonic feeder cell-conditioned medium (CCM⁺) consisting of DMEM F12+Glutamax, 15% Knock-out Serum Replacement, 1% non-essential amino acids (all Gibco), 100 μ M β -mercaptoethanol (Sigma), and 100 ng/mL bFGF (PeproTech; CCM⁺/100). Cells were passaged every three to four days by dissociation with Accutase and seeded onto Geltrex-coated (0.5%, Life Technologies) plasticware at a density of 5×10^4 cells per cm² in CCM⁺, containing the ROCK inhibitor Y-27632 (10 μ M, Selleckchem, #S1049). The ROCK inhibitor was eliminated from the CCM⁺ on the following days.

Tri-lineage differentiation of human iPSCs

To induce differentiation of human iPSCs into all three germ layers, human iPSC-colonies were detached from feeder layers using 0.4% (w/v) type IV collagenase and resuspended in differentiation medium consisting of IMDM + GlutaMAX supplemented with 20% (v/v) fetal calf serum, 1 mL L-Glutamine, 0.1 mM 2-mercaptoethanol, and 1% non-essential amino acid stock (all Thermo Scientific). Colonies were maintained for 7 days in suspension culture on 1% (w/v) agarose/IMDM coated 12-well plates to form 3D embryoid bodies (EBs). Subsequently, about 15-20 EBs were plated on 6-well plates coated with 0.1% (w/v) gelatine. After 24 days, EBs were harvested for qRT-PCR and replated for immunofluorescence (IF) analyses, respectively.

Karyotype analysis

After treatment of undifferentiated human iPSCs with a final concentration of 0.1 µg/mL Colcemid (Thermo Scientific) for 2 h, cells were detached with trypsin/EDTA (0.05/0.02%, Biochrom). After centrifugation, the pellet was resuspended in hypotonic solution (0.32% KCl with 0.2% (v/v) fetal calf serum) and incubated for 15 min at 37 °C. Cells were fixed in ice-cold methanol/acetic acid (3:1). G-banding was performed according to Seabright protocol [60]. Karyograms were imaged using the IKAROS software of MetaSystems (Altlufheim, Germany). The chromosome arrangement was investigated as previously described [23].

Cardiac differentiation of human iPSCs

Cardiac differentiation was performed in 3D suspension culture after aggregate formation in agarose microwells modified from established protocol [5, 35]. For differentiation in 3D suspension culture, agarose microwells (AMW) were generated from AggreWellTM400Ex plates (Stem Cell Technologies, #27840) containing 4700 microslots per AMW in a 6-well format [5]. For each AMW, 5x10⁶ undifferentiated human iPSCs were seeded in 3 mL CCM+/100 supplemented with 10 µM ROCK inhibitor Y-27632 (Selleckchem, #S1049). iPSCs formed uniform EBs during the initial 24 h on AMW, and were harvested and transferred to suspension culture in 15-cm dishes and placed on an orbital shaker at 60 rpm. Suspension EBs were cultivated for further 3 days in CCM+/100 before the start of cardiac differentiation. Differentiation was induced with the exchange of medium to RPMI 1640 supplemented with 1% (v/v) B27 without insulin (RB⁻, Thermo Scientific, #A18956-01). The GSK-3 inhibitor CHIR99021 (Selleckchem, #S1263) was added at 4 - 6 µM (depending on the iPSC line) for the first 24 h of differentiation, thereafter differentiations were kept in RB⁻ without small molecule inhibitors until day 3 (d3) before the WNT inhibitor IWR-1 (4 µM, Sigma,

#I0161) was added for 48 h. The first contracting EBs were observed between d5 and d7. From d7-d10, EBs were cultivated with RPMI 1640 supplemented with 1% (v/v) B27 with insulin (RB⁺, Thermo Scientific, #17504-044). Afterwards, a metabolic selection was performed for 10d (until d20) to eliminate all non-CM in RPMI minus glucose (Thermo Scientific, #11879-020) supplemented with human albumin (Sigma, #A0237), sodium DL-lactate (Sigma, #L4263), and L-ascorbic acid-2-phosphate (Sigma, #A8960) [64]. From d20 - d40, CBs were kept in RB⁺ medium. Depending on the experimental design, inhibition of MEK was started on d12 of differentiation by supplementing the medium with 0.1 and 0.2 µM PD0325901 (Sigma, #PZ0162). Medium was exchanged every two days until d20. Flow cytometric assessment of CM content was done on d20 by staining against cardiac troponin T (Life technologies) after dissociation of aggregates with Stemdiff CM dissociation kit (STEMCELL Technologies) following the manufacturer's protocol after adding Accutase to the enzyme mix (1:2). Aggregates with a purity of >95% were termed cardiac bodies (CBs) and further cultivated.

Bioartificial cardiac tissue (BCT) preparation, culture, and measurements

On day 21, non-MEK-inhibited CBs were dissociated as described above and a previously described protocol to generate myocardial tissue was employed [32]. In brief, a mixture of rat tail collagen type I (Cultrex) and Matrigel™ (Life Technologies) was mixed with CMs and gamma-irradiated human foreskin fibroblasts (HFFs) and poured into silicone molds (5x5x10 mm, w/d/h) with two horizontal titanium rods that serve as suspensions for the developing tissue at a distance of 6 mm. Resulting BCTs with a volume of 250 µL each containing 10⁶ CMs, 10⁵ HFFs, collagen type I (230 µg), and 10% Matrigel. BCTs were stretched by 200 µm every fourth day to support tissue maturation, and tissue development was documented by daily microscopic observation. Beating frequencies, active contraction, and passive forces were determined in a custom-made bioreactor system at 200 µm increments until the maximum contraction force was reached (L_{max}). Contractile and passive tension was calculated by dividing the force by the cross-sectional area of each BCT (mN/mm²).

Reverse transcriptase polymerase chain reaction

Cells were lysed using TRIzol™ (Ambion, Thermo Scientific, Germany) and total RNA was extracted via phenol-chloroform extraction. Remaining genomic DNA contaminations were removed using the DNA-free™ DNA Removal Kit (Ambion, Thermo Scientific, Germany).

DNase-treated RNA was transcribed into complementary DNA (cDNA) using the ImProm-II™ reverse transcription system and oligo-dT as primer (Promega, Germany). Quantitative real-time reverse transcriptase polymerase chain reaction (qPCR) was performed using SYBR Green (Thermo Scientific, #4309155 Germany). Primer sequences are listed in Supplementary Table S1. The $2^{-\Delta\Delta Ct}$ method was employed for estimating the relative mRNA expression levels and $2^{-\Delta Ct}$ for mRNA levels. Among six different housekeeping genes that we tested, *HPRT1* showed the lowest variation among different cell lines and conditions. Therefore, *HPRT1* was used for normalization in our qPCR analysis.

Flow cytometry

For flow cytometric analysis, single-cell suspensions of undifferentiated human iPSCs were obtained with Accutase and cells were washed with ice-cold phosphate-buffered saline (PBS)⁺. CBs were dissociated into single cells by incubation with Versene (EDTA-Solution, Thermo Scientific, #15040066) for 10 min in a Thermomixer at 37°C. Thereafter, TrypLE (Thermo Scientific, #A1285901) was added and samples were incubated for additional 10 min at 37 °C and 1200 rpm until the cellular aggregates have dissolved. Both cell types were fixed in 4% formaldehyde (Carl Roth, #P087.1) for 10 min on ice and permeabilized with 90% ice-cold methanol for 20 min followed by a blocking step with 1.5% BSA and 2.5% goat or donkey serum diluted in PBS for 1 h, at 4 °C. Cells were then stained with primary antibodies.

Immunoblotting

To extract the total protein, CBs were washed with PBS⁺ prior to cell lysis (lysis buffer: 50 mM Tris-HCl pH 7.5; 100 mM NaCl, 2 mM MgCl₂; 1% Triton X100; 10% glycerol; 20 mM beta-glycerol phosphate; 1 mM orthoNa₃VO₄; and EDTA-free protease inhibitor (Roche, Germany, #11873580001)). To further disrupt the cellular aggregates, a sonicator with 70% power was used prior to incubation in a rotor at 4 °C for 30 min. Protein concentrations were determined using the Bradford assay (Bio-Rad, #5000201). Equal amounts of cell lysates (10 - 50 µg) were subjected to sodium dodecyl sulfate polyacrylamide gel electrophoresis (SDS-PAGE). Following electrophoresis, proteins were transferred to a nitrocellulose membrane by electroblotting and probed with primary antibodies overnight at 4°C. All antibodies were diluted in Intercept® (TBS) Blocking Buffer (LI-COR #927-60001) mixed in a 1:3 ratio with Tris-buffered saline containing 0.02% Tween 20. The antibodies from Santa Cruz were diluted 1:200 while the remaining antibodies were diluted 1:1000 (see Table S2). Immunoblots

were developed with LI-COR Odyssey FX (LI-COR) and quantification of signals was performed by densitometry of scanned signals with the aid of Image Studio (version 5.2, LI-COR).

Immunocytochemistry

Immunostaining was performed as described previously [43]. The procedure for the single-cell suspensions of CBs was described in the flow cytometry section. Briefly, cells were washed twice with ice-cold PBS containing magnesium/calcium and fixed with 4% formaldehyde (Carl Roth, #P087.1) for 20 min at room temperature. To permeabilize cell membranes, cells were incubated in 0.25% Triton X-100/PBS for 5 min. Blocking was performed with 3% bovine serum albumin (Thermo Scientific, # 26140079) and 2% goat serum diluted in PBS containing 0.25% Triton X-100 for 1 h at room temperature. Incubation with primary antibodies was performed overnight. Cells were washed three times for 10 min with PBS and incubated with secondary antibodies for 2 h at room temperature. Slides were washed three times and ProLong® Gold Antifade mounting reagent containing DAPI (4',6-diamidino-2-phenylindole) (Thermo Scientific, #P10144) was applied to mount the coverslips.

Immunohistochemistry

From formalin fixed tissue, 3 µm sections were stained with H&E and Masson trichrome (Trichrome II Blue staining kit at Nexus special stainer; Roche). Immunohistochemical analysis was performed on cryosections and paraffin sections using a Bench Mark XT automatic staining platform (Ventana, Heidelberg, Germany) with the primary antibodies. The sections were examined using a Nikon Eclipse 80i equipped with a DS-Fi1 camera.

A myectomy was performed on the patient one with RAF mutation at the age of 5 years. After formalin-fixation of the surgically removed tissue, 3µm sections were stained with hematoxylin and eosin. Immunohistochemical analysis was performed on cryosections and paraffin sections using a Bench Mark XT automatic staining platform (Ventana, Heidelberg, Germany), using the primary antibodies listed in the supplementary table S2. The sections were examined using a Nikon Eclipse 80i equipped with a DS-Fi1 camera.

Immunohistochemistry of BCT samples was carried out using BCTs embedded and snap-frozen in Tissue-Tek® OCT resin (Sakura Finetek, #4583). The cryo-blocks were sliced into 8µm thick sections. Sections were fixed in 4% paraformaldehyde (Carl Roth, #P087.1) in 0.1 mol/L sodium phosphate buffer pH 7.4 for 10 min. Washing was performed in PBS and 0.2% saponin/PBS. After blocking with 10% normal goat serum (NGS) in 0.2% saponin/PBS for 1 h,

primary antibodies were incubated over night at 4°C. Secondary antibodies were incubated for 3 h at room temperature in the dark. The sections were mounted with ProLong® Gold Antifade Mountant, containing ProLDAPI (#P-36935, Invitrogen). Slides were analyzed with a ZEISS Airyscan LSM 880 confocal microscope (Center for Advanced Imaging, Heinrich Heine University, Düsseldorf, Germany). Pictures were taken with 63x objective and analyzed using ZEN 3.2 (blue edition) by Carl Zeiss AG.

Immunoprecipitation

For immunoprecipitation of RAF1, beads were initially incubated with an anti-RAF1 antibody and a non-specific anti-IgG for the negative control, respectively, and washed afterwards five times with immunoprecipitation buffer (20 mM Tris/HCl pH 7.4, 150 mM NaCl, 5 mM MgCl₂, 10 mM β-glycerophosphate, 0.5 mM Na₃VO₄, 10% glycerol, and EDTA-free protease inhibitor). Afterwards, iPSCs cells were lysed in lysis buffer (immunoprecipitation buffer with 0.5% NP-40) by 30 min rotation in a reaction tube at 4°C. Immunoprecipitation from total cell lysates was carried out for 1 h, at 4°C. Beads were washed five times with immunoprecipitation buffer, and eluted proteins were heated in SDS/Laemmli sample buffer at 95°C for 10 min before subjected to immunoblotting.

Analysis of cardiomyocyte cell surface

Analysis of CM cell surface was conducted using a Java-based open-source image processing software ImageJ. Software pixel length was calibrated to the μm scale bar on the used confocal images. After background elimination, the Region of Interest-tool (ROI) was used to mark the borders of single cells. For each condition, multiple confocal images were evaluated in order to evaluate a sufficient number of images. Finally, the cell area was extracted and compared between the conditions.

Transmission electron microscopy (TEM)

Small cardiac tissue samples were fixed with 6% glutaraldehyde/0.4 M phosphate buffered saline (PBS) and processed with a Leica EM TP tissue processor. Cardiac bodies were fixed with 3% glutaraldehyde/0.1 M Cacodylate buffer. The cell pellets were processed by hand according to the automated tissue processor. For electron microscopy of the small cardiac tissue samples, ultrathin sections were contrasted with 3% lead citrate trihydrate with a Leica EM AC20 (Ultrastain kit II) and were examined using a ZEISS EM 109 transmission electron microscope equipped with a

Slowscan-2K-CCD-digital camera (2K-wide-angle Sharp: eye), while CBs were imaged using a Hitachi H-7100.

Measurement of Ca²⁺ cycling in cardiac bodies

iPSC-derived CBs were dissociated and grown on gelatin coated cover slips for up to 7 d before loading with the fluorescent Ca²⁺ indicator Fura-2 by adding 1 μg Fura-2-AM/mL cell medium. After a 15 min incubation at 37°C, cells were washed in pre-warmed medium (37°C). A dual excitation (340 nm and 380 nm) fluorescence imaging recording system was used to measure Ca²⁺ transients of paced (0.5 Hz) and spontaneously beating cells (HyperSwitch Myocyte System, IonOptix Corp., Milton, MA, USA). Data were acquired as the ratio of measurements at 340 and 380 nm and analyzed using IonWizard software (Version 6.4, Ion Optix Corp).

Acknowledgements

We are grateful to Dr. Ehsan Amin and Prof. Dr. Thomas Wieland for helpful advices, and stimulating discussions. We are grateful to the CFEM (Core Facility Electron Microscopy) of the medical faculty of the Heinrich Heine University Düsseldorf. We gratefully thank the entire team from the Stem Cell Unit, University Medical Center Göttingen, for excellent technical assistance in iPSC generation and characterization. The authors thank Louisa Habich, Sarah Nourmohammadi, Hannah Schlierbach, David Skvorc, Marion Möckel and Kerstin Leib for excellent technical assistance in iPSC differentiation, CM selection and BCT production. We thank and give credit to “BioRender.com” which was used for design and creation of Fig. 1A.

Ethical Approval and Consent to participate

Blood samples and dermal fibroblasts were obtained by skin biopsy from two unrelated female patients with Noonan syndrome carrying the heterozygous substitution c.770C>T in exon 7 of RAF1 under protocols concerning research with biomaterials approved by the institution’s ethics committees (Justus-Liebig-University Giessen, Germany: AZ258/16 ; Otto von Guericke University Medical Center Magdeburg: 173/14; University Medical Center Göttingen: 10/9/15). Research with biomaterials was approved by the ethical committee of the Justus Liebig University of Giessen. Written informed consent was given by both parents of both individuals. One human iPSC line that was used in this study as a control, was generated from the human foreskin fibroblast-1 (HFF-1) cell line (ATCC).

Funding

This study was supported by the German Federal Ministry of Education and Research (BMBF) – German Network of RASopathy Research (GeNeRARE, grant numbers: 01GM1902A, 01GM1902C, 01GM1902D, 01GM1902F); the German Center for Cardiovascular Research (DZHK); the European Network on Noonan Syndrome and Related Disorders (EJP-RD; NSEuroNet, grant numbers: 01GM1921A, 01GM1921B); Deutsche Gesellschaft für Muskelkranke (DGM) e.V. (Sc22/11); German Research Foundation (DFG); grant numbers AH 92/8-1 to MRA, Ci216/2-1 to ICC, SFB 974, P3 to MRA and B9 to AR, SFB1002 S01 to LC, SFB1116-1/2 TPA02 to MK and JS, and(IRTG 1902 P6 to MRA.

Authors' contributions

Conception, design, and writing: MRA, SNR and FB

Development of methodology: SNR, FB, MB, JD, FH, MK, AB, RA, GK, LC

Acquisition of data, analysis and interpretation of data: SNR, FB, AVB, MB, FH, JD, FF, SK, AB, AVK, ASR, AS, MT, GK

Administrative, technical, or material support: MRA, GK, MZ, MK, AG, MJW, AS, ASR, AH, RPP, JS, LC

Study supervision and coordination: MRA, GK, SNR and MZ

Abbreviations

AC, adenylyl cyclase; ACTN1, actinin alpha 1; APF, alpha fetoprotein; α -SMA, alpha smooth muscle actin; BNP, brain natriuretic peptide; CACNA1C, calcium voltage-gated channel subunit alpha1 C; CB, cardiac body; CT, cardiac tissue; CM, cardiomyocytes; cTNT, cardiac troponin T; DUSP1, dual-specificity phosphatase; EB, embryoid body; EBNA1, Epstein-Barr nuclear antigen 1; EM, electron microscopy; ERK, extracellular regulated kinase; FOXO2, forkhead box A2; GSK3 β , glycogen synthase kinase 3 beta; HCM, hypertrophic cardiomyopathy; HDAC, histone deacetylase; HPRT1, hypoxanthine-guanine phosphoribosyltransferase; LTCC, L-type calcium channels; MAPK, mitogen-activated protein kinase; MEF2, myocyte enhancer factor 2; MEK, MAP/ERK kinase; MEKi, MAP/ERK kinase inhibitor; MYH, myosin heavy chain; MYL, myosin light chain 7; iPSC, induced pluripotent stem cells; NFAT, nuclear factor of activated T-cells; NC, nocodazole; NKX2.5, NK2 homeobox 5; NPPB, natriuretic

peptide B; NS, Noonan syndrome; OCT-4, octamer-binding transcription factor 4; PE, phenylephrine; p-H3, phospho-histone 3; PLN, phospholamban; RAF, rapidly accelerated fibrosarcoma; RT-PCR, reverse transcriptase polymerase chain; RyR2, ryanodine receptor type-2; SERCA2A, sarco/endoplasmic reticulum Ca²⁺-ATPase; SOX2, SRY-box transcription factor 2; TNNC1, troponin C1; TNNI3, troponin I3, cardiac type; TRP53, transformation related protein 53; TUBB3, tubulin beta 3 class III, WT, wild-type.

References

1. Broustas CG, Grammatikakis N, Eto M, Dent P, Brautigan DL, Kasid U (2001) Phosphorylation of the Myosin-binding Subunit of Myosin Phosphatase by Raf-1 and Inhibition of Phosphatase Activity. *J Biol Chem* 277:3053-3059 doi:10.1074/jbc.M106343200
2. Bueno OF, De Windt LJ, Tymitz KM, Witt SA, Kimball TR, Klevitsky R, Hewett TE, Jones SP, Lefer DJ, Peng CF, Kitsis RN, Molkentin JD (2000) The MEK1-ERK1/2 signaling pathway promotes compensated cardiac hypertrophy in transgenic mice. *EMBO J* 19:6341-50 doi:10.1093/emboj/19.23.6341
3. Calcagni G, Adorisio R, Martinelli S, Grutter G, Baban A, Versacci P, Digilio MC, Drago F, Gelb BD, Tartaglia M, Marino B (2018) Clinical Presentation and Natural History of Hypertrophic Cardiomyopathy in RASopathies. *Heart Fail Clin* 14:225-235 doi:10.1016/j.hfc.2017.12.005
4. Charron F, Paradis P, Bronchain O, Nemer G, Nemer M (1999) Cooperative interaction between GATA-4 and GATA-6 regulates myocardial gene expression. *Mol Cell Biol* 19:4355-65 doi:10.1128/mcb.19.6.4355
5. Dahlmann J, Kensah G, Kempf H, Skvorc D, Gawol A, Elliott DA, Dräger G, Zweigert R, Martin U, Gruh I (2013) The use of agarose microwells for scalable embryoid body formation and cardiac differentiation of human and murine pluripotent stem cells. *Biomaterials* 34:2463-71 doi:10.1016/j.biomaterials.2012.12.024
6. Daub M, Jockel J, Quack T, Weber CK, Schmitz F, Rapp UR, Wittinghofer A, Block C (1998) The RafC1 cysteine-rich domain contains multiple distinct regulatory epitopes which control Ras-dependent Raf activation. *Mol Cell Biol* 18:6698-710 doi:10.1128/mcb.18.11.6698
7. Del Re DP, Yang Y, Nakano N, Cho J, Zhai P, Yamamoto T, Zhang N, Yabuta N, Nojima H, Pan D, Sadoshima J (2012) Yes-associated Protein Isoform 1 (Yap1) Promotes Cardiomyocyte Survival and Growth to Protect against Myocardial Ischemic Injury. *J Biol Chem* 288:3977-3988 doi:10.1074/jbc.M112.436311
8. Desideri E, Cavallo AL, Baccarini M (2015) Alike but Different: RAF Paralogs and Their Signaling Outputs. *Cell* 161:967-970 doi:10.1016/j.cell.2015.04.045
9. Dhandapani PS, Fabris F, Tonk R, Illaste A, Karakikes I, Sorourian M, Sheng J, Hajjar RJ, Tartaglia M, Sobie EA, Lebeche D, Gelb BD (2011) Cyclosporine attenuates cardiomyocyte hypertrophy induced by RAF1 mutants in Noonan and LEOPARD syndromes. *J Mol Cell Cardiol* 51:4-15 doi:10.1016/j.yjmcc.2011.03.001
10. Dirks E, da Costa Martins PA, De Windt LJ (2013) Regulation of fetal gene expression in heart failure. *Biochim Biophys Acta* 1832:2414-24 doi:10.1016/j.bbdis.2013.07.023
11. Dorn GW, 2nd, Force T (2005) Protein kinase cascades in the regulation of cardiac hypertrophy. *J Clin Invest* 115:527-37 doi:10.1172/jci24178

12. Dougherty MK, Müller J, Ritt DA, Zhou M, Zhou XZ, Copeland TD, Conrads TP, Veenstra TD, Lu KP, Morrison DK (2005) Regulation of Raf-1 by direct feedback phosphorylation. *Mol Cell* 17:215-24 doi:10.1016/j.molcel.2004.11.055
13. Doyle MJ, Lohr JL, Chapman CS, Koyano-Nakagawa N, Garry MG, Garry DJ (2015) Human Induced Pluripotent Stem Cell-Derived Cardiomyocytes as a Model for Heart Development and Congenital Heart Disease. *Stem Cell Rev* 11:710-27 doi:10.1007/s12015-015-9596-6
14. Dumaz N, Marais R (2003) Protein kinase A blocks Raf-1 activity by stimulating 14-3-3 binding and blocking Raf-1 interaction with Ras. *J Biol Chem* 278:29819-29823 doi:10.1074/jbc.C300182200
15. Eisner DA, Caldwell JL, Kistamas K, Trafford AW (2017) Calcium and Excitation-Contraction Coupling in the Heart. *Circ Res* 121:181-195 doi:10.1161/circresaha.117.310230
16. Fabiato A (1983) Calcium-induced release of calcium from the cardiac sarcoplasmic reticulum. *Am J Physiol* 245:C1-14 doi:10.1152/ajpcell.1983.245.1.C1
17. Ferguson BS, Harrison BC, Jeong MY, Reid BG, Wempe MF, Wagner FF, Holson EB, McKinsey TA (2013) Signal-dependent repression of DUSP5 by class I HDACs controls nuclear ERK activity and cardiomyocyte hypertrophy. *Proc Natl Acad Sci U S A* 110:9806-11 doi:10.1073/pnas.1301509110
18. Gallo S, Vitacolonna A, Bonzano A, Comoglio P, Crepaldi T (2019) ERK: A Key Player in the Pathophysiology of Cardiac Hypertrophy. *Int J Mol Sci* 20 doi:10.3390/ijms20092164
19. Gelb BD, Roberts AE, Tartaglia M (2015) Cardiomyopathies in Noonan syndrome and the other RASopathies. *Prog Pediatr Cardiol* 39:13-19 doi:10.1016/j.ppedcard.2015.01.002
20. Gupta MP (2007) Factors controlling cardiac myosin-isoform shift during hypertrophy and heart failure. *J Mol Cell Cardiol* 43:388-403 doi:10.1016/j.yjmcc.2007.07.045
21. Habibi J, Ferguson BS (2018) The Crosstalk between Acetylation and Phosphorylation: Emerging New Roles for HDAC Inhibitors in the Heart. *Int J Mol Sci* 20 doi:10.3390/ijms20010102
22. Haghighi F, Dahlmann J, Nakhaei-Rad S, Lang A, Kutschka I, Zenker M, Kensah G, Piekorz RP, Ahmadian MR (2018) bFGF-mediated pluripotency maintenance in human induced pluripotent stem cells is associated with NRAS-MAPK signaling. *Cell Commun Signal* 16:96 doi:10.1186/s12964-018-0307-1
23. Hamta A, Adamovic T, Samuelson E, Helou K, Behboudi A, Levant G (2006) Chromosome ideograms of the laboratory rat (*Rattus norvegicus*) based on high-resolution banding, and anchoring of the cytogenetic map to the DNA sequence by FISH in sample chromosomes. *Cytogenet Genome Res* 115:158-68 doi:10.1159/000095237
24. Hanses U, Kleinsorge M, Roos L, Yigit G, Li Y, Barbarics B, El-Battrawy I, Lan H, Tiburcy M, Hindmarsh R (2020) Intronic CRISPR Repair in a Preclinical Model of Noonan Syndrome-Associated Cardiomyopathy. *Circulation* 142:1059-1076 doi:10.1161/CIRCULATIONAHA.119.044794
25. He A, Kong SW, Ma Q, Pu WT (2011) Co-occupancy by multiple cardiac transcription factors identifies transcriptional enhancers active in heart. *Proc Natl Acad Sci U S A* 108:5632-7 doi:10.1073/pnas.1016959108
26. Higgins EM, Bos JM, Dotzler SM, Kim CJ, Ackerman MJ (2019) MRAS Variants Cause Cardiomyocyte Hypertrophy in Patient-Specific iPSC-Derived Cardiomyocytes: Additional Evidence for MRAS as a Definitive Noonan Syndrome-Susceptibility Gene. *Circ Genom Precis Med* doi:10.1161/circgen.119.002648
27. Ho PD, Fan JS, Hayes NL, Saada N, Palade PT, Glembofski CC, McDonough PM (2001) Ras reduces L-type calcium channel current in cardiac myocytes. Corrective effects of L-channels and SERCA2 on [Ca(2+)](i) regulation and cell morphology. *Circ Res* 88:63-9 doi:10.1161/01.res.88.1.63
28. Huang H, Joseph LC, Gurin MI, Thorp EB, Morrow JP (2014) Extracellular signal-regulated kinase activation during cardiac hypertrophy reduces sarcoplasmic/endoplasmic reticulum calcium ATPase 2 (SERCA2) transcription. *J Mol Cell Cardiol* 75:58-63 doi:10.1016/j.yjmcc.2014.06.018
29. Jaffre F, Miller CL, Schanzer A, Evans T, Roberts AE, Hahn A, Kontaridis MI (2019) Inducible Pluripotent Stem Cell-Derived Cardiomyocytes Reveal Aberrant Extracellular Regulated Kinase 5 and Mitogen-Activated Protein Kinase Kinase 1/2 Signaling Concomitantly Promote Hypertrophic Cardiomyopathy in RAF1-Associated Noonan Syndrome. *Circulation* 140:207-224 doi:10.1161/circulationaha.118.037227
30. Josowitz R, Mulero-Navarro S, Rodriguez NA, Falce C, Cohen N, Ullian EM, Weiss LA, Rauen KA, Sobie EA, Gelb BD (2016) Autonomous and Non-autonomous Defects Underlie Hypertrophic Cardiomyopathy in BRAF-Mutant hiPSC-Derived Cardiomyocytes. *Stem Cell Reports* 7:355-369 doi:10.1016/j.stemcr.2016.07.018
31. Kaliman P, Llagostera E (2008) Myotonic dystrophy protein kinase (DMPK) and its role in the pathogenesis of myotonic dystrophy 1. *Cell Signal* 20:1935-1941 doi:10.1016/j.cellsig.2008.05.005
32. Kensah G, Roa Lara A, Dahlmann J, Zweigerdt R, Schwanke K, Hegermann J, Skvorc D, Gawol A, Azizian A, Wagner S, Maier LS, Krause A, Dräger G, Ochs M, Haverich A, Gruh I, Martin U (2013) Murine and human pluripotent stem cell-derived cardiac bodies form contractile myocardial tissue in vitro. *Eur Heart J* 34:1134-46 doi:10.1093/eurheartj/ehs349
33. Krüger M, Linke WA (2011) The Giant Protein Titin: A Regulatory Node That Integrates Myocyte Signaling Pathways. *J Biol Chem* 286:9905-9912 doi:10.1074/jbc.R110.173260
34. Lan F, Lee AS, Liang P, Sanchez-Freire V, Nguyen PK, Wang L, Han L, Yen M, Wang Y, Sun N, Abilez OJ, Hu S, Ebert AD, Navarrete EG, Simmons CS, Wheeler M, Pruitt B, Lewis R, Yamaguchi Y, Ashley EA, Bers DM, Robbins RC, Longaker MT, Wu JC (2013) Abnormal calcium handling properties underlie familial hypertrophic cardiomyopathy pathology in patient-specific induced pluripotent stem cells. *Cell Stem Cell* 12:101-13 doi:10.1016/j.stem.2012.10.010
35. Lian X, Zhang J, Azarin SM, Zhu K, Hazeltine LB, Bao X, Hsiao C, Kamp TJ, Palecek SP (2013) Directed cardiomyocyte differentiation from human pluripotent stem cells by modulating Wnt/beta-catenin signaling under fully defined conditions. *Nat Protoc* 8:162-75 doi:10.1038/nprot.2012.150
36. Liu YL, Huang CC, Chang CC, Chou CY, Lin SY, Wang IK, Hsieh DJ, Jong GP, Huang CY, Wang CM (2015) Hyperphosphate-Induced Myocardial Hypertrophy through the GATA-4/NFAT-3 Signaling Pathway Is Attenuated by ERK Inhibitor Treatment. *Cardiorenal Med* 5:79-88 doi:10.1159/000371454
37. MacLennan DH, Kranias EG (2003) Phospholamban: a crucial regulator of cardiac contractility. *Nat Rev Mol Cell Biol* 4:566-77 doi:10.1038/nrm1151
38. Maron BJ, Maron MS (2013) Hypertrophic cardiomyopathy. *The Lancet* 381:242-255 doi:10.1016/s0140-6736(12)60397-3
39. Miyata S, Minobe W, Bristow MR, Leinwand LA (2000) Myosin heavy chain isoform expression in the failing and nonfailing human heart. *Circ Res* 86:386-90 doi:10.1161/01.res.86.4.386
40. Mosqueira D, Mannhardt I, Bhagwan JR, Lis-Slimak K, Katili P, Scott E, Hassan M, Prondzynski M, Harmer SC, Tinker A, Smith JGW, Carrier L, Williams PM, Gaffney D, Eschenhagen T, Hansen A, Denning C (2018) CRISPR/Cas9 editing in human pluripotent stem cell-cardiomyocytes highlights arrhythmias, hypocontractility, and energy depletion as potential therapeutic

- targets for hypertrophic cardiomyopathy. *Eur Heart J* 39:3879-3892 doi:10.1093/eurheartj/ehy249
41. Nakao K, Minobe W, Roden R, Bristow MR, Leinwand LA (1997) Myosin heavy chain gene expression in human heart failure. *J Clin Invest* 100:2362-70 doi:10.1172/jci119776
42. Nakhaei-Rad S, Bahrami AR, Mirahmadi M, Matin MM (2012) New windows to enhance direct reprogramming of somatic cells towards induced pluripotent stem cells. *Biochem Cell Biol* 90:115-23 doi:10.1139/o11-064
43. Nakhaei-Rad S, Nakhaeizadeh H, Kordes C, Cirstea IC, Schmick M, Dvorsky R, Bastiaens PI, Haussinger D, Ahmadian MR (2015) The Function of Embryonic Stem Cell-expressed RAS (E-RAS), a Unique RAS Family Member, Correlates with Its Additional Motifs and Its Structural Properties. *J Biol Chem* 290:15892-903 doi:10.1074/jbc.M115.640607
44. Okita K, Matsumura Y, Sato Y, Okada A, Morizane A, Okamoto S, Hong H, Nakagawa M, Tanabe K, Tezuka K, Shibata T, Kunisada T, Takahashi M, Takahashi J, Saji H, Yamanaka S (2011) A more efficient method to generate integration-free human iPS cells. *Nat Methods* 8:409-12 doi:10.1038/nmeth.1591
45. Olivetto I, d'Amati G, Basso C, Van Rossum A, Patten M, Emdin M, Pinto Y, Tomberli B, Camici PG, Michels M (2015) Defining phenotypes and disease progression in sarcomeric cardiomyopathies: contemporary role of clinical investigations. *Cardiovasc Res* 105:409-423 doi:10.1093/cvr/cvv024
46. Ovchinnikova E, Hoes M, Ustyantsev K, Bomer N, de Jong TV, van der Mei H, Berezikov E, van der Meer P (2018) Modeling Human Cardiac Hypertrophy in Stem Cell-Derived Cardiomyocytes. *Stem Cell Reports* 10:794-807 doi:10.1016/j.stemcr.2018.01.016
47. Pandit B, Sarkozy A, Pennacchio LA, Carta C, Oishi K, Martinelli S, Pogna EA, Schackwitz W, Ustaszewska A, Landstrom A, Bos JM, Ommen SR, Esposito G, Lepri F, Faul C, Mundel P, López-Sigüero JP, Tenconi R, Selicorni A, Rossi C, Mazzanti L, Torrente I, Marino B, Digilio MC, Zampino G, Ackerman MJ, Dallapiccola B, Tartaglia M, Gelb BD (2007) Gain-of-function RAF1 mutations cause Noonan and LEOPARD syndromes with hypertrophic cardiomyopathy. *Nat Genet* 39:1007-1012 doi:10.1038/ng2073
48. Periasamy M, Bhupathy P, Babu GJ (2007) Regulation of sarcoplasmic reticulum Ca²⁺ ATPase pump expression and its relevance to cardiac muscle physiology and pathology. *Cardiovasc Res* 77:265-273 doi:10.1093/cvr/cvm056
49. Perkin J, Slater R, Del Favero G, Lanzicher T, Hidalgo C, Anderson B, Smith JE, 3rd, Sbaizero O, Labeit S, Granzier H (2015) Phosphorylating Titin's Cardiac N2B Element by ERK2 or CaMKII δ Lowers the Single Molecule and Cardiac Muscle Force. *Biophys J* 109:2592-2601 doi:10.1016/j.bpj.2015.11.002
50. Pfeleiderer P, Sumandea MP, Rybin VO, Wang C, Steinberg SF (2009) Raf-1: a novel cardiac troponin T kinase. *J Muscle Res Cell Motil* 30:67-72 doi:10.1007/s10974-009-9176-y
51. Raskin A, Lange S, Banares K, Lyon RC, Ziesenis A, Lee LK, Yamazaki KG, Granzier HL, Gregorio CC, McCulloch AD, Omens JH, Sheikh F (2012) A novel mechanism involving four-and-a-half LIM domain protein-1 and extracellular signal-regulated kinase-2 regulates titin phosphorylation and mechanics. *J Biol Chem* 287:29273-84 doi:10.1074/jbc.M112.372839
52. Rauen KA (2013) The RASopathies. *Annu Rev Genomics Hum Genet* 14:355-369 doi:10.1146/annurev-genom-091212-153523
53. Razzaque MA, Nishizawa T, Komoike Y, Yagi H, Furutani M, Amo R, Kamisago M, Momma K, Katayama H, Nakagawa M, Fujiwara Y, Matsushima M, Mizuno K, Tokuyama M, Hirota H, Muneuchi J, Higashinakagawa T, Matsuoka R (2007) Germline gain-of-function mutations in RAF1 cause Noonan syndrome. *Nat Genet* 39:1013-1017 doi:10.1038/ng2078
54. Rezaei Adariani S, Buchholzer M, Akbarzadeh M, Nakhaei-Rad S, Dvorsky R, Ahmadian MR (2018) Structural snapshots of RAF kinase interactions. *Biochem Soc Trans* 46:1393-1406 doi:10.1042/bst20170528
55. Roberts AE, Allanson JE, Tartaglia M, Gelb BD (2013) Noonan syndrome. *The Lancet* 381:333-342 doi:10.1016/S0140-6736(12)61023-X
56. Romano D, Nguyen LK, Matallanas D, Halasz M, Doherty C, Kholodenko BN, Kolch W (2014) Protein interaction switches coordinate Raf-1 and MST2/Hippo signalling. *Nat Cell Biol* 16:673-84 doi:10.1038/ncb2986
57. Rose BA, Force T, Wang Y (2010) Mitogen-activated protein kinase signaling in the heart: angels versus demons in a heart-breaking tale. *Physiol Rev* 90:1507-46 doi:10.1152/physrev.00054.2009
58. Rössler U, Hennig AF, Stelzer N, Bose S, Kopp J, Sør K, Cyganek L, Zifarelli G, Ali S, von der Hagen M (2021) Efficient generation of osteoclasts from human induced pluripotent stem cells and functional investigations of lethal CLCN7-related osteopetrosis. *J Bone Miner Res* doi:10.1002/jbmr.4322
59. Sakai T, Naito AT, Kuramoto Y, Ito M, Okada K, Higo T, Nakagawa A, Shibamoto M, Yamaguchi T, Sumida T, Nomura S, Umezawa A, Miyagawa S, Sawa Y, Morita H, Lee JK, Shiojima I, Sakata Y, Komuro I (2018) Phenotypic Screening Using Patient-Derived Induced Pluripotent Stem Cells Identified Pyr3 as a Candidate Compound for the Treatment of Infantile Hypertrophic Cardiomyopathy. *Int Heart J* 59:1096-1105 doi:10.1536/ihj.17-730
60. Seabright M (1971) A rapid banding technique for human chromosomes. *Lancet* 2:971-972 doi:10.1016/S0140-6736(71)90287-X
61. Sheikh F, Raskin A, Chu PH, Lange S, Domenighetti AA, Zheng M, Liang X, Zhang T, Yajima T, Gu Y, Dalton ND, Mahata SK, Dorn GW, 2nd, Brown JH, Peterson KL, Omens JH, McCulloch AD, Chen J (2008) An FHL1-containing complex within the cardiomyocyte sarcomere mediates hypertrophic biomechanical stress responses in mice. *J Clin Invest* 118:3870-80 doi:10.1172/JCI34472
62. Shimizu M, Wang W, Walch ET, Dunne PW, Epstein HF (2000) Rac-1 and Raf-1 kinases, components of distinct signaling pathways, activate myotonic dystrophy protein kinase. *FEBS letters* 475:273-277 doi:10.1016/S0014-5793(00)01692-6
63. Strunk A, Bhalla V, Clopton P, Nowak RM, McCord J, Hollander JE, Duc P, Storrow AB, Abraham WT, Wu AH (2006) Impact of the history of congestive heart failure on the utility of B-type natriuretic peptide in the emergency diagnosis of heart failure: results from the Breathing Not Properly Multinational Study. *Am J Med* 119:69. e1-69. e11 doi:10.1016/j.amjmed.2005.04.029
64. Tohyama S, Hattori F, Sano M, Hishiki T, Nagahata Y, Matsuura T, Hashimoto H, Suzuki T, Yamashita H, Satoh Y, Egashira T, Seki T, Muraoka N, Yamakawa H, Ohgino Y, Tanaka T, Yoichi M, Yuasa S, Murata M, Suematsu M, Fukuda K (2013) Distinct metabolic flow enables large-scale purification of mouse and human pluripotent stem cell-derived cardiomyocytes. *Cell Stem Cell* 12:127-37 doi:10.1016/j.stem.2012.09.013
65. von Gise A, Lin Z, Schlegelmilch K, Honor LB, Pan GM, Buck JN, Ma Q, Ishiwata T, Zhou B, Camargo FD, Pu WT (2012) YAP1, the nuclear target of Hippo signaling, stimulates heart growth through cardiomyocyte proliferation but not hypertrophy. *Proc Natl Acad Sci U S A* 109:2394-9 doi:10.1073/pnas.1116136109
66. Wang L, Kim K, Parikh S, Cadar AG, Bersell KR, He H, Pinto JR, Kryshtal DO, Knollmann BC (2018) Hypertrophic cardiomyopathy-linked mutation in troponin T causes myofibrillar disarray and pro-arrhythmic action potential changes in human iPSC cardiomyocytes. *J Mol Cell Cardiol* 114:320-327 doi:10.1016/j.jmcc.2017.12.002

67. Wang L, Kryshtal DO, Kim K, Parikh S, Cadar AG, Bersell KR, He H, Pinto JR, Knollmann BC (2017) Myofilament Calcium-Buffering Dependent Action Potential Triangulation in Human-Induced Pluripotent Stem Cell Model of Hypertrophic Cardiomyopathy. *J Am Coll Cardiol* 70:2600-2602 doi:10.1016/j.jacc.2017.09.033
68. Yang Y, Del Re DP, Nakano N, Sciarretta S, Zhai P, Park J, Sayed D, Shirakabe A, Matsushima S, Park Y, Tian B, Abdellatif M, Sadoshima J (2015) miR-206 Mediates YAP-Induced Cardiac Hypertrophy and Survival. *Circ Res* 117:891-904 doi:10.1161/circresaha.115.306624
69. Yu L, Daniels JP, Wu H, Wolf MJ (2015) Cardiac hypertrophy induced by active Raf depends on Yorkie-mediated transcription. *Sci Signal* 8:ra13 doi:10.1126/scisignal.2005719
70. Zhai Y, Luo Y, Wu P, Li D (2018) New insights into SERCA2a gene therapy in heart failure: pay attention to the negative effects of B-type natriuretic peptides. *J Med Genet* 55:287-296 doi:10.1136/jmedgenet-2017-105120
71. Zhao Z, Manser E (2015) Myotonic dystrophy kinase-related Cdc42-binding kinases (MRCK), the ROCK-like effectors of Cdc42 and Rac1. *Small GTPases* 6:81-88 doi:10.1080/21541248.2014.1000699
72. Zheng M, Dilly K, Dos Santos Cruz J, Li M, Gu Y, Ursitti JA, Chen J, Ross Jr J, Chien KR, Lederer JW (2004) Sarcoplasmic reticulum calcium defect in Ras-induced hypertrophic cardiomyopathy heart. *Am J Physiol Heart Circ Physiol* 286:H424-H433 doi:10.1152/ajpheart.00110.2003
73. Zhou Q, Li L, Zhao B, Guan KL (2015) The hippo pathway in heart development, regeneration, and diseases. *Circ Res* 116:1431-47 doi:10.1161/circresaha.116.303311

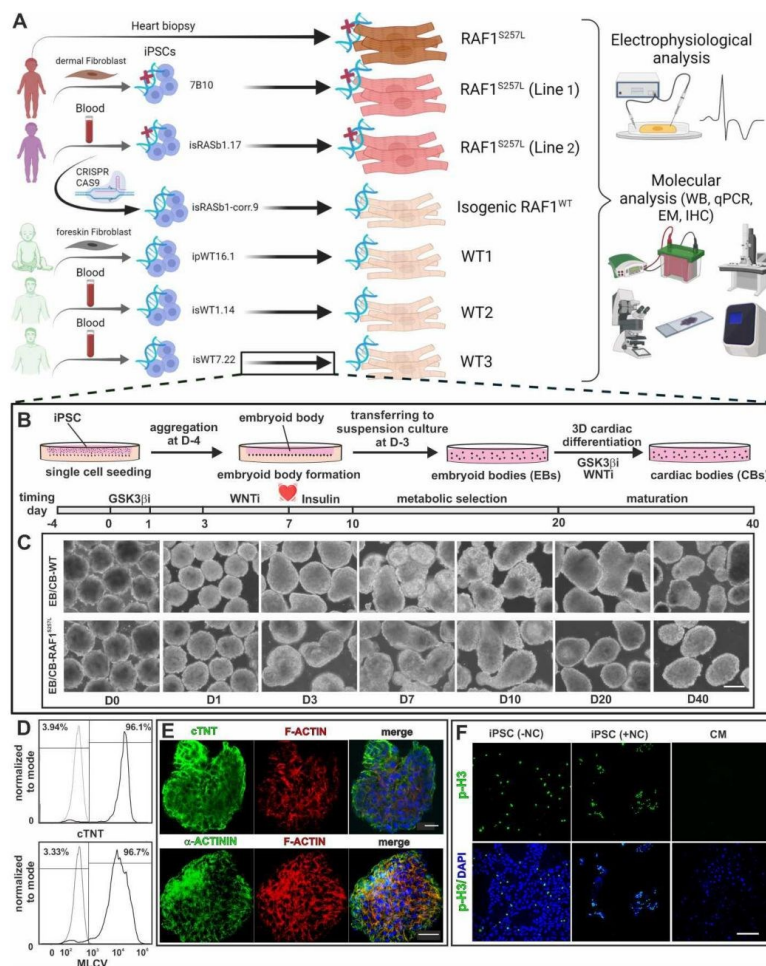


Figure 1. Study overview and details of 3D cardiac differentiation of iPSCs with WNT signaling modulation.
A) Summary of the donor cells and the iPSC lines together with an overview of different analysis approaches used in this study.
B) Schematic overview of embryoid body (EB) formation using agarose microwells combined with the stages and time lines of EBs differentiation to cardiac bodies (CBs).
C) Light microscopic pictures of EBs/CBs during the course of cardiac differentiation and metabolic selection. Scale bar, 200 μ m.
D) Exemplary histograms of flow cytometric analysis of dissociated CBs displayed efficient cardiac differentiation towards ventricular cardiomyocytes by analysis of MLCV2 and cTNT positive cells (RAF1^{S257L}-1). Isotype controls depicted in light gray.
E) Immunofluorescence staining of a representative CB for cTNT and α -actinin expression (RAF1^{S257L}-1). Scale bar, 20 μ m.
F) Illustration of mitotic cells stained with the mitotic marker p-H3 in iPSC cells and CMs. CMs showed no proliferative behavior as compared to iPSCs, which were arrested in mitosis by 100 nM nocodazole (NC) treatment. Scale bar, 200 μ m.

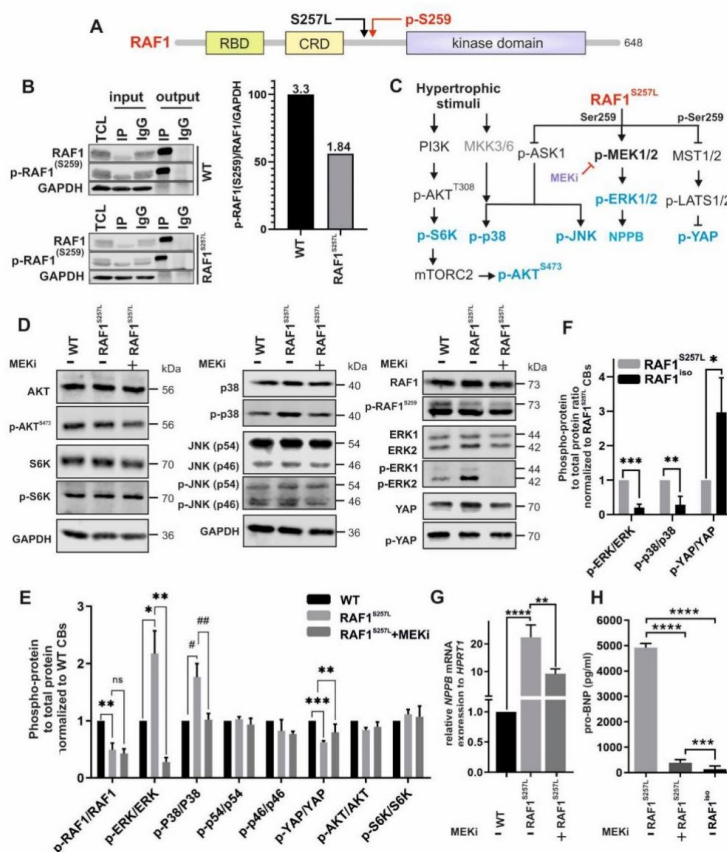


Figure 2. The effect of the RAF1^{S257L} variant on the activity of selected effector kinases downstream of RAF1. A) Domain organization of RAF1 kinase with the typical functional domains, including the RAS-binding domain (RBD), the cysteine-rich domain (CRD), and the kinase domain. The adjacent sites of S257L variant and the inhibitory S259 phosphorylation (p-S259) are highlighted. B) Immunoprecipitation and quantification of total and p-RAF1^{S259} in WT and RAF1^{S257L} iPSCs. Total RAF1 was pulled down from lysates of WT and RAF1^{S257L} iPSCs using an anti-RAF1 specific antibody. IgG was applied as an isotype control. Immunoblotting was carried out using anti-RAF1 and anti-p-RAF1^{S259} antibodies. For quantification, signal intensities of p-RAF1^{S259} were divided by those for total RAF1. GAPDH was used as a loading control. TCL, total cell lysate; IP, immunoprecipitation; IgG, Immunoglobulin G. C) Schematic diagram summarizing the signaling molecules investigated downstream of hypertrophic stimuli and RAF1. Proteins marked in blue letters were investigated at the protein level by immunoblotting. D) Representative immunoblots of p-AKT vs. AKT, p-S6K vs. S6K, p-RAF1^{S259} vs. RAF1, p-ERK1/2 vs. ERK1/2, p-YAP vs. YAP, p-p38 vs. p38, and p-JNK vs. JNK using cell lysates from WT and RAF1^{S257L} CBs (d24). E) Phospho-protein vs. total protein ratio quantification as shown in D. *P < 0.05, **P < 0.01, ***P < 0.001, ****P < 0.0001, unpaired 2-tail t-test. # P < 0.05, ## P < 0.01, unpaired 1-tail t-test. n≤2. F) Phospho-protein vs. total protein ratio quantification of western blot results for selected pathways in RAF1^{S257L} CBs vs. gene corrected line, RAF1^{iso} CBs (d24). *P < 0.05, **P < 0.01, ***P < 0.001, unpaired 2-tail t-test. n≤2. G) qPCR analysis of *NPPB* transcription levels. **P < 0.01, ***P < 0.0001, unpaired 2-tail t-test, n=3. H) ELISA analysis of pro-BNP levels released in the cell culture supernatant of CB's (pg/ml). ***P < 0.001, ****P < 0.0001, unpaired 2-tail t-test. n=8.

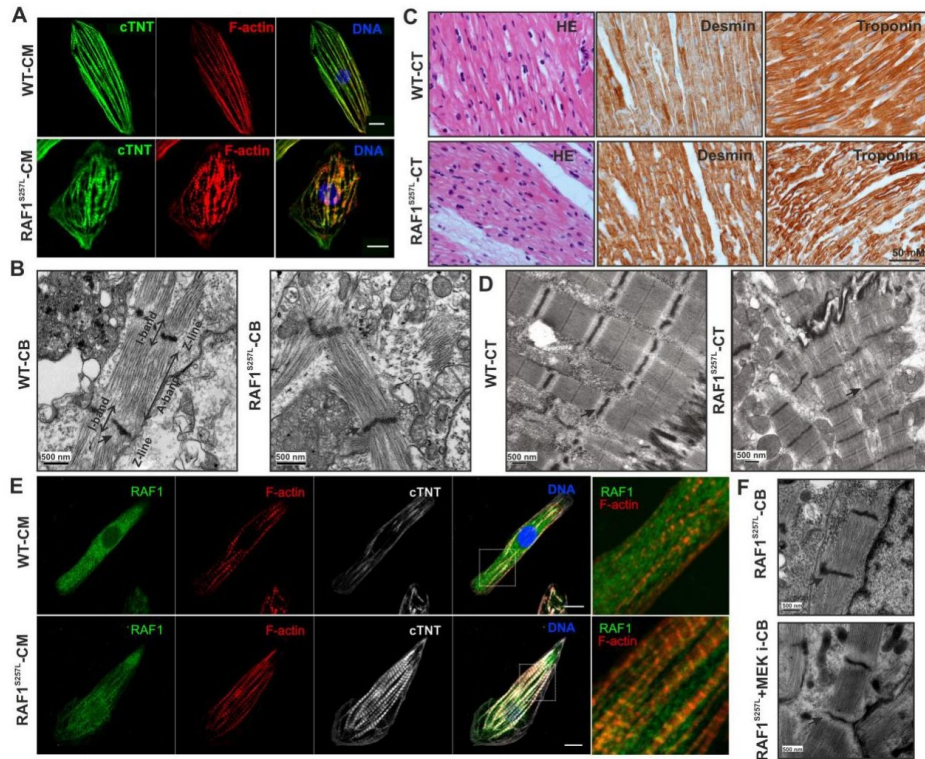


Figure 3. Aberrant RAF1^{S257L} activity impairs the cytoarchitecture of human iPSC-derived cardiomyocytes. A) Dissociated cardiac bodies were seeded on Geltrex-coated coverslips for 7 d and stained for cTNT and F-actin (Scale bar, 10 μm). B) Representative EM images from RAF1^{S257L} CBs revealed a stronger myofibrillar disarray accompanied by shortened I-bands and a thickened Z-line pattern as compared to WT CBs. C) IHC analysis of RAF1^{S257L} CTs from one of the NS individuals with *RAF1* c.770C>T variant for desmin and troponin showed myofilament disarray. D) Representative EM images of the same RAF1^{S257L} CTs as in C exhibited shortened I-bands and a thickened Z-line pattern consistent with RAF1^{S257L} CBs in B. E) Representative ICC images of RAF1^{S257L} and WT CMs at d90 post-differentiation showed RAF1 co-localization with cTNT and F-actin at the sarcomere (Scale bar, 10 μm). F) EM images of RAF1 mutated RAF1^{S257L} CBs (d40) treated with 0.2 μM MEKi from d12 of differentiation.

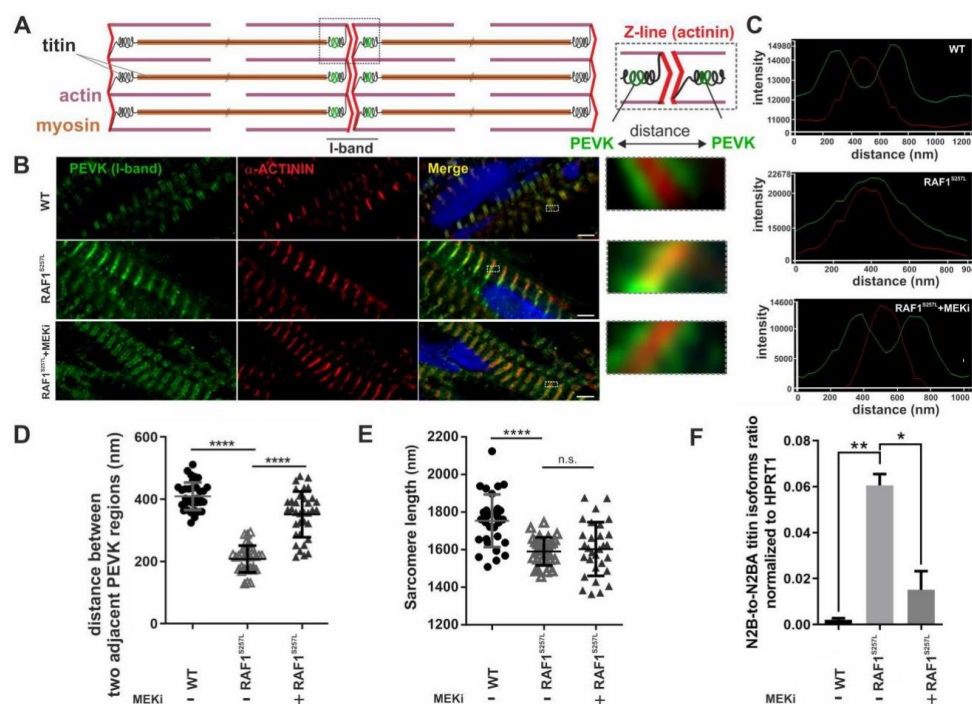


Figure 4. Hyperactive RAF1^{S257L} triggers a shorter I-band phenotype

A) Schematic view of the sarcomeric organization.

B) IHC analysis of 8-μm cryosections of WT and RAF1^{S257L} BCTs with PEVK segment of titin's I-band, α-actinin 2 as the Z-line marker, and DAPI for DNA staining.

C) Histogram of selected boxes on G were imported base on the intensity and overlaps of emitted fluorescent lights using the Zeiss LSM 880 Airyscan confocal microscope software.

D) Averaged distance (nm) between two adjacent PEVK segments was measured for more than 50 different sarcomeric units for each condition and statistically evaluated. ****P < 0.0001, unpaired 2-tailed t-test.

E) Averaged sarcomere length (nm) was measured for more than 50 different sarcomere units for each condition by measuring the distance between two parallel Z-lines (α-actinin) and statistically evaluated. ****P < 0.0001, unpaired 2-tailed t-test.

F) qPCR analysis of ratio of the N2B-to-N2BA titin isoforms expression levels in CBs. *P < 0.05, **P < 0.01, unpaired 2-tailed t-test.

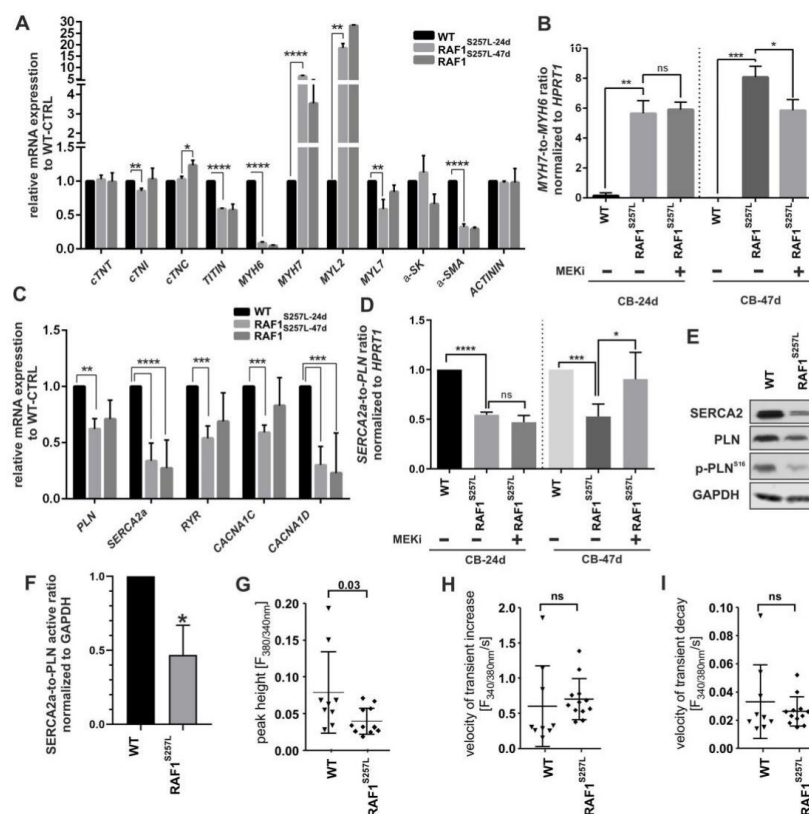


Figure 5. Abnormal expression of proteins involved in sarcomere function and calcium handling.

The experiments in A-F were conducted with WT CBs, RAF1^{S257L} CBs, and RAF1^{S257L} CBs treated with 0.2 μ M MEKi from d12 of differentiation. The data are averaged from three independent experiments in biological triplicates. *P < 0.05, **P < 0.01, ***P < 0.001, ****P < 0.0001, unpaired 2-tail t-test.

A) qPCR analysis of mRNAs related to sarcomere proteins.

B) MYH7-to-MYH6 ratio.

C) qPCR analysis of mRNAs related to regulation of calcium transients.

D) SERCA2a-to-PLN ratio.

E) Immunoblot analysis of SERCA2, PLN, and p-PLN^{Ser16} in CBs at d24.

F) The ratio of SERCA2 to PLN was calculated by measuring the ratio of SERCA2 to PLN/p-PLN^{Ser16}

G-I) Ca²⁺ transients were measured in Fura2-loaded CMs and expressed as the ratio of fluorescence emission at 340 nm and 380 nm. Bar graphs display the peak height of Ca²⁺ transients (G) and the velocities of cytosolic Ca²⁺ increase (H) and decrease (I). Each data point represents the average of 10 transients obtained from a single CM. Nine wild-type and twelve RAF1^{S257L} CMs were analyzed in total.

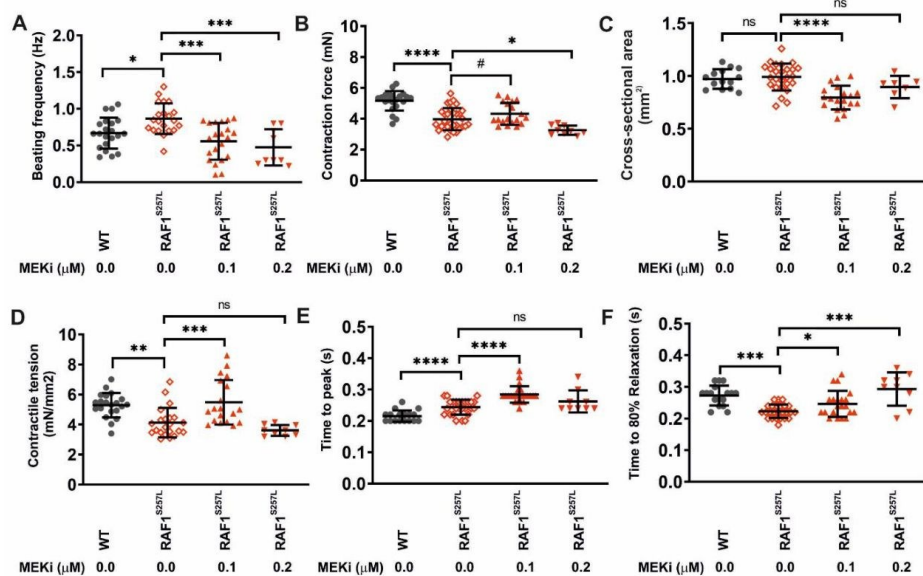


Figure 6. Aberrant contractility of RAF1^{S257L} BCTs and partial rescue by MEKi.

Physiological measurements were conducted on day 24-28 of culture using WT, RAF1^{S257L} and RAF1^{S257L} + MEKi BCTs. N = 9-26 individual tissue samples per group. Depending on the presence of normally distributed values, one-way ANOVA or Kruskal-Wallis test was applied. *P<0.05, **P<0.01, ***P<0.001, ****P<0.0001.

A) Spontaneous beating frequencies.

B) Quantification of cross-sectional areas.

C) Maximum contraction forces.

D) Maximum contractile tensions based on the cross-sectional areas.

E) Time to peak.

F) Time to 80% relaxation.

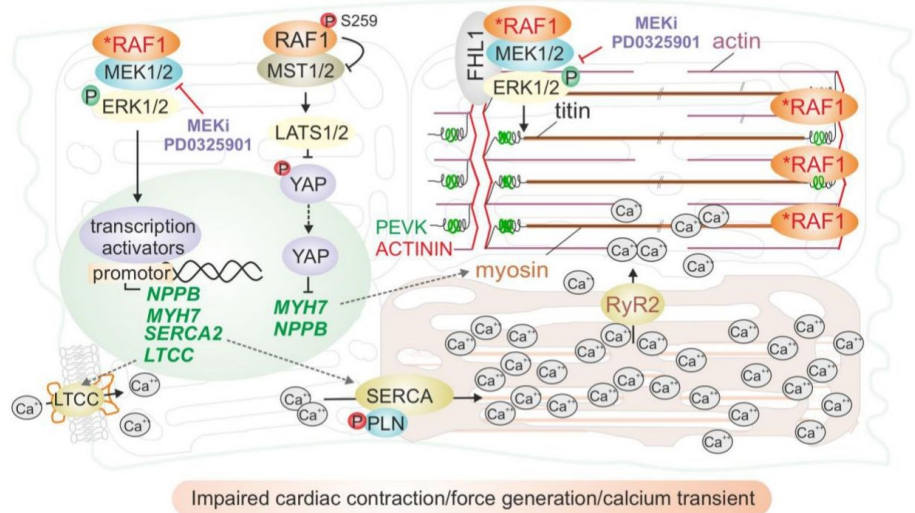
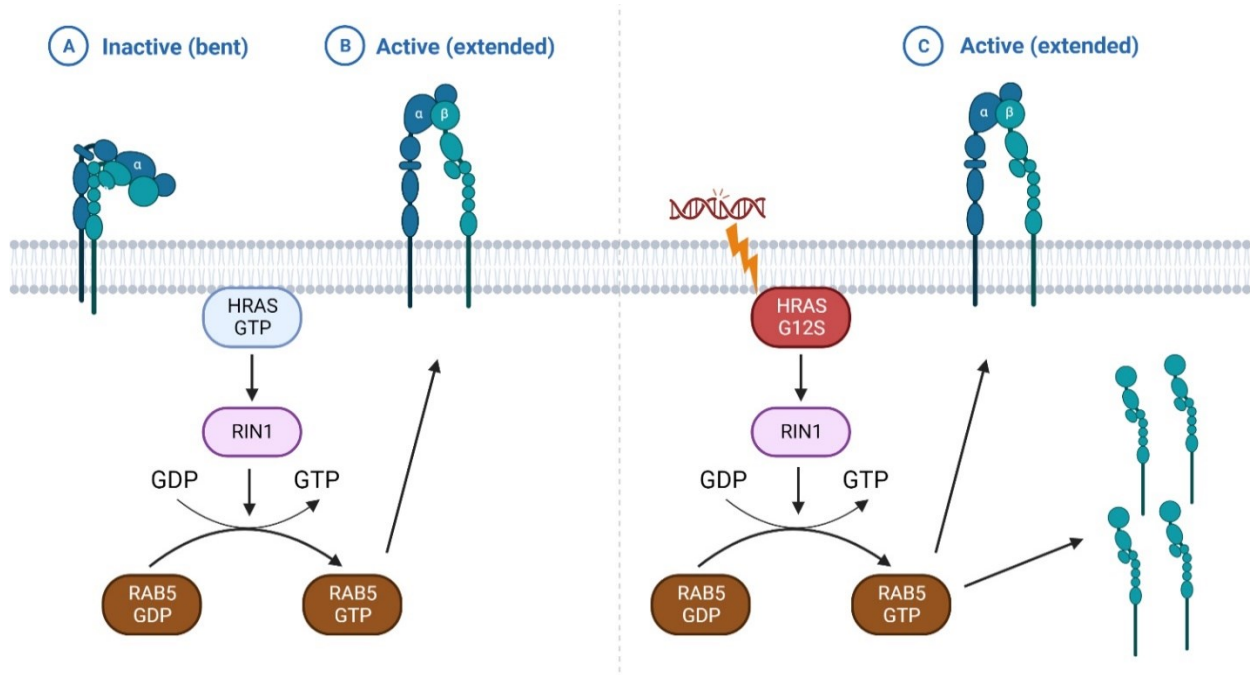


Figure 7. A proposed model of both *RAF1*-dependent cardiac signaling pathways, coupling calcium transients and contraction, and *RAF1*^{S259L}-enhanced impairment of cardiac contraction, force generation, and calcium transients (for details, see “Discussion”).

Chapter 3

Cutaneous manifestations in Costello syndrome: HRAS p.Gly12Ser affects RIN1-mediated integrin trafficking in immortalized epidermal keratinocytes



Status: published in Human Molecular Genetics, 15 January 2023

Impact factor: 6.15

Contribution: 30 %

Expression and purification of different variants of HRAS, RAB5 and RIN1 proteins, preparation of nucleotide-free and fluorescently labeled forms of HRAS variants, protein interaction analyses including fluorescence polarization measurements, GEF nucleotide exchange assay, figure preparation and illustration, drafting of manuscript and discussion.

Cutaneous manifestations in Costello syndrome: HRAS p.Gly12Ser affects RIN1-mediated integrin trafficking in immortalized epidermal keratinocytes

Theresa Nauth^{1,†}, Farhad Bazgir^{2,†}, Hannah Voß³, Laura I. Brandenstein¹, Niloufar Mosaddeghzadeh², Verena Rickassel¹, Sophia Deden¹, Christian Gorzelanny⁴, Hartmut Schlüter³, Mohammad R. Ahmadian² and Georg Rosenberger^{1,*}

¹Institute of Human Genetics, University Medical Center Hamburg-Eppendorf, 20246 Hamburg, Germany

²Institute of Biochemistry and Molecular Biology II, Medical Faculty and University Hospital Düsseldorf, Heinrich-Heine University, 40225 Düsseldorf, Germany

³Institute of Clinical Chemistry and Laboratory Medicine, Section Mass Spectrometry and Proteomics, University Medical Center Hamburg-Eppendorf, 20246 Hamburg, Germany

⁴Department of Dermatology and Venerology, University Medical Center Hamburg-Eppendorf, 20246 Hamburg, Germany

*To whom correspondence should be addressed at: Institute of Human Genetics, University Medical Center Hamburg-Eppendorf, Martinistraße 52, 20246 Hamburg, Germany. Tel: +49 40 741054534; Fax: +49 40 741055138; Email: rosenberger@uke.de

[†]TN and FB share the first-author position.

Abstract

Heterozygous germline missense variants in the HRAS gene underlie Costello syndrome (CS). The molecular basis for cutaneous manifestations in CS is largely unknown. We used an immortalized human cell line, HaCaT keratinocytes, stably expressing wild-type or CS-associated (p.Gly12Ser) HRAS and defined RIN1 as quantitatively most prominent, high-affinity effector of active HRAS in these cells. As an exchange factor for RAB5 GTPases, RIN1 is involved in endosomal sorting of cell-adhesion integrins. RIN1-dependent RAB5A activation was strongly increased by HRAS^{Gly12Ser}, and HRAS-RIN1-ABL1/2 signaling was induced in HRAS^{WT}- and HRAS^{Gly12Ser}-expressing cells. Along with that, HRAS^{Gly12Ser} expression decreased total integrin levels and enriched β 1 integrin in RAB5- and EEA1-positive early endosomes. The intracellular level of active β 1 integrin was increased in HRAS^{Gly12Ser} HaCaT keratinocytes due to impaired recycling, whereas RIN1 disruption raised β 1 integrin cell surface distribution. HRAS^{Gly12Ser} induced co-localization of β 1 integrin with SNX17 and RAB7 in early/sorting and late endosomes, respectively. Thus, by retaining β 1 integrin in intracellular endosomal compartments, HRAS-RIN1 signaling affects the subcellular availability of β 1 integrin. This may interfere with integrin-dependent processes as we detected for HRAS^{Gly12Ser} cells spreading on fibronectin. We conclude that dysregulation of receptor trafficking and integrin-dependent processes such as cell adhesion are relevant in the pathobiology of CS.

Introduction

Costello syndrome (CS) (OMIM #218040), a rare developmental disorder, is characterized by a multiorgan presentation with distinctive facial features, failure-to-thrive, developmental delay, cardiac manifestations and a history of polyhydramnios (1). Moreover, patients show distinct dermatologic features including loose, redundant and soft skin on the neck, hands and feet, deep palmar and plantar creases, hyperpigmentation and prematurely aged skin. With increasing age, patients develop palmoplantar keratoderma and facial papillomata, preferentially in the face and perianal region. Individuals with CS have sparse and curly hair, frontotemporal alopecia, brittle and thin fingernails and toenails as well as spatulate finger pads (1,2). CS is caused by pathogenic heterozygous germline variants in the proto-oncogene HRAS, which cause constitutive HRAS activation (3). Approximately, 80% of CS-associated HRAS variants result in the missense change p.Gly12Ser (1).

HRAS acts as molecular switch by alternating between an active guanosine triphosphate (GTP)-bound and inactive guanosine diphosphate (GDP)-bound state. Active HRAS binds to diverse effectors and, thereby, controls a variety of cellular signaling

pathways. Amongst HRAS effectors the serine/threonine RAF kinases, the catalytic subunits of phosphoinositide 3-kinases (PIK3CA), phospholipase C1 (PLCE1) and RAL guanine nucleotide dissociation stimulator (RALGDS) are best characterized (4). Less is known about the HRAS effector RAS and RAB interactor 1 (RIN1) and its associated signaling pathways (5,6): binding of active HRAS to RIN1 promotes the activation of RAB5 GTPases (7) and ABL1/2 tyrosine kinases (8). Through these two signaling branches, endosomal sorting events and cytoskeletal dynamics are coordinated (7–12). Translocation of RIN1 between cytoplasmic and membrane compartments is controlled in part by Ser³⁵¹ phosphorylation-dependent binding to 14-3-3 proteins (10,13).

The molecular pathophysiology caused by disease-associated HRAS variants has been investigated in various cell types including neuronal cells, heart muscle cells, fibroblasts and others (14–19). However, up to date the molecular basis for dermatologic/epidermal findings in CS and other RASopathies is largely unknown.

The epithelium of the skin, the epidermis, is composed of four layers of keratinocytes that undergo proliferation and programmed differentiation (20). This process—also known as epidermal stratification—is the prerequisite for a functional and

Received: March 9, 2022. Revised: July 15, 2022. Accepted: August 7, 2022

© The Author(s) 2022. Published by Oxford University Press. All rights reserved. For Permissions, please email: journals.permissions@oup.com

healthy skin, and HRAS has been shown to be an important modulator in keratinocyte stratification (21,22). The basal keratinocytes are highly proliferative and connect the epidermis with the extracellular matrix (ECM) and the dermis via focal adhesions and hemidesmosomes (20,23). Moreover, keratinocytes are in close contact with neighboring keratinocytes through cell-cell contacts, including adherens junctions, tight junctions, desmosomes and gap junction (20,23). All of these cell-cell and cell-ECM contacts are facilitated by diverse transmembrane and cell adhesion proteins such as cadherins, claudins and integrins (20,23). Transmembrane integrins connect the actin cytoskeleton of the cell with the ECM and transduce signals in both directions. Integrin receptors consist of alpha and beta subunits, and the majority of these heterodimers contain the $\beta 1$ subunit that plays a central role in the maintenance of epidermal stratification and adhesion to the basement membrane (23–25).

In line with the dynamic nature of the epidermis and to maintain epidermal homeostasis, keratinocytes continuously reorganize their cell-cell contacts and adhesion sites with neighboring cells and to the ECM, respectively (20). For this, a tightly regulated vesicle-based endosomal sorting (trafficking) machinery is essential to internalize, recycle back to the plasma membrane and/or degrade contact and adhesion proteins. Accordingly, the surface availability and activity of integrins in keratinocytes and, consequently, the efficiency to get in contact with the ECM and to appropriately respond to environmental cues is controlled by marked trafficking of these receptors within a cycle of endocytosis, recycling and lysosomal degradation (24,26). Notably, a large proportion of integrins is recycled back to the plasma membrane resulting in a remarkably protein half-life (12–24 hours) (24).

The RAB family of GTPases, in particular the RIN1 effector RAB5, regulates vesicle-dependent cellular distribution of integrins and, thereby, controls cell adhesion and adhesion-dependent processes such as cell spreading and migration (24,27). Spatiotemporal reorganization of the actin cytoskeleton is central for both integrin-dependent cell adhesion and motility (28), and the tyrosine kinases ABL1/2 downstream of RIN1 can promote actin polymerization during these processes (29,30).

Here we provide evidence for a critical function of the HRAS-RIN1 signaling node for adhesion-associated integrin trafficking in immortalized HaCaT keratinocytes, and we add a novel aspect in the molecular pathogenesis of CS.

Results

RIN1 is the quantitatively most prominent and high-affinity effector of HRAS in immortalized HaCaT keratinocytes

As an epidermal cellular model system, we used immortalized human keratinocyte cells (HaCaT) stably expressing HA-tagged HRAS^{WT} (HA-HRAS^{WT}) and HRAS^{Gly12Ser} (HA-HRAS^{Gly12Ser}), two clones each (indicated as 1 and 2). To identify keratinocyte-specific binding partners of HRAS, we affinity purified HA-HRAS^{WT} and HA-HRAS^{Gly12Ser} from HaCaT lysates and analyzed precipitates by differential quantitative proteomics. In total, 885 proteins were quantified (Supplementary Material, Table S1). A missing value tolerant nonlinear iterative partial least squares (NIPALS) principal component analysis (PCA) demonstrated the clear distinguishability of HA-HRAS^{WT} and HA-HRAS^{Gly12Ser} clones, based on the relative abundance of the proteins in the precipitates, according to principal component 1 (PC1, 78% of the explained variation) and PC2 (27%). Native and empty vector (EV)

transfected HaCaT cells formed a separate cluster (Fig. 1A). Quantitative comparison of HA-HRAS^{WT} and HA-HRAS^{Gly12Ser} samples identified 82 significantly differential abundant proteins ($P < 0.05$ or $= 1$ and FoldChange difference > 1.5 , Supplementary Results and Discussion, Supplementary Material, Table S1). Pearson's correlation-based hierarchical clustering was performed for all genes/proteins listed in the WP_RAS_SIGNALING gene-set (www.gsea-msigdb.org). Nineteen known HRAS-associated proteins were found (Fig. 1B). We identified the RAS and RAB interactor 1 (RIN1) (FC difference: 78) and Ras-related proteins Rap1a (RAP1A) and Rap1b (RAP1B) as highly abundant in HA-HRAS^{Gly12Ser} vs HA-HRAS^{WT} precipitates (Fig. 1B; Supplementary Material, Table S1). Notably, proteomic analyses of HaCaT cells expressing the oncogenic variant HA-HRAS^{Gly12Val} resulted in a similar but not identical pattern compared with CS-associated HA-HRAS^{Gly12Ser} expressing HaCaT keratinocytes (Supplementary Material, Fig. S1); this suggests mutation-specific consequences in addition to mutation effect overlaps. In this study, we focused on RIN1 (for details see Supplementary Material, Results and Discussion). Co-immunoprecipitation of endogenous RIN1 was increased by approximately 7-fold in HA-HRAS^{Gly12Ser} compared to HA-HRAS^{WT} expressing HaCaT keratinocytes cultured in 10% serum (Fig. 1C). Moreover, we used the GST-tagged RAS association domain of RIN1 (RIN1[RA]) and precipitated HA-tagged HRAS from HaCaT extracts. Whereas HA-HRAS^{WT} was pulled down (PD) weakly, HA-HRAS^{Gly12Ser} strongly co-precipitated with GST-RIN1[RA] demonstrating RIN1 binding with activated HRAS (Fig. 1D). By fluorescence polarization, we detected an approximately 2-fold increased binding affinity of RIN1[RA] with HRAS^{Gly12Ser} vs HRAS^{WT} (Fig. 1E and Supplementary Material, Fig. dS2). The mildly hyperactive HRAS^{Gly13Glu} showed an affinity to RIN1[RA] comparable with HRAS^{WT}, while no binding was detected for dominant negative HRAS^{Ser17Asp}. Finally, we compared expression of HRAS pathway proteins in HaCaT, HEK-293, HeLa cells as well as primary keratinocytes and primary fibroblasts. RIN1 is strongly expressed in HaCaT cells and primary keratinocytes, however, (very) weakly in primary fibroblasts and in HeLa cells (Fig. 1F). We did not detect RIN1 in HEK-293 cells. Similar to RIN1, strongest expression of HRAS was detected in HaCaT and primary keratinocytes (Fig. 1F). Whereas expression of PI3K and PLC α was robust in (HaCaT and primary) keratinocytes, RALGDS protein levels were moderate, each compared to the remaining cell types (Fig. 1F). RAF1 was well expressed in HEK-293 and HeLa cells but weakly in HaCaT keratinocytes (Supplementary Material, Fig. S3A). Accordingly, expression of HA-HRAS^{Gly12Ser} or HA-HRAS^{WT} did not significantly affect RAF-mediated phosphorylation of MEK1/2 and ERK1/2 (Supplementary Material, Fig. S3B). These data indicate that HRAS-RIN1 signaling is relevant in keratinocyte biology.

HRAS controls RIN1 effector pathways

RIN1 is a guanine nucleotide exchange factor for the RAS-related protein RAB5A and an activator of non-receptor tyrosine-protein kinases ABL1/2 (7,8). To determine HRAS-RIN1 stimulated RAB5A activation, we measured the release of fluorescently labeled GDP (mant-deoxy-GDP) from recombinant RAB5A. In the absence of active HRAS protein, recombinant RIN1[GEF-RA]^{WT} (comprising the guanine exchange factor and RAS association domains) did not affect nucleotide exchange on RAB5A. Upon addition of GppNHp-loaded HRAS^{WT}, HRAS^{Gly12Ser} or HRAS^{Gly13Glu}, the nucleotide exchange rate of RAB5A was significantly increased by 34-, 52- and 68-fold, respectively (Fig. 2A and Supplementary Material, Fig. S4). As a negative

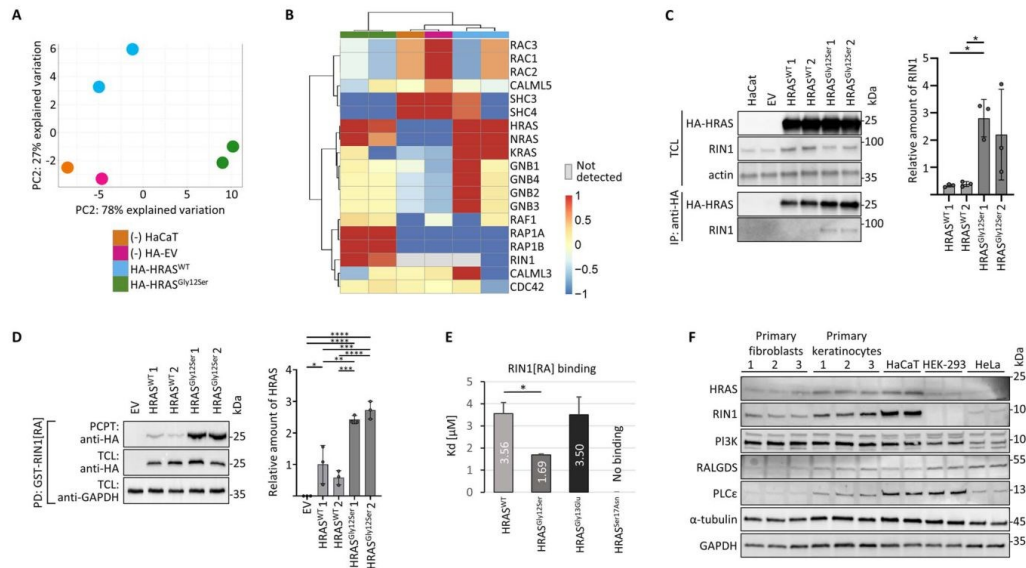


Figure 1. RIN1 is a highly abundant and high-affinity effector of HRAS in HaCaT keratinocytes. **(A)** Distinct proteomic relative quantitative differences between HaCaT keratinocytes expressing HRAS^{WT} and HRAS^{Gly12Ser}. HRAS was precipitated with anti-HA magnetic beads and subjected to LC-MS/MS analysis. Scatter plot distribution of HRAS^{WT} (blue) HRAS^{Gly12Ser} (green) native (HaCaT, orange) and EV (pink) transfected (HA-EV) samples for the top two principal components in NIPALS PCA, based on 885 proteins quantified. PC, principle component. **(B)** RIN1 is highly abundant in HA-HRAS^{Gly12Ser} precipitates. Pearson's correlation-based hierarchical clustering of HRAS^{WT}, HRAS^{Gly12Ser}, native (HaCaT) and EV transfected (HA-EV) samples, based on all quantified proteins implemented in the WP_RAS_SIGNALING (www.gsea-msigdb.org) gene-set. The relative protein abundance is coded by colors from red (high abundant) to blue (low abundant). **(C)** RIN1 strongly co-precipitates with HRAS^{Gly12Ser}. TCL of HaCaT cells stably expressing HA-tagged HRAS variants and controls were subjected to IP with anti-HA magnetic beads. Co-precipitation and input levels of endogenous RIN1 were assessed by anti-RIN1 immunoblotting. Actin was used as loading control. The graph shows relative amounts of co-immunoprecipitated RIN1 normalized to immunoprecipitated HA-HRAS and to total amounts of RIN1 and HA-HRAS in cell lysates ($n=3$). One-way ANOVA, Tukey's multiple comparison test, $P < 0.05$, $n=3$. **(D)** HRAS^{Gly12Ser} efficiently co-precipitates with RIN1 in GTPase pulldown assays. HA-HRAS was PD from cell extracts of HaCaT keratinocytes stably expressing HA-HRAS^{WT} or HA-HRAS^{Gly12Ser} by using GST-fused RIN1[RA]. Precipitates (PCPT) and TCL were subjected to immunoblotting as indicated. The graph shows mean relative protein amounts of precipitated HA-HRAS normalized to total HA-HRAS ($n=3$). One-way ANOVA, Tukey's multiple comparison test, $P < 0.05$. RIN1[RA], Ras and Rab interactor 1 [RAS association domain]. **(E)** RIN1 is a high-affinity effector of HRAS. Fluorescence polarization experiments were performed to determine the dissociation constants (Kd) by titrating mantGppNhp-bound HRAS variants with increasing concentrations of RIN1[RA]. mantGppNhp is a fluorescent, non-hydrolyzable GTP analog under the experimental conditions. **(F)** HaCaT and primary keratinocytes (strongly) express RIN1 and HRAS. TCLs of primary fibroblasts and primary keratinocytes, (derived from three juvenile individuals each), as well as HaCaT keratinocytes, HEK-293 cells and HeLa cells were subjected to immunoblotting as indicated. α -tubulin and GAPDH were used as loading controls. RIN1, RAS and RAB interactor 1; PI3K, phosphoinositide 3-kinase; RALGDS, RAL guanine nucleotide dissociation stimulator; PLC ϵ , phospholipase C1.

control, we used inactive HRAS^{Ser17Asn}. The RIN1[GEF-RA]^{Glu574Ala} variant with reduced RAB5A GEF activity (31) resulted in lower increase of RAB5A nucleotide exchange rates (by 16-, 20- and 38-fold for HRAS^{WT}, HRAS^{Gly12Ser} and HRAS^{Gly13Glu}, respectively) (Fig. 2A and Supplementary Material, Fig. S4). These findings suggest that the HRAS-RIN1-RAB5 signaling pathway is functional and depends on HRAS activity. As the cellular level of GTP is much higher than GDP, we conclude that increased RAB5A GDP release rates in the presence of HRAS^{Gly12Ser} (or HRAS^{Gly13Glu}) compared to HRAS^{WT} likely render RAB5A in an active GTP-bound state. To prove HRAS-RIN1-ABL signaling in immortalized keratinocytes, we generated RIN1-deficient HaCaT cells by using the Type II CRISPR-Cas system with tracrRNAs (32). As read-out, we determined Tyr²²¹ phosphorylation of the adaptor protein CRKII, a well-established ABL substrate (33). CRKII phosphorylation was significantly reduced in RIN1-deficient HaCaT cells vs native HaCaT cells (Fig. 2B). Conversely, cells stably overexpressing HRAS^{WT} or HRAS^{Gly12Ser} strongly increased CRKII

phosphorylation (by 4- to 5-fold) compared with control (EV) cells (Fig. 2B). HRAS-promoted CRKII phosphorylation does require RIN1, because transient overexpression of HA-HRAS^{WT} or HA-HRAS^{Gly12Ser} enhanced CRKII phosphorylation in native HaCaT cells but not in RIN1-deficient HaCaT cells (Fig. 2C). Finally, we detected strong and medium expression of p-CRKII in HaCaT and primary keratinocytes, respectively (Fig. 2D). Thus, HRAS and RIN1 control ABL kinase-mediated downstream signaling in keratinocytes. RIN1 is regulated by the phosphorylation of serine 351 (Ser³⁵¹), which enhances interaction with 14-3-3 adaptor proteins and reduces RIN1 membrane residence and RAS accessibility (13). Phospho-Ser³⁵¹ levels were only tententially but not significantly reduced in HaCaT cells expressing HRAS^{Gly12Ser} vs. HRAS^{WT} (Fig. 2E). However, transiently expressed EGFP-RIN1^{WT} was clearly enriched at the membrane of HRAS^{Gly12Ser} cells (Fig. 2F and Supplementary Material, Fig. S5). Taken together, these data suggest that HRAS^{Gly12Ser} affects RIN1-mediated signaling pathways.

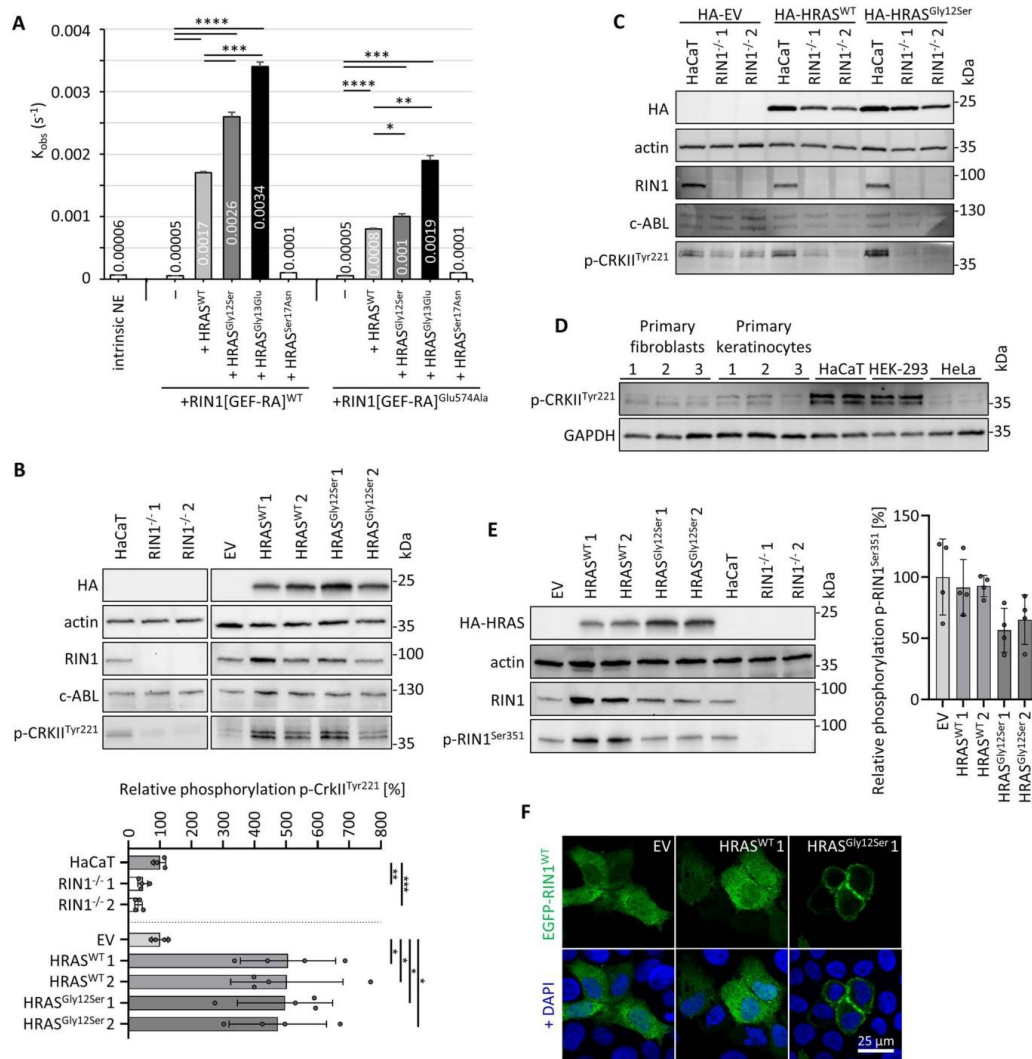


Figure 2. HRAS controls RIN1 effector pathways. **(A)** The HRAS-RIN1-RAB5 signaling axis is functional. The release of mant-deoxy-GDP from RAB5A was measured intrinsically (NE, nucleotide exchange) and in the presence of RIN1[GEF-RA] and HRAS variants as indicated in a fluorimeter instrument. K_{obs} (s^{-1}), observed fluorescent rates per second; *, $P < 0.05$; **, $P < 0.01$; ***, $P < 0.001$; ****, $P < 0.0001$; unpaired 2-tailed T-test. **(B)** HRAS stimulates activity of ABL. TCLs of native and RIN1-deficient HaCaT cells as well as HaCaT keratinocytes stably expressing HA-HRAS variants and EV-controls were subjected to immunoblotting as indicated. Phosphorylation levels of the c-ABL substrate CRKII (p-CRKII^{Tyr221}) were normalized to actin. The mean \pm SD of four independent experiments ($n=4$) each is shown relative to native HaCaT controls or EV-controls. One-way ANOVA; Sidak's multiple comparison test; *, $P < 0.05$; c-ABL, tyrosine kinase ABL1. **(C)** HRAS-promoted CRKII phosphorylation does require RIN1. Native and RIN1-deficient HaCaT cells were transiently transfected with EV (HA-EV), HA-HRAS^{WT} or HA-HRAS^{Gly12Ser} and TCLs were subjected to immunoblotting as indicated. Actin was used as loading control. **(D)** Phospho-CRKII is expressed in HaCaT and primary keratinocytes. TCLs of primary fibroblasts, primary keratinocytes, HaCaT keratinocytes, HEK-293 cells, and HeLa cells were subjected to immunoblotting using anti phospho-CRKII antibody (p-CRKII^{Tyr221}). GAPDH was used as loading control. **(E)** HRAS^{Gly12Ser} reduces RIN1^{Ser351} phosphorylation. Radioimmunoprecipitation assay buffer (RIPA) cell extracts were subjected to immunoblotting with antibodies against phosphorylated and total RIN1. Levels of phosphorylated RIN1^{Ser351} were double normalized to total RIN1 and actin. The graph shows relative phosphorylation of RIN1 (\pm SD) in four independent experiments ($n=4$); EV was considered as 100%. One-way ANOVA with Tukey's multiple comparison test ($P < 0.05$) showed no significant difference. **(F)** Expression of HA-HRAS^{Gly12Ser} promotes membrane localization of RIN1. HaCaT cells expressing HRAS^{WT} or HRAS^{Gly12Ser} and control cells (EV) were transiently transfected with EGFP-RIN1^{WT}, fixed and stained with DAPI to visualize nuclei. Cells were imaged by confocal microscopy, scale bar 25 μ m.

HRAS affects concentration and/or localization of integrins

Due to strong involvement of RAB5 GTPases and ABL kinases in integrin regulation (24,27–30), we compared levels of $\beta 1$ and $\beta 4$ integrin in various cell types. $\beta 1$ integrin was robustly expressed in primary fibroblasts and keratinocytes, in HaCaT and HeLa cells, but not in HEK-293 cells (Fig. 3A). $\beta 4$ integrin was detected only in HaCaT and primary keratinocytes but not in primary fibroblasts, HEK-293 and HeLa cells (Fig. 3A). Next, we examined the impact of HRAS and RIN1 on integrin expression in HaCaT cells. Immunoblotting analysis revealed a significant decrease of $\beta 4$ integrin level in cells expressing HRAS^{WT} or HRAS^{Gly12Ser} compared to control (EV) cells (Fig. 3B). The level of $\beta 1$ integrin was not significantly affected by the presence of HRAS^{WT} or HRAS^{Gly12Ser} (Fig. 3B). $\beta 1$ and $\beta 4$ integrin levels in RIN1-deficient HaCaT keratinocytes were similar to those in HaCaT control cells (Fig. 3B). Integrins are embedded in a dynamic cycle of endocytosis, recycling and degradation; depending on their activation state, they localize in endosomal structures or at the plasma membrane (34). We analyzed the distribution of $\beta 1$ integrin by immunocytochemistry. Both active and total $\beta 1$ integrin predominantly localize at the cell membrane in control (EV) and HRAS^{WT} expressing cells (Fig. 3C; Supplementary Material, Fig. S6). HaCaT cells expressing HRAS^{Gly12Ser} showed a strong enrichment of $\beta 1$ integrin positive vesicles inside the cell body (Fig. 3C and D; Supplementary Material, Fig. S6). Co-staining with RAB5, a marker protein for early endosomes (24,35), revealed co-localization of $\beta 1$ integrin with RAB5 at these intracellular vesicles (Fig. 3C; Supplementary Material, Fig. S6). We determined moderate occurrence of $\beta 1$ integrin-positive vesicles in RIN1-deficient cells, however these only marginally colocalized with RAB5 (Fig. 3C and D; Supplementary Material, Fig. S6). Next, we visualized the early endosomal marker protein EEA1 (35). We detected a rather weak co-localization of EEA1 with $\beta 1$ integrin both, in control (EV) and HRAS^{WT} expressing cells; the size of EEA1 positive vesicles was slightly increased in HRAS^{WT} cells compared to control cells (Supplementary Material, Fig. S7). HRAS^{Gly12Ser} expression was associated with clearly enlarged or clustered EEA1-positive vesicles and partial co-localization with $\beta 1$ integrin (Supplementary Material, Fig. S7). RIN1^{-/-} HaCaT keratinocytes showed very small EEA1-positive vesicles with very weak or without $\beta 1$ integrin co-localization, which was similar to native HaCaT cells (Supplementary Material, Fig. S7). Our data suggest that HRAS^{Gly12Ser} promotes enrichment of $\beta 1$ integrin in the early endosomal compartment. In addition to HRAS-induced deregulation of $\beta 1$ and $\beta 4$ integrin, we detected decreased abundance of $\alpha 6$ and $\alpha 2$ integrins in HaCaT cells expressing HRAS^{WT} (Supplementary Material, Fig. S8A). Finally, immunofluorescence analysis revealed a strong enrichment of E-cadherin positive intracellular vesicles in HRAS^{Gly12Ser} HaCaT cells (Supplementary Material, Fig. S8B). Taken together, altered HRAS signaling may interfere with a central cellular mechanism that controls abundance and distribution of diverse cell contact and adhesion molecules.

HRAS^{Gly12Ser} affects integrin trafficking

Surface availability and activity of integrins is controlled by trafficking within a cycle of endocytosis, recycling and lysosomal degradation (24,26). We used antibody TS2/16 specific for the active conformation, applied flow cytometry (34,36) and determined the amount of active integrin both on the cell surface before internalization and in intracellular compartments after internalization. HaCaT cells stably expressing HRAS^{WT} showed

a similar relative amount of active cell surface $\beta 1$ integrin as control cells (EV) (Fig. 4A). Stable over-expression of active HRAS^{Gly12Ser} slightly but not significantly reduced the relative amount of $\beta 1$ integrin at the cell surface in both HRAS^{Gly12Ser} cell lines (1 and 2) (Fig. 4A). Quantification of intracellular $\beta 1$ integrin over time revealed strongest differences between cell clones after 15 min internalization (Supplementary Material, Fig. S9). At this point, the fraction of internalized $\beta 1$ integrin was increased by approximately 1.5-fold in HaCaT keratinocytes expressing HRAS^{Gly12Ser} vs HRAS^{WT} or control (EV) cells (Fig. 4B). These results suggest that HRAS^{Gly12Ser} affects integrin trafficking by increasing the intracellular fraction of active $\beta 1$ integrin. To discriminate if HRAS^{Gly12Ser} stimulates endocytosis or impairs recycling of $\beta 1$ integrin, we performed internalization assays in the presence of the recycling inhibitor primaquine (37). Upon 15 min internalization, the amount of intracellular $\beta 1$ integrin was similar in HaCaT cells expressing HRAS^{Gly12Ser}, HRAS^{WT} or control cells (Fig. 4C). These data suggest that expression of CS-associated HA-HRAS^{Gly12Ser} interferes with recycling of active integrin. Knock out of RIN1 did not affect internalized $\beta 1$ integrin level, however, cell surface level was slightly—but not significantly—increased (Supplementary Material, Fig. S10). We could support these results by immunocytochemical examination using the marker protein SNX17 (sorting nexin 17) that promotes recycling of the receptor over lysosomal degradation at early and sorting endosomes (24,26,38). Stable expression of HRAS^{Gly12Ser} resulted in increased localization of active/total $\beta 1$ integrin at SNX17-positive vesicles (Fig. 4D, Supplementary Material, Fig. S11A). Knockout of RIN1 had no effect on this localization (Supplementary Material, Fig. S11B). Inactive $\beta 1$ integrins are rapidly recycled in a RAB4-dependent manner, whereas active receptors are trafficked through the RAB11 long-loop pathway (26). Expression of HRAS^{Gly12Ser} had no significant effect on the distribution of active/total integrin at RAB4-positive vesicles (Supplementary Material, Fig. S12A) and slightly increased localization of active $\beta 1$ integrin at RAB11-positive vesicles (Supplementary Material, Fig. S12B). RIN1-deficient cells showed an increased number of RAB4-positive vesicles without $\beta 1$ integrin co-localization (Supplementary Material, Fig. S12C). Taken together, our data suggest that CS-associated HRAS^{Gly12Ser} enriches $\beta 1$ integrin in the endosomal compartment on the cost of surface integrin. In line with this, visualization of RAB7, a marker for late endosomes, showed enhanced co-localization with total $\beta 1$ integrin in HRAS^{Gly12Ser} cells (Supplementary Material, Fig. S13). In contrast, by using lysosomal marker LAMP1 we detected no co-localization with $\beta 1$ integrin in these cells (Supplementary Material, Fig. S14). We conclude that over-expression of HRAS^{Gly12Ser} disturbs the balance between cell surface and intracellular $\beta 1$ integrin pools in HaCaT keratinocytes and HRAS-RIN1 signaling regulates $\beta 1$ integrin availability at the cell surface.

HRAS-RIN1 signaling controls HaCaT keratinocyte spreading on fibronectin

Integrin trafficking is directly implicated in the regulation of cell spreading and cell migration (24,39). We studied the consequences of HRAS-RIN1 signaling on spreading of HaCaT cells on fibronectin-coated coverslips. Cells expressing HRAS^{WT} or HRAS^{Gly12Ser} showed significantly fewer cell protrusions (i.e. filopodia) and a general decreased spreading ability compared to EV transfected cells (Fig. 5A). HaCaT cells deficient for RIN1 are rich of actin bundles, spread very quickly, and were significantly larger compared to native HaCaT cells (Fig. 5B). These findings

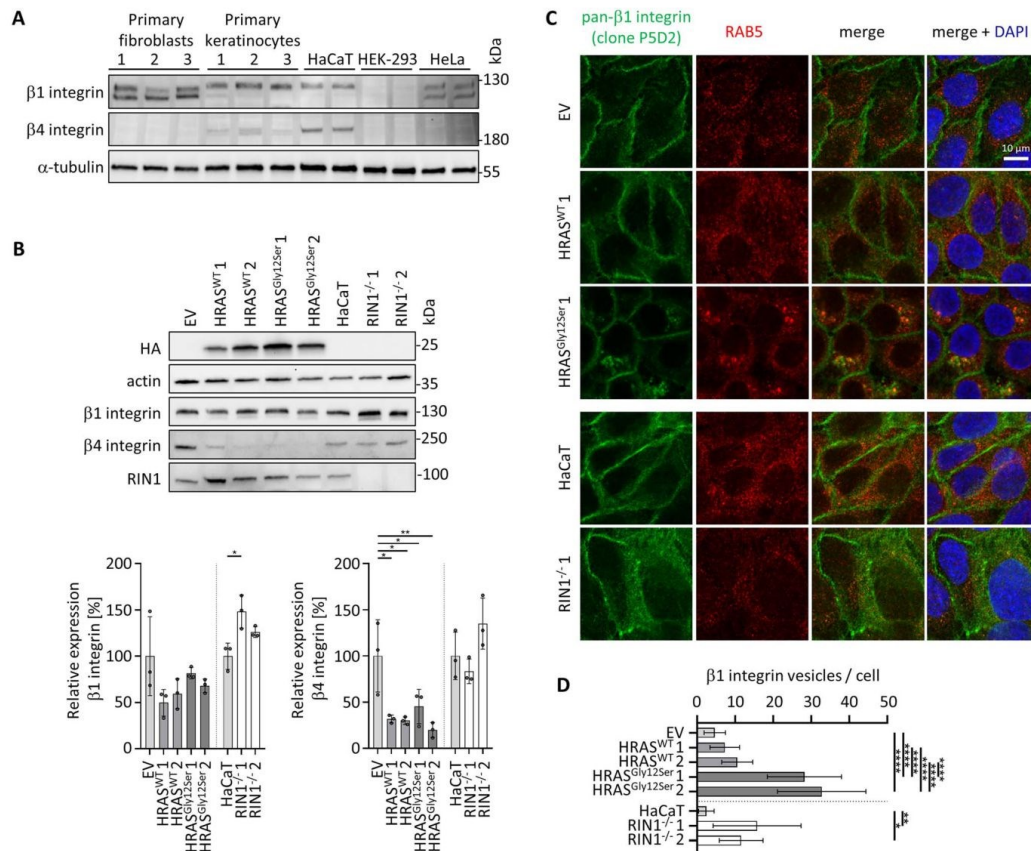


Figure 3. HRAS-RIN1 signaling controls expression and localization of integrins. (A) Primary and HaCaT keratinocytes express β1 and β4 integrin. TCLs of primary fibroblasts, primary keratinocytes, HaCaT keratinocytes, HEK-293 cells and HeLa cells were subjected to immunoblotting as indicated. Both, mature (upper band) and precursor (lower band) β1 integrin were detected. α-tubulin was used as loading control. (B) HRAS-RIN1 signaling modulates expression of integrins. TCLs of HaCaT keratinocytes stably expressing HA-HRAS variants, EV-controls, native HaCaT cells and RIN1-deficient cells were subjected to immunoblotting as indicated. Graphs show the mean (± SD) of β1 (left) and β4 (right) integrin levels from three independent experiments relative to EV and HaCaT cells. One-way ANOVA, Tukey's multiple comparison test, $P < 0.05$ was used. (C) β1 integrin is enriched in RAB5-positive vesicles in cells expressing HA-HRAS^{Gly12Ser}. HaCaT cells were plated on coverslips, fixed and Rab5 was stained by mouse anti-Rab5 antibody followed by anti-mouse Alexa Fluor 568-conjugated antibody. After blocking, cells were stained by directly conjugated mouse β1 integrin P5D2-Alexa 488. Nuclear DNA was labeled by DAPI. Scale 10 μm. $n = 3$. (D) β1 integrin positive vesicles are increased in HA-HRAS^{Gly12Ser} HaCaT keratinocytes. HaCaT keratinocytes stably expressing HRAS^{WT}, HRAS^{Gly12Ser} or EV-controls, as well as native HaCaT cells and RIN1-deficient cells were stained for β1 integrin. Microscopic images were analyzed for β1 integrin positive intracellular vesicles with Imaris as described in the methods section. Graph shows mean numbers of β1 integrin positive vesicles per cell (± SD) from 3–5 independent experiments. One-way ANOVA, Tukey's multiple comparison test, $P < 0.05$ was used.

suggest that HRAS-RIN1 signaling is a key pathway to control cell spreading.

Discussion

The epidermal manifestation in patients with CS raises the question on the functional impact of CS-associated HRAS variants in keratinocytes, the major cell type in the human skin. We report here for the first time on the crucial function of HRAS-RIN1 signaling in endocytic sorting of integrin receptors in immortalized epidermal HaCaT keratinocytes. Expression of the CS-typical HRAS variant p.Gly12Ser essentially affected integrin trafficking, suggesting a role of altered integrin availability in the pathogenesis of the epidermal manifestation in CS. In line with this, β1

integrin dysfunction has been associated with CS-typical epidermal manifestations including epidermal thickening, prematurely aged skin, keratosis and papillomata as well hair abnormalities (for details see Supplementary Material, Results and Discussion) (40–45).

HRAS-RIN1 signaling in HaCaT keratinocytes

We showed that the previously less perceived HRAS effector RIN1 is strongly expressed both in permanent and primary keratinocytes and greatly enriched in HRAS^{Gly12Ser} precipitates. RIN1 binds with high affinity and specificity to activated HRAS (6,13,46). Similarly, we found a high binding affinity of RIN1 with HRAS^{Gly12Ser}. It has been demonstrated that RIN1 efficiently competed with RAF1 for binding to activated RAS *in vitro* (13).

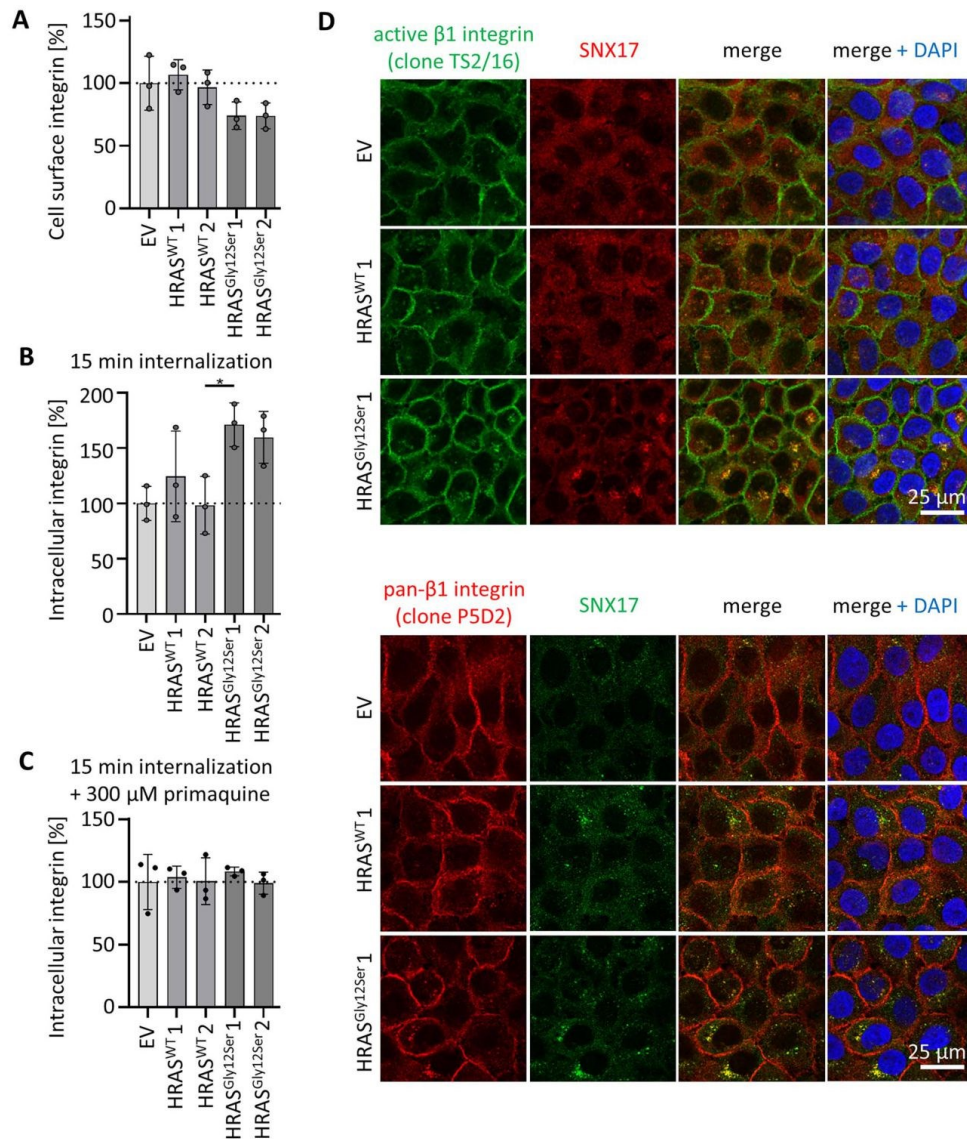


Figure 4. (A–C) HRAS^{Gly12Ser} interferes with integrin trafficking. Cells were starved, incubated on ice, labeled with antibodies against active $\beta 1$ integrin (TS2/16-Alexa Fluor 488) and further processed as described in methods. Graphs show the mean (\pm SD) amounts of $\beta 1$ integrin on the cell surface before internalization (A), intracellular $\beta 1$ integrin after 15 min internalization (B) and intracellular $\beta 1$ integrin after 15 min internalization in the presence of primaquine (C) from three independent experiments each ($n = 3$). After internalization, remaining fluorescence on the cell surface was quenched by acidic wash treatment and fluorescence intensities of internalized $\beta 1$ integrin (B and C) were normalized against total cell surface fluorescence intensities from (A). Fluorescent intensities of EV-transfected control cells were considered as 100%. P values were calculated by one-way ANOVA with Tukey's multiple comparison test ($P < 0.05$). (D) $\beta 1$ integrin is enriched at SNX17-positive vesicles in HaCaT keratinocytes expressing HA-HRAS^{Gly12Ser}. HaCaT cells stably expressing HA-HRAS variants or transfected with EV were seeded on coverslips, fixed and stained with rabbit anti-SNX17 antibody followed by anti-rabbit Alexa Fluor 568 (red) and Alexa Fluor 488-conjugated mouse anti $\beta 1$ integrin TS2/16 (green) antibodies (upper part of the figure). To visualize total $\beta 1$ integrin, cells were stained with mouse anti- $\beta 1$ integrin (clone P5D2) and rabbit anti-SNX17 antibody followed by anti-mouse Alexa Fluor 568 (red) and anti-rabbit Alexa Fluor 488 (green) antibodies. Nuclear DNA was labeled by DAPI. Scale 25 μ m. $n = 3$.

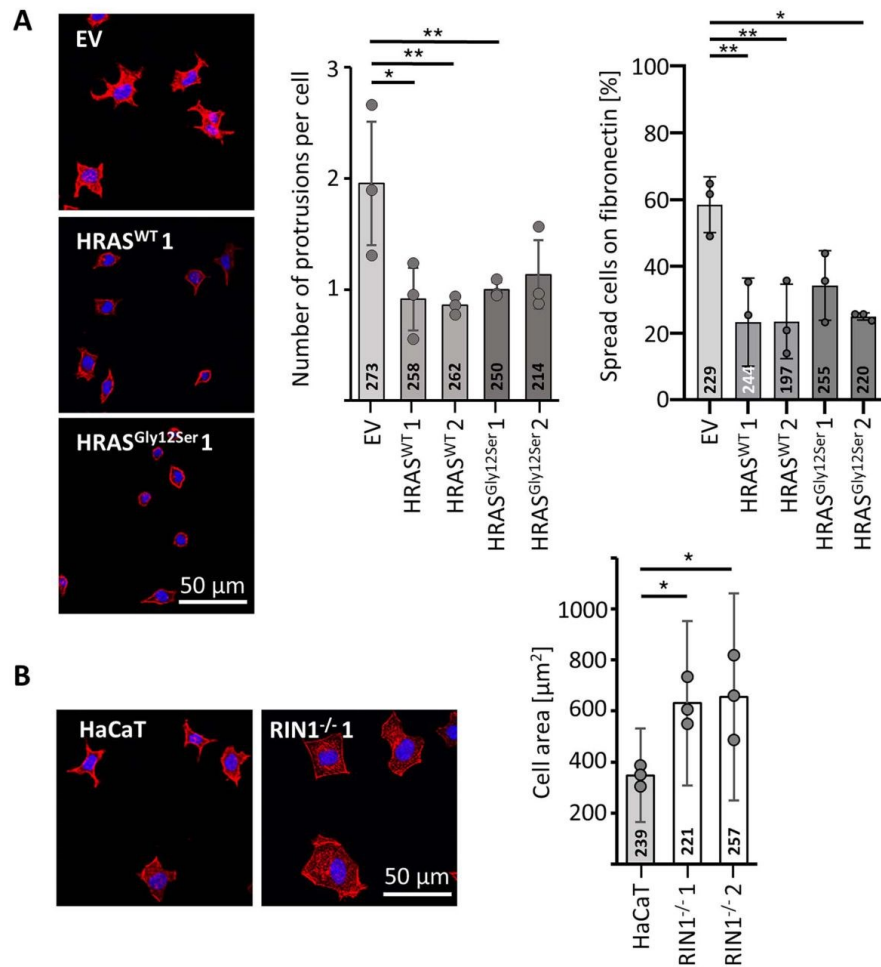


Figure 5. HRAS-RIN1 signaling controls spreading of HaCaT keratinocytes on fibronectin (FN). HaCaT cells stably expressing HA-HRAS variants, EV-controls, native HaCaT cells and RIN1-deficient cells were starved and plated on FN-coated coverslips. After 60 min, cells were fixed and F-actin was stained by using Texas Red-phalloidin. Nuclear DNA was labeled by DAPI. Scale 50 μm . **(A)** Expression of HRAS^{WT} or HRAS^{Gly12Ser} inhibits protrusion formation and spreading. The number of cell protrusions was counted by microscopic analysis of EV transfected and HRAS variant expressing cells. Representative pictures of cells during spreading are given. The left graph shows the mean number (\pm SD) of actin protrusions per cell (left graph) determined in three independent experiments. The right graph shows the mean number (\pm SD) of spread cells from three independent experiments. The exact numbers of analyzed cells are given. One-way ANOVA, Tukey's multiple comparison test, $P < 0.05$. **(B)** Knockout of RIN1 promotes cell spreading. Cells were visualized by microscopy and cell areas were measured by using ImageJ. Representative pictures of spreading cells are given. The graph shows the mean areas (\pm SD) of >200 spread cells determined in three independent experiments each. One-way ANOVA, Tukey's multiple comparison test, $P < 0.05$.

In HaCaT keratinocytes, however, RAF1 was expressed at low levels suggesting that RAF1 is a rather minor competitor of RIN1 in this cell type. Accordingly, RAF-MAPK signaling was only marginally altered by expression of active HRAS^{Gly12Ser} in HaCaT cells. This is in contrast to data from neuronal cells or fibroblasts, in which RAS-RAF kinase signaling was significantly altered by CS-associated HRAS variants (15–17). A particular relevance of the HRAS-RIN1 signaling axis has been demonstrated in neuronal cells, mammary epithelial cells, mouse fibroblasts and in various heterologous cell lines, such as HeLa, HEK293T, NIH3T3 and A549 cells (7,8,10,11,31,47–49). Briefly, binding of active HRAS to RIN1

promotes the activation of RAB5 GTPases (7) and ABL1/2 tyrosine kinases (8). In line with these previous data, we found that HRAS and RIN1 control RAB5- and ABL kinase-dependent signaling in HaCaT cells. Taken together, our results suggest that RIN1 is a major HRAS effector in epidermal keratinocytes.

HRAS-RIN1 signaling in integrin trafficking

A function of RIN1 in the regulation of endocytic trafficking is well established: RIN1 stimulates ligand-induced receptor internalization in fibroblasts, epithelial cells and cancer cells (7,10–12,31,50–52). Moreover, RIN1 has strong impact on endosome

morphology and endosome fusion (7,12,53–55). On the other hand, an involvement of RIN1 in endocytic sorting of integrin receptors has not yet been described in any cell type. A role of HRAS as a regulator of endocytic sorting has not gained much attention to date.

Here, we show that HRAS-RIN1 signaling controls integrin trafficking and, therefore, the availability of integrins on the cell surface of epidermal HaCaT keratinocytes, a cell type that upkeeps a potent and tightly controlled integrin trafficking machinery (23,24). Based on our results we suggest that activation of HRAS-RIN1 signaling enhances the intracellular $\beta 1$ integrin fraction at the expense of surface $\beta 1$ integrin (for an overview of relevant results, see Supplementary Material, Table S2). In line with this, most of available data indicate that HRAS-RIN1 signaling increases the intracellular fraction of cell surface receptors (10,31,50,51).

There are significant data on the HRAS homologues GTPase RRAS and its involvement in integrin regulation (56). Previous overexpression studies showed that RRAS promotes endocytosis, spatio-temporal clustering and recycling of $\beta 1$ integrin (57). Moreover, it was demonstrated that RRAS induces active $\beta 1$ integrin endocytosis depending on RIN2 and RAB5 (58). Our data suggest a different function for HRAS-RIN1 signaling in integrin trafficking; activation of this cascade promotes intracellular enrichment of $\beta 1$ integrin by acting on trafficking between different endosomal compartments because: First, active/total $\beta 1$ integrin was enriched in SNX17-positive vesicles in cells expressing HRAS^{Gly12Ser} (Supplementary Material, Table S2); SNX17 promotes receptor recycling over lysosomal degradation at early and sorting endosomes (24,26,38). In this context, it has previously been shown, that HRAS forms a complex with SNX17 (59), supporting a role of HRAS-RIN1 at early and sorting endosomes. And second, we detected increased levels of active/total $\beta 1$ integrin in RAB7-positive vesicles (late endosomes) but not in lysosomes of cells overexpressing HRAS^{Gly12Ser} (Supplementary Material, Table S2). Based on the postulated function of RRAS as a positive regulator of $\beta 1$ integrin endocytosis and recycling and, thereby enhancement of integrin function in cell adhesion and spreading (57), we suggest a complementary function for HRAS. The latter rather holds back $\beta 1$ integrin in the endosomal compartment and thus decreases its surface availability. In line with this, HRAS and RRAS have been reported to play opposite and counteracting roles in integrin-mediated adhesion in some cell types (60).

The function of HRAS in the epidermis

The epidermal manifestation in patients with CS (1,2) proves a critical function of HRAS signaling in epidermal development and/or homeostasis. Mice expressing an activated HRAS^{Gly12Val} transgene showed aberrant $\beta 1$ and $\beta 4$ integrin expression and developed massive hyperplastic skin papillomas at sites of wounding (61–63). RAS function in epidermal homeostasis has mainly been attributed to RAF-MAP kinase and PI3 kinase signaling (21,22,63). Here, we put forward the HRAS-RIN1 signaling axis that regulates the expression and/or distribution of integrin receptors. Integrins underlie the ability of keratinocytes for adhesion to the ECM (23–25,39) and an altered cellular distribution of integrin is in well agreement with affected cell adhesion. In line with this, we show that expression of HRAS^{Gly12Ser} affects HaCaT keratinocyte spreading on fibronectin. Notably, overexpression of wild-type HRAS (HRAS^{WT}) is also sufficient to induce the observed effects on HaCaT keratinocyte adhesion, suggesting a dose effect in this specific cellular context. Finally, knockout of RIN1 resulted in an overspread HaCaT cell phenotype. We conclude that

HRAS-RIN signaling likely controls cell adhesion by acting on integrin availability.

In addition to dysregulated $\beta 1$ integrin that is core constituent of focal adhesions (20,23,25), we detected reduced levels of $\beta 4$ integrin in HaCaT keratinocytes over-expressing HRAS^{WT} or HRAS^{Gly12Ser}. Together with $\alpha 6$ integrin, $\beta 4$ integrin forms the central core of the hemidesmosome (23). Available data suggest that dysregulation of $\beta 4$ integrin results in defective basement membrane adhesion and migration deficits (for details see Supplementary Material, Results and Discussion) (20,25). Since $\beta 4$ integrin, similar to $\beta 1$ integrin, is sorted via endosomal compartments (64,65), it is plausible, that trafficking defects may affect the cellular distribution and/or amount of $\beta 4$ integrin. Moreover, we detected altered expression or distribution of other contact and adhesion molecules in cells overexpressing HRAS^{WT} or HRAS^{Gly12Ser} (for details see Supplementary Material, Discussion). Taken together we suggest that HRAS controls subcellular distribution and availability of various contact and adhesion proteins in keratinocytes.

Integrin-mediated adhesion and spreading results in intracellular reactive oxygen species (ROS) production and modulation of various signaling pathways (66–69). *Vice versa*, intracellular ROS levels have an effect on integrin mediated signaling and thereby influence cell adhesion and migration (70). Oncogenic RAS proteins also promote the generation of ROS, which in turn modulate multiple signaling pathways (71,72). Accordingly, primary fibroblasts from subjects with CS showed increased levels of ROS resulting in enhanced AMP-activated protein kinase α (AMPK α) and p38 activation as well as dysregulated energetic metabolism (73). In conclusion, HRAS^{Gly12Ser}-associated defects in integrin trafficking, as we describe in our study for HaCaT keratinocytes, as well as increased ROS levels, as shown in CS fibroblasts (73), may conjointly contribute to specific cellular pathophysiological features, such as adhesion and migration deficits.

Dysregulated endosomal sorting is a novel pathomechanism in RASopathies

CS belongs to the RASopathies, a group of disorders caused by germline variants in genes encoding components or regulators of RAS signaling pathways. Mostly gain-of function or hyperactivation of the RAS-MAPK pathway is cited to explain the molecular consequences of pathogenic variants. Our data point to a novel aspect in the molecular pathogenesis of RASopathies as we describe HRAS-RIN1 as regulatory signaling axis for (integrin) trafficking in HaCaT keratinocytes. Defective endocytic sorting of receptors, i.e. EGFR and glutamate receptors, has been already proposed and demonstrated as a pathomechanistic basis for Noonan syndrome related phenotypes (74–76). In analogy, bi-allelic pathogenic variants in RIN2, an ubiquitously expressed protein that interacts with RAB5 and is involved in the regulation of endocytic trafficking, cause a syndromic disorder characterized by a significant skin manifestation (77). In conclusion, altered endosomal sorting of cell surface receptors may explain certain epidermal manifestations in various RASopathies and related disorders.

Limitations

This study also has limitations. As a cellular model, we used HaCaT cells that is a spontaneously immortalized epithelial cell line with loss-of-function variants in tumor protein p53 (TP53) (78,79). TP53 is involved in the regulation of keratinocyte homeostasis (growth, differentiation and senescence) (80), thus, it

cannot be excluded that the loss of TP53 influences experimental results in HaCaT cells.

Materials and Methods

Cell culture

The HaCaT keratinocyte cell line is a spontaneously immortalized and non-tumorigenic cell line that maintains typical characteristics of keratinocytes and is widely used for *in vitro* skin models (81). HaCaT cells were cultured in Dulbecco's Modified Eagle Medium (DMEM; Gibco, Thermo Fisher Scientific, Inc., Waltham, MA, USA) containing 10% serum (Sigma-Aldrich, Merck, Darmstadt, Germany) and penicillin-streptomycin (100 U/ml and 100 mg/ml, respectively) (Sigma-Aldrich) at 37°C and 5% CO₂. Human primary keratinocytes were freshly isolated from juvenile foreskin as previously reported (82). Briefly, foreskin tissue was cut into small pieces, which were incubated in trypsin solution (0.25% v/v in phosphate buffered saline, Merck) to separate epidermis and dermis. Mechanical dissociation of the epidermal layer produced a suspension of keratinocytes that were cultivated for 5 days at 37°C and 5% CO₂ in serum-free EpiLife medium (Life Technologies, Thermo Fisher Scientific). Primary fibroblasts obtained from skin biopsies of three juvenile individuals were cultured in DMEM (Gibco, Thermo Fisher Scientific) supplemented with 10% fetal bovine serum (GE Healthcare, Chalfont St Giles, UK) and penicillin-streptomycin (100 U/ml and 100 mg/ml, respectively; ThermoFisher).

Generation of stable cell lines

The coding sequences of HA-tagged HRAS^{WT} (GenBank accession number NM_005343.4) and the HRAS mutants c.34G>A (p.Gly12Ser) and c.35G>T (p.Gly12Val) were sub-cloned into pcDNA 3.2-DEST Mammalian Expression Vector (Thermo Fisher Scientific). HaCaT cells were transfected by electroporation using the Neon transfection system (Thermo Fisher Scientific) according to the manufacturer's instructions (pulse voltage 1600 V; pulse width 10 ms; pulse number 3). Cells were selected with 500 µg/ml Geneticin (Gibco, Thermo Fisher Scientific) according to the manufacturer's instructions. Cells were single cell sorted by fluorescence activated cell sorting (FACS) (FACS Aria III; BD Biosciences, San Jose, CA, USA) and single cell clones were analyzed for expression.

Generation of RIN1 knockout cells

Two specific crRNAs targeting RIN1 (Design ID: Hs.Cas9.RIN1.1.AA: CATTGGGCACGTACATACAGT; Hs.Cas9.RIN1.1.AC: CAGATGAGCTG-GACTAGTGC), the tracrRNA and Cas9 protein were synthesized by Integrated DNA Technologies (IDT, Inc.; Iowa, USA). The assembly of the ribonucleoprotein (RNP) complex and the delivery by Neon electroporation system (Thermo Fisher Scientific) were performed according to the manufacturers' instructions. Briefly, crRNA and tracrRNA were hybridized at the same molar ratios in IDT duplex buffer (30 mM HEPES, pH 7.5; 100 mM potassium acetate) at 95°C for 5 min and were allowed to slowly cool to 20°C. To generate Cas9 RNPs, Cas9 protein and RNAs duplex (crRNA:tracrRNA) were incubated in Resuspension Buffer R (from Neon System Kit) for 20 min at room temperature. 5 × 10⁵ HaCaT cells were resuspended in Resuspension Buffer R and RNPs were added. Electroporation was performed with a 10 µL Neon System Kit (pulse voltage 1600 V, pulse width 10 ms, pulse number 3). Cells were grown under normal conditions, single cell sorted into 96 well plates using FACS sorter (FACS Aria III; BD Biosciences) and analyzed for RIN1 knockout clones by immunoblotting.

Sample preparation for proteomics

In-gel digestion was done following established protocols (83). Shrinking and swelling was performed with 100% acetonitrile (ACN) and 100 mM NH₄HCO₃. In-gel reduction was achieved with 10 mM dithiothreitol (dissolved in 100 mM NH₄HCO₃). Alkylation was performed with 55 mM iodoacetamide (dissolved in 100 mM NH₄HCO₃). Proteins in the gel pieces were digested by covering them with a trypsin solution (8 ng/µl sequencing-grade trypsin, dissolved in 50 mM NH₄HCO₃ containing 10% ACN) and incubating the mixture at 37°C for overnight. Tryptic peptides were yielded by extraction with 2% formic acid (FA), 80% ACN. The extract was evaporated. For liquid chromatography-mass spectrometry (LC-MS/MS) analysis, samples were dissolved in 20 µL 0.1% FA.

Differential quantitative proteomics

Chromatographic separation of peptides was achieved by nano ultra-performance liquid chromatography (UPLC, nanoAcquity system, Waters, Milford, MA, USA) with a two-buffer system (buffer A: 0.1% FA in water, buffer B: 0.1% FA in ACN). Attached to the UPLC was a peptide trap (180 µm × 20 mm, 100 Å pore size, 5 µm particle size, Symmetry C18, Waters) for online desalting and purification followed by a 25-cm C18 reversed-phase column (75 µm × 200 mm, 130 Å pore size, 1.7 µm particle size, Peptide BEH C18, Waters). Peptides were separated using an 80-min gradient with linearly increasing ACN concentration from 2% to 30% ACN in 65 minutes. The eluting peptides were analyzed on a Quadrupole Orbitrap hybrid mass spectrometer (QExactive, Thermo Fisher Scientific). Here, the ions being responsible for the 12 highest signal intensities per precursor scan (1 × 10⁶ ions, 70 000 Resolution, 240 ms fill time) were analyzed by MS/MS (higher-energy collisional dissociation (HCD) at 25 normalized collision energy, 1 × 10⁵ ions, 17 500 resolution, 50 ms fill time) in a range of 400–1200 m/z. A dynamic precursor exclusion of 20 s was used.

LC-MS/MS data were searched with the Sequest algorithm integrated in the Proteome Discoverer software (v 2.41.15, Thermo Fisher Scientific) against a reviewed human Swissprot database, obtained in April 2020, containing 20 365 entries. Carbamidomethylation was set as fixed modification for cysteine residues and the oxidation of methionine, and pyro-glutamate formation at glutamine residues at the peptide N-terminus, as well as acetylation of the protein N-terminus were allowed as variable modifications. A maximum number of 2 missing tryptic cleavages was set. Peptides between 6 and 144 amino acids were considered. A strict cutoff (false discovery rate (FDR) < 0.01) was set for peptide and protein identification.

Constructs, recombinant proteins and nucleotide loading

pGEX vectors were used for bacterial overexpression of RIN1 [GEF-RA] (amino acids 293–716) variants (wild-type and p.Glu574Ala), full length variants of HRAS [wild-type, c.34G>A (p.Gly12Ser), c.38_39delG/CinsAA (p.Gly13Glu) and c.50G>A (p.Ser17Asn)] and full length RAB5A. Proteins were isolated as glutathione S-transferase (GST) fusion proteins in *Escherichia coli* BL21 (DE3) and purified after cleavage of the GST tag via gel filtration (Superdex 75 or 200; GE Healthcare). Nucleotide-free and fluorescent nucleotide-bound proteins (RAB5A and HRAS) were prepared using alkaline phosphatase (Roche, Basel, Switzerland) and phosphodiesterase (Sigma-Aldrich) at 4°C. Methylanthraniloyl

(mant-) GppNHp (guanosine 5'- β , γ -imidotriphosphate), a non-hydrolysable GTP analog and methylantraniloyl (mant-) dGDP (deoxyguanosine-5'-diphosphate) were used as fluorescent nucleotides. The mant-GppNHp content of each labeled protein was determined by HPLC using a buffer containing 20–25% acetonitrile. All proteins were analyzed by sodium dodecyl-sulfate polyacrylamide gel electrophoresis (SDS-PAGE) and stored at -80°C .

Fluorescence polarization

Increasing amounts of RIN1[RA] were titrated to mantGppNHp-bound HRAS proteins (1 μM) in a buffer, containing 30 mM Tris/HCl (pH 7.5), 150 mM NaCl, 5 mM MgCl₂, 3 mM dithiothreitol and a total volume of 200 μL at 25°C . For excitation, wavelength of 362 nm (slit width: 8 micron) was used for the mant fluorophore and 450 nm was used for emission (slit width: 10 micron). The dissociation constants (K_d) were calculated by fitting the concentration-dependent binding curve using a quadratic ligand-binding equation. Fluorescence experiments were performed in a Fluoromax 4 fluorimeter in polarization mode.

Fluorimeter measurements

Guanine nucleotide exchange reactions were performed with a Fluoromax 4 fluorimeter instrument. The excitation and emission wavelengths for mant-deoxy-GDP were 360 nm and 450 nm, respectively. For nucleotide exchange reactions, 1 μM mant-deoxy-GDP RAB5A, 100 μM GDP, 10 μM RIN1 [GEF-RA] and 1 μM GppNHp-bound HRAS were used in 200 μL of measurement buffer containing 30 mM Tris/HCl, pH 7.5, 10 mM K₂HPO₄/KH₂PO₄, 2 mM MgCl₂ and 3 mM dithiothreitol at 25°C .

GTPase pull down assay

The RAS-association (RA) domains of RIN1 (amino acids 624–716) was used to specifically pull down GTP-bound HRAS from cell extracts. Preparation of GST-RA beads, cell lysis and precipitation of GTP-bound GTPases have been described previously (14).

(Co-)Immunoprecipitation

Cells were washed and scraped off in ice-cold PBS. Cell pellets were lysed on ice for 60 min in ice-cold co-immunoprecipitation buffer (50 mM Tris-HCl pH 8.0, 120 mM NaCl, 0.5% Nonidet P40, supplemented with complete Mini Protease Inhibitors and PhosStop (Roche)) and clarified by centrifugation (14 000 rpm, 15 min, 4°C). After removing small aliquots (total cell lysates – TCL), supernatants were incubated with 20 μL Pierce Anti-HA magnetic beads (#88836, Thermo Fisher Scientific) at 4°C with rotation for 60 min. Beads were magnetically separated from cell lysates and subsequently washed (3x) with Co-IP-buffer by rotation for 3 min at room temperature. After final wash, beads were supplemented with sample buffer, heated to 95°C and precipitated proteins were subjected to SDS-PAGE and immunoblotting or to sample preparation for proteomics.

Immunoblotting and antibodies

Cells were cultured as specified, washed with PBS and scraped off in ice-cold PBS. Cell pellets were lysed on ice for 60 min with cell lysis buffer (50 mM Tris-HCl, pH 8.0; 150 mM NaCl; 1% Nonidet P-40; supplemented with complete Mini Protease Inhibitors

and PhosStop (Roche)). Cell lysates were clarified by centrifugation (14 000 rpm, 15 min, 4°C) and supernatants were supplemented with sample buffer. Proteins were separated on SDS-polyacrylamide gels and transferred to PVDF membranes. Following blocking (20 mM Tris-HCl, pH 7.4; 150 mM NaCl; 0.1% Tween-20; 5% non-fat dry milk) and washing (20 mM Tris-HCl, pH 7.4; 150 mM NaCl; 0.1% Tween-20), membranes were incubated in primary antibody solution (20 mM Tris-HCl, pH 7.4; 150 mM NaCl; 0.1% Tween-20; 5% BSA or 5% non-fat dry milk) containing the appropriate antibodies. Rabbit polyclonal antibodies against RIN1 (Thermo Fisher Scientific; PA5-57292, 1:1000/Sigma; HPA035491 1:1000), PI3K (Upstate Biotechnology Inc., Thermo Fisher Scientific; 06-195, 1:1000), PLCE1 (Abnova Ltd, Biozol, Cambridge, UK; abx147622, 1:1000), RAF-1 (Santa Cruz Biotechnology Inc., Dallas, Texas, USA; sc-7267, 1:200), RALGDS (Thermo Fisher Scientific; PA5-49099, 1:1000), MEK1/2 (Cell Signaling Tech., Danvers, MA; no. 9122; 1:1000), phospho-MEK1/2 (Ser217/221) (Cell Signaling Tech.; no. 9121; 1:1000), p44/42 MAP kinase (ERK1/2) (Cell Signaling Tech.; no. 9102, 1:1000), phospho-p44/42 MAP kinase (ERK1/2) (Thr202/Tyr204) (Cell Signaling Tech.; no. 9101, 1:1000), Akt1/2/3 (Cell Signaling Tech.; no. 9272; 1:1000), phospho-Akt1/2/3 (Ser473) (Cell Signaling Tech.; no. 9271; 1:1000), HRAS (Proteintech; 18 295-1-AP, 1:1000), actin (Sigma; A5060, 1:250), c-ABL (Cell signaling; 2862, 1:1000), and p-CrkII Tyr221 (Cell signaling; 3491, 1:1000) as well as rabbit monoclonal phospho-RIN1 antibodies (abcam; ab172976, [EPR2734(2)] phospho Ser351, 1:1000) were used. Mouse monoclonal antibodies against α -Tubulin (Sigma-Aldrich; clone DM1A, T9026 1: 3000), GAPDH (abcam, Cambridge, UK; ab8245, 1:10 000), CD29 β 1 integrin (BD; 610467, 1:500), CD104 β 4 integrin (BD; 611233; 1:500), RAB5 (BD; 610724, 1:500) were applied. Rat monoclonal HA-HRP (Roche; 12 013 819 001, 1:10 000) was used to detect HA-HRAS. Membranes were washed and incubated with secondary horseradish peroxidase (HRP)-coupled anti-rabbit (NA934V) and anti-mouse (NA931V) antibodies (GE Healthcare; 1: 7500) or with goat anti-mouse IgG StarBright Blue 700 Fluorophore antibodies (BioRad; 12 004 159, 1:10 000). After final washing, proteins were visualized using the ChemiDoc MP Imaging System (Bio-Rad Laboratories, Inc.; Hercules, CA, USA). Data shown are representative of three independent experiments.

Immunocytochemistry and antibodies

HaCaT cells were seeded on coverslips (300 000 cells/3.5 cm²) and cultivated overnight. For transient expression of RAB4 (pEGFP-C1 Rab4B WT), RAB7 (pmEGFP-C1 Rab7a WT), RAB11 (pmEGFP-C1 RAB11A WT), LAMP1 (plasmid RFP-LAMP1, addgene #1817) and EV RFP-N1 (control), cells were transfected with jetOPTIMUS (1:1.25) for 24 h according to manufacturer's protocol (Polyplus transfection, Illkirch, France). Subsequently, cells were rinsed with PBS, fixed with 4% paraformaldehyde (Sigma-Aldrich) in PBS and washed three times with PBS. After treatment with permeabilization/blocking solution (2% BSA, 3% goat serum, 0.5% Nonidet P40 in PBS), cells were incubated in antibody solution (3% goat serum and 0.1% Nonidet P40 in PBS) containing appropriate primary antibodies: Alexa Fluor 488 or unconjugated mouse monoclonal β 1 integrin antibody clone P5D2 (abcam; total β 1 integrin; ab193591/ab24693, 1:200); Alexa Fluor 488 or unconjugated mouse monoclonal β 1 integrin clone TS2/16 (Santa Cruz Biotechnology; active β 1 integrin, TS2/16, sc-53711, 1:100); mouse monoclonal RAB5 antibody (BD Biosciences; 610724, 1:100); rabbit monoclonal anti-RAB5 antibody (cell signaling Tech., 3547, 1:100); rabbit monoclonal EEA1 (Cell Signaling Tech.; 3288S, 1:100); rabbit polyclonal SNX17 antibody (Novus Biologicals; NBP1-92417, 1:100); rabbit monoclonal E-cadherin antibody

(abcam; ab40772 [EP700Y], 1:250). Cells were washed with PBS and incubated with Fluorophore-conjugated secondary goat anti-mouse Alexa Fluor488 antibody, Alexa Fluor568 antibody or Texas Red-X phalloidin (Life Technologies,) in antibody solution. After extensive washing with PBS, cells were embedded in ProLong Diamond Antifade Mountant with DAPI (P36962, Life Technologies). Fixed samples were analyzed with Zeiss Axiovert 200 M with ApoTome for structured illumination (63x Plan-Apochromat Oil DIC, NA 1.4; Carl Zeiss Microscopy, Jena, Germany) and confocal laser scanning microscopes (Leica TCS SP5/SP8, 63x HC PL APO Oil CS2, NA 1.4; Leica Microsystems, Wetzlar, Germany) were used for image acquisition, respectively. Confocal images of $\beta 1$ integrin labeled HaCaT keratinocytes were analyzed for intracellular vesicles using Imaris (v7.6.1, Oxford Instruments, Abingdon, UK). After background subtraction, relevant vesicles were identified applying an automatic threshold based segmentation algorithm (i.e. surface tool), followed by a sphericity filter (sphericity parameter ≥ 0.87) on the segmented objects.

Antibody-based integrin internalization assay

Cells were kept under serum-deprived conditions (0.1% serum) for 2–3 h and harvested with StemProAccutase (Thermo Fisher Scientific). Cells were incubated on ice and cell surface $\beta 1$ integrins were stained with directly conjugated antibody clone TS2/16-Alexa Fluor 488 (detects the active conformation of $\beta 1$ integrin, sc-53711 AF488, Santa Cruz Biotechnology) or isotype control mouse IgG1, κ (14-4714-82, Invitrogen) diluted 1:100 in FACS-buffer (PBS containing 0.5% BSA and 2 mM EDTA) for 60 min at 4°C and rotation. After 1 h cells were washed twice with FACS-buffer. To start integrin internalization, cells were incubated in pre-warmed media (0.1% serum/DMEM) at 37°C for 15, 30 or 60 min. After internalization, cells were immediately transferred on ice and cooled down. The remaining cell surface bound antibody was removed by acidic wash buffer (0.2 M acetic acid, 0.5 M NaCl, pH 2.2) in three washing steps (3 min each), followed by neutralization with 0.3% BSA/DMEM. In parallel, antibody treated cells were left on ice (0 min internalization) as a control for endocytosis. Controls and isotype controls confirmed functionality and antibody specificity of the internalization assay (data not shown). To measure the total amount of cell surface integrin stained by the $\beta 1$ integrin antibody, cells were left on ice without acid wash. Fluorescent intensities of total cell surface and internalized $\beta 1$ integrin of 20000 cells per condition were measured with FACS Canto II (BD Biosciences). Viable, single cells were gated by forward scatter (FSC) and side scatter (SSC) dot blot (Flowing Software by Perttu Terho, Turku Centre for Biotechnology, Finland). Fluorescence intensities of internalized $\beta 1$ integrin were normalized against total cell surface fluorescence intensities. Relative fluorescent intensities of HaCaT/EV and HaCaT control cells were considered as 100%. To inhibit integrin recycling, cells were treated with 300 μ M primaquine during 15 min internalization.

Analysis of cell spreading and protrusion numbers

Cells were kept under serum-deprived conditions (0.1% serum) over-night and then seeded on fibronectin-coated coverslips. Beforehand, coverslips were coated with 10 μ g/ml fibronectin (F2006, Sigma) in PBS over night at 4°C, washed with PBS and blocked in 1% BSA/PBS for 60 min at 37°C. Cells were harvested with StemProAccutase (Thermo Fisher Scientific), washed with PBS, and seeded in DMEM/0.3% BSA. After 1 h at 37°C, samples were fixed with 4% PFA for 10 min at room temperature and subsequently treated with permeabilization/blocking solution

(2% BSA, 3% goat serum, 0.5% Nonidet P40 in PBS), followed by antibody solution (3% goat serum and 0.1% Nonidet P40 in PBS) containing Phalloidin TexasRed (Life Technologies). After extensive washing with PBS cells were embedded in ProLong Diamond Antifade Mountant with DAPI (P36962, Life Technologies). Cells were visualized by using a confocal laser scanning microscope (Leica TCS SP5, 63x HC PL APO Oil CS2, NA 1.4; Leica Microsystems, Wetzlar, Germany) and images were taken. The numbers of spread and not spread cells were determined by visual inspection, with only solitary cells with a clear flat spread out cell morphology being considered as fully spread. The number of cell protrusions (i.e. filopodia) was determined by visual inspection of confocal images and the area of cells was measured using ImageJ area measurement tool.

Statistical analysis

Fluorescent signals on blots from three independent experiments were quantified by densitometric analysis using the Image Lab software (v6.0.0, Bio-Rad Laboratories). A ONE-WAY-ANOVA in combination with Tukey's or Sidak's post-hoc multiple comparison test was used to determine the significance of the difference between cells overexpressing HRAS^{WT} and HRAS^{Gly12Ser}. Values are presented as the mean \pm standard deviation and were considered significant at P-value < 0.05. For differential quantitative proteomics, obtained relative differences of protein abundances where log2 transformed. Median normalization was performed for each sample. Missing value-tolerant NIPALS PCA calculation and visualization were performed, using the MixOmics package implemented in the R software environment (84). Details and background information on NIPALS PCA calculations are described in the Supplementary Materials and Methods. To investigate the abundance distribution of HRAS signaling-associated proteins, Pearson's correlation-based hierarchical clustering was performed, based on all proteins present in the WikiPathways-RAS signaling genset (85), obtained from the Molecular Signature Database (MsigDB) (86). Heatmap visualization of clustering results was performed using the pheatmap package, implemented in the R software environment. To test for the overrepresentation of GO terms and pathways across differential abundant interactors between WT and Gly12Ser HRAS gene-set enrichment analysis (GSEA) (version 4.1) was used (86). Log2 transformed, centered protein abundances were tested against gene ontology gene-sets (Cellular Component, Biological Process, Molecular function) and curated gene-sets from the WikiPathway database. Permutation was performed based on gene-sets. A weighted enrichment statistic was applied, using the signal-to-noise ratio as a metric for gene ranking. Balancing and normalization where disabled within GSEA. Gene-sets with a P-value < 0.01 and an FDR < 0.25 were considered significantly enriched. Enriched gene-sets where plotted according to their normalized enrichment score using Microsoft Excel. T-testing was performed in Perseus (Version 1.6.5.0). Proteins with a P-value < 0.05, exceeding a FoldChange difference of > 1.5 between HRAS^{WT} and HRAS^{Gly12Ser}-derived IPs were considered as statistically significant differential abundant.

Supplementary Material

Supplementary Material is available at HMG online

Acknowledgements

cDNA constructs for transient expression of RAB4 (pEGFP-C1 Rab4B^{WT}) and RAB7 (pmEGFP-C1 Rab7a^{WT}) were obtained from

Juan Bonifacio, for transient expression of RAB11 (pmEGFP-C1 RAB11A^{WT}) from Frederike Harms, and for transient expression of human RIN1 (pEGFP-RIN1^{WT}) from Angelika Haußer. We thank the UKE Microscopy Imaging Facility and UKE FACS Sorting Core Unit for assistance.

Conflict of Interest statement. The authors have declared that no conflict of interest exists.

Funding

This work was supported by the German Federal Ministry of Education and Research (BMBF) within the German Network of RASopathy Research (GeNeRARE; funding codes 01GM1902C and 01GM1902E to FB, MRA and GR); within the European Network on Noonan Syndrome and Related Disorders (NSEuroNet; funding code 01GM1621B to NM and MRA); and by grants from the Deutsche Forschungsgemeinschaft (DFG) [funding codes IRTG 1902-p6 (International Research Training Group 'Intra- and interorgan communication of the cardiovascular system'), INST 337/15-1, INST 337/16-1 and INST 152/837-1].

Ethics Statement

For skin biopsies and juvenile foreskin preparations, informed written consent was obtained from all subjects or their legal guardians under protocols approved by the local ethics board of the Hamburg Medical Chamber (PV7038 and WF-061/12).

Authors' Contributions

G.R. conceived and designed the project. H.S., C.G., M.R.A. and G.R. coordinated and supervised experimental work. T.N., F.B., H.V., L.I.B., N.M., V.R. and S.D. conducted the experiments and acquired and analyzed data. T.N., F.B., H.S., M.R.A. and G.R. interpreted the data and defined follow up experiments. T.N., F.B., H.V., C.G. and G.R. drafted the manuscript with contributions of all authors. M.R.A. and G.R. reviewed and finalized the manuscript.

The research was performed in four laboratories (principle investigators: H.S., C.G., M.R.A. and G.R.). T.N. did most of the experiments and data curation; therefore, she merited the first place in the order of the first authors. The contribution of F.B. was critical for the manuscript (e.g. to demonstrate that the HRAS-RIN1 signaling axis is functional) and it was felt that F.B. merited the second place on the shared first authorship. Both first authors agreed to this order of first authorship.

References

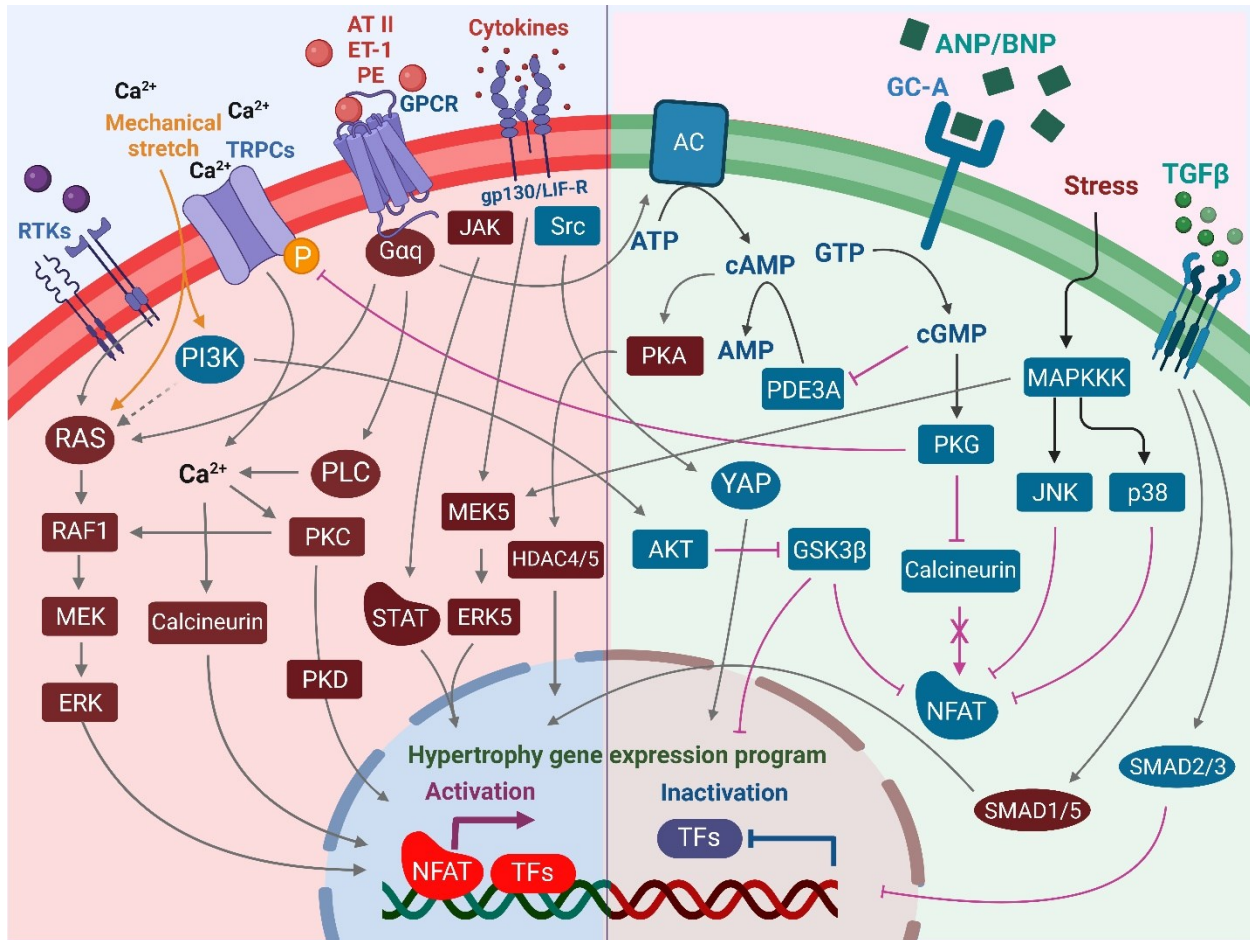
- Gripp, K.W., Morse, L.A., Axelrad, M., Chatfield, K.C., Chidekel, A., Dobyns, W., Doyle, D., Kerr, B., Lin, A.E., Schwartz, D.D. et al. (2019) Costello syndrome: clinical phenotype, genotype, and management guidelines. *Am. J. Med. Genet. A*, **179**, 1725–1744.
- Siegel, D.H., Mann, J.A., Krol, A.L. and Rauen, K.A. (2012) Dermatological phenotype in Costello syndrome: consequences of Ras dysregulation in development. *Br. J. Dermatol.*, **166**, 601–607.
- Gripp, K.W. and Lin, A.E. (2012) Costello syndrome: a Ras/mitogen activated protein kinase pathway syndrome (rasopathy) resulting from HRAS germline mutations. *Genet. Med.*, **14**, 285–292.
- Simanshu, D.K., Nissley, D.V. and McCormick, F. (2017) RAS proteins and their regulators in human disease. *Cell*, **170**, 17–33.
- Bliss, J.M., Venkatesh, B. and Colicelli, J. (2006) The RIN family of Ras effectors. *Methods Enzymol.*, **407**, 335–344.
- Han, L. and Colicelli, J. (1995) A human protein selected for interference with Ras function interacts directly with Ras and competes with Raf1. *Mol. Cell. Biol.*, **15**, 1318–1323.
- Tall, G.G., Barbieri, M.A., Stahl, P.D. and Horazdovsky, B.F. (2001) Ras-activated endocytosis is mediated by the Rab5 guanine nucleotide exchange activity of RIN1. *Dev. Cell*, **1**, 73–82.
- Hu, H., Bliss, J.M., Wang, Y. and Colicelli, J. (2005) RIN1 is an ABL tyrosine kinase activator and a regulator of epithelial-cell adhesion and migration. *Curr. Biol.*, **15**, 815–823.
- Sziber, Z., Liliom, H., Morales, C.O., Ignacz, A., Ratkai, A.E., Ellwanger, K., Link, G., Szucs, A., Hausser, A. and Schlett, K. (2017) Ras and Rab interactor 1 controls neuronal plasticity by coordinating dendritic filopodial motility and AMPA receptor turnover. *Mol. Biol. Cell*, **28**, 285–295.
- Balaji, K., Mooser, C., Janson, C.M., Bliss, J.M., Hojjat, H. and Colicelli, J. (2012) RIN1 orchestrates the activation of RAB5 GTPases and ABL tyrosine kinases to determine the fate of EGFR. *J. Cell Sci.*, **125**, 5887–5896.
- Balaji, K. and Colicelli, J. (2013) RIN1 regulates cell migration through RAB5 GTPases and ABL tyrosine kinases. *Commun. Integr. Biol.*, **6**, e25421.
- Barbieri, M.A., Kong, C., Chen, P.-I., Horazdovsky, B.F. and Stahl, P.D. (2003) The Src homology 2 domain of Rin1 mediates its binding to the epidermal growth factor receptor and regulates receptor endocytosis. *J. Biol. Chem.*, **278**, 32027–32036.
- Wang, Y., Waldron, R.T., Dhaka, A., Patel, A., Riley, M.M., Rozen-gurt, E. and Colicelli, J. (2002) The RAS effector RIN1 directly competes with RAF and is regulated by 14-3-3 proteins. *Mol. Biol. Cell*, **22**, 916–926.
- Rosenberger, G., Meien, S. and Kutsche, K. (2009) Oncogenic HRAS mutations cause prolonged PI3K signaling in response to epidermal growth factor in fibroblasts of patients with Costello syndrome. *Hum. Mutat.*, **30**, 352–362.
- Niihori, T., Aoki, Y., Okamoto, N., Kurosawa, K., Ohashi, H., Mizuno, S., Kawame, H., Inazawa, J., Ohura, T., Arai, H. et al. (2011) HRAS mutants identified in Costello syndrome patients can induce cellular senescence: possible implications for the pathogenesis of Costello syndrome. *J. Hum. Genet.*, **56**, 707–715.
- Krencik, R., Hokanson, K.C., Narayan, A.R., Dvornik, J., Rooney, G.E., Rauen, K.A., Weiss, L.A., Rowitch, D.H. and Ullian, E.M. (2015) Dysregulation of astrocyte extracellular signaling in Costello syndrome. *Sci. Transl. Med.*, **7**, 286ra266.
- Paquin, A., Hordo, C., Kaplan, D.R. and Miller, F.D. (2009) Costello syndrome H-Ras alleles regulate cortical development. *Dev. Biol.*, **330**, 440–451.
- Tidyman, W.E., Lee, H.S. and Rauen, K.A. (2011) Skeletal muscle pathology in Costello and cardio-facio-cutaneous syndromes: developmental consequences of germline Ras/MAPK activation on myogenesis. *Am. J. Med. Genet. C Semin. Med. Genet.*, **157C**, 104–114.
- Hinek, A., Teitell, M.A., Schoyer, L., Allen, W., Gripp, K.W., Hamilton, R., Weksberg, R., Kluppel, M. and Lin, A.E. (2005) Myocardial storage of chondroitin sulfate-containing moieties in Costello syndrome patients with severe hypertrophic cardiomyopathy. *Am. J. Med. Genet. A*, **133**, 1–12.
- Simpson, C.L., Patel, D.M. and Green, K.J. (2011) Deconstructing the skin: cytoarchitectural determinants of epidermal morphogenesis. *Nat. Rev. Mol. Cell Biol.*, **12**, 565–580.

21. Drosten, M., Lechuga, C.G. and Barbacid, M. (2013) Genetic analysis of Ras genes in epidermal development and tumorigenesis. *Small GTPases*, **4**, 236–241.
22. Drosten, M., Lechuga, C.G. and Barbacid, M. (2014) Ras signaling is essential for skin development. *Oncogene*, **33**, 2857–2865.
23. Hegde, S. and Raghavan, S. (2013) A skin-depth analysis of integrins: role of the integrin network in health and disease. *Cell Commun. Adhes.*, **20**, 155–169.
24. Moreno-Layseca, P., Icha, J., Hamidi, H. and Ivaska, J. (2019) Integrin trafficking in cells and tissues. *Nat. Cell Biol.*, **21**, 122–132.
25. Rippa, A.L., Vorotelyak, E.A., Vasiliev, A.V. and Tersikh, V.V. (2013) The role of integrins in the development and homeostasis of the epidermis and skin appendages. *Acta Nat.*, **5**, 22–33.
26. De Franceschi, N., Hamidi, H., Alanko, J., Sahgal, P. and Ivaska, J. (2015) Integrin traffic - the update. *J. Cell Sci.*, **128**, 839–852.
27. Yuan, W. and Song, C. (2020) The emerging role of Rab5 in membrane receptor trafficking and signaling pathways. *Biochem. Res. Int.*, **2020**, 4186308.
28. Parsons, J.T., Horwitz, A.R. and Schwartz, M.A. (2010) Cell adhesion: integrating cytoskeletal dynamics and cellular tension. *Nat. Rev. Mol. Cell Biol.*, **11**, 633–643.
29. Woodring, P.J., Hunter, T. and Wang, J.Y. (2003) Regulation of F-actin-dependent processes by the Abl family of tyrosine kinases. *J. Cell Sci.*, **116**, 2613–2626.
30. Khatri, A., Wang, J. and Pendergast, A.M. (2016) Multifunctional Abl kinases in health and disease. *J. Cell Sci.*, **129**, 9–16.
31. Hu, H., Milstein, M., Bliss, J.M., Thai, M., Malhotra, G., Huynh, L.C. and Colicelli, J. (2008) Integration of transforming growth factor beta and RAS signaling silences a RAB5 guanine nucleotide exchange factor and enhances growth factor-directed cell migration. *Mol. Biol. Cell*, **28**, 1573–1583.
32. Chylinski, K., Le Rhun, A. and Charpentier, E. (2013) The tracrRNA and Cas9 families of type II CRISPR-Cas immunity systems. *RNA Biol.*, **10**, 726–737.
33. Colicelli, J. (2010) ABL tyrosine kinases: evolution of function, regulation, and specificity. *Sci. Signal.*, **3**, re6.
34. Arjonen, A., Alanko, J., Veltel, S. and Ivaska, J. (2012) Distinct recycling of active and inactive beta1 integrins. *Traffic*, **13**, 610–625.
35. Jovic, M., Sharma, M., Rahajeng, J. and Caplan, S. (2010) The early endosome: a busy sorting station for proteins at the crossroads. *Histol. Histopathol.*, **25**, 99–112.
36. Su, Y., Xia, W., Li, J., Walz, T., Humphries, M.J., Vestweber, D., Cabafias, C., Lu, C. and Springer, T.A. (2016) Relating conformation to function in integrin $\alpha 5 \beta 1$. *Proc. Natl. Acad. Sci. U. S. A.*, **113**, E3872–E3881.
37. van Weert, A.W., Geuze, H.J., Groothuis, B. and Stoorvogel, W. (2000) Primaquine interferes with membrane recycling from endosomes to the plasma membrane through a direct interaction with endosomes which does not involve neutralisation of endosomal pH nor osmotic swelling of endosomes. *Eur. J. Cell Biol.*, **79**, 394–399.
38. Böttcher, R.T., Stremmel, C., Meves, A., Meyer, H., Widmaier, M., Tseng, H.-Y. and Fässler, R. (2012) Sorting nexin 17 prevents lysosomal degradation of $\beta 1$ integrins by binding to the $\beta 1$ -integrin tail. *Nat. Cell Biol.*, **14**, 584–592.
39. Paul, N.R., Jacquemet, G. and Caswell, P.T. (2015) Endocytic trafficking of integrins in cell migration. *Curr. Biol.*, **25**, R1092–R1105.
40. Brakebusch, C., Grose, R., Quondamatteo, F., Ramirez, A., Jorcano, J.L., Pirro, A., Svensson, M., Herken, R., Sasaki, T., Timpl, R. et al. (2000) Skin and hair follicle integrity is crucially dependent on beta 1 integrin expression on keratinocytes. *EMBO J.*, **19**, 3990–4003.
41. Carroll, J.M., Romero, M.R. and Watt, F.M. (1995) Suprabasal integrin expression in the epidermis of transgenic mice results in developmental defects and a phenotype resembling psoriasis. *Cell*, **83**, 957–968.
42. Bosset, S., Bonnet-Duquennoy, M., Barre, P., Chalou, A., Lazou, K., Kurfurst, R., Bonte, F., Schnebert, S., Disant, F., Le Varlet, B. et al. (2003) Decreased expression of keratinocyte beta1 integrins in chronically sun-exposed skin in vivo. *Br. J. Dermatol.*, **148**, 770–778.
43. Giangreco, A., Goldie, S.J., Failla, V., Saintigny, G. and Watt, F.M. (2010) Human skin aging is associated with reduced expression of the stem cell markers beta1 integrin and MCSP. *J. Invest. Dermatol.*, **130**, 604–608.
44. Ferreira, M., Fujiwara, H., Morita, K. and Watt, F.M. (2009) An activating beta1 integrin mutation increases the conversion of benign to malignant skin tumors. *Cancer Res.*, **69**, 1334–1342.
45. Lee, C.H., Chen, J.S., Sun, Y.L., Liao, W.T., Zheng, Y.W., Chai, C.Z., Chen, G.S. and Yu, H.S. (2006) Defective beta1-integrins expression in arsenical keratosis and arsenic-treated cultured human keratinocytes. *J. Cutan. Pathol.*, **33**, 129–138.
46. Han, L., Wong, D., Dhaka, A., Afar, D., White, M., Xie, W., Herschman, H., Witte, O. and Colicelli, J. (1997) Protein binding and signaling properties of RIN1 suggest a unique effector function. *Proc. Natl. Acad. Sci. U. S. A.*, **94**, 4954–4959.
47. Dhaka, A., Costa, R.M., Hu, H., Irvin, D.K., Patel, A., Komblum, H.I., Silva, A.J., O'Dell, T.J. and Colicelli, J. (2003) The RAS effector RIN1 modulates the formation of aversive memories. *J. Neurosci.*, **23**, 748–757.
48. Dzudor, B., Huynh, L., Thai, M., Bliss, J.M., Nagaoka, Y., Wang, Y., Ch'ng, T.H., Jiang, M., Martin, K.C. and Colicelli, J. (2010) Regulated expression of the Ras effector Rin1 in forebrain neurons. *Mol. Cell. Neurosci.*, **43**, 108–116.
49. Deininger, K., Eder, M., Kramer, E.R., Ziegler, W., Dodt, H.U., Dormmair, K., Colicelli, J. and Klein, R. (2008) The Rab5 guanylate exchange factor Rin1 regulates endocytosis of the EphA4 receptor in mature excitatory neurons. *Proc. Natl. Acad. Sci. U. S. A.*, **105**, 12539–12544.
50. Hunker, C.M., Giambini, H., Galvis, A., Hall, J., Kruk, I., Veisaga, M.L. and Barbieri, M.A. (2006) Rin1 regulates insulin receptor signal transduction pathways. *Exp. Cell Res.*, **312**, 1106–1118.
51. Tomshine, J.C., Severson, S.R., Wigle, D.A., Sun, Z., Belefard, D.A., Shridhar, V. and Horazdovsky, B.F. (2009) Cell proliferation and epidermal growth factor signaling in non-small cell lung adenocarcinoma cell lines are dependent on Rin1. *J. Biol. Chem.*, **284**, 26331–26339.
52. Trino, S., De Luca, L., Simeon, V., Laurenzana, I., Morano, A., Caivano, A., La Rocca, F., Pietrantonio, G., Bianchino, G., Grieco, V. et al. (2016) Inverse regulation of bridging integrator 1 and BCR-ABL1 in chronic myeloid leukemia. *Tumor Biol.*, **37**, 217–225.
53. Jozic, I., Saliba, S.C. and Barbieri, M.A. (2012) Effect of EGF-receptor tyrosine kinase inhibitor on Rab5 function during endocytosis. *Arch. Biochem. Biophys.*, **525**, 16–24.
54. Galvis, A., Giambini, H., Villasana, Z. and Barbieri, M.A. (2009) Functional determinants of ras interference 1 mutants required for their inhibitory activity on endocytosis. *Exp. Cell Res.*, **315**, 820–835.
55. Jozic, I., Blanco, G. and Barbieri, M.A. (2011) Inhibition of Rab5 activation during insulin receptor-mediated endocytosis. *Curr. Cell. Biochem.*, **1**, 20–32.
56. Weber, S.M. and Carroll, S.L. (2021) The role of R-Ras proteins in normal and pathologic migration and morphologic change. *Am. J. Pathol.*, **191**, 1499–1510.

57. Conklin, M.W., Ada-Nguema, A., Parsons, M., Riching, K.M. and Keely, P.J. (2010) R-Ras regulates beta1-integrin trafficking via effects on membrane ruffling and endocytosis. *BMC Mol. Cell Biol.*, **11**, 14.
58. Sandri, C., Caccavari, F., Valdembrì, D., Camillo, C., Veltel, S., Santambrogio, M., Lanzetti, L., Bussolino, F., Ivaska, J. and Serini, G. (2012) The R-Ras/RIN2/Rab5 complex controls endothelial cell adhesion and morphogenesis via active integrin endocytosis and Rac signaling. *Cell Res.*, **22**, 1479–1501.
59. Ghai, R., Mobli, M., Norwood, S.J., Bugarcic, A., Teasdale, R.D., King, G.F. and Collins, B.M. (2011) Phox homology band 4.1/ezrin/radixin/moesin-like proteins function as molecular scaffolds that interact with cargo receptors and Ras GTPases. *Proc. Natl. Acad. Sci. U. S. A.*, **108**, 7763–7768.
60. Kinbara, K., Goldfinger, L.E., Hansen, M., Chou, F.L. and Ginsberg, M.H. (2003) Ras GTPases: integrins' friends or foes? *Nat. Rev. Mol. Cell Biol.*, **4**, 767–776.
61. Greenhalgh, D.A., Rothnagel, J.A., Quintanilla, M.I., Orenco, C.C., Gagne, T.A., Bundman, D.S., Longley, M.A. and Roop, D.R. (1993) Induction of epidermal hyperplasia, hyperkeratosis, and papillomas in transgenic mice by a targeted v-Ha-ras oncogene. *Mol. Carcinog.*, **7**, 99–110.
62. Bailleul, B., Surani, M.A., White, S., Barton, S.C., Brown, K., Blessing, M., Jorcano, J. and Balmain, A. (1990) Skin hyperkeratosis and papilloma formation in transgenic mice expressing a ras oncogene from a suprabasal keratin promoter. *Cell*, **62**, 697–708.
63. Dajee, M., Tarutani, M., Deng, H., Cai, T. and Khavari, P.A. (2002) Epidermal Ras blockade demonstrates spatially localized Ras promotion of proliferation and inhibition of differentiation. *Oncogene*, **21**, 1527–1538.
64. Yoon, S.O., Shin, S. and Mercurio, A.M. (2005) Hypoxia stimulates carcinoma invasion by stabilizing microtubules and promoting the Rab11 trafficking of the alpha6beta4 integrin. *Cancer Res.*, **65**, 2761–2769.
65. Jeong, H., Lim, K.M., Kim, K.H., Cho, Y., Lee, B., Knowles, B.C., Roland, J.T., Zwerner, J.P., Goldenring, J.R. and Nam, K.T. (2019) Loss of Rab25 promotes the development of skin squamous cell carcinoma through the dysregulation of integrin trafficking. *J. Pathol.*, **249**, 227–240.
66. Chiarugi, P. (2008) From anchorage dependent proliferation to survival: lessons from redox signalling. *IUBMB Life*, **60**, 301–307.
67. Goitre, L., Pergolizzi, B., Ferro, E., Trabalzini, L. and Retta, S.F. (2012) Molecular crosstalk between integrins and cadherins: do reactive oxygen species set the talk? *J. Sign. Transduct.*, **2012**, 807682.
68. Mushtaq, U., Bashir, M., Nabi, S. and Khanday, F.A. (2021) Epidermal growth factor receptor and integrins meet redox signaling through P66shc and Rac1. *Cytokine*, **146**, 155625.
69. Svineng, G., Ravuri, C., Rikardsen, O., Huseby, N.E. and Winberg, J.O. (2008) The role of reactive oxygen species in integrin and matrix metalloproteinase expression and function. *Connect. Tissue Res.*, **49**, 197–202.
70. Gregg, D., de Carvalho, D.D. and Kovacic, H. (2004) Integrins and coagulation: a role for ROS/redox signaling? *Antioxid. Redox Signal.*, **6**, 757–764.
71. Bartolacci, C., Andreani, C., El-Gammal, Y. and Scaglioni, P.P. (2021) Lipid metabolism regulates oxidative stress and ferroptosis in RAS-driven cancers: a perspective on cancer progression and therapy. *Front. Mol. Biosci.*, **8**, 706650.
72. Ferro, E., Goitre, L., Retta, S.F. and Trabalzini, L. (2012) The interplay between ROS and Ras GTPases: physiological and pathological implications. *J. Sign. Transduct.*, **2012**, 365769.
73. Carpentieri, G., Leoni, C., Pietraforte, D., Cecchetti, S., Iorio, E., Belardo, A., Pietrucci, D., Di Nottia, M., Pajalunga, D., Megiorni, F. et al. (2022) Hyperactive HRAS dysregulates energetic metabolism in fibroblasts from patients with Costello syndrome via enhanced production of reactive oxidizing species. *Hum. Mol. Genet.*, **31**, 561–575.
74. Martinelli, S., De Luca, A., Stellacci, E., Rossi, C., Checquolo, S., Lepri, F., Caputo, V., Silvano, M., Buscherini, F., Consoli, F. et al. (2010) Heterozygous germline mutations in the CBL tumor-suppressor gene cause a Noonan syndrome-like phenotype. *Am. J. Med. Genet. A*, **87**, 250–257.
75. Brand, K., Kentsch, H., Glashoff, C. and Rosenberger, G. (2014) RASopathy-associated CBL germline mutations cause aberrant ubiquitylation and trafficking of EGFR. *Hum. Mutat.*, **35**, 1372–1381.
76. Altmüller, F., Pothula, S., Annamneedi, A., Nakhaei-Rad, S., Montenegro-Venegas, C., Pina-Fernandez, E., Marini, C., Santos, M., Schanze, D., Montag, D. et al. (2017) Aberrant neuronal activity-induced signaling and gene expression in a mouse model of RASopathy. *PLoS Genet.*, **13**, e1006684.
77. Basel-Vanagaite, L., Sarig, O., Hershkovitz, D., Fuchs-Telem, D., Rapoport, D., Gat, A., Isman, G., Shirazi, I., Shohat, M., Enk, C.D. et al. (2009) RIN2 deficiency results in macrocephaly, alopecia, cutis laxa, and scoliosis: MACS syndrome. *Am. J. Hum. Genet.*, **85**, 254–263.
78. Boukamp, P., Petrussevska, R.T., Breitkreutz, D., Hornung, J., Markham, A. and Fusenig, N.E. (1988) Normal keratinization in a spontaneously immortalized aneuploid human keratinocyte cell line. *J. Cell Biol.*, **106**, 761–771.
79. Lehman, T.A., Modali, R., Boukamp, P., Stanek, J., Bennett, W.P., Welsh, J.A., Metcalf, R.A., Stampfer, M.R., Fusenig, N., Rogan, E.M. et al. (1993) p53 mutations in human immortalized epithelial cell lines. *Carcinogenesis*, **14**, 833–839.
80. Abbadie, C., Pluquet, O. and Pourtier, A. (2017) Epithelial cell senescence: an adaptive response to pre-carcinogenic stresses? *Cell. Mol. Life Sci.*, **74**, 4471–4509.
81. Colombo, I., Sangiovanni, E., Maggio, R., Mattozzi, C., Zava, S., Corbett, Y., Fumagalli, M., Carlino, C., Corsetto, P.A., Scaccabarozzi, D. et al. (2017) HaCaT cells as a reliable in vitro differentiation model to dissect the inflammatory/repair response of human keratinocytes. *Mediat. Inflamm.*, **2017**, 7435621.
82. Pollok, S., Pfeiffer, A.C., Lobmann, R., Wright, C.S., Moll, I., Martin, P.E. and Brandner, J.M. (2011) Connexin 43 mimetic peptide Gap27 reveals potential differences in the role of Cx43 in wound repair between diabetic and non-diabetic cells. *J. Cell. Mol. Med.*, **15**, 861–873.
83. Shevchenko, A., Tomas, H., Havlis, J., Olsen, J.V. and Mann, M. (2006) In-gel digestion for mass spectrometric characterization of proteins and proteomes. *Nat. Protoc.*, **1**, 2856–2860.
84. Rohart, F., Gautier, B., Singh, A. and Le Cao, K.A. (2017) mixOmics: an R package for 'omics feature selection and multiple data integration. *PLoS Comp. Biol.*, **13**, e1005752.
85. Martens, M., Ammar, A., Riutta, A., Waagmeester, A., Slenter, D.N., Hanspers, K., R. A.M., Digles, D., Lopes, E.N., Ehrhart, F. et al. (2021) WikiPathways: connecting communities. *Nucleic Acids Res.*, **49**, D613–D621.
86. Subramanian, A., Tamayo, P., Mootha, V.K., Mukherjee, S., Ebert, B.L., Gillette, M.A., Paulovich, A., Pomeroy, S.L., Golub, T.R., Lander, E.S. et al. (2005) Gene set enrichment analysis: a knowledge-based approach for interpreting genome-wide expression profiles. *Proc. Natl. Acad. Sci. U. S. A.*, **102**, 15545–15550.

Chapter 4

The microenvironment of hypertrophic cardiomyopathy



Status: Under review at American Journal of Physiology-Heart and Circulatory Physiology

Impact factor: 5.12

Contribution: 40 %

Preparation of the figures 1, 2, 3 and 4, writing the manuscript, reference management and discussion.

The microenvironment of hypertrophic cardiomyopathy

Julia Nau^{1,*}, Farhad Bazgir^{1,*}, Saeideh Nakhaei-Rad^{1,2}, Ehsan Amin³, Matthew J. Wolf⁴, Jeffrey Saucerman⁵, Kristina Lorenz^{6,7}, Mohammad R. Ahmadian¹

¹ Institute of Biochemistry and Molecular Biology II, Medical Faculty and University Hospital Düsseldorf, Heinrich Heine University Düsseldorf, 40225 Düsseldorf, Germany.

² Stem Cell Biology, and Regenerative Medicine Research Group, Institute of Biotechnology, Ferdowsi University of Mashhad, Mashhad, Iran.

³ Institute of Neural and Sensory Physiology, Medical Faculty and University Hospital Düsseldorf, Heinrich Heine University Düsseldorf, 40225 Düsseldorf, Germany.

⁴ Department of Medicine and Robert M. Berne Cardiovascular Research Center, University of Virginia, USA.

⁵ Department of Biomedical Engineering, University of Virginia; Charlottesville, Virginia 22908, USA.

⁶ Institute of Pharmacology and Toxicology, University of Würzburg, Würzburg, Germany.

⁷ Leibniz-Institut für Analytische Wissenschaften – ISAS- e.V., Bunsen-Kirchhoff-Str. 11, 44139 Dortmund, Germany.

* Author sharing the first authorship.

Abstract

Pathological cardiac hypertrophy is a key risk factor for the development of heart failure and predisposes individuals to cardiac arrhythmia and sudden death. While physiological cardiac hypertrophy is adaptive, hypertrophy resulting from conditions comprising hypertension, aortic stenosis, or genetic mutations, such as hypertrophic cardiomyopathy, is maladaptive. Here, we highlight the essential role and reciprocal interactions involving both cardiomyocytes and non-myocardial cells in response to pathological conditions. Prolonged cardiovascular stress causes cardiomyocytes and non-myocardial cells to enter an activated state releasing numerous pro-hypertrophic, pro-fibrotic, and pro-inflammatory mediators such as vasoactive hormones, growth factors, and cytokines, i.e., commencing signaling events that collectively cause cardiac hypertrophy. Fibrotic remodeling is mediated by cardiac fibroblasts as the central players, but also endothelial cells and resident and infiltrating immune cells enhance these processes. Many of these hypertrophic mediators are now being integrated into computational models that provide system-level insights and will help to translate our knowledge into new pharmacological targets. This perspective article summarizes the last decades' advances in cardiac hypertrophy research and discusses the herein-involved complex myocardial microenvironment and signaling components.

Key words: cardiac hypertrophy; cardiomyocytes; heart failure; myocardial microenvironment; myofibroblasts; pressure overload; scar formation; vasoactive hormones

1. General introduction

Myocardial remodeling associated with cardiac hypertrophy is one of the critical causes in the development of heart failure ^{1,2}. The pathogenesis of heart dysfunction is one of the primary causes of morbidity and mortality in elderly people ¹.

Cardiac hypertrophy is the most frequently compensatory or adaptive process to numerous physiological or pathological conditions (Table 1) ³. Hypertrophic enlargement is characterized by an increase in the cell size of cardiomyocytes. The heart can dynamically change its muscle mass to cope with the stimuli of development, physiological conditions of exercise and pregnancy, or pathological disease stimuli (Table 1) ⁴. Increased workload as a consequence of volume or pressure overload due to pathological or physiological stimuli increases tension

on the cardiac walls of the heart chambers^{5,6}. This ultimately triggers stress signals released by different cell types of the microenvironment to compensate for the wall tension increase, resulting in a hypertrophic growth response^{5,6}. Individual cardiomyocytes can increase in length and/or width in response to hypertrophic stimuli depending on the intracellular signaling cascades involved^{7,8}.

Physiological and pathological cardiac hypertrophy is associated with distinct molecular characteristics (Table 1) involving alterations in the expression of fetal genes, and contractile and calcium-handling proteins⁹. A major molecular characteristic of pathological hypertrophy is the re-expression of fetal genes. Pathological settings such as hypertension cause the induction of the stress program that involves increased expression of atrial natriuretic peptide (ANP), B-type natriuretic peptide (BNP), and alpha-skeletal actin (α -sk actin)¹⁰. In contrast, an important characteristic of physiological hypertrophy is the absence of molecular stress programs¹¹. In addition, expression of cardiac contractile proteins, such as alpha- and beta-myosin heavy chain and calcium-handling proteins, e.g., sarcoplasmic reticulum Ca^{2+} -ATPase 2a (SERCA2a) remain unchanged during physiological cardiac hypertrophy, whereas pathological cardiac hypertrophy is closely associated with alterations in the above-named genes and proteins¹⁰.

While the events associated with physiological hypertrophy are generally reversible, those associated with pathological cardiac hypertrophy are commonly irreversible and impose a high risk of heart failure (Table 1). A common disease stimulus, such as long-standing hypertension usually causes pressure overload and increases systolic wall stress¹². In this case, individual cardiomyocytes typically grow in width more than in length, leading to the thickening of the cardiac walls, a condition referred to as concentric hypertrophy^{4,13}. Hypertrophic changes have been rationalized employing Laplace's law, which says wall stress (or tension) is an inverse function of wall thickness (tension= (pressure x radius)/ 2x wall thickness). Thus, compensated growth of the cardiac muscle is a physiological response to decrease wall tension and thereby maintain cardiac pump function⁵. Prolonged pathological stress, however, causes maladaptive changes at the cellular and molecular level resulting in pathological cardiac hypertrophy. Untreated pathological cardiac hypertrophy predisposes individuals to heart failure, arrhythmia, and sudden death^{7,8}.

Triggers of pathological cardiac hypertrophy include extrinsic drives such as pressure overload due to long-standing hypertension or valvular stenosis, as well as volume overload due to mitral regurgitation or aortic insufficiency (Table 1), loss of contractile mass (myocardial infarction), or intrinsic causes such as hereditary defects^{3,14}. Although a notable feature of physiological and pathological cardiac hypertrophy is the increase in heart size, pathological cardiac hypertrophy involves the loss of myocytes and fibrotic replacement, leading to cardiac dysfunction, heart failure, and/or sudden death¹⁵⁻¹⁷. Despite views that the length of stress has a significant impact on the distinction between pathological and physiological cardiac hypertrophy, the nature of stress and the intracellular signaling cascades involved are thought to be more important in the development of maladaptive cardiac dysfunction than the chronic duration of exposure¹⁸.

The role of the heart's microenvironment and the inter-cell communication in the cardiac niche has become more evident for future studies and therapeutic interventions, as also recently highlighted by Tazhor *et al.*¹⁹, challenging the traditional view on the heart as a cardiomyocyte-centered and directed regenerative and therapeutic target in cardiovascular disease. Future therapeutic and mechanistic investigations should take into account the fact that immune cells, fibroblasts, and endothelial cells collectively outnumber cardiomyocytes by a significant margin as the resident cells in the heart, making this viewpoint increasingly important as a crucial element in the study of the intercellular communications and the treatment of heart disease. Therefore, the aim of this review article was to focus on these processes related to the onset, progression, and pathogenesis of hypertrophic cardiomyopathy and to complement previous

work by incorporating molecular axes and details of intercellular communication in the cardiac microenvironment that have not yet been illuminated.

2. An interplay of different cells in hypertrophic remodeling

The heart consists of various cell types, including myocytes, endothelial cells, fibroblasts, vascular smooth muscle cells, sympathetic neurons, and immune cells, which collectively account for a synchronized cardiac function^{20, 21}. However, it has been shown that owing to their enormous size, cardiomyocytes in particular account for the majority of heart mass, increase in size and reprogram transcription in the process of cardiac hypertrophy^{3, 22}. Crosstalks between cardiomyocytes and non-myocytes lead to the secretion of bioactive mediators, which operate in an autocrine and paracrine manner (Table 2). This is followed by microenvironmental stimulation of different cell types and the activation of various signaling pathways within the cells (Fig. 1,2)^{20, 23}. Altogether these complex processes result in cardiomyocyte hypertrophy, fibroblast hyperplasia, interstitial tissue composition changes, and remodeling of the ventricular chambers²⁴.

Fibroblast remodeling. Pressure overload triggers resident cardiac fibroblasts originating from the epicardium and endocardium to undergo rapid expansion and activation, rather than previously reported hematopoietic precursor-derived fibroblasts or endothelial-to-mesenchymal transition (EndMT) as a contributing source (Fig. 1,3)^{25, 26}. Despite this, the exact origins of cardiac fibroblasts as well as the delineation of their characteristics and plasticity remain a field of the current investigation and controversy²⁷. Like cardiomyocytes, fibroblasts respond to external stress stimuli, but in a slightly different manner. Mechanical stress promotes fibroblast differentiation to a myofibroblast-like phenotype (Fig. 1,3)^{28, 29}, which has been shown to develop from tissue-derived fibroblasts rather than endothelial or smooth muscle cells²⁶ with the expression of α -skeletal actin³⁰. Myofibroblasts overproduce and release extracellular matrix (ECM) components and pro-hypertrophic mediators, including TGF- β (Table 2), and are engaged in a wide range of pathological conditions, particularly fibrosis and tissue remodeling (Fig. 3)³¹. Notably, myofibroblasts do not reside in normal cardiac tissue except the valve leaflets³². Enhanced release of ECM by myofibroblasts contributing to mechanical stiffness accompanied by increasing fibrosis evolves into severe consequences causing cardiac diastolic dysfunction (Fig. 4)³³. Moreover, progressing fibrosis can affect systolic function by building a barrier between the resident cardiomyocytes, thereby provoking defective electrical coupling within the myocardium³⁴. Additionally, an increased level of ECM, such as collagen, can disrupt the oxygen diffusion capacity leading to hypoxia in the affected myocytes a process that may further enhance pathological remodeling³⁵. In conclusion, cardiac fibroblasts react to pressure overload-induced injury with activation, accumulation, and excessive ECM deposition (Fig. 1,3). The resulting conditions including mechanical stiffness, myocyte uncoupling, and ischemia comprise key contributors to heart failure²⁵. These lines of evidence also emphasize the identification of mechanical stress in cardiac hypertrophy as an independent risk factor for arrhythmias, myocardial infarction, and sudden death (Fig. 4)¹⁵.

Endothelial cell activation. In response to pressure overload, cardiac endothelial cells, similar to cardiac fibroblasts, are capable of changing their phenotype (Fig. 1). It has been reported that endothelial cells can undergo an EndMT, differentiate into myofibroblast-like cells, and thereby contribute to cardiac fibrosis³⁶. Others outlined that EndMT recruits circulating hematopoietic progenitors to the heart thereby generating significant numbers of cardiac fibroblasts (reviewed in³⁷) but also their origin from tissue-resident fibroblasts is being discussed^{25, 26}. Altogether, left ventricular myocardial tissue of end-stage cardiac failure patients revealed dramatically increased expression levels of EndMT-related genes³⁸, indicating the need for further investigation to clarify the exact contribution of EndMT.

Major factors secreted by cardiac endothelial cells (Table 2) comprise nitric oxide (NO), endothelin 1 (ET-1), prostaglandin I₂ (PI₂), and angiotensin II (AT-II), which directly influence

cardiac metabolism, growth, contractile performance, and rhythmicity of the adult heart³⁹. In response to various stimuli, activated endothelial cells express adhesion molecules, including intercellular adhesion molecule-1 (ICAM-1) and vascular cell adhesion molecule-1 (VCAM), which attract and further promote the infiltration of immune cells into the myocardium (Fig. 1). One major mediator produced and secreted by endothelial cells is NO (Table 2; Fig. 1). Among the numerous functional influences of NO are cardiac-related functions, including key regulators of vasodilation, reduction of permeability and thrombogenesis, and inhibition of inflammation⁴⁰. Another active mediator secreted by endothelial cells is CNP (Table 2). Together, NO and C-type natriuretic peptide (CNP) contribute to the suppression of cardiac hypertrophy by up-regulating cyclic GMP (cGMP)-dependent protein kinase 1 (PKG1) signaling⁴¹ by inhibiting calcineurin (Fig. 2). Another endothelium-derived factor next to NO and CNP is ET-1 (Table 2)⁴². Originally identified as an endothelium-derived vasoconstrictor⁴³, ET-1 contributes to cardiac hypertrophy and fibrosis as a major growth factor. Aside from endothelial cells, ET-1 is, amongst others, also expressed in non-endothelial cells, such as fibroblasts and cardiomyocytes (Table 2; Fig. 1). Functioning in an autocrine and paracrine manner, ET-1 seems to have important effects during the development of cardiomyocyte hypertrophy⁴⁴. ET-1 exhibits a positive inotropic effect⁴² as well as triggers cardiomyocyte hypertrophy responses⁴⁵. Moreover, cardiac endothelial cells carry enzymes with protease activities, like the angiotensin-converting enzyme (ACE) and chymase (Table 2; Fig. 1), which may contribute to changes in local levels of AT-II⁴⁶. Besides fibroblasts, endothelial cells may also contribute to cardiac fibrosis (Fig. 3). For example, it is known that endothelial cells and pericytes as the capillary lining cells wrapped around them, control cardiac fibroblast numbers^{36, 47}. Whether this contribution is similarly relevant as the proliferation and activation of resident fibroblasts upon exposure to pressure overload awaits further investigation²⁵.

The role of immune cells in cardiac hypertrophy

The pathogenesis of pressure overload and heart failure has been suggested to be in close context with the activation of inflammatory cells and the release of inflammatory mediators (Fig. 1)⁴⁸.

Cardiac mast cells. Identification of the presence of mast cells in the heart tissue of animals⁴⁹, and humans⁵⁰⁻⁵³, as well as the discovery of mast cells as the source of an array of mediators (Table 2)⁵⁴, clearly emphasize the crucial participation of innate immune cells, especially cardiac mast cells, in cardiac hypertrophy and remodeling (reviewed in^{55, 56}).

Activated cardiac mast cells were identified in spontaneously hypertensive rats as a major source of growth factors (Fig. 1), such as TGF- β and bFGF, in areas of myocardial fibrosis⁵⁷. This is consistent with findings that the release of TGF- β provokes an increase in collagen production alongside the differentiation of fibroblasts to myofibroblasts (Fig. 1)⁵⁸, and indicates that cardiac mast cells also contribute to the key steps of cardiac tissue fibrosis⁵⁹. Another major mediator that is released upon mast cell degranulation in the heart is histamine (Table 2)⁵¹. Histamine is a neurohormonal mediator that binds to histamine H1, H2, and H3 receptors, thereby inducing various cellular functions^{60, 61} as well as cardiac hypertrophy (Fig. 1)⁶². Notably, cardiomyocytes express the histamine H2 receptor, which is coupled to the beta receptor and Gs proteins⁶³⁻⁶⁷. Consistently, histamine triggers positive inotropic effects^{65, 68}. In contrast, blocking the histamine H2 receptors decreases cardiac output⁶⁸. The application of famotidine, a histamine H2 receptor antagonist, in chronic heart failure (CHF) patients, was found to decrease left ventricular remodeling⁶⁹.

Another characteristic of mast cells involves their strategic location often at a perivascular site, thereby exerting regulatory functions on endothelial cells. Mast cells synthesize several endothelial cell activators comprising, amongst others, the platelet-activating factor (PAF), IL-1 β , IL-4, and tumor necrosis factors alpha (TNF α)⁷⁰⁻⁷². Several studies have indicated mast cell degranulation as a major source of TNF α (Table 2; Fig. 1)⁷³⁻⁷⁶. Even though many cardiac cells have been described to generate TNF α , cardiac mast cells appear to constitutively

express TNF α ^{75, 76} and activate TNF α /nuclear factor kappa B (NF- κ B)/IL-6 cascades⁵⁷. Activation of the TNF α /NF- κ B axis leads to the activation of p38-MAPK (Fig. 2), collectively causing hypertrophy and dysfunction of the heart^{77, 78}. Moreover, mast cells release other cytokines including IL-1 and IL-6 (Table 2; Fig. 1)^{54, 79}. IL-6 cytokine family binds the common coreceptor glycoprotein 130 (gp130) and thereby potentially takes an active role in cardiac hypertrophy induction via the JAK/STAT pathway (Fig. 2)^{80, 81}.

Although several studies suggest that cardiac mast cells are a source of renin, released upon mast cell degranulation (Table 2)^{82, 83}, the major source of renin in the myocardial microenvironment is complex^{84, 85}. Mast cells release the proteolytic enzyme chymase, which catalyzes, independently of ACE, the conversion of angiotensin I to AT-II (Fig. 1)⁸⁶. Thus, mast cell renin and chymase may serve as an alternative way to upregulate AT-II levels in the myocardial microenvironment, and it has been demonstrated in rat models that mast cell inhibition using mast cell stabilizer cromolyn sodium reduces pathological left ventricular remodeling⁸⁷.

Monocytes & Macrophages. Healthy and injured cardiac tissues possess heterogeneous populations of macrophages, in both humans and mice (Fig. 1)⁸⁸. Most macrophages within the heart are established embryonically from the yolk sac and fetal liver progenitors, similar to tissue macrophages of the liver or brain. Local proliferation in contrast to monocyte recruitment serves to maintain resident macrophage subsets^{89, 90}. In the absence of disease, self-renewal serves to maintain local tissue macrophage populations⁹¹. Despite this, in response to pressure overload or ischemic injuries, the majority of macrophages are derived from the recruitment and differentiation of blood monocytes⁹².

Cardiac macrophages are key effector cells mediating tissue remodeling and fibrosis (Fig. 3)⁹³. The initial and significant event for vascular lesion formation results from inflammatory cytokine and growth factor-producing migrating macrophages (Fig. 1)⁹⁴. The accumulation of macrophages has been found in the perivascular space, where they co-localize with fibroblasts collectively producing collagen during cardiac hypertrophy (Fig. 3)^{95, 96}. Consistent with this, other studies have found that pressure overload initiates endothelial cells of the intramyocardial arteries to exhibit intercellular adhesion molecule (ICAM)-1, and that accumulation of macrophages occurs adjacent to the ICAM-1 expressing arteries in the perivascular space (Fig. 1)⁹⁷. Additionally, vascular cells and monocytes synthesize and express monocyte chemoattractant protein (MCP)-1, a potent monocyte chemoattractant⁹⁸, primarily regulating the recruitment of macrophages to the vessels⁹⁹. For example, the continuous infusion of angiotensin II (AT II) or norepinephrine in hypertensive rats demonstrated that MCP-1 induction was associated with adventitial macrophage accumulation in the aortic wall⁹⁸.

Collectively, this suggests that resident and recruited macrophages actively take part in the early responses to stress preceding hypertrophic remodeling.

Neutrophils. Under normal reparative conditions, neutrophil granulocytes are recruited to areas of acute inflammation, where they perform functions such as the clearance of dead cells and matrix debris (Fig. 3) (95, 96). As key components of the inflammatory response, neutrophils also act on the recruitment, activation, and programming of antigen-presenting cells (APCs). Specifically, they attract monocytes and dendritic cells (DCs) by generating chemotactic signals, thereby influencing the differentiation of macrophages into a predominantly pro- or anti-inflammatory state (97-99). Because neutrophil granulocytes are one of the most important cellular components of the body for the destruction of microorganisms, there is also the possibility that these cells damage host cells and tissues (100, 101). Accordingly, they may have deleterious effects on cardiac tissue when recruited to sites where pressure overload is present (Fig. 3).

Several studies have reported that in response to hypertrophy triggered by pressure overload, the first leukocytes to appear in the myocardium within 3 days of injury are neutrophils (Fig. 3) (102, 103). Activation of endothelial cells and subsequent expression of adhesion molecules allow the transmigration of neutrophils (Fig. 3) (104, 105). In addition, inflammatory mediators such as TNF- α , IL1 β , and mast cell-derived histamine enhance this process (106-108). Additionally, macrophage and neutrophil infiltration appeared in the first 3 days after injury next to ICAM-1 containing coronary arteries in the left and right ventricle, using a mouse model with inter-renal aortic banding. Moreover, these alterations of macrophage and neutrophil content occurred ahead in perivascular fibrosis (10 days), and cardiomyocyte hypertrophy (28 days) ¹⁰⁰.

Neutrophils have been described to produce cytokines such as TNF- α that drive macrophage and dendritic cell differentiation ¹⁰¹⁻¹⁰³. Additionally, neutrophilic nicotinamide adenine dinucleotide phosphate (NADPH) oxidase gets activated in response to pressure overload injury ¹⁰⁴, resulting in the degranulation of neutrophils and thereby release of pro-fibrotic proteases (Fig. 3) as well as reactive oxygen species (ROS) ¹⁰⁵.

Sympathetic neurons. ET-1-induced norepinephrine (NE) release by sympathetic nerve terminals has been reported to mediate arrhythmia effects, contribute to cardiac remodeling events, and increase the prevalence of heart failure due to reduced ejection fraction volume (Fig. 4) (113-116).

Substantial amounts of renin released in the cardiac microenvironment result in both AT-II formation within striking distance of AT1 receptor-expressing cardiac sympathetic nerve terminals and enhanced NE release (Fig. 1) and arrhythmias (Fig. 4) (117, 118). The fact that these events can be prevented by mast cell-stabilizing agents confirms the central role of cardiac mast cell-derived renin in AT1 receptor signaling (78). Locally produced AT-II thus activates the AT1 receptor at sympathetic nerve endings, resulting in increased NE release (Fig. 1) (78).

3. Mediators of cardiac remodeling

Mechanical stretch and neurohumoral mechanisms identify the most proximal stimuli for initiating hypertrophic signaling pathways (Fig. 1) ⁴. Due to hemodynamic overload, cardiomyocytes undergo mechanical stress and thereby release autocrine and paracrine signaling factors, such as growth factors, hormones, cytokines, and chemokines (Table 2) ¹⁰. Furthermore, mechanical stress is sensed by both cardiac fibroblasts resulting in the production and release of signaling mediators (Fig. 1) ¹⁰⁶, and cardiac endothelial cells, which communicate with cardiomyocytes by secretion of autocrine and paracrine mediators ^{41, 107}. Cardiomyocytes sense these ligands through a multitude of G-protein-coupled receptors, growth factor receptors, and cytokine receptors (Fig. 1,2) ⁴. Orchestrated mechanisms of the induction, maintenance, and progression of cardiac hypertrophy, particularly left ventricular hypertrophy, underlie a series of events that follows the activation of cardiomyocytes upon pressure overload/mechanical stress.

Activation of the local renin-angiotensin system (RAS). In addition to the classical circulating renin-angiotensin system (RAS) (121, 122), the heart has a local RAS that mediates autocrine, paracrine, and intracrine effects (Fig. 1) (122-124). Components of the RAS, including angiotensinogen (AGT), renin, ACE, AT-I, and AT-II, are expressed in the heart (125, 126), and component expression is upregulated in cardiomyocytes *in vitro* in response to stretch (127, 128). Several studies have indicated that hemodynamic overload activates the local RAS and highlighted the crucial role of the AT1 receptor in strain-induced cardiac hypertrophy (127, 129-137). Thus, mechanical stress can be considered the major upstream trigger that activates the local RAS and leads to increased AT-II levels throughout the microenvironment.

Reactive oxygen species (ROS). Reactive oxygen species (ROS) such as superoxide anion (O_2^-), hydroxyl (OH), and hydrogen peroxide (H_2O_2), and reactive nitrogen species including nitric oxide (NO) and peroxynitrite ($ONOO^-$) classify reactive species involved in redox signaling. The latter results from the reaction of (O_2^-) with NO¹⁰⁸. Data suggest that both direct and indirect mechanisms resulting from redox signaling within and between endothelial cells and cardiomyocytes are responsible for functional communication between these cells (17). Moreover, redox signaling not only influences many physiological processes in the heart but also plays an important role in pathological cardiac remodeling (139, 140). In cardiac cells, several sources of ROS have been described, such as mitochondria¹⁰⁹, xanthine oxidase (XO)¹¹⁰, uncoupled NO synthases (NOS)¹¹¹, and NADPH oxidases (NOXs)¹¹². The interactions of NOX proteins with NOS-derived NO have been highlighted to be particularly important for redox signaling in the development of heart failure (Fig. 1)¹¹²⁻¹¹⁴.

An increase in the cardiac generation of ROS and therefore an increase in oxidative stress has been implicated in pressure-overload-induced left ventricular cardiac hypertrophy (LVH) and heart failure (Fig. 1)¹¹⁵⁻¹¹⁷. Additionally, the development of cellular hypertrophy and remodeling has been found to implicate increased ROS production, and activation of the mitogen-activated protein kinase (MAPK) superfamily, where redox-sensitive protein kinases, are known to be partly responsible. Moreover, cardiomyocyte apoptosis and necrosis may be due to increased oxidative stress (Fig. 4), which is described to be associated with the transition from compensated pressure-overload-induced hypertrophy to heart failure. Furthermore, alterations in the redox-sensitive activity of several key proteins including sarcolemma ion channels and exchangers and sarcoplasmic reticulum calcium release channels, which collectively account for excitation-contraction coupling, contribute to myocardial contractile dysfunction (Fig. 4). Beyond that, the consequent generation of peroxynitrite ($ONOO^-$) as a result of increased inactivation of NO has been attributed to indirect effects of ROS, leading to coronary vascular endothelial dysfunction and peroxynitrite-induced inhibition of myocardial respiration¹¹⁸.

Several mediators including AT-II, ET-1, alpha-adrenergic agonists, TNF- α , and mechanical forces trigger NOX2 activation. Via induction of four cytosolic regulatory subunits (p47^{phox}, p67^{phox}, p40^{phox}, and RAC1), these mediators initiate O_2^- production¹¹⁹, indicating that pressure overload subsequently increases O_2^- levels (Fig. 1). Excessive O_2^- levels interact extremely rapidly with NO, resulting in peroxynitrite formation, thereby disrupting physiological NO signaling^{114, 120}. Hence, pressure overload shifts the balance towards increased ROS (Fig. 1), a condition that suppresses the physiological functions of NO. Consistently, O_2^- has long been recognized to be implicated in severe cardiovascular diseases. Moreover, reports indicate that NOS may generate O_2^- instead of NO, a condition referred to as uncoupled NOS. The switch to O_2^- generation appears as a consequence of tetrahydrobiopterin (BH4) depletion (usually through oxidation to BH2) or as NOS enzymes undergo post-translational modification¹²¹. Consistent, increased levels of O_2^- and $ONOO^-$ may be implicated in an amplifying mechanism that aggravates NOS uncoupling through oxidation of BH4¹²².

Hence as outlined above, reactive oxygen species should be considered as a group of key mediators driving pathological remodeling in the microenvironment of cardiac hypertrophy (Fig. 1), especially regarding pressure overload.

Endogenous storage pools of AT-II in secretory granules. AT-II secretion into the culture medium upon mechanical stress of isolated cardiomyocytes has been observed and provides some evidence supporting the concept of increased local concentrations of AT-II¹²³. Potential autocrine and paracrine regulatory mechanisms of AT-II may activate the AT1 receptor on cardiomyocytes and surrounding cells (Table 2)¹²⁴. This in turn has been proposed to induce the release of autocrine and paracrine mediators, including vasoactive peptides, growth

factors, cytokines, and ECM components, such as collagen (Fig. 1)^{44, 125-127}. Potentiated or sustained AT1 receptor activation is likely associated with cardiomyocyte hypertrophy, fibroblast hyperplasia, and fibrosis (Fig. 4)¹²⁸⁻¹³⁰. Alternative mechanisms have been proposed to contribute to the activation of the AT1 receptor upon binding of AT-II¹³¹, including membrane stretch and mechanoactivation that can in turn promote distinct conformational rearrangements in the receptor, leading to alternative signaling outcomes^{132, 133}. Several proteins have been implicated as sensors of mechanical stretches, such as muscle LIM proteins, integrins, and their associated signaling pathways^{134, 135}. Network models have been developed to predict how these mechano-sensitive proteins work together to coordinate cardiomyocyte hypertrophy^{136, 137}. Mechanisms that integrate these events and propagate the stress signal to the AT1 receptor after activation by mechanical stress remain areas of active investigation. Interestingly, despite the absence of AT-II/AT1 signaling, cardiac hypertrophy, systolic dysfunction, and fibrosis occurred in response to pressure overload (Fig. 4)¹²⁹.

The two faces of the TGF- β signaling. AT-II-activated fibroblasts release TGF- β and ET-1 in a paracrine manner into cardiomyocytes, leading to hypertrophy (Table 2)⁴⁴. Similar to mechanical stress, autocrine TGF- β signaling promotes fibroblast proliferation and ECM production (Fig. 1), especially collagen and fibronectin, whereas degradation of these components is reduced¹³⁸. Several studies report that the canonical TGF- β /SMAD2/3 signaling pathways (Fig. 2) induce the expression of genes related to collagen, fibronectin, and other ECM proteins¹³⁹⁻¹⁴², which concomitantly contribute to cardiac fibrosis (Fig. 1)¹⁴³. Experiments using pressure-overload rats demonstrated that a TGF- β neutralizing antibody inhibited fibroblast activation and proliferation, and diastolic dysfunction¹⁴³. These data suggest TGF- β as a central target and the inhibition of TGF- β signaling as beneficial. In line with this, cardiac fibrosis was attenuated in SMAD3 deficient mice subjected to cardiac pressure overload, but interestingly cardiac hypertrophy and cardiac dysfunction were aggravated¹⁴⁴. Also, another rat model revealed that worsened cardiac remodeling and increased mortality correlate with a reduction of ECM using a TGF- β neutralizing antibody after myocardial infarction¹⁴⁵. Transforming growth factor beta (TGF- β)-activated kinase 1 (TAK1) binds directly to type II (TBR1) TGF β receptors. Identification of this interaction links TAK1 to the TGF- β signaling cascade, implicating an additional way of hypertrophy induction in cardiomyocytes by TGF- β signaling¹⁴⁶. Thus, aside from contributing to cardiac fibrosis, the non-canonical TGF- β /TGF- β activated kinase 1 (TAK 1) signaling pathway has also been reported to promote cardiac hypertrophy (Fig. 2)¹⁴⁷. Altogether, TGF- β is released from cardiomyocytes, fibroblasts, and endothelial cells in the healthy heart (Table 2)^{148, 149} and in the context of injury and repair also from myofibroblasts and infiltrating immune cells^{150, 151}. Thus, TGF- β seems to be involved in adaptive or maladaptive processes most likely depending on the context, and may locally trigger interactions between different cell types such as cardiomyocytes and fibroblasts (Fig. 1) and thereby impact cardiac hypertrophy, fibrosis, and the development of heart failure (Fig. 4).

Endothelin-1 effects. Endothelin-1 (ET-1) is an endothelium-derived vasoconstrictor of 21 amino acids. Later, two additional homologs (ET-2 and ET-3) were identified. ET-1 is released from vascular endothelium and other cells including cardiomyocytes (Fig. 1) after cleavage from a large precursor peptide¹⁵². ET-1 is the predominant endothelin in the heart and is identified as a potent hypertrophic stimulus in neonatal cardiomyocytes¹⁵³. ET-1 is a ligand for two GPCRs: ET-A and ET-B where 90% of the endothelin receptors on cardiomyocytes belong to the ET-A subtype (Fig. 2)¹⁵⁴. In rat hearts, the ET-A is predominant and identified to be coupled to both the Gq and Gi subfamily of G-proteins (Fig. 2)¹⁵⁵. In addition, a characteristic pattern of gene expression is induced by ET-1 in ventricular neonatal rat cardiomyocytes (NRC) including immediate early genes (c-FOS, c-JUN, EGR-1), early genes (ANF, β -MHC, α -sk actin), and later on, ventricular MLC-2 and α -cd actin¹⁵⁶. The Gq-RAS-RAF-ERK pathway may be involved in these transcriptional changes (Fig. 2). Furthermore, ET-1 activates

the Ras-MEKK1-SEK-JNK pathway contributing to the hypertrophy-associated gene expression program field ¹⁵⁷.

ET-1 causes cell damage in cardiomyocytes *in vivo*, and experiments with long-term treatment with the ET-A receptor blocker BQ-123 showed improved survival of rats with heart failure ¹⁵⁸.

The release of ANP and BNP from cardiomyocytes can also be triggered by AT-II and ET-1, though cardiomyocyte stretch is the main regulatory mechanism for ANP and BNP production ¹⁵⁹.

FGF-2 effects in scar formation. In general, considering the epigenetic state and very low proliferative potential of adult cardiomyocytes, consensus exists that there is only a small ability to regenerate injured myocardium through the proliferation of cardiomyocytes ^{160, 161}. Instead, scar formation occurs through infiltrating highly proliferative cardiac fibroblasts (Fig. 1,3) ¹⁶². A key player is FGF-2 (bFGF), which is expressed by numerous cell types in the adult myocardium. FGF-2 is released upon cardiac injury from its “storage site” (Table 2) thereby potentially activating cell surface receptors, such as FGFR (Fig. 2) ¹⁶³. Moreover, AT-II, ET-1, and FGF-2 itself are known to promote FGF-2 gene expression (Table 2) ^{163, 164}. Accordingly, FGF-2 increases both fibroblast and myofibroblast proliferation ^{165, 166}, therefore contributing to both enhanced scar formation and stiffness during cardiac injury (Fig. 3). Noteworthy, FGF-2 exists as an isoform with a high molecular weight (Hi-FGF-2) and low molecular weight (Lo-FGF-2) ¹⁶⁷, thus it is important to determine the potential effects of both in the context of cardiac hypertrophy and tissue remodeling. In the past, several *in vitro* studies revealed evidence for an important role of FGF-2 in cardiac hypertrophy (Fig. 1). Consistent with reports Lo-FGF-2 alters the gene profile of contractile proteins from “adult” to “fetal” programs when added to cultured neonatal cardiomyocytes ¹⁶⁸, a distinct characteristic that is attributed to pressure overload-induced cardiac hypertrophy *in vivo*. Although data seems contradictory as others reported that cardiomyocyte hypertrophy is stimulated only by Hi-FGF-2, both *in vivo* and *in vitro* ¹²⁷. Hi-FGF-2 accumulates preferentially in response to stress stimuli (Fig. 1), including AT-II ¹⁶⁹ and oxidative stress ¹⁷⁰. This is further supported by others who found that Hi-FGF-2 is preferentially accumulated and released by cardiac fibroblasts which induce paracrine cardiomyocyte hypertrophy (Table 2) ¹²⁸. Once released, Hi-FGF-2 may directly interact and activate the tyrosine kinase receptor FGFR-1 (Fig. 2) ¹⁷¹, and downstream mitogen-activated protein kinase signaling ^{126, 172}. Lo-FGF-2 exhibits cardioprotective effects, especially against post-ischemic cardiac dysfunction ¹⁷³. One mechanism for the effects of Lo-FGF-2 is its potent angiogenic activity that may increase resistance to ischemic injury and cardioprotection ^{163, 174, 175}. In conclusion, these data imply that Hi-FGF-2 is a contributor to cardiac hypertrophy, fibrosis, and heart failure (Fig. 4), while Lo-FGF-2 seems to exert opposite functions as a component of adaptive responses in the injured myocardium ¹⁷⁶.

FGF-2 null mice had a marked reduction of the hypertrophic response in cardiomyocytes in response to pressure overload ¹⁷⁷; however, questions remain whether the entire blockade of FGF-2 signaling is therapeutically beneficial. Considering data highlighting the role of FGF-2 in the progression of many cancer types ¹⁷⁸⁻¹⁸², blocking of FGF-2 may have beneficial effects as shown in reports on the elimination of tumor angiogenesis ¹⁸³. But, in the context of ischemic heart disease, inhibition of FGF-2 signaling may be detrimental, since an angiogenic effect by Lo-FGF-2 upregulation may be desirable ^{163, 174, 175}. Although data suggests functions for Hi-FGF-2 and Lo-FGF-2 in the myocardium, further investigations are certainly needed to understand a) the precise outcomes of targeting one or the other isoform, b) the effects on exact organs/cells, and c) to define the precise function of the isoforms in the context of cardiomyocyte hypertrophy and fibrosis. Additionally, unwanted effects of Hi-FGF-2 and Lo-FGF-2 need to be considered. Moreover, in addition to FGF-2, TGF- β , AT-II, catecholamines, and other molecules as well orchestrate the response to hemodynamic stress (Fig. 1), which suggests that targeting just one mediator may not be sufficient.

ERK as the most prominent downstream effector of FGF-2 signaling plays a predominant role in the development of both physiological and pathological cardiac hypertrophy (Fig. 2). While cytosolic functions of ERK upon activation through pressure overload and mediators are believed to promote the development of physiological hypertrophic conditions, nuclear transcriptional activations mediated by ERK promote a pathological hypertrophic response in CMs (Fig. 2)^{184, 185}. Hypertrophic stimuli such as angiotensin II, ET-1, cytokines, catecholamines, and biomechanical stress may also contribute to detrimental ROS formation in cardiomyocytes, and additional autophosphorylation of ERK1/2 has been reported to trigger pathological ERK1/2-mediated cardiac hypertrophy (Fig. 2)^{186, 187}. These changes can then activate several hypertrophic signaling mediators regulated by ERK1/2^{185, 188}.

Hyperactivation of ERK1/2 activity is most frequently linked to HCMs caused by genetic abnormalities^{189, 190}. While genetic variant-induced hyperactivation of ERK is closely linked to pathogenic remodeling, normalization of ERK activation by simvastatin treatment restores contractility and protects against fibrosis in animal models^{191, 192}.

One study reported different cardiac hypertrophic responses using both mice that completely lacked ERK1/2 protein in the heart and mice that expressed an activated MEK1 in the heart. Inhibiting MEK-ERK1/2 in mice lacking ERK1/2 in the heart causes eccentric cardiac growth with elongated cardiomyocytes, whereas activation of MEK1-ERK1/2 signaling by the overexpression of an active MEK1 mutant appears to be responsible for the concentric type of hypertrophy with thicker cells¹⁹³. Thus, increased pre- versus afterload have been described to result in typical hypertrophic responses, and ERK1/2 seem to exhibit a central role, partially regulating the underlying molecular mechanisms. Induction of ERK1/2 translocation to the nucleus in adult rat myocytes, corresponded to reduced myocyte lengths and increased width, under both baseline and chronic pacing conditions¹⁹⁴, pointing to the critical role played by ERK signaling in balancing concentric and eccentric hypertrophic growth (Fig. 2).

Cytokines and inflammasome in cardiac remodeling. Cytokines of the interleukin-6 (IL6) family are key molecules for the local regulation of hypertrophic responses in cardiomyocytes (Fig. 1). Pressure overload acts as a strong trigger for the upregulation of genes related to leukemia inhibitory factor (LIF) and cardiotrophin-1 (CT-1) in the adult human myocardium^{195, 196}. Cardiomyocytes and cardiac fibroblasts produce leukemia LIF and CT-1 (Table 2)^{197, 198}. The release of Hi-FGF-2 from cardiac fibroblasts (Table 2) has been suggested to act in an autocrine way and trigger the release of pro-hypertrophic CT-1^{126, 199, 200}. Moreover, cardiomyocytes also express autocrine-acting CT-1, and CT-1 induces hypertrophy of cardiomyocytes *in vitro*²⁰¹. Increased production and release of LIF, CT-1, and IL-6 in cardiac fibroblasts in response to AT-II can contribute to cardiomyocyte hypertrophy by paracrine activation of the gp130-linked downstream signaling (Fig. 2)²⁰². Interestingly, IL-6 contributes to the induction of massive collagen release by cardiac fibroblasts in response to AT-II and norepinephrine stimulation^{203, 204}, consistent with a pro-hypertrophic response. Alternatively, LIF stimulates several beneficial effects including reduction of collagen production and matrix metalloproteinase activity in cardiac fibroblasts, resulting in an inhibition of differentiation of cardiac fibroblast to myofibroblast²⁰⁵. Likewise, the role of CT-1 seems unclear as consistent with reports describing CT-1 as having a potent hypertrophic effect on cultured cardiomyocytes²⁰⁶ in addition to cardioprotective effects such as promoting cardiomyocyte survival²⁰⁷. In conclusion, during the process of developing cardiac hypertrophy, cytokine release is increased in response to a variety of stress stimuli, including pressure overload, injury, and mediators like AT-II. However, since IL-6 has a negative inotropic effect, its function is still unclear,²⁰⁸ suggesting the possibility of detrimental impacts by IL-6 driving hypertrophy toward heart failure.

According to data binding of all IL-6-type cytokines to their common receptor subunit gp130 potentially activates STAT3 and to a lesser extent STAT1 (Fig. 2)²⁰⁹. Transgenic mice with cardiac-specific STAT3 over-expression found that STAT3 holds a key role in hypertrophic and

protective signaling, respectively. STAT3 induced the expression of cardiac protective factors and guarded against decreases in the expression rates of cardiac contractile genes in the case of doxorubicin-induced cardiomyopathy ²¹⁰. In line with this, another study that used pressure overload on ventricular-restricted gp130 receptor knockout mice found a rapid onset of dilated cardiomyopathy and induction of cardiomyocyte apoptosis. In comparison, a normal cardiac structure and function were found under basal conditions, and compensated hypertrophy was found in control mice under pressure overload ²¹¹. These observations suggest a key role of the gp130/STAT pathway in cardiomyocytes for transmitting adaptive and protective functions in response to pressure overload and injury. However, a study on transgenic mice that expressed a dominant negative mutant of gp130 (to decrease activation of this pathway) reported concomitant to a suppressed STAT3 activation a significantly smaller hypertrophic response when subjected to pressure overload ²¹², suggesting a pro-hypertrophic function for STAT3. Whether the effects of the gp130 signaling pathway are beneficial or detrimental remains unclear. Since pressure overload triggers hypertrophic responses in cardiomyocytes via GPCRs in turn activating PKC and PKD (Fig. 2) ²¹³, potential crosstalk of signaling pathways could be involved. Likewise, neonatal rat cardiomyocytes showed that stretch induces a transient activation in a sequential time order on PKC and other downstream targets as the successive components of the MAPK signaling cascade (Fig. 2) ²¹⁴.

In contrast, YAP1, a downstream effector of Hippo signaling regulating proliferation, survival, and organogenesis in mammalian cells, that can also be activated through SRC-mediated gp130 activation in cardiomyocytes ²¹⁵, is involved in cardio-protective mechanisms against pressure overload stimulation of cardiac hypertrophy (Fig. 2). Under chronic pressure overload conditions, activation of YAP transcriptional activity reduces the development of cardiac hypertrophy. Additionally, apoptosis and fibrosis effects on cardiomyocytes that can be prerequisites for myocardial infarction are reduced ²¹⁶. The transcriptional activity of YAP mediates compensatory cardiac hypertrophy under pressure overload conditions ²¹⁷ to stop the progression of wall stress into myocardial infarction, while CMs are driven toward heart failure by the detrimental effects of YAP signaling loss-of-function ²¹⁸.

Concomitant hypertrophic responses via activation of PKC and MAP kinases can also be triggered by AT-II (Fig. 2). Cardiomyocytes under mechanical stress secrete AT-II ¹²³. Here, active PKC, with its numerous nuclear and cytosolic substrates ²¹⁹, specifies the extensive crosstalk of signaling pathways in response to pressure overload. The alpha-isoform of PKC directly activates RAF1 ²²⁰, providing evidence for a complex link between the signaling pathway downstream of growth factor receptors in the context of cardiac hypertrophy. Others have reported that GPCR signaling can be crosslinked directly to RAS (Fig. 2) ¹²⁴, and GTP-bound RAS interacts with many downstream effectors which in turn transmit the signal for activating multiple signaling pathways ²²¹, potentially promoting hypertrophic responses in cardiomyocytes. Additionally, others reported that the C-terminus of the AT1 receptor associates with JAK2 upon binding of the ligand, resulting in JAK2/STAT3 pathway activation ²²²⁻²²⁵, indicating another example of the crosstalk interaction of signaling pathways in response to hypertrophy-associated stress signals. These lines of evidence indicate that the discrepancy of data regarding the gp130 signaling pathway may be due to the extensive crosstalk between intracellular signaling pathways (Fig. 2). Taken together, there are contradictory reports regarding the individual effects of IL-6, LIF, CT-1 and their signaling via the gp130 pathway in cardiac hypertrophy, thus further investigation is necessary for elucidating the exact mechanisms.

Calcineurin/NFAT in cardiac hypertrophy. Calcineurin as a Ca²⁺-dependent serine/threonine protein-phosphatase has been found to exhibit central pro-hypertrophic functions in the myocardium (Fig. 2) ²²⁶. Calcineurin contains two subunits: the 57-61-kDa catalytic subunit (CnA) and the 19-kDa regulatory subunit (CnB). Activation of this dimeric protein occurs through direct binding of the Ca²⁺-saturated adaptor protein calmodulin ²²⁷. The mammalian heart only expresses CnA α , CnA β , and CnB1, although there are three genes

including CnA α , β and γ encoding for CnA, and two genes (*CnB1* and *B2*) encode for CnB. Calcineurin becomes activated in response to increased Ca²⁺ levels, which enables binding to transcription factors of the nuclear factor of activated T cells (NFAT) family (Fig. 2)²²⁷.

Pro-hypertrophic gene expression is activated upon binding, and through dephosphorylation of conserved serine residues at the N terminus of NFAT by calcineurin, resulting in NFAT translocating into the nucleus (Fig. 2)²²⁷. Here, NFAT regulates the expression of cardiac genes *via* association with GATA4 and myocyte enhancer factor 2 (MEF2), which are also transcription factors^{228, 229}. Noteworthy, several studies indicate that NFAT transcription factors act as primary calcineurin effectors in the heart, as they have been identified as necessary and sufficient mediators promoting cardiac hypertrophy^{226, 228}. Moreover, cardiomyocytes contain structural proteins located in the repetitive Z-disc that have been found to regulate calcineurin in addition to the activation *via* increased Ca²⁺²³⁰⁻²³³.

GPCR stimulation with hypertrophic agonists, including AT-II and PE on cultured neonatal rat cardiomyocytes indicated an increase in calcineurin enzymatic activity, which was induced by increased calcineurin A β (CnA β) mRNA and protein, compared to CnA α or CnA γ ²³⁴. By that, human hypertrophied and failing hearts (Fig. 4) also exhibit increased calcineurin activity²³⁵, as well as in ventricular muscle with exposure to AT-II, ET-1, and Urotensin II in human failing heart²³⁶. Significantly, hypertrophied hearts in rodents subjected to aortic banding displayed upregulated calcineurin activity²³⁷⁻²⁴¹ and profound cardiac hypertrophy with rapid progression to dilated cardiomyopathy, extensive fibrosis, congestive heart failure, and sudden death (Fig. 4) were observed in active calcineurin expressing transgenic mice²²⁶.

Upregulated NFAT activity has been observed upon both physiological stimuli (exercise training, growth hormone-IGF1 infusion) and pathological stimuli (pressure overload, myocardial infarction) (Table 1)¹¹. In contrast, the hypertrophic response to pressure overload and GPCR agonists was impaired in a model of transgenic mice exhibiting a targeted inactivation of calcineurin A β ²⁴² and in transgenic mice expressing a dominant negative form of calcineurin A²⁴⁰. Furthermore, cardiac hypertrophy was prevented in a model using pharmacological inhibition of calcineurin A activity on transgenic mice with constitutively active calcineurin A²²⁶.

These lines of evidence taken together indicate that calcineurin/NFAT plays a major role in the conversion of pathogenic stimuli into pathological cardiac remodeling, suggesting it is a key target in the setup of clinical prevention of cardiac hypertrophic (Fig. 4). But data seems contradictory, as a study reported accentuated hypertrophy, impaired histopathology as well as risk for early death when applying calcineurin inhibitors²⁴³. Thus, further investigation is necessary to clarify if calcineurin/NFAT could be considered as a key target.

ANP/BNP in cardiac hypertrophy. Development of pathological cardiac hypertrophy is frequently linked to increased mRNA expression of atrial natriuretic peptide (ANP) and B-type natriuretic peptide (BNP), according to studies in both human and animal models^{244, 245}, as well as an increase in the plasma levels of ANP and BNP with the severity of heart failure. Under critical conditions, more BNP than ANP is secreted, largely in the ventricles and atria, respectively. However, as heart failure worsens, ANP is also secreted in the ventricles; for this reason, the ventricles are crucial locations for both BNP and ANP²⁴⁶. Both ANP and BNP, as well as their more stable cleavage products, NT-proANP and NT-proBNP, respectively, are efficient biomarkers in the clinical diagnosis and management of heart failure (Fig. 4)^{247, 248}.

Besides the physiological effects of ANP and BNP such as vasodilation, regulation of sodium reabsorption and water balance as well as inhibition of the renin-angiotensin-aldosterone (RAA) system, collectively directed towards responding to cardiac pressure and volume dynamics and suppression of heart failure^{249, 250}, ANP/BNP causes the cGMP-dependent PKG

to be activated (Fig. 2), which in turn prompts the Ca^{2+} /calmodulin-dependent endothelial nitric oxide (NO) synthase to aid in the production of more NO, which relaxes the vascular smooth muscle cells and lowers systemic blood pressure^{249, 251, 252}. ANP/BNP and NO can also counteract NE effects on the size expansion of cardiomyocytes, presumably through the cGMP-PKG-mediated cardioprotective axis resulting in the reduction of NE-stimulated Ca^{2+} influx^{251, 253}.

Moreover, while ANP and BNP expression is being regulated by pro-hypertrophic transcriptional activation of NFAT, on the other hand, ANP and BNP can counteract as negative regulators of hypertrophy by PKG-mediated inhibition of calcineurin to curb nuclear translocation of NFAT (Fig. 2)²⁵⁴⁻²⁵⁶.

4. Computational models of cardiac hypertrophy

Many mediators and pathways implicated in cardiac hypertrophy hinder the field's ability to integrate individual findings into a common framework. To address this, several computational models have been developed that provide systems-level insight into how cardiac hypertrophy is regulated. In the first model of hypertrophic signaling, Cooling et al. examined the factors that control the kinetics of IP3²⁵⁷. They found that ET-1 induced a much more sustained IP3 signal than AT-II, which was best explained by differences in receptor kinetics. To obtain a more global view of hypertrophic signaling, Ryall et al. used a logic-based modeling framework²⁵⁸ to simulate 193 reactions integrated across 14 pathways²⁵⁹. Comprehensive knockout simulations supported the conclusion that Ras is the hub of a bow-tie control structure, which integrates signals from many receptors and stimulates hypertrophy through partially redundant MAPK pathways. This was validated in new experiments comparing the effects of inhibition of RAS, MEK, p38, and JNK²⁵⁹.

While neonatal cardiomyocytes have been extremely useful in the study of cardiac hypertrophy, it is well-known that they show limited maturity compared to adult cells²⁶⁰. But quantitatively, to what extent are *in vitro* data predictive of *in vivo* cardiac hypertrophy? To address this question comprehensively, Frank et al. used the model of neonatal cardiomyocyte hypertrophy²⁵⁹ to attempt to predict the *in vivo* hypertrophy for 52 cardiac-specific transgenic mice²⁶¹. Strikingly, they found that the model correctly predicted 78% of cardiac outputs, including four double-transgenic mouse models. Differences between model predictions and *in vivo* experiments may indicate differences between *in vitro* and *in vivo* mechanisms or specific transgenic mice whose hypertrophic phenotype depends on specific contexts (e.g., hormones, genetic background).

Indeed, examination of context-dependent regulation can elucidate new aspects of signaling networks. Khalilimeybodi et al. developed a computational method called CLASSSED to systematically revise the previous model of Ryall et al.²⁵⁸ using context-dependent experimental data from 550 experimental data from 230 literature articles. Examining areas of a model-experiment disagreement using CLASSSED, they identified the reactions that should be removed or added from the network. They also found new crosstalks between $\text{G}\beta\gamma$ and CaMKII or calcineurin, which were validated in neonatal cardiomyocytes²⁵⁸. Most recently, models of cardiomyocyte signaling are being incorporated into models of multiscale integration of mechanics and signaling in pressure overload, hormones²⁶², or pregnancy²⁶³. Recently, researchers have attempted to mature iPSC-CMs by prolonged culture duration, metabolic substrates, and mechanical and electrical stimulation to model HCM and measure cellular morphology, contractility, electrophysiological property, calcium handling, and metabolism^{264, 265}. Therefore, network model reparameterization for iPSC-CM will be advantageous from the perspective of translational applications. Cardiac hypertrophy is associated with an increased occurrence of ventricular arrhythmia²⁶⁶. Interestingly, several nodes in the signaling network of hypertrophy (such as CaMKII, PKA, and calcineurin) modulate the ion channels^{267, 268}. Therefore, the involvement of these node states in multiscale electromechanical models may predict the association of hypertrophy and arrhythmia.

5. Concluding remarks and future directions

The microenvironment involved in the development of cardiac hypertrophy involves cardiomyocytes and non-myocardial cells, and the accompanying release of numerous pro-hypertrophic, pro-fibrotic, and pro-inflammatory mediators facilitating reciprocal interactions.

Cardiac fibroblasts are the main players in the development of fibrosis, nevertheless, endothelial cells that can undergo EndMT toward a myofibroblast-like phenotype are closely involved as well. Resident and infiltrating immune cells (mast cells, macrophages, neutrophils) enhance these processes while simultaneously contributing to tissue inflammation. Thus, considering all these mechanisms in the hypertrophic microenvironment, it appears that tailoring an efficient treatment regimen is extremely complex. Sophisticated strategies and most likely multidirectional approaches are needed and should be well-approachable using computational modeling systems that allow the integration of all signaling components.

Since it is not feasible to discuss every cellular and molecular process involved in the development of different types of cardiac hypertrophy, we aimed to outline the main drivers of the hypertrophic microenvironment and the respective signaling pathways being affected. A necessary future approach will be the identification of the precise involvement of different cell types, cellular mediators released by them, and the respective activation of second messengers. This will allow us to evaluate the known and thus far unrecognized molecular signaling axes during disease development. Moreover, such data collection within a computational model will help to guide effective and selective targeting strategies in cardiac hypertrophy. Given the high prevalence of heart disease in the Western world, an important future effort should be to translate the knowledge gained into new pharmacological targets that help to delay or even stop the remodeling process and the severe consequences that patients experience after diagnosis of a diastolic or systolic dysfunction.

Acknowledgments

We thank Professor Joachim Schmitt of the Institute of Pharmacology, Faculty of Medicine, Heinrich Heine University, Düsseldorf, for the critical review of the manuscript.

Competing interests

The authors declare that they have no competing interests.

Funding

This study was supported by the International Research Training Group 1902 Intra- and Interorgan Communication of the Cardiovascular System (Grant number: IRTG 1902-P6), the German Federal Ministry of Education and Research (BMBF), German Network of RASopathy Research (GeNeRARE, grant numbers: 01GM1902C), the European Network on Noonan Syndrome and Related Disorders (NSEuroNet, grant number: 01GM1602B), the German Research Foundation (grant number: SFB1525/453989101) and TRR 296/1 2020, and the National Institutes of Health (grant number: NIH R01HL162925).

Abbreviations

AC, adenylate cyclase; ACE, angiotensin converting enzyme; α -cd actin, alpha-cardiac actin; aFGF, acidic fibroblast growth factor; AGT, angiotensinogen; AKT/PKB, protein kinase B; α -MHC, α -myosin heavy chain; AMP, adenosine monophosphate; ANP, atrial natriuretic peptide; APCs, antigen-presenting cells; α -sk actin, alpha skeletal muscle actin; α -sm actin, alpha smooth muscle actin; AT-I, angiotensin I; AT-II, angiotensin II; AT1R, angiotensin II type 1 receptor; ATP, adenosine triphosphate; bFGF, basic fibroblast growth factor; FGF-2, fibroblast growth factor 2; BH4, tetrahydrobiopterin; β -MHC, β -myosin heavy chain; BNP, brain natriuretic peptide; Ca^{2+} , Calcium ion; CaMK, calmodulin-dependent kinase; cAMP, cyclic adenosine monophosphate; CHF, chronic heart failure; CMs, cardiomyocytes; CnA β , calcineurin A β ; CNP, c-type natriuretic peptide; CR, cytokine receptor; CT-1, cardiotrophin-1; DCs, dendritic cells; ECM, extracellular-matrix; EndMT, endothelial-to-mesenchymal transition; ERK, extracellular signal regulated kinase; ET-1, endothelin-1; FGFR, FGF receptor; GPCR, G-protein-coupled receptor; gp130, glycoprotein 130; GSK3 β , glycogen synthase kinase-3 β ; GTP, guanosine-5'-triphosphate; HCM, hypertrophic cardiomyopathy; HDAC4/5, histone deacetylases; Hi-bFGF, high molecular weight FGF-2; H₂O₂, hydroxyl and hydrogen peroxide; ICAM-1, intercellular adhesion molecule-1; IGF1, Insulin like growth factor-1; IL-1, Interleukin-1; IL-1b, Interleukin-1b; IP3, inositol-1,4,5-trisphosphate; iPSC, induced pluripotent stem cells; Janus kinase; JNK, c-Jun N-terminal kinase; LIF, leukemia inhibitory factor; Lo-FGF-2, low molecular weight FGF-2; MAPK, mitogen-activated protein kinase; MAPKKK, mitogen-activated kinase kinase kinase; MCP-1, monocyte chemoattractant protein-1; MEF2, myocyte enhancer factor 2; MEK, mitogen activated ERK activating kinase; MLC, myosin light chain; NADPH, nicotinamide adenine dinucleotide phosphate; NFAT, nuclear factor of activated T cells; NE, norepinephrine; NF- κ B, nuclear factor kappa B; NO, nitric oxide; NOS, uncoupled NO synthases; NOX, nicotinamide adenine dinucleotide phosphate oxidase; NRCs, neonatal rat cardiomyocytes; O₂⁻, superoxide anion; ONOO⁻, peroxynitrite; PDE3A, phosphodiesterase-3a; PAF, platelet-activating factor; PDGF, platelet-derived growth factor; PE, phenylephrine; PI2, prostaglandin I2; PKA, protein kinase-A; PKC, protein kinase-C; PKD, protein kinase-D; PI3K, phosphoinositide 3-kinase; PKGI, cyclic GMP (cGMP)-dependent protein kinase 1; PLC, phospholipase-C; RAAS, renin-angiotensin-aldosterone system; Rac, RAS-related C3 botulinum toxin substrate; Raf, rapidly accelerated fibrosarcoma; RAS, renin-angiotensin system; Ras, rat sarcoma; ROS, reactive oxygen species; SERCA2, Ca-pump of sarcoplasmic reticulum; SMAD, Suppressor of Mothers Against Decapentaplegic; Src, sarcoma; STAT, signal transducer and activator of transcription; TGF- β , transforming growth factor beta; TFs, transcription factors; TNF α , tumor necrosis factor- α ; VCAM-1, vascular cell adhesion molecule-1; LVH, ventricular cardiac hypertrophy; XO, xanthine oxidase; YAP, yes-associated protein.

References

1. Zhu L, Li C, Liu Q, Xu W, Zhou X. Molecular biomarkers in cardiac hypertrophy. *Journal of cellular and molecular medicine*. 2019;23:1671-1677.
2. Peter AK, Bjerke MA, Leinwand LA. Biology of the cardiac myocyte in heart disease. *Molecular biology of the cell*. 2016;27:2149-2160.
3. Schaub MC, Hefti MA, Harder BA, Eppenberger HM. Various hypertrophic stimuli induce distinct phenotypes in cardiomyocytes. *Journal of molecular medicine*. 1997;75:901-920.
4. Heineke J, Molkentin JD. Regulation of cardiac hypertrophy by intracellular signalling pathways. *Nature reviews. Molecular cell biology*. 2006;7:589-600.
5. Mailliet M, van Berlo JH, Molkentin JD. Molecular basis of physiological heart growth: fundamental concepts and new players. *Nat Rev Mol Cell Biol*. 2013;14:38-48.
6. Ovchinnikova E, Hoes M, Ustyantsev K, et al. Modeling Human Cardiac Hypertrophy in Stem Cell-Derived Cardiomyocytes. *Stem Cell Reports*. 2018;10:794-807.
7. Berenji K, Drazner MH, Rothermel BA, Hill JA. Does load-induced ventricular hypertrophy progress to systolic heart failure? *American journal of physiology. Heart and circulatory physiology*. 2005;289:H8-H16.
8. Haider AW, Larson MG, Benjamin EJ, Levy D. Increased left ventricular mass and hypertrophy are associated with increased risk for sudden death. *Journal of the American College of Cardiology*. 1998;32:1454-1459.
9. Nakamura M, Sadoshima J. Mechanisms of physiological and pathological cardiac hypertrophy. *Nature reviews. Cardiology*. 2018;15:387-407.
10. Bernardo BC, Weeks KL, Pretorius L, McMullen JR. Molecular distinction between physiological and pathological cardiac hypertrophy: experimental findings and therapeutic strategies. *Pharmacology & therapeutics*. 2010;128:191-227.
11. Wilkins BJ, Dai YS, Bueno OF, et al. Calcineurin/NFAT coupling participates in pathological, but not physiological, cardiac hypertrophy. *Circulation research*. 2004;94:110-118.
12. Grossman W, Jones D, McLaurin LP. Wall stress and patterns of hypertrophy in the human left ventricle. *The Journal of clinical investigation*. 1975;56:56-64.
13. Dorn GW, 2nd. The fuzzy logic of physiological cardiac hypertrophy. *Hypertension*. 2007;49:962-970.
14. Shenasa M, Shenasa H. Hypertension, left ventricular hypertrophy, and sudden cardiac death. *International journal of cardiology*. 2017;237:60-63.
15. Levy D, Garrison RJ, Savage DD, Kannel WB, Castelli WP. Prognostic implications of echocardiographically determined left ventricular mass in the Framingham Heart Study. *The New England journal of medicine*. 1990;322:1561-1566.
16. Weber KT, Brilla CG, Janicki JS. Myocardial fibrosis: functional significance and regulatory factors. *Cardiovascular research*. 1993;27:341-348.
17. Cohn JN, Bristow MR, Chien KR, et al. Report of the National Heart, Lung, and Blood Institute Special Emphasis Panel on Heart Failure Research. *Circulation*. 1997;95:766-770.
18. Perrino C, Prasad SVN, Mao L, et al. Intermittent pressure overload triggers hypertrophy-independent cardiac dysfunction and vascular rarefaction. *The Journal of clinical investigation*. 2006;116:1547-1560.
19. Tzahor E, Dimmeler S. A coalition to heal—the impact of the cardiac microenvironment. *Science*. 2022;377:eabm4443.

20. Hefti MA, Harder BA, Eppenberger HM, Schaub MC. Signaling pathways in cardiac myocyte hypertrophy. *Journal of molecular and cellular cardiology*. 1997;29:2873-2892.
21. Zhang M, Shah AM. ROS signalling between endothelial cells and cardiac cells. *Cardiovascular research*. 2014;102:249-257.
22. Peter AK, Bjerke MA, Leinwand LA. Biology of the cardiac myocyte in heart disease. *Molecular biology of the cell*. 2016;27:2149-2160.
23. Takeda N, Manabe I. Cellular Interplay between Cardiomyocytes and Nonmyocytes in Cardiac Remodeling. *International journal of inflammation*. 2011;2011:535241.
24. Jane-Lise S, Corda S, Chassagne C, Rappaport L. The extracellular matrix and the cytoskeleton in heart hypertrophy and failure. *Heart failure reviews*. 2000;5:239-250.
25. Moore-Morris T, Guimaraes-Camboa N, Banerjee I, et al. Resident fibroblast lineages mediate pressure overload-induced cardiac fibrosis. *The Journal of clinical investigation*. 2014;124:2921-2934.
26. Kanisicak O, Khalil H, Ivey MJ, et al. Genetic lineage tracing defines myofibroblast origin and function in the injured heart. *Nature communications*. 2016;7:1-14.
27. Tallquist MD, Molkentin JD. Redefining the identity of cardiac fibroblasts. *Nature reviews. Cardiology*. 2017;14:484-491.
28. Powell DW, Mifflin RC, Valentich JD, Crowe SE, Saada JI, West AB. Myofibroblasts. I. Paracrine cells important in health and disease. *The American journal of physiology*. 1999;277:C1-9.
29. Tomasek JJ, Gabbiani G, Hinz B, Chaponnier C, Brown RA. Myofibroblasts and mechano-regulation of connective tissue remodelling. *Nature reviews. Molecular cell biology*. 2002;3:349-363.
30. Sappino AP, Schurch W, Gabbiani G. Differentiation repertoire of fibroblastic cells: expression of cytoskeletal proteins as marker of phenotypic modulations. *Laboratory investigation; a journal of technical methods and pathology*. 1990;63:144-161.
31. Desmouliere A, Geinoz A, Gabbiani F, Gabbiani G. Transforming growth factor-beta 1 induces alpha-smooth muscle actin expression in granulation tissue myofibroblasts and in quiescent and growing cultured fibroblasts. *The Journal of cell biology*. 1993;122:103-111.
32. Manabe I, Shindo T, Nagai R. Gene expression in fibroblasts and fibrosis: involvement in cardiac hypertrophy. *Circulation research*. 2002;91:1103-1113.
33. Chaturvedi RR, Herron T, Simmons R, et al. Passive stiffness of myocardium from congenital heart disease and implications for diastole. *Circulation*. 2010;121:979-988.
34. Spach MS, Boineau JP. Microfibrosis produces electrical load variations due to loss of side-to-side cell connections: a major mechanism of structural heart disease arrhythmias. *Pacing and clinical electrophysiology : PACE*. 1997;20:397-413.
35. Sabbah HN, Sharov VG, Lesch M, Goldstein S. Progression of heart failure: a role for interstitial fibrosis. *Molecular and cellular biochemistry*. 1995;147:29-34.
36. Zeisberg EM, Tarnavski O, Zeisberg M, et al. Endothelial-to-mesenchymal transition contributes to cardiac fibrosis. *Nature medicine*. 2007;13:952-961.
37. Cheng W, Li X, Liu D, Cui C, Wang X. Endothelial-to-mesenchymal transition: role in cardiac fibrosis. *Journal of Cardiovascular Pharmacology and Therapeutics*. 2021;26:3-11.

38. Xu X, Tan X, Tampe B, et al. Epigenetic balance of aberrant Rasal1 promoter methylation and hydroxymethylation regulates cardiac fibrosis. *Cardiovascular research*. 2015;105:279-291.
39. Brutsaert DL. Cardiac endothelial-myocardial signaling: its role in cardiac growth, contractile performance, and rhythmicity. *Physiological reviews*. 2003;83:59-115.
40. Esper RJ, Nordaby RA, Vilarino JO, Paragano A, Cacharron JL, Machado RA. Endothelial dysfunction: a comprehensive appraisal. *Cardiovascular diabetology*. 2006;5:4.
41. Kuhn M. Cardiology: A big-hearted molecule. *Nature*. 2015;519:416-417.
42. Moravec CS, Reynolds EE, Stewart RW, Bond M. Endothelin is a positive inotropic agent in human and rat heart in vitro. *Biochemical and biophysical research communications*. 1989;159:14-18.
43. Yanagisawa M, Kurihara H, Kimura S, et al. A novel potent vasoconstrictor peptide produced by vascular endothelial cells. *Nature*. 1988;332:411-415.
44. Gray MO, Long CS, Kalinyak JE, Li HT, Karliner JS. Angiotensin II stimulates cardiac myocyte hypertrophy via paracrine release of TGF-beta 1 and endothelin-1 from fibroblasts. *Cardiovascular research*. 1998;40:352-363.
45. Drawnel FM, Archer CR, Roderick HL. The role of the paracrine/autocrine mediator endothelin-1 in regulation of cardiac contractility and growth. *British journal of pharmacology*. 2013;168:296-317.
46. Urata H, Hoffmann S, Ganten D. Tissue angiotensin II system in the human heart. *European heart journal*. 1994;15 Suppl D:68-78.
47. Sartore S, Chiavegato A, Faggini E, et al. Contribution of adventitial fibroblasts to neointima formation and vascular remodeling: from innocent bystander to active participant. *Circulation research*. 2001;89:1111-1121.
48. Liu X, Shi GP, Guo J. Innate Immune Cells in Pressure Overload-Induced Cardiac Hypertrophy and Remodeling. *Frontiers in cell and developmental biology*. 2021;9:659666.
49. Assem E, Ghanem N, Abdullah N, Repke H, Foreman J, Hayes N. Substance P and Arg-Pro-Lys-Pro-NH-C12-H25-induced mediator release from different mast cell subtypes of rat and guinea-pig. *Immunopharmacology*. 1989;17:119-128.
50. Ghanem N, Assem E, Leung K, Pearce F. Cardiac and renal mast cells: morphology, distribution, fixation and staining properties in the guinea pig and preliminary comparison with human. *Agents and actions*. 1988;23:223-226.
51. Dvorak AM. Mast-cell degranulation in human hearts. *N Engl J Med*. 1986;315:969-970.
52. Estensen R. Eosinophilic myocarditis: a role for mast cells? *Archives of pathology & laboratory medicine*. 1984;108:358-359.
53. Forman MB, Oates JA, Robertson D, Robertson RM, Roberts LJ, Virmani R. Increased adventitial mast cells in a patient with coronary spasm. *New England Journal of Medicine*. 1985;313:1138-1141.
54. Mekori YA, Metcalfe DD. Mast cells in innate immunity. *Immunological reviews*. 2000;173:131-140.
55. Liu X, Shi G-P, Guo J. Innate immune cells in pressure overload-induced cardiac hypertrophy and remodeling. *Frontiers in cell and developmental biology*. 2021;9.
56. Balakumar P, Singh AP, Ganti SS, Krishan P, Ramasamy S, Singh M. Resident cardiac mast cells: are they the major culprit in the pathogenesis of cardiac hypertrophy? *Basic & clinical pharmacology & toxicology*. 2008;102:5-9.

57. Shiota N, Rysa J, Kovanen PT, Ruskoaho H, Kokkonen JO, Lindstedt KA. A role for cardiac mast cells in the pathogenesis of hypertensive heart disease. *Journal of hypertension*. 2003;21:1935-1944.
58. Petrov VV, Fagard RH, Lijnen PJ. Stimulation of collagen production by transforming growth factor-beta1 during differentiation of cardiac fibroblasts to myofibroblasts. *Hypertension*. 2002;39:258-263.
59. Weber KT. Fibrosis and hypertensive heart disease. *Current opinion in cardiology*. 2000;15:264-272.
60. Leurs R, Bakker RA, Timmerman H, de Esch IJ. The histamine H3 receptor: from gene cloning to H3 receptor drugs. *Nature reviews. Drug discovery*. 2005;4:107-120.
61. Hough LB. Genomics meets histamine receptors: new subtypes, new receptors. *Molecular pharmacology*. 2001;59:415-419.
62. Barka T, van der Noen H, Shaw PA. Proto-oncogene fos (c-fos) expression in the heart. *Oncogene*. 1987;1:439-443.
63. Matsuda N, Jesmin S, Takahashi Y, et al. Histamine H1 and H2 receptor gene and protein levels are differentially expressed in the hearts of rodents and humans. *The Journal of pharmacology and experimental therapeutics*. 2004;309:786-795.
64. Hill SJ, Ganellin CR, Timmerman H, et al. International Union of Pharmacology. XIII. Classification of histamine receptors. *Pharmacological reviews*. 1997;49:253-278.
65. Eckel L, Gristwood RW, Nawrath H, Owen DA, Satter P. Inotropic and electrophysiological effects of histamine on human ventricular heart muscle. *The Journal of physiology*. 1982;330:111-123.
66. Du XY, Schoemaker RG, X462P, Bos E, Saxena PR. Effects of histamine on porcine isolated myocardium: differentiation from effects on human tissue. *Journal of cardiovascular pharmacology*. 1993;22:468-473.
67. Hattori Y. Cardiac histamine receptors: their pharmacological consequences and signal transduction pathways. *Methods and findings in experimental and clinical pharmacology*. 1999;21:123-131.
68. Kirch W, Halabi A, Hinrichsen H. Hemodynamic effects of quinidine and famotidine in patients with congestive heart failure. *Clinical pharmacology and therapeutics*. 1992;51:325-333.
69. Kim J, Ogai A, Nakatani S, et al. Impact of blockade of histamine H2 receptors on chronic heart failure revealed by retrospective and prospective randomized studies. *Journal of the American College of Cardiology*. 2006;48:1378-1384.
70. Galli SJ. New concepts about the mast cell. *The New England journal of medicine*. 1993;328:257-265.
71. Bradding P, Feather IH, Howarth PH, et al. Interleukin 4 is localized to and released by human mast cells. *The Journal of experimental medicine*. 1992;176:1381-1386.
72. Ohkawara Y, Yamauchi K, Tanno Y, et al. Human lung mast cells and pulmonary macrophages produce tumor necrosis factor-alpha in sensitized lung tissue after IgE receptor triggering. *American journal of respiratory cell and molecular biology*. 1992;7:385-392.
73. Gordon JR, Galli SJ. Mast cells as a source of both preformed and immunologically inducible TNF-alpha/cachectin. *Nature*. 1990;346:274-276.
74. Kaartinen M, Penttila A, Kovanen PT. Mast cells in rupture-prone areas of human coronary atheromas produce and store TNF-alpha. *Circulation*. 1996;94:2787-2792.
75. Frangogiannis NG, Lindsey ML, Michael LH, et al. Resident cardiac mast cells degranulate and release preformed TNF-alpha, initiating the cytokine cascade in

- experimental canine myocardial ischemia/reperfusion. *Circulation*. 1998;98:699-710.
76. Gilles S, Zahler S, Welsch U, Sommerhoff CP, Becker BF. Release of TNF-alpha during myocardial reperfusion depends on oxidative stress and is prevented by mast cell stabilizers. *Cardiovascular research*. 2003;60:608-616.
 77. Barnes PJ, Karin M. Nuclear factor-kappaB: a pivotal transcription factor in chronic inflammatory diseases. *The New England journal of medicine*. 1997;336:1066-1071.
 78. Sugden PH, Clerk A. "Stress-responsive" mitogen-activated protein kinases (c-Jun N-terminal kinases and p38 mitogen-activated protein kinases) in the myocardium. *Circulation research*. 1998;83:345-352.
 79. Prussin C, Metcalfe DD. 5. IgE, mast cells, basophils, and eosinophils. *The Journal of allergy and clinical immunology*. 2006;117:S450-456.
 80. Yamauchi-Takahara K, Hirota H, Kunisada K, et al. Roles of gp130 signaling pathways in cardiac myocytes: recent advances and implications for cardiovascular disease. *Journal of cardiac failure*. 1996;2:S63-68.
 81. Plenz G, Song ZF, Tjan TD, et al. Activation of the cardiac interleukin-6 system in advanced heart failure. *European journal of heart failure*. 2001;3:415-421.
 82. Silver RB, Reid AC, Mackins CJ, et al. Mast cells: a unique source of renin. *Proceedings of the National Academy of Sciences of the United States of America*. 2004;101:13607-13612.
 83. Mackins CJ, Kano S, Seyedi N, et al. Cardiac mast cell-derived renin promotes local angiotensin formation, norepinephrine release, and arrhythmias in ischemia/reperfusion. *The Journal of clinical investigation*. 2006;116:1063-1070.
 84. Dostal DE, Baker KM. The cardiac renin-angiotensin system: conceptual, or a regulator of cardiac function? *Circulation research*. 1999;85:643-650.
 85. Krop M, Danser AH. Circulating versus tissue renin-angiotensin system: on the origin of (pro)renin. *Current hypertension reports*. 2008;10:112-118.
 86. McEuen AR, Sharma B, Walls AF. Regulation of the activity of human chymase during storage and release from mast cells: the contributions of inorganic cations, pH, heparin and histamine. *Biochimica et Biophysica Acta (BBA)-Molecular Cell Research*. 1995;1267:115-121.
 87. Wang H, da Silva J, Alencar A, et al. Mast cell inhibition attenuates cardiac remodeling and diastolic dysfunction in middle-aged, ovariectomized Fischer344x Brown Norway rats. *Journal of cardiovascular pharmacology*. 2016;68:49.
 88. Azzawi M, Kan SW, Hillier V, Yonan N, Hutchinson IV, Hasleton PS. The distribution of cardiac macrophages in myocardial ischaemia and cardiomyopathy. *Histopathology*. 2005;46:314-319.
 89. Epelman S, Lavine KJ, Beaudin AE, et al. Embryonic and adult-derived resident cardiac macrophages are maintained through distinct mechanisms at steady state and during inflammation. *Immunity*. 2014;40:91-104.
 90. Heidt T, Courties G, Dutta P, et al. Differential contribution of monocytes to heart macrophages in steady-state and after myocardial infarction. *Circulation research*. 2014;115:284-295.
 91. Hashimoto D, Chow A, Noizat C, et al. Tissue-resident macrophages self-maintain locally throughout adult life with minimal contribution from circulating monocytes. *Immunity*. 2013;38:792-804.
 92. Molawi K, Wolf Y, Kandalla PK, et al. Progressive replacement of embryo-derived cardiac macrophages with age. *The Journal of experimental medicine*. 2014;211:2151-2158.

93. Mosser DM, Edwards JP. Exploring the full spectrum of macrophage activation. *Nat Rev Immunol*. 2008;8:958-969.
94. Ross R. Atherosclerosis--an inflammatory disease. *The New England journal of medicine*. 1999;340:115-126.
95. Hinglais N, Heudes D, Nicoletti A, et al. Colocalization of myocardial fibrosis and inflammatory cells in rats. *Laboratory investigation; a journal of technical methods and pathology*. 1994;70:286-294.
96. Nicoletti A, Heudes D, Mandet C, Hinglais N, Bariety J, Michel JB. Inflammatory cells and myocardial fibrosis: spatial and temporal distribution in renovascular hypertensive rats. *Cardiovascular research*. 1996;32:1096-1107.
97. Kuwahara F, Kai H, Tokuda K, et al. Roles of intercellular adhesion molecule-1 in hypertensive cardiac remodeling. *Hypertension*. 2003;41:819-823.
98. Capers Qt, Alexander RW, Lou P, et al. Monocyte chemoattractant protein-1 expression in aortic tissues of hypertensive rats. *Hypertension*. 1997;30:1397-1402.
99. Reape TJ, Groot PH. Chemokines and atherosclerosis. *Atherosclerosis*. 1999;147:213-225.
100. Higashiyama H, Sugai M, Inoue H, et al. Histopathological study of time course changes in inter-renal aortic banding-induced left ventricular hypertrophy of mice. *International journal of experimental pathology*. 2007;88:31-38.
101. Bennouna S, Bliss SK, Curiel TJ, Denkers EY. Cross-talk in the innate immune system: neutrophils instruct recruitment and activation of dendritic cells during microbial infection. *Journal of immunology*. 2003;171:6052-6058.
102. Tsuda Y, Takahashi H, Kobayashi M, Hanafusa T, Herndon DN, Suzuki F. Three different neutrophil subsets exhibited in mice with different susceptibilities to infection by methicillin-resistant *Staphylococcus aureus*. *Immunity*. 2004;21:215-226.
103. van Gisbergen KP, Sanchez-Hernandez M, Geijtenbeek TB, van Kooyk Y. Neutrophils mediate immune modulation of dendritic cells through glycosylation-dependent interactions between Mac-1 and DC-SIGN. *The Journal of experimental medicine*. 2005;201:1281-1292.
104. Li JM, Gall NP, Grieve DJ, Chen M, Shah AM. Activation of NADPH oxidase during progression of cardiac hypertrophy to failure. *Hypertension*. 2002;40:477-484.
105. Ciz M, Denev P, Kratchanova M, Vasicek O, Ambrozova G, Lojek A. Flavonoids inhibit the respiratory burst of neutrophils in mammals. *Oxidative medicine and cellular longevity*. 2012;2012:181295.
106. MacKenna D, Summerour SR, Villarreal FJ. Role of mechanical factors in modulating cardiac fibroblast function and extracellular matrix synthesis. *Cardiovascular research*. 2000;46:257-263.
107. Paulus WJ, Tschope C. A novel paradigm for heart failure with preserved ejection fraction: comorbidities drive myocardial dysfunction and remodeling through coronary microvascular endothelial inflammation. *Journal of the American College of Cardiology*. 2013;62:263-271.
108. Pacher P, Beckman JS, Liaudet L. Nitric oxide and peroxynitrite in health and disease. *Physiological reviews*. 2007;87:315-424.
109. Tsutsui H, Kinugawa S, Matsushima S. Mitochondrial oxidative stress and dysfunction in myocardial remodelling. *Cardiovascular research*. 2009;81:449-456.

110. Nishino T, Okamoto K, Eger BT, Pai EF, Nishino T. Mammalian xanthine oxidoreductase - mechanism of transition from xanthine dehydrogenase to xanthine oxidase. *The FEBS journal*. 2008;275:3278-3289.
111. Carnicer R, Crabtree MJ, Sivakumaran V, Casadei B, Kass DA. Nitric oxide synthases in heart failure. *Antioxidants & redox signaling*. 2013;18:1078-1099.
112. Zhang M, Perino A, Ghigo A, Hirsch E, Shah AM. NADPH oxidases in heart failure: poachers or gamekeepers? *Antioxidants & redox signaling*. 2013;18:1024-1041.
113. Zhang Y, Tocchetti CG, Krieg T, Moens AL. Oxidative and nitrosative stress in the maintenance of myocardial function. *Free radical biology & medicine*. 2012;53:1531-1540.
114. Nediani C, Raimondi L, Borch E, Cerbai E. Nitric oxide/reactive oxygen species generation and nitroso/redox imbalance in heart failure: from molecular mechanisms to therapeutic implications. *Antioxidants & redox signaling*. 2011;14:289-331.
115. Dhalla NS, Temsah RM, Netticadan T. Role of oxidative stress in cardiovascular diseases. *Journal of hypertension*. 2000;18:655-673.
116. Sugden PH, Clerk A. Cellular mechanisms of cardiac hypertrophy. *Journal of molecular medicine*. 1998;76:725-746.
117. Chien KR. Stress pathways and heart failure. *Cell*. 1999;98:555-558.
118. Shah AM, MacCarthy PA. Paracrine and autocrine effects of nitric oxide on myocardial function. *Pharmacology & therapeutics*. 2000;86:49-86.
119. Brown DI, Griendling KK. Nox proteins in signal transduction. *Free radical biology & medicine*. 2009;47:1239-1253.
120. Hare JM. Nitroso-redox balance in the cardiovascular system. *The New England journal of medicine*. 2004;351:2112-2114.
121. Chen CA, Wang TY, Varadharaj S, et al. S-glutathionylation uncouples eNOS and regulates its cellular and vascular function. *Nature*. 2010;468:1115-1118.
122. Landmesser U, Dikalov S, Price SR, et al. Oxidation of tetrahydrobiopterin leads to uncoupling of endothelial cell nitric oxide synthase in hypertension. *The Journal of clinical investigation*. 2003;111:1201-1209.
123. Sadoshima J, Xu Y, Slayter HS, Izumo S. Autocrine release of angiotensin II mediates stretch-induced hypertrophy of cardiac myocytes in vitro. *Cell*. 1993;75:977-984.
124. Sadoshima J, Izumo S. The heterotrimeric G q protein-coupled angiotensin II receptor activates p21 ras via the tyrosine kinase-Shc-Grb2-Sos pathway in cardiac myocytes. *The EMBO journal*. 1996;15:775-787.
125. Harada M, Itoh H, Nakagawa O, et al. Significance of ventricular myocytes and nonmyocytes interaction during cardiocyte hypertrophy: evidence for endothelin-1 as a paracrine hypertrophic factor from cardiac nonmyocytes. *Circulation*. 1997;96:3737-3744.
126. Pellieux C, Foletti A, Peduto G, et al. Dilated cardiomyopathy and impaired cardiac hypertrophic response to angiotensin II in mice lacking FGF-2. *The Journal of clinical investigation*. 2001;108:1843-1851.
127. Jiang ZS, Jeyaraman M, Wen GB, et al. High- but not low-molecular weight FGF-2 causes cardiac hypertrophy in vivo; possible involvement of cardiotrophin-1. *Journal of molecular and cellular cardiology*. 2007;42:222-233.
128. Harada K, Komuro I, Zou Y, et al. Acute pressure overload could induce hypertrophic responses in the heart of angiotensin II type 1a knockout mice. *Circulation research*. 1998;82:779-785.

129. Harada K, Komuro I, Shiojima I, et al. Pressure overload induces cardiac hypertrophy in angiotensin II type 1A receptor knockout mice. *Circulation*. 1998;97:1952-1959.
130. Sadoshima J, Izumo S. Molecular characterization of angiotensin II--induced hypertrophy of cardiac myocytes and hyperplasia of cardiac fibroblasts. Critical role of the AT1 receptor subtype. *Circulation research*. 1993;73:413-423.
131. Tóth AD, Turu G, Hunyady L, Balla A. Novel mechanisms of G-protein-coupled receptors functions: AT1 angiotensin receptor acts as a signaling hub and focal point of receptor cross-talk. *Best Practice & Research Clinical Endocrinology & Metabolism*. 2018;32:69-82.
132. Wang J, Hanada K, Gareri C, Rockman HA. Mechanoactivation of the angiotensin II type 1 receptor induces β -arrestin-biased signaling through Gai coupling. *Journal of cellular biochemistry*. 2018;119:3586-3597.
133. Hunyady L, Turu G. The role of the AT1 angiotensin receptor in cardiac hypertrophy: angiotensin II receptor or stretch sensor? *Trends in Endocrinology & Metabolism*. 2004;15:405-408.
134. Brancaccio M, Fratta L, Notte A, et al. Melusin, a muscle-specific integrin beta1-interacting protein, is required to prevent cardiac failure in response to chronic pressure overload. *Nature medicine*. 2003;9:68-75.
135. Knoll R, Hoshijima M, Hoffman HM, et al. The cardiac mechanical stretch sensor machinery involves a Z disc complex that is defective in a subset of human dilated cardiomyopathy. *Cell*. 2002;111:943-955.
136. Saucerman JJ, Tan PM, Buchholz KS, McCulloch AD, Omens JH. Mechanical regulation of gene expression in cardiac myocytes and fibroblasts. *Nature reviews. Cardiology*. 2019;16:361-378.
137. Tan PM, Buchholz KS, Omens JH, McCulloch AD, Saucerman JJ. Predictive model identifies key network regulators of cardiomyocyte mechano-signaling. *PLoS computational biology*. 2017;13:e1005854.
138. Border WA, Noble NA. Transforming growth factor beta in tissue fibrosis. *The New England journal of medicine*. 1994;331:1286-1292.
139. Yang YC, Piek E, Zavadil J, et al. Hierarchical model of gene regulation by transforming growth factor beta. *Proceedings of the National Academy of Sciences of the United States of America*. 2003;100:10269-10274.
140. Verrecchia F, Chu ML, Mauviel A. Identification of novel TGF-beta /Smad gene targets in dermal fibroblasts using a combined cDNA microarray/promoter transactivation approach. *The Journal of biological chemistry*. 2001;276:17058-17062.
141. Bujak M, Ren G, Kweon HJ, et al. Essential role of Smad3 in infarct healing and in the pathogenesis of cardiac remodeling. *Circulation*. 2007;116:2127-2138.
142. Ryer EJ, Hom RP, Sakakibara K, et al. PKCdelta is necessary for Smad3 expression and transforming growth factor beta-induced fibronectin synthesis in vascular smooth muscle cells. *Arteriosclerosis, thrombosis, and vascular biology*. 2006;26:780-786.
143. Kuwahara F, Kai H, Tokuda K, et al. Transforming growth factor-beta function blocking prevents myocardial fibrosis and diastolic dysfunction in pressure-overloaded rats. *Circulation*. 2002;106:130-135.
144. Divakaran V, Adroge J, Ishiyama M, et al. Adaptive and maladaptive effects of SMAD3 signaling in the adult heart after hemodynamic pressure overloading. *Circulation. Heart failure*. 2009;2:633-642.

145. Frantz S, Hu K, Adamek A, et al. Transforming growth factor beta inhibition increases mortality and left ventricular dilatation after myocardial infarction. *Basic research in cardiology*. 2008;103:485-492.
146. Watkins SJ, Jonker L, Arthur HM. A direct interaction between TGFbeta activated kinase 1 and the TGFbeta type II receptor: implications for TGFbeta signalling and cardiac hypertrophy. *Cardiovascular research*. 2006;69:432-439.
147. Zhang D, Gaussin V, Taffet GE, et al. TAK1 is activated in the myocardium after pressure overload and is sufficient to provoke heart failure in transgenic mice. *Nature medicine*. 2000;6:556-563.
148. Bujak M, Frangogiannis NG. The role of TGF-beta signaling in myocardial infarction and cardiac remodeling. *Cardiovascular research*. 2007;74:184-195.
149. Euler G. Good and bad sides of TGFbeta-signaling in myocardial infarction. *Frontiers in physiology*. 2015;6:66.
150. Lindahl GE, Chambers RC, Papakrivopoulou J, et al. Activation of fibroblast procollagen alpha 1(I) transcription by mechanical strain is transforming growth factor-beta-dependent and involves increased binding of CCAAT-binding factor (CBF/NF-Y) at the proximal promoter. *The Journal of biological chemistry*. 2002;277:6153-6161.
151. Wipff PJ, Rifkin DB, Meister JJ, Hinz B. Myofibroblast contraction activates latent TGF-beta1 from the extracellular matrix. *The Journal of cell biology*. 2007;179:1311-1323.
152. Suzuki T, Kumazaki T, Mitsui Y. Endothelin-1 is produced and secreted by neonatal rat cardiac myocytes in vitro. *Biochemical and biophysical research communications*. 1993;191:823-830.
153. Shubeita HE, McDonough PM, Harris AN, et al. Endothelin induction of inositol phospholipid hydrolysis, sarcomere assembly, and cardiac gene expression in ventricular myocytes. A paracrine mechanism for myocardial cell hypertrophy. *The Journal of biological chemistry*. 1990;265:20555-20562.
154. Kedzierski RM, Yanagisawa M. Endothelin system: the double-edged sword in health and disease. *Annual review of pharmacology and toxicology*. 2001;41:851-876.
155. Hilal-Dandan R, Merck DT, Lujan JP, Brunton LL. Coupling of the type A endothelin receptor to multiple responses in adult rat cardiac myocytes. *Molecular pharmacology*. 1994;45:1183-1190.
156. Sugden PH, Bogoyevitch MA. Endothelin-1-dependent signaling pathways in the myocardium. *Trends in cardiovascular medicine*. 1996;6:87-94.
157. Bogoyevitch MA, Andersson MB, Gillespie-Brown J, et al. Adrenergic receptor stimulation of the mitogen-activated protein kinase cascade and cardiac hypertrophy. *The Biochemical journal*. 1996;314 (Pt 1):115-121.
158. Sakai S, Miyauchi T, Kobayashi M, Yamaguchi I, Goto K, Sugishita Y. Inhibition of myocardial endothelin pathway improves long-term survival in heart failure. *Nature*. 1996;384:353-355.
159. de Lemos JA, McGuire DK, Drazner MH. B-type natriuretic peptide in cardiovascular disease. *Lancet*. 2003;362:316-322.
160. Anversa P, Nadal-Ginard B. Myocyte renewal and ventricular remodelling. *Nature*. 2002;415:240-243.
161. Pasumarthi KB, Field LJ. Cardiomyocyte cell cycle regulation. *Circulation research*. 2002;90:1044-1054.
162. Greenberg B. Treatment of heart failure: state of the art and prospectives. *Journal of cardiovascular pharmacology*. 2001;38 Suppl 2:S59-63.

163. Detillieux KA, Sheikh F, Kardami E, Cattini PA. Biological activities of fibroblast growth factor-2 in the adult myocardium. *Cardiovascular research*. 2003;57:8-19.
164. Jimenez SK, Sheikh F, Jin Y, et al. Transcriptional regulation of FGF-2 gene expression in cardiac myocytes. *Cardiovascular research*. 2004;62:548-557.
165. Galzie Z, Kinsella AR, Smith JA. Fibroblast growth factors and their receptors. *Biochemistry and cell biology = Biochimie et biologie cellulaire*. 1997;75:669-685.
166. Hoerstrup SP, Zund G, Schnell AM, et al. Optimized growth conditions for tissue engineering of human cardiovascular structures. *The International journal of artificial organs*. 2000;23:817-823.
167. Liu L, Doble BW, Kardami E. Perinatal phenotype and hypothyroidism are associated with elevated levels of 21.5- to 22-kDa basic fibroblast growth factor in cardiac ventricles. *Developmental biology*. 1993;157:507-516.
168. Parker TG, Packer SE, Schneider MD. Peptide growth factors can provoke "fetal" contractile protein gene expression in rat cardiac myocytes. *The Journal of clinical investigation*. 1990;85:507-514.
169. Peng H, Myers J, Fang X, et al. Integrative nuclear FGFR1 signaling (INFS) pathway mediates activation of the tyrosine hydroxylase gene by angiotensin II, depolarization and protein kinase C. *Journal of neurochemistry*. 2002;81:506-524.
170. Vagner S, Touriol C, Galy B, et al. Translation of CUG- but not AUG-initiated forms of human fibroblast growth factor 2 is activated in transformed and stressed cells. *The Journal of cell biology*. 1996;135:1391-1402.
171. Gualandris A, Urbinati C, Rusnati M, Ziche M, Presta M. Interaction of high-molecular-weight basic fibroblast growth factor with endothelium: biological activity and intracellular fate of human recombinant M(r) 24,000 bFGF. *Journal of cellular physiology*. 1994;161:149-159.
172. Bogoyevitch MA, Glennon PE, Andersson MB, Lazou A, Marshall CJ, Sugden PH. Acidic fibroblast growth factor or endothelin-1 stimulate the MAP kinase cascade in cardiac myocytes. *Biochemical Society transactions*. 1993;21:358S.
173. Liao S, Bodmer J, Pietras D, Azhar M, Doetschman T, Schultz J. Biological functions of the low and high molecular weight protein isoforms of fibroblast growth factor-2 in cardiovascular development and disease. *Developmental dynamics : an official publication of the American Association of Anatomists*. 2009;238:249-264.
174. Jiang ZS, Padua RR, Ju H, et al. Acute protection of ischemic heart by FGF-2: involvement of FGF-2 receptors and protein kinase C. *American journal of physiology. Heart and circulatory physiology*. 2002;282:H1071-1080.
175. Jiang ZS, Srisakuldee W, Soulet F, Bouche G, Kardami E. Non-angiogenic FGF-2 protects the ischemic heart from injury, in the presence or absence of reperfusion. *Cardiovascular research*. 2004;62:154-166.
176. Santiago J-J, McNaughton LJ, Koleini N, et al. High molecular weight fibroblast growth factor-2 in the human heart is a potential target for prevention of cardiac remodeling. *PloS one*. 2014;9:e97281.
177. Schultz JE, Witt SA, Nieman ML, et al. Fibroblast growth factor-2 mediates pressure-induced hypertrophic response. *The Journal of clinical investigation*. 1999;104:709-719.
178. Morrison RS, Yamaguchi F, Saya H, et al. Basic fibroblast growth factor and fibroblast growth factor receptor I are implicated in the growth of human astrocytomas. *Journal of neuro-oncology*. 1994;18:207-216.

179. Reed MJ, Purohit A, Duncan LJ, et al. The role of cytokines and sulphatase inhibitors in regulating oestrogen synthesis in breast tumours. *The Journal of steroid biochemistry and molecular biology*. 1995;53:413-420.
180. Halaban R. Growth factors and melanomas. *Semin Oncol*. 1996;23:673-681.
181. Kumar-Singh S, Weyler J, Martin MJ, Vermeulen PB, Van Marck E. Angiogenic cytokines in mesothelioma: a study of VEGF, FGF-1 and -2, and TGF beta expression. *The Journal of pathology*. 1999;189:72-78.
182. Dow JK, deVere White RW. Fibroblast growth factor 2: its structure and property, paracrine function, tumor angiogenesis, and prostate-related mitogenic and oncogenic functions. *Urology*. 2000;55:800-806.
183. Auguste P, Gursel DB, Lemiere S, et al. Inhibition of fibroblast growth factor/fibroblast growth factor receptor activity in glioma cells impedes tumor growth by both angiogenesis-dependent and -independent mechanisms. *Cancer research*. 2001;61:1717-1726.
184. Lorenz K, Schmitt JP, Schmitteckert EM, Lohse MJ. A new type of ERK1/2 autophosphorylation causes cardiac hypertrophy. *Nature medicine*. 2009;15:75-83.
185. Tomasovic A, Brand T, Schanbacher C, et al. Interference with ERK-dimerization at the nucleocytoplasmic interface targets pathological ERK1/2 signaling without cardiotoxic side-effects. *Nature communications*. 2020;11:1733.
186. Laskowski A, Woodman OL, Cao AH, et al. Antioxidant actions contribute to the antihypertrophic effects of atrial natriuretic peptide in neonatal rat cardiomyocytes. *Cardiovascular research*. 2006;72:112-123.
187. Ruppert C, Deiss K, Herrmann S, et al. Interference with ERK(Thr188) phosphorylation impairs pathological but not physiological cardiac hypertrophy. *Proceedings of the National Academy of Sciences of the United States of America*. 2013;110:7440-7445.
188. Takimoto E, Kass DA. Role of oxidative stress in cardiac hypertrophy and remodeling. *Hypertension*. 2007;49:241-248.
189. Towbin JA. Inherited cardiomyopathies. *Circulation journal : official journal of the Japanese Circulation Society*. 2014;78:2347-2356.
190. Alcalai R, Seidman JG, Seidman CE. Genetic basis of hypertrophic cardiomyopathy: from bench to the clinics. *Journal of cardiovascular electrophysiology*. 2008;19:104-110.
191. Patel R, Nagueh SF, Tsybouleva N, et al. Simvastatin induces regression of cardiac hypertrophy and fibrosis and improves cardiac function in a transgenic rabbit model of human hypertrophic cardiomyopathy. *Circulation*. 2001;104:317-324.
192. Robinson P, Liu X, Sparrow A, et al. Hypertrophic cardiomyopathy mutations increase myofilament Ca(2+) buffering, alter intracellular Ca(2+) handling, and stimulate Ca(2+)-dependent signaling. *The Journal of biological chemistry*. 2018;293:10487-10499.
193. Kehat I, Davis J, Tiburcy M, et al. Extracellular signal-regulated kinases 1 and 2 regulate the balance between eccentric and concentric cardiac growth. *Circulation research*. 2011;108:176-183.
194. Davis J, Davis LC, Correll RN, et al. A Tension-Based Model Distinguishes Hypertrophic versus Dilated Cardiomyopathy. *Cell*. 2016;165:1147-1159.
195. Pemberton CJ, Raudsepp SD, Yandle TG, Cameron VA, Richards AM. Plasma cardiotrophin-1 is elevated in human hypertension and stimulated by ventricular stretch. *Cardiovascular research*. 2005;68:109-117.

196. Pan J, Fukuda K, Kodama H, et al. Involvement of gp130-mediated signaling in pressure overload-induced activation of the JAK/STAT pathway in rodent heart. *Heart and vessels*. 1998;13:199-208.
197. King KL, Winer J, Phillips DM, Quach J, Williams PM, Mather JP. Phenylephrine, endothelin, prostaglandin F2alpha' and leukemia inhibitory factor induce different cardiac hypertrophy phenotypes in vitro. *Endocrine*. 1998;9:45-55.
198. Kuwahara K, Saito Y, Harada M, et al. Involvement of cardiotrophin-1 in cardiac myocyte-nonmyocyte interactions during hypertrophy of rat cardiac myocytes in vitro. *Circulation*. 1999;100:1116-1124.
199. Aoyama T, Takimoto Y, Pennica D, et al. Augmented expression of cardiotrophin-1 and its receptor component, gp130, in both left and right ventricles after myocardial infarction in the rat. *Journal of molecular and cellular cardiology*. 2000;32:1821-1830.
200. Freed DH, Moon MC, Borowiec AM, Jones SC, Zahradka P, Dixon IM. Cardiotrophin-1: expression in experimental myocardial infarction and potential role in post-MI wound healing. *Molecular and cellular biochemistry*. 2003;254:247-256.
201. Wollert KC, Taga T, Saito M, et al. Cardiotrophin-1 activates a distinct form of cardiac muscle cell hypertrophy. Assembly of sarcomeric units in series VIA gp130/leukemia inhibitory factor receptor-dependent pathways. *The Journal of biological chemistry*. 1996;271:9535-9545.
202. Sano M, Fukuda K, Kodama H, et al. Interleukin-6 family of cytokines mediate angiotensin II-induced cardiac hypertrophy in rodent cardiomyocytes. *The Journal of biological chemistry*. 2000;275:29717-29723.
203. Briest W, Rassler B, Deten A, et al. Norepinephrine-induced interleukin-6 increase in rat hearts: differential signal transduction in myocytes and non-myocytes. *Pflügers Archiv : European journal of physiology*. 2003;446:437-446.
204. Sarkar S, Vellaichamy E, Young D, Sen S. Influence of cytokines and growth factors in ANG II-mediated collagen upregulation by fibroblasts in rats: role of myocytes. *American journal of physiology. Heart and circulatory physiology*. 2004;287:H107-117.
205. Wang F, Trial J, Diwan A, et al. Regulation of cardiac fibroblast cellular function by leukemia inhibitory factor. *Journal of molecular and cellular cardiology*. 2002;34:1309-1316.
206. Pennica D, King KL, Shaw KJ, et al. Expression cloning of cardiotrophin 1, a cytokine that induces cardiac myocyte hypertrophy. *Proceedings of the National Academy of Sciences of the United States of America*. 1995;92:1142-1146.
207. Sheng Z, Knowlton K, Chen J, Hoshijima M, Brown JH, Chien KR. Cardiotrophin 1 (CT-1) inhibition of cardiac myocyte apoptosis via a mitogen-activated protein kinase-dependent pathway. Divergence from downstream CT-1 signals for myocardial cell hypertrophy. *The Journal of biological chemistry*. 1997;272:5783-5791.
208. Finkel MS, Oddis CV, Jacob TD, Watkins SC, Hattler BG, Simmons RL. Negative inotropic effects of cytokines on the heart mediated by nitric oxide. *Science*. 1992;257:387-389.
209. Heinrich PC, Behrmann I, Muller-Newen G, Schaper F, Graeve L. Interleukin-6-type cytokine signalling through the gp130/Jak/STAT pathway. *The Biochemical journal*. 1998;334 (Pt 2):297-314.
210. Kunisada K, Negoro S, Tone E, et al. Signal transducer and activator of transcription 3 in the heart transduces not only a hypertrophic signal but a protective signal

- against doxorubicin-induced cardiomyopathy. *Proceedings of the National Academy of Sciences of the United States of America*. 2000;97:315-319.
211. Hirota H, Chen J, Betz UA, et al. Loss of a gp130 cardiac muscle cell survival pathway is a critical event in the onset of heart failure during biomechanical stress. *Cell*. 1999;97:189-198.
 212. Uozumi H, Hiroi Y, Zou Y, et al. gp130 plays a critical role in pressure overload-induced cardiac hypertrophy. *The Journal of biological chemistry*. 2001;276:23115-23119.
 213. Dorn GW, 2nd, Force T. Protein kinase cascades in the regulation of cardiac hypertrophy. *The Journal of clinical investigation*. 2005;115:527-537.
 214. Yamazaki T, Komuro I, Kudoh S, et al. Mechanical stress activates protein kinase cascade of phosphorylation in neonatal rat cardiac myocytes. *The Journal of clinical investigation*. 1995;96:438-446.
 215. Li Y, Feng J, Song S, et al. gp130 Controls Cardiomyocyte Proliferation and Heart Regeneration. *Circulation*. 2020;142:967-982.
 216. Byun J, Del Re DP, Zhai P, et al. Yes-associated protein (YAP) mediates adaptive cardiac hypertrophy in response to pressure overload. *The Journal of biological chemistry*. 2019;294:3603-3617.
 217. Yang Y, Del Re DP, Nakano N, et al. miR-206 Mediates YAP-Induced Cardiac Hypertrophy and Survival. *Circulation research*. 2015;117:891-904.
 218. Kashiwara T, Mukai R, Oka SI, et al. YAP mediates compensatory cardiac hypertrophy through aerobic glycolysis in response to pressure overload. *The Journal of clinical investigation*. 2022;132.
 219. Nishizuka Y. Protein kinase C and lipid signaling for sustained cellular responses. *FASEB journal : official publication of the Federation of American Societies for Experimental Biology*. 1995;9:484-496.
 220. Kolch W, Heidecker G, Kochs G, et al. Protein kinase C alpha activates RAF-1 by direct phosphorylation. *Nature*. 1993;364:249-252.
 221. Marshall CJ. Ras effectors. *Current opinion in cell biology*. 1996;8:197-204.
 222. Seta K, Nanamori M, Modrall JG, Neubig RR, Sadoshima J. AT1 receptor mutant lacking heterotrimeric G protein coupling activates the Src-Ras-ERK pathway without nuclear translocation of ERKs. *The Journal of biological chemistry*. 2002;277:9268-9277.
 223. Marrero MB, Schieffer B, Paxton WG, et al. Direct stimulation of Jak/STAT pathway by the angiotensin II AT1 receptor. *Nature*. 1995;375:247-250.
 224. Ali MS, Sayeski PP, Dirksen LB, Hayzer DJ, Marrero MB, Bernstein KE. Dependence on the motif YIPP for the physical association of Jak2 kinase with the intracellular carboxyl tail of the angiotensin II AT1 receptor. *The Journal of biological chemistry*. 1997;272:23382-23388.
 225. Ali MS, Sayeski PP, Bernstein KE. Jak2 acts as both a STAT1 kinase and as a molecular bridge linking STAT1 to the angiotensin II AT1 receptor. *The Journal of biological chemistry*. 2000;275:15586-15593.
 226. Molkentin JD, Lu JR, Antos CL, et al. A calcineurin-dependent transcriptional pathway for cardiac hypertrophy. *Cell*. 1998;93:215-228.
 227. Wilkins BJ, Molkentin JD. Calcium-calcineurin signaling in the regulation of cardiac hypertrophy. *Biochemical and biophysical research communications*. 2004;322:1178-1191.
 228. Wilkins BJ, De Windt LJ, Bueno OF, et al. Targeted disruption of NFATc3, but not NFATc4, reveals an intrinsic defect in calcineurin-mediated cardiac hypertrophic growth. *Molecular and cellular biology*. 2002;22:7603-7613.

229. Frey N, Olson EN. Cardiac hypertrophy: the good, the bad, and the ugly. *Annual review of physiology*. 2003;65:45-79.
230. Heineke J, Ruetten H, Willenbockel C, et al. Attenuation of cardiac remodeling after myocardial infarction by muscle LIM protein-calceineurin signaling at the sarcomeric Z-disc. *Proceedings of the National Academy of Sciences of the United States of America*. 2005;102:1655-1660.
231. Frey N, Barrientos T, Shelton JM, et al. Mice lacking calsarcin-1 are sensitized to calcineurin signaling and show accelerated cardiomyopathy in response to pathological biomechanical stress. *Nature medicine*. 2004;10:1336-1343.
232. Frey N, Richardson JA, Olson EN. Calsarcins, a novel family of sarcomeric calcineurin-binding proteins. *Proceedings of the National Academy of Sciences of the United States of America*. 2000;97:14632-14637.
233. Li HH, Kedar V, Zhang C, et al. Atrogin-1/muscle atrophy F-box inhibits calcineurin-dependent cardiac hypertrophy by participating in an SCF ubiquitin ligase complex. *The Journal of clinical investigation*. 2004;114:1058-1071.
234. Taigen T, De Windt LJ, Lim HW, Molkentin JD. Targeted inhibition of calcineurin prevents agonist-induced cardiomyocyte hypertrophy. *Proceedings of the National Academy of Sciences of the United States of America*. 2000;97:1196-1201.
235. Haq S, Choukroun G, Kang ZB, et al. Glycogen synthase kinase-3beta is a negative regulator of cardiomyocyte hypertrophy. *The Journal of cell biology*. 2000;151:117-130.
236. Li J, Wang J, Russell FD, Molenaar P. Activation of calcineurin in human failing heart ventricle by endothelin-1, angiotensin II and urotensin II. *British journal of pharmacology*. 2005;145:432-440.
237. Shimoyama M, Hayashi D, Takimoto E, et al. Calcineurin plays a critical role in pressure overload-induced cardiac hypertrophy. *Circulation*. 1999;100:2449-2454.
238. Lim HW, De Windt LJ, Steinberg L, et al. Calcineurin expression, activation, and function in cardiac pressure-overload hypertrophy. *Circulation*. 2000;101:2431-2437.
239. De Windt LJ, Lim HW, Bueno OF, et al. Targeted inhibition of calcineurin attenuates cardiac hypertrophy in vivo. *Proceedings of the National Academy of Sciences of the United States of America*. 2001;98:3322-3327.
240. Zou Y, Hiroi Y, Uozumi H, et al. Calcineurin plays a critical role in the development of pressure overload-induced cardiac hypertrophy. *Circulation*. 2001;104:97-101.
241. Saito T, Fukuzawa J, Osaki J, et al. Roles of calcineurin and calcium/calmodulin-dependent protein kinase II in pressure overload-induced cardiac hypertrophy. *Journal of molecular and cellular cardiology*. 2003;35:1153-1160.
242. Bueno OF, Wilkins BJ, Tymitz KM, et al. Impaired cardiac hypertrophic response in Calcineurin Abeta -deficient mice. *Proceedings of the National Academy of Sciences of the United States of America*. 2002;99:4586-4591.
243. Fatkin D, McConnell BK, Mudd JO, et al. An abnormal Ca(2+) response in mutant sarcomere protein-mediated familial hypertrophic cardiomyopathy. *The Journal of clinical investigation*. 2000;106:1351-1359.
244. Iemitsu M, Miyauchi T, Maeda S, et al. Physiological and pathological cardiac hypertrophy induce different molecular phenotypes in the rat. *American Journal of Physiology-Regulatory, Integrative and Comparative Physiology*. 2001;281:R2029-R2036.

245. Takahashi T, Allen PD, Izumo S. Expression of A-, B-, and C-type natriuretic peptide genes in failing and developing human ventricles. Correlation with expression of the Ca (2+)-ATPase gene. *Circulation research*. 1992;71:9-17.
246. Yoshimura M, Yasue H, Ogawa H. Pathophysiological significance and clinical application of ANP and BNP in patients with heart failure. *Canadian journal of physiology and pharmacology*. 2001;79:730-735.
247. Dunn ME, Manfredi TG, Agostinucci K, et al. Serum Natriuretic Peptides as Differential Biomarkers Allowing for the Distinction between Physiologic and Pathologic Left Ventricular Hypertrophy. *Toxicol Pathol*. 2017;45:344-352.
248. Engle SK, Watson DE. Natriuretic Peptides as Cardiovascular Safety Biomarkers in Rats: Comparison With Blood Pressure, Heart Rate, and Heart Weight. *Toxicological sciences : an official journal of the Society of Toxicology*. 2016;149:458-472.
249. Wong PC, Guo J, Zhang A. The renal and cardiovascular effects of natriuretic peptides. *Advances in physiology education*. 2017;41:179-185.
250. de Bold AJ, Borenstein HB, Veress AT, Sonnenberg H. A rapid and potent natriuretic response to intravenous injection of atrial myocardial extract in rats. *Life sciences*. 1981;28:89-94.
251. Gorbe A, Giricz Z, Szunyog A, et al. Role of cGMP-PKG signaling in the protection of neonatal rat cardiac myocytes subjected to simulated ischemia/reoxygenation. *Basic research in cardiology*. 2010;105:643-650.
252. Elesgaray R, Caniffi C, Ierace DR, et al. Signaling cascade that mediates endothelial nitric oxide synthase activation induced by atrial natriuretic peptide. *Regulatory peptides*. 2008;151:130-134.
253. Calderone A, Thaik CM, Takahashi N, Chang DL, Colucci WS. Nitric oxide, atrial natriuretic peptide, and cyclic GMP inhibit the growth-promoting effects of norepinephrine in cardiac myocytes and fibroblasts. *The Journal of clinical investigation*. 1998;101:812-818.
254. Takimoto E, Champion HC, Li M, et al. Chronic inhibition of cyclic GMP phosphodiesterase 5A prevents and reverses cardiac hypertrophy. *Nature medicine*. 2005;11:214-222.
255. Fiedler B, Lohmann SM, Smolenski A, et al. Inhibition of calcineurin-NFAT hypertrophy signaling by cGMP-dependent protein kinase type I in cardiac myocytes. *Proceedings of the National Academy of Sciences of the United States of America*. 2002;99:11363-11368.
256. Li X, Lan Y, Wang Y, Nie M, Lu Y, Zhao E. Telmisartan suppresses cardiac hypertrophy by inhibiting cardiomyocyte apoptosis via the NFAT/ANP/BNP signaling pathway. *Molecular medicine reports*. 2017;15:2574-2582.
257. Cooling M, Hunter P, Crampin EJ. Modeling hypertrophic IP3 transients in the cardiac myocyte. *Biophysical journal*. 2007;93:3421-3433.
258. Kraeutler MJ, Soltis AR, Saucerman JJ. Modeling cardiac beta-adrenergic signaling with normalized-Hill differential equations: comparison with a biochemical model. *BMC Syst Biol*. 2010;4:157.
259. Ryall KA, Holland DO, Delaney KA, Kraeutler MJ, Parker AJ, Saucerman JJ. Network reconstruction and systems analysis of cardiac myocyte hypertrophy signaling. *The Journal of biological chemistry*. 2012;287:42259-42268.
260. Molkentin JD, Robbins J. With great power comes great responsibility: using mouse genetics to study cardiac hypertrophy and failure. *Journal of molecular and cellular cardiology*. 2009;46:130-136.

261. Frank DU, Sutcliffe MD, Saucerman JJ. Network-based predictions of in vivo cardiac hypertrophy. *Journal of molecular and cellular cardiology*. 2018;121:180-189.
262. Estrada AC, Yoshida K, Saucerman JJ, Holmes JW. A multiscale model of cardiac concentric hypertrophy incorporating both mechanical and hormonal drivers of growth. *Biomech Model Mechanobiol*. 2021;20:293-307.
263. Yoshida K, Saucerman JJ, Holmes JW. Multiscale model of heart growth during pregnancy: integrating mechanical and hormonal signaling. *Biomech Model Mechanobiol*. 2022;21:1267-1283.
264. Johansson M, Ulfenborg B, Andersson CX, et al. Cardiac hypertrophy in a dish: a human stem cell based model. *Biology open*. 2020;9.
265. Li J, Feng X, Wei X. Modeling hypertrophic cardiomyopathy with human cardiomyocytes derived from induced pluripotent stem cells. *Stem cell research & therapy*. 2022;13:232.
266. Bockstall KE, Link MS. A primer on arrhythmias in patients with hypertrophic cardiomyopathy. *Current cardiology reports*. 2012;14:552-562.
267. Yang JH, Saucerman JJ. Phospholemman is a negative feed-forward regulator of Ca²⁺ in beta-adrenergic signaling, accelerating beta-adrenergic inotropy. *Journal of molecular and cellular cardiology*. 2012;52:1048-1055.
268. Morotti S, Edwards AG, McCulloch AD, Bers DM, Grandi E. A novel computational model of mouse myocyte electrophysiology to assess the synergy between Na⁺ loading and CaMKII. *The Journal of physiology*. 2014;592:1181-1197.
269. Heiden S, Vignon-Zellweger N, Masuda S, et al. Vascular endothelium derived endothelin-1 is required for normal heart function after chronic pressure overload in mice. *PloS one*. 2014;9:e88730.
270. Kardami E, Fandrich RR. Basic fibroblast growth factor in atria and ventricles of the vertebrate heart. *The Journal of cell biology*. 1989;109:1865-1875.
271. Vlodavsky I, Folkman J, Sullivan R, et al. Endothelial cell-derived basic fibroblast growth factor: synthesis and deposition into subendothelial extracellular matrix. *Proceedings of the National Academy of Sciences of the United States of America*. 1987;84:2292-2296.
272. Cheng GC, Briggs WH, Gerson DS, et al. Mechanical strain tightly controls fibroblast growth factor-2 release from cultured human vascular smooth muscle cells. *Circulation research*. 1997;80:28-36.
273. Ku PT, D'Amore PA. Regulation of basic fibroblast growth factor (bFGF) gene and protein expression following its release from sublethally injured endothelial cells. *Journal of cellular biochemistry*. 1995;58:328-343.
274. McNeil PL, Muthukrishnan L, Warder E, D'Amore PA. Growth factors are released by mechanically wounded endothelial cells. *The Journal of cell biology*. 1989;109:811-822.
275. Qu Z, Liebler JM, Powers MR, et al. Mast cells are a major source of basic fibroblast growth factor in chronic inflammation and cutaneous hemangioma. *The American journal of pathology*. 1995;147:564-573.
276. Pennington DW, Lopez AR, Thomas PS, Peck C, Gold WM. Dog mastocytoma cells produce transforming growth factor beta 1. *The Journal of clinical investigation*. 1992;90:35-41.
277. Lindstedt KA, Wang Y, Shiota N, et al. Activation of paracrine TGF-beta1 signaling upon stimulation and degranulation of rat serosal mast cells: a novel function for chymase. *FASEB journal : official publication of the Federation of American Societies for Experimental Biology*. 2001;15:1377-1388.

278. Ancey C, Corbi P, Froger J, et al. Secretion of IL-6, IL-11 and LIF by human cardiomyocytes in primary culture. *Cytokine*. 2002;18:199-205.
279. Ancey C, Menet E, Corbi P, et al. Human cardiomyocyte hypertrophy induced in vitro by gp130 stimulation. *Cardiovascular research*. 2003;59:78-85.
280. Bowers SL, Banerjee I, Baudino TA. The extracellular matrix: at the center of it all. *Journal of molecular and cellular cardiology*. 2010;48:474-482.
281. Kanekar S, Hirozanne T, Terracio L, Borg TK. Cardiac fibroblasts form and function. *Cardiovascular pathology : the official journal of the Society for Cardiovascular Pathology*. 1998;7:127-133.
282. Lee DI, Zhu G, Sasaki T, et al. Phosphodiesterase 9A controls nitric-oxide-independent cGMP and hypertrophic heart disease. *Nature*. 2015;519:472-476.
283. Campbell DJ. Circulating and tissue angiotensin systems. *The Journal of clinical investigation*. 1987;79:1-6.
284. Dinh DT, Frauman AG, Johnston CI, Fabiani ME. Angiotensin receptors: distribution, signalling and function. *Clinical science*. 2001;100:481-492.
285. Lindpaintner K, Ganten D. The cardiac renin-angiotensin system. An appraisal of present experimental and clinical evidence. *Circulation research*. 1991;68:905-921.
286. Baker KM, Booz GW, Dostal DE. Cardiac actions of angiotensin II: Role of an intracardiac renin-angiotensin system. *Annual review of physiology*. 1992;54:227-241.
287. Lee MA, Bohm M, Paul M, Ganten D. Tissue renin-angiotensin systems. Their role in cardiovascular disease. *Circulation*. 1993;87:IV7-13.
288. Campbell DJ, Habener JF. Angiotensinogen gene is expressed and differentially regulated in multiple tissues of the rat. *The Journal of clinical investigation*. 1986;78:31-39.
289. McEuen AR, Sharma B, Walls AF. Regulation of the activity of human chymase during storage and release from mast cells: the contributions of inorganic cations, pH, heparin and histamine. *Biochimica et biophysica acta*. 1995;1267:115-121.

Table 1. Characteristics of physiological and pathological cardiac hypertrophy^a

Characteristic	Physiological cardiac hypertrophic	Pathological cardiac hypertrophic
Stimuli	Exercise, pregnancy	i.a. pressure or volume overload
Cardiomyocyte size	Increased	Increased
Concentric or eccentric	eccentric > concentric	concentric or eccentric
Adaptivity	yes	initially yes/ advanced maladaptive
Contractility	preserved or increased	preserved or decreased
Cardiac metabolism		
- Fatty acid oxidation	increased	decreased
- Glycolysis	increased	increased
Structural and functional		
- Replacement	no	yes
- Interstitial fibrosis	no	yes
- Cardiomyocyte apoptosis	no	yes
- Capillary network	sufficient	insufficient
Molecular characteristics		
- Fetal gene expression	unmodified	upregulated
- Contractile linked genes	normal or increased	downregulated
Cardiac function	normal or increased	depressed
Reversible	yes	no
Heart failure	unlikely	Prone

^a Adapted from Bernardo et al., 2010 (Ref. 10) and, Nakamura and Sadoshima, 2018 (Ref. 9).

Table 2. Mediators influencing the microenvironment in cardiac hypertrophy

Vasoactive peptides	Secretion from/ Location	References
AT-II	cardiomyocyte	124, 130
AT-II	endothelial cell	39
ET-1	cardiomyocyte	44, 269
ET-1	fibroblast	44, 125, 126, 269
ET-1	endothelial cell	39, 42, 44, 269
Catecholamines	Secretion from/ Location	References
NE	sympathetic nerve ending	83
Growth factors	Secretion from/ Location	References
FGF (aFGF, bFGF)	cardiomyocyte	163, 270
FGF (aFGF, bFGF)	non-myocyte	270
FGF-2 (bFGF)	fibroblast	126, 163, 172
FGF-2 (bFGF)	endothelial cell	271-274
FGF-2 (bFGF)	mast cell	54, 79, 275
High-FGF-2 (Hi-bFGF)	fibroblast	126
TGF- β	cardiomyocyte	143, 148, 149
TGF- β	fibroblast	44, 125, 126, 143, 148, 149
TGF- β	endothelial cell	143, 148, 149
TGF- β	mast cell	54, 79, 276, 277
TGF- β	myofibroblast	31, 150, 151
Cytokines	Secretion from/ Location	References
IL-6, CT-1, LIF	cardiomyocyte	197, 198, 201, 278, 279
IL-6, CT-1, LIF	fibroblast	197, 198, 278, 279
IL-6	mast cell	54, 79
IL-1	mast cell	54, 79
TNF α	mast cell	54, 73-76, 79
Various other components	Secretion from/ Location	References
VCAM-1, ICAM-1	endothelial cell	40
ECM components	cardiomyocyte	280
ECM components	fibroblast	280
ECM components	endothelial cell	280
ECM components	myofibroblast	31, 281
Histamine	mast cell	51
Chemotactic factors	mast cell	54, 79
Anti-hypertrophic peptides	Secretion from/ Location	References
ANP, BNP	cardiomyocyte	41, 282
NO	endothelial cell	39, 40
CNP	endothelial cell	41
Enzymatic activities	Secretion from/ Location	References
Local RAS	cardiac tissue	283-285
AGT, renin, ACE, AT1, AT2	cardiac tissue	286, 287
AGT	cardiomyocyte	288
AGT	fibroblast	288
Renin	mast cell	82, 83
ACE	endothelial cell	46
Chymase (alternative ACE)	endothelial cell	46
Chymase (alternative ACE)	mast cell	54, 79, 289

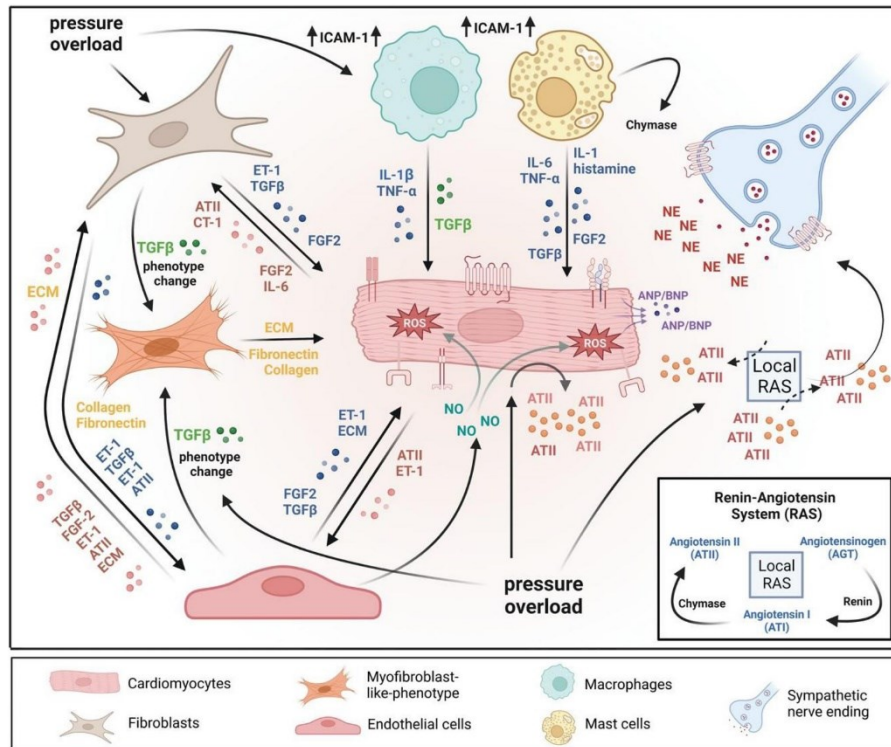


Figure 1. A microenvironmental model of pressure overload-induced cardiac hypertrophy. The model also illustrates multiple cell types' substantial roles and reciprocal interactions in the myocardium. In response to pressure overload cardiomyocyte and non-myocardial cells are transformed into an “activated state”, releasing numerous pro-hypertrophic, pro-fibrotic, and pro-inflammatory mediators. In addition, vasoactive hormones, various growth factors, cytokines, and the local renin-angiotensin system (RAS) act in an autocrine and/or paracrine mode. Collectively, the above-mentioned mechanisms orchestrate effects that contribute to pathological remodeling processes leading to cardiac hypertrophy, fibrosis, and inflammation. AT II: angiotensin II; CT-1: Cardiotrophin-1; ECM: extracellular matrix; ET-1: endothelin-1; FGF-2: fibroblast growth factor 2; ICAM-1: Intercellular Adhesion Molecule 1; IL-1: interleukin-1; IL-6: interleukin-6; NE: norepinephrine; TGF-β: transforming growth factor-β; TNFα: tumor necrosis factor-α.

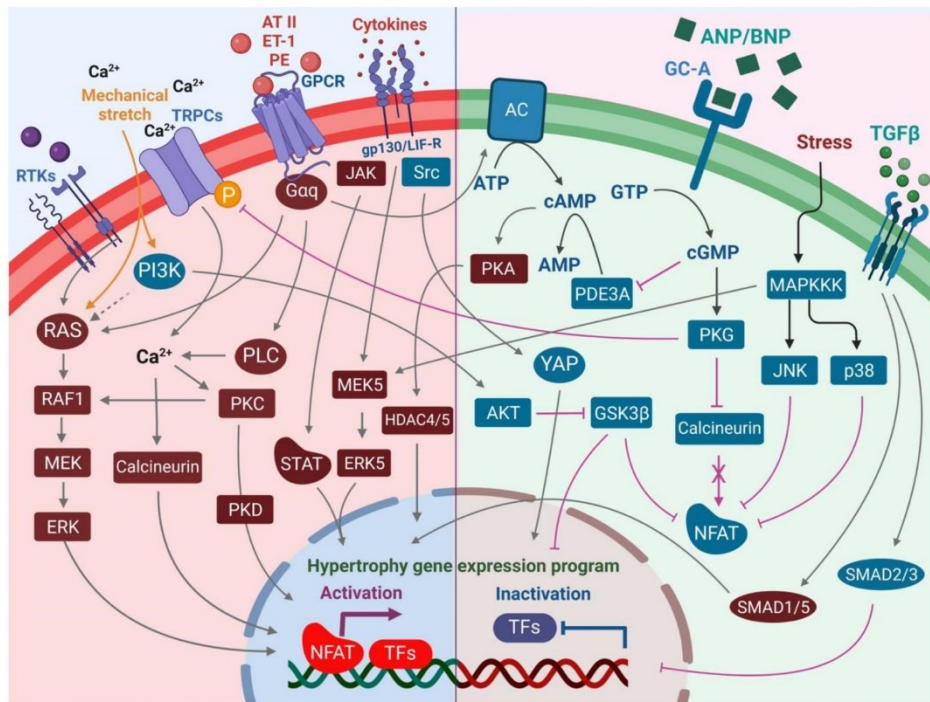


Figure 2. An overview of the pro-hypertrophic (left panel) and anti-hypertrophic (right panel) signaling pathways regulating the hypertrophic response in the cardiomyocyte. Increased intracellular Ca^{2+} levels mediated by TRPCs and Ca^{2+} import promote pro-hypertrophic transcriptional signaling events via calcineurin-NFAT and activation of PKC. PLC may contribute to these axes in the activation of alpha-adrenergic receptor signaling. Although canonical MAPK signaling via RTKs including FGFR-1 promotes pro-hypertrophic signaling, the PI3K-AKT axis plays an opposing role in hypertrophic signaling via inhibition of GSK3 β and activation of YAP transcriptional activity. Increased secretion of cytokines promotes transcriptional activation of the pro-hypertrophic gene program in the nucleus not only via JAK-STAT but also the MEK5-ERK5 axis. On the other hand, increased pressure overload in cardiac tissue promotes secretion of ANP and BNP by cardiomyocytes, leading to vasodilation and an anti-hypertrophic response in cells via an increase in intracellular cGMP levels, which leads to activation of PKG, in turn mediating reduced hypertrophic growth. Activation of JNK and p38 stress signaling events in the cardiomyocytes, although leading to cardiomyopathy and heart failure, results in inhibition of NFAT through phosphorylation events that prevent its nuclear localization and pro-hypertrophic transcriptional regulation activities, thereby blocking the calcineurin axis. Increased secretion of TGF β during increased pressure stress can lead to mixed responses, with canonical TGF β -SMAD2/SMAD3 signaling leading to anti-hypertrophic responses, whereas activation of noncanonical SMAD1/SMAD5 leads to pro-hypertrophic responses.

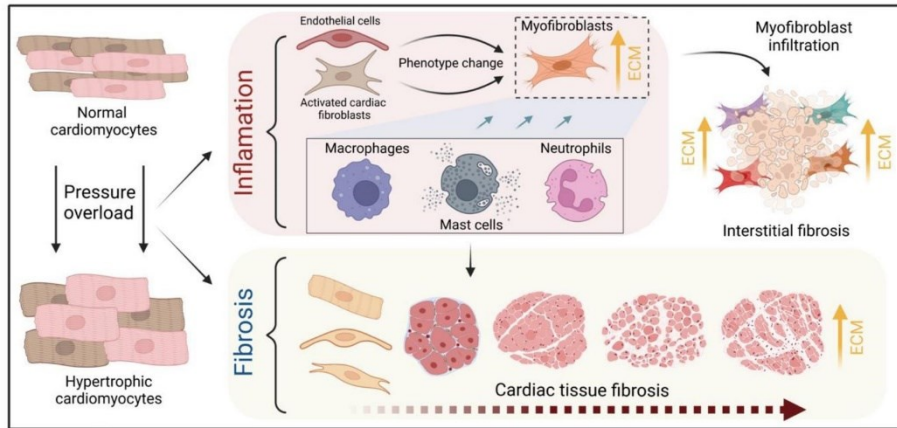


Figure 3. Schematic illustration of the process of fibrotic scar formation at the cellular level. The myocardium develops cardiomyocyte hypertrophy under pressure overload conditions, triggering concomitant inflammatory processes and fibrotic scar formation. The evidence discussed in the text suggests a central role for resident fibroblasts, nonetheless cardiac endothelial cells may also contribute to myofibroblast-like cells and drive cardiac fibrosis. Resident and infiltrating immune cells, including mast cells, macrophages, and neutrophils, enhance this phenotype change by releasing TGF- β while mediating tissue inflammation *via* cytokines such as TNF α , IL-6, and IL-1. These mechanisms increase the number of myofibroblasts and the accumulation of collagen, which accelerates fibrotic scar formation in the microenvironment of cardiac hypertrophy.

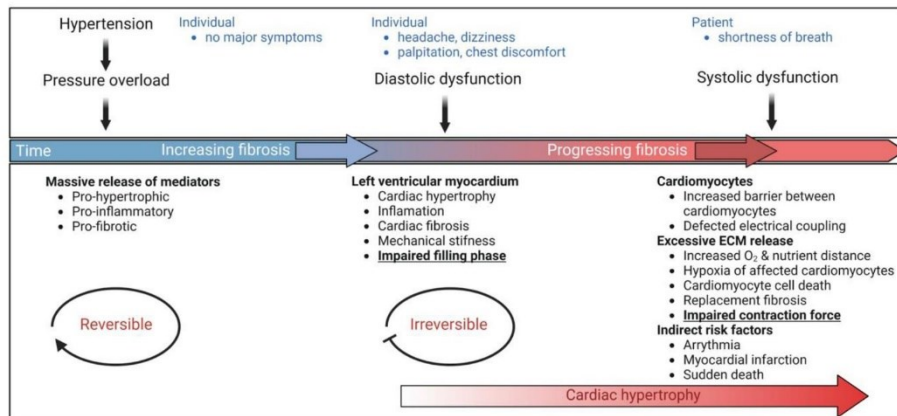
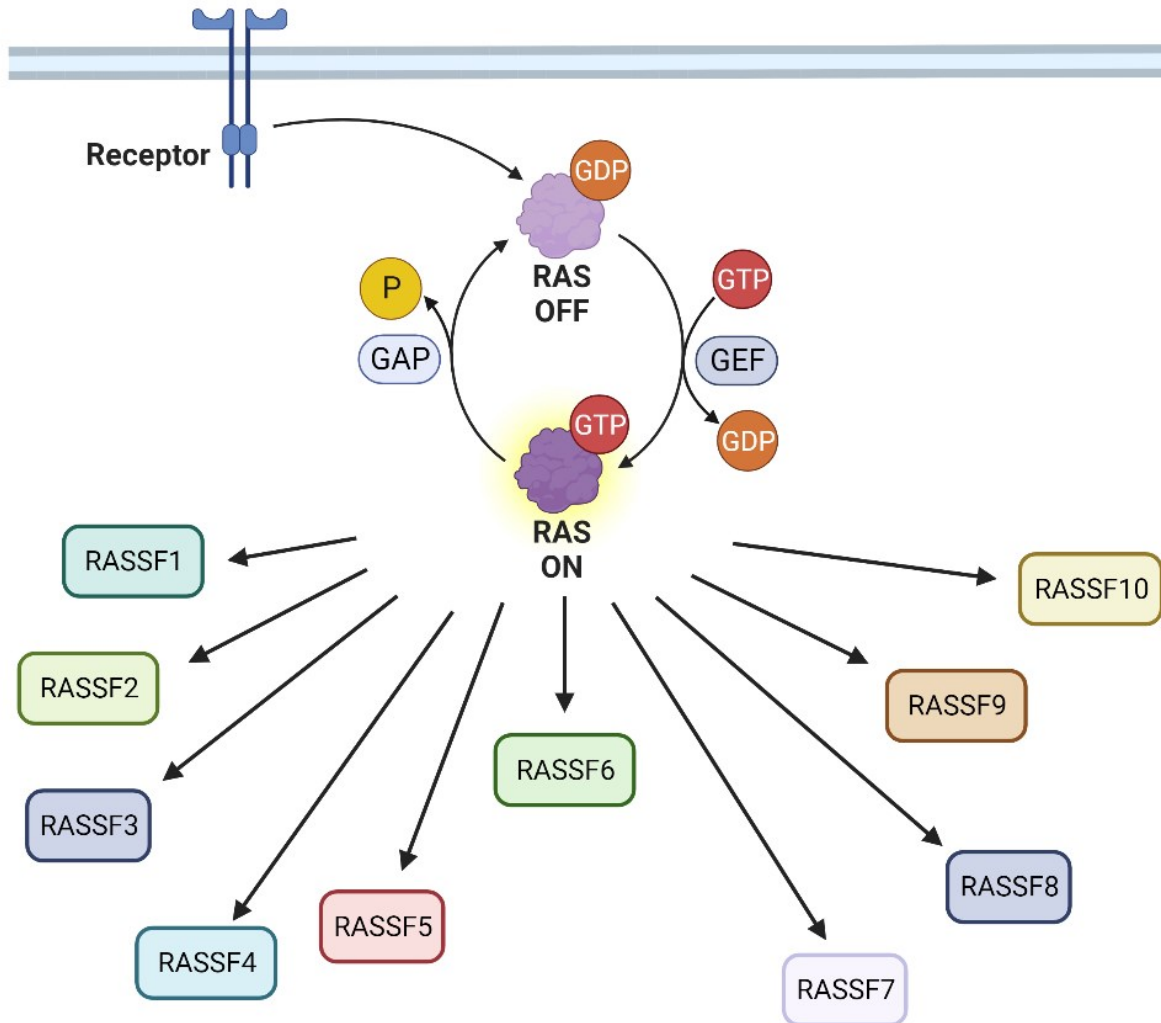


Figure 4. Schematic diagram of how changes in the microenvironment affect cardiac function. Hypertension, a common cardiovascular disease, causes pressure overload followed by a massive release of pro-hypertrophic, pro-fibrotic, and pro-inflammatory mediators. At this stage, when individuals do not experience symptoms, hypertension and its accompanying microenvironmental complications may be reversible with strategies such as lifestyle modification, however without any intervention, this could evolve into cardiac hypertrophy and fibrotic remodeling. Increasing fibrosis leads to mechanical stiffness and impaired filling phase, both prominent features of diastolic dysfunction. Common symptoms include headache, dizziness, palpitations, and chest discomfort. Notably, this phase is not reversible and requires pharmacological management. Late diagnosis or inadequate treatment leads to progressive fibrosis and detrimental changes at the molecular level, such as a barrier between cardiomyocytes at the cellular level, impaired electrical coupling, and hypoxia of affected cardiomyocytes, collectively resulting in cardiomyocytes' cell death. The subsequent decreased contractile force characterizes systolic dysfunction while having severe consequences as individuals suffer from shortness of breath. Biomarker identification in a diagnostic screening approach could help detect early onset diastolic dysfunction in affected individuals, setting the platform for early management and preventive course of action to avoid the subsequent detrimental outcomes of the developing condition.

Chapter 5

A comprehensive analysis of RAS-effector interactions reveals interaction hotspots and new binding partners



Status: published in Journal of Biological Chemistry, January 2021

Impact factor: 5.48

Contribution: 15 %

Expression and purification of RAS GTPases and RASSF proteins, preparation of nucleotide-free and fluorescently labeled forms of GTPases, protein interaction analyses including fluorescence polarization measurements, Cell culture and transfection, Pull-down and western blotting, figure preparation and illustration, drafting of manuscript and discussion.



A comprehensive analysis of RAS-effector interactions reveals interaction hotspots and new binding partners

Received for publication, January 19, 2021, and in revised form, March 25, 2021. Published, Papers in Press, April 28, 2021.
<https://doi.org/10.1016/j.jbc.2021.100626>

Soheila Rezaei Adariani^{1,†}, Neda S. Kazeminejad^{1,†}, Farhad Bazgir^{1,*}, Christoph Wittich¹, Ehsan Amin^{1,2,*}, Claus A. M. Seidel³, Radovan Dvorsky¹, and Mohammad R. Ahmadian^{1,*}

From the ¹Medical Faculty, Institute of Biochemistry and Molecular Biology II, ²Medical Faculty, Institute of Neural and Sensory Physiology, ³Chair of Molecular Physical Chemistry, Heinrich Heine University, Düsseldorf, Germany

Edited by Henrik Dohlman

RAS effectors specifically interact with GTP-bound RAS proteins to link extracellular signals to downstream signaling pathways. These interactions rely on two types of domains, called RAS-binding (RB) and RAS association (RA) domains, which share common structural characteristics. Although the molecular nature of RAS-effector interactions is well-studied for some proteins, most of the RA/RB-domain-containing proteins remain largely uncharacterized. Here, we searched through human proteome databases, extracting 41 RA domains in 39 proteins and 16 RB domains in 14 proteins, each of which can specifically select at least one of the 25 members in the RAS family. We next comprehensively investigated the sequence–structure–function relationship between different representatives of the RAS family, including HRAS, RRAS, RALA, RAP1B, RAP2A, RHEB1, and RIT1, with all members of RA domain family proteins (RASFFs) and the RB-domain-containing CRAF. The binding affinity for RAS-effector interactions, determined using fluorescence polarization, broadly ranged between high (0.3 μ M) and very low (500 μ M) affinities, raising interesting questions about the consequence of these variable binding affinities in the regulation of signaling events. Sequence and structural alignments pointed to two interaction hotspots in the RA/RB domains, consisting of an average of 19 RAS-binding residues. Moreover, we found novel interactions between RRAS1, RIT1, and RALA and RASFF7, RASFF9, and RASFF1, respectively, which were systematically explored in sequence–structure–property relationship analysis, and validated by mutational analysis. These data provide a set of distinct functional properties and putative biological roles that should now be investigated in the cellular context.

RAS family proteins control activities of multiple signaling pathways and consequently a wide array of cellular processes, including survival, growth, adhesion, migration, and differentiation (1). Any dysregulation of these pathways leads, thus, to cancer, developmental disorders, metabolic and cardiovascular diseases (2). Signal transduction implies a physical association of RAS proteins with a spectrum of

functionally diverse downstream effectors, e.g., CRAF, PI3K α , TIAM1, RALGDS, PLC ϵ , and RASFF5 (3–11). RAS-effector interaction essentially requires RAS association with membranes (12), and its activation by specific regulatory proteins (e.g., guanine nucleotide exchange factors or GEFs), leading to the formation of GTP-bound, active RAS (13–15). Notably, RAS proteins change their conformation mainly at two mobile regions, designated as a switch I (residues 30–40) and switch II (residues 60–68) (16–18). Only in GTP-bound form, the switch regions of the RAS proteins provide a platform for the association of the effector proteins (19, 20).

To date, two types of domains, the RAS-binding (RB) and RAS association (RA) domains, have been defined for various effectors. They are comprised of 80 to 100 amino acids and have a similar ubiquitin-like topology (8, 21–24). Considering different RAS effectors, RB and RA domain interactions with RAS proteins do not exhibit the same mode of interaction between different RAS effectors. However, CRAF RB and RALGDS RA domains share a similar structure and contact the switch I region *via* a similar binding mode (25, 26). In contrast, PI3K α RB, RASFF5 RA, and PLC ϵ RA domains do not share sequence and structural similarity but commonly associate with the switch regions, particularly switch I (27–29). RAS-effector interaction strikingly shares a similar binding mode adopted by three components: two antiparallel β -sheets of the RA/RB domains and the RAS switch I region, respectively, and the first α -helix of the RA/RB domains (30).

In this study, we conducted an in-depth database search in the human proteome and extracted 57 RA/RB domains. We used ten RASFF RA domains to analyze their interactions with seven representatives of the RAS proteins family, including HRAS, RRAS1, RAP1B, RAP2A, RALA, RIT1, and RHEB1. CRAF RB domain was used as control. The binding analysis was performed under the same conditions using fluorescence polarization. Obtained dissociation constants (K_d) with a broad range (0.3–500 μ M) along with a matrix for a potential interaction of 25 RAS proteins and 57 RA/RB domains provide us a detailed view of the sequence–structure–property relationships of RAS-effector binding capabilities.

[†] These authors equally contributed to this study.

* For correspondence: Mohammad R. Ahmadian, reza.ahmadian@hhu.de.



RAS-RASSF selectivity

Results

Human proteome contains 39 RA and 14 RB domain-containing proteins

Mining in the UniProt database led to the extraction of 130 RB and 145 RA-domain-containing proteins, respectively. In a parallel search using HMMER, 127 RB and 164 RA-domain-containing proteins were extracted. These numbers were reduced to 46 RB and 97 RA-domain-containing proteins by excluding proteins containing RHO-binding domains, mitochondrial proton/calcium antiporter domain, and receptors. In the last step, all isoforms with identical sequences of the RB and RA domains were excluded using multiple sequence alignments generated with the ClustalW algorithm. This approach identified a total number of 16 RB domains in 14 RB-domain-containing proteins and 41 RA domains in 39 RA-domain-containing proteins, (Fig. S1; Tables S1 and S2). Both types of RAS effector domains share sequence identity of 10.5% and 9.2% and sequence similarity of 25.5% and 20.2% (Figs. S2 and S3).

The direct interaction of different RA-domain-containing proteins with RAS proteins has been comprehensively analyzed (23, 31). However, the majority of proteins with a RA domain remain uncharacterized (Table S1). The RAS association domain family (RASSF), which controls a broad range of signaling pathways (8, 32), is the largest RA-domain-containing protein family (Fig. 1). Their RA domains differently interact with classical RAS proteins (8, 24). Among them, only the interaction of RASSF1 and RASSF5/NORE1 RA domains has been characterized quantitatively so far (23, 31). Other characterized RA-domain-containing proteins, including RALGDS-like proteins, PLC ϵ , AF6, RIN1/2, and PDZGEF1/2, regulate diverse cellular processes. They share high structural similarity and exhibit differential selectivity for HRAS and RAP1B (23, 31).

RB-domain-containing proteins are mostly kinases (Table S2). The serine/threonine RAF kinase family proteins

(A/B/CRAF; (33)) activate the MEK-ERK axis and control cell proliferation and differentiation (34, 35). PI3K α generates phosphatidylinositol (3,4,5)-trisphosphate (PIP₃) and regulates cell growth, cell survival, cytoskeleton reorganization, and metabolism (36). RGS12/14, which usually act as inactivators of G α proteins (37), physically interact with various members of the RAS family. They appear to facilitate the assembly of the components of the MAPK pathway through direct association with activated HRAS (38). TIAM1/2, which act as specific GEFs for the RHO family proteins and control cell migration (39, 40), have been suggested to recognize activated RAS proteins (41). However, their direct interaction with RAS proteins has not been shown to date (23). Moreover, a few proteins, reported as RAS effectors, do not apparently contain an RA/RB domain (Table S3).

Variable affinities for the RAS-effector interactions

To determine the binding capability between the effector domains and diverse proteins of the RAS family, the following proteins were selected for this study: (i) all ten RASSF family proteins as representative RA-domain-containing effector proteins; (ii) CRAF RB domain (Fig. 1) was used as a representative of the RB-domain-containing proteins; and (iii) the RAS family includes 23 genes coding for at least 25 proteins, which share, considering their G domains, sequence identity of 48.6% and sequence similarity of 61.5% (Fig. S4). Based on sequence identity, structure, and function of their G domains, the RAS proteins were divided into eight paralog groups (Table S4): RAS, RRAS, RAP, RAL, RIT, RHEB, RASD, and DIRAS (42). RAS-related proteins RASLs, RERG, RERGL, NKIRAS1/2 were excluded from this list and study due to their major sequence deviations.

To monitor binding we applied a fluorescence polarization assay (21) to determine the dissociation constants (K_d) for the RAS-effector interactions. For this, we prepared HRAS, RRAS, RAP1B, RAP2A, RALA, RIT1, and RHEB1 in complex with a

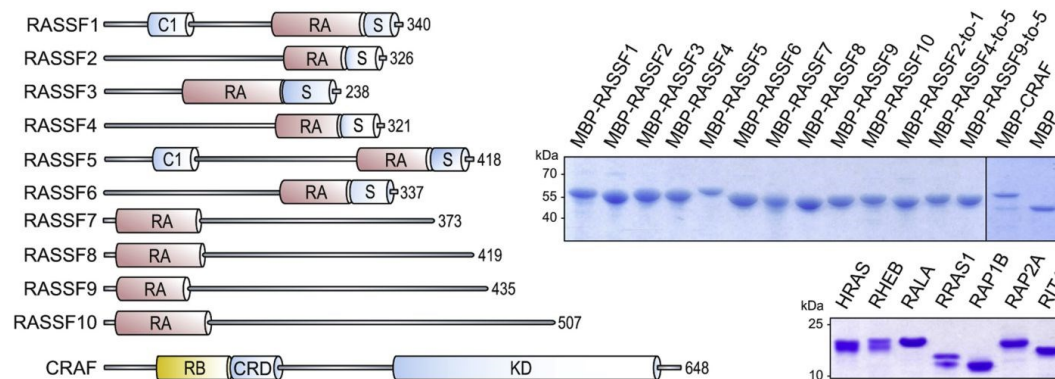


Figure 1. Domain organization of effector proteins. Schematic representation of RASSF1–10 proteins and CRAF. Different domains are highlighted, including RAS association domain (RA) in red, RAS-binding domain (RB) in yellow and other domains in blue. Based on their domain organization, the RASSF family proteins are divided in group 1 (RASSF1–6) and group 2 with N-terminal RA domains (RASSF7–10). Coomassie brilliant blue stained SDS gels show purified RAS proteins as well as the RA/RB domains purified as MBP fusion proteins.

nonhydrolyzable, fluorescent analog of GTP, called mGppNHp. Representatives of RASD and DIRAS groups were not applied due to their physical instability *in vitro*. Small-sized RB and RA domains were fused to maltose-binding protein (MBP, 42 kDa) to increase their overall molecular weight and to ensure a homogeneous monomeric form of the fusion proteins. Figure 1 shows SDS gels for all purified proteins used in this study.

Increasing concentrations of MBP-fused effector proteins were titrated to RAS•mGppNHp proteins to assess the binding capability of the respective interaction pairs. We observed a significant change in fluorescence polarization for the majority of the measurements (Figs. S5 and S6A). However, evaluated K_d values ranged from 0.3 to more than 500 μM . These data are summarized in Table S5 and illustrated in Figure 2. Under these experimental conditions, the CRAF RB domain revealed the highest affinity for HRAS and RRAS1 while the RASSF5 RA domain exhibited a relatively high affinity for HRAS, RAP1B, and RAP2A (Fig. 2, A and B, green bars). The intermediate affinities were obtained for the interaction of the CRAF RB domain with RAP1B as well as RASSF1 with RAP1B, RAP2A and RALA, RASSF9 with RIT1 and RASSF7 with RRAS1 (Fig. 2, A and B; blue bars). The majority of the interaction pairs showed, however, low and very low affinities (Fig. 2B, red and black bars, respectively). Among them, RHEB notably

revealed the majority of low-affinity interactions. No binding was observed for 12 pairwise interactions.

Purified MBP, which was titrated to HRAS•mGppNHp as a negative control, exhibited no interaction (Fig. S7A). The reproducibility of the fluorescence polarization measurements was assessed by determining the K_d value for the interaction between HRAS•mGppNHp with RASSF1-RA in three different experiments.

Identification of common RAS-binding site pattern in RA/RB domains

To understand the atomic interactions between RAS and effector proteins and explain observed variable affinities, we analyzed various structures of RAS-effector protein complexes. To date, 13 structures of RAS-effector protein complexes exist in the PDB (Table S6). As some of them contain more than one complex in the unit cell, there were altogether 19 complexes available for the analysis. In order to map atomic interactions responsible for observed variable affinities, we have extracted information about interacting interface from all of the abovementioned complex structures (Figs. S8 and S9) and combined them with their sequence alignments (Figs. S2–S4). It is important to note that some amino acids, aligned according to the sequence, were quite distant in the space. Therefore, we edited the sequence alignment to synchronize it with the structural alignment. Our python code finally took

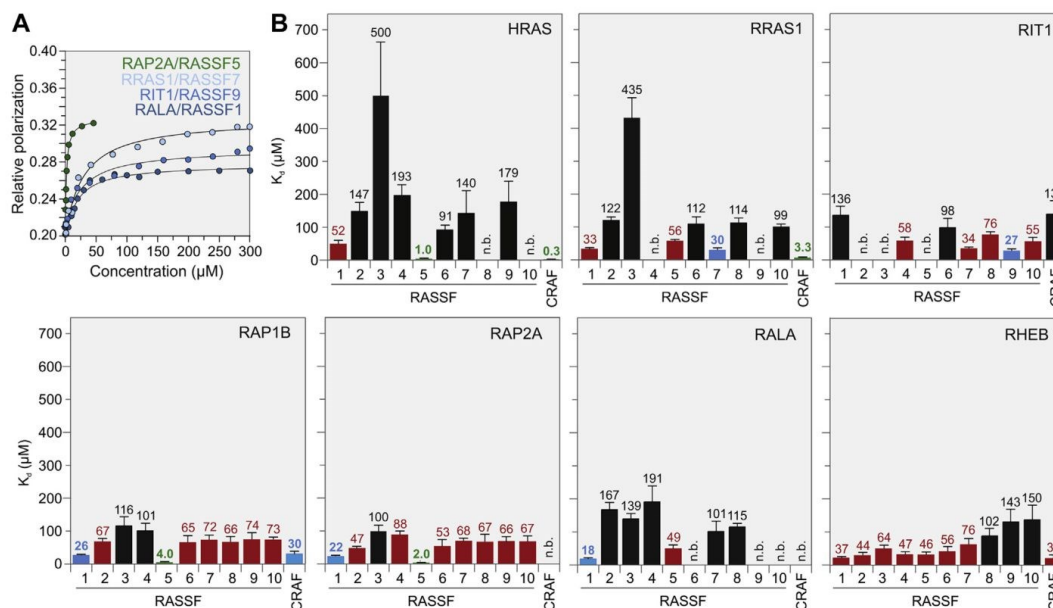


Figure 2. Differential binding affinities for the RA/RB domain interactions with various RAS subfamily members. The interactions between seven RAS subfamily members with 11 effector proteins (ten RA domains of the RASSF protein family and CRAF RB domain) were determined by titrating mGppNHp-bound, active forms of RAS proteins (1 μM , respectively) with increasing concentrations of the respective effector domains as MBP fusion proteins (Figs. S5 and S6). A, data of four representative experiments are shown for the interaction of RALA, RAP2A, RRAS1, and RIT1 with RASSF1, 5, 7, and 9, respectively. B, evaluated K_d values (above the bars; Table S5) were divided in high affinity (0.1–5 μM ; green), intermediate affinity (6–30 μM ; blue), low affinity (31–90 μM ; red), and very low affinity (91–510 μM ; black). No binding (n.b.) stands for K_d values higher than 500 μM . The error bars were derived from the fitting errors.

RAS-RASSF selectivity

sequence alignments with PDB files of complex structures as inputs and calculated all interaction pairs in analyzed complex structures in the form of an interaction matrix. The resultant matrix comprehensively relates the interacting residues on both sides of the complexes, with RAS paralogs as rows and the RA/RB domains as columns (Fig. 3). All numbering in this study is based on HRAS on the one side and CRAF and RASSF5, for RB and RA domains respectively, on the other side.

Each element of the matrix that can be accounted for a “hotspot” relates one homologous residue from RAS proteins to one homologous residue from the RA/RB domains. The number value of this element, ranging from 0 to 19, represents the number of complex structures in which these residues interact (Fig. 3). Thus, 0 means that these two residues do not contact each other in any structure while a maximal value 19 means that this particular interaction exists in all analyzed complex structures of the RAS-RA/RB domains. We have sorted the residues at both sides of the matrix according to their conservation *versus* variability. As can be seen in Figs. S4 and S9, the majority of the residues (14 out of 20) on the side of 25 RAS proteins are conserved, nine of which (Q/N25, D/

E33, I/V36, E37, D38, S/T39, Y40, R/K41 in switch I, and Y64 in the switch II; HRAS numbering) account for major hotspots (Fig. 3). On the other side, and in contrast, the majority of 19 RAS interacting residues in RA/RB domains are variable and only two distant residues are conserved (R/K59 and K/R84; CRAF numbering; R/K241 and K/R308; RASSF5 numbering) (Fig. 3 and Fig. S9).

However, what is striking is the middle cluster of the matrix with the most frequent interactions between the conserved residues in the switch I region of the RAS proteins (β2-strand residues 36–41; HRAS numbering) and the variable residues of the RA/RB domains (β2-strand residues 64–71; CRAF numbering; residues 284–291; RASSF5 numbering) (Fig. 3 and Fig. S9). This cluster adopts an arrangement of intermolecular β-sheet interactions in an antiparallel fashion (Fig. S8). A substantial number of the contacts in this cluster are mediated by main-chain/main-chain interactions, which typically involve hydrogen bonds between the N-H group and the carbonyl oxygen of the amino acids 37 to 39 from the RAS side and positions 66 to 69 (CRAF numbering) and 286 to 289 (RASSF5 numbering) from the side of the RA/RB domains.

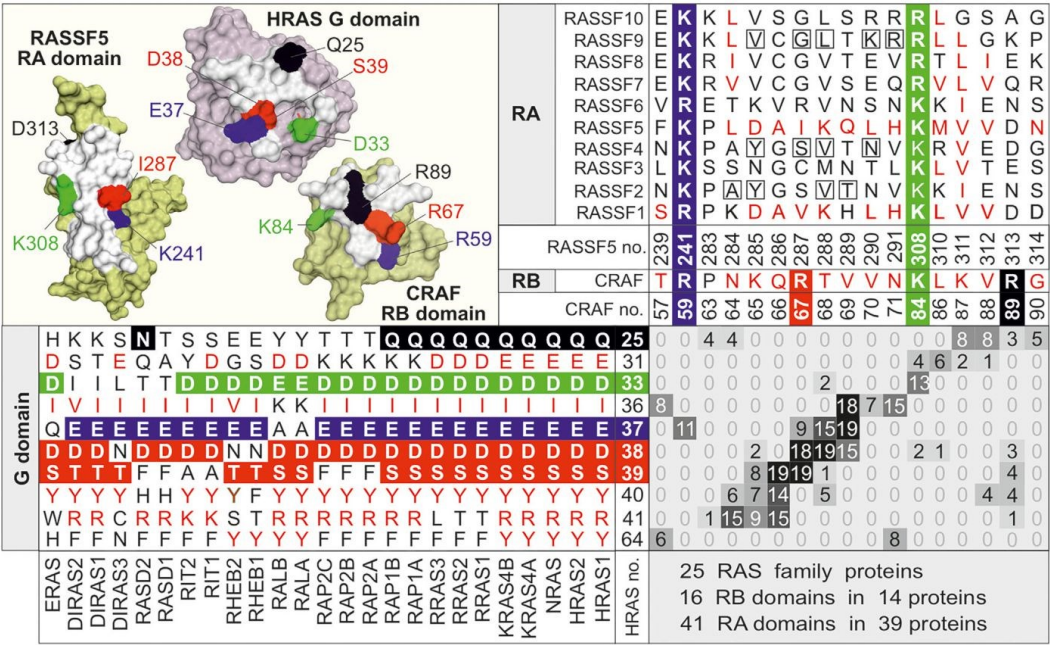


Figure 3. Interaction matrix adapted for the structures of RAS complexes with effector domains. Interaction matrix of RAS family proteins with the RA/RB proteins used in this study is generated to demonstrate interacting residues in respective structures (see Table S6). It comprises the amino acid sequence alignments of the RAS proteins (lower left panel) and the effector domains (upper right panel), respectively, extracted from the complete alignments in Figs. S2–S4. Each element corresponds to a possible interaction of RAS residues (row; HRAS numbering) and effector (column; CRAF and RASSF5 numbering, respectively). The number of actual contact sites between RAS and the effector domains (with distances of 4 Å or less) were calculated and are indicated with positive numbers for matrix elements. Extracted structures of HRAS (in orange) and the RA domain of RASSF5 and RB domain of CRAF (in olive) from their surface complexes are presented (top left panel). Key interaction hotspots with the same color codes are highlighted on the surface structures as well as in the interaction matrix and the secondary structures, respectively. Boxed residues in RASSF2, 4, and 9 were replaced to RASSF1 and 5, respectively, to validate the impact of these hotspot residues on the interaction with RAS family proteins (Fig. 4).

Switched RASSF-binding selectivity by hotspots residue swapping

To prove the impact of the hotspot residues on the selectivity of the RASSF RA domain interactions with RAS family proteins, we selected the weak and strong RAS-RASSF interactions, and substituted 4 to 5 amino acids in the hotspot region (Fig. 3, boxed residues) RASSF2 to RASSF1 as well as RASSF4 and RASSF9 to RASSF5. The variants, RASSF2-to-1, RASSF4-to-5, and RASSF9-to-5 (Fig. 1), were successfully expressed and purified. Their binding affinities for HRAS, RIT1, RALA, RAP2A and RRAS1 were measured using fluorescence polarization (Fig. S10).

Remarkable differences in binding affinities of the analyzed RASSF variants are summarized in Figure 4 for comparison. RASSF2-to-1 variant revealed a significant increase of RALA ($p < 0.006$) and RRAS1 ($p < 0.014$) binding affinity compared with RASSF2 but declined compared with RASSF1. In contrast, RIT1, which did not show any binding to RASSF2 and a very low affinity to RASSF1, now exhibited a reasonable K_d value of 65 μM for RASSF2-to-1. The RASSF4-to-5 variant, on the one hand, showed a tremendous increase in affinity for HRAS of about 20-fold ($p < 0.0118$) and, on the other hand, diminished RIT1 property to bind RASSF4 by threefold ($p < 0.0351$). These data suggest that the hotspot residues favor RASSF4 binding to RIT1, whereas those residues of RASSF5 counteract RIT1 binding. Similarly, the RASSF4-to-5 affinity for RAP2A was increased by 2.5-fold (n.s., $p < 0.087$), which emphasizes the high-affinity RAP2A-RASSF5 interaction. The RASSF9-to-5 variant showed a 4.5-fold increase in HRAS-binding affinity as compared with RASSF9 ($p < 0.008$) that can be attributed to the high-affinity interaction of HRAS with RASSF5. The intermediate affinity of RASSF9 for RIT1 of 27 μM is validated by the RASSF9-to-5 variant, which revealed a 5.5-fold higher K_d value ($p < 0.005$). The interaction of the RASSF9-to-5 variant with RALA was drastically enhanced

($K_d = 35 \mu\text{M}$) considering the lack of RASSF9 binding to RALA.

Our data on residue swapping in RASSF proteins successfully validated the key role of hotspot residues in the RAS-RASSF interaction, particularly RASSF1-RALA, RASSF5-HRAS, and RASSF9-RIT1.

RIT1 pull-down from cell lysates by RASSF7 and RASSF9

To prove physiological relevance of identified RIT1 interactions with RASSF7 and RASSF9, we transfect Human Embryonic Kidney (HEK) 293T cells with human RIT1 and used His-tagged RA domains of RASSF7 and RASSF9 to pull down HA-tagged RIT1 from the cell lysates. As a control, we used lysates of HRAS-transfected cells and His-tagged RASSF5 RA domain to pull down FLAG-HRAS. As shown in Figure 5A, RIT1 bound to RASSF7 and RASSF9 but not to RASSF5, which was, in contrast, able to pull down HRAS. Data of three independent experiments were quantified by a Li-Cor Odyssey imaging system and expressed as signal intensity (Fig. 5B), confirmed the significance of the RIT1 interaction with RASSF7 and RASSF9 ($p < 0.01$).

Discussion

Effector selection and activation by a RAS protein in a proper cellular context and appropriate protein network are known to initiate a cascade of biochemical reactions and thus control defined cellular functions in all types of cells. It is also increasingly clear that functionalization of the effectors with various modular building blocks, mainly the RA/RB domains, is a prerequisite for successful orchestration of a series of spatiotemporal events, including recruitment, subcellular localization, assembly of proactive protein complexes, and ultimately association with and activation *via* the RAS protein. An issue that is investigated in-depth in this study is how many effectors for RAS proteins exist in the human proteome and

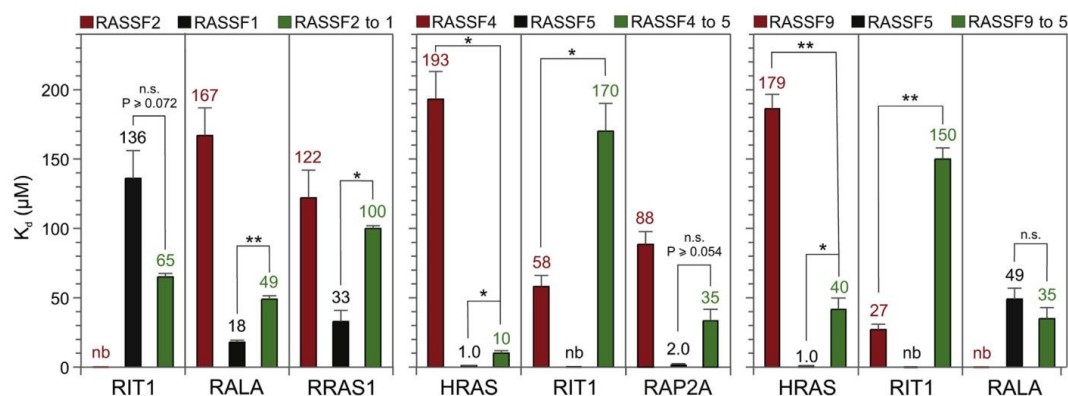


Figure 4. Validation of RAS-RASSF selectivity by hotspots residue swapping in RASSF RA domains. The interactions of the RASSF hotspot variants (RASSF2-to-1: A186K/Y187D/V190K/T191H, RASSF4-to-5: Y185D/S187I/V188K/N188L and RASSF9-to-5: V40D/G42I/L43K/K45L/R46H; see Fig. 3, boxed residues) with various RAS family proteins (RIT1, RALA, RRAS1, HRAS, and RAP2A) were determined by fluorescence polarization (see Fig. S10), and evaluated K_d values were plotted as bar charts together with K_d values of wild-type RASSF1, 2, 4, 5, and 9. (* $p < 0.05$; ** $p < 0.01$). Color codes highlight RASSF wild types (red and black) and RASSF variants (green). The error bars were derived from the fitting errors.

RAS-RASSF selectivity

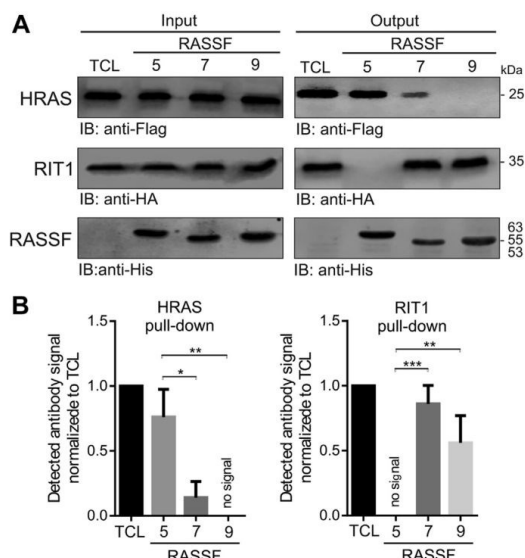


Figure 5. Binding analysis of RIT1 and HRAS with RASSF1-RA, RASSF7-RA, and RASSF9-RA using pull-down assay. A, HA-RIT1 and FLAG-HRAS, overexpressed in HEK 293T cells, were pulled down using the His-tagged MBP-RA domains of RASSF5, RASSF7, and RASSF9, respectively, and immunoblotted (IB) using anti-HA and anti-FLAG antibodies. Immunoblots of total cell lysates (TCL) were served as a loading control to detect HA-RIT1 and FLAG-HRAS. An anti-His antibody was used for detection of the His-tagged MBP-RA domains of RASSF5, RASSF7, and RASSF9 as an input loading control (more detail in Fig. S11). B, the graphs represent densitometric analysis of three independent experiments under the same conditions as shown in (A). All values were normalized to the loading control. All data are expressed as the mean of triplicate experiments \pm standard deviation (unpaired t-test, * p < 0.05, ** p < 0.01, and *** p < 0.001).

how they achieve the desired affinity and selectivity for their cognate RAS protein.

The total numbers of RAS effectors differ from study to study. A SMART database search has provided 108 RA and 20 RB-domain-containing proteins in one of the early and first comprehensive studies on RAS-effector interactions (23). These numbers have been slightly reduced to 100 RA domains and only a few members of RB-domain-containing proteins, including A/B/CRAF, TIAM1/2, and RGS12/14 proteins (31). In the next studies, Kiel *et al.* (43) have come to around 70 human proteins, containing RA and RB domains. Ibáñez Gaspar *et al.* (44) have analyzed in their very recent, comprehensive study 56 established and predicted RAS effectors with the potential ability to bind to RAS oncoproteins. Our search, using the UniProt database and the program HMMER, alongside with a cross-check of each individual sequence, ended up with 41 RA in 39 RA-domain-containing proteins and 16 RB in 14 RB-domain-containing proteins (Fig. S1). Thus, our lists contain 53 proteins, also including RALGDSL2 and SNX17 (Tables S1 and S2). SNX17 along with SNX27 and SNX31, which possess a FERM-like domain, has been shown to directly bind to GTP-bound HRAS (45) and may thus be involved in endosomal RAS signaling processes

(46). However, we exclude RASGEF3-5, KRIT1, and RGL4. Sequences, related to RA or RB domains, were not found in other proteins (Table S3), such as SIN1, SNX31, HK1 (Hexokinase 1), and SHANK2-3, which have been recently described as new RAS effector proteins (45, 47–50).

In order to refine a comprehensive list of RAS proteins and their effectors regarding their capabilities of mutual binding, we have investigated pairwise interaction between selected proteins (Fig. 2), related them to available structural data (Fig. 3), and combined them with data described in previous studies (Fig. S9).

The RASSF family contains ten members and is divided into two groups; RASSF1–6 typically have C-terminal RA and SARAH domains and RASSF7–10 an N-terminal RA domain (Fig. 1) (51). However, RAS-binding residues are not conserved in group 2 of the RASSF family and overall, the RA domains of these two RASSF groups are about 25% identical. Our data showed a much lower binding affinity between RAS family members and RA domains of group 2 (Fig. 2).

In a very recent study, Dhanaraman *et al.* have performed RASSF pull-down experiments under similar conditions as previously published by Chan *et al.* (8, 24). As already stated by the reviewer, this approach has limitations to detect affinities lower than 10 to 30 μ M, which is dependent on several variables such as the buffer and centrifugation speed. Chan *et al.* have observed HRAS interactions with RASSF6 and RASSF7 as well, which were determined in the present study, although with very high K_d values (Fig. 2). RASSF5 binding to KRAS and HRAS, as reported by Dhanaraman *et al.*, also confirms a previous study by Nakhaeizadeh *et al.*, which has shown similar binding affinities of the effector domains, including RASSF5-RA, toward the RAS paralogs, HRAS, KRAS, and NRAS (21). In contrast, Dhanaraman *et al.* have examined RAP1A and RASSF5, consistent with our study with RAP1B and RAP2A (Fig. 2), but did not consider them as interactions, again due to the approach limitation of 10 μ M (see below).

RASSF1 and RASSF5 RA domains share the highest sequence homology and several residues, including L282, D285, A286, I/V287, K288, H291, K308, V311, V312, and D313 (RASSF5 numbering), involved in RAS interaction (Fig. 3), are almost identical. These RASSFs have been described in many studies as effectors for H/K/NRAS, RRAS1, and RAP1A (19, 32, 52, 53). Accordingly, we have determined high and intermediate affinities for their association with RAS family members in this study (Fig. 2) and in part also in a previous report (21). Interestingly, RASSF proteins turned out to interact with several other RAS-related proteins, beyond the classical RAS paralogs. Shifman and colleagues have recently shown by immunoprecipitation experiments that RASSF1 also interacts with ERAS and DIRAS3 (54), which are atypical members of the RAS family (42). Similarly, Dhanaraman *et al.* (24) have very recently demonstrated the interaction of RASSF1 with GEM, REM1, REM2 and RSL12 GTPase proteins. These GTPases, which belong to the RGK GTPase family, regulate voltage-dependent calcium channels and cell shape (24). The present study showed that RIT1 interacts RASSF7 and RASSF9, and RALA with RASSF1. These

interactions, which successfully validated the key role of hotspot residues in the RAS-RASSF interaction (Fig. 4), confirmed our predicted interaction model (Fig. 3). The RALA-RASSF1 interaction seems rather relevant since the presence of four RASSF1 hotspot residues in RASSF2 considerably enhanced RALA binding (Fig. 4). RALA and RALB contain lysine and alanine at positions 36 and 37, respectively (HRAS numbering), rather different residues than isoleucine and glutamate in other RAS proteins, which are known to be critical for the RAS-effector interactions (55). RALA-RASSF1 interaction has not been reported to date and awaits further cell-based investigations, especially because the RASSF2-to-1 variant gained binding affinity toward RALA (Fig. 4). Similarly, RALA-RASSF5 interaction appears rather relevant as the RASSF9-to-5 variant affected the binding of RALA. This has been also demonstrated by hotspots residue swapping of RASSF9 to RASSF5. While RALA showed a K_d value of 35 μ M for RASSF9-to-5 while it did not show any binding to RASSF9, suggesting that very few key residues are sufficient to generate the appropriate binding surface. This notion presumes that analyzed RA domains share a conserved mode of RAS recognition based on the formation of an intermolecular, antiparallel β sheet (21, 24).

Among all RASSF family members, only RASSF1 and RASSF5 interact in high or intermediate affinities with all investigated RAS family members, with an exception of RIT1 (Fig. 2). RASSF7-9 RA domains share high sequence similarity and are different from RASSF10 (Fig. S2). A common signature of the RASSF members is the existence of the K/R241 and K/R308 hotspots (Fig. 3). They revealed, with a few exceptions, comparable K_d values for different representatives of the RAS family (Fig. 2). RIT1-RASSF7 and RIT1-RASSF9 interactions with affinities of 34 and 27 μ M are quite remarkable, especially because these proteins have not been reported yet as RAS effectors. RIT1 contains an alanine instead of the conserved S/T39 (HRAS numbering), and RASSF9 contains two negatively charged glutamic acids instead of the positively charged lysine residues at 307 and 308 (RASSF5 numbering; Fig. S2). These two drastic deviations may be responsible for the very low affinity of RASSF9 for HRAS due to electrostatic repulsion with D33. However, RIT1 contains also an aspartic acid at the corresponding position and yet shows an intermediate affinity for RASSF9. The relevance of RIT1-RASSF9 interaction was successfully validated by residue swapping. Substitution of five RASSF9 to RASSF5 residues, which did not bind RIT1, significantly impaired the interaction (Fig. 4). Moreover, cell-based pulldown experiments confirmed the relevance of RASSF7 and RASSF9 as potential RIT1 effectors and support the notion that K_d values of about 30 μ M can be considered physiologically relevant. It is important to note that GTPase-effector interactions in the cell take place in a context of multivalent platform very different from the isolated domains and bimolecular interaction under cell-free conditions. Effectors are full-length, associated with accessory proteins, and eventually the cell membrane, and are subjected to distinct control mechanisms, including posttranslational modifications. Validated antibodies against these proteins will enable us

in near future to take the next step namely determining the appropriate cell type that endogenously expresses the desired proteins and to unambiguously verify RIT1-RASSF interaction.

RHEB broadly exhibited low-affinity interaction with RASSF1-7, particularly RASSF1 (Fig. 2), which may be based on a large number of amino acid deviations in both switch regions (Fig. 3 and Fig. S4). It has been proposed that RHEB may complex with RASSF1 to coordinate signaling pathways, after processing by MST/LATS and TOR kinases (56). In the presence of RASSF1, RHEB has been shown to stimulate the MST/LATS/YAP pathways but is suppressed in its ability to activate the TOR pathway. The physical interaction of RHEB with RASSFs remains to be shown in cells, like it has been shown for other RAS and RAS-like proteins (54).

CRAF RB domain is one of the most and best studied RAS effectors with the highest selectivity for the H/K/NRAS paralogs and to a certain extent also for the RRAS proteins (21). CRAF RB domain revealed an intermediate affinity for RAP1B and RHEB1 but not for RIT1 or RAP2A (Fig. 2). The RAP1 and RAP2 subgroups differ at positions 25 and 39 (HRAS numbering), which are in the case of RAP1 proteins occupied by favorable glutamine and serine (Fig. 3). The two orders of magnitude lower affinity of RAP1B for the CRAF RB domain stems from the drastic deviation at position 31 (HRAS numbering). K31 in RAP proteins obviously collides with the K84 in CRAF and disfavors a RAP-CRAF interaction (Fig. S9); this was the reason why RAP1A mutated at this site was used for successful determination of the complex structure between RAP1A and the CRAF RB domain (26). Phosphorylation of RAP1A at S11 has been recently proposed to promote RAP1A-CRAF RB domain interaction (57). Devanand and colleagues have proposed that phosphorylation of S11 allosterically modulates the dynamics of RAP1A switch regions, which consequently promotes the RAP1A-CRAF complex formation and downstream signaling (58).

An intermediate affinity for CRAF RB domain interaction with RHEB G domain (Fig. 2) points to previous reports of a direct relationship between these two crucial signaling molecules. PKA-dependent phosphorylation of CRAF at S43 has been shown to reciprocally potentiate RHEB-CRAF interaction and to decrease CRAF interaction with HRAS (59). An asparagine instead of D38 (HRAS numbering) in the switch I region seems to be critical for the unique CRAF-binding properties of RHEB. In a different study, Henske and co-workers have shown that RHEB interacts with and inhibits BRAF (60). In this context, RHEB not only hinders the BRAF association with HRAS but also interferes with BRAF activation and its heterodimerization with CRAF. As the RB domains of the RAF paralogs are conserved (33), mainly regarding their RAS-binding residues (Fig. S3), differences between BRAF and CRAF interactions with RHEB may stem from deviations outside the RB domains or from different phosphorylation states. Heard *et al.* (61) have recently reported a strong interaction between RHEB-GTP and BRAF (but not with CRAF) and that RHEB overexpression decreases and RHEB knockdown increases RAF/MEK/ERK activation. They have shown that a variant of RHEB (Y35 to asparagine; Y32 in

RAS-RASSF selectivity

HRAS) impedes RHEB interaction with BRAF leading to an increased BRAF/CRAF heterodimerization and thus activation of the MAPK pathway. Accordingly, they have proposed a dual function for RHEB, suppression of the MAPK pathway and mTORC1 activation (61).

RIT1-CRAF interaction has been frequently proposed due to their critical roles in developmental disorders, collectively called RASopathy (62), but not directly shown. We observed a very low affinity for these two proteins (Fig. 2), which may stem from the sequence deviation between RIT1 and HRAS in their switch I region (Fig. 3). In an early study on biochemical characterization of RIT, Andres and coworkers have shown that RIT1 interacts with RA domains of RALGDS and AF6 but not with the CRAF RB domain (63). In a different study, they have shown that RIT1 binds and activates BRAF but not CRAF (64). This may again implicate those additional regions may exist outside the conserved RB domains of the RAF paralogs, which differently facilitate the interaction with the RAS proteins, such as RIT1 or RHEB.

An ever-present central concern in the biophysical investigation of protein–protein interactions is the relevance of low (10–30 μ M) to very low ($>> 30 \mu$ M) affinity interactions in the regulation of signaling events. These protein complexes rely on weak, transient interactions that are emerging as important components of large signaling complexes at the plasma membrane that are required to respond to external stimuli. Cellular membranes play a critical role in the localization and orientation of protein complexes and in fine-tuning of protein functions (65). The activity of RAS and RAF paralogs is regulated through different parameters, including membrane association. Analysis of dynamic interactions between KRAS4B and lipid bilayer membrane has revealed that association of ARAF RB domain with active KRAS4B not only reorients KRAS4B at the membrane surface but also facilitates membrane binding of ARAF RBD itself (66). Four basic residues, K28, K66, R68, and K69, are engaged in lipid binding. Another emerging concept is based on the physical interaction of the G domain itself with a lipid membrane. A membrane-based, nucleotide-dependent conformational switch operates through distinct regions on the surface of RAS proteins, including the hypervariable region (HVR), which reorients with respect to the plasma membrane (67–76). Mazhab-Jafari and colleagues have proposed two different orientations of KRAS4B facing toward the membrane (66). KRAS4B in an exposed GDP-bound form favors $\alpha 4/\alpha 5$ helices, which considerably reorients upon activation, and favors $\beta 1$ – $\beta 3$ sheets and $\alpha 2/\alpha 3$ helices from the G domain, and K167/K172 from HVR, in an occluded GTP-bound form. G-domain-membrane interaction may not only stabilize protein complexes but may also contribute to the specificity of signal transduction. A critical aspect in this context is the organization of RAS proteins into protein–lipid complexes. These so-called nanoclusters concentrate RAS at the plasma membrane. They are the sites of effector recruitment and activation and are essential for signal transmission (67, 70, 77, 78).

A frequently encountered issue in the enhancement of RAS-effector interaction is posttranslational modification. Thurman *et al.* (79) have recently demonstrated that the ubiquitylation of KRAS at L147 impairs RAS-RASGAP interaction and facilitates RAS-CRAF association and MAPK signaling. Barceló *et al.* (80) have shown that PKC-catalyzed phosphorylation of KRAS at S181 results in an increased interaction of KRAS with CRAF and PI3K α . Several studies have previously shown that the CRAF CR domain undergoes direct interaction with HRAS, which appears to be enhanced by the farnesyl moiety if using farnesylated RAS (15, 81–86). A possible HRAS-CRAF CR domain interaction has been proposed to be, contrary to the CRAF RB domain, outside of the switch regions of HRAS and thus independent of its nucleotide-bound state. In contrast, Y32 and Y64 phosphorylation by SRC alters the conformation of switch I and II regions, markedly reduces RAS binding to CRAF, and concomitantly increases binding to RASGAPs and the rate of GTP hydrolysis (87, 88).

Another aspect related to very low affinity interactions involves a secondary RAS-binding site, in addition to the RA/RB domain, in terms of a two-step, two-domain binding model. The two-domain model accommodates at least two different enhancer mechanisms. One is the direct enhancement of a selective RAS-effector interaction required for effector activation, proposed for the interactions of yeast RAS2 with two sites in adenylyl cyclase (89), HRAS with RB and CR domains of CRAF (33), and HRAS with two RA domains of PLC ϵ (90). The latter may involve a high-affinity, GTP-dependent binding of the RA2 domain accompanied by low-affinity, GTP-independent binding of the RA1 domain. The deletion of one of the RA domains inhibits HRAS-induced PLC ϵ activation (90). Notably, AF6 also possesses two RA domains and two RGS12/14 RB domains, respectively (44). Such a tandem arrangement of RA with RB domains may enhance their affinity toward RAS, increase effector occupancy by additional endogenous events and thus the signaling output. An emerging concept, therefore, is the action of membrane-binding CR domain that stabilizes RAS-CRAF RB domain interaction accompanied by S621 phosphorylation and 14-3-3 binding that collectively facilitates RAF activation (82, 83, 91–94).

The formation of multiprotein complexes underlies a multistep assembly mechanism that follows a defined and probably short path from the cytoplasm, just underneath the membrane, to the membrane where membrane-associated proteins, for example, RAS proteins, are anchored. The first step, which has been designated as the piggyback mechanism (95), most likely increases local concentrations of protein components in a small volume and may drive cytoplasmic phase separations (96–98). The second step is the site-specific association of assembled protein complex with membrane-associated components, such as RAS proteins, which in turn are connected to receptors and coreceptors (44, 97, 98). In this way, a machinery of signaling molecules is orchestrated before the ligand activates the receptor. This is fine-tuned and prepared for an efficient signal transduction. Of course, it remains

to be figured out why some interactions are in the nanomolar range (e.g., 20 nM) and some in the micromolar range (e.g., 20 μ M or more). Given that the latter is involved in the initiation of multivalent macromolecular interactions, the final complex formation comes along after multivalent interactions have proceeded (99). This obviously increases significantly both the number of interacting complexes and overall binding affinity by orders of magnitude (44). The nanomolar affinity, however, may determine the selectivity for a sequential formation of two complexes. These interactions are often characterized by fast association and slow dissociation rates, indicating the formation of stable complexes (100–102).

Experimental procedures

Constructs

Gene fragments encoding RAs of RASSF1 (accession number Q9NS23; amino acids or aa 194–288), RASSF2 (P50749; aa 176–264), RASSF3 (Q86WH2; aa 79–187), RASSF4 (Q9H2L5; aa 174–262), RASSF5 (Q5EBH1; aa 200–358), RASSF6 (Q6ZTQ3; aa 218–306), RASSF7 (Q02833; aa 6–89), RASSF8 (Q8NHQ8, aa 1–82), RASSF9 (O75901, aa 25–119), and RASSF10 (A6NK89; aa 4–133) as well as CRAF RB domain (P04049, aa 51–131) were cloned into pMal-c5X-His vector. The variants RASSF2-to-1 (A186K/Y187D/V190K/T191H), RASSF4-to-5 (Y185D/S187I/V188K/N188L) and RASSF9-to-5 (V40D/G42I/L43K/K45L/R46H) were generated by BioCat Gene Synthesis (BioCat GmbH) in pMal-c5X-His vector. Constructs for the prokaryotic expression of human HRAS, RRAS, RALA, RHEB1, RIT1, RAP2A, and RAP1B isoforms were described previously (6). For mammalian expression, human HRAS and RIT1 were cloned in pcDNA3.1-Flag and pMT2-HA vectors, respectively.

Proteins

All RASSF and RAS proteins were expressed in *Escherichia coli* using the pMal-His and pGEX expression systems and purified using Ni-NTA and glutathione-based affinity chromatography as described previously (103). RAS•mGppNHp was prepared as described (103). mGppNHp is a fluorescent, nonhydrolyzable analog of GTP; m stands for the methylantraniloyl (m) and GppNHp for Guanosine-5'-[(β,γ)-imido] triphosphate.

Fluorescence polarization

Increasing concentrations of RA/RB domains (0.002–300 μ M) were added to the solution of mGppNHp-bound RAS family proteins (1 μ M) in a buffer, containing (30 mM Tris-HCl, pH 7.4, 100 mM NaCl, 5 mM MgCl₂, 3 mM DTT) using fluorescence polarization on a Fluoromax 4 fluorimeter as described previously (75). The excitation wavelength was 360 nm and the emission wavelength 450 nm. The dissociation constants (K_d) for the RAS-effector interaction were evaluated using a quadratic ligand-binding equation.

Bioinformatics

Information about RB and RA domains was obtained either from annotations in the UniProt database or in parallel using the program suite HMMER [<http://hmmer.org/>]. HMMER uses a Hidden Markov Model to compare sequences. Unlike CLUSTAL, which directly compares corresponding amino acids in the alignment, HMMER also takes adjacent amino acids into account. To do so, it calculates a Profile HMM before sequence comparison. It determines which amino acids are suitable at a given position. In the context of some protein domain, Profile can be viewed as a mapping of its characteristic features required for the domain structure, function, or interaction. Sequence alignments were performed in the Bioedit program using the ClustalW algorithm (104). By using Chimera, the sequence alignments were adjusted with superimposed structures (25). An interaction matrix is based on intermolecular contacts in complex structures (21). A python code was written to match sequence alignments with complex structures and calculated intermolecular contacts were put in the form of the interaction matrix. The intermolecular contacts were defined as pair residues with a distance of 4.0 Å between effectors and RAS proteins in available complex structures in the protein data bank (<http://www.pdb.org>). Biopython modules (105) were also used to elucidate corresponding residues in all available complex structures. The structural representation was generated using Pymol viewer (<http://www.pymol.org>).

Cell-based assays

In total, 3.2 millions of HEK 293T cells were seeded in 10 cm plates in DMEM supplemented with 10% fetal bovine serum (FBS) 14 h prior to transfection. The cells were transfected at 80% to 90% confluency using TurboFect transfection reagent (R0532, Thermo Scientific), with Flag-tagged HRAS and HA-tagged RIT1 constructs, or no plasmid as a negative control. At 24 h posttransfection, cells were washed in ice-cold phosphate-buffered saline (PBS) and lysed in ice-cold lysis buffer, containing 50 mM Tris/HCl pH 7.5, 5 mM MgCl₂, 100 mM NaCl, 1% Igepal CA-630, 10% glycerol, 20 mM β -glycerolphosphate, 1 mM Na-orthovanadate, EDTA-free inhibitor cocktail 1 tablet/50 ml. In total, 200 μ g cell lysate was added to 20 μ g His-tagged MBP-RASSF proteins coupled with 100 μ l Ni-NTA beads. The samples were incubated for 30 min on the rotator at 4 °C. After three washing with the lysis buffer and centrifugation steps (30 s at 300g), the samples were subjected to SDS-PAGE (12.5% polyacrylamide). HRAS and RIT1 were detected by immunoblotting using a rabbit anti-His (RM146) antibody (Thermo Fisher), a rabbit polyclonal anti-FLAG (F7425) antibody (Sigma), and a rabbit polyclonal anti-HA (SC-805) antibody (Santa Cruz), respectively. The immunoblots were evaluated using an Odyssey Fc Imaging System (LI-CORE Biosciences).

RAS-RASSF selectivity

Data availability

All the data are in the article.

Supporting information—This article contains supporting information.

Acknowledgments—We thank C. Herrmann and Mathilda Katan and Alfred Wittinghofer for sharing plasmids and Kotsene Loumonvi for technical assistance.

Authors contributions—M. R. A. conceived and coordinated the study; S. R. A., N. S. K. J., and M. R. A. designed and wrote the paper; S. R. A., N. S. K. J., C. W., and F. B. designed, performed, and analyzed the experiments; S. R. A., R. D., and E. A. performed structural analysis; C. A. M. S. contributed to the conception of this work and provided critical feedback on data interpretation; all the authors reviewed the results and approved the final version of the article.

Funding and additional information—This study was supported by the European Network on Noonan Syndrome and Related Disorders (NSEuroNet, grant number: 01GM1621B); the German Research Foundation (Deutsche Forschungsgemeinschaft or DFG) through the International Research Training Group “Intra- and interorgan communication of the cardiovascular system” (grant number: IRTG 1902-p6); the German Federal Ministry of Education and Research (BMBF)—German Network of RASopathy Research (GeNeRARE, grant numbers: 01GM1902C).

Conflict of interest—The authors declare that they have no conflicts of interest with the contents of this article.

Abbreviations—The abbreviations used are: AF6, ALL1-fused gene from chromosome 6; CR domain, cysteine-rich domain; ERK, extracellular signal-regulated kinase; GAP, GTPase-activating protein; GEF, guanine nucleotide exchange factor; GTP, guanosine triphosphate; GTPase, guanosine triphosphatase; HK1, hexokinase-1; HRAS, Harvey rat sarcoma; KRAS, Kristen rat sarcoma; MAPK, mitogen-activated protein kinase; MBP, maltose binding protein; MEK, MAPK/ERK kinase; NKIRAS, NF-kappa-B inhibitor-interacting RAS-like protein; NORE1, novel RAS effector; NRAS, neuroblastoma RAS; PDZGEF, PDZ-domain-containing guanine nucleotide exchange factor; PI3K, phosphoinositide 3-kinase; PKC, protein kinase C; PLC ϵ , phospholipase C epsilon; RA, RAS association domain; RAF, rapidly accelerated fibrosarcoma; RALA, RAS-like protein A; RALGDS, RAL guanine nucleotide dissociation stimulator; RAP, RAS proximate; RAS, rat sarcoma; RASD, dexamethasone-induced RAS-related; RASSF, RAS association domain family; RB, RAS-binding domain; RERG, RAS-related and estrogen-regulated growth inhibitor; RERGL, RAS-related and estrogen-regulated growth inhibitor-like protein; RGL, RAL guanine nucleotide dissociation stimulator-like; RGS, regulator of G protein signaling; RHEB, RAS homologous enriched in brain; RHO, RAS homologous; RIN, RAS and RAB interactor; RIT, RAS-like protein expressed in many tissues; RRAS, RAS-related protein; SARA, Salvador-RASSF-Hippo domain; SHANK, SH3 and multiple ankyrin repeat domain; SIN1, stress-activated protein kinase-interacting protein 1; SNX17, sorting nexin-17; TIAM, T-lymphoma invasion and metastasis protein.

References

1. Jaiswal, M., Dvorsky, R., Amin, E., Risse, S. L., Fansa, E. K., Zhang, S. C., Taha, M. S., Gauhar, A. R., Nakhaei-Rad, S., Kordes, C., Koessmeier, K. T., Cirstea, I. C., Olayioye, M. A., Haussinger, D., and Ahmadian, M. R. (2014) Functional cross-talk between ras and rho pathways: A Ras-specific GTPase-activating protein (p120RasGAP) competitively inhibits the RhoGAP activity of deleted in liver cancer (DLC) tumor suppressor by masking the catalytic arginine finger. *J. Biol. Chem.* **289**, 6839–6849.
2. Simanshu, D. K., Nissley, D. V., and McCormick, F. (2017) RAS proteins and their regulators in human disease. *Cell* **170**, 17–33.
3. Gutierrez-Erlandsson, S., Herrero-Vidal, P., Fernandez-Alfara, M., Hernandez-Garcia, S., Gonzalo-Flores, S., Mudarra-Rubio, A., Fresno, M., and Cubelos, B. (2013) R-RAS2 overexpression in tumors of the human central nervous system. *Mol. Cancer* **12**, 127.
4. Karnoub, A. E., and Weinberg, R. A. (2008) Ras oncogenes: Split personalities. *Nat. Rev. Mol. Cell Biol.* **9**, 517–531.
5. Herrmann, C. (2003) Ras-effector interactions: After one decade. *Curr. Opin. Struct. Biol.* **13**, 122–129.
6. Nakhaei-Rad, S., Nakhaeizadeh, H., Götze, S., Kordes, C., Sawitza, I., Hoffmann, M. J., Franke, M., Schulz, W. A., Scheller, J., and Piekorz, R. P. (2016) The role of embryonic stem cell-expressed RAS (ERAS) in the maintenance of quiescent hepatic stellate cells. *J. Biol. Chem.* **291**, 8399–8413.
7. Castellano, E., and Downward, J. (2010) Role of RAS in the regulation of PI 3-kinase. *Curr. Top. Microbiol. Immunol.* **346**, 143–169.
8. Chan, J. J., Flatters, D., Rodrigues-Lima, F., Yan, J., Thalassinou, K., and Katan, M. (2013) Comparative analysis of interactions of RASSF1-10. *Adv. Biol. Regul.* **53**, 190–201.
9. Bunney, T. D., and Katan, M. (2011) PLC regulation: Emerging pictures for molecular mechanisms. *Trends Biochem. Sci.* **36**, 88–96.
10. Ferro, E., and Trabalzini, L. (2010) RalGDS family members couple Ras to Ral signalling and that's not all. *Cell Signal.* **22**, 1804–1810.
11. Rajalingam, K., Schreck, R., Rapp, U. R., and Albert, S. (2007) Ras oncogenes and their downstream targets. *Biochim. Biophys. Acta* **1773**, 1177–1195.
12. Nussinov, R., Tsai, C.-J., Muratcioglu, S., Jang, H., Gursoy, A., and Keskin, O. (2015) Principles of K-Ras effector organization and the role of oncogenic K-Ras in cancer initiation through G1 cell cycle deregulation. *Expert Rev. Proteomics* **12**, 669–682.
13. Ahearn, I. M., Haigis, K., Bar-Sagi, D., and Philips, M. R. (2012) Regulating the regulator: Post-translational modification of RAS. *Nat. Rev. Mol. Cell Biol.* **13**, 39.
14. Hennig, A., Markwart, R., Esparza-Franco, M. A., Ladds, G., and Rubio, I. (2015) Ras activation revisited: Role of GEF and GAP systems. *Biol. Chem.* **396**, 831–848.
15. Fischer, A., Hekman, M., Kuhlmann, J., Rubio, I., Wiese, S., and Rapp, U. R. (2007) B- and C-RAF display essential differences in their binding to Ras: the isotype-specific N terminus of B-RAF facilitates Ras binding. *J. Biol. Chem.* **282**, 26503–26516.
16. Mott, H. R., and Owen, D. (2015) Structures of Ras superfamily effector complexes: What have we learnt in two decades? *Crit. Rev. Biochem. Mol. Biol.* **50**, 85–133.
17. Vetter, I. R., and Wittinghofer, A. (2001) The guanine nucleotide-binding switch in three dimensions. *Science* **294**, 1299–1304.
18. Filchtinski, D., Sharabi, O., Rüppel, A., Vetter, I. R., Herrmann, C., and Shifman, J. M. (2010) What makes Ras an efficient molecular switch: A computational, biophysical, and structural study of Ras-GDP interactions with mutants of Raf. *J. Mol. Biol.* **399**, 422–435.
19. Erijman, A., and Shifman, J. M. (2016) RAS/effector interactions from structural and biophysical perspective. *Mini Rev. Med. Chem.* **16**, 370–375.
20. Nassar, N., Horn, G., Herrmann, C., Block, C., Janknecht, R., and Wittinghofer, A. (1996) Ras/Rap effector specificity determined by charge reversal. *Nat. Struct. Biol.* **3**, 723–729.
21. Nakhaeizadeh, H., Amin, E., Nakhaei-Rad, S., Dvorsky, R., and Ahmadian, M. R. (2016) The RAS-effector interface: Isoform-specific differences in the effector binding regions. *PLoS One* **11**, e0167145.

22. Repasky, G. A., Chenette, E. J., and Der, C. J. (2004) Renewing the conspiracy theory debate: Does Raf function alone to mediate Ras oncogenesis? *Trends Cell Biol.* **14**, 639–647
23. Wohlgemuth, S., Kiel, C., Krämer, A., Serrano, L., Wittinghofer, F., and Herrmann, C. (2005) Recognizing and defining true Ras binding domains I: Biochemical analysis. *J. Mol. Biol.* **348**, 741–758
24. Dhanaraman, T., Singh, S., Killoran, R. C., Singh, A., Xu, X., Shifman, J. M., and Smith, M. J. (2020) RASSF effectors couple diverse RAS subfamily GTPases to the Hippo pathway. *Sci. Signal.* **13**, eabb477
25. Goddard, T. D., Huang, C. C., Meng, E. C., Pettersen, E. F., Couch, G. S., Morris, J. H., and Ferrin, T. E. (2018) UCSF ChimeraX: Meeting modern challenges in visualization and analysis. *Protein Sci.* **27**, 14–25
26. Nassar, N., Horn, G., Herrmann, C. A., Scherer, A., McCormick, F., and Wittinghofer, A. (1995) The 2.2 Å crystal structure of the Ras-binding domain of the serine/threonine kinase c-Raf1 in complex with Rap1A and a GTP analogue. *Nature* **375**, 554
27. Bunney, T. D., Harris, R., Gandarillas, N. L., Josephs, M. B., Roe, S. M., Sorli, S. C., Paterson, H. F., Rodrigues-Lima, F., Esposito, D., and Ponting, C. P. (2006) Structural and mechanistic insights into Ras association domains of phospholipase C epsilon. *Mol. Cell* **21**, 495–507
28. Stieglitz, B., Bee, C., Schwarz, D., Yildiz, Ö., Moshnikov, A., Khokhlatchev, A., and Herrmann, C. (2008) Novel type of Ras effector interaction established between tumour suppressor NORE1A and Ras switch II. *EMBO J.* **27**, 1995–2005
29. Pacold, M. E., Suire, S., Perisic, O., Lara-Gonzalez, S., Davis, C. T., Walker, E. H., Hawkins, P. T., Stephens, L., Eccleston, J. F., and Williams, R. L. (2000) Crystal structure and functional analysis of Ras binding to its effector phosphoinositide 3-kinase γ . *Cell* **103**, 931–944
30. Smith, M. J., Ottoni, E., Ishiyama, N., Goudreau, M., Haman, A., Meyer, C., Tucholska, M., Gasmi-Seabrook, G., Menezes, S., and Laister, R. C. (2017) Evolution of AF6-RAS association and its implications in mixed-lineage leukemia. *Nat. Commun.* **8**, 1–13
31. Kiel, C., Wohlgemuth, S., Rousseau, J., Schymkowitz, J., Ferkinghoff-Borg, J., Wittinghofer, F., and Serrano, L. (2005) Recognizing and defining true Ras binding domains II: In silico prediction based on homology modelling and energy calculations. *J. Mol. Biol.* **348**, 759–775
32. Donniger, H., Schmidt, M. L., Mezzanotte, J., Barnoud, T., and Clark, G. J. (2016) Ras signaling through RASSF proteins. *Semin. Cell Dev. Biol.* **58**, 86–95
33. Rezaei Adariani, S., Buchholzer, M., Akbarzadeh, N., Nakhaei-Rad, S., Dvorsky, R., and Ahmadian, M. R. (2018) Structural snapshots of RAF kinase interactions. *Biochem. Soc. Trans.* **46**, 1393–1406
34. Haghighi, F., Dahlmann, J., Nakhaei-Rad, S., Lang, A., Kutschka, I., Zenker, M., Kensah, G., Piekorz, R. P., and Ahmadian, M. R. (2018) bFGF-mediated pluripotency maintenance in human induced pluripotent stem cells is associated with NRAS-MAPK signaling. *Cell Commun. Signal.* **16**, 96
35. Desideri, E., Cavallo, A. L., and Baccarini, M. (2015) Alike but different: RAF paralogs and their signaling outputs. *Cell* **161**, 967–970
36. Castellano, E., and Downward, J. (2011) RAS interaction with PI3K: More than just another effector pathway. *Genes Cancer* **2**, 261–274
37. Ross, E. M., and Wilkie, T. M. (2000) GTPase-activating proteins for heterotrimeric G proteins: regulators of G protein signaling (RGS) and RGS-like proteins. *Annu. Rev. Biochem.* **69**, 795–827
38. Willard, F. S., Willard, M. D., Kimple, A. J., Soundararajan, M., Oestreich, E. A., Li, X., Sowa, N. A., Kimple, R. J., Doyle, D. A., and Der, C. J. (2009) Regulator of G-protein signaling 14 (RGS14) is a selective H-Ras effector. *PLoS One* **4**, e4884
39. Malliri, A., and Collard, J. G. (2003) Role of Rho-family proteins in cell adhesion and cancer. *Curr. Opin. Cell Biol.* **15**, 583–589
40. Rooney, C., White, G., Nazgiewicz, A., Woodcock, S. A., Anderson, K. I., Ballestrem, C., and Malliri, A. (2010) The Rac activator STEF (Tiam2) regulates cell migration by microtubule-mediated focal adhesion disassembly. *EMBO Rep.* **11**, 292–298
41. Yamauchi, J., Miyamoto, Y., Tanoue, A., Shooter, E. M., and Chan, J. R. (2005) Ras activation of a Rac1 exchange factor, Tiam1, mediates neutrophin-3-induced Schwann cell migration. *Proc. Natl. Acad. Sci. U. S. A.* **102**, 14889–14894
42. Nakhaei-Rad, S., Haghighi, F., Nouri, P., Rezaei Adariani, S., Lissy, J., Kazemine Jasemi, N. S., Dvorsky, R., and Ahmadian, M. R. (2018) Structural fingerprints, interactions, and signaling networks of RAS family proteins beyond RAS isoforms. *Crit. Rev. Biochem. Mol. Biol.* **53**, 130–156
43. Kiel, C., Foglierini, M., Kuemmerer, N., Beltrao, P., and Serrano, L. (2007) A genome-wide Ras-effector interaction network. *J. Mol. Biol.* **370**, 1020–1032
44. Ibáñez Gaspar, V., Catozzi, S., Ternet, C., Luthert, P. J., and Kiel, C. (2021) Analysis of Ras-effector interaction competition in large intestine and colorectal cancer context. *Small GTPases* **12**, 209–225
45. Ghai, R., Mobli, M., Norwood, S. J., Bugarcic, A., Teasdale, R. D., King, G. F., and Collins, B. M. (2011) Phox homology band 4.1/ezrin/radixin/moesin-like proteins function as molecular scaffolds that interact with cargo receptors and Ras GTPases. *Proc. Natl. Acad. Sci. U. S. A.* **108**, 7763–7768
46. Ghai, R., and Collins, B. (2011) PX-FERM proteins: A link between endosomal trafficking and signaling? *Small GTPases* **2**, 7763–7768
47. Amendola, C. R., Mahaffey, J. P., Parker, S. J., Ahearn, I. M., Chen, W.-C., Zhou, M., Court, H., Shi, J., Mendoza, S. L., and Morten, M. J. (2019) KRAS4A directly regulates hexokinase 1. *Nature* **576**, 482–486
48. Chowdhury, D., and Hell, J. W. (2020) How CBP/Shank3 guards Rap and H-Ras. *Structure* **28**, 274–276
49. Cai, Q., Hosokawa, T., Zeng, M., Hayashi, Y., and Zhang, M. (2020) Shank3 binds to and stabilizes the active form of Rap1 and HRas GTPases via its NTD-ANK tandem with distinct mechanisms. *Structure* **28**, 290–300.e294
50. Miyan, J., Asif, M., Malik, S. A., Dubey, P., Singh, V., Singh, K., Mitra, K., Pandey, D., Haq, W., and Amita, H. (2019) Direct physical interaction of active Ras with mSIN1 regulates mTORC2 signaling. *BMC Cancer* **19**, 1–16
51. Iwasa, H., Hossain, S., and Hata, Y. (2018) Tumor suppressor C-RASSF proteins. *Cell Mol. Life Sci.* **75**, 1773–1787
52. Gordon, M., and Baksh, S. (2011) RASSF1A: Not a prototypical Ras effector. *Small GTPases* **2**, 5729–5740
53. van der Weyden, L., and Adams, D. J. (2007) The Ras-association domain family (RASSF) members and their role in human tumorigenesis. *Biochim. Biophys. Acta* **1776**, 58–85
54. Thillaivillalan, D., Singh, S., Killoran, R. C., Singh, A., Xu, X., Shifman, J., and Smith, M. J. (2020) RASSF effectors couple diverse RAS subfamily GTPases to the Hippo pathway. *bioRxiv*. <https://doi.org/10.1101/2020.02.05.923433>
55. Bauer, B., Mirey, G., Vetter, I. R., García-Ranea, J. A., Valencia, A., Wittinghofer, A., Camonis, J. H., and Cool, R. H. (1999) Effector recognition by the small GTP-binding proteins Ras and Ral. *J. Biol. Chem.* **274**, 17763–17770
56. Nelson, N., and Clark, G. J. (2016) Rheb may complex with RASSF1A to coordinate Hippo and TOR signaling. *Oncotarget* **7**, 33821
57. Devanand, T., Venkatraman, P., and Vemparala, S. (2018) Phosphorylation promotes binding affinity of Rap-Raf complex by allosteric modulation of switch loop dynamics. *Sci. Rep.* **8**, 1–15
58. Devanand, T., Krishnaswamy, S., and Vemparala, S. (2019) Interdigitation of lipids induced by membrane-active proteins. *J. Membr. Biol.* **252**, 331–342
59. Yee, W. M., and Worley, P. F. (1997) Rheb interacts with Raf-1 kinase and may function to integrate growth factor- and protein kinase A-dependent signals. *Mol. Cell. Biol.* **17**, 921–933
60. Karbowiczek, M., Robertson, G. P., and Henske, E. P. (2006) Rheb inhibits C-raf activity and B-raf/C-raf heterodimerization. *J. Biol. Chem.* **281**, 25447–25456
61. Heard, J. J., Phung, I., Potes, M. L., and Tamanoi, F. (2018) An oncogenic mutant of RHEB, RHEB Y35N, exhibits an altered interaction with BRAF resulting in cancer transformation. *BMC Cancer* **18**, 69
62. Yaoita, M., Niihori, T., Mizuno, S., Okamoto, N., Hayashi, S., Watanabe, A., Yokozawa, M., Suzumura, H., Nakahara, A., and Nakano, Y. (2016) Spectrum of mutations and genotype-phenotype analysis in Noonan syndrome patients with RIT1 mutations. *Hum. Genet.* **135**, 209–222

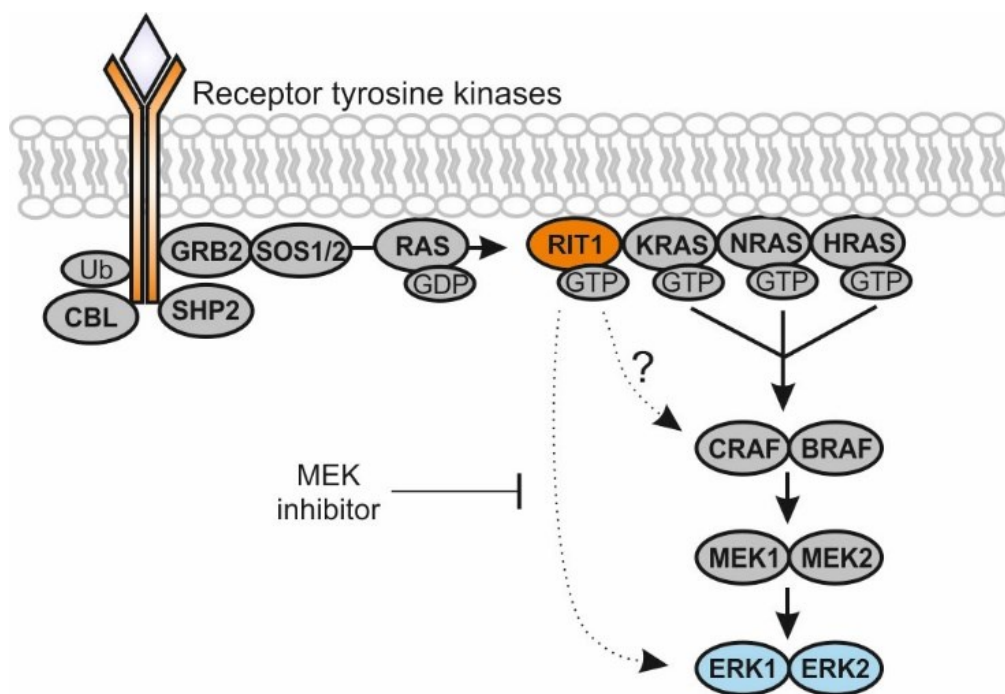
RAS-RASSF selectivity

63. Shao, H., Kadono-Okuda, K., Finlin, B. S., and Andres, D. A. (1999) Biochemical characterization of the Ras-related GTPases Rit and Rin. *Arch. Biochem. Biophys.* **371**, 207–219
64. Shi, G.-X., and Andres, D. A. (2005) Rit contributes to nerve growth factor-induced neuronal differentiation via activation of B-Raf-extracellular signal-regulated kinase and p38 mitogen-activated protein kinase cascades. *Mol. Cell. Biol.* **25**, 830–846
65. Chavan, T. S., Muratcioglu, S., Marszalek, R., Jang, H., Keskin, O., Gursoy, A., Nussinov, R., and Gaponenko, V. (2015) Plasma membrane regulates Ras signaling networks. *Cell Logist.* **5**, e1136374
66. Mazhab-Jafari, M. T., Marshall, C. B., Smith, M. J., Gasmi-Seabrook, G. M., Stathopoulos, P. B., Inagaki, F., Kay, L. E., Neel, B. G., and Ikura, M. (2015) Oncogenic and nanodomain-associated K-RAS mutations relieve membrane-dependent occlusion of the effector-binding site. *Proc. Natl. Acad. Sci. U. S. A.* **112**, 6625–6630
67. Abankwa, D., Gofe, A. A., and Hancock, J. F. (2007) Ras nanoclusters: Molecular structure and assembly. *Semin. Cell Dev. Biol.* **18**, 599–607
68. Abankwa, D., Gofe, A. A., Inder, K., and Hancock, J. F. (2010) Ras membrane orientation and nanodomain localization generate isoform diversity. *Proc. Natl. Acad. Sci. U. S. A.* **107**, 1130–1135
69. Cirstea, I. C., Kutsche, K., Dvorsky, R., Gremer, L., Carta, C., Horn, D., Roberts, A. E., Lepri, F., Merbitz-Zahradnik, T., Konig, R., Kratz, C. P., Pantaleoni, F., Dentici, M. L., Joshi, V. A., Kucherlapati, R. S., et al. (2010) A restricted spectrum of NRAS mutations causes Noonan syndrome. *Nat. Genet.* **42**, 27–29
70. Zhou, Y., and Hancock, J. F. (2018) Deciphering lipid codes: K-Ras as a paradigm. *Traffic* **19**, 157–165
71. Kapoor, S., Triola, G., Vetter, I. R., Erklamp, M., Waldmann, H., and Winter, R. (2012) Revealing conformational substates of lipidated N-Ras protein by pressure modulation. *Proc. Natl. Acad. Sci. U. S. A.* **109**, 460–465
72. Vogel, A., Nikolaus, J., Weise, K., Triola, G., Waldmann, H., Winter, R., Herrmann, A., and Huster, D. (2014) Interaction of the human N-Ras protein with lipid raft model membranes of varying degrees of complexity. *Biol. Chem.* **395**, 779–789
73. Sperlich, B., Kapoor, S., Waldmann, H., Winter, R., and Weise, K. (2016) Regulation of K-Ras4B membrane binding by calmodulin. *Biophys. J.* **111**, 113–122
74. Erwin, N., Patra, S., Dwivedi, M., Weise, K., and Winter, R. (2017) Influence of isoform-specific Ras lipidation motifs on protein partitioning and dynamics in model membrane systems of various complexity. *Biol. Chem.* **398**, 547–563
75. Nouri, K., Fansa, E. K., Amin, E., Dvorsky, R., Gremer, L., Willbold, D., Schmitt, L., Timson, D. J., and Ahmadian, M. R. (2016) IQGAP1 interaction with RHO family proteins revisited kinetic and equilibrium evidence for multiple distinct binding sites. *J. Biol. Chem.* **291**, 26364–26376
76. Yoon, S. Y., Tefferi, A., and Li, C. Y. (2000) Cellular distribution of platelet-derived growth factor, transforming growth factor-beta, basic fibroblast growth factor, and their receptors in normal bone marrow. *Acta Haematol.* **104**, 151–157
77. Nussinov, R., Tsai, C. J., and Jang, H. (2018) Is nanoclustering essential for all oncogenic KRas pathways? Can it explain why wild-type KRas can inhibit its oncogenic variant? *Semin. Cancer Biol.* **54**, 114–120
78. Nussinov, R., Tsai, C.-J., and Jang, H. (2020) Ras assemblies and signaling at the membrane. *Curr. Opin. Struct. Biol.* **62**, 140–148
79. Thurman, R., Siraliev-Perez, E., and Campbell, S. L. (2020) RAS ubiquitylation modulates effector interactions. *Small GTPases* **11**, 180–185
80. Barceló, C., Paco, N., Morell, M., Alvarez-Moya, B., Bota-Rabasedas, N., Jaumot, M., Vilardell, F., Capella, G., and Agell, N. (2014) Phosphorylation at Ser-181 of oncogenic KRAS is required for tumor growth. *Cancer Res.* **74**, 1190–1199
81. Thapar, R., Williams, J. G., and Campbell, S. L. (2004) NMR characterization of full-length farnesylated and non-farnesylated H-Ras and its implications for Raf activation. *J. Mol. Biol.* **343**, 1391–1408
82. Li, Z.-L., Prakash, P., and Buck, M. (2018) A “tug of war” maintains a dynamic protein–membrane complex: Molecular dynamics simulations of C-Raf RBD-CRD bound to K-Ras4B at an anionic membrane. *ACS Cent. Sci.* **4**, 298–305
83. Li, S., Jang, H., Zhang, J., and Nussinov, R. (2018) Raf-1 cysteine-rich domain increases the affinity of K-Ras/Raf at the membrane, promoting MAPK signaling. *Structure* **26**, 513–525.e512
84. Hu, C.-D., Kariya, K.-i., Tamada, M., Akasaka, K., Shirouzu, M., Yokoyama, S., and Kataoka, T. (1995) Cysteine-rich region of Raf-1 interacts with activator domain of post-translationally modified Ha-Ras. *J. Biol. Chem.* **270**, 30274–30277
85. Williams, J. G., Drugan, J. K., Yi, G.-S., Clark, G. J., Der, C. J., and Campbell, S. L. (2000) Elucidation of binding determinants and functional consequences of Ras/Raf-cysteine-rich domain interactions. *J. Biol. Chem.* **275**, 22172–22179
86. Ke, H., Matsumoto, S., Murashima, Y., Taniguchi-Tamura, H., Miyamoto, R., Yoshikawa, Y., Tsuda, C., Kumasaka, T., Mizohata, E., and Edamatsu, H. (2017) Structural basis for intramolecular interaction of post-translationally modified H-Ras• GTP prepared by protein ligation. *FEBS Lett.* **591**, 2470–2481
87. Bunda, S., Heir, P., Srikumar, T., Cook, J. D., Burrell, K., Kano, Y., Lee, J. E., Zadeh, G., Raught, B., and Ohh, M. (2014) Src promotes GTPase activity of Ras via tyrosine 32 phosphorylation. *Proc. Natl. Acad. Sci. U. S. A.* **111**, E3785–E3794
88. Kano, Y., Gebregiorgis, T., Marshall, C. B., Radulovich, N., Poon, B. P., St-Germain, J., Cook, J. D., Valencia-Sama, I., Grant, B. M., and Herrera, S. G. (2019) Tyrosyl phosphorylation of KRAS stalls GTPase cycle via alteration of switch I and II conformation. *Nat. Commun.* **10**, 1–14
89. Shima, F., Okada, T., Kido, M., Sen, H., Tanaka, Y., Tamada, M., Hu, C.-D., Yamawaki-Kataoka, Y., Kariya, K.-i., and Kataoka, T. (2000) Association of yeast adenylyl cyclase with cyclase-associated protein CAP forms a second Ras-binding site which mediates its Ras-dependent activation. *Mol. Cell. Biol.* **20**, 26–33
90. Kelley, G. G., Reks, S. E., Ondrako, J. M., and Smrcka, A. V. (2001) Phospholipase Cε: A novel Ras effector. *EMBO J.* **20**, 743–754
91. Travers, T., López, C. A., Van, Q. N., Neale, C., Tonelli, M., Stephen, A. G., and Gnanakaran, S. (2018) Molecular recognition of RAS/RAF complex at the membrane: Role of RAF cysteine-rich domain. *Sci. Rep.* **8**, 1–15
92. Lakshman, B., Messing, S., Schmid, E. M., Clogston, J. D., Gillette, W. K., Esposito, D., Kessing, B., Fletcher, D. A., Nissley, D. V., and McCormick, F. (2019) Quantitative biophysical analysis defines key components modulating recruitment of the GTPase KRAS to the plasma membrane. *J. Biol. Chem.* **294**, 2193–2207
93. Park, E., Rawson, S., Li, K., Kim, B.-W., Ficarro, S. B., Gonzalez-Del Pino, G., Sharif, H., Marto, J. A., Jeon, H., and Eck, M. J. (2019) Architecture of autoinhibited and active BRAF–MEK1–14-3-3 complexes. *Nature* **575**, 545–550
94. Jang, H., Zhang, M., and Nussinov, R. (2020) The quaternary assembly of KRas4B with Raf-1 at the membrane. *Comput. Struct. Biotechnol. J.* **18**, 737–748
95. Kholodenko, B. N., Hoek, J. B., and Westerhoff, H. V. (2000) Why cytoplasmic signalling proteins should be recruited to cell membranes. *Trends Cell Biol.* **10**, 173–178
96. Sukenik, S., Ren, P., and Gruebele, M. (2017) Weak protein–protein interactions in live cells are quantified by cell-volume modulation. *Proc. Natl. Acad. Sci. U. S. A.* **114**, 6776–6781
97. Case, L. B., Ditlev, J. A., and Rosen, M. K. (2019) Regulation of transmembrane signaling by phase separation. *Annu. Rev. Biophys.* **48**, 465–494
98. Bratek-Skicky, A., Pancsa, R., Meszaros, B., Van Lindt, J., and Tompa, P. (2020) A guide to regulation of the formation of biomolecular condensates. *FEBS J.* **287**, 1924–1935
99. Banani, S. F., Lee, H. O., Hyman, A. A., and Rosen, M. K. (2017) Biomolecular condensates: Organizers of cellular biochemistry. *Nat. Rev. Mol. Cell Biol.* **18**, 285–298
100. Kiel, C., Selzer, T., Shaul, Y., Schreiber, G., and Herrmann, C. (2004) Electrostatically optimized Ras-binding Ral guanine dissociation stimulator mutants increase the rate of association by

- stabilizing the encounter complex. *Proc. Natl. Acad. Sci. U. S. A.* **101**, 9223–9228
101. Kiel, C., Filchtinski, D., Spoerner, M., Schreiber, G., Kalbitzer, H. R., and Herrmann, C. (2009) Improved binding of Raf to Ras· GDP is correlated with biological activity. *J. Biol. Chem.* **284**, 31893–31902
102. Schreiber, G., Haran, G., and Zhou, H.-X. (2009) Fundamental aspects of protein– protein association kinetics. *Chem. Rev.* **109**, 839–860
103. Gremer, L., Merbitz-Zahradnik, T., Dvorsky, R., Cirstea, I. C., Kratz, C. P., Zenker, M., Wittinghofer, A., and Ahmadian, M. R. (2011) Germline KRAS mutations cause aberrant biochemical and physical properties leading to developmental disorders. *Hum. Mutat.* **32**, 33–43
104. Hall, T. A. (1999) BioEdit: A user-friendly biological sequence alignment editor and analysis program for Windows 95/98/NT. In *Nucleic Acids Symposium Series*, Information Retrieval Ltd, London: c1979–c2000
105. Cock, P. J., Antao, T., Chang, J. T., Chapman, B. A., Cox, C. J., Dalke, A., Friedberg, I., Hamelryck, T., Kauff, F., and Wilczynski, B. (2009) Biopython: Freely available Python tools for computational molecular biology and bioinformatics. *Bioinformatics* **25**, 1422–1423

Chapter 6

Functional Testing of Novel Mosaic RIT1 Mutations Identified in Patients with Arteriovenous Malformations Paves the Way for Targeted Therapy



Status: In preparation

Impact factor: N/A

Contribution: 25 %

Preparation of the patient specific constructs, cell culture and expression assay, western blotting, figure preparation and illustration, drafting of the manuscript and discussion.

Brief Definitive Report

Title:

Assessment of Somatic *RIT1* Indels Identified in Arteriovenous Malformations Enables Targeted Therapy

Running Title:

RIT1 mutations in AVM

Authors:

Friedrich G. Kapp¹ ^{*,#}, Farhad Bazgir² ^{*}, Nagi Mahammadzade¹ ^{*}, Annegret Holm^{1,3}, Axel Karow⁴, Caroline Seebauer⁵, Erik Vassella⁶, Walter A. Wohlgemuth⁷, Charlotte M. Niemeyer¹, Mohammad R Ahmadian², Yvonne Döhring^{8,9,10}, Martin Zenker¹¹, Whitney Eng¹², Iris Baumgartner^{7,8} ^{*}, Jochen Rössler^{1,13} ^{*,#}

¹ *Division of Pediatric Hematology and Oncology, Department of Pediatrics and Adolescent Medicine, Medical Center-University of Freiburg, Faculty of Medicine, University of Freiburg, 79106 Freiburg, Germany, VASCERN VASCA European Reference Centre*

² *Institute of Biochemistry and Molecular Biology II, Medical Faculty and University Hospital, Heinrich-Heine University, Düsseldorf, Germany*

³ *Vascular Biology Program, Department of Surgery, Boston Children's Hospital, Harvard Medical School, Boston, MA, United States.*

⁴ *Department of Pediatrics and Adolescent Medicine, Friedrich-Alexander-Universität Erlangen-Nürnberg (FAU), D-91054 Erlangen, Germany*

⁵ *Department of Otorhinolaryngology, Regensburg University Medical Center, Franz-Josef-Strauß-Allee 11, 93053 Regensburg, Germany.*

⁶ *Institute of Pathology, University of Bern, Bern, Switzerland*

⁷ *University Clinic and Policlinic of Radiology at the Martin-Luther-Universität Halle-Wittenberg, Halle, Germany*

⁸ *Division of Angiology, Swiss Cardiovascular Center, Inselspital, Bern University Hospital, Bern, Switzerland*

⁹ *Department for BioMedical Research (DBMR), University of Bern, Switzerland*

¹⁰ *Institute for Cardiovascular Prevention (IPEK), Ludwig-Maximilians University Munich, Pettenkoferstr 9, 80336, Munich, Germany.*

¹¹ *Institute of Human Genetics, University Hospital Magdeburg, 39120 Magdeburg, Germany*

¹² *Division of Hematology/Oncology, Boston Children's Hospital and Harvard Medical School, Boston, MA, USA*

¹³ *Division of Paediatric Hematology and Oncology, Department of Paediatrics, Inselspital, Bern University Hospital, University of Bern, Switzerland*

* These authors contributed equally to this work

*Corresponding authors Email: friedrich.kapp@uniklinik-freiburg.de;
jochen.roessler@insel.ch*

Summary:

We identified novel mosaic *RIT1* indels in three patients with peripheral arteriovenous malformations. We performed functional testing *in vitro* and *in vivo* that shows activation of the RAS pathway and aberrant vascular development, respectively. We also present clinical data on targeted treatment in one patient.

Keywords & Subject Areas

Vascular anomalies

Vascular malformations

Arteriovenous malformations

RIT1

Targeted treatment

Zebrafish

Counts:

Title: 100 characters (Limit 100 characters including spaces)

Summary: 44 words (aim: ~40 words)

Abstract: 156 / 160 words

Main text: XX characters (20,000 characters (not including spaces, figure legends, methods, or references))

Number of Tables and Figures: 4 figures

Number of online only files: 2 Supplemental Figures, 2 Supplemental Videos,

References: XX

Abstract

Peripheral arteriovenous malformations (AVMs) are benign vascular malformations prone to complications such as pain, bleeding and progressive growth. Treatment is often difficult and relapse after therapy is common. AVMs are caused by somatic mutations in the RAS/RAF/MEK/ERK pathway; however, a respective mutation cannot be identified in all patients. Using NGS sequencing of AVM tissue, we identified three novel *RIT1* indel mutations, a gene of the RAS pathway. After expression in HEK293T cells, we observed a strong increase of ERK1/2 activation, which was suppressed by MEK inhibition. After mosaic endothelial-specific overexpression all three *RIT1* indels led to formation of AVMs in zebrafish embryos and did so at a significantly higher rate than expression of *RIT1* wildtype (66-75% vs 24%). Targeted treatment with the MEK inhibitor trametinib led to a significant decrease in bleeding episodes and size of the AVM in patient P1. Our findings expand the genetic spectrum of AVMs and pave the way for clinical trials evaluating targeted treatment in AVM patients.

Introduction

Vascular anomalies are classified according to the Classification of the International Society for the Study of Vascular Anomalies (ISSVA) and are grouped into vascular tumors and vascular malformations (REF). While vascular tumors show increased proliferation, vascular malformations represent non-proliferative lesions that are caused by errors in vascular development. However, when transplanted into mice, vascular malformations e.g. venous malformations (REF), and arteriovenous malformations (AVMs) almost always progress in size (REF), suggesting that these lesions may have some tumor-like characteristics. Most vascular malformations are caused by a somatic mutation in the affected tissue, that leads to an activation of the PIK3CA/AKT/mTOR pathway in venous and lymphatic malformations (REFs) and the RAS/RAF/MEK/ERK pathway in AVMs (REFs). This overactivation might be a target for drug therapy, with the mTOR inhibitor sirolimus now being a commonly used drug in venous and lymphatic malformations. Targeted therapies such as with the PIK3CA inhibitor alpelisib (REFs) or the MEK inhibitor trametinib (REFs) have been reported as successful in case reports and small case series, and are being evaluated in clinical studies.

Location of peripheral AVM is usually at the extremities in the soft tissue or rarely in bones. Clinically presentation can be swelling, pain, pulsations and bleeding. In some cases, the skin can be harmed due to steal phenomenon caused by the AVM. AVMs located in the face may lead to major symptoms and complications with disfigurement (REF – recent review on AVM). AVMs belong to the most aggressive and difficult to treat vascular anomalies, as they have an extremely high rate of progression (REF), which may lead to pain, necrosis, bleeding and heart failure. This progression has been classified by Schobinger into four stages, I to IV (REF Schobinger). Treatment is mainly interventional and surgical with embolization and resection, however, relapse after therapy is common (REF Boston). This makes the need for novel treatment strategies evident.

In this project we identified novel mosaic indel variants in *RIT1*, that were found in AVM tissue of three patients. This gene of the RAS/RAF/MEK/ERK pathway has so far not been implicated in the development of AVMs. We performed an *in vitro* and *in vivo* characterization of these variants and assessed their effect on ERK phosphorylation *in vitro* and on vascular development *in vivo*. We also present data on the off-label use of trametinib in one patient.

Results

Novel *RITI* indel variants could be identified in three patients with AVMs

Patient 1 (P1) was a 2 year-old girl with an AVM of the right face. A capillary malformation and an inconspicuous swelling of the right cheek was noticed at birth (Fig. 1A). A diagnosis of an infantile hemangioma was made at an external hospital and a therapy with propranolol was initiated at one month of age. The lesion did not respond to this therapy and a first episode of epistaxis occurred at 4 months of age. After an MRI of the head was performed, the patient was referred to a vascular anomaly center, where an AVM of the bones and the soft tissue was diagnosed (Fig. 1, A' and A''). At 6 months of age, a first catheter embolization with Onyx was performed, with two additional embolizations until the age of 22 months, the last intervention being combined with bleomycine electro-sclerotherapy. Unfortunately, the lesion did not respond to this therapy and the AVM progressed with intermittent life-threatening bleeding episodes (Fig. S1 and Fig. S2). Due to the progressive symptoms, the patient was then treated at another vascular anomaly center, where a more extensive Onyx embolization of the AVM was performed, a molar in the maxilla within the AVM that caused recurrent bleeding was removed, and a biopsy was taken for genetic analysis. These interventions slightly ameliorated the symptoms and the patient was referred to a third vascular anomaly center for evaluation of an off-label drug treatment, since interventional and surgical options were not available anymore. Due to the extent of the disease, resection of the maxilla was considered, however, due to infiltration of the AVM into the orbita, it was unlikely that this very invasive approach would be curative and we thus initiated treatment with thalidomide at the age of 2 years. Under this treatment – and after extensive embolization performed at the referring center – the severity of the bleeding episodes improved over the next weeks and months before worsening again after four months. In the biopsy, a *RITI* indel variant was identified

(c.=/246_248delinsCCCTCT p.=/T83delinsPL (referred to as *RITI*^{P1}, hereafter), with a variant allele frequency (VAF) of 3.3%.

Patient 2 (P2) was a 42-year-old man with a first episode of neck pain at the age of 35 years followed by a continuously growing and pulsating lesion. MRI angiography showed an AVM connected to the subclavian and the thyrocervical trunk on the right side with soft tissue involvement including the splenius capitis muscle (Fig. 1, B and B'). A medical therapy with sirolimus was introduced but stopped again after a few weeks due to limited effect. At the age of 39 years, he received three direct intraarterial embolizations with alcohol in monthly intervals without success. One year later, a debulking surgery was performed, histology showed typical findings of an AVM. Ten months later, progression was again noted and finally a combined embolization with Onyx and a gross total resection was conducted. Since then, the patient is without complaints and has a stable minimal radiological residuum. In this resected tissue, a *RITI* indel variant was identified (c.=/242_248delinsTCCCTCT p.=/E81_T83delinsVPL (referred to as *RITI*^{P2}, hereafter) with a VAF of 6.0 %

P3 (USA)

P3 was a 17 year-old girl, who presented with a persistent prominence in the left forearm noted the year prior (Fig. 1C). At the time of initial presentation, there was no associated pain, no functional deficit, no overlying skin changes and only minimal swelling. An initial ultrasound was notable for a 5.4 cm x 1.1 cm x 4.7 cm intramuscular mass in the left forearm with diffuse internal vascularity seen on Doppler examination. An MRI of the lesion was obtained which was notable for a solid enhancing mass in the left pronator teres muscle with imaging findings consistent of a solid neoplasm (Fig. 1C'). She underwent IR-guided biopsy of the lesion.

8

Histopathology was consistent with intramuscular fast-flow vascular anomaly. She was followed for the next two years and had progressive swelling of the lesion associated with pain. Given the worsening of her symptoms, she underwent resection of the lesion. There were no complications and she has had minimal pain since. In the resected tissue, a *RIT1* indel variant was identified (c./229delinsTTGGATACAA p./A77delinsLDTT (referred to as *RIT1*^{P3}, hereafter) with a variant allele frequency of 13%.

***RIT1* indels lead to ERK hyperactivation in HEK293T cells**

All three novel *RIT1* indels were localized in or close to the GTP binding domain of the Switch 2 region (Fig. 1, D and E). To assess whether these mutations would lead to an activation of the RAS-MAPK pathway, we assessed ERK phosphorylation by western blotting after expression of *RIT1* in HEK293T cell. We expressed *RIT1*^{P1}, *RIT1*^{P2}, and *RIT1*^{P3}, *RIT1* wildtype (*RIT1*^{wt}) as well as two *RIT1* mutations found in Noonan syndrome (p.F82L and p.M90I). All three novel *RIT1* indels led to a significant increase in ERK phosphorylation, while expression of *RIT1*^{wt} and the two Noonan *RIT1* mutations only induced a minor ERK hyperphosphorylation (Fig. 2, A and B).

Hyperphosphorylation can be reversed by treatment by MEK but not SHP2 inhibition

Since *RIT1* is downstream of SHP2, but upstream of MEK and ERK in the RAS/RAF/MEK/ERK signaling pathway, we hypothesized that *RIT1*-induced ERK hyperphosphorylation would exhibit a differential response to treatment with SHP2 and MEK inhibition. Indeed, when we treated HEK293T cells with the SHP2 inhibitor SHP099, ERK

phosphorylation remained unchanged. In contrast, MEK inhibition with PD0325901 returned ERK phosphorylation to normal levels (Fig. 2, C and D)

***RIT1* indel variants lead to the formation of AVMs in the zebrafish model**

As we could show that the *RIT1* indels identified in AVM patients indeed resulted in an activation of the RAS pathway, we next assessed, whether this would lead to aberrant vascular development in the tail vasculature of zebrafish embryos. After endothelial-specific mosaic expression was achieved by injecting UAS:*RIT1* plasmids into *Tg(fli1a:Gal4, UAS:RFP)* embryos at the one-cell stage (Fig. 3A), we observed a significantly higher rate of AVMs in embryos expressing *RIT1*^{P1-P3} indels compared to *RIT1*^{wt} at 48 hpf (66-75% vs 24%, Fig. 3B). AVMs were characterized by aberrant connections between the dorsal aorta and the caudal vein, the most severe phenotypes exhibited a fusion of these two arterial and venous vessels (Fig. 3, C-G). In some embryos, the vessels downstream of the AVM were dilated, while the distal part of the tail vasculature was hypoplastic (Fig. 3, E and F, and Videos S1 and S2). Next, we treated injected embryos with 0.1 μ M trametinib during early development. This early treatment could indeed prevent the formation of AVMs (Fig. 3B), further indicating that AVM formation was dependent on overactivation of the RAS pathway.

Trametinib induced a reduction in AVM size and bleeding frequency in P1

As described above, P1 had a refractory disease and recurrent life-threatening bleeding. Due to this aggressive course of disease, treatment with thalidomide (REF) was started but was only transiently effective before symptoms worsened again (Fig. 4, A-C). Because of increasing disease severity, we began treatment with trametinib, which led to a significant clinical response

(Fig. 4D) and a decrease in bleeding episodes. Additionally, the size of the AVM was regressing as assessed by MRI (Fig. 4, E and F). Due to improved disease control, the patient was able to visit preschool for the first time in her life. Treatment tolerance was good without any significant adverse events related to trametinib and treatment could be continued. It was then noted, that the patient had a frontoethmoidal encephalocele, that could not be closed sufficiently with surgery at the age of XX years and a ventriculoperitoneal shunt was put in place when the patient was under trametinib therapy for XX months. This shunt needed to be replaced after XX months due to a parietal skin defect above the shunt line; considering the known cutaneous side effects of trametinib, this adverse event was considered as possibly related. Unfortunately, the patient later developed a pneumococcal meningitis with cerebral edema and herniation leading to death at the age of XX years. We attribute this fatal event to the underlying insufficiently closed frontoethmoidal encephalocele, and consider this fatal event as unrelated to the ongoing trametinib treatment.

Discussion

We describe three novel somatic activating *RIT1* indel mutations in patients with peripheral AVMs. All three mutations are located close to the Switch 2 domain of *RIT1*, a domain that also harbors *RIT1* germline mutations commonly associated with Noonan syndrome.

Interestingly, indel variants of RAS GTPases have been described in *KRAS* and *HRAS* – also in close proximity to their Switch 2 region – in vascular anomalies (REF by Ejikelenbloom et al.). Biochemically, the indel mutations led to an ERK hyperphosphorylation that was much more pronounced than in Noonan-associated *RIT1* mutations. Considering the location of *RIT1* in the RAS/RAF/MEK/ERK signaling pathway, treatment with a SHP2 inhibitor – as expected – did not influence ERK phosphorylation in cells transfected with the indel variants.

In contrast, MEK inhibition normalized ERK phosphorylation. These data suggest that *RIT1* indels activate the RAS pathway in a canonical manner.

To assess the novel mutations further functionally, we used our established approach of observing vascular development in the zebrafish after mosaic vascular expression of genes with variants of unknown significance (REF Bell). To this end, we used plasmids, which contain the transcriptional activating sequence UAS that controls the expression of *RIT1* (wt or mutated, without stop codon) linked to GFP with the self-cleaving peptide P2A. These plasmids were injected in the one-cell stage of *Tg(fli1a:Gal4; UAS:RFP)* embryos. While the plasmid integrated randomly in the DNA of cells of the zebrafish embryo, expression of *RIT1*-P2A-GFP was limited to endothelial cells that expressed Gal4 under the control of the endothelial *fli1a* promoter. Using this approach, we could mimic the mosaic endothelial expression that also occurs in patients. In previous work we have shown that the dichotomy of the genetics of vascular malformations – with activation of the PI3K/mTOR pathway leading to venous and lymphatic malformations and activation of the RAS pathway leading to arteriovenous malformations – can also be observed in the zebrafish. Endothelial-specific mosaic expression of *TEK* mutations induced venous malformations in zebrafish embryos, while *MAP2K1* mutations led to the development of AVMs (REF). In the current work, we observed that *RIT1* mutations induced AVMs in zebrafish embryos, further confirming the activation of the RAS signaling pathway caused by *RIT1* indels and their deleterious effect on vascular development. We could also show that treatment with the MEK inhibitor normalized the activation of the RAS pathway *in vitro* and allowed for normal vascular development, further confirming that AVM formation was due to an activated RAS signaling pathway.

These data paved the way for the off-label use of the cancer drug trametinib, a selective MEK inhibitor in our severely affected patient P1. It must however be considered that prevention of the formation of an AVM in zebrafish embryos likely has a different molecular and cellular

underpinning than the vascular remodeling and regression of the AVM in a patient with a fully developed AVM. Nonetheless, patient P1 responded very well with a significant reduction of AVM size and associated complaints, such as bleeding episodes. Unfortunately, the patient died due to an unrelated infectious complication (meningitis due to an encephalocele). While we consider this event as not related to trametinib treatment, it further highlights the need for controlled studies in the field of vascular anomalies, to assess treatment efficacy and tolerability and advance care for patients with these diseases into an era of evidence-based medicine.

In summary, our work highlights *RIT1* as a novel gene that is implicated in the development of AVMs. After functional *in vitro* and *in vivo* testing we could show the activation of the RAS pathway and its influence on development of AVMs, and present first promising data on the use of trametinib treatment in a patient with a somatic *RIT1* mutation.

Materials and methods

Patients

Ethical Approval and Informed Consent Forms

The patient from University Hospital of Bern, Switzerland has been identified from a prospective ongoing cohort of congenital extracranial/extraspinal vascular malformations that has been enrolling consecutive patients since 2008 (VASCOM cohort) (REF). As of October 2020, following the advances in the realm of theranostics and precision medicine for vascular malformations, genetic testing is performed on tissue available from diagnostic biopsies of vascular malformations, using the TruSight Oncology 500 (TSO500; Illumina) Next Generation Sequencing (NGS) gene panel. Patients (or their legal guardians) are required to submit a written general informed consent (IC) form for anonymized data collection and analysis and

genetic testing. An approval of the Ethics Committee of the Canton of Bern has been obtained (local ethics board number 2017--01960).

USA: IRB-P00025772

Regensburg: 17-854-101

Cell culture and Western Bot

Three million of HEK293T cells were seeded in 10 cm cell culture plates supplemented with DMEM containing 10% fetal bovine serum (FBS) 12 hours prior to transfection. At around 70% confluency levels cells were transfected using TurboFect transfection reagent (Thermo Fisher #R0532), with Flag-tagged RIT1 variants in pCDNA constructs or empty vector (EV) as negative control. The medium was refreshed the next day and at 48 hours' post-transfection, cells were washed in ice-cold phosphate-buffered saline (PBS) and lysed in ice-cold lysis buffer, containing 50 mM Tris/HCl pH 7.5, 5 mM MgCl₂, 100 mM NaCl, 1% Igepal CA-630, 10% glycerol, 20 mM β-glycerolphosphate, 1 mM Na-orthovanadate, EDTA-free inhibitor cocktail 1 tablet/50 ml. After addition of Laemmli sample buffer, the samples were subjected to SDS-PAGE (12.5% polyacrylamide). Blots were detected by immunoblotting using a mouse anti-γ-Tubulin antibody (Sigma #T5326), a mouse anti-FLAG antibody (Sigma #F3165), a rabbit anti-ERK antibody (Cell signaling technology #9102), and a rabbit anti-p-ERK antibody (Cell signaling technology #4370), respectively. The immunoblots were detected and analyzed using an Odyssey Fc Imaging System (LI-CORE Biosciences).

Zebrafish husbandry

Maintenance and breeding of zebrafish (*Danio rerio*) was performed in the fish facility of the Developmental Biology, Institute for Biology I, University Freiburg under standard conditions. Only embryos up to 5 days post-fertilization were used. All experiments were carried out in accordance with German laws for animal care and the Regierungspräsidium Freiburg.

Plasmid preparation

Plasmids were designed using ApE—A plasmid editor version 3.0.8. *Homo sapiens RIT1* sequence was obtained from the online database Ensembl (Transcript ID: ENST00000368323.8), minimally codon optimized for *D. rerio* and ordered as a plasmid including Tol2 sites, a UAS promoter, RIT1^{Bern}, and P2A-GFP from Twist Bioscience (South San Francisco, CA, USA). Plasmids were purified using Wizard Plus SC Minipreps DNA Purification Systems (Promega, Walldorf, Germany, A1330) according to the manufacturer's instructions.

Mutagenesis

RIT1^{wt} as well as all other *RIT1* mutations analyzed in this study were derived from the UAS:RIT1^{Bern}-P2A-GFP construct using Q5 Site-Directed Mutagenesis (New England Biolabs, E0554S). Corresponding mutagenesis primers were designed using NEBaseChanger version 1.3.3. All plasmids were sequenced to confirm the expected sequence.

Plasmid injection

The construct was then injected into *Tg(fli1a:Gal4FF^{ubs3}; UAS:RFP)* embryos at the one-cell stage together with Tol2 mRNA (21), both at a concentration of 30 ng/μl. For better readability, *Tg(fli1a:Gal4FF^{ubs3}; UAS:RFP)* embryos injected with a gene of interest (e.g. UAS:RIT1^{Bern}-P2A-GFP) are abbreviated as *Tg(fli1a:RIT1^{Bern})G0 mosaic* instead of *Tg(fli1a:Gal4FF^{ubs3}; UAS:RFP)* and *Tg(UAS:RIT1^{Bern}-P2A-GFP)G0 mosaic*.

Pharmacological treatments

For pharmacological treatments, injected zebrafish embryos were randomized into control and treatment groups. From the 10-somite stage on, embryos of the treatment group were transferred in E3 Medium (5 mM NaCl, 0.17 mM KCl, 0.33 mM CaCl₂, 0.33 mM MgSO₄) containing 0.2 mM 1-phenyl 2-thiourea (PTU; Sigma, Taufkirchen, Germany, P7629) and either mTOR inhibitor Sirolimus (Rapamycin; Selleckchem, S1039; 1 μ M) or MEK1/2 inhibitor Trametinib (Cayman Chemical, 16 292; 50 nM) using 100 \times stock solutions dissolved in dimethyl sulfoxide (DMSO; Sigma, D2650). Treatment doses of sirolimus and trametinib were chosen by assessing the highest tolerated dose that still allowed for normal embryonic development, defined as less than 20% of the embryos showing any maldevelopment (such as heart edema, yolk sac edema, curved body axis or death) at 5 dpf. The data from three independent experiments, each with $n = 15$ embryos (sirolimus) or $n = 16$ embryos (trametinib), are summarized in [Supplementary Material, Figure S5](#). These data were the rationale for choosing a concentration of 1 μ M of sirolimus and 50 nM of trametinib for the following experiments.

Embryos of the control group were raised in E3 medium with 0.2 mM PTU and 1 μ M or 50 nM DMSO (equal amounts to treatment group).

Acknowledgments

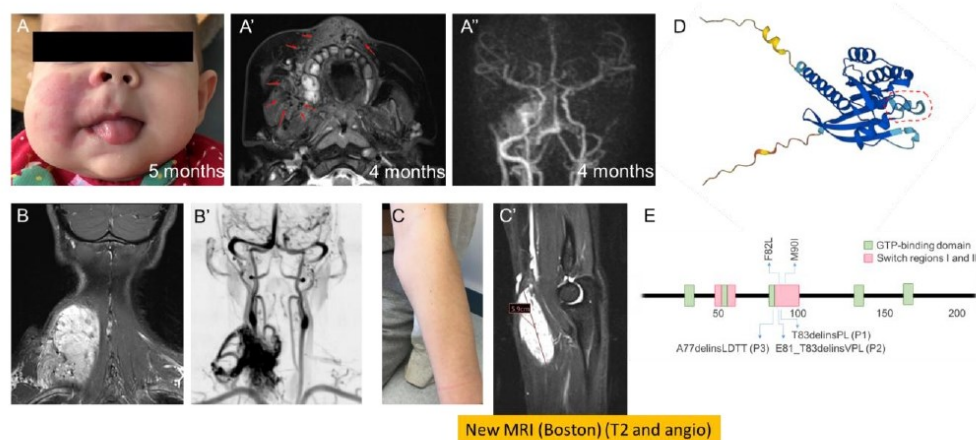
The authors acknowledge the contribution of the Center Vascular Anomalies at the Freiburg Center for Rare Diseases, and the Hilda Biobank at the Department of Pediatrics and Adolescent Medicine, Freiburg, Germany. Four of the authors of this publication are members of the Vascular Anomalies Working Group (VASCA WG) of the European Reference Network for Rare Multisystemic Vascular Diseases (VASCERN)—Project ID: 769036 .

Abbreviations:

AVM – arteriovenous malformation

MRI – magnetic resonance imaging

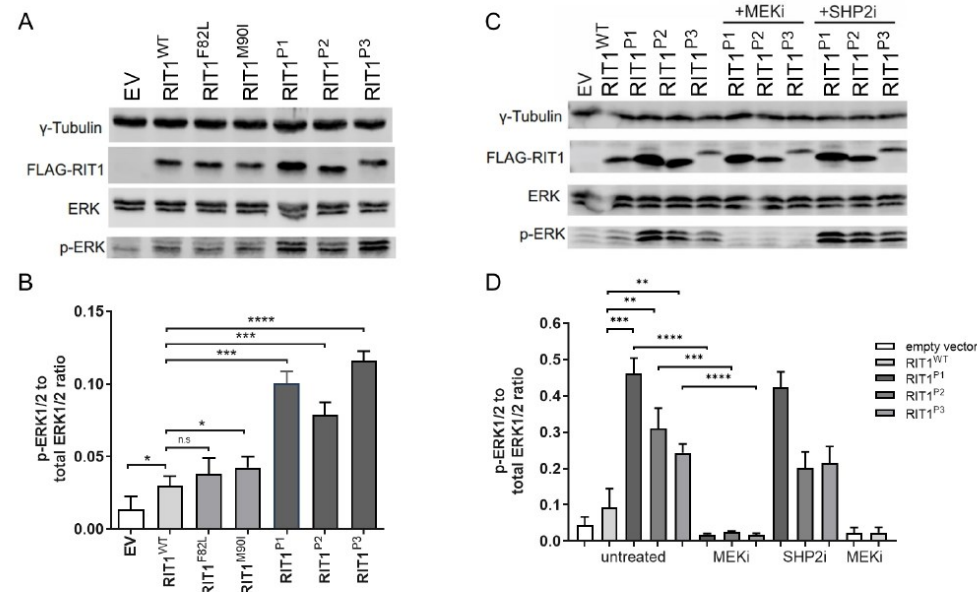
Figure 1



Three patients with somatic RIT1 variants identified in AVM tissue

(A) P1 was born with a capillary malformation and swelling of the right side of the face. (A') MRI of P1 at the age of 4 months, image of a transversal T2 TSE sequence, in which an AVM could be detected; the extent of the disease is labeled with red arrows indicating soft tissue edema and flow-voids. (A'') The MRI angiography shows an increased perfusion on the right side of the face. (B) MRI of P2, image of a coronal T2 sequence with fat saturation, which shows evident edema, flow-voids, and an intramuscular location. (B') Hyperperfusion of the lesion can be noted on MR angiography. (C) Clinical aspect of the swelling on the left forearm, close to the medial side of the elbow. (C') MRI shows typical aspects of an intramuscular fast flow anomaly with intramuscular location, edema and flow voids. (D) Predicted protein structure (predicted by AlphaFold (REFs), accessed through ensemble.org) of RIT1. The area labeled by the dashed red line indicated the switch 2 domain. (E) Schematic drawing of functional domains of human RIT1 protein (green boxes = GTP-binding regions; red boxes = switch regions I and II; blue arrows (upward) = two mutations typically found in Noonan syndrome; blue arrows (downward) = mutations identified in AVM patients.

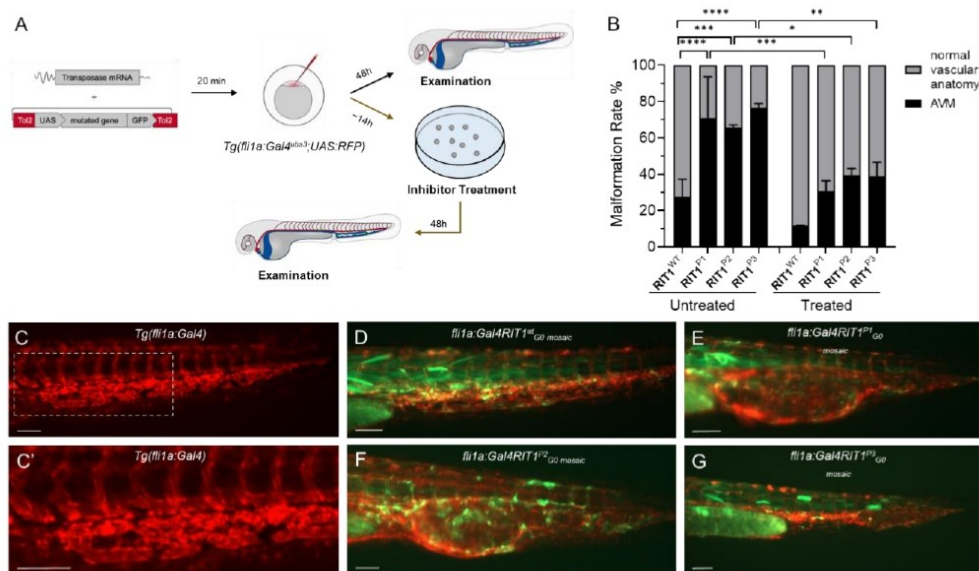
Figure 2



ERK phosphorylation after expression of RIT1 variants *in vitro* in HEK293T cells

(A) Western blot after expression of *RIT1* variants to assess activation of the RAS pathway. Gamma tubulin serves as loading control, FLAG-RIT1 confirms the expression of the construct, total ERK levels serve as a control to exclude differential expression of ERK, and p-ERK measures the level of phosphorylate of ERK as an marker of RAS pathway activation. (B) Quantification of the ERK phosphorylation measured in a total of three western blots. (C) Western blot after expression of *RIT1* variants and with or without treatment using a MEK inhibitor or SHP2 inhibitor. The same parameters were assessed as in panel (A). (D) Quantification of the ERK phosphorylation measured in a total of three western blots.

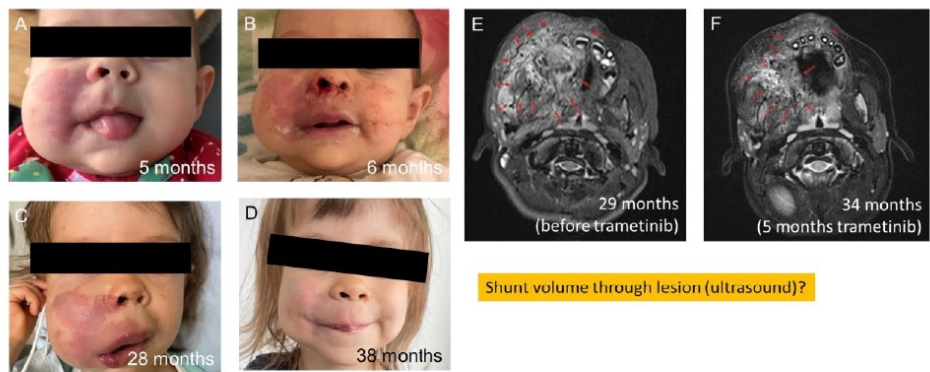
Figure 3



Mosaic endothelial-specific expression of *RIT1* variants leads to the formation of AVMs in zebrafish embryos.

(A) . (B) . (C) . (C') . (D) . (E) . (F) . (G) .

Figure 4



Response to targeted therapy in P1

(A) . (B) . (C) . (D) . (E) . (F).

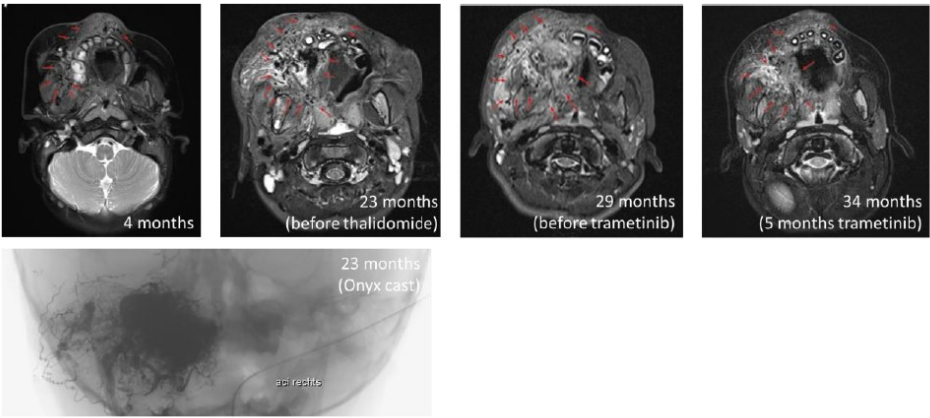
Supplementary data

Figure S1



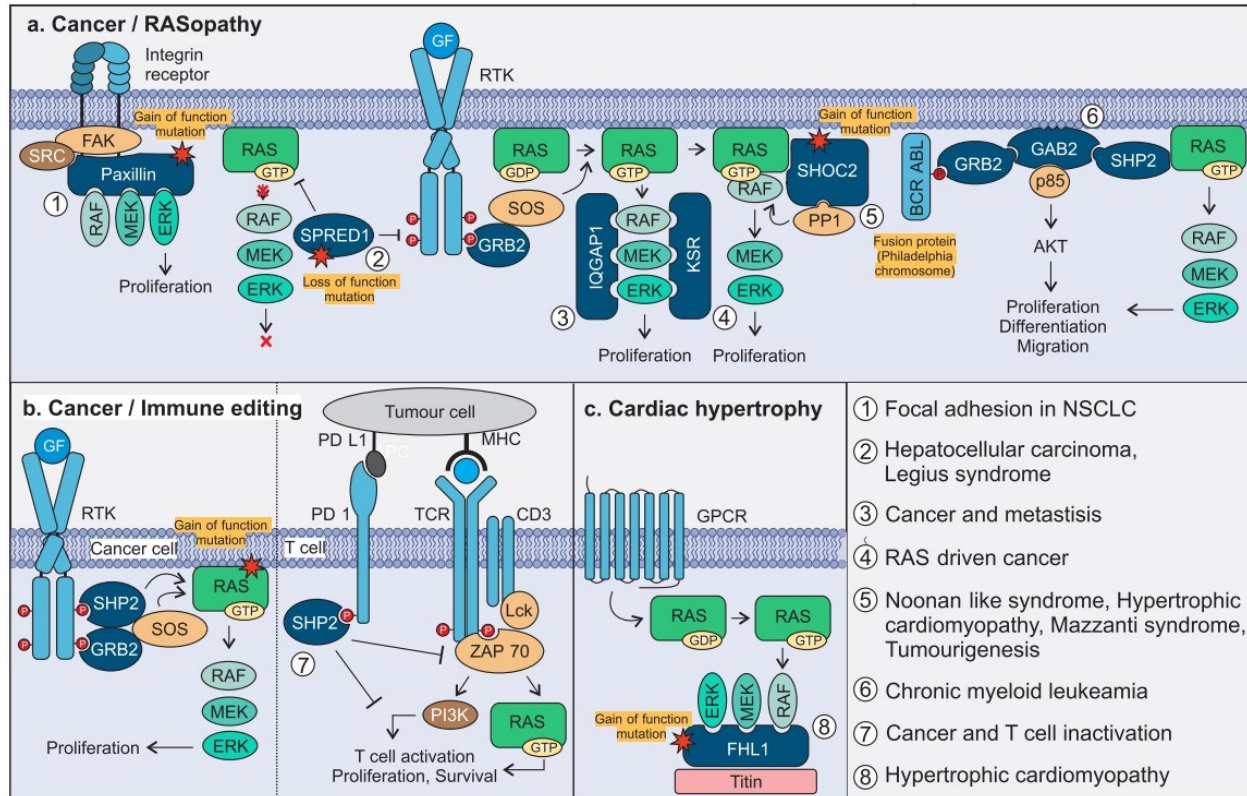
Patient P1 – Clinical Evolution of diseases

Figure S2



Patient P1 – Radiological Evolution of disease

Accessory proteins of the RAS-MAPK pathway: moving from the side line to the front line



Status: published in Nature-Communications Biology, 8th June 2021

Impact factor: 6.54

Contribution: 15 %

Writing and drafting of the manuscript, reference management and discussion.

Accessory proteins of the RAS-MAPK pathway: moving from the side line to the front line

Silke Pudewell¹, Christoph Wittich¹, Neda S. Kazemineh Jasemi¹, Farhad Bazgir¹ & Mohammad R. Ahmadian¹  

Health and disease are directly related to the RTK-RAS-MAPK signalling cascade. After more than three decades of intensive research, understanding its spatiotemporal features is afflicted with major conceptual shortcomings. Here we consider how the compilation of a vast array of accessory proteins may resolve some parts of the puzzles in this field, as they safeguard the strength, efficiency and specificity of signal transduction. Targeting such modulators, rather than the constituent components of the RTK-RAS-MAPK signalling cascade may attenuate rather than inhibit disease-relevant signalling pathways.

ature has evolved sophisticated, cell type-specific mechanisms to sense, amplify and integrate diverse external signals, and ultimately generate the appropriate cellular response. Signals are processed by evolutionarily conserved signalling cassettes that comprise specific constituent components acting as receptors, mediators, effectors and regulatory proteins. Activated receptor tyrosine kinases (RTKs), for instance, link the RAS activator SOS1 to RAS paralogs, e.g., the proto-oncogene KRAS4B, which in turn regulate various signalling pathways, including the mitogen-activated protein kinase (MAPK) pathway¹. This pathway contains a three-tiered kinase cascade comprising the serine/threonine kinases ARAF/BRAF/CRAF, the dual specificity kinase MEK1/2 and the serine/threonine kinases ERK1/2^{1,2}. The RTK-RAS-MAPK axis is a highly conserved, intracellular signalling pathway that has an essential role throughout mammalian development, from embryogenesis to tissue-specific cellular homeostasis in the adult³. Dysregulation of components or regulators of this cascade is frequently associated with tumour growth and a distinct subset of developmental disorders called the RAS-MAPK syndromes or RASopathies^{4–6}. This signalling cascade has rapidly taken centre stage in cancer and RASopathy therapies (see below).

However, the strength, efficiency, specificity and accuracy of signal transduction are controlled by mechanisms that increase the connectivity of the signalling molecules and thus increase their local concentration and reduce their dimensionality. This state can be achieved by liquid–liquid phase separation (LLPS), a mechanism in which two separate liquid phases with different protein compositions emerge from one mixed solution⁷. A large number of proteins, hereafter, collectively designated as the ‘accessory proteins’, fulfil the requirements to drive LLPS and have been reported to act as adaptor, anchoring, docking or scaffold proteins. Accessory proteins link constituent components of individual signal transduction pathways by forming physical complexes. What the functions of the accessory proteins are, why are they crucial for signal transduction, and whether they represent better therapeutic targets for different human diseases are questions that will be addressed in this article in the context of the RTK-RAS-MAPK signalling pathway.

Structural and functional variety of accessory proteins. Rapidly emerging reports on signalling networks support the idea that various signalling molecules operate together in functional protein complexes. For example, activated protein nanoclusters in specialised membrane

¹ Institute of Biochemistry and Molecular Biology II, Medical Faculty of the Heinrich-Heine University, Düsseldorf, Germany. [✉]email: reza.ahmadian@hhu.de

microdomains selectively connect with and subsequently activate cytosolic signalling components or complexes^{8,9}. RAS nanoclusters form and locally increase the concentration of RAS paralogs in membrane microdomains¹⁰.

Membrane-resident signalling proteins, such as transmembrane (TM) and membrane-associated proteins, are predominantly trafficked to the plasma membrane via the secretory pathways¹¹. But how are the cytosolic proteins trafficked to their cognate membrane nanoclusters? Mounting evidence has emerged recently that a large number of membraneless compartments (also called non-membrane-bound organelles or biomacromolecular condensates) are assembled via LLPS¹². The formation of cytosolic signalling condensates is based on two processes. First multivalent molecules undergo phase separation, whereas in a second step other proteins are able to diffuse into the phase without considerably contributing to the stability of the phase. This process can increase local concentrations of molecules by several folds. One example is the enrichment of kinases in membrane-associated liquid droplets around T-cell receptors while phosphatases are excluded¹³.

An essential group of proteins that are themselves not constituent components of signal transduction but allow assembly and spatiotemporal organisation of a signalling cascade are accessory proteins. These proteins have the features to interact with and assemble other biomolecules, ranging from lipids, over proteins to nucleic acids. They mostly lack enzymatic activity but are equipped with different types of protein–protein interaction domains, motifs and intrinsically disordered regions (IDRs). Thus, accessory proteins dictate the local formation of macromolecular protein complexes through modular multivalent interactions, and thereby organise and facilitate signal transduction.

Accessory proteins bind and connect at least two constituent components to orchestrate their spatiotemporal localisation and enhance their assembly by reducing the dimensionality of interactions and/or increasing local concentrations of interacting proteins^{14–16}. They can be categorised in four distinct groups based on their structure and mode of action: (1) scaffold proteins are cytosolic multidomain proteins that bind two or more distinct components to organise them in a functional unit and modulate their function. (2) Adaptor proteins link two partners usually via SH2 and/or SH3 domains and may also regulate their specific downstream signalling pathways. (3) Anchoring proteins bind to the membrane and other proteins, which are usually protein kinases, and therefore, bring them to their site of action. (4) Docking proteins assemble signalling complexes by binding to effectors and RTKs or G-proteins at the membrane.

Accessory proteins of the RTK-RAS-MAPK pathway. New discoveries and concepts regarding the receptor-driven RAS-MAPK signal transduction have emerged during the last three decades: novel pathway components, structure elucidation, biophysical principles, biomimetic strategies and clinical drug candidates. By focusing particularly on the signalling process itself, the emphasis of this article is on the implementation of the accessory proteins, which bind molecular components and orchestrate their assembly and eventually activity in a context-dependent manner. We believe that the spatial arrangements of such biophysical features over time determine specificity, efficiency, fidelity of signal transduction and safeguard against any deleterious effects.

A multitude of accessory proteins, which largely vary in size and domain architecture (Fig. 1), are involved in orchestrating RTK-RAS-MAPK signal transduction. The high variability of scaffold proteins is—due to their high interaction specificity—comprehensible. Certain domains or repeats frequently exist in

individual proteins, for example, LDs (repeated leucine-rich sequence) in Paxillin, WDs (WD-repeat) in MORG1, RRM (RNA recognition motif) in nucleolin and LIMs in FHL1/2. Furthermore, IDRs are found in several proteins, which may fold upon interaction with their binding partner. IDRs are also involved in oligomerization for example in galectin-3¹⁷. Anchoring proteins contain membrane-binding domains, such as the PH domain in CNK1 and GAB1/2, and TM segment, e.g., in LAT, NTAL and SEF1. PAQR10/11 contain 7 TM segments and anchor RAS to the Golgi apparatus via their N-terminal cytoplasmic tail¹⁸. The PHB domain of FLOT1 has been reported to be a membrane association domain as it is post-translationally modified by palmitoylation¹⁹. This leads to FLOT1 association with lipid rafts of phagosomes and the plasma membrane. Docking proteins frequently possess both PH domains, which increase their residence time at the membrane, and PTB domains, which enable them to interact specifically with activated RTKs. Adaptor proteins are specialised in linking activated RTKs via SH2 domains with their downstream signalling molecules, in most cases, via SH3 domains.

Linking TM receptors to RAS. GRB2 links activated RTKs or anchoring proteins, such as LAT, with SOS1/2 to activate RAS paralogs (Fig. 2a)²⁰. The adaptor protein function of GRB2 is accomplished by a central SH2 domain that binds to the tyrosine-phosphorylated RTK and two flanking SH3 domains, which bind to the C-terminal proline-rich domain of SOS1 and translocate it to the plasma membrane^{21,22}. Activated SOS1, in turn, stimulates, as a RASGEF, the GDP/GTP exchange of RAS paralogs and thereby activates amongst others the MAPK cascade²³.

Furthermore, direct GRB2 association with activated RTKs leads to the recruitment of GAB1 and CBL. GAB1 provides a docking platform for several signalling molecules, e.g., SHP2, PLC γ and PI3K, thereby cross-linking different signalling pathways²⁴. CBL was originally described to act as an adaptor protein as it contains several domains and motifs for protein–protein interactions (Fig. 1). Later, it was identified as a RING-dependent E3-ubiquitin-protein-ligase that transfers the ubiquitin to RTKs for endocytic internalisation, and recycling or degradation²⁵. It also regulates signalling processes of the non-RTKs SYK, ZAP70 and SRC²⁶. CBL constitutively interacts with GRB2, mediating hematopoietic cell proliferation²⁷, and T-cell and B-cell receptor and cytokine receptor signalling via interaction with CRKL SH2 domain²⁸. As CBL and SOS1 bind to the same region of GRB2, the overexpression of CBL inhibits complex formation between SOS1 and GRB2 underlining the fine-tuning mechanism of accessory proteins by binding other pathway modulators²⁹.

Engagement of GRB2 is versatile and leads to different outcomes depending on the cellular context. GRB2 can bind indirectly to RTKs via interaction with the tyrosine-phosphorylated adaptor proteins SHC and FRS2. SHC links activated TRKA receptors to GRB2 in PC12nnr5 cells^{21,22,30}, which can recruit SOS to the PM and control the extent of RAS activation²³. Upon activation of the B-cell antigen receptor (BCR) in B-lymphocytes, the tyrosine kinase SYK phosphorylates SHC which leads to translocation of GRB2-SOS1 and activation of membrane-associated RAS signalling³¹. The SHC–GRB2 complex, downstream of cytokine receptors, also activates the PI3K pathway to control cell survival and/or proliferation³². A similar mechanism of GRB2-SOS-RAS activation is operated via FRS2, which acts downstream of TRKA in neurons²¹, and FGFR in embryonic stem cells^{33,34}. FRS2 has multiple tyrosine phosphorylation sites to activate, in response to a wide range of agonists, PI3K and RAS-MAPK pathways in various cell types via binding

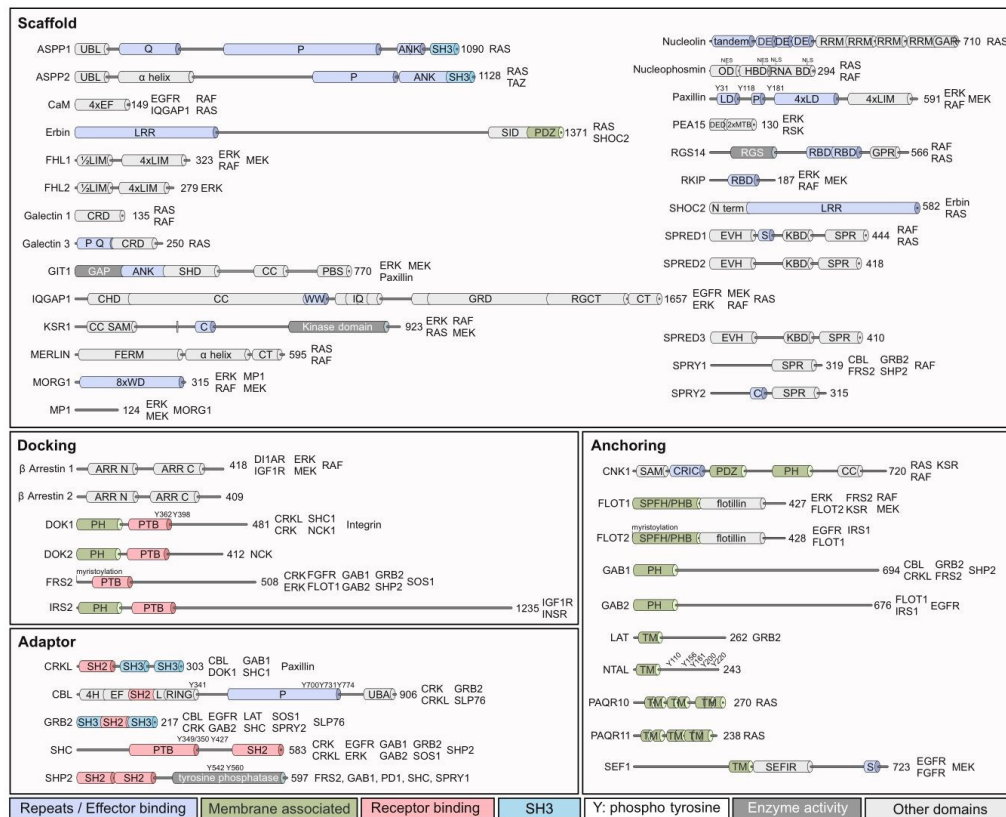


Fig. 1 Domain organisation and crucial interactions of RTK-RAS-MAPK accessory proteins. Schematic representation of relevant domains in scaffold, docking, adaptor and anchoring proteins. Direct binding partners, which are part of the RTK-RAS-MAPK pathway, are mentioned next to the amino-acid numbers at the right side of the proteins. Please check the list of abbreviations in the supplemental table for more details. Abbreviations are summarised in Supplementary Table 1.

to GRB2 and SHP2, respectively^{35–39}. The binding of the ubiquitous protein tyrosine phosphatase SHP2 to GRB2, induces recruitment by the FRS2-SHP2 complex, which controls retinal precursor proliferation and lens development⁴⁰.

Modulating the RAS cycle. The RAS cycle between an inactive, GDP-bound state and an active, GTP-bound state is strictly controlled by multidomain regulatory proteins^{41–44}. Unlike the well-understood cellular process of RAS activation by RASGEFs, such as SOS1 little is known about the recruitment and activation of RASGAPs. The first evidence has emerged that the RASGAPs neurofibromin and p120 are recruited to the plasma membrane and RAS•GTP by two distinct scaffold proteins, SPRED1 and merlin (Fig. 2b). The EVH domain of SPRED1, a member of the sprouty family, binds the GAP domain of neurofibromin without interfering with its GAP function^{45,46}. SPRED1 appears to directly contact BRAF and thus to interfere with KRAS signalling⁴⁷. Merlin, a member of the ERM family, directly binds to, on the one hand, p120 and RAS (probably KRAS4B), a mechanism that potentiates RAS inactivation in Schwann cells, and on the other hand, CRAF and blocks its interaction with RAS^{48,49}. p120 modulates many regulators and signalling

proteins via its N-terminal protein interaction domains, apparently independent of its GAP function^{50,51}.

RAS-RAF connection. Lipidation and clustering of the RAS paralogs are critical steps for a tight control of signal transduction through the MAPK pathway. This process connects two distinct macromolecular clusters, plasma membrane-associated RAS-containing clusters⁹ and cytosolic RAF/MEK/ERK-containing clusters⁵².

The scaffold proteins galectin 1 and 3 are carbohydrate-binding proteins that are involved in many physiological functions. While galectin 1 homodimer binds to HRAS-RAF complex and stabilises HRAS•GTP at the plasma membrane^{10,53}, galectin 3 selectively binds and clusters KRAS4B•GTP (Fig. 2c)⁵⁴. The nucleolar phosphoproteins nucleophosmin and nucleolin shuttle between nucleus and PM and are different types of RAS scaffold proteins, which have been reported to stabilise KRAS4B levels in a nucleotide-independent manner at the plasma membrane. Nucleophosmin also increases the KRAS4B•GTP clusters and enhances MAPK signal transduction⁵⁵.

Another type of clustering is performed by the scaffold protein SHOC2 (also known as SUR8), which connects activated RAS with the RAF kinases (Fig. 2d). SHOC2 is an integral element of a heterotrimeric holoenzyme complex with PP1 and MRAS, which

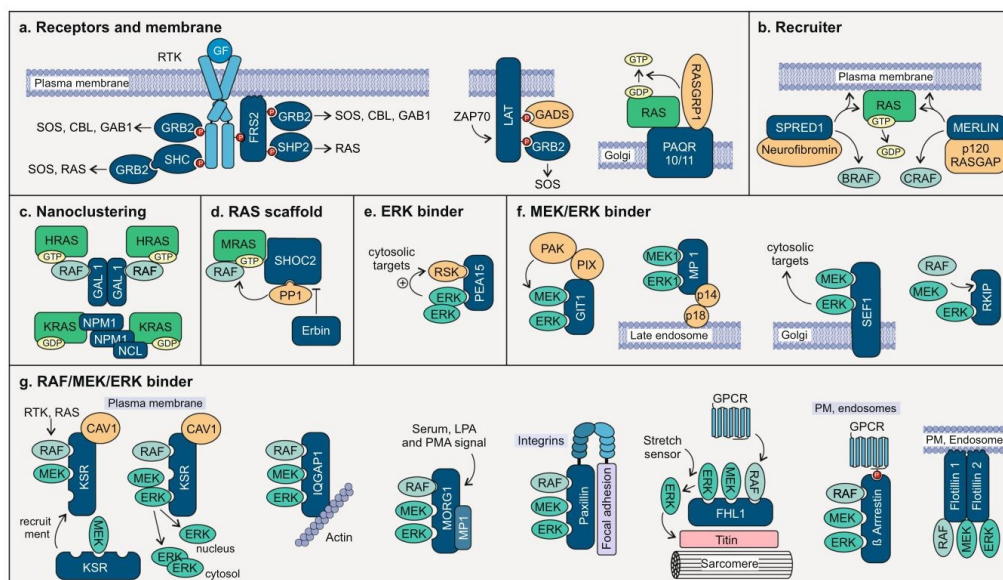


Fig. 2 Involvement of RTK-RAS-MAPK accessory proteins in signal transduction. Accessory proteins are involved in every step of the RTK-RAS-MAPK pathway and increase the connectivity between signalling components. Adaptor proteins and docking proteins interact with phosphorylated receptors, in contrast to anchoring proteins, which are directly associated with the membrane (a). Recruiter translocate binding partner towards the site of action, e.g., a GTPase activating protein to activated RAS at the plasma membrane (b). Scaffold proteins that induce nanoclustering, increase the local concentration of their binding partner in lipid rafts (c). RAS scaffold proteins bind RAS and other components of the RTK-RAS-MAPK pathway (d), whereas ERK binder (e), MEK/ERK binder (f) and RAF/MEK/ERK binder (g) can connect one, two, or all three members of the MAPKs, bringing them close together, regulate their activity and determine their localisation. See text for more details.

dephosphorylates and releases RAF from its inhibited state^{56,57}, and subsequently activates the MAPK pathway⁵⁸. The scaffold protein Erbin interferes with this process⁵⁹. It binds and sequesters SHOC2 from its RAS/RAF complex, and inhibits ERK activation⁶⁰. Erbin is a large scaffold protein (Fig. 1). As such, it links different pathways by binding, besides SHOC2, also various other accessory proteins, including GRB2⁶¹, CBL⁶², Merlin⁶³ and KSR1^{2,64}.

RAF/MEK/ERK cascade. RAF kinase translocation to the plasma membrane and activation by direct interaction with RAS•GTP is well described^{2,65–67}. Activated BRAF/CRAF heterodimer phosphorylates MEK1/2, which in turn phosphorylates ERK1/2 at the TEY motif in the activation loop^{68,69}. Activated ERK1/2 are ultimately recruited to their substrates in various subcellular compartments^{70,71}. The assembly of macromolecular complexes of the MAPK components and their connection with RAS nanoclusters at the membrane, which constitutes the RAS-ERK axis, is arranged by homo- and heterodimerization of the members of this pathway⁶⁸. To achieve signal diversity, specificity and fine-tuning, the spatiotemporal flux through the pathway is organised by various distinct accessory proteins, which bind either ERK, MEK/ERK, or RAF/MEK/ERK^{1,70,72}.

PEA15 modulates ERK activity towards its cytosolic substrates, including RSK2. It enhances ERK-dependent phosphorylation of RSK2 by binding both of them independently (Fig. 2e)⁷³. PEA15 phosphorylation by PKC, AKT, or CaMKII inhibits this process. In addition, PEA15 steers subcellular localisation of ERK by facilitating its nucleocytoplasmic export⁷⁴.

The MEK/ERK accessory proteins are illustrated in Fig. 2f. GIT1 binds MEK1 and ERK1 in response to integrin, RTK and GPCR activation. Its activity is directly regulated by different downstream effectors, such as PIX/PAK complex⁷⁵. MP1 binds and translocates MEK1 and ERK1 to late endosomes by associating with p14 and p18^{76,77}. The anchoring protein SEF binds activated MEK on the Golgi apparatus, and subsequently binds ERK, leading to activation of ERK and finally its cytosolic substrates such as RSK2⁷⁸. The latter phosphorylates SEF and induces its translocation to the plasma membrane, where it directly inhibits FGFRs, and enhances EGFR signalling instead⁷⁹. RKIP acts as a competitive inhibitor of MEK phosphorylation. It binds ERK and mutually exclusively RAF or MEK, and thus, dissociates active RAF/MEK complexes⁸⁰. The phosphorylation of RKIP by PKC results in the release of RAF1 and enables the activation of the MAPK pathway⁸¹.

The scaffolding of RAF/MEK/ERK is dependent on several factors, including the tissue specificity, cellular localisation of the signalling complexes and the type of upstream signals (Fig. 2g). KSR1 is one of the best-studied scaffolds that binds to all three members of the RAF/MEK/ERK cascade⁷². KSR1 translocates, upon RTK-RAS activation, in a complex with MEK to CAV1-rich microdomains in the plasma membrane to bind activated RAF and modulate MEK and ERK activation. Feedback phosphorylation of KSR1 and BRAF by ERK promotes their dissociation and results in the release of KSR1/MEK from the plasma membrane⁸². In this way, MEK is sequestered from upstream signals and cannot itself regulate ERK activation.

The multidomain protein IQGAP1 scaffolds and activates the RAF/MEK/ERK kinases by directly associating with the EGF

receptor^{83,84}. With over 100 binding partners, the localisation and effect of IQGAP1 interaction reach from actin cytoskeleton reorganisation in the context of neurite outgrowth, migration or vascular barrier integrity to insulin secretion via exocytosis or cell proliferation and differentiation via ERK signalling. The extensive interactions of IQGAP1 vary according to cell types and environmental conditions⁸⁵. In contrast, MORG1, FHL1, paxillin and β -arrestin act EGF-independent (Fig. 2g). MORG1 exists in a complex with MP1 and facilitates ERK1/2 activation in response to LPA and PMA, and GPCR activation⁸⁶. The focal adhesion protein paxillin modulates the activation of the RAF/MEK/ERK complex through the binding of other proteins, controlling the remodelling of the actin cytoskeleton⁸⁷. FHL1 scaffolds RAF/MEK/ERK on the N2B domain of the giant protein titin at the sarcomere of the mammalian muscle cells⁸⁸. β -arrestin stimulates ERK signalling in response to activation of GPCR or other receptors on the plasma membrane but also on endosomes. FLOT1/2 are membrane raft-associated proteins that form heterodimers. They are not only involved in the EGF receptor clustering and activation, but also directly bind CRAF, MEK and ERK enhancing their activity upon stimulation⁸⁹. CNK1 physically interacts with RAF facilitating its activation by assisting RAF membrane localisation and oligomerization upon RAS activation⁹⁰, whereas being able to interact with RAS as well via the N-terminal regions⁹¹.

Accessory proteins as in human disease. Even if dysregulated constituent components of the RTK-RAS-MAPK pathway are among the most intensively studied target structures for disease treatment, new emphasis should be laid on accessory proteins (Fig. 3). Their loss-of-function or gain-of-function mutations are mostly and frequently associated with the initiation and progression of human diseases and disorders. The hyperactivation of the RTK-RAS-MAPK pathway is a known cause of many diseases, like cancer and developmental disorders, including RASopathies.

Cancer. The upregulation of activating proteins or the down-regulation of inhibiting proteins leads to gain-of-function of the RTK-RAS-MAPK pathway in almost all types of cancer (Fig. 3a). The expression of accessory proteins is tightly controlled and often dysregulated in tumours. Paxillin is a scaffold protein, which is involved in focal adhesion. A gain-of-function mutation in *Paxillin* has been found in 9% of all non-small cell lung cancers (NSCLC) (1)⁹². Furthermore, genomic amplification of *Paxillin* in lung cancer promotes tumour growth, invasion and migration⁹³. SPRED1/2, negative modulators of RAS signalling, are down-regulated in 84% of patients with hepatocellular carcinoma (2)⁹⁴. The scaffold protein IQGAP1 promotes tumour formation,

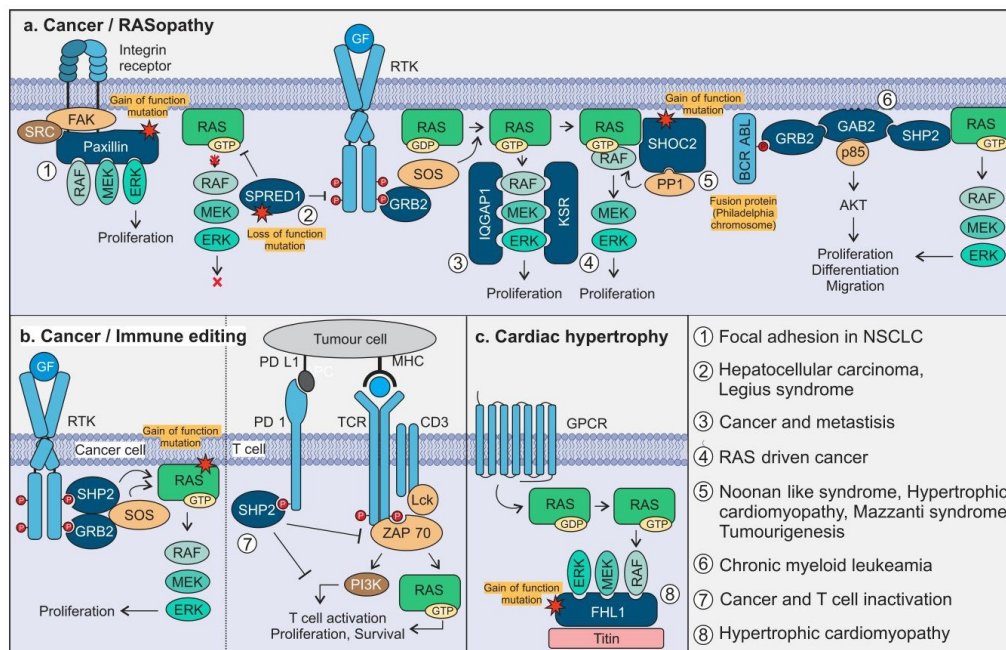


Fig. 3 Involvement of accessory proteins in diseases. The canonical RAS/MAPK pathway is tightly regulated by many proteins, attenuators and negative feedback mechanisms. Mutations in regulators like accessory proteins can lead to a dysregulated RAS/MAPK pathway and therefore to a variety of diseases as cancer and RASopathies (a). The genomic amplification of Paxillin is found in many NSCLC patients and activates the focal adhesion complex downstream of integrins (1). Loss-of-function mutations of SPRED1 activate the RAS-MAPK pathway and lead to Legius syndrome (germline) and hepatocellular carcinoma (somatic) (2). IQGAP1 mutations are often associated with tumour formation and metastasis (3), whereas KSR is a central player in KRAS-driven cancers, inducing proliferation and survival (4). Mild gain-of-function mutations of SHOC2 lead to Noonan-like syndrome with loose anagen hair or Mazzanti syndrome, other somatic mutations can lead to hypertrophic cardiomyopathy or tumorigenesis (5). The signalling of BCR-ABL-positive cells in chronic myeloid leukaemia is also dependent on GAB2 activation, cross-linking AKT and RAS pathway (6). The adaptor protein SHP2 is not only part of hyperactive RAS signalling in cancer cells, but is of major importance in the inactivation of T cells, inhibiting the TCR signal in response to ligand binding to PD-1 (b). FHL1 is involved in the development of cardiac hypertrophy, which is caused by a gain-of-function mutation, leading to increased ERK signalling (c).

transformation, invasion and metastasis in various cancer types (3)⁹⁵. A study of a *KSR*^{-/-} mouse model proves the resistance against RAS-dependent tumour formation⁹⁶, highlighting the pro-oncogenic function of KSR in RAS-driven cancers (4). SHOC2 mediates tumourigenesis and metastasis in different cancer types via tethering RAS and CRAF proteins in close proximity and thus promoting RAS-mediated CRAF activation^{97,98}. Knockout models of SHOC2 in KRAS mutated lung adenocarcinoma in mice have revealed a significant reduction of tumour growth, as well as a prolonged survival, accentuating the scaffold protein as a potential therapeutic target (5)⁹⁹. GAB2 has been implicated as a central modulator for oncogenic BCR-ABL signalling¹⁰⁰. GAB2-deficient mice have exhibited resistance against cancer cell transformation of myeloid progenitors in the presence of BCR-ABL, which is found in 90% of patients with chronic myeloid leukemia (6)^{100,101}. SHP2 is not only associated with a large number of cancers but plays a central role in PD-L1/PD-1 singling that inhibits the TCR-activated pathways, including RAS-MAPK, in T cells (Fig. 3b (7))¹⁰². This leads to an inactivation of the T cells, guarding the tumour cells against the immune system. Thus, SHP2 inhibitors have a dual role as a possible therapeutic target by reducing RAS signalling and inducing the body's immune response.

RASopathies. RASopathies or RAS-MAPK syndromes are defined as a group of developmental disorders that are caused by mild gain-of-function germline mutations in genes related to not only the constituent members of the RTK-RAS-MAPK pathway¹⁰³ but also various accessory proteins, including CBL, SHP2, SPRED1 and SHOC2 (Fig. 3a)¹⁰³.

Germline *CBL* mutations exhibit a wide phenotypic variability related to Noonan syndrome, which is characterised by a relatively high frequency of neurological features, predisposition to juvenile myelomonocytic leukaemia and low prevalence of cardiac defects, reduced growth and cryptorchidism¹⁰⁴. The mutations are mainly located in the central region of CBL, which is known to abolish the ubiquitination of RTKs by impairing CBLs E3 ligase activity¹⁰⁴. Legius syndrome-associated mutations in *SPRED1*, mostly result in loss-of-function of the scaffold protein, and gain-of-function of the RAS-MAPK pathway^{105,106}. In contrast, mutations in genes encoding SHP2 and SHOC2 lead to a gain-of-function and contribute to MAPK signalling upregulation that causes diverse developmental phenotypes^{56,59,107}. A recurrent activating mutation at the very N-terminus of SHOC2 (Ser-2 to Gly) leads to N-myristoylation of SHOC2, confers continuous membrane association and consequently causes Mazzanti syndrome, a RASopathy characterised by features resembling Noonan syndrome^{107,108}. Another RASopathy-causing *SHOC2* mutation (Gln-269 to His and His-270 to Tyr) has been recently identified to be associated with prenatal-onset hypertrophic cardiomyopathy¹⁰⁷. This mutation changes the relative orientation of the two leucine-rich repeat domains of SHOC2 and enhances its binding to MRAS and PPP1CB, two other RASopathy genes¹⁰⁹, and thus, increased signalling through the MAPK cascade¹⁰⁷.

Other diseases. Moyamoya angiopathy is characterised by progressive stenosis of the terminal portion of the internal carotid arteries and the development of a network of abnormal collateral vessels. This is a rare condition that can be caused by de novo *CBL* mutations even in the absence of obvious signs of RASopathy¹¹⁰. Evidence linking CNK1 dysfunction to autosomal recessive intellectual disability in patients emphasises the importance of this anchoring protein in the orchestration of the RTK-RAS-MAPK signalling in brain development and

cognition¹¹¹. The scaffold proteins FHL1/2 link RAS-MAPK signalling to the sarcomere and is a critical component of the hypertrophy signalling in cardiac cells (Fig. 3c)⁸⁸. FHL1/2 mutations are associated with cardiac diseases¹¹². FLOT1 has been implicated in the development of Alzheimer and type 2 diabetes and could be a promising proteomic biomarker^{113,114}.

Accessory proteins as therapeutic targets. Direct targeting of constituent members of the RTK-RAS-MAPK axis in the context of disease treatment, such as cancer, is a big challenge. Therapies for KRAS mutated cancers remain a major clinical need, despite allele-specific inhibitors that trap and inactivate mutant KRAS (G12C)^{115,116}. Three decades of research led to significant advances in tumour treatment¹¹⁷. However, the side-effects can still be severe and more-specific treatments could ease patient suffering. Unfortunately, many of the expectations for RAS pathway-targeted drugs have not been fulfilled. High toxicity and resistance acquisition have hampered many of the drugs developed to date^{117,118}. An alternative therapeutic strategy to treat KRAS mutant cancers aims at protein degradation via proteolysis targeting chimeras (PROTACs)¹¹⁹. The ablation of CRAF in advanced tumours driven by KRAS oncogene leads to significant tumour regression with no detectable appearance of resistance mechanisms and limited toxicities¹²⁰. In this context, a recent study has reported first progress to develop degrader molecules that target KRAS oncogene in NSCLC¹²¹.

Emerging evidence suggests that constituent signalling proteins assemble into macromolecular complexes and co-operate in clusters at specific sites of the cell. Therefore, it is important to note that the stoichiometric imbalance of each subunit of a complex—either by gene overexpression on the one side, and depletion, knockout or targeted protein degradation on the other—perturbs the equilibrium, and interferes at some level with the function of the protein or its complex¹²². With accessory proteins being of immense relevance for the whole signalling machinery and operating particularly from the side line, we propose that functional interference with a defined site of accessory proteins may attenuate rather than inhibit the signalling of hyperactivated RTK-RAS-MAPK axis.

The knockout or knockdown of accessory proteins in cell-based or animal models could already show the importance of these modulators in cancer signalling. The scaffold protein SHOC2 has an important role in embryogenesis, therefore, loss-of-SHOC2 is embryonically lethal. In contrast, the systemic knockout in adult mice as well as in human cell lines is quite well tolerated and leads to growth inhibition of RAS-mutated NSCLC cell lines⁹⁹. Furthermore, the depletion of SHOC2 leads to a sensitisation towards MEK inhibitor treatment, by interfering with the feedback-loop of MEK inhibition via BRAF/CRAF dimerisation, which is SHOC2 dependent⁹⁹. Therefore, dual targeting of SHOC2 and MEK appears as a promising treatment strategy in RAS-mutated cancers. Another approach deals with the scaffold protein GIT1. The knockdown of GIT1 in human osteosarcoma cells has shown in vivo and in vitro reduced tumour cell growth, invasion and angiogenesis, which could make GIT1 a potential target in gene therapy¹²³.

There is a number of approaches to target specific functions of accessory proteins (Table 1). The CNK1 inhibitor PHT-7.3 binds to its PH domain and prevents the colocalisation with prenylated KRAS4B on the plasma membrane¹²⁴. PHT-7.3 successfully inhibits the growth of tumour cells induced by mutated but not wild type KRAS4B. The interference of GRB2 mRNA by liposome-incorporated nuclease-resistant antisense oligodeoxynucleotides in BCR-ABL fusion protein-positive cancer cells, leads to reduced tumour growth in Xenograft models¹²⁵. It

Table 1 Accessory proteins as attractive therapeutic targets.

Accessory protein	Disease	Drug	State of art	Comment	Ref.
CNK1	Cancers with KRAS mutations	PHT-7.3	Cell-based model	PHT-7.3 binds selectively to CNK1 PH domain, interferes its colocalisation with KRAS4B on the plasma membrane and diminishes RAF/MEK/ERK signalling	¹²⁴
GRB2	BCR-ABL-positive leukaemia	Anti-miDNA L-GRB2	Xenograft model	L-GRB2 selectively targets GRB2 mRNA and inhibits its translation	¹²⁵
IQGAP1	Cancers with KRAS mutations	WW competitive peptide	Mouse model	WW competitive peptide antagonist of IQGAP1 interferes with its scaffolding ERK interaction; it is applied in combination with the BRAF inhibitor vemurafenib (PLX-4032) against KRAS4B oncogene	¹²⁶
KSR	Cancers with KRAS mutations	APS-2-79	Cell-based model	APS-2-79 binds and stabilises KSR in its inactive state, interferes with KSR/RAF heterodimerization and inhibit oncogenic KRAS4B signalling	^{128,129}
SHP2	Cancers	SHP099	Xenograft model	SHP099 binds SHP2 as an allosteric inhibitor, stabilises its autoinhibited state and inhibit oncogenic Ras signalling	¹³⁰⁻¹³³

interferes with the RAS/MAPK pathway and the cross-talk towards AKT pathway via GAB2. A WW-peptide of IQGAP1 binds ERK and competes with endogenous IQGAP1, which leads to attenuation of ERK activation¹²⁶. This treatment together with the BRAF inhibitor vemurafenib (PLX-4032), was very successful in tumour mouse models¹²⁶. It has later been shown that not the WW-domain but the IQ domain is necessary to bind ERK¹²⁷. The effects on the tumour growth suppression may stem from the interference with another yet unknown binding partner of IQGAP1 as an integral element of its complex scaffolding function. Another interesting example of accessory proteins as a therapeutic target is the small molecule APS-2-79, which binds KSR in its inactive state and interferes with RAF binding and thus blocks MEK phosphorylation¹²⁸. The cell-based experiments with APS-2-79 have shown not only reduced ERK activation and growth inhibition in combination with the MEK inhibitor trametinib, but also antagonising its resistance mechanism¹²⁹. Besides active site inhibitors, an allosteric inhibitor of SHP2 SHP099 stabilises the autoinhibited state and interferes with the enzymatic activity as well as its adaptor protein function to bind, for example, the GRB2-SOS complex¹³⁰. A combination of SHP099 with a MEK inhibitor has been shown to interfere with the feedback mechanism via SHP2 and to block the resistance initiation observed in KRAS4B-driven cancer therapy¹³⁰⁻¹³². In addition, SHP2 inhibition by SHP099 has been shown to have a positive effect on anti-tumour immunity in colon cancer xenograft models, especially in a co-treatment with an anti-PD-1 antibody¹³³.

Given that the majority of accessory proteins are now emerging as attractive therapeutic targets, still a very small number of accessory inhibitors have been discovered yet.

Concluding remarks and outlook

Accessory proteins tightly control signal transduction by fine-tuning spatiotemporal organisation of signalling components and maintaining specificity and function of the pathway on a cell type and even subcellular level. They operate from the side line, from which they specifically leverage their multivalent domains on the formation of macromolecular clusters, as highlighted in this article. Even though interest in accessory proteins has grown in the past few years, the possibilities to practically visualise them, track their pathway and experimentally and selectively affect their functions in human cells are keys to address questions about their cell type specificities, subcellular distribution and physical interactions in a context-dependent manner. To investigate the impact of an accessory protein in the context of RAS-MAPK signalling,

we suggest the following approach: (i) It is necessary to first determine a cell line that expresses the gene related to the accessory protein of interest using quantitative real-time PCR. (ii) It is crucial to investigate the accessory protein at the endogenous levels. The overexpression studies cause in spite of their experimental advantages various difficulties¹²². A prominent example is KSR overexpression that has been erroneously identified as a suppressor of RAS signalling. (iii) The major challenges faced and likely to be faced in near future are the difficult task of the direct use of antibodies post-purchase without careful validation¹³⁴. It is of major importance to validate the antibody specificity by immunoblotting purified protein or protein fragments, and cell lysates overexpressing gene or gene fragments encoding the accessory protein. (iv) Cell fractionation and confocal imaging under-stimulated and non-stimulated conditions will prove if the proteins pre-assemble in complexes with their binding partners (as predicted for KSR-MEK) and where they are located within the cell; as we expect the accessory proteins to orchestrate the RTK-RAS-MAPK signalling in specific subcellular compartments (e.g., plasma membrane, early endosomes, lysosomes, Golgi or ER). (v) Gene knockout cell lines, generated by CRISPR/Cas9 technology, will allow measuring the impact of the accessory proteins as positive or negative modulators of the RAS-MAPK pathway, by determining the p-ERK/ERK ratio. Moreover, this approach will give an idea about possible feedback or compensation mechanisms of accessory proteins among each other. Thus, exploring these concepts in greater detail will provide the framework for future research that will fill existing gaps in our knowledge and expand our understanding of more effective therapies.

Received: 12 February 2021; Accepted: 23 April 2021;
Published online: 08 June 2021

References

- McKay, M. M. & Morrison, D. K. Integrating signals from RTKs to ERK/MAPK. *Oncogene* **26**, 3113–3121 (2007).
- Lavoie, H. & Therrien, M. Regulation of RAF protein kinases in ERK signalling. *Nat. Rev. Mol. Cell Biol.* **16**, 281–298 (2015).
- Nakhaei-Rad, S. et al. Structural fingerprints, interactions, and signaling networks of RAS family proteins beyond RAS isoforms. *Crit. Rev. Biochem. Mol. Biol.* **53**, 130–156 (2018).
- Tartaglia, M. & Gelb, B. D. Disorders of dysregulated signal traffic through the RAS-MAPK pathway: phenotypic spectrum and molecular mechanisms. *Ann. N. Y. Acad. Sci.* **1214**, 99–121 (2010).
- Dhillon, A. S., Hagan, S., Rath, O. & Kolch, W. MAP kinase signalling pathways in cancer. *Oncogene* **26**, 3279–3290 (2007).

6. Castel, P., Rauen, K. A. & McCormick, F. The duality of human oncoproteins: drivers of cancer and congenital disorders. *Nat. Rev. Cancer* **20**, 383–397 (2020).
7. Lyon, A. S., Peeples, W. B. & Rosen, M. K. A framework for understanding the functions of biomolecular condensates across scales. *Nat. Rev. Mol. Cell Biol.* **18**, 285–298 (2020).
8. Kholodenko, B. N., Hancock, J. F. & Kolch, W. Signalling ballet in space and time. *Nat. Rev. Mol. Cell Biol.* **11**, 414–426 (2010).
9. Zhou, Y., Prakash, P., Gorfe, A. A. & Hancock, J. F. Ras and the plasma membrane: a complicated relationship. *Cold Spring Harb. Perspect. Med.* **8**, a031831 (2018).
10. Blažević, O. et al. Galectin-1 dimers can scaffold Raf-effectors to increase H-ras nanoclustering. *Sci. Rep.* **6**, 24165 (2016).
11. Omerovic, J. & Prior, I. A. Compartmentalized signalling: ras proteins and signalling nanoclusters. *FEBS J.* **276**, 1817–1825 (2009).
12. Banani, S. F., Lee, H. O., Hyman, A. A. & Rosen, M. K. Biomolecular condensates: organizers of cellular biochemistry. *Nat. Rev. Mol. Cell Biol.* **18**, 285–298 (2017).
13. Su, X. et al. Phase separation of signaling molecules promotes T cell receptor signal transduction. *Science* **352**, 595–599 (2016).
14. Hunter, T. Signaling - 2000 and beyond. *Cell* **100**, 113–127 (2000).
15. Tian, T. et al. Plasma membrane nanoswitches generate high-fidelity Ras signal transduction. *Nat. Cell Biol.* **9**, 905–914 (2007).
16. Ivakhno, S. & Armstrong, J. D. Non-linear dimensionality reduction of signaling networks. *BMC Syst. Biol.* **1**, 1–17 (2007).
17. Lin, Y. H. et al. The intrinsically disordered N-terminal domain of galectin-3 dynamically mediates multisite self-association of the protein through fuzzy interactions. *J. Biol. Chem.* **292**, 17845–17856 (2017).
18. Jin, T. et al. PAQR10 and PAQR11 mediate Ras signaling in the Golgi apparatus. *Cell Res.* **22**, 661–676 (2012).
19. Morrow, I. C. et al. Flotillin-1/raggie-2 traffics to surface raft domains via a novel Golgi-independent pathway. Identification of a novel membrane targeting domain and a role for palmitoylation. *J. Biol. Chem.* **277**, 48834–48841 (2002).
20. Huang, W. Y. C. et al. A molecular assembly phase transition and kinetic proofreading modulate Ras activation by SOS. *Science* **363**, 1098–1103 (2019).
21. MacDonald, J. I. S., Gryz, E. A., Kubu, C. J., Verdi, J. M. & Meakin, S. O. Direct binding of the signaling adapter protein Grb2 to the activation loop tyrosines on the nerve growth factor receptor tyrosine kinase, TrkA. *J. Biol. Chem.* **275**, 18225–18233 (2000).
22. Biernat, W. Epidermal growth factor receptor in glioblastoma. *Folia Neuropathol.* **43**, 123–132 (2005).
23. Ravichandran, K. S., Lorenz, U., Shoelson, S. E. & Burakoff, S. J. Interaction of Shc with Grb2 regulates association of Grb2 with mSOS. *Mol. Cell. Biol.* **15**, 593–600 (1995).
24. Wöhrl, F. U., Daly, R. J. & Brummer, T. Function, regulation and pathological roles of the Gab/DOS docking proteins. *Cell Commun. Signal.* **7**, 22 (2009).
25. Joazeiro, C. A. P. et al. The tyrosine kinase negative regulator c-Cbl as a RING-type, E2-dependent ubiquitin-protein ligase. *Science* **286**, 309–312 (1999).
26. Sanjay, A., Horne, W. C. & Baron, R. The Cbl family: ubiquitin ligases regulating signaling by tyrosine kinases. *Sci. Signal.* **2001**, pe40–pe40 (2001).
27. Brizzi, M. F. et al. Discrete protein interactions with the Grb2/c-Cbl complex in SCF- and TPO-mediated myeloid cell proliferation. *Oncogene* **13**, 2067–2076 (1996).
28. Elly, C. et al. Tyrosine phosphorylation and complex formation of Cbl-b upon T cell receptor stimulation. *Oncogene* **18**, 1147–1156 (1999).
29. Wong, A., Lamothe, B., Lee, A., Schlessinger, J. & Lax, I. FRS2α attenuates FGF receptor signaling by Grb2-mediated recruitment of the ubiquitin ligase Cbl. *Proc. Natl Acad. Sci. USA* **99**, 6684–6689 (2002).
30. Stephens, R. M. et al. Trk receptors use redundant signal transduction pathways involving SHC and PLC-γ1 to mediate NGF responses | TSpace Repository. *Neuron* **3**, 691–705 (1994).
31. Harmer, S. L. & DeFranco, A. L. Shc contains two Grb2 binding sites needed for efficient formation of complexes with SOS in B lymphocytes. *Mol. Cell. Biol.* **17**, 4087–4095 (1997).
32. Gu, H. et al. New role for Shc in activation of the phosphatidylinositol 3-kinase/Akt pathway. *Mol. Cell. Biol.* **20**, 7109–7120 (2000).
33. Kouhara, H. et al. A lipid-anchored Grb2-binding protein that links FGF-receptor activation to the Ras/MAPK signaling pathway. *Cell* **89**, 693–702 (1997).
34. Murohashi, M. et al. An FGF4-FRS2α-Cdx2 axis in trophoblast stem cells induces Bmp4 to regulate proper growth of early mouse embryos. *Stem Cells* **28**, 113–121 (2010).
35. Zhang, S. Q. et al. Shp2 regulates Src family kinase activity and Ras/Erk activation by controlling Csk recruitment. *Mol. Cell* **13**, 341–355 (2004).
36. Hadari, Y. R., Kouhara, H., Lax, I. & Schlessinger, J. Binding of Shp2 tyrosine phosphatase to FRS2 is essential for fibroblast growth factor-induced PC12 cell differentiation. *Mol. Cell. Biol.* **18**, 3966–3973 (1998).
37. Dance, M., Montagner, A., Salles, J. P., Yart, A. & Raynal, P. The molecular functions of Shp2 in the Ras/mitogen-activated protein kinase (ERK1/2) pathway. *Cell. Signal.* **20**, 453–459 (2008).
38. Tajan, M., de Rocca Serra, A., Valet, P., Edouard, T. & Yart, A. SHP2 sails from physiology to pathology. *Eur. J. Med. Genet.* **58**, 509–525 (2015).
39. Chen, P. Y. & Friesel, R. FGFR1 forms an FRS2-dependent complex with mTOR to regulate smooth muscle marker gene expression. *Biochem. Biophys. Res. Commun.* **382**, 424–429 (2009).
40. Gotoh, N. et al. Tyrosine phosphorylation sites on FRS2α responsible for Shp2 recruitment are critical for induction of lens and retina. *Proc. Natl Acad. Sci. USA* **101**, 17144–17149 (2004).
41. Quilliam, L. A., Rebhun, J. F. & Castro, A. F. A growing family of guanine nucleotide exchange factors is responsible for activation of ras-family GTPases. *Prog. Nucleic Acid Res. Mol. Biol.* **71**, 391–444 (2002).
42. Scheffzek, K. & Shivalingaiah, G. Ras-specific gtpase-activating proteins—structures, mechanisms, and interactions. *Cold Spring Harb. Perspect. Med.* **9**, a031500 (2019).
43. Simanshu, D. K., Nissley, D. V. & McCormick, F. Ras proteins and their regulators in human disease. *Cell* **170**, 17–33 (2017).
44. Haghighi, F. et al. bFGF-mediated pluripotency maintenance in human induced pluripotent stem cells is associated with NRAS-MAPK signaling. *Cell Commun. Signal.* **16**, 96 (2018).
45. Stowe, I. B. et al. A shared molecular mechanism underlies the human rasopathies Legius syndrome and Neurofibromatosis-1. *Genes Dev.* **26**, 1421–1426 (2012).
46. Duzendortorfer-Matt, T., Mercado, E. L., Maly, K., McCormick, F. & Scheffzek, K. The neurofibromin recruitment factor Spred1 binds to the GAP related domain without affecting Ras inactivation. *Proc. Natl Acad. Sci. USA* **113**, 7497–7502 (2016).
47. Siljamäki, E. & Abankwa, D. SPRED1 interferes with K-ras but Not H-ras membrane anchorage and signaling. *Mol. Cell. Biol.* **36**, 2612–2625 (2016).
48. Cui, Y. et al. The NF2 tumor suppressor merlin interacts with Ras and RasGAP, which may modulate Ras signaling. *Oncogene* **38**, 6370–6381 (2019).
49. Cui, Y. et al. Merlin cooperates with neurofibromin and Spred1 to suppress the Ras-Erk pathway. *Hum. Mol. Genet.* **29**, 3793–3806 (2020).
50. Pamonsinlapatham, P. et al. P120-Ras GTPase activating protein (RasGAP): a multi-interacting protein in downstream signaling. *Biochimie* **91**, 320–328 (2009).
51. Jaiswal, M. et al. Functional cross-talk between ras and rho pathways: a ras-specific gtpase-activating protein (p120RasGAP) competitively inhibits the rhoGAP activity of deleted in liver cancer (DLC) tumor suppressor by masking the catalytic arginine finger. *J. Biol. Chem.* **289**, 6839–6849 (2014).
52. An, S. et al. Raf-interactome in tuning the complexity and diversity of Raf function. *FEBS J.* **282**, 32–53 (2015).
53. Belanis, L., Plowman, S. J., Rotblat, B., Hancock, J. F. & Kloog, Y. Galectin-1 is a novel structural component and a major regulator of H-Ras nanoclusters. *Mol. Biol. Cell* **19**, 1404–1414 (2008).
54. Shalom-Feuerstein, R. et al. K-Ras nanoclustering is subverted by overexpression of the scaffold protein galectin-3. *Cancer Res.* **68**, 6608–6616 (2008).
55. Inder, K. L. et al. Nucleophosmin and nucleolin regulate K-ras plasma membrane interactions and MAPK signal transduction. *J. Biol. Chem.* **284**, 28410–28419 (2009).
56. Young, L. C. et al. SHOC2-MRAS-PP1 complex positively regulates RAF activity and contributes to Noonan syndrome pathogenesis. *Proc. Natl Acad. Sci. USA* **115**, E10576–E10585 (2018).
57. Rodriguez-Viciana, P., Osés-Prieto, J., Burlingame, A., Fried, M. & McCormick, F. A phosphatase holoenzyme comprised of Shoc2/Sur8 and the catalytic subunit of PP1 functions as an M-Ras effector to modulate Raf activity. *Mol. Cell* **22**, 217–230 (2006).
58. del Río, I. B. et al. SHOC2 complex-driven RAF dimerization selectively contributes to ERK pathway dynamics. *Proc. Natl Acad. Sci. USA* **116**, 13330–13339 (2019).
59. Jang, H., Stevens, P., Gao, T. & Galperin, E. The leucine-rich repeat signaling scaffolds Shoc2 and Erbin: cellular mechanism and role in disease. *FEBS J.* **288**, 721–739 (2020).
60. Dai, P., Xiong, W. C. & Mei, L. Erbin inhibits RAF activation by disrupting the Sur-8-Ras-Raf complex. *J. Biol. Chem.* **281**, 927–933 (2006).
61. Zheng, Z. et al. miR-183-5p inhibits occurrence and progression of acute myeloid leukemia via targeting erbin. *Mol. Ther.* **27**, 542–558 (2019).
62. Yao, S. et al. Erbin interacts with c-Cbl and promotes tumorigenesis and tumour growth in colorectal cancer by preventing c-Cbl-mediated ubiquitination and down-regulation of EGFR. *J. Pathol.* **236**, 65–77 (2015).

63. Wilkes, M. C. et al. Erbin and the NF2 tumor suppressor merlin cooperatively regulate cell-type-specific activation of PAK2 by TGF- β . *Dev. Cell* **16**, 433–444 (2009).
64. Stevens, P. D. et al. Erbin suppresses KSR1-mediated Ras/RAF signaling and tumorigenesis in colorectal cancer. *Cancer Res.* **78**, 4839–4852 (2018).
65. Matallanas, D. et al. Raf family kinases: old dogs have learned new tricks. *Genes Cancer* **2**, 232–60 (2011).
66. Rezaei Adariani, S. et al. Structural snapshots of RAF kinase interactions. *Biochem. Soc. Trans.* **46**, 1393–1406 (2018).
67. Terrell, E. M. & Morrison, D. K. Ras-mediated activation of the Raf family kinases. *Cold Spring Harb. Perspect. Med.* **9**, a033746 (2019).
68. Santos, E. & Crespo, P. The RAS-ERK pathway: a route for couples. *Sci. Signal.* **11**, eaav0917 (2018).
69. Roskoski, R. ERK1/2 MAP kinases: structure, function, and regulation. *Pharmacol. Res.* **66**, 105–143 (2012).
70. Wortzel, I. & Seger, R. The ERK cascade: distinct functions within various subcellular organelles. *Genes Cancer* **2**, 195–209 (2011).
71. Kolch, W. Meaningful relationships: The regulation of the Ras/Raf/MEK/ERK pathway by protein interactions. *Biochem. J.* **351**, 289–305 (2000).
72. Kolch, W. Coordinating ERK/MAPK signalling through scaffolds and inhibitors. *Nat. Rev. Mol. Cell Biol.* **6**, 827–837 (2005).
73. Vaidyanathan, H. et al. ERK MAP kinase is targeted to RSK2 by the phosphoprotein PEA-15. *Proc. Natl Acad. Sci. USA* **104**, 19837–19842 (2007).
74. Formstecher, E. et al. PEA-15 mediates cytoplasmic sequestration of ERK MAP kinase. *Dev. Cell* **1**, 239–250 (2001).
75. Zhang, N. et al. GIT1 is a novel MEK1-ERK1/2 scaffold that localizes to focal adhesions. *Cell Biol. Int.* **34**, 41–47 (2009).
76. Teis, D., Wunderlich, W. & Huber, L. A. Localization of the MP1-MAPK scaffold complex to endosomes is mediated by p14 and required for signal transduction. *Dev. Cell* **3**, 803–814 (2002).
77. Nada, S. et al. The novel lipid raft adaptor p18 controls endosome dynamics by anchoring the MEK-ERK pathway to late endosomes. *EMBO J.* **28**, 477–489 (2009).
78. Kovalenko, D., Yang, X., Nadeau, R. J., Harkins, L. K. & Friesel, R. Sef inhibits fibroblast growth factor signaling by inhibiting FGFR1 tyrosine phosphorylation and subsequent ERK activation. *J. Biol. Chem.* **278**, 14087–14091 (2003).
79. Ren, Y. et al. Tyrosine 330 in hSef is critical for the localization and the inhibitory effect on FGF signaling. *Biochem. Biophys. Res. Commun.* **354**, 741–746 (2007).
80. Yeung, K. et al. Suppression of Raf-1 kinase activity and MAP kinase signalling by RKIP. *Nature* **401**, 173–177 (1999).
81. Keller, E. T., Fu, Z. & Brennan, M. The role of Raf kinase inhibitor protein (RKIP) in health and disease. *Biochem. Pharmacol.* **68**, 1049–1053 (2004).
82. McKay, M. M., Ritt, D. A. & Morrison, D. K. Signaling dynamics of the KSR1 scaffold complex. *Proc. Natl Acad. Sci. USA* **106**, 11022–11027 (2009).
83. McNulty, D. E., Li, Z., White, C. D., Sacks, D. B. & Annan, R. S. MAPK scaffold IQGAP1 binds the EGF receptor and modulates its activation. *J. Biol. Chem.* **286**, 15010–15021 (2011).
84. Bañón-Rodríguez, I. et al. EGFR controls IQGAP basolateral membrane localization and mitotic spindle orientation during epithelial morphogenesis. *EMBO J.* **33**, 129–145 (2014).
85. Hedman, A. C., Smith, J. M. & Sacks, D. B. The biology of IQGAP proteins: beyond the cytoskeleton. *EMBO Rep.* **16**, 427–446 (2015).
86. Vomastek, T. et al. Modular construction of a signaling scaffold: MORG1 interacts with components of the ERK cascade and links ERK signaling to specific agonists. *Proc. Natl Acad. Sci. USA* **101**, 6981–6986 (2004).
87. Turner, C. E. Paxillin and focal adhesion signalling. *Nat. Cell Biol.* **2**, E231–E236 (2000).
88. Sheikh, F. et al. An FHL1-containing complex within the cardiomyocyte sarcomere mediates hypertrophic biomechanical stress responses in mice. *J. Clin. Invest.* **118**, 3870–3880 (2008).
89. Amaddii, M. et al. Flotillin-1/Reggie-2 protein plays dual role in activation of receptor-tyrosine kinase/mitogen-activated protein kinase signaling. *J. Biol. Chem.* **287**, 7265–7278 (2012).
90. Therrien, M., Wong, A. M. & Rubin, G. M. CNK, a RAF-binding multidomain protein required for RAS signaling. *Cell* **95**, 343–353 (1998).
91. Therrien, M., Wong, A. M., Kwan, E. & Rubin, G. M. Functional analysis of CNK in RAS signaling. *Proc. Natl Acad. Sci. USA* **96**, 13259–13263 (1999).
92. Mackinnon, A. C. et al. Paxillin expression and amplification in early lung lesions of high-risk patients, lung adenocarcinoma and metastatic disease. *J. Clin. Pathol.* **64**, 16–24 (2011).
93. Jagadeeswaran, R. et al. Paxillin is a target for somatic mutations in lung cancer: implications for cell growth and invasion. *Cancer Res.* **68**, 132–142 (2008).
94. Yoshida, T. et al. Spreds, inhibitors of the Ras/ERK signal transduction, are dysregulated in human hepatocellular carcinoma and linked to the malignant phenotype of tumors. *Oncogene* **25**, 6056–6066 (2006).
95. White, C. D., Brown, M. D. & Sacks, D. B. IQGAPs in cancer: a family of scaffold proteins underlying tumorigenesis. *FEBS Lett.* **583**, 1817–1824 (2009).
96. Nguyen, A. et al. Kinase suppressor of Ras (KSR) is a scaffold which facilitates mitogen-activated protein kinase activation in vivo. *Mol. Cell. Biol.* **22**, 3035–3045 (2002).
97. Kaduwal, S. et al. Sur8/Shoc2 promotes cell motility and metastasis through activation of Ras-PI3K signaling. *Oncotarget* **6**, 33091–33105 (2015).
98. Lee, Y. M. et al. Sur8 mediates tumorigenesis and metastasis in colorectal cancer. *Exp. Mol. Med.* **48**, e249 (2016).
99. Jones, G. G. et al. SHOC2 phosphatase-dependent RAF dimerization mediates resistance to MEK inhibition in RAS-mutant cancers. *Nat. Commun.* **10**, 2532 (2019).
100. Gu, S. et al. Distinct GAB2 signaling pathways are essential for myeloid and lymphoid transformation and leukemogenesis by BCR-ABL1. *Blood* **127**, 1803–1813 (2016).
101. Shivelman, E., Lifshitz, B., Gale, R. P. & Canaani, E. Fused transcript of abl and bcr genes in chronic myelogenous leukaemia. *Nature* **315**, 550–554 (1985).
102. Patsoukis, N. et al. Selective effects of PD-1 on Akt and ras pathways regulate molecular components of the cell cycle and inhibit T cell proliferation. *Sci. Signal.* **5**, ra46 (2012).
103. Tajan, M., Paccoud, R., Branka, S., Edouard, T. & Yart, A. The RASopathy family: consequences of germline activation of the RAS/MAPK pathway. *Endocr. Rev.* **39**, 676–700 (2018).
104. Martinelli, S. et al. Molecular diversity and associated phenotypic spectrum of germline CBL mutations. *Hum. Mutat.* **36**, 787–796 (2015).
105. Brems, H. & Legius, E. Legius syndrome, an update: molecular pathology of mutations in SPRED1. *Keio J. Med.* **62**, 107–112 (2013).
106. Yan, W. et al. Structural Insights into the SPRED1-Neurofibromin-KRAS Complex and Disruption of SPRED1-Neurofibromin Interaction by Oncogenic EGFR. *Cell Rep.* **32**, 107909 (2020).
107. Motta, M. et al. Clinical and functional characterization of a novel RASopathy-causing SHOC2 mutation associated with prenatal-onset hypertrophic cardiomyopathy. *Hum. Mutat.* **40**, 23767 (2019).
108. Cordeddu, V. et al. Mutation of SHOC2 promotes aberrant protein N-methylstylation and causes Noonan-like syndrome with loose anagen hair. *Nat. Genet.* **41**, 1022–1026 (2009).
109. Motta, M. et al. Activating MRAS mutations cause Noonan syndrome associated with hypertrophic cardiomyopathy. *Hum. Mol. Genet.* **29**, 1772–1783 (2019).
110. Guey, S. et al. De novo mutations in CBL causing early-onset paediatric moyamoya angiopathy. *J. Med. Genet.* **54**, 550–557 (2017).
111. Kazeminasab, S. et al. CNKSRI gene defect can cause syndromic autosomal recessive intellectual disability. *Am. J. Med. Genet. Part B Neuropsychiatr. Genet.* **177**, 691–699 (2018).
112. Liang, Y., Bradford, W. H., Zhang, J. & Sheikh, F. Four and a half LIM domain protein signaling and cardiomyopathy. *Biophys. Rev.* **10**, 1073–1085 (2018).
113. Angelopoulou, E., Paudel, Y. N., Shaikh, M. F. & Piperi, C. Flotillin: a promising biomarker for alzheimer's disease. *J. Pers. Med.* **10**, 20 (2020).
114. Galazis, N., Afrentiou, T., Xenophontos, M., Diamanti-Kandarakis, E. & Aiotomo, W. Proteomic biomarkers of type 2 diabetes mellitus risk in women with polycystic ovary syndrome. *Eur. J. Endocrinol.* **168**, R33–R43 (2013).
115. Moore, A. R., Rosenberg, S. C., McCormick, F. & Malek, S. RAS-targeted therapies: is the undruggable drugged? *Nat. Rev. Drug Discov.* **19**, 533–552 (2020).
116. Ostrem, J. M., Peters, U., Sos, M. L., Wells, J. A. & Shokat, K. M. K-Ras(G12C) inhibitors allosterically control GTP affinity and effector interactions. *Nature* **503**, 548–551 (2013).
117. Matallanas, D. & Crespo, P. New druggable targets in the Ras pathway? *Curr. Opin. Mol. Ther.* **12**, 674–683 (2010).
118. Vasan, N., Basella, J. & Hyman, D. M. A view on drug resistance in cancer. *Nature* **575**, 299–309 (2019).
119. Khan, S. et al. PROteolysis TARgeting Chimeras (PROTACs) as emerging anticancer therapeutics. *Oncogene* **39**, 4909–4924 (2020).
120. Sanclemente, M. et al. c-RAF ablation induces regression of advanced Kras/Trp53 mutant lung adenocarcinomas by a mechanism independent of MAPK signaling. *Cancer Cell* **33**, 217–228.e4 (2018).
121. Zeng, M. et al. Exploring targeted degradation strategy for oncogenic KRASG12C. *Cell Chem. Biol.* **27**, 19–31.e6 (2020).
122. Prelich, G. Gene overexpression: uses, mechanisms, and interpretation. *Genetics* **190**, 841–854 (2012).
123. Zhang, Z., Hu, P., Xiong, J. & Wang, S. Inhibiting GIT1 reduces the growth, invasion and angiogenesis of osteosarcoma. *Cancer Manag. Res.* **10**, 6445–6455 (2018).
124. Indarte, M. et al. An inhibitor of the pleckstrin homology domain of CNK1 selectively blocks the growth of mutant KRAS cells and tumors. *Cancer Res.* **79**, 3100–3111 (2019).

125. Tari, A. M. et al. Liposome-incorporated Grb2 antisense oligodeoxynucleotide increases the survival of mice bearing bcr-abl-positive leukemia xenografts. *Int. J. Oncol.* **31**, 1243–1250 (2007).
126. Jameson, K. L. et al. IQGAP1 scaffold-kinase interaction blockade selectively targets RAS-MAP kinase-driven tumors. *Nat. Med.* **19**, 626–630 (2013).
127. Bardwell, A. J., Lagunes, L., Zebarjedi, R. & Bardwell, L. The WW domain of the scaffolding protein IQGAP1 is neither necessary nor sufficient for binding to the MAPKs ERK1 and ERK2. *J. Biol. Chem.* **292**, 8750–8761 (2017).
128. Dhawan, N. S., Scompton, A. P. & Dar, A. C. Small molecule stabilization of the KSR inactive state antagonizes oncogenic Ras signalling. *Nature* **537**, 112–116 (2016).
129. Neilsen, B. K., Frodyma, D. E., Lewis, R. E. & Fisher, K. W. KSR as a therapeutic target for Ras-dependent cancers. *Expert Opin. Ther. Targets* **21**, 499–509 (2017).
130. Xie, J. et al. Allosteric inhibitors of SHP2 with therapeutic potential for cancer treatment. *J. Med. Chem.* **60**, 10205–10219 (2017).
131. Mainardi, S. et al. SHP2 is required for growth of KRAS-mutant non-small-cell lung cancer in vivo letter. *Nat. Med.* **24**, 961–967 (2018).
132. Ruess, D. A. et al. Mutant KRAS-driven cancers depend on PTPN11/SHP2 phosphatase. *Nat. Med.* **24**, 954–960 (2018).
133. Zhao, M. et al. SHP2 inhibition triggers anti-tumor immunity and synergizes with PD-1 blockade. *Acta Pharm. Sin. B* **9**, 304–315 (2019).
134. Acharya, P., Quinlan, A. & Neumeister, V. The ABCs of finding a good antibody: how to find a good antibody, validate it, and publish meaningful data. *F1000Res.* **6**, 851 (2017).

Acknowledgements

We are grateful to our colleagues Ehsan Amin, Ion C. Cirstea, Oliver Krumbach, Niloufar Mosaddeghzadeh, Saeideh Nakhaei-Rad and K. Nouri, for stimulating discussion. This study was supported by the Research Committee of the Medical Faculty of the Heinrich Heine University Düsseldorf (grant number: 2020-70/9772617), the German Research Foundation (Deutsche Forschungsgemeinschaft or DFG; grant number: AH 92/8-1), the German Research Foundation (Deutsche Forschungsgemeinschaft or DFG) through the International Research Training Group 'Intra- and interorgan communication of the cardiovascular system' (grant number: IRTG 1902-p6), the European Network on Noonan Syndrome and Related Disorders (NSEuroNet; grant number: 01GM1621B); the German Federal Ministry of Education and Research (BMBF)—German Network of RASopathy Research (GeNeRARe; grant numbers: 01GM1902C).

Author contributions

S.P., N.S.K.J., F.B. and C.W. systematically searched and read the literature using the PubMed database; C.W. generated Fig. 1, and S.P. generated Figures 2 and 3. All authors, including M.R.A. designed, wrote and approved the final version of the manuscript.

Funding

Open Access funding enabled and organized by Projekt DEAL.

Competing interests

The authors declare no competing interests.

Additional information

Supplementary information The online version contains supplementary material available at <https://doi.org/10.1038/s42003-021-02149-3>.

Correspondence and requests for materials should be addressed to M.R.A.

Reprints and permission information is available at <http://www.nature.com/reprints>

Publisher's note Springer Nature remains neutral with regard to jurisdictional claims in published maps and institutional affiliations.

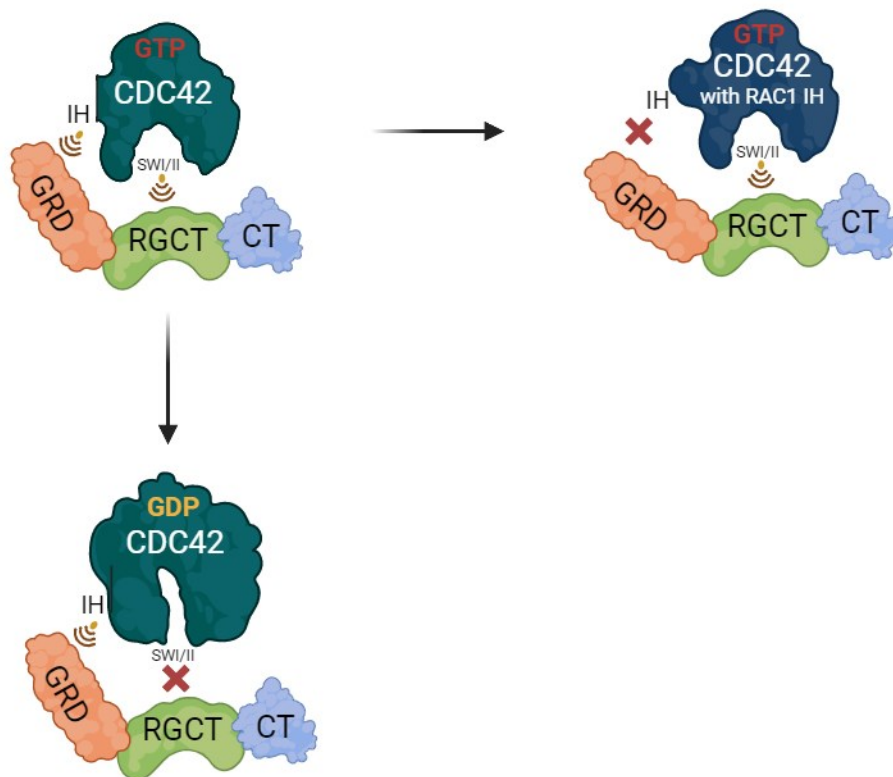


Open Access This article is licensed under a Creative Commons Attribution 4.0 International License, which permits use, sharing, adaptation, distribution and reproduction in any medium or format, as long as you give appropriate credit to the original author(s) and the source, provide a link to the Creative Commons license, and indicate if changes were made. The images or other third party material in this article are included in the article's Creative Commons license, unless indicated otherwise in a credit line to the material. If material is not included in the article's Creative Commons license and your intended use is not permitted by statutory regulation or exceeds the permitted use, you will need to obtain permission directly from the copyright holder. To view a copy of this license, visit <http://creativecommons.org/licenses/by/4.0/>.

© The Author(s) 2021, corrected publication 2021

Chapter 8

CDC42-IQGAP Interactions Scrutinized: New Insights into the Binding Properties of the GAP-Related Domain



Status: published in International Journal of Molecular Sciences, August 2022

Impact factor: 6.20

Contribution: 20 %

Expression and purification of RAS GTPases, p120 GAP and NF1 GAP, preparation of nucleotide-free forms of RAS GTPases, HPLC and GAP assay, figure preparation and illustration, drafting of the manuscript and discussion.



Article

CDC42-IQGAP Interactions Scrutinized: New Insights into the Binding Properties of the GAP-Related Domain

Niloufar Mosaddeghzadeh ^{1,†}, Silke Pudewell ^{1,†}, Farhad Bazgir ¹, Neda S. Kazemineh Jasemi ¹,
Oliver H. F. Krumbach ¹, Lothar Gremer ^{2,3}, Dieter Willbold ^{2,3}, Radovan Dvorsky ^{1,4}
and Mohammad R. Ahmadian ^{1,*}

¹ Institute of Biochemistry and Molecular Biology II, Medical Faculty and University Hospital Düsseldorf, Heinrich Heine University Düsseldorf, 40225 Düsseldorf, Germany

² Institute of Physical Biology, Heinrich Heine University Düsseldorf, 40225 Düsseldorf, Germany

³ Institute of Biological Information Processing, Structural Biochemistry (IBI-7), Forschungszentrum Jülich, 52425 Jülich, Germany

⁴ Center for Interdisciplinary Biosciences, P. J. Šafárik University, Jesenná 5, 040 01 Košice, Slovakia

* Correspondence: reza.ahmadian@uni-duesseldorf.de; Tel.: +49-211-811-2384

† These authors contributed equally to this work.



Citation: Mosaddeghzadeh, N.; Pudewell, S.; Bazgir, F.; Kazemineh Jasemi, N.S.; Krumbach, O.H.F.; Gremer, L.; Willbold, D.; Dvorsky, R.; Ahmadian, M.R. CDC42-IQGAP Interactions Scrutinized: New Insights into the Binding Properties of the GAP-Related Domain. *Int. J. Mol. Sci.* **2022**, *23*, 8842. <https://doi.org/10.3390/ijms23168842>

Academic Editor: Alexandre Baykov

Received: 23 June 2022

Accepted: 6 August 2022

Published: 9 August 2022

Publisher's Note: MDPI stays neutral with regard to jurisdictional claims in published maps and institutional affiliations.



Copyright: © 2022 by the authors. Licensee MDPI, Basel, Switzerland. This article is an open access article distributed under the terms and conditions of the Creative Commons Attribution (CC BY) license (<https://creativecommons.org/licenses/by/4.0/>).

Abstract: The IQ motif-containing GTPase-activating protein (IQGAP) family composes of three highly-related and evolutionarily conserved paralogs (IQGAP1, IQGAP2 and IQGAP3), which fine tune as scaffolding proteins numerous fundamental cellular processes. IQGAP1 is described as an effector of CDC42, although its effector function yet re-mains unclear. Biophysical, biochemical and molecular dynamic simulation studies have proposed that IQGAP RASGAP-related domains (GRDs) bind to the switch regions and the insert helix of CDC42 in a GTP-dependent manner. Our kinetic and equilibrium studies have shown that IQGAP1 GRD binds, in contrast to its C-terminal 794 amino acids (called C794), CDC42 in a nucleotide-independent manner indicating a binding outside the switch regions. To resolve this discrepancy and move beyond the one-sided view of GRD, we carried out affinity measurements and a systematic mutational analysis of the interfacing residues between GRD and CDC42 based on the crystal structure of the IQGAP2 GRD-CDC42^{Q61L} GTP complex. We determined a 100-fold lower affinity of the GRD1 of IQGAP1 and of GRD2 of IQGAP2 for CDC42 mGppNHp in comparison to C794/C795 proteins. Moreover, partial and major mutation of CDC42 switch regions substantially affected C794/C795 binding but only a little GRD1 and remarkably not at all the GRD2 binding. However, we clearly showed that GRD2 contributes to the overall affinity of C795 by using a 11 amino acid mutated GRD variant. Furthermore, the GRD1 binding to the CDC42 was abolished using specific point mutations within the insert helix of CDC42 clearly supporting the notion that CDC42 binding site(s) of IQGAP GRD lies outside the switch regions among others in the insert helix. Collectively, this study provides further evidence for a mechanistic framework model that is based on a multi-step binding process, in which IQGAP GRD might act as a ‘scaffolding domain’ by binding CDC42 irrespective of its nucleotide-bound forms, followed by other IQGAP domains downstream of GRD that act as an effector domain and is in charge for a GTP-dependent interaction with CDC42.

Keywords: CDC42; GAP; GAP-related domain; GRD; GTPase activating protein; IQGAP; nucleotide-independent binding; RASGAP; RHO GTPases; scaffold protein; scaffolding protein; switch regions

1. Introduction

RHO GTPases act, with some exceptions [1], as molecular switches by cycling between an inactive (GDP-bound) and an active (GTP-bound) state. Their functions at the plasma membrane are usually controlled by three groups of regulatory proteins: guanine nucleotide dissociation inhibitors (GDIs), guanine nucleotide exchange factors (GEFs) and GTPases activating proteins (GAPs) [2]. The formation of the active GTP-bound state of

RHO GTPases, such as CDC42, is accompanied by a conformational change in two regions, known as switch I and II (encompassing amino acids or aa 29–42 and 62–68, respectively); these regions provide a platform for a GTP-dependent, high-affinity association of structurally and functionally diverse effector proteins, e.g., ACK, PAK1, WASP, ROCK1, DIA and IQGAP1, through their so-called GTPase-binding domains (GBDs) [3–13] (reviewed in [14]). GTPase-effector signaling activates further a wide variety of pathways in all eukaryotic cells [2].

A unique feature distinguishing the RHO family from other small GTPase families is the presence of a 12 amino-acid insertion (aa 124–135 in CDC42) that protrudes from the G domain structure by forming a short helix, the so-called insert helix (IH) [15]. This IH is highly charged and variable among the members of the RHO family [15]. The IH has been very recently shown to have larger conformational flexibility in the GDP-bound CDC42 than in the GTP-bound CDC42 [16]. IH is a binding site for RHOGDI1, p50GAP, DIA, FMNL2, PLD1 and IQGAP2 [10,12,17–21], and appears rather essential for downstream activation of RHO GTPases [21–23].

IQGAP1 is ubiquitously expressed and shares a similar domain structure with its human paralogs IQGAP2 and IQGAP3 (Figure 1A), including an N-terminal calponin homology domain (CHD), a coiled-coil repeat region (CC), a tryptophan-containing proline-rich motif-binding region (WW), four isoleucine/glutamine-containing motifs (IQ), a RASGAP-related domain (GRD), a RASGAP C-terminal domain (RGCT) and a very C-terminal domain (CT). IQGAPs interact with a large number of proteins and modulate the spatiotemporal distributions of distinct signal-transducing protein complexes [24–34]. As multidomain scaffold proteins, they safeguard the magnitude, efficiency and specificity of signal transduction [35]. They have been localized at multiple subcellular sites orchestrating different signaling pathways and thus controlling a variety of cellular functions [36–42]. Notably, IQGAP1 has been implicated as a drug target due to its vital regulatory roles in cancer development [42–49] although the molecular mechanism of its functions is unclear.

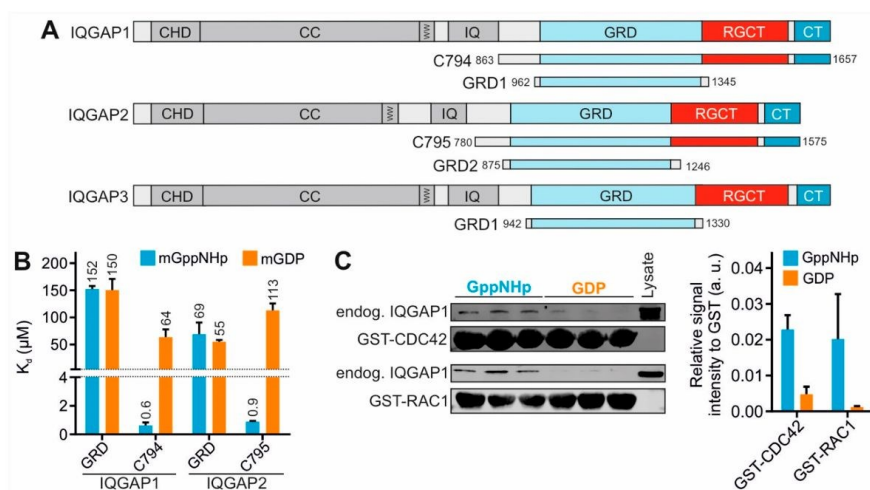


Figure 1. IQGAP GRD binding is nucleotide independent. (A) Domain organization of the IQGAP paralogs along with their GRDs and C-terminal fragments assessed in this study (see text for more details). (B) Fluorescence polarization analysis of IQGAP1 and IQGAP2 proteins with mGppNHp- and mGDP-bound CDC42. (C) Pull-down of endogenous IQGAP1 FL from HEK293 lysates with GppNHp- or GDP-bound GST-CDC42 and GST-RAC1, respectively. Densitometry evaluation of relative IQGAP1 binding to GST-CDC42 proteins (a. u., arbitrary unit) from a triplicate experiment is shown as bar charts.

Earlier studies analyzed the crucial role of IQGAP RGCT in high-affinity binding to the switch regions of the GTP-bound, active CDC42 and proposed it as an IQGAP ‘effector domain’ [5,50,51]. Accordingly, Swart-Mataraza et al. reported that the CDC42 GppNHp can still bind to IQGAP-ΔGRD (lacking aa 1122–1324) [52]. Moreover, Li et al. mapped the CDC42 and IQGAP binding regions and determined that switch I and surrounding regions (residues 29–55) together with the insert region (residues 122–134) are required for high affinity binding to IQGAP1 [53]. LeCour et al., however, solved a crystal structure of constitutively active CDC42(Q61L) in complex with the IQGAP2 GRD (GRD2) and proposed that CDC42 binds GRD2 from two different sites in a 4:2 stoichiometry [12,54]. One is the ‘GAPex-mode binding site’ (ex stands for ‘extra’ subdomains consisting of variable N- and C-terminal flanking regions) and the other is the ‘RASGAP-mode binding site’ very much resembling the RASGAP and CDC42GAP structures [18,55] with a conserved core domain (GAPc). Analyzing this structure, Ozdemir et al. proposed that CDC42 IH binding to the GAPex-domain induces GRD2 dimerization and changes the RASGAP site allosterically, which subsequently create another interaction interface for CDC42 binding (leading to a 2:1 stoichiometry of GRD2 and CDC42) [54].

A number of biophysical and biochemical studies have provided valuable insights into the structural and binding properties of the C-terminal domains of IQGAP1 (C794) and IQGAP2 (C795), encompassing the GRD, RGCT and CT domains, with CDC42 [12,50,52–54,56–63]. Evidently, all three domains bind with different affinities to CDC42 [5]. However, the mechanistic principles behind these interactions have remained unclear. Moreover, there are conflicting views regarding the assignment of a ‘CDC42-specific GBD’ for IQGAPs. One model proposes the GRD and its RASGAP-mode binding with the switch regions of CDC42 [12,54,56,58,64], whereas the other model excludes GRD and marks RGCT, located distal to the GRD, as crucial for high-affinity binding to CDC42 in a GTP-dependent manner [5,26,50–52]. Aiming to shed light on this discrepancy and to understand the molecular basis of CDC42-IQGAP interaction we comprehensively investigated the nature of the GRD interaction with CDC42 in this study and determined the role of the IH of CDC42 in contributing to GRD association. Furthermore, we studied the binding characteristics of C794 regarding the switch region and IH contact sites by mutational analysis, and verified the results in cell-based studies with endogenous IQGAP1. Collectively, our results consolidate and refine the importance of IQGAP RGCT as the true GBD in the recognition of CDC42 and its binding in a GTP-dependent manner. The GRD, although not a central effector domain, is evidently necessary for scaffolding CDC42 and facilitating its recruitment to preexisting cues.

2. Results and Discussion

IQGAP1 and IQGAP2 proteins were analyzed in this study to critically evaluate the function of the respective GRD domains. First, we determined the CDC42 binding properties of different IQGAP proteins, including IQGAP1 full-length (FL). Second, we examined the role of amino-acids crucial for the interplay between IQGAP2 and CDC42 using mutational IQGAPs and CDC42 variants. Third, we analyzed the impact of CDC42 IH as an IQGAP binding site. Fourth, we investigated the RASGAP activity of IQGAP1 GRD towards eight different members of the RAS family and examined the introduction of a catalytic arginine finger in the GRD.

2.1. GRD Is Not the Prominent Binding Domain for High IQGAP-CDC42 Affinity

2.1.1. GRD Binds to CDC42 with Very Low Affinity in a Nucleotide-Independent Manner

Different domains and fragments of the IQGAPs, including GRD1 and C794 of IQGAP1, as well as GRD2 and C795 of IQGAP2 (Figure 1A), were purified to determine their binding affinities for mGDP- and mGppNHp-bound CDC42 using fluorescence polarization. Obtained dissociation constants (K_d ; Figure 1B) clearly show that all IQGAP constructs are able to bind CDC42 but with different affinities and preferences for the nucleotide-bound forms of CDC42. GRDs of both IQGAPs are low-affinity binders and do

not discriminate between the active and the inactive states of CDC42. Similar observations were made for GRD3 and the CT of IQGAP1 (Supplementary Figure S1). In contrast, C794 and C795, encompassing in addition to both GRD and CT also the central RGCT (Figure 1A), exhibited K_d values of 0.6 and 0.9 μM , respectively, indicating an around 100-fold higher affinity for the GTP-bound active CDC42 as compared to CDC42 GDP (Figure 1B). This result clearly suggests that RGCT but not GRD represents a ‘CDC42-specific GBD’ for at least IQGAP1 and IQGAP2, by directly associating with the switch regions of CDC42 GTP. Unfortunately, our efforts to obtain IQGAP1 RGCT (aa 1276–1575) and IQGAP3 C790 (aa 841–1631) for determining their binding affinities to the members of the RHO GTPase family, including CDC42, has been remaining unsuccessful [26,51]. Purified IQGAP1 RGCT tends to assemble into higher oligomeric or polymeric states, and, thus, is disabled in binding CDC42 [51].

Several lines of evidence support the crucial role of RGCT rather than GRD as the IQGAP effector domain for CDC42: (i) Here we can show that proteins containing RGCT bind with a more than 100-fold affinity to CDC42 mGppNHp as compared to isolated GRD or CT (Figure 1B and Figure S1), (ii) substitution of the Serine 1443 for glutamate (a phosphomimetic mutation) drastically impaired IQGAP1 binding to CDC42 mGppNHp [5,51]; (iii) an IQGAP1 protein, lacking the GRD (aa1122–1324), only binds CDC42 GppNHp, in contrast to IQGAP1 itself, that binds both GppNHp-bound and GDP-bound CDC42 [52]. The latter has been also demonstrated in other studies [63,64] and support our previous [26,51] and current findings that IQGAP domains, including GRD and CT, bind CDC42 GDP as strong as CDC42 GppNHp (Figure 1B).

2.1.2. Endogenous IQGAP1 also Binds CDC42 GDP

Serum-stimulated HEK293 cells, endogenously expressing IQGAP1 full-length (FL), were now used to carry out a pull-down assay with purified GST-fusion proteins of CDC42 and RAC1 in either GDP-bound or GppNHp-bound forms. IQGAP1 FL bound to these GTPases, regardless of their nucleotide status even though the binding to GDP-bound proteins was observed to be much weaker than the GppNHp-bound proteins (Figure 1C). This pattern corresponds to the binding behavior of C794 and not with the binding of GRD1 alone. Densitometric evaluation of three independent pull-down experiments showed that IQGAP1 FL binding to CDC42 GDP is much stronger than to RAC1 GDP (Figure 1C).

Altogether, our data suggest that IQGAP1 forms a complex with CDC42 through different sites in both nucleotide-dependent and nucleotide-independent manner.

2.2. Switch Regions of CDC42 Are Not the Main Binding Sites for the GRDs

Timpson’s and our group have provided evidence that the IQGAP RGCT is essential for high affinity binding to the switch regions of the GTP-bound, active CDC42 and thus acts as an IQGAP ‘effector domain’ [5,50,51]. This critical issue has now been further expanded with additional experiments as described above (Figure 1), and confirms the crucial role of the RGCT as an IQGAP ‘effector domain’ that selectively associates with CDC42 GTP and carries out the high affinity association. Other groups have, in contrast, used the constitutive active CDC42(Q61L) in their structural and biochemical analysis and proposed that CDC42(Q61L) GTP GRD forms a GTPase-effector complex [12,54,56,57]. Such a role of the GRD in associating with CDC42 GTP is astonishing considering the afore mentioned studies on both GRD1-CT that binds CDC42 with a higher affinity as compared with GRD and an IQGAP1 variant, lacking the RASGAP domain (aa 1122–1324), which equally interacts with CDC42 as compared with IQGAP1 wild type [52]. To clarify this discrepancy, we have carefully examined ‘the RASGAP-mode binding site’ of CDC42 using mutational approaches coupled with kinetic and equilibrium measurements. Results of this examination are discussed in following subsections.

2.2.1. Mutations in CDC42 Switch Regions Only Mildly Affect GRD Binding

Proposed interacting mode of GRD with the switch regions of CDC42 (RASGAP mode binding) was deduced from the IQGAP2 GRD2 structure in complex CDC42^{Q61L} GTP [12] and two CDC42 mutation variants within the switch I and II regions (2xSW and 8xSW) and a 11-residues mutant variant within the GRD of IQGAP2 C795 (11xGRD) were generated as illustrated in Figure 2A. Identical and highly conserved residues within the interacting interface highlighted in Figure 2B, were all replaced by alanine. All variants were stable in their purified forms and Far-UV CD spectroscopic measurements excluded any improper folding as compared to the wild-type proteins (Supplementary Figure S2).

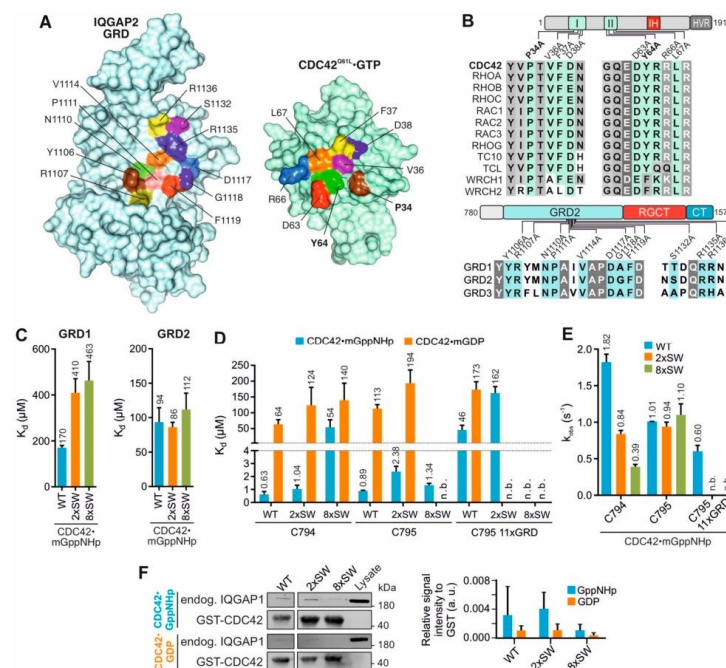


Figure 2. Analysis of CDC42 switch region and IQGAP1 GRD mutants. (A) The selection of GRD2 and CDC42 mutations is based on the GRD2/CDC42^{Q61L} structure (PDB: 5CJP). Interacting residues colored on both proteins were selected for mutational analysis. For more details see also Table S1. (B) Multiple sequence alignments of switch regions of RHO GTPases and IQGAPs highlight identical or homologous interacting residues that have been replaced in this study by alanine for analyzing their impact on IQGAP binding. Conserved residues are shaded in grey. Mutations in CDC42 switch regions include 2xSW (bolded residues) and 8xSW (all eight residues, as indicated), and 11xGRD in IQGAP2 C795. (C) Fluorescence polarization measurements of mGppNHp-bound CDC42 WT, 2xSW and 8xSW with IQGAP1 GRD1 or IQGAP2 GRD2. (D) The K_d values for the interactions of IQGAP1 C794, IQGAP2 C795 and C795 11xGRD with the CDC42 variants in mGppNHp- and mGDP-bound form were determined using fluorescence polarization. n.b. stands for no binding observed. C794 and C795 CDC42 WT measurements are included from Figure 1B for simple comparison. (E) Observed rate constants (k_{obs}) for the IQGAPs association with mGppNHp-bound CDC42 WT, 2xSW and 8xSW were measured using stopped-flow fluorimetry. (F) Pull-down of endogenous IQGAP1 FL from HEK293 lysates with GST-CDC42 in GppNHp-bound or GDP-bound state. Cell lysate was used as an input control. Densitometry evaluation of relative IQGAP1 binding to GST-CDC42 proteins (a. u., arbitrary unit) from triplicate experiments is shown as bar charts.

We first determined the K_d values for the GRD1 and GRD2 interaction with the mGppNHp-bound CDC42 WT, 2xSW and 8xSW. Interestingly, we found a two to three-fold reduction in the binding affinity of GRD1 but no notable reduction for GRD2 with the CDC42 variants as compared to CDC42 WT (Figures 1B, 2C and S3). As the effect of 2x and 8x introduced mutations on the proposed crucial interaction sites of CDC42 and GRD2 did not result in a decrease of affinity, our data clearly indicates that the association of CDC42 switch regions with IQGAP must be through other sites rather than the GRD.

2.2.2. IQGAP C794/C795 Binding Is Impaired by Switch Region and GRD Mutations

Next, we measured the K_d values for the interaction of IQGAP1 C794 or IQGAP2 C795, containing the GRD, RGCT and CT domains, with mGDP-bound and mGppNHp-bound CDC42 variants. Data shown in Figure 2D (Supplementary Figure S4) indicate that the substitution of two amino acids in the switch regions was not sufficient to largely impair the CDC42-C794 interaction. However, mGppNHp-bound, but not mGDP-bound CDC42 8xSW exhibited a drastic reduction (86-fold) in its binding affinity for C794. For mGDP-bound CDC42, introduction of SW mutations only slightly decreased the affinity of C794. The IQGAP2 C795 binding to the CDC42 switch regions was not impaired by neither 2x nor 8x mutants of CDC42 in mGppNHp-bound state. Interestingly, IQGAP2 C795 showed a slightly decreased binding to the mGDP-bound CDC42 2xSW mutant but no binding to the 8xSW mutant, a much different result than obtained for GRD2 binding alone. The data from real-time stopped-flow fluorescence spectrometry (Figure 2E and Figure S5) showed both IQGAPs associated with similar k_{obs} values, as observed in Figure 2D.

The next question addressed was to what extent CDC42 binding of IQGAP1 FL was affected by the switch region mutations. Therefore, endogenous IQGAP1 was pulled down from HEK293 lysates using GDP-bound and GppNHp-bound GST-CDC42 WT, 2xSW and 8xSW. As shown in Figure 2F, IQGAP1 binding to CDC42 did not change with two amino acid substitution of the switch regions but was disrupted with the eight mutations. These experiments support our kinetic and equilibrium measurements and clearly indicate that the switch regions are significant for the IQGAP1 interaction with both GDP-bound and GppNHp-bound CDC42.

Taken together, the presented data suggest a slightly different binding behavior of IQGAP1 and IQGAP2 variants for CDC42. Our results do not support the interacting mode between IQGAP and CDC42 based on the crystal structure [12] and the central role of the GRD in it [54] since the introduction of SW mutations of CDC42 clearly affected C795/C794 binding but only little the GRD binding. We, in contrary, propose that the interactions sites on IQGAP for complex formation with CDC42 GTP are clearly within the RGCT and might be different between IQGAP1 and IQGAP2.

2.3. Insert Helix Contributes to the Binding Affinity of CDC42 for IQGAP1 GRD

The question arises as which regions on CDC42 could bind GRD if we can now exclude the switch regions. A region/site that has attracted our attention is the IH of CDC42 for valid reasons. We have shown that IQGAPs bind to RAC-like and CDC42-like proteins but not to the other members of the RHO family [26] and the IH consistently is a highly variable region among the RHO GTPases (Figure 3A) [15]. Several CDC42-binding proteins, including RHOGDI1, p50GAP, FMNL2 and IQGAP2 have been shown to contact the IH [10,12,17,18,20]. Thus, mutational analysis of the CDC42 IH was performed, using four different single residue mutations and a quadruple mutation (Figure 3A and Table S1). Note that variable residues were replaced in CDC42 by the corresponding residues of RAC1. Most remarkably and in sharp contrast to the SW mutations (Figure 2), all IH mutations abolished GRD1-CDC42 interaction irrespective of the nucleotide-bound states of CDC42 (Figures 3B and S6), which underlines the central role of CDC42 IH in GRD binding. The scenario was rather different for C794, which binds mGDP-bound CDC42 with 3-fold and mGppNHp-bound CDC42 with 20-fold lower affinities (Figure 3B). These

In the GTP-bound CDC42, Q61 acts as a ‘catalytic residue’ that is involved in hydrogen bonding with a catalytic water molecule, an arginine finger of GAP and the γ -phosphate of GTP, initiating a nucleophilic attack that hydrolyzes GTP (Figure 4A) [18,65]. L61 does not, however, undergo these functionally critical hydrogen bonds but rather points towards protein surface without causing significant structural changes (Figure 4A). As a result, the substitution of Q61 by leucine drastically increases the binding affinity of IQGAPs for CDC42^{Q61L} GTP by up to 15-fold as was clearly demonstrated previously [5,26,51]. Despite this fact, many groups use this CDC42 variant for the interaction analysis of effectors, such as IQGAPs [12,54,56,57]. Thus, we revisited this issue and have comparatively analyzed the interaction of IQGAP1 GRD with CDC42^{Q61L} and CDC42^{wt} using fluorescence polarization and size exclusion chromatography (SEC). Equilibrium measurements shown in Figure 4B clearly revealed that the Q61L mutation results in a strong enhancement of GRD1 and GRD2 binding with the mGppNHp-bound CDC42, but not with mGDP-bound CDC42. The binding affinity of mGppNHp-bound CDC42^{Q61L} rises from a low affinity 186 μ M/69 μ M binding to a high 2.7 μ M/2.5 μ M binding for GRD1/GRD2, respectively (Figures 4B and S7). This is a change of 30–50-fold and might explain the huge differences of CDC42 interactions with GRD. Moreover, SEC analysis showed that GRD1 forms a 2:2 stoichiometry with CDC42^{wt} GppNHp but 2:1 stoichiometry with CDC42^{Q61L} GppNHp (Figure 4C–F). The latter is remarkably consistent with the previous reports on a high-affinity binding of IQGAP2 GRD2 with CDC42^{Q61L} GTP and 4:2 and 2:1 stoichiometry, respectively [12,54]. These findings verified the clear difference between CDC42^{wt} and CDC42^{Q61L} and how replacement of Q61 by L changes the binding properties (affinity and stoichiometry) of CDC42 interaction with IQGAP GRDs.

Chen et al. have reported that the Q61L mutation strengthen hydrogen bond interactions between CDC42 and the γ -phosphate of GTP [66]. Analyzing the Cdc42^{Q61L} GTP GRD2 structure, Ozdemir et al. proposed that CDC42 IH binding to the GAPex-domain induces allosteric changes in the RASGAP site, which in turn facilitate GRD dimerization, and enable the second CDC42^{Q61L} to bind to this site (yielding a 2:1 stoichiometry) [54]. Collectively, we recapitulate that CDC42^{Q61L} is not an ideal analog of CDC42^{wt} especially in studying the interaction of the downstream effectors. G12V and Q61L mutations of CDC42 cause GAP insensitivity leading to sustained hyperactivation of CDC42 [16,18,55,65,66]. Thus, we suggest CDC42^{wt} GppNHp and even CDC42^{G12V} GTP variants as more suitable species for the investigation of CDC42-effector interaction rather than CDC42^{Q61L} GTP.

2.5. GRD Lacks the Structural Fingerprints to Induce the GAP Activity

The structure of the RAS-RASGAP complex shows GAP-334 interacting predominantly with the switch regions of RAS [55]. Three regions (finger loop, FLR motif and helix α 7/variable loop) constitute structural fingerprints of the RASGAP p120 and neurofibromin that form critical RAS binding sites in order to apply an arginine finger into the active center of RAS [67,68]. Amino acid sequence analysis of these RASGAPs with the three IQGAP paralogs showed that major parts of these fingerprints are different in IQGAPs (Figure 5A). Moreover, the catalytic arginine is missing and there is instead a threonine (T1045 in IQGAP1; Figure 5A). Thus, it is quite understandable why IQGAP1 did not display RASGAP activities towards HRAS [60]. It is, however, known that GAPs specific for other members of the RAS superfamily use other catalytic residues than an arginine (reviewed in [69,70]).

We set out to examine a possible GAP activity of IQGAP1 GRD towards different RAS family GTPases. Figure 5B shows that IQGAP1 GRD is a pseudo-RASGAP domain with no obvious catalytic ability (orange bars). Earlier studies have shown that the substitution of the arginine finger of the RASGAPs to other amino acids completely abolishes their GAP activity [67,68]. Therefore, threonine 1046 of IQGAP1 GRD was replaced by an arginine and the impact of T1046R on the GTP hydrolysis of the eight RAS proteins was measured. Data shown in Figure 5B revealed no apparent GAP activities of IQGAP1 GRD^{T1046R} (green bars)

as expected for a RASGAP. These data suggest that IQGAPs, besides lacking an arginine finger, do not contain critical RAS-binding residues of the $\alpha 7$ /variable loop (Figure 5A).

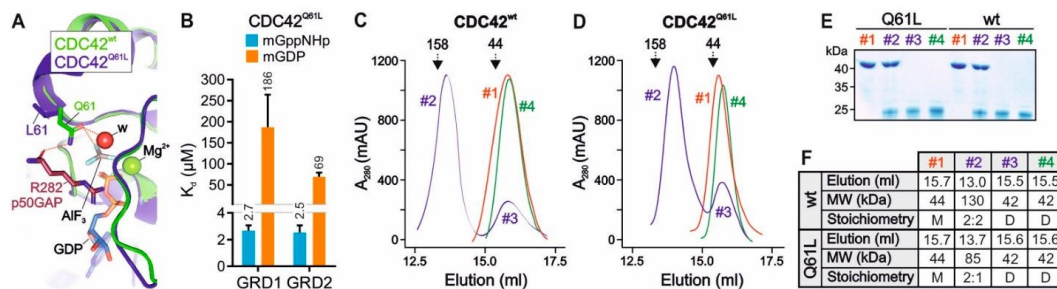


Figure 4. Comparative analysis of IQGAP1 GRD1 interaction with CDC42^{Q61L} and CDC42^{WT}. (A) Structural overlay of CDC42^{WT} GDP AIF₃ p50GAP (green; PDB: 1GRN) on CDC42^{Q61L} GTP IQGAP2 (blue; PDB: 5CJP) with the focus on Q61 hydrogen bonds (red dashed lines). GDP AIF₃ mimics the transition state of the GTP hydrolysis reaction and is coordinated with the magnesium ion (Mg²⁺) and the nucleophilic water molecule (w) and the arginine finger (R282) of p50GAP. Aluminum trifluoride (AlF₃) mimics the γ -phosphate of GTP in the transition state. In contrast to L61, Q61 is critical for the catalysis of the GTP hydrolysis reaction through three hydrogen bonds (see text). (B) Fluorescence polarization data of IQGAP GRD1 with CDC42 mGppNHp and CDC42 mGDP. (C–F) IQGAP GRD1 differently forms complexes with CDC42^{WT} and CDC42^{Q61L}, respectively, when applied on an analytical SEC. For this purpose, CDC42^{WT} GppNHp (C) or CDC42^{Q61L} GppNHp (D) were mixed with IQGAP1 GRD1 and SEC was performed on a Superdex 200 10/300 column using an ÄKTA purifier (flow rate of 0.5 mL/min, fraction volume of 0.5 mL) and a buffer, containing 30 mM Tris/HCl, pH 7.5, 150 mM NaCl, and 5 mM MgCl₂. The elution profiles represented one peak for the respective CDC42 proteins (#1), two peaks for the respective mixtures of respective CDC42 proteins with GRD (#2 and #3) and one peak for the GRD1 (#4). (E) Coomassie brilliant blue staining of the corresponding elution volumes indicated that only peaks #2 contain GRD1 complexes with CDC42^{WT} or CDC42^{Q61L}, respectively. Peaks #3 only contain the CDC42 proteins as compared to the peaks #1 and #4. (F) The SEC profiles of CDC42^{WT} and CDC42^{Q61L} are summarized for each peak regarding the elution volume, the molecular weight (MW) and the stoichiometry. M stands for monomeric and D for dimeric. The theoretical MWs of CDC42 (21.2 kDa) and GRD (43 kDa) were calculated using the ExPASy ProtParam tool. The presented MWs for each peak was calculated based on the calibration curve (aldolase 158 kDa and ovalbumin 44 kDa, respectively) and partition coefficient plot ($K_{av} = V_e - V_0 / V_c - V_0$) versus the logarithm of MWs; V_e : elution volume number; V_0 : void volume (8 mL); V_c : geometric column volume (24 mL)). Accordingly, peaks #2 correspond to a heterotetrameric complex between CDC42^{WT} GppNHp and GRD1 with a MW of 130 kDa, and a heterotrimeric complex of GRD and CDC42^{Q61L} GppNHp with a MW of 85 kDa.

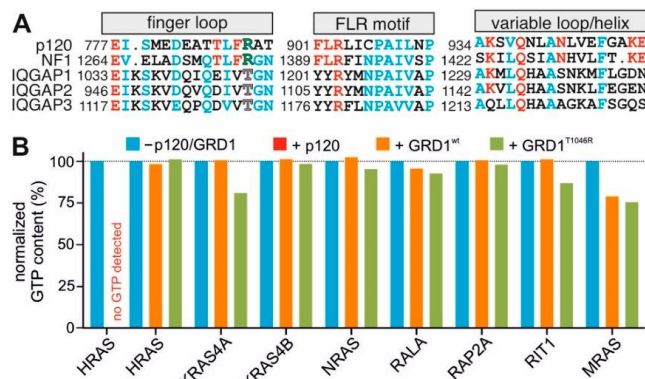


Figure 5. Deviation in RAS-binding residues in GRDs cause lack of RASGAP activity. **(A)** Sequence alignment of human RASGAPs p120, neurofibromin (NF1) and the three IQGAP paralogs highlights distinctive deviations in three signature motifs (grey boxes): the finger loop, FLR region and a7/variable loop. RAS-binding residues are shown in red and conserved residues in blue. The catalytic arginine (green) is substituted by threonine in IQGAPs. The numbers correspond to the amino acids of the respective proteins. **(B)** GTP hydrolysis of various RAS family GTPases was measured in the absence (blue) and in the presence of p120 GAP domain (red; positive control, where no GTP detected) or GRD1^{wt} (orange) and GRD1^{T1046R} (green). The GTP hydrolysis of the RAS proteins (10 μ M) was measured via HPLC and the GTP content normalized to 100% before adding p120 or GRD1, respectively, at 100 μ M concentrations and 1 min incubation time.

3. Material and Methods

3.1. Constructs

The pGEX4T1 encoding an N-terminal glutathione S-transferase (GST) fusion protein was used to overexpress human IQGAP1 (accession number P46940) GRD1 (aa 962–1345), C794 (aa 863–1657) and CT (aa 1576–1657); human IQGAP2 (accession number Q13576) GRD2 (aa 875–1246) and C795 (aa 780–1575); human IQGAP3 (accession number P60953) GRD3 (aa 942–1330); human CDC42 (accession number P60953; aa 1–178). All constructs and related variants are listed in Supplementary Table S1. For purification of these proteins, pGEX-4T1 constructs were transformed in *Escherichia coli* and proteins were isolated via affinity chromatography using a glutathione Sepharose column on a ÄKTA start protein purification system (Cytiva, US) [71]. GST-cleavage was carried out by incubation with thrombin (#T6884-1KU, Sigma Aldrich, Taufkirchen, Germany) at 4 °C until full digestion of the fusion protein. Quality of the proteins was checked via SDS-PAGE and Coomassie staining. CDC42 variants were further verified for their activity in HPLC by determining the amount of bound nucleotide [71]. Nucleotide free proteins were prepared by incubating the proteins with alkaline phosphatase (#P0762-250UN, Sigma Aldrich, Germany) and phosphodiesterase (#P3243-1VL, Sigma Aldrich, Taufkirchen, Germany) at 4 °C [71]. CDC42 variants were labelled with either GDP (#51060, Sigma Aldrich, Taufkirchen, Germany), GppNHp (#NU-401, Jena Bioscience, Jena, Germany), mant-GDP (#NU-204, Jena Bioscience, Jena, Germany) or mant-GppNHp (#NU-207, Jena Bioscience, Jena, Germany).

3.2. Circular Dichroism (CD) Spectrometry

Far-UV-CD spectroscopy of protein samples was performed on a JASCO J-715 CD spectropolarimeter (Jasco, Gross-Umstadt, Germany) using quartz cuvettes (Helma, Mühlheim, Germany) with 1 mm path length. Spectra were recorded at protein concentrations of 20 μ M CDC42 WT and variants in 1 mM NaPi buffer, pH 7.0 or 8 μ M IQGAP WT and variants in 12.5 mM TRIS/HCl pH 7.4, 37.5 mM NaCl, 1.25 mM MgCl₂, at 22 °C with instrument settings as follows: 0.1 nm step size, 50 nm min^{−1} scan speed, 1 nm

band with. Signal-to-noise ratio was improved by accumulation of 10 scans per sample. The mean residue ellipticity $[\theta]_{\text{mrw}}$ in $\text{deg}\cdot\text{cm}^2\cdot\text{dmol}^{-1}$ was calculated from the equation $[\theta]_{\text{mrw}} = (\theta_{\text{obs}} \times \text{MRW}) / (c \times d \times 10)$, with θ_{obs} , observed ellipticity (in degrees); c , concentration (in g/mL); d , cell path length (in cm); MRW (mean residue weight), molecular weight divided by number of peptide bonds.

3.3. Cell Culture and Lysis

HEK293 cells were cultured in Dulbecco's Modified Eagle's Medium (DMEM) (#12320032, Thermo Fisher, Waltham, CA, USA) supplemented with 10 % FBS and 1% Penicillin/Streptomycin in an exponential growth phase at 37 °C with 5% CO₂ and 95% humidity. Lysis was performed by washing the cells with PBS^{−/−} and scraping them down with FISH buffer (50 mM Tris/HCl pH 7.5, 100 mM NaCl, 2 mM MgCl₂, 10% glycerol, 20 mM β-glycerolphosphate, 1 mM Na₃VO₄, 1× protease inhibitor cocktail and 1% IGPAL). Cells were lysed for 10 min on ice and then centrifuged for 10 min at 15,000× *g*. Supernatant was used for affinity pull down measurements.

3.4. GST-Pull-Down

The pull-down of endogenously expressed proteins with purified GST-fused proteins was performed using glutathione agarose beads (#745500.10, Macherey-Nagel, Düren, Germany). Beads were coupled to the GST-fused protein for one hour at 4 °C while mixing and centrifuged for 5 min at 500× *g*. Excess protein was removed by three washing steps. Coupled beads were incubated with HEK293 lysate for one hour at 4 °C on a rotor and again washed 3 times. In the final step, beads were mixed with 1× Laemmli buffer and proteins were denatured at 95 °C for 5 min. Samples were evaluated via SDS-PAGE and western blotting using anti-GST (own antibody, mouse) and anti-IQGAP1 (NBP1-06529, Novus, Wiesbaden Nordenstadt, Germany, rabbit) primary antibodies and secondary antibodies: IRDye® 800 CW anti-Rabbit IgG and IRDye® 680 RD anti-Mouse IgG from LiCor. Values were analyzed by using multiple t test analysis in GraphPad Prism 6 (one unpaired t test per row, fewer assumptions by analyzing each row individually).

3.5. Fluorescence Stopped-Flow Spectrometry

All kinetic parameters (k_{obs}) evaluated in this study were analyzed using a previously described kinetic analysis protocol [72]. The kinetic parameters were monitored with a stopped-flow apparatus (HiTech Scientific, Applied Photophysics SX20, Leatherhead, UK). The excitation was set for mant at the wavelength of 362 nm, and emission was detected through a cutoff filter of 408 nm. The observed rate constants were calculated by fitting the data as single exponential decay using GraFit program.

3.6. Fluorescence Polarization

To determine the dissociation constant K_d of direct protein–protein interaction (including weak interactions) fluorescence polarization analysis was performed in a Fluoromax 4 fluorimeter (Horiba Scientific, Loos, France). Here, 1 μM mant-GDP or mant-GppNHp labelled CDC42 proteins were prepared in a total volume of 170 μL in a three directional cuvette. Measurement was performed in polarization mode versus time with an excitation wavelength of 360 nm (slit width: 8 μm) and an emission wavelength of 450 nm (slit width: 10 μm). K_d values were calculated in GraFit 5 by fitting the concentration-dependent binding curve using a quadratic ligand binding equation.

3.7. GTP Hydrolysis Measurements

GTP hydrolysis rates of a set of different GTPases in presence and absence of GRD1 and its T1046R mutant containing the arginine residue were measured by high-performance liquid chromatography (HPLC) analysis. GTP-bound HRAS in presence of p120 GAP was used as control. Then, 10 μM of each GTPase in the GTP bound state was injected into the HPLC mixing chamber after 1 min of incubation in absence (intrinsic) and presence

(GAP stimulated) of 100 μ M of GRD1 WT and T1046R variant. The GTP content for each measurement was calculated by dividing the intensity of the GTP detection peak to the sum of the intensities of the GTP plus GDP peaks.

4. Conclusions

The exact binding site of the IQGAP GRD and CDC42 is still not completely clear to date. This article provides evidence that the IQGAP GRD does not act as the primary or leading effector binding domain of CDC42 and counterevidence the role of IQGAP GRD in CDC42 binding deduced from a crystal structure of an IQGAP2 GRD2-CDC42Q61L GTP complex. We could show that the GRD does not bind to CDC42 in a nucleotide-dependent manner and that even multiple mutations of the suggested main residues of interaction do not abolish the direct physical interaction in cells and under cell-free conditions. Our data support the binding model of Ozdemir et al. [54] and propose the CDC42 IH as a key binding site for GRD. Furthermore, we shed light once more into the interaction difference of CDC42^{wt} and CDC42^{Q61L} that might be one of the main reasons of the discrepancies in the published data as discussed above. By our comparative measurements of IQGAP1 and IQGAP2 variants, we found differences in their binding strength and specificity towards CDC42^{wt} but also towards various CDC42 variants. Our efforts to investigate also IQGAP3 were so far not successful. The exact binding residues and interaction sites of IQGAP1 and IQGAP2 with the switch regions of CDC42 will still remain to be identified in the future.

Supplementary Materials: The following supporting information can be downloaded at: <https://www.mdpi.com/article/10.3390/ijms23168842/s1>.

Author Contributions: M.R.A. conceived and coordinated the study; N.M., S.P., F.B., N.S.K.J. and O.H.F.K. designed, performed and analyzed the experiments; N.M., L.G. and D.W. performed the CD experiments; R.D. performed structural analysis; N.M. and M.R.A. directed the experiments, analyzed the data and wrote the paper. All authors have read and agreed to the published version of the manuscript.

Funding: This study was supported by the European Network on Noonan Syndrome and Related Disorders (NSEuroNet, grant number: 01GM1621B to N.S.K.J. and M.R.A.), the German Research Foundation (Deutsche Forschungsgemeinschaft or DFG) through the International Research Training Group ‘Intra- and interorgan communication of the cardiovascular system’ (grant number: IRTG 1902-p6 701158241 to F.B. and M.R.A.), the German Federal Ministry of Education and Research (BMBF)—German Network of RASopathy Research (GeNeRARE, grant numbers: 01GM1902C to N.M. and M.R.A.), the Research Committee of the Medical Faculty of the Heinrich Heine University (grant number: 9772764 to S.P. and M.R.A) and the Operational Program Integrated Infrastructure ERDF: Open scientific community for modern interdisciplinary research in medicine (OPENMED; grant number: ITMS2014+: 313011V455 to R.D.).

Institutional Review Board Statement: Not applicable.

Informed Consent Statement: Not applicable.

Data Availability Statement: All the data are in the manuscript.

Acknowledgments: We thank Roland Piekorz and Kotsene Loumonvi for support and discussions.

Conflicts of Interest: The authors declare no conflict of interest.

References

1. Ahmadian, M.R.; Jaiswal, M.; Fansa, E.K.; Dvorsky, R. New insight into the molecular switch mechanism of human Rho family proteins: Shifting a paradigm. *Biol. Chem.* **2013**, *394*, 89–95. [CrossRef]
2. Mosaddeghzadeh, N.; Ahmadian, M.R. The RHO Family GTPases: Mechanisms of Regulation and Signaling. *Cells* **2021**, *10*, 1831. [CrossRef] [PubMed]
3. Abdul-Manan, N.; Aghazadeh, B.; Liu, G.A.; Majumdar, A.; Ouerfelli, O.; Simlnovitch, K.A.; Rosen, M.K. Structure of Cdc42 in complex with the GTPase-binding domain of the “Wiskott-Aldrich syndrome” protein. *Nature* **1999**, *399*, 379–383. [CrossRef] [PubMed]

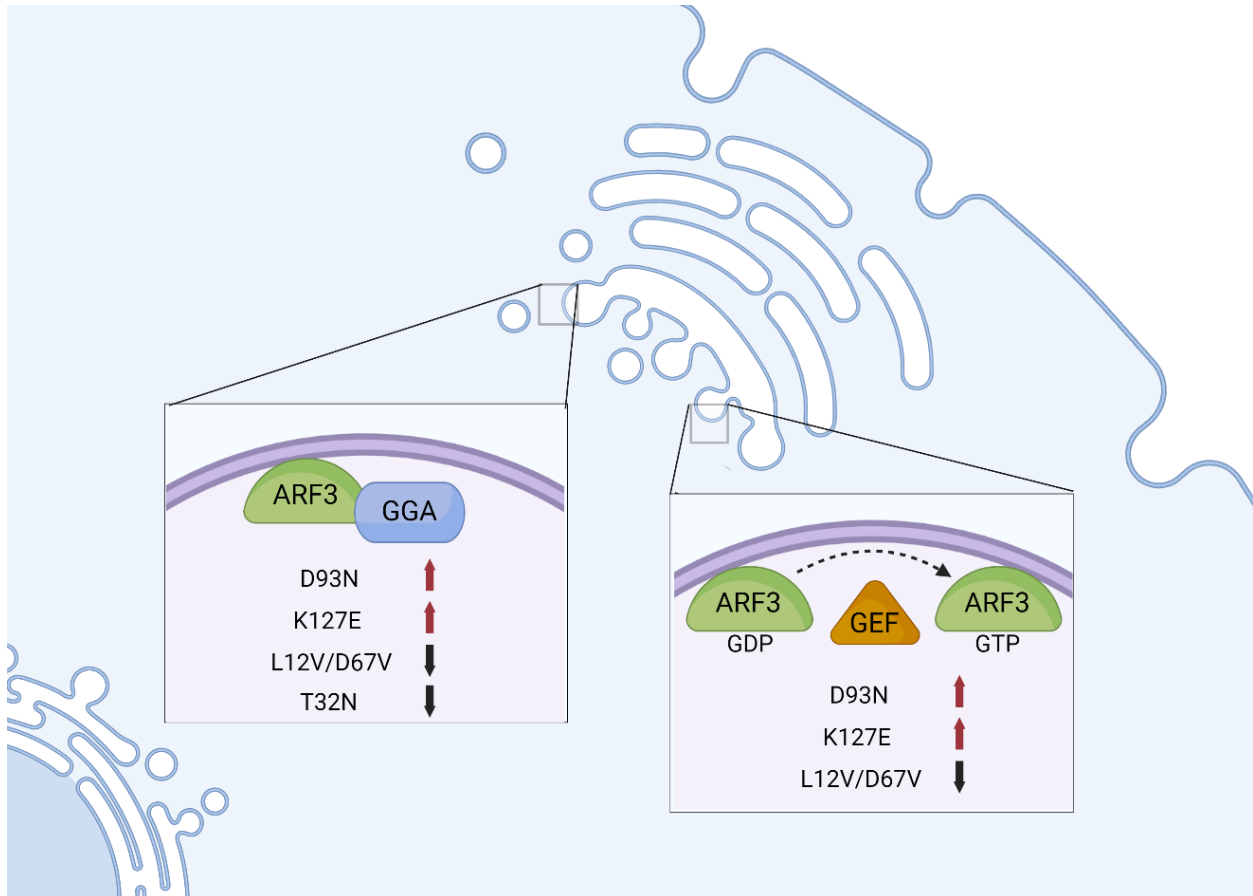
4. Mott, H.R.; Owen, D.; Nietlispach, D.; Lowe, P.N.; Manser, E.; Lim, L.; Laue, E.D. Structure of the small G protein Cdc42 bound to the GTPase-binding domain of ACK. *Nature* **1999**, *399*, 384–388. [\[CrossRef\]](#)
5. Nouri, K.; Timson, D.J.; Ahmadian, M.R. New model for the interaction of IQGAP1 with CDC42 and RAC1. *Small GTPases* **2020**, *11*, 16–22. [\[CrossRef\]](#)
6. Morreale, A.; Venkatesan, M.; Mott, H.R.; Owen, D.; Nietlispach, D.; Lowe, P.N.; Laue, E.D. Structure of Cdc42 bound to the GTPase binding domain of PAK. *Nat. Struct. Biol.* **2000**, *7*, 384–388. [\[CrossRef\]](#)
7. Dvorsky, R.; Ahmadian, M.R. Always look on the bright site of Rho: Structural implications for a conserved intermolecular interface. *EMBO Rep.* **2004**, *5*, 1130–1136. [\[CrossRef\]](#)
8. Dvorsky, R.; Blumenstein, L.; Vetter, I.R.; Ahmadian, M.R. Structural Insights into the Interaction of ROCK1 with the Switch Regions of RhoA. *J. Biol. Chem.* **2004**, *279*, 7098–7104. [\[CrossRef\]](#) [\[PubMed\]](#)
9. Hemsath, L.; Dvorsky, R.; Fiegen, D.; Carlier, M.F.; Ahmadian, M.R. An electrostatic steering mechanism of Cdc42 recognition by Wiskott-Aldrich syndrome proteins. *Mol. Cell* **2005**, *20*, 313–324. [\[CrossRef\]](#)
10. Rose, R.; Weyand, M.; Lammers, M.; Ishizaki, T.; Ahmadian, M.R.; Wittinghofer, A. Structural and mechanistic insights into the interaction between Rho and mammalian Dia. *Nature* **2005**, *435*, 513–518. [\[CrossRef\]](#)
11. Hall, A. Rho family GTPases. In *Biochemical Society Transactions*; Portland Press: London, UK, 2012; Volume 40, pp. 1378–1382.
12. LeCour, L.; Boyapati, V.K.; Liu, J.; Li, Z.; Sacks, D.B.; Worthylake, D.K. The Structural Basis for Cdc42-Induced Dimerization of IQGAPs. *Structure* **2016**, *24*, 1499–1508. [\[CrossRef\]](#) [\[PubMed\]](#)
13. Owen, D.; Mott, H.R. CRIB effector disorder: Exquisite function from chaos. *Biochem. Soc. Trans.* **2018**, *46*, 1289–1302. [\[CrossRef\]](#) [\[PubMed\]](#)
14. Mott, H.R.; Owen, D. Structures of Ras superfamily effector complexes: What have we learnt in two decades? *Crit. Rev. Biochem. Mol. Biol.* **2015**, *50*, 85–133. [\[CrossRef\]](#) [\[PubMed\]](#)
15. Thapar, R.; Karnoub, A.E.; Campbell, S.L. Structural and Biophysical Insights into the Role of the Insert Region in Rac1 Function. *Biochemistry* **2002**, *41*, 3875–3883. [\[CrossRef\]](#) [\[PubMed\]](#)
16. Haspel, N.; Jang, H.; Nussinov, R. Active and Inactive Cdc42 Differ in Their Insert Region Conformational Dynamics. *Biophys. J.* **2021**, *120*, 306. [\[CrossRef\]](#) [\[PubMed\]](#)
17. Wu, W.J.; Leonard, D.A.; Cerione, R.A.; Manor, D. Interaction between Cdc42Hs and RhoGDI Is Mediated through the Rho Insert Region. *J. Biol. Chem.* **1997**, *272*, 26153–26158. [\[CrossRef\]](#)
18. Nassar, N.; Hoffman, G.R.; Manor, D.; Clardy, J.C.; Cerione, R.A. Structures of Cdc42 bound to the active and catalytically compromised forms of Cdc42GAP. *Nat. Struct. Biol.* **1998**, *5*, 1047–1052. [\[CrossRef\]](#) [\[PubMed\]](#)
19. Lammers, M.; Meyer, S.; Köhlmann, D.; Wittinghofer, A. Specificity of Interactions between mDia Isoforms and Rho Proteins. *J. Biol. Chem.* **2008**, *283*, 35236–35246. [\[CrossRef\]](#) [\[PubMed\]](#)
20. Kühn, S.; Erdmann, C.; Kage, F.; Block, J.; Schwenkmezger, L.; Steffen, A.; Rottner, K.; Geyer, M. The structure of FMNL2–Cdc42 yields insights into the mechanism of lamellipodia and filopodia formation. *Nat. Commun.* **2015**, *6*, 7088. [\[CrossRef\]](#) [\[PubMed\]](#)
21. Walker, S.J.; Brown, H.A. Specificity of Rho insert-mediated activation of phospholipase D1. *J. Biol. Chem.* **2002**, *277*, 26260–26267. [\[CrossRef\]](#) [\[PubMed\]](#)
22. Karnoub, A.E.; Der, C.J.; Campbell, S.L. The Insert Region of Rac1 Is Essential for Membrane Ruffling but Not Cellular Transformation. *Mol. Cell. Biol.* **2001**, *21*, 2847–2857. [\[CrossRef\]](#) [\[PubMed\]](#)
23. Zong, H.; Kaibuchi, K.; Quilliam, L.A. The Insert Region of RhoA Is Essential for Rho Kinase Activation and Cellular Transformation. *Mol. Cell. Biol.* **2001**, *21*, 5287–5298. [\[CrossRef\]](#) [\[PubMed\]](#)
24. Fukata, M.; Watanabe, T.; Noritake, J.; Nakagawa, M.; Yamaga, M.; Kuroda, S.; Matsuura, Y.; Iwamatsu, A.; Perez, F.; Kaibuchi, K. Rac1 and Cdc42 capture microtubules through IQGAP1 and CLIP-170. *Cell* **2002**, *109*, 873–885. [\[CrossRef\]](#)
25. Watanabe, T.; Wang, S.; Noritake, J.; Sato, K.; Fukata, M.; Takefuji, M.; Nakagawa, M.; Izumi, N.; Akiyama, T.; Kaibuchi, K. Interaction with IQGAP1 links APC to Rac1, Cdc42, and actin filaments during cell polarization and migration. *Dev. Cell* **2004**, *7*, 871–883. [\[CrossRef\]](#) [\[PubMed\]](#)
26. Mosaddeghzadeh, N.; Nouri, K.; Krumbach, O.H.F.; Amin, E.; Dvorsky, R.; Ahmadian, M.R. Selectivity determinants of rho gtpase binding to iqgaps. *Int. J. Mol. Sci.* **2021**, *22*, 12596. [\[CrossRef\]](#) [\[PubMed\]](#)
27. Roy, M.; Li, Z.; Sacks, D.B. IQGAP1 Binds ERK2 and Modulates Its Activity. *J. Biol. Chem.* **2004**, *279*, 17329–17337. [\[CrossRef\]](#) [\[PubMed\]](#)
28. Roy, M.; Li, Z.; Sacks, D.B. IQGAP1 Is a Scaffold for Mitogen-Activated Protein Kinase Signaling. *Mol. Cell. Biol.* **2005**, *25*, 7940. [\[CrossRef\]](#) [\[PubMed\]](#)
29. Ren, J.G.; Li, Z.; Sacks, D.B. IQGAP1 modulates activation of B-Raf. *Proc. Natl. Acad. Sci. USA* **2007**, *104*, 10465–10469. [\[CrossRef\]](#) [\[PubMed\]](#)
30. Benseñor, L.B.; Kan, H.M.; Wang, N.; Wallrabe, H.; Davidson, L.A.; Cai, Y.; Schafer, D.A.; Bloom, G.S. IQGAP1 regulates cell motility by linking growth factor signaling to actin assembly. *J. Cell Sci.* **2007**, *120*, 658–669. [\[CrossRef\]](#) [\[PubMed\]](#)
31. Le Clainche, C.; Schlaepfer, D.; Ferrari, A.; Klingauf, M.; Grohmanova, K.; Veligodskiy, A.; Didry, D.; Le, D.; Egile, C.; Carlier, M.F.; et al. IQGAP1 stimulates actin assembly through the N-wasp-Arp2/3 pathway. *J. Biol. Chem.* **2007**, *282*, 426–435. [\[CrossRef\]](#)
32. Kaur, R.; Yuan, X.; Lu, M.L.; Balk, S.P. Increased PAK6 expression in prostate cancer and identification of PAK6 associated proteins. *Prostate* **2008**, *68*, 1510–1516. [\[CrossRef\]](#)

33. Usatyuk, P.V.; Gorshkova, I.A.; He, D.; Zhao, Y.; Kalari, S.K.; Garcia, J.G.N.; Natarajan, V. Phospholipase D-mediated Activation of IQGAP1 through Rac1 regulates hyperoxia-induced p47phox translocation and reactive oxygen species generation in lung endothelial cells. *J. Biol. Chem.* **2009**, *284*, 15339–15352. [\[CrossRef\]](#) [\[PubMed\]](#)
34. Pelikan-Conchaudron, A.; Le Clainche, C.; Didry, D.; Carlier, M.F. The IQGAP1 protein is a calmodulin-regulated barbed end capper of actin filaments: Possible implications in its function in cell migration. *J. Biol. Chem.* **2011**, *286*, 35119–35128. [\[CrossRef\]](#) [\[PubMed\]](#)
35. Pudewell, S.; Wittich, C.; Kazeminejad, N.S.; Bazgir, F.; Ahmadian, M.R. Accessory proteins of the RAS-MAPK pathway: Moving from the side line to the front line. *Commun. Biol.* **2021**, *4*, 696. [\[CrossRef\]](#) [\[PubMed\]](#)
36. Watanabe, T.; Wang, S.; Kaibuchi, K. IQGAPs as Key Regulators of Actin-cytoskeleton Dynamics Mini-review and Review. *Cell Struct. Funct.* **2015**, *40*, 69–77. [\[CrossRef\]](#)
37. Abel, A.M.; Schuld, K.M.; Rajasekaran, K.; Hwang, D.; Riese, M.J.; Rao, S.; Thakar, M.S.; Malarkannan, S. IQGAP1: Insights into the function of a molecular puppeteer. *Mol. Immunol.* **2015**, *65*, 336–349. [\[CrossRef\]](#) [\[PubMed\]](#)
38. Hedman, A.C.; Smith, J.M.; Sacks, D.B. The biology of IQGAP proteins: Beyond the cytoskeleton. *EMBO Rep.* **2015**, *16*, 427–446. [\[CrossRef\]](#) [\[PubMed\]](#)
39. Smith, J.M.; Hedman, A.C.; Sacks, D.B. IQGAPs choreograph cellular signaling from the membrane to the nucleus. *Trends Cell Biol.* **2015**, *25*, 171–184. [\[CrossRef\]](#)
40. Choi, S.; Anderson, R.A. IQGAP1 is a phosphoinositide effector and kinase scaffold. *Adv. Biol. Regul.* **2016**, *60*, 29–35. [\[CrossRef\]](#) [\[PubMed\]](#)
41. Tanos, B.E.; Yeaman, C.; Rodriguez-Boulant, E. An emerging role for IQGAP1 in tight junction control. *Small GTPases* **2018**, *9*, 375–383. [\[CrossRef\]](#) [\[PubMed\]](#)
42. Nussinov, R.; Zhang, M.; Tsai, C.J.; Jang, H. Calmodulin and IQGAP1 activation of PI3K α and Akt in KRAS, HRAS and NRAS-driven cancers. *Biochim. Biophys. Acta Mol. Basis Dis.* **2018**, *1864*, 2304–2314. [\[CrossRef\]](#) [\[PubMed\]](#)
43. White, C.D.; Li, Z.; Dillon, D.A.; Sacks, D.B. IQGAP1 Protein Binds Human Epidermal Growth Factor Receptor 2 (HER2) and Modulates Trastuzumab Resistance. *J. Biol. Chem.* **2011**, *286*, 29734. [\[CrossRef\]](#) [\[PubMed\]](#)
44. Liu, C.; Billadeau, D.D.; Abdelhakim, H.; Leof, E.; Kaibuchi, K.; Bernabeu, C.; Bloom, G.S.; Yang, L.; Boardman, L.; Shah, V.H.; et al. IQGAP1 suppresses T β RII-mediated myofibroblastic activation and metastatic growth in liver. *J. Clin. Invest.* **2013**, *123*, 1138–1156. [\[CrossRef\]](#) [\[PubMed\]](#)
45. Jameson, K.L.; Mazur, P.K.; Zehnder, A.M.; Zhang, J.; Zarnegar, B.; Sage, J.; Khavari, P.A. IQGAP1 scaffold-kinase interaction blockade selectively targets RAS-MAP kinase-driven tumors. *Nat. Med.* **2013**, *19*, 626–630. [\[CrossRef\]](#) [\[PubMed\]](#)
46. Choi, S.; Hedman, A.C.; Sayedyahosseini, S.; Thapa, N.; Sacks, D.B.; Anderson, R.A. Agonist-stimulated phosphatidylinositol-3,4,5-trisphosphate generation by scaffolded phosphoinositide kinases. *Nat. Cell Biol.* **2016**, *18*, 1324–1335. [\[CrossRef\]](#) [\[PubMed\]](#)
47. Peng, X.; Wang, T.; Gao, H.; Yue, X.; Bian, W.; Mei, J.; Zhang, Y. The interplay between IQGAP1 and small GTPases in cancer metastasis. *Biomed. Pharmacother.* **2021**, *135*, 111243. [\[CrossRef\]](#)
48. Wei, T.; Lambert, P.F. Role of IQGAP1 in Carcinogenesis. *Cancers* **2021**, *13*, 3940. [\[CrossRef\]](#)
49. Rotoli, D.; Díaz-Flores, L.; Gutiérrez, R.; Morales, M.; Ávila, J.; Martín-Vasallo, P. AmotL2, IQGAP1, and FKBP51 Scaffold Proteins in Glioblastoma Stem Cell Niches. *J. Histochem. Cytochem.* **2022**, *70*, 9–16. [\[CrossRef\]](#)
50. Elliott, S.F. Biochemical analysis of the interactions of IQGAP1 C-terminal domain with CDC42. *World J. Biol. Chem.* **2012**, *3*, 53. [\[CrossRef\]](#)
51. Nouri, K.; Fansa, E.K.; Amin, E.; Dvorsky, R.; Gremer, L.; Willbold, D.; Schmitt, L.; Timson, D.J.; Ahmadian, M.R. IQGAP1 interaction with RHO family proteins revisited kinetic and equilibrium evidence for multiple distinct binding sites. *J. Biol. Chem.* **2016**, *291*, 26364–26376. [\[CrossRef\]](#)
52. Swart-Mataraza, J.M.; Li, Z.; Sacks, D.B. IQGAP1 is a component of Cdc42 signaling to the cytoskeleton. *J. Biol. Chem.* **2002**, *277*, 24753–24763. [\[CrossRef\]](#) [\[PubMed\]](#)
53. Li, R.; Debreceni, B.; Jia, B.; Gao, Y.; Tigyi, G.; Zheng, Y. Localization of the PAK1-, WASP-, and IQGAP1-specifying regions of Cdc42. *J. Biol. Chem.* **1999**, *274*, 29648–29654. [\[CrossRef\]](#) [\[PubMed\]](#)
54. Sila Ozdemir, E.; Jang, H.; Gursoy, A.; Keskin, O.; Li, Z.; Sacks, D.B.; Nussinov, R. Unraveling the molecular mechanism of interactions of the Rho GTPases Cdc42 and Rac1 with the scaffolding protein IQGAP2. *J. Biol. Chem.* **2018**, *293*, 3685–3699. [\[CrossRef\]](#) [\[PubMed\]](#)
55. Scheffzek, K.; Ahmadian, M.R.; Kabsch, W.; Wiesmüller, L.; Lautwein, A.; Schmitz, F.; Wittinghofer, A. The Ras-RasGAP complex: Structural basis for GTPase activation and its loss in oncogenic ras mutants. *Science* **1997**, *277*, 333–338. [\[CrossRef\]](#) [\[PubMed\]](#)
56. Owen, D.; Campbell, L.J.; Littlefield, K.; Evetts, K.A.; Li, Z.; Sacks, D.B.; Lowe, P.N.; Mott, H.R. The IQGAP1-Rac1 and IQGAP1-Cdc42 interactions: Interfaces differ between the complexes. *J. Biol. Chem.* **2008**, *283*, 1692–1704. [\[CrossRef\]](#)
57. Kurella, V.B.; Richard, J.M.; Parke, C.L.; LeCour, L.F.; Bellamy, H.D.; Worthylake, D.K. Crystal structure of the GTPase-activating protein-related domain from IQGAP1. *J. Biol. Chem.* **2009**, *284*, 14857–14865. [\[CrossRef\]](#)
58. Gorisse, L.; Li, Z.; Wagner, C.D.; Worthylake, D.K.; Zappacosta, F.; Hedman, A.C.; Annan, R.S.; Sacks, D.B. Ubiquitination of the scaffold protein IQGAP1 diminishes its interaction with and activation of the Rho GTPase CDC42. *J. Biol. Chem.* **2020**, *295*, 4822–4835. [\[CrossRef\]](#)

59. McCallum, S.J.; Wu, W.J.; Cerione, R.A. Identification of a putative effector for Cdc42Hs with high sequence similarity to the RasGAP-related protein IQGAP1 and a Cdc42Hs binding partner with similarity to IQGAP2. *J. Biol. Chem.* **1996**, *271*, 21732–21737. [\[CrossRef\]](#)
60. Hart, M.J.; Callow, M.G.; Souza, B.; Polakis, P. IQGAP1, a calmodulin-binding protein with a rasGAP-related domain, is a potential effector for cdc42Hs. *EMBO J.* **1996**, *15*, 2997–3005. [\[CrossRef\]](#)
61. Zhang, B.; Chernoff, J.; Zheng, Y. Interaction of Rac1 with GTPase-activating proteins and putative effectors. A comparison with Cdc42 and RhoA. *J. Biol. Chem.* **1998**, *273*, 8776–8782. [\[CrossRef\]](#)
62. Kuroda, S.; Fukata, M.; Nakagawa, M.; Fujii, K.; Nakamura, T.; Ookubo, T.; Izawa, I.; Nagase, T.; Nomura, N.; Tani, H.; et al. Cdc42 and Rac1 Regulate the Interaction of IQGAP1 with β^2 -Catenin. *J. Biol. Chem.* **1999**, *274*, 26044–26050. [\[CrossRef\]](#)
63. Grohmanova, K.; Schlaepfer, D.; Hess, D.; Gutierrez, P.; Beck, M.; Kroschewski, R. Phosphorylation of IQGAP1 modulates its binding to Cdc42, revealing a new type of Rho-GTPase regulator. *J. Biol. Chem.* **2004**, *279*, 48495–48504. [\[CrossRef\]](#) [\[PubMed\]](#)
64. Mataraza, J.M.; Briggs, M.W.; Li, Z.; Frank, R.; Sacks, D.B. Identification and characterization of the Cdc42-binding site of IQGAP1. *Biochem. Biophys. Res. Commun.* **2003**, *305*, 315–321. [\[CrossRef\]](#)
65. Scheffzek, K.; Ahmadian, M.R.; Wittinghofer, A. GTPase-activating proteins: Helping hands to complement an active site. *Trends Biochem. Sci.* **1998**, *23*, 257–262. [\[CrossRef\]](#)
66. Chen, S.; Shu, L.; Zhao, R.; Zhao, Y. Molecular dynamics simulations reveal the activation mechanism of mutations G12V and Q61L of Cdc42. *Proteins Struct. Funct. Bioinform.* **2022**, *90*, 1376–1389. [\[CrossRef\]](#)
67. Ahmadian, M.R.; Stege, P.; Scheffzek, K.; Wittinghofer, A. Confirmation of the arginine-finger hypothesis for the GAP-stimulated GTP-hydrolysis reaction of Ras. *Nat. Struct. Biol.* **1997**, *4*, 686–689. [\[CrossRef\]](#) [\[PubMed\]](#)
68. Ahmadian, M.R.; Kiel, C.; Stege, P.; Scheffzek, K. Structural fingerprints of the Ras-GTPase activating proteins neurofibromin and p120GAP. *J. Mol. Biol.* **2003**, *329*, 699–710. [\[CrossRef\]](#)
69. Scheffzek, K.; Shivalingaiah, G. Ras-specific gtpase-activating proteins— structures, mechanisms, and interactions. *Cold Spring Harb. Perspect. Med.* **2019**, *9*, a031500. [\[CrossRef\]](#)
70. Scheffzek, K.; Ahmadian, M.R. GTPase activating proteins: Structural and functional insights 18 years after discovery. *Cell. Mol. Life Sci.* **2005**, *62*, 3014–3038. [\[CrossRef\]](#)
71. Jaiswal, M.; Dubey, B.N.; Koessmeier, K.T.; Gremer, L.; Ahmadian, M.R. Biochemical assays to characterize Rho GTPases. *Methods Mol. Biol.* **2012**, *827*, 37–58. [\[CrossRef\]](#)
72. Hemsath, L.; Ahmadian, M.R. Fluorescence approaches for monitoring interactions of Rho GTPases with nucleotides, regulators, and effectors. *Methods* **2005**, *37*, 173–182. [\[CrossRef\]](#) [\[PubMed\]](#)

Chapter 9

Dominant ARF3 variants disrupt Golgi integrity and cause a neurodevelopmental disorder recapitulated in zebrafish



Status: published in Nature Communications, 11th November 2022

Impact factor: 17.69

Contribution: 5 %

Stopped-flow measurements and intrinsic nucleotide exchange assay, intrinsic GTP hydrolysis assay, discussion.


Article

Dominant *ARF3* variants disrupt Golgi integrity and cause a neurodevelopmental disorder recapitulated in zebrafish

Received: 2 July 2021

Accepted: 24 October 2022

Published online: 11 November 2022

 Check for updates

Giulia Fasano^{1,20}, Valentina Muto^{1,20}, Francesca Clementina Radio^{1,20}, Martina Venditti¹, Niloufar Mosaddeghzadeh², Simona Coppola³, Graziamaria Paradisi^{1,4}, Erika Zara^{1,5}, Farhad Bazgir², Alban Ziegler^{6,7}, Giovanni Chillemi^{4,8}, Lucia Bertuccini⁹, Antonella Tinari¹⁰, Annalisa Vetro¹¹, Francesca Pantaleoni¹, Simone Pizzi¹, Libenzio Adrian Conti¹², Stefania Petrini¹², Alessandro Bruselles¹³, Ingrid Guarnetti Prandi⁴, Cecilia Mancini¹, Balasubramanian Chandramouli¹⁴, Magalie Barth⁷, Céline Bris^{6,7}, Donatella Milani¹⁵, Angelo Selicorni¹⁶, Marina Macchiaiolo¹, Michaela V. Gonfiantini¹, Andrea Bartuli¹, Riccardo Mariani¹⁷, Cynthia J. Curry¹⁸, Renzo Guerrini¹¹, Anne Slavotinek¹⁸, Maria Iascone¹⁹, Bruno Dallapiccola¹, Mohammad Reza Ahmadian², Antonella Lauri¹✉ & Marco Tartaglia¹✉

Vesicle biogenesis, trafficking and signaling *via* Endoplasmic reticulum-Golgi network support essential developmental processes and their disruption lead to neurodevelopmental disorders and neurodegeneration. We report that de novo missense variants in *ARF3*, encoding a small GTPase regulating Golgi dynamics, cause a developmental disease in humans impairing nervous system and skeletal formation. Microcephaly-associated *ARF3* variants affect residues within the guanine nucleotide binding pocket and variably perturb protein stability and GTP/GDP binding. Functional analysis demonstrates variably disruptive consequences of *ARF3* variants on Golgi morphology, vesicles assembly and trafficking. Disease modeling in zebrafish validates further the dominant behavior of the mutants and their differential impact on brain and body plan formation, recapitulating the variable disease expression. In-depth *in vivo* analyses traces back impaired neural precursors' proliferation and planar cell polarity-dependent cell movements as the earliest detectable effects. Our findings document a key role of *ARF3* in Golgi function and demonstrate its pleiotropic impact on development.

The Golgi apparatus is a polarized, membrane network-built organelle organized as a series of flattened, stacked pouches (*cisternae*) held together by matrix proteins and microtubules and structured into the *cis* and *trans*-Golgi compartments. It is responsible for transporting, modifying, and packaging proteins and lipids into vesicles for their

targeted delivery^{1–4}. Golgi also provides signaling platforms for the regulation of a wide range of cellular processes (e.g., cell polarity, stress response, and mitosis) suggesting a role as a cell sensor and regulator similarly to other organelles, which ultimately orchestrates development^{4–6}. Golgi function is highly depending upon its rapid

A full list of affiliations appears at the end of the paper. ✉ e-mail: antonella.lauri@opbg.net; marco.tartaglia@opbg.net

structural remodeling in response to different physiological stimuli, which is attained via tightly regulated processes involving ribbon disassembly, tubulovesicular conversion as well as stacks repositioning^{4,7}. Of note, stimulus-dependent Golgi repositioning in the apical radial glia precursors is crucial to maintain stem cell identity, likely controlling polarized trafficking during corticogenesis⁸.

In the last years, several Mendelian disorders have causally been related to the defective or aberrant function of components of the transport machinery⁹. In particular, disruption of Golgi organization underlies several diseases, most of which share altered neurodevelopment and early-onset neurodegeneration^{10–12}. In these disorders, collectively named “Golgiopathies”, recurrent features include microcephaly, CNS defects (e.g., delayed myelination, cortical atrophy, abnormal corpus callosum, and pontocerebellar hypoplasia) and developmental delay (DD)/intellectual disability (ID)^{12,13}. More generally, defective vesicle formation and unbalanced trafficking have been recognized as prominent patho-mechanisms in several neurodevelopmental disorders with CNS malformations and microcephaly^{14–16}, and neurodegenerative conditions^{17,18}.

The six members of the ADP-ribosylation factors (ARF) family of small GTPases (ARF1, ARF3–6, and ARF2, missing in primates) regulate key events of Golgi structure and function, vesicular biogenesis and cargo transport. ARF function is broadly overlapping and redundant in cells^{19,20}, where they participate in bidirectional membrane trafficking required for endocytosis and anterograde/retrograde transport, including protein recycling to the membranes or their degradation^{20–24}.

These proteins bind to guanine nucleotides with high affinity and specificity and cycle between a GTP (active) and GDP (inactive)-bound form^{22,23}. Similar to other members of the RAS superfamily, release of GDP is stimulated by specific guanine nucleotide exchange factors (ARFGEFs), indirectly favoring binding to GTP^{22,26,27}. As a consequence of the conformational change promoted by GTP, the *N*-terminal myristoylated region is exposed, allowing anchoring of the active GTPase to membranes of different organelles, including *cis* and *trans*-Golgi, plasma membrane and endosomes, where these proteins exert their function^{22,25,28–30}. Moreover, the conformational rearrangement of the switch 1 [SW1] and switch 2 [SW2] regions controls the interaction with a number of effectors and regulators^{30–32}. The intrinsic slow GTPase activity of ARFs is accelerated by specific GTPase-activating proteins (ARFGAPs), which result in protein inactivation and release from membrane^{22,29,33,34}.

By interacting with coat and adaptor proteins via this switch system¹²², ARF proteins support various steps of the biosynthetic trafficking, such as COP-I vesicle formation and budding, which are essential for anterograde/retrograde cargo transport^{35,36}. ARF proteins can also recruit non-coat Golgi-specific factors to membranes (e.g., Golgin-160 and GCC88)³⁷, which are fundamental for Golgi structural integrity^{38,39}, and thereby contribute to the control of Golgi and organelle structural organization and function^{20,23,40,41}.

The use of constitutively active (CA, GTP-bound) and dominant negative (DN, GDP-bound) ARF mutants as well as ARF silencing in cells has demonstrated the variable consequences of aberrant ARF function on Golgi integrity, morphology, vesicle formation, and recycling^{20,36}, and the redundant roles among the various ARF proteins. CA mutants (i.e., ARF1/3^{Q71L}) produce loss of the Golgi ribbon-like structure with an overall expansion of the Golgi and COP-I compartments due to conspicuous vesiculation^{20,23}. Conversely, DN mutants (e.g., ARF3^{N126I}) induce a different pattern of Golgi fragmentation, with the dispersion of the coat proteins and COP-I disassembly⁴⁰. The latter resembles the ARF poisoning effect triggered by brefeldin A (BFA), which blocks the normal activation of all ARF proteins by binding ARF1-GDP-GEF⁴².

ARF-regulated Golgi dynamics during mitosis are crucial for cell division and cytokinesis^{43–45}. Ultimately, by controlling Golgi structure, function, cargo sorting, and trafficking, ARFs actively participate in the fine regulation of key events during embryogenesis (i.e., cell polarity

establishment and migration during gastrulation, neuronal maturation, and tissue morphogenesis)⁴⁶. A hyperactive or reduced *arf1* function in zebrafish results in altered body plan and head development^{47,48}. In particular, hyperactive *arf1* induces body plan alterations that are consistent with altered planar cell polarity (PCP)⁴⁷.

Notwithstanding their emerging pivotal roles in development, mutations in *ARF* genes have only recently been linked to human disease, with activating missense variants of *ARF1* (MIM: 103180) causing a rare dominant malformation of cortical development resulting from defective neuronal migration (MIM: 618185)⁴⁹. More recently, during the revision of this work, two pathogenic variants in *ARF3* were described in three individuals with a variable neurodevelopmental phenotype, and microcephaly in the most severe case⁵⁰.

Here, we report five de novo missense *ARF3* variants underlying a similar disorder affecting CNS and skeletal development. In silico and in vitro analyses provide evidence of a variable impact of mutations on protein stability, activity, Golgi integrity, vesicle formation, and cargo recycling. In-depth investigation in zebrafish corroborates the dominant nature of mutations, confirms a diverse effect on Golgi morphology during early embryogenesis, and recapitulates the variable brain and axial defects observed in patients. Experiments in live embryos further trace back the effect of aberrant ARF3 function to an altered balance of cell proliferation and death within the anterior developing brain and to impaired PCP-dependent cell axes formation.

Results

ARF3 mutations cause a developmental disorder affecting CNS and skeletal formation

In the frame of a research program dedicated to subjects affected by unclassified diseases, trio-based exome sequencing allowed us to identify a previously unreported de novo *ARF3* variant, c.379A>G (p.Lys127Glu; NM_001659.2), as the putative disease-causing event in a girl (Subject 1) with a severe syndromic neurodevelopmental disorder characterized by growth restriction, severe microcephaly, progressive diffuse cortical atrophy, hypoplasia of corpus callosum and other brain anomalies at MRI (i.e., lateral ventricular enlargement, severe brainstem hypoplasia particularly affecting the pons, cerebellar inferior vermis hypoplasia), seizures, profound DD/ID and skeletal involvement (i.e., 11 rib pairs and severe scoliosis), inguinal hernia and congenital heart defects (CHD). (Supplementary Fig. 1, Supplementary Tables 1 and 2 and clinical reports). Whole exome sequencing (WES) data analysis excluded the presence of other relevant variants compatible with known Mendelian disorders based on their expected inheritance model and associated clinical presentation, and high-resolution SNP array analysis excluded the occurrence of genomic rearrangements. The missense change, which had not previously been reported in population databases, affected an invariantly conserved residue among orthologs, paralogs, and other structurally related GTPases of the RAS family (Supplementary Fig. 2a). Through networking and GeneMatcher⁵¹, we identified four additional subjects with de novo *ARF3* missense variants, which had not been reported in ExAC/gnomAD and involved amino acid residues located in regions highly constrained for variation (Supplementary Table 2, Supplementary Fig. 2a, b). No additional candidate variants in clinically associated genes were identified in any patients (WES statistics and data output, Supplementary Tables 3–7). Affected residues but Leu¹² were conserved among ARF3 orthologs and paralogs, and three of them were also conserved among other RAS GTPases (Supplementary Fig. 2a). The identified missense variants affected residues whose corresponding positions in other GTPases of the RAS superfamily had previously been associated with human disease (Supplementary Table 8). Among these, the same Lys-to-Glu substitution at codon 127 in Subject 1 was recently reported to affect the corresponding residue in ARF1 in a patient with DD, microcephaly, periventricular heterotopia, progressive cerebral atrophy, and epilepsy⁴⁹.

Affected subjects showed variable degrees of DD/ID associated with brain and skeletal anomalies (Supplementary Fig. 1, Supplementary Table 1 and clinical reports). No characteristic craniofacial gestalt was noted, with only minor craniofacial features reported in single patients, mainly related to microcephaly (Supplementary Fig. 1a, b). Similar to Subject 1, Subject 2 (p.Leu12Val; p.Asp67Val) showed microcephaly, profound DD/ID, absence of speech and language development, progressive diffuse cortical atrophy with diminished hemispheric white matter, thin corpus callosum, progressive pontocerebellar hypoplasia without the involvement of the cerebellar vermis, hypotonia, microsomia, and consistent skeletal defects (Supplementary Fig. 1b, c; Supplementary Table 1 and clinical reports). A comparable but less severe condition was also observed in Subject 4 (p.Asp93Asn), who manifested hypotonia, severe DD/ID, delayed speech and language development, post-natal microcephaly, thinning of the corpus callosum as well as milder skeletal defects (Supplementary Fig. 1, Supplementary Table 1 and clinical reports). Subject 3 (p.Pro47Ser) and Subject 5 (p.Thr32Asn) showed the mildest phenotype with DD/ID and delayed (Subject 3) or severely delayed (Subject 5) speech and language development. Subject 3 also shows early-onset seizures and severe hypoplasia of the anterior part of the temporal lobe associated with hypomyelination and thin corpus callosum, while Subject 5 showed hypoplasia of the corpus callosum, mild white matter involvement in periventricular and supraventricular areas, and a large cisterna magna with a milder skeletal involvement (Supplementary Fig. 1b, c, Supplementary Table 1 and clinical reports).

Disease-associated ARF3 variants variably affect protein stability and function

The identified disease-associated variants affected residues spotted throughout the coding sequence except for the C-terminal region (Fig. 1a). First, we examined the possible functional consequences of each amino acid substitution using a three-dimensional structure of the GTPase recently solved by X-ray diffraction⁵² as reference. All residues except for Leu¹² cluster within or close to the GTP/GDP binding pocket (Fig. 1b). Lys¹²⁷ is one of the four residues of the NKXD motif directly mediating binding to the ribose ring of GTP/GDP⁵², and substitution of the positively charged residue with a negatively charged glutamate was predicted to affect nucleotide binding (Fig. 1c). Similarly, Thr³² contributes to stabilizing the GTP/GDP binding via direct hydrogen bonding with one oxygen atom of the α phosphate (Fig. 1c). While the conservative Thr to Asn substitution was predicted to result in a steric hindrance, Asp⁹³ does not directly contact GTP, even though it participates in the overall structure of the nucleotide-binding pocket by a direct hydrogen bond with the lateral chain of Lys¹²⁷ (Fig. 1c). The Asp-to-Asn change was anticipated to disrupt the interaction between the two residues, destabilizing GTP/GDP binding (Fig. 1d). Pro⁴⁷ and Asp⁶⁷ were predicted to affect ARF3 GTPase activity. Pro⁴⁷ is located within the SW1 region, which plays a key role in the catalytic activity of the GTPase and the conformational rearrangement mediating binding to effectors^{22,32}. Substitution of this non-polar residue with a polar serine was expected to strongly perturb the functional behavior of the protein. Similarly, Asp⁶⁷ participates in the coordination of the Mg²⁺ ion through direct hydrogen bonds with a water molecule⁵³ (Fig. 1c), and contributes to the regulation of GDP/GTP binding upon the “inter-switch toggle” mechanism⁵³; its substitution with valine was predicted to considerably perturb GTP/GDP binding³⁰ and the overall organization of the nucleotide-binding pocket. Similar pathogenic variants in RAS proteins were predicted to destabilize the binding to GTP/GDP^{54,55} and ARF1 substitutions in Lys¹²⁷, Asp⁶⁷, and Asp⁹³ were documented to have a deleterious effect in yeast⁵⁶. Leu¹² (in *cis* with p.Asp67Val in Subject 2) is located within the flexible N-terminal myristoylated alpha helix implicated in membrane-cytoplasm shuttling^{22,30}, a region that has not been resolved structurally. No obvious consequence could be hypothesized for p.Leu12Val. However,

a possible impact on nucleotide binding and GTPase activity cannot be excluded⁵⁷. Of note, while Thr³², Asp⁹³, and Lys¹²⁷ map regions of the GTPase not directly involved in intermolecular contacts, Pro⁴⁷ and Asp⁶⁷ lie in regions close to the surface of the GTPase interacting with effectors/regulators⁵⁸, which does not rule out the possibility of a more complex functional behavior of the p.Pro47Ser and p.Asp67Val changes. To explore the structural and functional consequences of these two substitutions, we built a model of ARF3 interacting with the cytosolic coat protein complex (COP) formed by γ -COP (COPG1) and ζ -COP (COPZ1) starting from an available GTP-bound ARF1:COPG1-COPZ1 complex (PDB: 3TJZ) as template⁵⁹ (Fig. 1e–h). The model for the wild-type (WT) ARF3 protein was validated by a 500-ns molecular dynamics (MD) simulation, documenting the conservation of all known interactions with GTP and Mg²⁺ (Fig. 1e, f; Supplementary Table 9). The ARF3:COPG1 interface is stabilized by an intermolecular hydrogen bonding network involving Arg¹⁹, Thr⁴⁸, and Asn⁸⁴ ARF3 residues (Supplementary Table 10). We assessed the structural perturbations due to the introduced p.Pro47Ser and p.Asp67Val changes using the same time frame. A minor impact on the ARF3 surface interacting with COPG1 was evident in the simulation when introducing the p.Asp67Val substitution (Fig. 1g; Supplementary Table 10). As predicted by the structural inspection, this change resulted instead in a significant rearrangement of the nucleotide-binding pocket with a reduction of the interactions of Lys¹²⁷ and Thr⁴⁵ with GTP (Supplementary Table 9). The Pro-to-Ser substitution at codon 47 did not significantly affect ARF3 binding to GTP (Supplementary Table 9), while a dramatic perturbation of the intermolecular binding network with COPG1 due to a substantial rearrangement of the SW1 region was observed (Fig. 1h; Supplementary Table 10). Consistently, essential dynamics analysis documented a major effect of p.Pro47Ser in terms of global fluctuations and long-range-correlated movements, compared to the other simulations (Supplementary Fig. 3). These structural analyses predicted that all variants but p.Leu12Val affect ARF3 GTP/GDP binding and/or the GTPase activity. A more articulated impact on conformational rearrangements mediating binding to effectors was suggested for p.Pro47Ser.

To experimentally validate the predicted consequences on ARF3 function, we examined the protein levels of each mutant in transiently transfected COS-1 cells, basally and after 3 and 6 hour-treatment with the protein synthesis inhibitor, CHX. The immunoblotting analysis documented levels of ARF3^{D93N} and ARF3^{T32N} comparable to the WT protein while showing a slightly reduced level for ARF3^{P47S} and a marked reduction for ARF3^{K127E} and particularly ARF3^{K127E/D67V} (Fig. 2a; Supplementary Fig. 4a), the latter also confirmed in zebrafish embryos (Supplementary Fig. 4b), which was not related to a significant reduction in the mRNA levels (Supplementary Fig. 5a). A similar reduction in expression was confirmed by quantitative imaging analysis in COS-1 cells expressing mCherry-tagged ARF3^{K127E} and ARF3^{K127E/D67V} (Supplementary Fig. 5b, c). Treatment with MG132 and bafilomycin A1, partially rescued the reduced levels of ARF3^{K127E} and ARF3^{K127E/D67V}, indicating an involvement of both the proteasomal pathway and autophagy in degradation (Fig. 2a').

In its active GTP-bound state, ARF3 is able to bind to the Golgi-associated gamma-adaptin ear-containing ARF-binding protein 3 (GGA3) to regulate downstream events controlling *trans*-Golgi function and intracellular trafficking⁶⁰. Thereby, we performed pull-down experiments using the GGA3 protein-binding domain (PBD) on cell lysates from transfected COS-1 cells to compare the relative amounts of GTP-bound fraction of WT and mutant ARF3 proteins. In the same assay, we parallelly assessed ARF3^{Q71L} and ARF3^{T32N} as CA and the DN mutants, respectively^{23,41}. Compared to cells expressing ARF3^{WT}, those expressing the ARF3^{K127E}, ARF3^{K127E/D67V}, and ARF3^{T32N} mutants showed a statistically significant reduction of the absolute ARF3 GTP-bound fraction, while a significant increase and a trend in the same direction were documented for ARF3^{D93N} and ARF3^{P47S}, respectively (Fig. 2b, c).

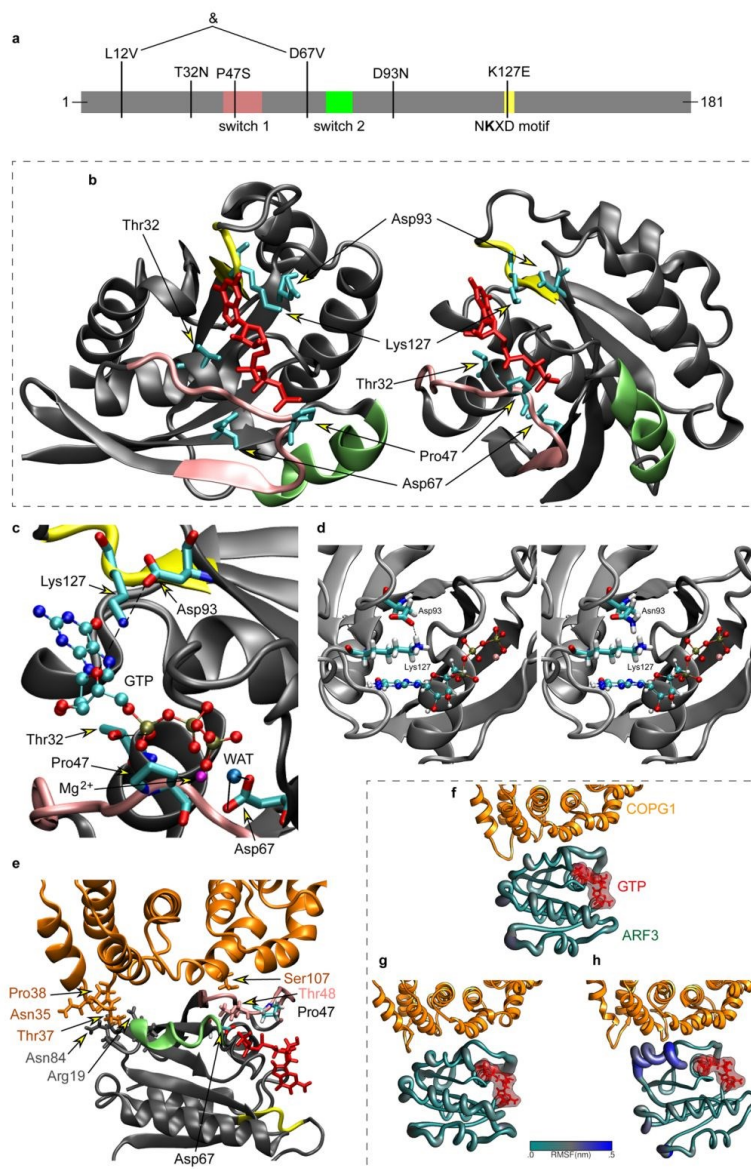


Fig. 1 | Structural organization of ARF3, location of mutated residues, and molecular dynamics analyses. **a** Domain organization of ARF3 excluding the unstructured C-terminal tail. Switch 1, switch 2 and the NKXD fingerprint motif are highlighted in pink, green and yellow, respectively. The variants identified in affected subjects are also reported. **b** 3D structure in two different orientations of GTP-bound ARF3 interacting with the MARTX toxin (PDB 6ii6). Side chains of the ARF3 residues mutated in the affected subjects and GTP are in cyan and red, respectively. Main chain of residues belonging to switch 1, switch 2 and NKXD fingerprint motif are colored as above. **c** Enlargement of the ARF3 GTP binding pocket with the five mutated residues. The direct hydrogen bond between the N atom in the Lys127 lateral chain and the oxygen atom of the GTP ribose ring is highlighted in dashed line. The Mg^{2+} ion is colored in magenta, while the oxygen atom of the water molecule, mediating the interaction between Asp⁶⁷ and the

manganese ion, is shown in light blue color. The two hydrogen bonds between Asp⁶⁷ and the water molecule are highlighted with dotted lines. **d** Zoom showing the structural organization around residue 93. Left: view of the WT Asp⁹³ forming a hydrogen bond with Lys¹²⁷. Right: structure with the p.Asp93Asn mutation and hydrogen bond breaking. The Mg^{2+} ion is colored in magenta. **e** Homology model of GTP-bound ARF3 interacting with the cytosolic coat protein complex COPG1-COPZ1 (PDB: 3TJZ) validated by a 500-ns molecular dynamics (MD) simulation. The region of contact between ARF3 and COPG1 (orange color) is shown in (e). **f-h** MD simulations of wild-type (f), p.Asp67Val (g), and p.Pro47Ser (h) ARF3 complexed with COPG1-COPZ1. Residues involved in the contact are shown with their side chain and colored as the respective protein/region. ARF3 backbone is represented with a diameter proportional to its per-residue fluctuations (RMSF).

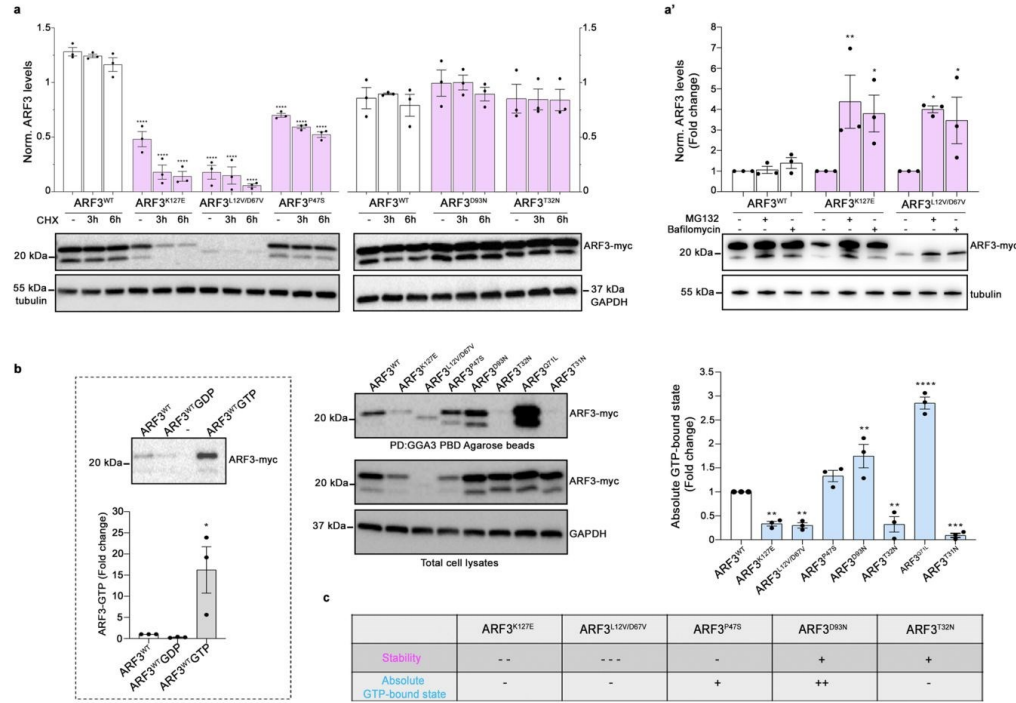


Fig. 2 | Expression, stability, and GTPase activity of WT and mutant ARF3 proteins in COS-1 cells. **a, a'** Western blot analysis showing the protein levels of myc-tagged ARF3^{WT} and all the identified mutants in transfected COS-1 cells, basally and after treatment with cycloheximide (CHX) (10 µg/ml) for the indicated time points (**a**), and with MG132 (100 µM), or bafilomycin A1 (200 nM) for six hours (**a'**). **b** Pull-down assay using GGA3-conjugated beads shows ARF3 activation in COS-1 cells transiently transfected with WT or mutant myc-tagged ARF3 expression constructs. Active and total ARF3 levels are monitored using anti-myc antibodies. GAPDH and beta-tubulin are used as loading controls. Pull-down assays of ARF3^{WT} transfected cells performed in the presence of an excess of GDP and γGTP are used as negative and positive controls, respectively (**b**, left panel). Pulldown samples in **b** (left and right), are loaded on different blots and processed parallelly.

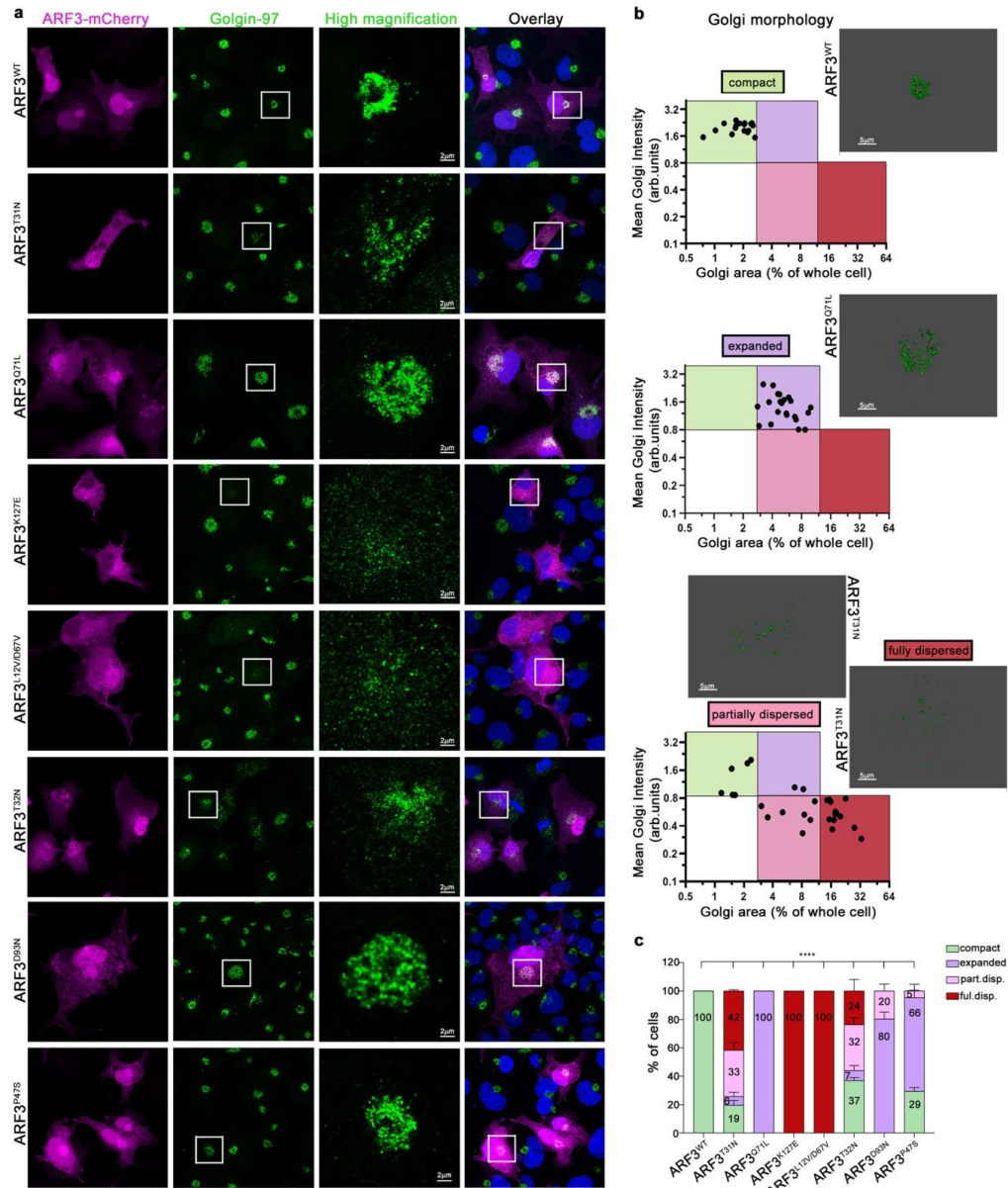
Representative blots are shown and data are expressed as mean ± SEM of three independent experiments. Two-way ANOVA followed by Tukey's *post hoc* test (**a**, WT vs. all mutants, *****p* < 0.0001; **a'**, K127E vs. K127E + MG132 ***p* = 0.0052; K127E vs. K127E + Bafilomycin **p* = 0.0195; L12V/D67V vs. L12V/D67V + MG132 **p* = 0.0123; L12V/D67V vs. L12V/D67V + Bafilomycin **p* = 0.0411). One-way ANOVA followed by Sidak's *post hoc* test (**b** left panel, WT vs. WT + GTP **p* = 0.0197). One-way ANOVA followed by Dunnett's *post hoc* test (**b**, WT vs. K127E ***p* = 0.0088; WT vs. L12V/D67V ***p* = 0.0058; WT vs. D93N ***p* = 0.0035; WT vs. T32N ***p* = 0.0075; WT vs. T47S *****p* < 0.0001; WT vs. T31N *****p* = 0.0006) are used to assess statistical significance. **c** Summary table of the data obtained relative to the stability and activity of the different ARF3 mutants. Source data are provided as a Source Data file.

Next, by employing a cell-free system and fluorescence polarization we examined the biochemical behavior of a subset of mutants for which we obtained purified proteins. Compared to the WT protein, we observed an increased intrinsic (i.e., GEF-independent) nucleotide exchange for the ARF3^{K127E} and ARF3^{D93N} mutants. A reduced exchange rate was instead registered for ARF3^{L12V/D67V}, while ARF3^{T32N} did not show significant alterations (Supplementary Fig. 6a, a'). By inspecting the GTP hydrolysis of the purified proteins, we failed to note major changes compared to ARF3^{WT} (Supplementary Fig. 6b, b'). Altogether, these data suggest a stabilized GTP-bound conformation and an overall hyperactive behavior for ARF3^{D93N} and, to a minor extent, ARF3^{T47S}, while a DN behavior could be established for the ARF3^{T32N} variant. These findings could not unambiguously functionally classify the ARF3^{K127E}, and ARF3^{L12V/D67V} behavior.

Disease-associated ARF3 mutants differentially impact on Golgi morphology

Next, we assessed the specific Golgi phenotype resulting from the overexpression of the individual mutants in cells. Given the role of ARF proteins in maintaining proper Golgi integrity, organization, and

function^{4,20,36,41,61}, we performed confocal microscopy analysis of COS-1 cells overexpressing mCherry-tagged WT and ARF3 mutants and labeled for the resident *trans*-Golgi protein Golgin-97⁶². To specifically ascribe the observed phenotype to known dysregulated ARF function and derive possible insights into the mechanism, we directly compared Golgin-97 patterns to that obtained by known CA (p.Q71L) and DN (p.T31N) ARF3 proteins. Four major Golgi morphotypes were identified (Fig. 3a, b). As expected, ARF3^{WT}-expressing cells showed diffuse cytoplasmic ARF3 localization. Perinuclear (PN) localization of the protein was also observed, partially co-localizing with Golgin-97 (i.e., GTP-bound ARF3), which showed a canonical, compact ribbon-like morphology (Fig. 3a, upper row, Supplementary Fig. 7). Conversely, only in a minority of cells expressing the DN ARF3^{T31N}, the *trans*-Golgi was recognizable as a discrete compact entity, while most cells showed partial or total dispersion of Golgin-97 within the cytosol (Fig. 3a, 2nd row, Supplementary Fig. 7), in line with previous reports^{41,50}, indicating occurrence of massive Golgi disassembly. In striking contrast, cells expressing the CA ARF3^{Q71L} protein showed a compact and expanded Golgin-97 staining, likely reflecting an expansion in the size of the *trans*-Golgi (Fig. 3a, 3rd row, Supplementary Fig. 7), as previously



reported²³. Dot plot representation of the Golgin-97 mean intensity (I) and area (A) in cells expressing ARF3^{WT}, ARF3^{D71L} and ARF3^{T31N} allowed classifying these distinct Golgi structural rearrangements into discrete classes: compact, expanded, partially or totally dispersed (Fig. 3b, Supplementary Fig. 7), providing an unbiased tool for the Golgi morphology assessment. Notably, altered Golgi morphology was not only characterized by an increase in area, but also by a significant decrease in Golgin-97 signal intensity with respect to compact Golgi. The three altered Golgi morphotypes were variably observed in cells expressing the identified *ARF3* variants, and variable severity of the phenotype was

documented. Cells expressing the ARF3^{K127E}, ARF3^{L12V/D67V}, and ARF3^{D93N} showed Golgi structural alterations in all analyzed cells, while compact Golgi organization was observed in a fraction of cells expressing the ARF3^{T32N} and ARF3^{R47S} (Fig. 3a, c), which is suggestive of a milder impact of these mutants, in line with the mild clinical features of patients (Supplementary Table 1 and clinical reports). Notably, similar to what was observed for the DN mutant, ARF3^{K127E}, ARF3^{L12V/D67V}, and ARF3^{T32N} mainly induced variable Golgi dispersal, which was observed in all cells expressing either ARF3^{K127E} or ARF3^{L12V/D67V} (Fig. 3a, 4th and 5th row, c). Cells expressing ARF3^{T32N} were characterized by a milder

Fig. 3 | ARF3 mutants induce variable Golgi morphological alterations in COS-1 cells. **a** Maximum intensity confocal z-projections showing immunostaining against Golgin-97 (*trans*-Golgi marker) (green) performed in fixed COS-1 cells transiently transfected with mCherry-tagged ARF3^{WT}, ARF3^{T32N}, and ARF3^{Q71L} (DN and CA variants, respectively) or mutants identified (magenta) for 48 h. Composite colocalization images are shown in the right panels with nuclei (DAPI staining) in blue. The images are representative of three independent experiments. Scale bars = 2 μ m (high magnification) and 10 μ m (all the other images). **b** Golgi means intensity and area define distinct Golgi morphotypes. Dot plots of mean intensity (MI) and area of Golgi in cells transiently transfected with mCherry-tagged ARF3^{WT}, or ARF3^{Q71L} and ARF3^{T32N} mutants (up, middle, bottom panels) are shown. Golgi MI and area (% of the whole cell) of cells were measured based on Golgin-97 staining. Whole-cell area was determined using the area covered by mCherry fluorescence as a mask. Representative 3D rendering images of the observed Golgi staining are

shown. Cell populations located in different gates are characterized by distinct Golgi morphologies: Compact: A < 2.6 and MI > 1.5 (green gate); expanded Golgi: 2.7 < A < 12 and MI > 0.8, (purple gate); partially dispersed Golgi: 2.7 < A < 12 and MI < 0.8 (pink gate); totally dispersed Golgi: A > 12 and MI < 0.8 (bordeaux gate). **c** Incidence of *trans*-Golgi morphotypes. The bar graph represents the percentage of cells showing compact, expanded, partially or fully dispersed distribution (part.disp and ful.disp.) of Golgi in mCherry-tagged ARF3 transfected cells, based on the classification described above in (b). No. of cells = 26 (WT); 22 (Q71L); 29 (T32N); 20 (K127E); 20 (L12V/D67V); 21 (P47S); 28 (D93N) and 27 (T32N). Data are expressed as mean \pm SEM of three independent experiments. Two-sided Chi-square's test in a 2 \times 2 contingency table (WT vs. all mutants, compact vs. all phenotypes ****p < 0.0001) is used to assess statistical significance. Arb.units = arbitrary units. Source data are provided as a Source Data file.

reorganization of the Golgi with only a minority of cells showing total dispersion (23%, Fig. 3a, 6th row, c). On the other hand, resembling the effect of the CA mutant, ARF3^{D93N} and ARF3^{P47S} showed a significant increase of cells with expanded Golgi (79% and 67%) (Fig. 3a, 7th and 8th row, c). Of note, a more severe effect was documented for ARF3^{D93N}, with a fraction of cells also exhibiting partial dispersion, while a compact Golgi was observed in approximately 30% of cells expressing ARF3^{P47S} (Fig. 3c). These findings provide evidence of a differential functional impact of the identified *ARF3* variants on Golgi structural morphology (Fig. 3c).

Next, we further investigated Golgi morphology via ultrastructure inspection by performing transmission electron microscopy (TEM) on cells expressing ARF3^{K127E} and ARF3^{D93N}, which showed the “fully dispersed” and “expanded” *trans*-Golgi morphotypes, respectively. While perinuclear Golgi mini-stacks well organized in ribbons were recognizable in cells expressing ARF3^{WT} (Supplementary Fig. 8a, a'), those expressing ARF3^{K127E} exhibited Golgi fragmentation characterized by an integrity loss of the mini-stacks with numerous diffused vesicles and small cisternae scattered in a wide area (Supplementary Fig. 8b, b'). Cells expressing ARF3^{D93N} displayed a different pattern with loss of the typical ultrastructure of Golgi elements and a marked increase in swollen cisternae and diffuse vesiculation, which were confined within the defined area normally occupied by Golgi (Supplementary Fig. 8c, c'). A similar fragmentation pattern had previously been described^{4,23,63,64}, also for CA ARF and ARF-like mutants^{4,23,63,64}. We cannot exclude the occurrence of more complex morphological alterations, whose assessment would require electron tomography analysis or 3D super-resolution microscopy.

To further validate these findings within an organismal context, we next set out to examine the *trans*-Golgi in zebrafish embryos expressing ARF3^{K127E} and ARF3^{D93N}, for which opposite effects were observed in cells. Zebrafish harbors two paralogs, *arf3a* and *arf3b*, which share common ancestry with mammalian *ARF3* and conservation of the amino acids involved in the identified mutations (Supplementary Fig. 2a). *arf3a* and *arf3b* are both expressed during early embryonic development, and *arf3b* shows a higher level of expression after maternal-to-zygotic transition (MZT) throughout gastrulation and somitogenesis (Supplementary Fig. 9), indicating its predominant role during these developmental stages. Next, we overexpressed mRNAs encoding ARF3^{WT}, ARF3^{K127E}, and ARF3^{D93N}, and used specific cellular and subcellular markers to assess *trans*-Golgi morphology in precursor cells of the envelope layer (ELV) in early gastrula (Fig. 4a). We reasoned that the complexity of the physiological Golgi dynamics in vivo and the expected occurrence of fragmented Golgi in proliferating cells⁴³ might limit our ability to distinguish the specific pathogenic effect of the mutants on Golgi in fish. Thereby, we first verified whether the dispersion of Golgi elements due to the expression of ARF3^{K127E} could be observed in early zebrafish embryos. To this aim, we injected mRNAs encoding the mCherry-tagged ARF3^{WT} and

ARF3^{K127E} in the first batch of siblings, together with a fluorescent membrane marker and EGFP-tagged GalT (galactosidase T⁸⁵), a marker of *trans*-Golgi. By using this marker, we parallelly confirmed ARF3^{K127E}-mediated Golgi elements dispersal in a live time-lapse of COS-1 cells (Fig. 4a–c; Supplementary Movie 1) and in alive zebrafish embryos (Fig. 4d, e). In embryos, we observed a diffused distribution of ARF3^{WT} partially overlapping EGFP-GalT staining. The latter was structured in ribbon-like elements. Conversely, in ARF3^{K127E} expressing fish, EGFP-GalT signal distribution appeared less intense and organized in small and large puncta, some of which also co-localized with ARF3 (indicating Golgi-localization) (Fig. 4d, e, Supplementary Fig. 10a). Next, we compared the EGFP-GalT staining associated with ARF3^{K127E} and ARF3^{D93N}, using the patterns resulting from CA and DN ARF3 mutants as reference. Again, we observed a reduced number of ribbon-like Golgi in cells expressing ARF3^{K127E} (<20%) as compared to WT, similar to the DN ARF3-expressing embryos (Supplementary Fig. 10b, c). Despite the changes in Golgi morphology being subtler in fish expressing with ARF3^{D93N}, the loss of typical Golgi ribbon-like structures was evident. This pattern was accompanied by instances of large EGFP-GalT⁺ structures (39%), also documented in fish expressing the known CA mutant (Supplementary Fig. 10b, c).

Overall, the collected in vitro and in vivo findings suggest that the identified pathogenic variants in *ARF3* have a variable dominant impact on protein stability, activity, and Golgi morphology. The Golgi morphotype analysis established the presence of different functional classes of disease-causing ARF3 mutants, broadly ascribing to a DN or CA mechanism. Notably, their variable strength appeared to correlate with the severity of clinical features observed in patients.

ARF3 mutants impair COP-I vesicle formation and cargo recycling in COS-1 cells

Given the known involvement of ARF GTPases in vesicles budding, endosomal transport, and recycling, and considering the observed Golgi phenotypes, we then asked whether and how ARF3 mutants impact the formation and activity of the endolysosomal compartments along the endocytic-recycling pathway. First, we examined the integrity of COP-I vesicles by immunostaining the β -COP subunit of COP-I. In line with the Golgi phenotypes and previous reports on DN and CA ARF3^{20,65}, cells expressing ARF3^{K127E} and ARF3^{L12V/D67V} were characterized by a sparse distribution of the signal throughout the cytoplasm, indicating a disassembly of COP-I vesicles. Differently, a large number of cells expressing ARF3^{P47S} and ARF3^{D93N} showed an expanded β -COP signal, which is indicative of an enlarged COP-I compartment. Cells expressing ARF3^{T32N} did not show a clear-cut phenotype, with a minor incidence of cells showing partial/complete disassembly, indicative of a mild effect of the mutant (Fig. 5a, b).

Next, to follow cargos destiny within the endocytic-recycling pathway, we continuously incubated COS-1 cells with fluorescently labeled transferrin (Tfn) at 37 °C for 5 or 30 min to trigger

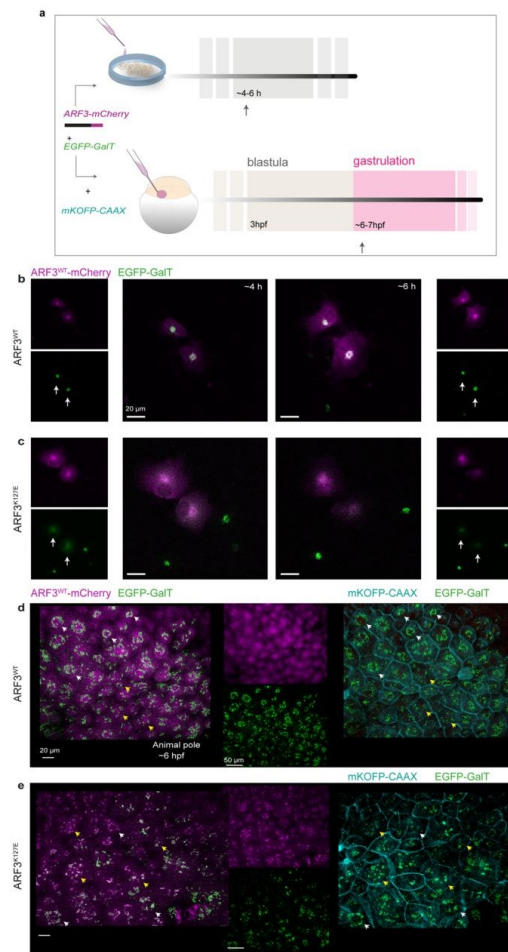


Fig. 4 | Trans-Golgi fragmentation visualized by EGFP-GalT in cells and zebrafish embryos expressing the mutant mCherry-tagged ARF3^{K127E}. **a** Schematic representation of the experimental setup in both in vitro and in vivo systems. COS-1 cells are transfected with DNA constructs expressing WT and mutant ARF3-mCherry (magenta) and EGFP-GalT (*trans*-Golgi marker, green) and analyzed by live confocal microscopy between 4 and 6 h post-transfection. Zebrafish embryos are injected at 1 cell stage with WT and mutant ARF3-mCherry and EGFP-GalT mRNA. mKOPF-CAAX mRNA is used as a membrane marker (cyan). Animals are analyzed by live confocal microscopy during gastrulation (~6–7 hpf). **b, c** Maximum intensity projections of confocal images of a single time-lapse experiment (Supplementary Movie 1) performed in transfected COS-1 cells at 15 min (~4 h post-transfection) and 120 min later (~6 h post-transfection) from the start of the time-lapse experiment. The images show diffused EGFP-GalT signal (*trans*-Golgi fragmentation) in ARF3^{K127E} over time (white arrows). Scale bar = 20 μ m. **d, e** 3D image reconstructions from live confocal acquisitions of the animal pole in developing zebrafish embryos expressing ARF3^{WT} and ARF3^{K127E} at the mid-gastrulation stage (~6 hpf). White arrowheads indicate a compact *trans*-Golgi morphology surrounding the nucleus (“ribbon”) in the EVL cells. Yellow arrowheads indicate cells showing “*punta*” morphology of the *trans*-Golgi dispersed throughout the cytosol. Scale bars = 20 and 50 μ m. The images are representative of embryos from two independent batches. Quantification is shown in Supplementary Fig. 10a. Source data are provided as a Source Data file.

internalization and trafficking of the endocytic vesicles containing labeled Tfn/TfnR complex to the endolysosomal compartment⁶⁶. The subcellular distribution of vesicles in these two-time points was assessed by confocal microscopy. In a normal scenario, upon 5 min incubation, Tfn is internalized and found along the endocytic pathway; following longer incubation time, the majority of the Tfn⁺ cargo is expected to have recycled back to the cell surface, such that limited Tfn levels are observed in the PN compartment^{67,68}. Upon 5 min incubation, the distribution of Tfn appeared nonuniform in ARF3^{WT} expressing cells, with sparse Tfn⁺ vesicles clusters observed throughout the cell, mostly within the PN space (“semi-clustered”), similar to non-transfected cells (Supplementary Fig. 11a, b). In contrast, a higher fraction of the cells expressing ARF3^{K127E} and ARF3^{L12V/D67V} showed Tfn⁺ vesicles enriched within the PN region (“clustered”) (Supplementary Fig. 11a, b’). In cells incubated for a longer time with Tfn, both mutants showed an even stronger cargo accumulation (Fig. 6a, b’; Supplementary Fig. 11c).

To further assess possible defects in recycling, cells incubated for 30 min with Tfn were stained for Rab5 and Rab11, early (EE), and recycling (RE) endosome markers, respectively^{68–71}. The fraction of internalized Tfn co-localizing with Rab5⁺ vesicles was significantly higher in ARF3^{K127E} and ARF3^{L12V/D67V} expressing cells compared to the control cells (Fig. 6c, d). A similar trend was observed with respect to Rab11, which was statistically significant for ARF3^{L12V/D67V} (Supplementary Fig. 12). These findings indicate a dominant behavior of ARF3^{K127E} and ARF3^{L12V/D67V} in causing cargo transport delay. None of the other mutants showed altered behavior.

Not recycled Tfn is normally eliminated via the lysosomal pathway^{72–75}. To evaluate mis-targeting of the Tfn to lysosomes or overload of the degradative pathway, cells incubated with Tfn for 30 min were stained with the lysosomal marker Lamp2. Compared to cells expressing ARF3^{WT}, only cells expressing ARF3^{D93N} showed a significant increase in the fraction of Tfn colocalized with Lamp2 at the PN. Nevertheless, expression of all mutants except ARF3^{P47S} was associated with a significantly increased fraction of Lamp2⁺ vesicles colocalized with Tfn (Supplementary Fig. 13). Hence, despite the mutation-specific patterns, lysosomes seem to generally increase their Tfn loading in the majority of the mutants.

Functional validation in zebrafish confirms the pathogenicity and dominant mechanism of action of ARF3 variants

We expanded our in vivo validation by investigating a possible variable impact of all the identified ARF3 mutants on embryogenesis. To this aim, myc-tagged WT and mutant ARF3 mRNAs were microinjected at one-cell stage zebrafish embryos (Fig. 7a). As anticipated, endogenous *arf3* is detected at early stages of embryogenesis (i.e., before MZT) and it accumulates only later starting at late blastula/early gastrula period (Supplementary Fig. 9). In the injected embryos, we profiled the expression timing of myc-tagged protein and determined a subtle expression of both WT and mutant ARF3 before MZT, with a clear increase only later during development. This pattern mimicked the endogenous *arf3* expression (Supplementary Fig. 14).

Injected embryos were sorted based on the expression of GFP-CAAX (used as injection marker), and developmental progression was followed from early time points of gastrulation till 48 hours post fertilization (hpf) (long-pec stage) (Fig. 7a, b’), when morphogenesis is nearly completed and sub-compartmentalization of different neural structures can be appreciated⁷⁶. Embryos expressing each of the tested ARF3 mutants showed significant phenotypic alterations compared to siblings expressing ARF3^{WT} and not injected controls. Compared to normal development (class I), mutant embryos showed variable degrees of survival rate and developmental delay (class II) (Fig. 7c–c’, Supplementary Fig. 15a). A statistically significant decrease in the

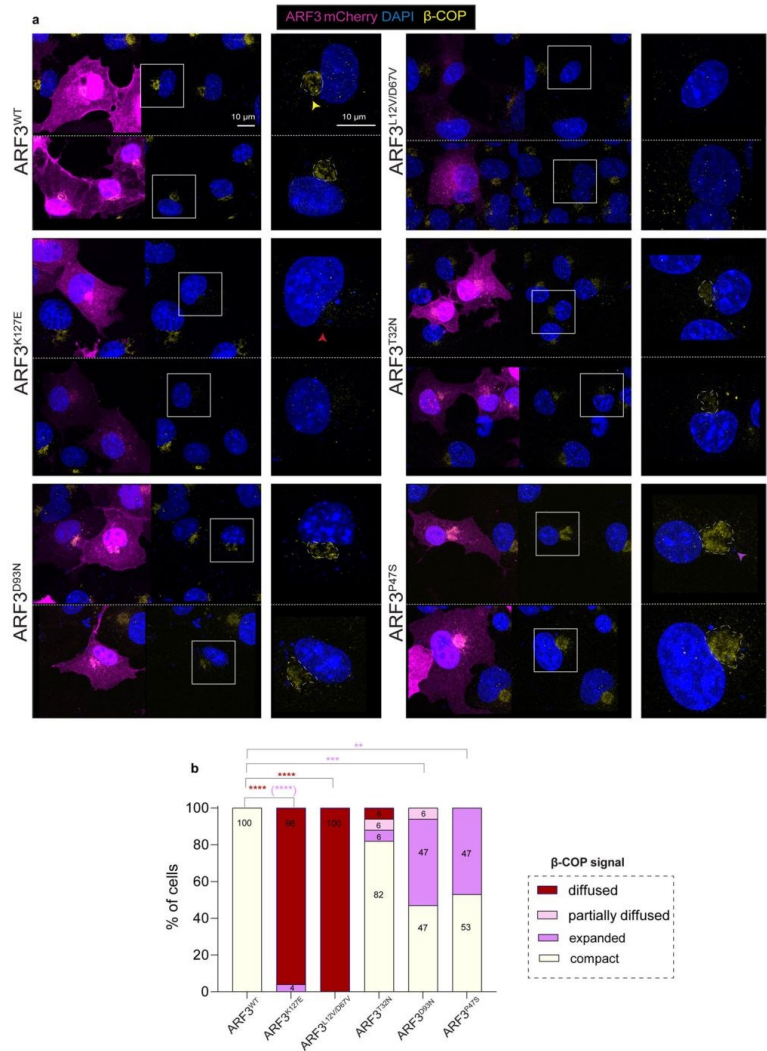


Fig. 5 | Variable impact of *ARF3* mutations on COP-I vesicle assembly.

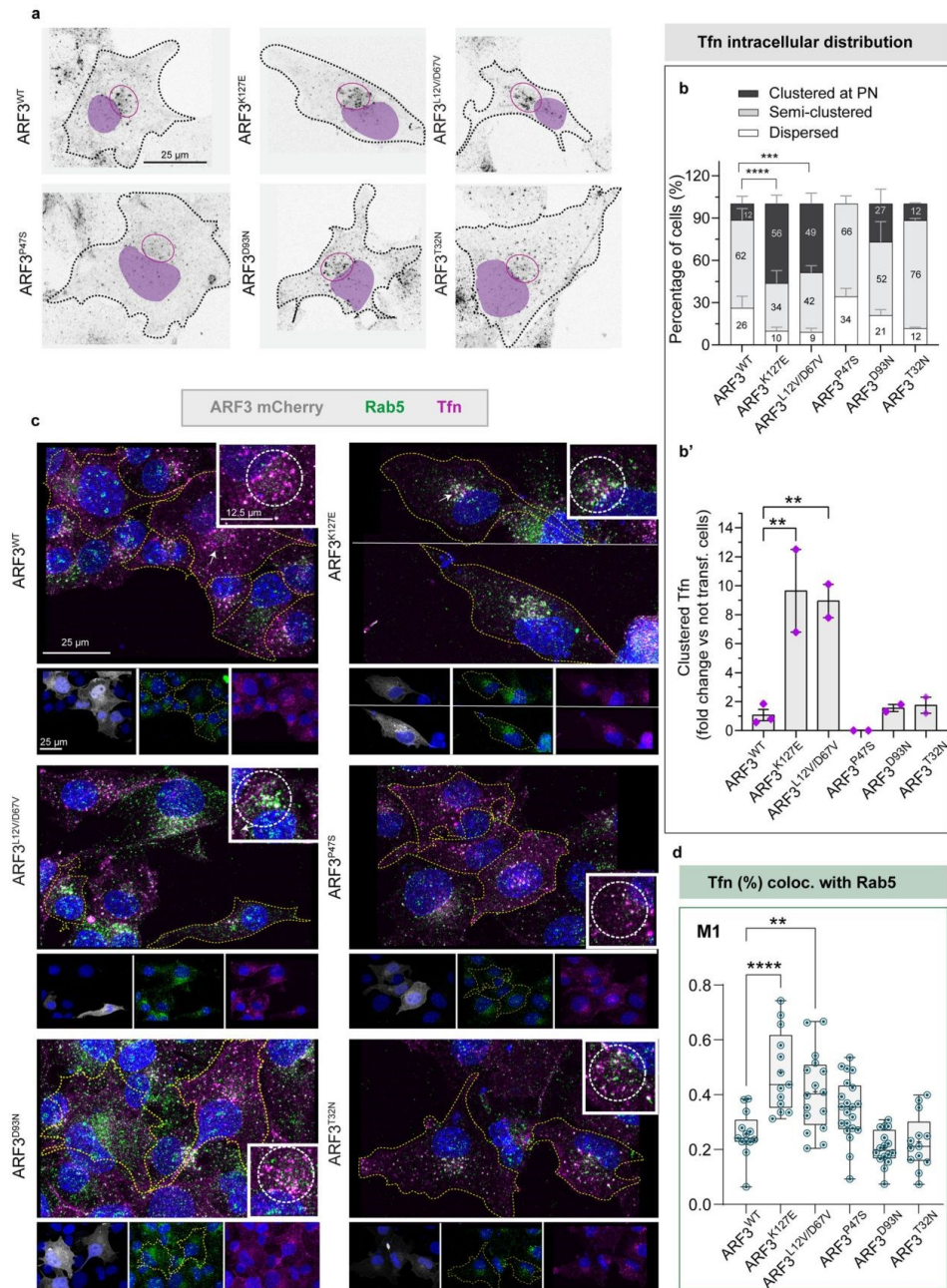
a Maximum intensity confocal z-projections of COS-1 cells expressing mCherry-tagged *ARF3*^{WT} and all identified mutants and stained for the β-subunit of COP-I. The right panel shows a magnification of β-COP signal. Nuclei are labeled with DAPI (blue). Yellow and red and purple arrowheads: normal, diffused, and expanded β-COP signal, respectively. Scale bar is 10 μm. The images are representative of cells from a single experiment. **b** Quantification of the percentage of WT and *ARF3* mutant cells showing different classes of phenotypes as indicated in the legend

(compact and expanded: clustered signal visible at the PN region and with a ratio between COP-I area/nucleus area ≤0.25 or >0.25, respectively). No. of cells = 18 (WT); 26 (K127E, compact vs. diffused *****p* < 0.0001, compact vs. expanded *****p* < 0.0001); 16 (L12V/D67V, compact vs. diffused *****p* < 0.0001); 18 (T32N); 15 (D93N, compact vs. expanded ****p* = 0.0007) and 15 (P47S, compact vs. expanded ***p* = 0.011). Two-sided Chi-square test in 2 × 2 contingency table is used to assess statistical significance. Source data are provided as a Source Data file.

survival rate of embryos expressing *ARF3*^{K127E} was documented (Fig. 7c'), and morphogenesis appeared particularly perturbed both at the level of the head and trunk for a significant fraction of embryos. For the majority of the analyzed mutants, a substantial fraction of embryos (≥25%) showed mild or severe phenotypes (class III and IV, respectively) that were characterized by reduced head size, with/without micropthalmia, and/or mild shortening and lateral bending of body axis (class III), or considerably reduced head (microcephaly or

anencephaly) and eye size, with marked reduction of the trunk, defective body elongation and severe lateral bending (kinked notochord, class IV) (Fig. 7c–c", Supplementary Fig. 15a).

To validate the mechanism of action and further test the dominant behavior of the *ARF3* variants in vivo, we directly compared the observed *ARF3* overexpression phenotype with that obtained by downregulating endogenous *arf3* via translation blocking morpholino (MO) approach, targeting both *arf3a* and *arf3b* maternal and zygotic



translation. At 24 hpf, fish injected with MO against *arf3a* and *arf3b* showed a subtler phenotype, with a prevalence of class II phenotype (developmental delay), and only a small percentage (<8%) of animals showing the characteristic body curvatures observed in fish expressing ARF3 mutants (Fig. 7d, d'). These defects increased only later in development but remained <20% on average (Fig. 7d''). Moreover,

contrary to fish expressing ARF3 mutants, we did not observe severely affected embryos among the *arf3* MO-injected embryos (Fig. 7d-d'') nor significant death (Supplementary Fig. 15b). Notably, the incidence of the observed phenotype increased with increasing MO doses (Fig. 7d-d''), and by 48 hpf a significant rescue of the phenotype could be observed when co-injecting mRNA encoding ARF3^{WT} (Fig. 7e-e''),

Fig. 6 | Internalized Tfn accumulates in the perinuclear region and in Rab5 + endosomes of COS-1 cells expressing ARF3^{K127E} and ARF3^{L12V/D67V}. **a** Maximum intensity confocal z-projections showing the distribution of Tfn-488 (black dots) upon 30 min of incubation in COS-1 cells expressing mCherry-tagged ARF3^{WT} and all identified mutants. Red circle indicates Tfn signal at the perinuclear region (PN). Outlines (black in a and yellow in c) depict the boundaries of representative transfected cells. The black and white images are rendered by inverting the original LUT in Fiji and nuclei are pseudo-colored (purple) in the images. The images are representative of two independent experiments. **b–b'** Incidence of cells showing “clustered”, “semi-clustered” or “dispersed” Tfn staining (**b**) and the ratio of the cells (%) showing “clustered” Tfn phenotype normalized by not-transfected cells (NT) with the same phenotype (**b'**, internal control). No. of cells = 42 (WT); 22 (K127E, ****p* < 0.0001); 33 (L12V/D67V, ****p* = 0.0002); 31 (P47S); 26 (D93N); and 25 (T32N). Data are expressed as mean ± SEM (**b, b'**) of three (WT) and two (all the other mutants) independent experiments. **c** Maximum intensity confocal z-projections showing COS-1 cells expressing ARF3^{WT} and all identified mutants,

incubated with Tfn-488 for 30 min followed by immunostaining against Rab5 (marker of early endosomes). For all the panels single channels (ARF3mCherry: gray, Tfn-488: magenta, Rab5: green), the merge showing the co-localization between Tfn and Rab5 are shown. The insets in the white square show a zoom on the PN co-localization signal. Nuclei are stained with DAPI. The images are representative of cells from a single experiment. **d** Colocalization analysis showing the spatial co-occurrence of Tfn and Rab5+ signals at the PN region in the z-stacks analyzed, no. of cells = 13 (WT; K127E ****p* < 0.0001; T32N), 16 (L12V/D67V, ***p* = 0.0016; D93N), 21 (P47S). The fraction (%) of Tfn' signal co-localized with Rab5+ vesicles at the PN (thresholded Mander's coefficient M1) is reported as box-and-whisker with median (middle line), 25th–75th percentiles (box), and min-max values (whiskers) of a single experiment. All the data points and the mean (“+”) are also shown. Two-sided Chi-square's test in a 2 × 2 contingency table (semi-clustered and dispersed vs. clustered, **b**), One-way ANOVA followed by Dunnett's multiple comparison *post hoc* test (**b', d**) are used to assess the statistical significance. Source data are provided as a Source Data file.

demonstrating the specificity of the phenotype in relation to *arf3* downregulation.

The MO approach had previously been used as a tool to test the genetic mechanism of action in vivo, assuming that downregulation of endogenous protein expression alleviates the phenotypes associated with CA mutants but exacerbates the phenotype of DN mutants⁷⁷. Therefore, we performed a set of experiments in which each of the pathogenic *ARF3* alleles was co-injected with *arf3a/b* MO (+MO). When we statistically assessed the incidence of phenotypes in “+MO” conditions against those observed by injecting solely mutant *ARF3* mRNA (–MO), a significant worsening of the most severe traits was documented for ARF3^{K127E} (class IV), ARF3^{L12V/D67V} and ARF3^{T32N} (both for class III). On the other hand, we observed a significant alleviation of the phenotype (class III) in embryos expressing ARF3^{D93N} and co-injected with *arf3a/b* MO. We did not observe any substantial change in the phenotype severity for ARF3^{P47S} (Fig. 7f). A ratio between the percentage of embryos showing the most severe traits, including class IV and V (deceased fish) with or without MO confirmed the trend for most of the mutants (Fig. 7f). Altogether, these data provided in vivo evidence of a dominant mechanism of the identified disease-causing variants, clearly distinguishable from the *arf3* loss-of-function effect. Moreover, corroborating the in vitro results, these findings support a DN mechanism for p.K127E, p.L12V/p.D67V, and p.T32N, and a CA behavior for p.D93N.

Zebrafish embryos expressing ARF3 mutants recapitulate the variable disease severity

To explore further the consequences of *ARF3* mutations on neurodevelopment, we more accurately characterized zebrafish head and brain phenotype. At 24 and 48 hpf, compared to not injected controls and siblings expressing ARF3^{WT}, we registered a significant reduction of the head area for p.K127E and p.L12V/D67V, with the most severe cases lacking the frontal part of the brain and eyes (Figs. 7b'; 8a, b). Phenotypic assessment at later stages (4.5 days post fertilization, dpf) documented the appearance of microcephaly also in embryos expressing ARF3^{D93N}, while none of the other mutants showed significant changes (Fig. 8b').

These in vivo measurements resembled the variable clinical traits reported in patients, with only Subjects 1 (p.K127E) and Subject 2 (p.L12V/p.D67V) showing severe microcephaly at birth, and Subject 4 (p.D93N) displaying post-natal microcephaly (Fig. 8b", Supplementary Fig. 1, Supplementary Table 1 and clinical reports).

Next, taking advantage of our live whole-brain/embryos samples, we examined the anterior brain volume in fish exhibiting early- and late-onset microcephaly as well as in embryos expressing ARF3^{P47S}, which was associated with a mild reduction within the developing forebrain in Subject 3 (Supplementary Fig. 1, Supplementary Table 1 and clinical reports). To this aim, we employed the *NBT:dsRed*

transgenic line, labeling differentiated neurons. Volumetric reconstructions from live confocal z-stack acquisitions confirmed a significant reduction of the brain volume for ARF3^{K127E} and ARF3^{L12V/D67V} (Fig. 8c, c').

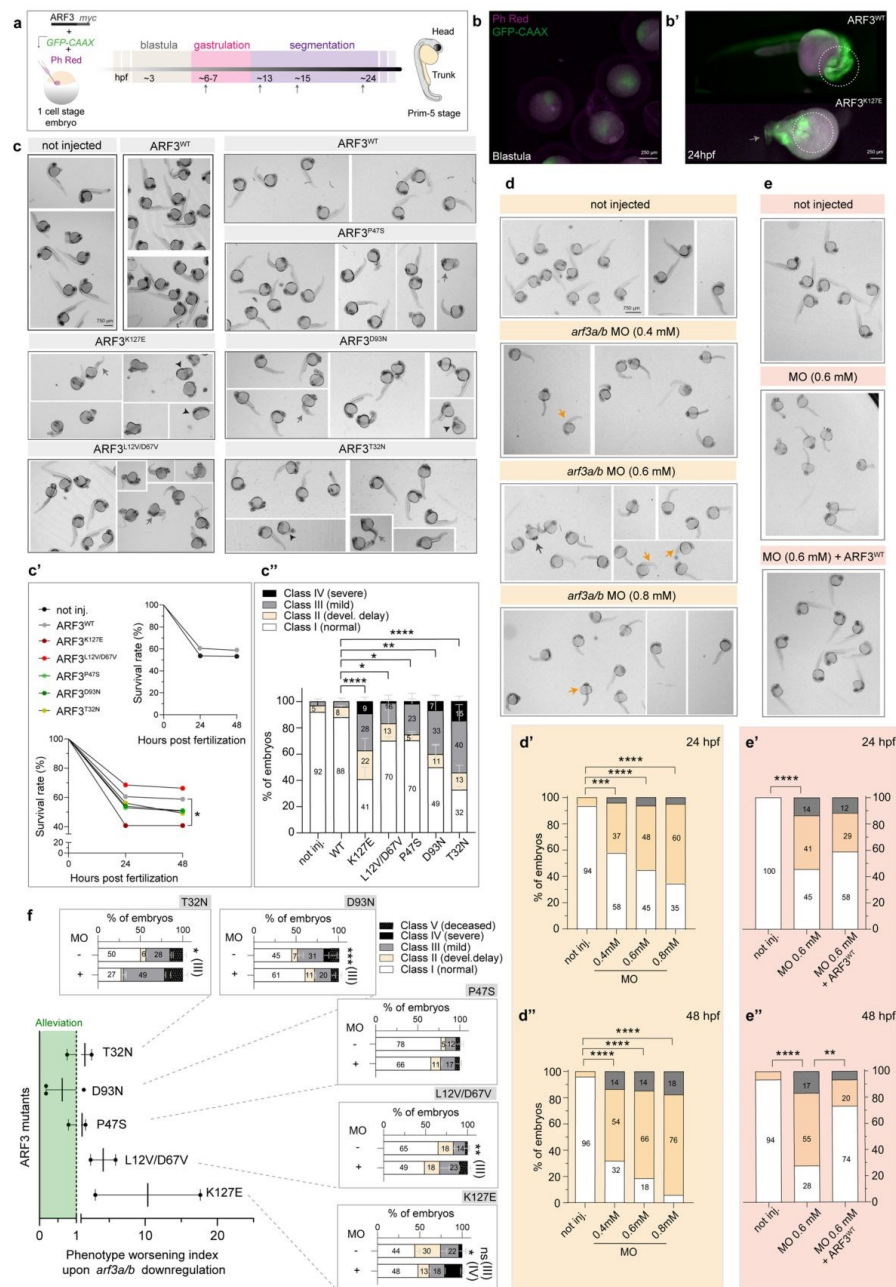
Additional volumetric measurements obtained from fixed specimens at 48 hpf by labeling mature axonal and neuronal structures confirmed the observed brain volume reduction for ARF3^{K127E} (Supplementary Fig. 16). Of note, despite head measurements documented only a delayed effect of ARF3^{D93N} and did not show significant changes for ARF3^{P47S}, the volumetric analysis of the anterior brain at 48 hpf was able to capture a significant reduction of brain mass for both mutants (Fig. 8c, c').

Defective formation of the forebrain commissural fibers of the corpus callosum (CC) is a common feature of all patients. No evolutionary-related structure has been described in teleost fish; nevertheless, the anterior commissure (AC) is the major white matter structure within the developing zebrafish telencephalon. Similar to the CC, the AC in zebrafish consists of thick axonal bundles connecting the two hemispheres of the telencephalic forebrain⁷⁸. To expand our brain phenotyping, we therefore assessed AC formation in 48 hpf fish injected with WT and mutant *ARF3* mRNA by using staining against anti-acetylated tubulin to visualize the axonal bundles. A significant reduction in the width of the AC lateral bundles was observed for all the ARF3 mutants. A stronger effect was recorded for ARF3^{K127E}, ARF3^{L12V/D67V}, and ARF3^{D93N} when the width of the entire AC was considered (Supplementary Fig. 17).

Altogether, the morphometric parameters measured in vivo are consistent with the variable degree of impaired brain development as a distinctive feature of the disease and support the occurrence of telencephalic white matter defects as a common trait of this new Golgiopathy. Our findings further document a severe effect on brain development for the p.K127E and p.L12V/D67V ARF3 substitutions in zebrafish, which captures the severity of phenotype observed in Subjects 1 and 2.

Aberrant ARF3 function induces proliferation and cell cycle defects within the anterior brain

Cortical malformations resulting in microcephaly are often caused by aberrant neurogenesis underlying altered proliferation and cell cycle progression, which ultimately lead to premature stem cell death^{79–81}. To test this hypothesis and probe into the mechanism causing reduced brain volume in mutant embryos, we examined the proliferative status and quantified cell death. By performing whole-brain immunohistochemistry using anti-proliferating cell nuclear antigen (PCNA) and anti-phospho-histone 3 (pH3) antibodies, we queried the proliferative and mitotic ability of precursor cells at 48 hpf within the forebrain proliferative zone (pz), which is clearly discernible from ventral confocal images (Fig. 9a, b). The number of pH3+ cells within this region



was significantly reduced in embryos expressing ARF3^{K127E}, a similar trend was observed for ARF3^{L12V/D67V} and ARF3^{D93N} expressing fish (Fig. 9b, c). In addition, we detected changes in the overall distribution of proliferative cells within the dorsal brain domain, which ectopically invaded the midbrain territory normally populated by differentiated neurons and nerve bundles (tectal neuropil)^{82,83}, with a stronger effect

observed for ARF3^{K127E} and ARF3^{D93N} (Supplementary Fig. 18a-h). This pattern indicates the occurrence of a complex impairment of the developmental processes within the anterior brain. No major changes in the total number of pH3⁺ cells were observed except for an increase in the cerebellum in ARF3^{D93N} expressing fish (Supplementary Fig. 18i-k).

Fig. 7 | Expression of mutant ARF3 and downregulation of endogenous *arf3* induce distinct phenotypes in zebrafish. a Experimental strategy in zebrafish models. Injected with WT and mutant ARF3-encoding mRNAs at 1 cell stage and phenotyped at different stages. **b–b'** Images and close-ups of ARF3^{WT} and ARF3^{K127E} expressing embryos at 24 hpf, co-injected with GFP-CAAX-encoding mRNA and Phenol-Red (dashed circle depicts cephalic region). **c** Bright-field images of embryos expressing WT and mutant ARF3. The images are representative of embryos from two (**b, b'**) and five (**c**) independent batches. **c'** Embryo survival, no. of embryos = 246, 114, 53, 86, 85, 161, 114 (not injected, WT, K127E, **p* = 0.03, L12V/D67V, P47S, D93N, T32N) from pooled batches. **c''** Incidence of gross phenotypes at 24 hpf (classes: I, II = yellow arrows, III, IV = gray and black arrows, respectively), no. of embryos = 132 (not injected); 69 (WT); 21 (K127E, *****p* < 0.0001); 58 (L12V/D67V, **p* = 0.02); 45 (P47S, **p* = 0.03); 86 (D93N, ***p* = 0.0018); 64 (T32N, *****p* < 0.0001). Data are expressed as mean ± SEM of four (not injected, WT), three (D93N), and two (K127E, L12V/D67V, P47S, T32N) independent batches. **d–d''** Bright-field images (**d**) and phenotype incidence at 24 and 48 hpf of *arf3a/arf3b* MO-injected embryos (**d'**, **d''**). Respectively, in **d'** and **d''** no. of embryos = 50, 48 (not injected); 25, 22 (MO 0.4 mM, ****p* = 0.0002, *****p* < 0.0001); 31, 27 (MO 0.6 mM *****p* < 0.0001); 21, 17 (MO 0.8 mM, *****p* < 0.0001) of one batch. **e–e''** Bright-field images (**e**) and phenotype incidence at 24 and 48 hpf (**e'**, **e''**) of *arf3a/arf3b* MO-injected embryos (0.6 mM

–/+ARF3^{WT}-encoding mRNA. The images in **d** and **e** are representative of embryos of one batch. Respectively in **e'** and **e''**, no. of embryos = 47 (not injected); 22, 18 (MO 0.6 mM, *****p* < 0.0001); 17, 15 (MO 0.6 mM + ARF3, ***p* = 0.0091 in **e'**) of one batch. **f** Phenotype worsening index at 48 hpf (fold-change) for ARF3 mutants (severe + deceased) compared to controls (co-injected with *arf3* MO). In the scatter plot the values < 0 (green) are found in the “alleviation window” depicted with green shading. Dots represent the “worsening index” for each experiment, calculated by dividing the percentage of severely diseased fish (class IV–V) in “MO+” condition by the same percentage obtained in “MO–” condition of two (K127E, L12V/D67V, P47S, T32N) or three (D93N) independent batches. The mean effect of MO for each mutation is also shown as bar graph. No. of embryos = 21 and 36 (K127E – and + MO **p* = 0.0307); 58 and 47 (L12V/D67V – and + MO, **p* = 0.0068); 45 and 54 (P47S – and + MO); 86 (D93N+ and – MO, ****p* = 0.0004); 64 and 35 (T32N – and + MO, **p* = 0.0370). Data in the bar graphs are expressed as a mean ± SEM of two independent batches. Survival is assessed by Log-Rank (Mantel–Cox) test (**c'**). Two-sided Chi-square's test in a 2 × 2 contingency table (class II, III and IV vs. I in **c'**, **d'**, **d''**, **e'**, **e''**) or Two-sided One sample *t*-test (class III/ IV vs. I in **f**) testing null hypothesis *H*₀, represented by the expected mean value of the control population, are used to assess statistical significance. Source data are provided as a Source Data file.

Next, by assessing the known chromatin morphology through the inspection of pH3 staining appearance, we profiled cells with respect to the cell cycle stage⁹⁴. Compared to controls, significant alterations in the relative proportion of mitotic cells between early phases (prophase/prometaphase), metaphase, or late phases (anaphase/telophase) were observed in embryos expressing the ARF3 mutants with the exception of ARF3^{P47S}. Specifically, precursor cells scored a higher percentage of pH3⁺ cells in prophase/prometaphase at the expense of later cell cycle stages, suggesting a delay or arrest in early mitosis (Fig. 9b, d, e).

Precursor cells failing to progress through the cell cycle are normally targeted to apoptosis via mitotic surveillance systems⁹⁵. Similar mechanisms activated during aberrant neurogenesis deplete the pool of stem cells available for neurogenesis and brain growth and result in microcephaly^{86,87}. To test this possibility, we next assessed the cell death rate within the forebrain of our fish mutants by live embryo staining with acridine orange (AO). The analysis showed a significant increase of AO⁺ spots (i.e., dying cells and/or apoptotic bodies) in ARF3^{K127E} and ARF3^{L12V/D67V} expressing fish (Fig. 9f, g, upper graph). This finding is in line with the clinical and functional in vivo data reporting p.K127E and p.L12V/D67V as the ARF3 amino acid substitutions associated with the most severe phenotype characterized by early-onset microcephaly in patients and severe head area reduction in fish, respectively. Increased cell death was also recorded for ARF3^{P47S} and ARF3^{D93N} expressing fish when a larger area of the forebrain including the eyes was examined (Fig. 9g, lower graph).

Last, given the importance of Golgi for the establishment and the dynamics of mitotic spindles in dividing precursors^{88–90}, we asked whether spindle aberrations could at least partially explain the cell cycle alterations observed in fish, as previously reported in a number of cortical malformations with microcephaly^{91–93}. We took advantage of the transgenic line *Tg(XlEef1a1:clck2DeltaK-GFP)* marking microtubules in early embryos and investigated metaphase spindles morphology within the anterior ventral brain in live embryos expressing ARF3^{WT}, ARF3^{K127E} and ARF3^{D93N}, causing early- vs. late-onset microcephaly. Compared to controls, aberrantly elongated spindle morphology was recorded for both mutants (Supplementary Fig. 19), indicating a common effect on spindle microtubule organization, likely explaining the similar impact on the cell cycle.

Collectively these data suggest a complex impact of different ARF3 mutants on neurogenesis and point to an impaired balance between precursors' cell mitosis and cell death as a mechanism contributing to the observed neurodevelopmental phenotypes.

ARF3 mutants variably impact PCP-dependent axes formation in early zebrafish development

We next detailed the morphological defects and developmental processes implicated in the observed body curvature. We focused on the notochord, which supports the body elongation along the anterior to the posterior axis (AP) and spine formation⁹⁴, and whose altered development has been associated with CA ARF1 in fish⁹⁷. We documented the occurrence of multiple notochord curvatures of variable degrees in animals expressing each of the ARF3 mutants except ARF3^{P47S} (Fig. 10a–c). Quantification of the degree of bending (180°: normal; 179° ≥ angle ≥ 110°: mild; angle ≤ 109°: severe) showed a similar incidence of mild and severe bending (in >90% of embryos) in fish expressing ARF3^{K127E} and ARF3^{L12V/D67V} (Fig. 10b, c), in line with the overall severity of the skeletal phenotype characterizing subjects 1 and 2 (Supplementary Fig. 1, Supplementary Table 1 and clinical reports). Overall, all mutants except ARF3^{P47S} showed a significantly higher number of notochord curvatures (Fig. 10c').

We further examined the underlying causes of the perturbed body trunk and notochord morphogenesis by tracing back axes establishment in development. First, we examined patterning and morphogenesis in animals in their segmentation stage (15 hpf). During this period, the embryo AP and mediolateral (ML) axes are already established and somitogenesis occurs. mRNA levels of *Krox20* and *MyoD* (markers of the hindbrain rhombomeres in the anterior cephalic domain and of developing somites from the paraxial mesoderm, respectively) were assessed in whole-mount embryos by in situ hybridization (ISH). While proper patterning of the cephalic region and paraxial mesoderm was in place, we observed a variable perturbation of the AP and ML axes in the ARF3 mutants (Fig. 10d, e). Embryos expressing ARF3 mutants showed a clear shortening of the AP length compared to WT (Fig. 10e, f). Consistently, the number of somites in mutant embryos was also reduced (Supplementary Fig. 20). Expansion of the paraxial tissue in the ML axis was also apparent for some mutants (Fig. 10e). The data pointed to a defective convergence-extension (CE) process, which was evident for all mutants except ARF3^{P47S} when the CE index (i.e., the ratio between the AP extend and ML extend of the anterior somites) was assessed (Fig. 10e, g). For both AP and ML axes defects, severely affected embryos were more prevalent among those expressing ARF3^{K127E}.

Lastly, benefiting from the transparent and fast zebrafish development, we assessed the time occurrence of axes defects linked to gastrulation (and thereby CE) perturbation by investigating earlier stages (Supplementary Fig. 21a). Already between 10 and 13 hpf, when segmentation has just started, brain thickenings and tail bud are visible at the very anterior and posterior end of the embryo, respectively, as a

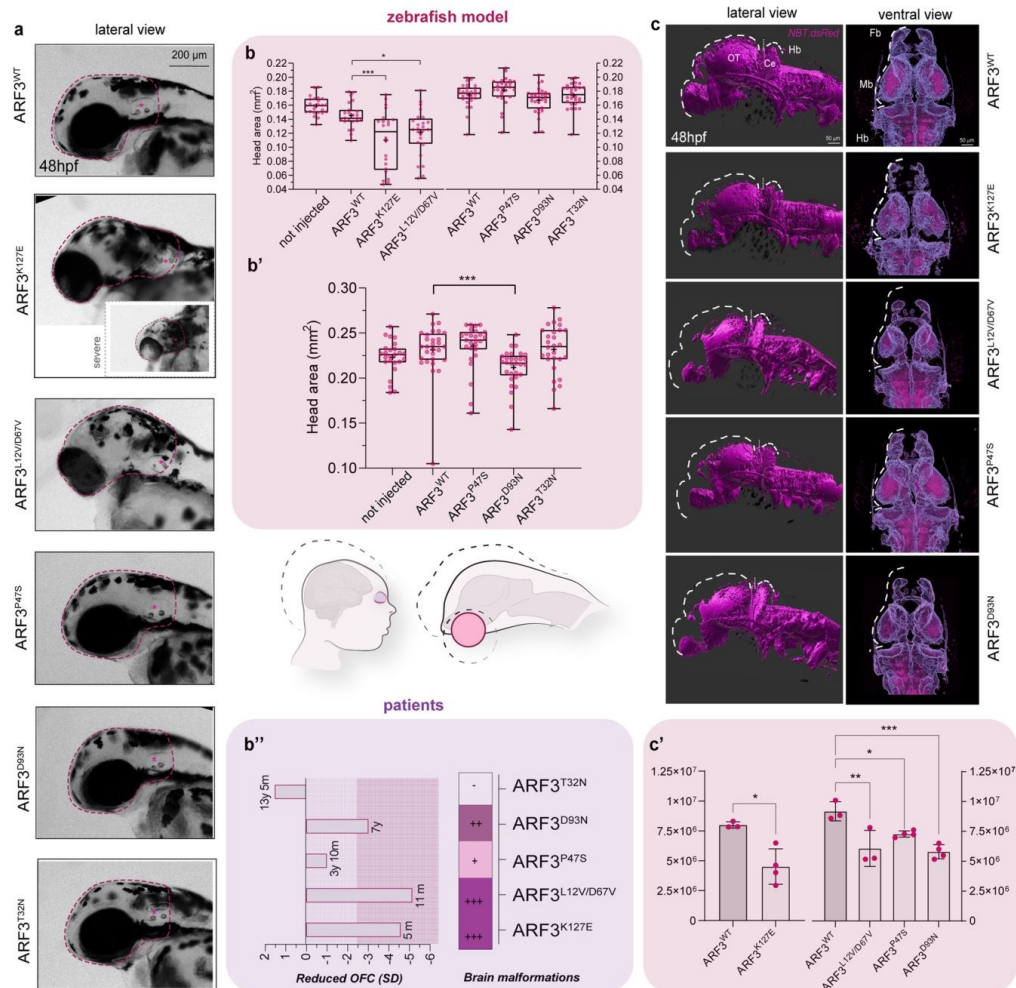


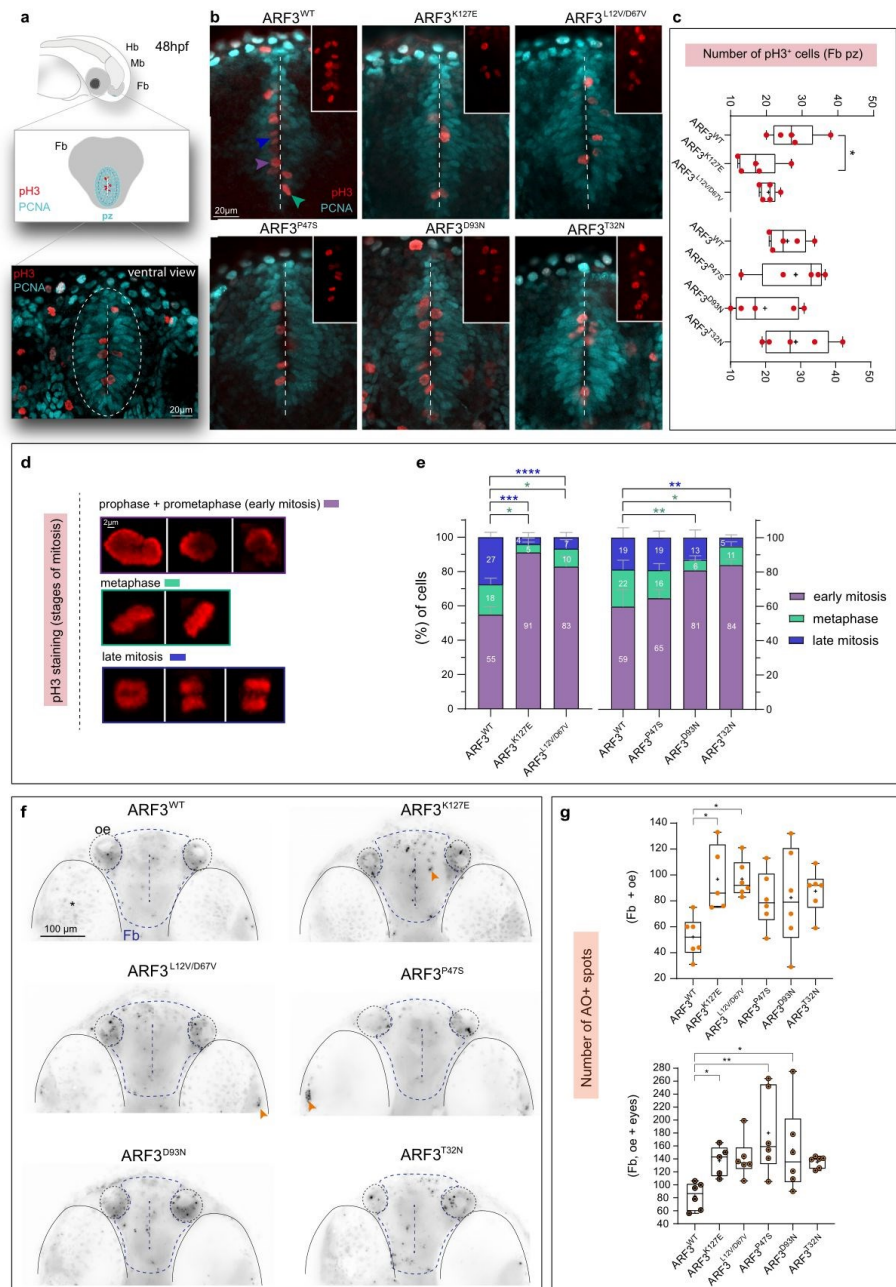
Fig. 8 | Occurrence of microcephaly and reduced brain volume in zebrafish expressing a subset of ARF3 mutants. **a** Bright-field images of the head (purple dashed line) in fish expressing WT and mutant ARF3 at 48 hpf (the inset for ARF3^{K127E} documents a severe case). The images are representative of embryos from two independent batches. **b-b'** Head area quantification at 48 hpf (**b**) and 4.5 dpf (**b'**). In **b**, set 1: no. of embryos = 25 (not injected), 23 (WT); 22 (K127E, *** $p = 0.0002$) and 25 (L12V/D67V, * $p = 0.0106$) of one batch; set 2: no. of embryos = 29 (WT); 28 (P47S); 30 (D93N); 29 (T32N). In **b'**, no. of embryos = 30 (not injected); 30 (WT); 27 (P47S); 30 (D93N, *** $p = 0.0006$) and 28 (T32N) of one batch. Data are expressed as box-and-whisker with median (middle line), 25th–75th percentiles (box), and min–max values (whiskers). All the data points and the mean (“+”) are also shown. **b''** Schematics of the brain volume reduction in human patients harboring a subset of ARF3 mutants and in zebrafish models generated in this study. The human brain in the illustration was created with BioRender.com and modified using Illustrator (Adobe). A summary of OFC and brain malformations data from patients in this study are depicted below (no sign of brain malformation (–), mild (+), moderate (+

+), and severe (+++) malformations). **(c)** Volumetric reconstructions (**c**) and anterior brain volume (white dashed line) from live confocal acquisitions from whole brains of 48hpf *Tg(NBT:dsRed)* fish injected with mRNA encoding WT and ARF3 mutants. The images are representative of embryos from two independent batches for WT, K127E, and L12V/D67V and from one batch for the other mutants. OT: optic tectum, Ce: cerebellum, Fb: forebrain, Mb: midbrain, Hb: hindbrain. **c'** Quantification of the brain volume. Set 1: no. of embryos = 4 (WT); 4 (K127E, * $p = 0.0163$) from one batch; set 2: no. of embryos = 3 (WT); 3 (L12V/D67V, ** $p = 0.0029$); 4 (P47S, * $p = 0.0350$) and D93N, *** $p = 0.0010$) of one batch. Data are expressed as mean \pm SEM. Different datasets for the same measurement are shown in adjacent plots with the internal WT control for each set, not injected controls between batches are not significantly different. One-way ANOVA followed by Dunnett’s multiple comparison *post hoc* test (**b**, left panel; **c'**, right panel), Kruskal–Wallis followed by Dunn’s multiple comparison *post hoc* test (**b**, right panel; **b'**), unpaired *t*-test with Welch’s correction (**c'**, left panel) are used to assess statistical significance. Source data are provided as a Source data file.

result of correctly orchestrated gastrulation movements⁷⁶. By measuring the angle between the developed cephalic and caudal structures at this stage, we documented a reduced embryo elongation (likely due to aberrant/delay gastrulation) for ARF3^{K127E} and ARF3^{D93N}

(Supplementary Fig. 21b, c), indicating an early impact of these mutants on axes formation.

Perturbed cell movements were further confirmed in live embryos expressing ARF3^{K127E}, which exhibited the strongest effect in terms of



axis elongation (AP, ML). Early embryos (6–7 hpf) showed reduced epiboly and impaired gastrulation, which ultimately resulted in defective head and tail bud formation (Supplementary Fig. 21d, e). Of note, cells expressing the mutant appeared mostly round, with a reduced number of protrusions, with respect to cells expressing the WT protein (Supplementary Fig. 21d–f), suggesting the occurrence of

altered polarity establishment and cytoskeletal organization as an early molecular event, in line with the emerging roles of Golgi in instructing cell polarity⁴⁵.

These *in vivo* findings demonstrate impairment of axes formation of variable degree as a common trait of the mutants causing skeletal deformities in patients, broadly recapitulating the severity of the

Article

Fig. 9 | Increased number of cells in early mitosis and cell death within the developing forebrain of zebrafish expressing a subset of ARF3 mutants.

a Schematics of the forebrain (Fb, gray) proliferative zone (pz, cyan) and a confocal scan of the ventral Fb in zebrafish expressing ARF3^{WT} (dashed white circle) showing proliferative and mitotic cells (PCNA and pH3 staining in red and cyan, respectively). Mb: midbrain, Hb: hindbrain. **b** Maximum intensity z-projections from a subset of confocal sections showing pH3⁺ mitotic cells within the ventral Fb (vFb) in zebrafish expressing WT and mutant ARF3. The images are representative of embryos from one batch. Dashed white line indicates the Fb ventricle, insets show zooms on pH3⁺ cells. Arrowheads indicate examples of pH3⁺ cells in different stages of mitosis: early mitosis (purple); metaphase (green) and late mitosis (blue). **c** Quantification of the total number of pH3⁺ cells in pz, no. of embryos = 5 (WT and K127E, **p* = 0.0217) of one batch. Data are expressed as box-and-whisker with median (middle line), 25th–75th percentiles (box), and min-max values (whiskers). All the data points and the mean ("*") are also shown. **d, e** Incidence of pH3⁺ cells in the different mitosis stages. No. of cells = 111 and 110 (WT); 61 (K127E, early mitosis vs. metaphase **p* = 0.0168, early vs. late mitosis ****p* = 0.0003); 88 (L12V/D67V, early mitosis vs. metaphase **p* = 0.0115, early vs. late mitosis *****p* < 0.0001); 75 (D93N,

early mitosis vs. metaphase ***p* = 0.0028); 110 (P47S); 109 cells (T32N, early mitosis vs. metaphase **p* = 0.0267, early vs. late mitosis ***p* = 0.0069) from five embryos of one batch. Data are expressed as mean ± SEM. In **c** and **e** different datasets for the same measurement are shown in adjacent plots with the internal WT control for each set. **f** Maximum intensity z-projections of the ventral brain stained with the acridine orange (AO). The black and white images are rendered by inverting the original LUT in Fiji. The images are representative of embryos from two independent batches. Orange arrowheads indicate specific staining. vFb pz, ventricle, eyes, and olfactory epithelium (OE) are outlined for morphological guidance, *indicates eyes with pigmentation background. **g** Quantification of the number of AO⁺ spots. No. of embryos = 6 (WT); 5 (K127E, **p* = 0.0163, **p* = 0.0461 for upper and lower graphs, respectively); 6 (L12V/D67V, **p* = 0.0109); 6 (P47S, ***p* = 0.0017 and D93N, **p* = 0.0387) of one batch. Data are expressed as box-and-whisker with median (middle line), 25th–75th percentiles (box), and min-max values (whiskers). All the data points and the mean ("*") are also shown. Two-sided Chi-square's test in a 2 × 2 contingency table (**e**), One-way ANOVA followed by Dunnett's (**c** and **g**, upper graph) or Kruskal–Wallis followed by Dunn's (**g**, lower graph) *post hoc* tests are used to assess statistical significance. Source data are provided as a source data file.

clinical phenotype, and tracing back the mechanism to a compromised PCP-dependent CE cell movement for the severe cases.

Discussion

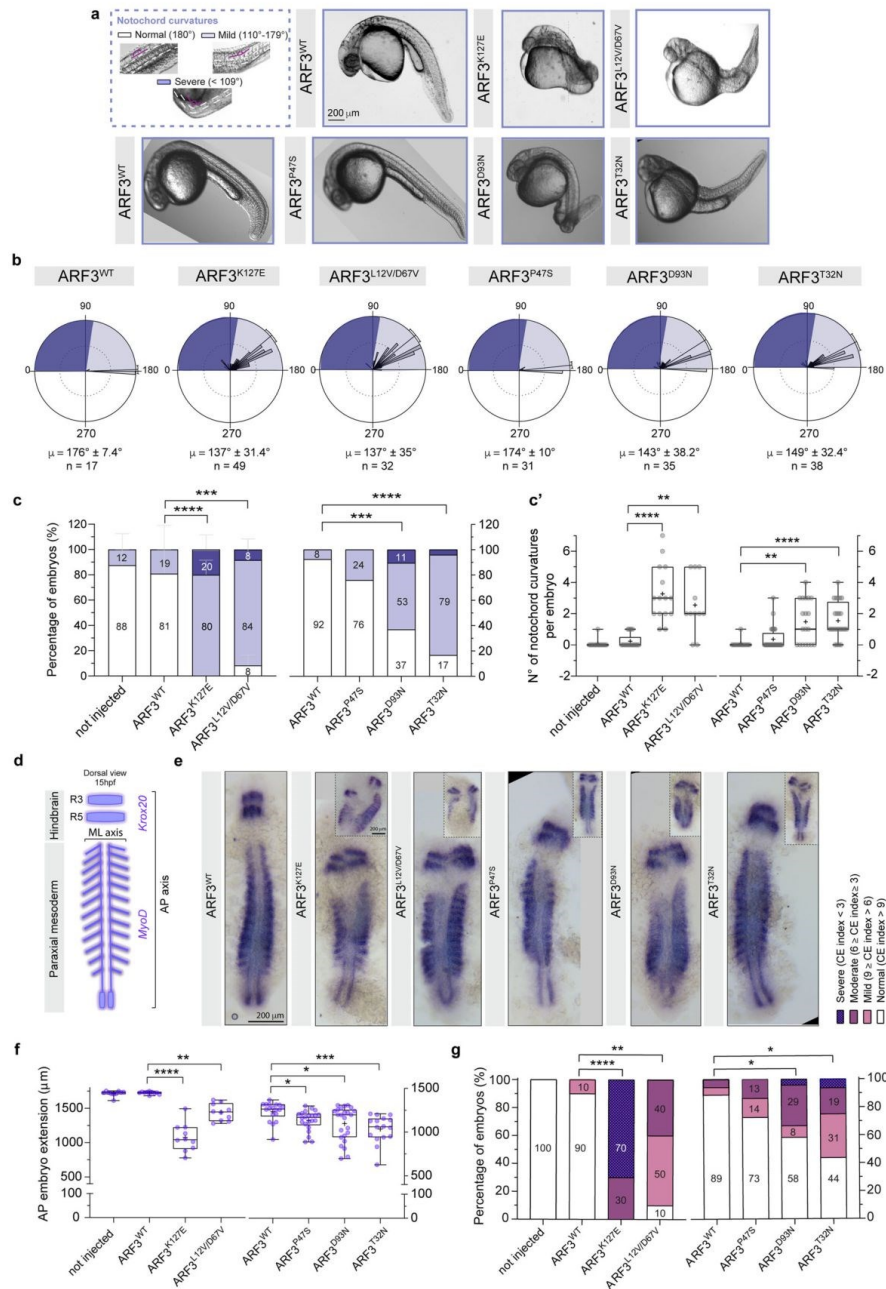
Controlling organelle stability, targeted trafficking of proteins and lipids, and signaling, the highly conserved ARF GTPases contribute to cell polarity, division, and migration ultimately instructing development^{14,47}. Here we identify *de novo* missense ARF3 variants as the molecular event underlying a clinically variable neurodevelopmental disorder characterized by DD/ID and variable CNS defects as common features. Microcephaly and progressive cerebral atrophy occurred in most affected individuals, while epilepsy and skeletal abnormalities were variably documented as associated traits. The clinical phenotype of this disorder is reminiscent of the condition caused by activating mutations in *ARF1*⁴⁹, characterized by DD/ID, microcephaly, delayed myelination, cortical and cerebellar atrophy, periventricular heterotopia and seizures as major features, but also showing periventricular heterotopia. A related neurodevelopmental disorder characterized by DD/ID, progressive microcephaly, failure to thrive, and periventricular heterotopia has been linked to allelic inactivating variants of *ARFGEF2* (ARPHM, MIM: 608097)¹⁶, encoding ARF-specific GEF stimulating the GTPase activation. Consistent with the observed clinical variability, our *in vitro* data demonstrate variable consequences of the identified disease-causing ARF3 variants on protein stability, nucleotide binding activity, and exchange, as well as on *trans*-Golgi and vesicle integrity and function. The differential impact of DN and CA on Golgi integrity is supported by *in vivo* validation. Zebrafish models, which recapitulate the pleiotropic effect and the variable strength of each ARF3 variant on developing brain and body axes, offer further insights into the underlying sub-cellular and cellular pathogenic mechanisms.

The activity of ARF3 at the *trans*-Golgi is tightly regulated via a conformational switch controlled by reversible GDP-to-GTP binding, which determines Golgi stability and trafficking^{22,32}. Our structural inspection indicates that the majority of the disease-causing ARF3 mutations affect conserved residues involved in GDP/GTP binding/exchange, previously reported to be mutated in other GTPases of the RAS superfamily (e.g., ARF1, HRAS, KRAS, NRAS, MRAS, RRAS, RAS2), which cause neurodevelopmental syndromes or contribute to oncogenesis^{49,96–101} (COSMIC database, Supplementary Fig. 2a and Supplementary Table 8). Lys¹²⁷ in ARF3 (mutated in Subject 1) is homologous to Lys¹¹⁷ in HRAS (MIM: 190020), which if mutated causes Costello syndrome (CS [MIM: 218040])¹⁰². Pro⁴⁷ (mutated in Subject 3) is homologous to Pro³⁴ in HRAS, KRAS, and NRAS. The same Pro-to-Ser change has previously been reported as a somatic event in *HRAS* underlying vascular tumors¹⁰³, and other changes affecting this residue

in KRAS, HRAS, and NRAS have been described in RASopathies^{104–106} (ClinVar IDs: VCV000040454, VCV001052630, VCV000039647). Furthermore, a missense change affecting the adjacent residue in ARF1 (p.Thr48Ile) was observed in a patient with clinical features overlapping with the present series¹⁰⁶. In *HRAS* and *KRAS*, mutations affecting Thr³⁸, which is adjacent to the aspartic acid residue homologous to Asp⁶⁷ in ARF3 (mutated in Subject 2), have causally been linked to RASopathies^{104,107,108}. Consistent with our findings, a recent report identified two missense changes affecting Asp⁶⁷ and Arg⁹⁹ of ARF3 in patients showing severe microcephaly at birth and progressive cortical and brainstem atrophy and epileptic seizures, and neurodevelopmental delay, cerebellar hypoplasia, and epilepsy, respectively⁵⁰. Finally, both p.Pro47Ser and p.Asp67Val affect a conserved hydrophobic region of ARF3 involved in effector binding^{24,30,109}, with molecular dynamics simulations suggesting a major perturbation exerted by p.Pro47Ser on ARF3 binding to effectors. These considerations stimulate future studies aimed to demonstrate whether effector binding in these mutants is qualitatively and/or quantitatively altered.

Our *in vitro* data show an altered behavior of all ARF3 mutants in terms of stability and GTP binding. Among these, two amino acid changes, p.D93N and p.P47S were classified as CA, with the former exhibiting the strongest activation, in line with the severe and milder phenotypes observed in patients harboring these variants, respectively. The GTP binding behavior of the p.T32N substitution could be classified as DN, while a more complex behavior emerged for p.K127E and p.L12V/D67V variants. The dramatically accelerated degradation of the two ARF3 mutants and reduced absolute levels of their GTP-bound forms cannot rule out the possibility of a loss-of-function behavior, which is in contrast with the activating role of the p.Lys117Arg substitution in *HRAS* causing upregulation of MAPK signaling in Costello syndrome^{102,110}. Similar to this variant, however, a biochemical investigation performed on purified proteins in a cell-free system demonstrates an increased nucleotide exchange rate and excludes any significant impact on the GTPase catalytic activity. The reduced activity of the purified ARF3^{L12V/D67V} is instead in line with the structural prediction, anticipating a destabilization of both GTP and GDP binding via impaired coordination with Mg²⁺. It should be noted that myristylation is not achieved in the bacterial expression system employed to purify the proteins and the used cell-free assay does not account for the relevance of the lipid bilayer on the structural rearrangement of the GTPase and its and function^{20,111}. Future dedicated experiments are required to more accurately examine the biochemistry of these mutants.

To functionally characterize the behavior of ARF3 mutants we profiled their impact on Golgi morphology. While depletion of ARF1 or ARF3 was not reported to affect Golgi structure¹⁰, a differential impact of DN and CA forms are known. Golgi fragmentation with the



dispersion of specific Golgi associated and coat proteins (β -COP) is reported for DN ARF mutants^{20,50,61}, while an extension of the Golgi compartment, with swelling of Golgi and COP-I vesicles resulting in sustained vesiculation, has been associated with expression of constitutively active mutants^{23,61}. The observed *trans*-Golgi and vesicle morphotypes identify different functional classes, mirroring CA and

DN behaviors. The pathophysiological relevance of these findings for embryonic development is supported by *in vivo* analysis of live *trans*-Golgi morphology in early zebrafish embryos overexpressing ARF3^{K127E} and ARF3^{D93N}. Nevertheless, the molecular mechanism by which aberrant ARF3 function causes different Golgi fragmentation patterns and the extent to which antero-retrograde transport might be impaired

Fig. 10 | Aberrant ARF3 function causes axial defects with notochord curvatures and defective axes formation in zebrafish. **a** Notochord curvatures of variable severity (purple angles schematics) and bright field images of WT and mutant ARF3 expressing fish at 30 hpf. The images are representative of embryos from three (WT, K127E, and L12V/D67V), two (P47S), and one batch (other mutations). **b** Rose diagrams showing notochord angles, no. of angles = 17 (WT); 49 (K127E); 32 (L12V/D67V); 31 (P47S); 35 (D93N) and 38 (T32N) pooled from a total n of embryos indicated below (c). Mean vector (μ) \pm circular SD is shown. Dark and light violet shadings in the rose diagrams represent mild and severe classes of notochord curvatures, respectively. **c** Incidence of embryos with mild or severe notochord curvatures, set 1: no. of embryos = 9 (not injected); 17 (WT); 15 (K127E, **** p < 0.0001) and 11 (L12V/D67V, **** p = 0.0005) of three independent batches; set 2: no. of embryos = 13 (WT); 28 (P47S); 19 (D93N, *** p = 0.0003) and 24 (T32N, **** p < 0.0001) of one batch. Data are expressed as mean \pm SEM (set 1) or mean (set 2). **c'** Quantification of the number of notochord curvatures per embryo from one batch (same n of embryos as in c): K127E, **** p < 0.0001; L12V/D67V, ** p = 0.0015; D93N, ** p = 0.0022 and T32N, **** p < 0.0001. **d** Schematics of *Krox20* and *MyoD* expression at 15 hpf. Black square brackets indicate AP and ML axes. R3 and R5:

rhombomeres 3 and 5. **e** Bright-field images showing *Krox20* and *MyoD* in situ mRNA staining (insets show severe cases). The images are representative of embryos from two independent batches for WT, K127E and L12V/D67V and from one batch for the other mutations. **f** Quantification of AP embryo extension, set 1: no. of embryos = 10 (not injected); 10 (WT); 10 (K127E, **** p < 0.0001); 10 (L12V/D67V, ** p = 0.0078); set 2: no. of embryos 18 (WT); 22 (P47S, * p = 0.0169); 24 (D93N, * p = 0.0207) and 16 (T32N, *** p = 0.0002) of one batch. In **c'** and **f** data are expressed as box-and-whisker with median (middle line), 25th–75th percentiles (box), and min-max values (whiskers). All the data points and the mean ("+") are also shown. **g** Incidence of fish with different convergence and extension (CE) index values (same no. of embryos as in **f**) **** p < 0.0001 (K127E and L12V/D67V), ** p = 0.0015; * p = 0.0251 (D93N), * p = 0.039 (T32N). Different datasets for the same measurement are shown in adjacent plots with the internal WT control for each set. Not injected controls between batches are not significantly different. Non-parametric Kruskal–Wallis followed by Dunn's multiple comparison *post hoc* test (**c'**, **f**). Two-sided Chi-square's test in 2 \times 2 contingency table (**c**, **g**, normal vs. phenotype) are used to assess statistical significance. Source data are provided as a Source Data file.

due to defective COP-I assembly and function remains to be determined. In this context, it should be noted that the specific Golgi phenotype shown by p.K127E, p.L12V/D67V, and, to a less extent, p.T32N are reminiscent of the BFA-induced effect in cells. Upon treatment with BFA, the ARF–GDP–GEF complex titrates the available GEF molecules away from the other ARF proteins, inhibiting their function⁴². Indeed, only co-occurring loss of function of multiple ARF proteins is able to perturb organelle and vesicle integrity^{20,112}.

Defective Golgi stability and activity is an emerging cause of cortical malformation⁴². The finding of fragmented Golgi in cells and embryos expressing the disease-associated ARF3 mutants assigns this disorder to the recently defined family of "Golgiopathies", a group of heterogeneous neurodevelopmental disorders clinically characterized by a wide spectrum of CNS abnormalities^{12,13}. Even if not detailed and therefore not easily comparable to our work, the recent functional investigation carried out by Sakamoto et al. on two *ARF3* mutations causing a similar neurodevelopmental condition corroborates the present findings.

Regulated transport through the endolysosomal system assists the differential targeting of cargos containing signaling molecules, polarity, and morphogenic factors to the membrane or to the *trans*-Golgi network for retrieval or to lysosomal degradation. The importance of healthy machinery to support this choice is just starting to gain attention in the context of development and disease^{73,113}. Of note, our experiments with fluorescently labeled Tfn in combination with staining for EE, RE, and lysosomes unravel a cargo accumulation and delayed recycling in cells expressing ARF3 mutants specifically leading to early-onset microcephaly and severe skeletal defects. Interestingly, only an increased lysosomal Tfn cargo delivery seems to occur for p.D93N causing late-onset microcephaly and mild skeletal deformities. The data also suggest a general overload of the lysosomal system for all mutants, the relevance of which should be further investigated. Thereby, besides the clear distinction in Golgi morphological patterns, a variable impact on the efficiency of sorting and transport seem to underlie the variable severity observed in our patients. Adding to our evidence, impaired endosomal trafficking of EGF signaling components and Tfn recycling underlie proliferative defects recently identified as a major cause of a neurodevelopmental disorder with microcephaly^{114,115}.

The attentive *in vivo* investigation performed here makes a strong case for the importance of correct ARF3 function during a number of processes supporting embryogenesis. First, the extensive phenotypic characterization in zebrafish provides sufficient evidence of the pathogenicity of all the identified *ARF3* variants and their dominant nature. In line with the Golgi phenotype observed *in vitro*, overexpression of ARF3 mutants and downregulation of endogenous *arf3* in zebrafish embryos corroborate the DN (p.K127E, p.L12V/D67V, and p.T32N) and CA (p.D93N) behaviors *in vivo*.

Independently of the specific mechanism of dominance, all mutants modeled in fish recapitulated the involvement of brain and axes malformations and the variable strength of the disease manifestation. Strikingly, similar to patients, overexpression of ARF3^{K127E} and ARF3^{L12V/D67V} produce early-onset severe microcephaly in fish, while fish expressing ARF3^{D93N} show late-onset microcephaly. Furthermore, in-depth brain analysis documents underlying brain volume reduction and validates defective forebrain white matter as a common feature of this neurodevelopmental disease. In line with these results, a severe vs. mild clinical phenotype was anticipated in the yeast *arf1* mutants involving Lys¹²⁷ and Asp⁹³, documenting complete or incomplete dominant lethal phenotypes, respectively⁵⁶.

Mechanistically, our *in vivo* work also provides insights into the processes that might hinder neurogenesis and contribute to neurodevelopmental defects. Our cell cycle profiling experiments indicate a possible delay of the mitosis in the early stages and an increased cell death within the developing anterior brain for the majority of the ARF3 fish mutants. A "Golgi checkpoint" sensing Golgi integrity and correct segregation has been suggested as an additional level to control cell cycle progression¹¹⁶, whose contribution to the observed brain growth and morphogenesis defects is worth further investigation. On the other hand, our live imaging of the developing fish forebrain determined the occurrence of altered spindle morphology in microcephaly-causing ARF3 mutants, which might ultimately underlie mitotic arrest and cell death. Supporting this hypothetical scenario, mitotic arrest resulting in increased apoptosis of cells with aberrant spindle are appreciated as pathological mechanisms underlying conditions characterized by cortical malformations and microcephaly, some of which have already been successfully modeled in zebrafish^{80,81,92,93,117}. The involvement of Golgi function in cell division, microtubule organization, and spindle formation is recognized^{88,89}. In line with our data, elongated spindles result from the depletion of the constituent Golgi proteins, which keep the integrity of the organelle in mouse oocyte⁹⁰. The role of ARF1 in mediating Golgi morphological changes during mitosis⁴³, and the function of class I ARF proteins in controlling proliferation have been reported^{118,119}, including the ARF3 involvement in cell cycle progression and apoptosis in gastric cancer¹¹⁸. Our zebrafish data show variably penetrant effects on cell proliferation and death, especially for p.P47S and p.T32N. This resembles the milder effect of these two mutants observed in cells in terms of Golgi integrity, vesicle assembly and recycling and anticipated by the mildest clinical traits associated with them. An investigation including a larger sample size might further clarify the presence of subtler effects. Conversely, additional, and not explored mechanisms might produce the mild phenotypes observed.

Lastly, strengthening the causal association of the described *ARF3* mutations to the observed skeletal traits, variable degrees of axial

malformations have been highlighted in the generated fish models recapitulating the severity of the disease in humans. Likewise in patients, similar defects are associated with DN and CA mutations, with p.K127E and p.L12V/D67V producing the most severe effects. Morphometric and live imaging analysis in early embryonic stages traced back the first assessable effect to defective PCP-mediated cell motility. CE movements, which require a fine-tuning of cell polarity factors within cells and are needed to shape the AP and ML axes^{120–122}, are evidently affected by ARF3 mutants. Of note, biosynthetic trafficking and correct function of ER and Golgi is essential during animal development for regulating morphogens' distribution^{46,47,123}, and required for cell polarity establishment and migration, as shown in vitro¹²⁴, nematodes¹²⁵, and zebrafish¹²⁶. Consistent with our findings, fish expressing the CA microcephaly-associated ARF1 mutant show similar PCP-related axial defects⁴⁷. Moreover, fish mutants for ARF-interacting COP-I/COP-II coat components exhibit skeletal and notochord abnormalities associated with Golgi disassembly^{127,128}. On the other hand, post-Golgi trafficking and sorting of polarity components also contribute to brain development, underlying correct asymmetric cell division and migration in vertebrate neurogenesis, axon arborization, and synaptogenesis^{46,129}. Along these lines, the impaired function of ARFGEF2 underlying the microcephalic traits observed in patients with ARPHM has been indeed linked to proliferative and migratory defects due to *trans*-Golgi to membrane trafficking of E-cadherins and beta-catenin¹⁶. The direct contribution of the impaired recycling found in cells to the observed brain defects in vivo remains to be assessed.

In conclusion, our work identifies *ARF3* as a gene implicated, when mutated, in a clinically variable neurodevelopmental disorder belonging to the emerging class of "Golgiopathies"^{42,13}. Our findings specifically highlight the role of ARF3 in the maintenance of *trans*-Golgi integrity and document an obligate dependence of early developmental processes and brain morphogenesis on the proper function of this GTPase. The generated in vivo models represent a tool that can be exploited to deepen our understanding of the pathological mechanisms underlying the disease.

Methods

Subjects

The study has been approved by the local Institutional Ethical Committee of the Ospedale Pediatrico Bambino Gesù IRCCS (OPBG), Rome (1702.OPBG.2018). Subject 1 was analyzed in the frame of a research project dedicated to undiagnosed disorders (Undiagnosed Patients Program, OPBG), while the other subjects were referred for diagnostic genetic testing. Clinical data and DNA samples were collected, stored, and used following procedures in accordance with the ethical standards of the Declaration of Helsinki protocols, and after signed consent from the participating families. The authors affirm that human research participants provided informed consent for the publication of the images in Supplementary Fig. 1 and of clinical information potentially identifying individuals.

Exome sequencing analysis

In all families, WES was performed using DNA samples obtained from leukocytes and a trio-based strategy was used. Target enrichment kits, sequencing platforms, data analysis, and WES statistics are reported in Supplementary Tables 3–7 and in the Supplementary Methods. WES data processing, read alignment to the GRCh37/hg19 version of genome assembly, and variant filtering and prioritization by allele frequency, predicted functional impact, and inheritance models were performed as previously reported^{130–134}. WES data output is summarized in Supplementary Tables 3–7. Cloning of the genomic portion encompassing the c.34C>G and c.200A>T missense substitutions (p.Leu12Val and p.Asp67Val; Subject 2) was used to confirm that both variants were on the same allele. Variant validation and segregation were assessed by Sanger sequencing in all the subjects included in the study.

Structural analysis and molecular dynamics simulations

The structural impact of the disease-associated missense changes was assessed using the available three-dimensional structures of human ARF3 complexed with GTP and *V. vulnificus* multifunctional-autoprocessing repeats-in-toxin (MARTX) (PDB 6ii6, <https://www.rcsb.org/structure/6ii6>)⁵². The structure was visualized using the VMD visualization software v.1.9.3¹³⁵. A model of GTP-bound ARF3 interacting with the cytosolic coat protein complex subunits γ -COP (COPG1) and ζ -COP (COPZ1) was built using the SWISS-MODEL automated protein structure homology modeling server (<http://swissmodel.expasy.org>)¹³⁶ using the 2.90 Å resolution X-ray structure (PDB 3TJZ)⁵⁹. The alignment of template and model amino acid sequences is reported in Supplementary Fig. 21. The p.Asp67Val and p.Pro47Ser mutations were introduced using the UCSF Chimera v.1.15¹³⁷. The side-chain orientations were obtained with the Dunbrack backbone-dependent rotamer library¹³⁸, choosing the best rotamer with minimal/no steric clashes with neighboring residues. Following the protonation of titratable amino acids at pH = 7, proteins were added in cubic boxes and solvated in water. Counter-ions were added to neutralize the charges of the system with the genion GROMACS tool¹³⁹. After energy minimizations, the systems were slowly relaxed for 5 ns by applying positional restraints of 1000 kJ mol⁻¹ m⁻² to atoms. Unrestrained simulations were carried out for a length of 500 ns with a time step of 2 fs using GROMACS 2020.2. The CHARMM36 all-atom force field¹⁴⁰ was used for the protein description and water molecules were described by the TIP3P model¹⁴¹. V-rescale temperature coupling was employed to keep the temperature constant at 300 K¹⁴². The Particle-Mesh Ewald method was used for the treatment of the long-range electrostatic interactions¹⁴³. The first 5 ns portion of the trajectory was excluded from the analysis. All analyses were performed using GROMACS utilities.

Expression constructs and in vitro mRNA synthesis

The full-length coding sequence of WT human ARF3 (NM_001659.3) was obtained by PCR and cloned into the pcDNA3.1/myc-6His eukaryotic expression vector (Life Technologies). The disease-associated substitutions were introduced in the pcDNA3.1/myc-6His expressing ARF3 WT and into pcDNA3.1/hArf3(WT)-mCherry (plasmid 79420, Addgene)¹⁴⁴ by site-directed mutagenesis (QuikChange II Site-Directed Mutagenesis Kit, Agilent Technologies, 200522-5). For zebrafish expression experiments, the myc-tagged (C-terminus) WT and mutant ARF3 sequences or mCherry-tagged plasmids were subcloned into the pCS-Dest vector (plasmid 22423, Addgene)¹⁴⁴ via LRllI clonease-mediated recombination (ThermoFisher, 12538120). pCS-Dest-mKOPF2-CAAX and pCS-Dest-EGFP-GalT were generated by subcloning the ADDGENE plasmids 75155¹⁴⁵ and 11929¹⁴⁶, respectively. Plasmids were digested and linearized with *KpnI*-HF (NEB New England Biolabs, R3142S), and mRNA was produced using mMessage mMachine SP6 transcription kit and poly(A) tailing kit (Thermo Fisher, AM1340). All cloned sequences were confirmed by bidirectional DNA sequencing.

COS-1 cell culture and transient transfection assays

COS-1 cells (CRL-1650-ATCC) were cultured in Dulbecco's modified Eagle's medium supplemented with 10% heat-inactivated fetal bovine serum (FBS, GIBCO, 10270-106), 1x sodium pyruvate (EUROCLONE, 11360-039) and 1x penicillin-streptomycin (EUROCLONE, ECB3001D), at 37 °C with 5% CO₂. Subconfluent cells were transfected with plasmids encoding myc- or mCherry-tagged WT and mutant ARF3, EGFP-GalT (Addgene, 11929¹⁴⁶) and GFP-rab11 (Addgene, Plasmid #12674)¹⁴⁷ using FuGENE 6 (Promega, E2691), according to the manufacturer's instructions.

Zebrafish husbandry

Zebrafish NHGRI, *Tg(Xla.Tubb:DsRed)*¹⁴⁸ and *Tg(XlEef1a1:dcIk2DeltaK-GFP)*¹⁴⁹ were cultured following standard protocols. Fish were housed in a water-circulating system (Tecniplast ®) under controlled

conditions (light/dark 14:10, 28 °C, 350–400 μ S, pH 6.8–7.2) and fed daily with dry and live food. All animal experiments were conducted under the approval of the Italian Ministry of Health (DGSA - Direzione generale della sanità animale e dei farmaci veterinari, 23/2019-PR).

ARF3-myc immunoblotting in COS-1 and in zebrafish embryos

Transfected COS-1 cells were lysed in radio-immunoprecipitation assay (RIPA) buffer, pH 8.0, containing phosphatase and protease inhibitors (Sigma-Aldrich, P5726, P0044, P8340). Lysates were kept on ice for 30 min and centrifuged at 16,000 \times g for 20 min at 4 °C. Samples containing an equal amount of total proteins (15 μ g) were resolved by 12% sodium dodecyl sulfate (SDS)–polyacrylamide gel (Biorad, 1610185). Proteins were transferred to nitrocellulose membrane using a dry transfer system (Biorad), and blots were blocked with 5% non-fat milk powder (Biorad, 170-6404) in Phosphate-buffered saline (PBS) containing 0.1% Tween-20 for 1 h at 4 °C and incubated with mouse monoclonal anti-Myc (1:1000, Cell Signaling, 2276 S), mouse monoclonal anti- β -tubulin (1:1000, Thermo Fisher, 32-2600), mouse monoclonal anti-GAPDH (1:1000, Santa Cruz, sc-32233) and anti-mouse HRP-conjugated secondary antibody (1:3000, Thermo Fisher, 31450). For zebrafish immunoblots experiments, total protein lysates from a pool of non-injected control zebrafish embryos and from siblings injected with myc-tagged ARF3^{WT} and mutant ARF3 different stages of development were obtained by syringe homogenization in cold lysis buffer (Tris-HCl 10 mM pH 7.4; EDTA 2 mM; NaCl 150 mM; Triton X-100 1% supplemented with 1X protease inhibitors cocktail (Roche, 11836170001) and equal amounts of protein extracts (40 μ g) were separated on a 12% Sodium dodecyl sulfate (SDS)-polyacrylamide gel. The total protein concentration was determined by the Bradford assay (Bio-Rad) using Infinite M Plex (Tecan). After electrophoresis, the proteins were transferred to PVDF membrane using a wet transfer system (Biorad, for myc-tagged ARF3 mutants at 6 and 12 hpf) or nitrocellulose membrane using Trans-Blot Turbo Transfer System (Biorad, myc-tagged ARF3 mutants from 1.75 to 3.7 hpf). Blots were blocked with 5% non-fat milk powder (Biorad) or bovine serum albumin (BSA, Sigma-Aldrich, A8022-100G) in PBS containing 0.1% Tween-20 (Sigma-Aldrich, P2287) overnight at 4 °C constantly shaking and incubated with the primary antibody in blocking solution. The following primary antibodies were used: mouse monoclonal anti-myc (Cell Signaling, dilution 1:1000, 2276), rabbit polyclonal anti-GAPDH (1:1000, Genetex, GTX124503). Following washes in PBST 0.1%, membranes were incubated with anti-mouse- (1:3000, Thermo Fisher, 31450) and anti-rabbit-HRP-conjugated secondary antibodies (1:3000, Thermo Fisher, 31460). Immunoreactive proteins were detected by enhanced chemiluminescence (ECL) detection kit (Thermo Fisher, 34095) according to the manufacturer's instructions, and an Alliance Mini HD9 with Q9 Mini 18.02-SN software (Uvitec) was used for chemiluminescence detection. Uncropped blots are provided in the Source data file and Supplementary information.

In vitro ARF3 protein stability assays

COS-1 cells were seeded at 3×10^5 in six-well plates and the following day was transfected with WT or mutant myc-tagged ARF3 expression constructs for 24 hours. A subset of transfected cells was then treated with CHX (10 μ g/ml) (Sigma-Aldrich, C7698) for 3 and 6 h and with proteasome inhibitor MG132 (100 μ M) (Sigma-Aldrich, C2211) or with the autophagy inhibitor bafilomycin A1 (200 nM) (Sigma-Aldrich, B1793) for 6 h to assess protein stability and degradation pathways. Alliance Mini HD9 with Q9 Mini 18.02-SN software (Uvitec) was used for chemiluminescence detection. Uncropped blots are provided in the Source data file and Supplementary information.

ARF3 activity (GTP-bound state) assay in COS-1 cells

COS-1 cells (1×10^6) were seeded in 100 mm Petri dishes and transfected with myc-tagged ARF3 expression constructs. Twenty-four

hours after transfection, cells were washed twice with ice-cold PBS and collected in 50 mM Tris (pH 7.4), 150 mM NaCl, 10 mM MgCl₂, 10% Glycerol, 1% NP-40 with proteases and phosphatase inhibitors (Sigma-Aldrich, P5726, P0044, P8340). Cell lysates were further subjected to pull-down using GGA3-conjugated agarose beads (Cell Biolabs, STA-419) and incubated at 4 °C for 60 min. Control samples were pre-incubated with 100 μ M GDP (Cell Biolabs, 240104) or the GTP analog guanosine-5'-(γ -thio)-triphosphate (GTP γ S) (Cell Biolabs, 240103) for 30 min and then pulled-down according to the manufacturer's instructions (Cell Biolabs, STA-407-1). For immunoblotting analyzes, pulled-down samples including GTP γ S/GDP controls and whole cell lysates were combined with a 2 \times sample buffer and denatured at 95 °C for 5 min. Samples were then separated by SDS-PAGE and incubated with mouse monoclonal anti-Myc and mouse monoclonal anti-GAPDH antibodies. GTP-bound protein level was detected by an ECL detection kit (Thermo Fisher, 34577). Alliance Mini HD9 with Q9 Mini 18.02-SN software (Uvitec) was used for chemiluminescence detection. Uncropped blots are provided in the Source data file.

Protein expression and purification, nucleotide exchange, and GTP hydrolysis measurements

Proteins were isolated as glutathione S-transferase (GST) fusion proteins in *E. coli* strain CodonPlusRIL, purified after cleavage of the GST tag via gel filtration Superdex 75 or 200 (GE Healthcare, 28989333, 28989335). Nucleotide-free and fluorescent nucleotide-bound ARF3 proteins were using alkaline phosphatase (Sigma-Aldrich, P0762-250UN) and phosphodiesterase (Sigma-Aldrich, P3243-1VL) at 4 °C. Various fluorescence reporter groups, including Mant and Tamra, have been coupled to 2'-(3'-hydroxyl group of the ribose moiety of GDP and GppNHp (Tamra GTP from Jena Bioscience, #NU-820-TAM, MantdGDP from Jena Bioscience, #NU-205L). All proteins were analyzed by SDS-PAGE and stored at –80 °C. Fluorescence polarization experiments were performed in a Fluoromax 4 fluorimeter in polarization mode. The excitation and emission wavelengths for Mant-deoxy-GDP were 360 nm (slit width: 8 μ m) and 450 nm (slit width: 10 μ m), respectively. For nucleotide exchange reactions, 1 μ M Mant-deoxy-GDP ARF3, 100 μ M GDP, 10 μ M ARFGEF BIG2 were used in 200 μ l of measurement buffer containing 30 mM Tris/HCl, pH 7.5, 10 mM K₂HPO₄/KH₂PO₄, 2 mM MgCl₂ and 3 mM dithiothreitol at 25 °C. For GTP hydrolysis activity 1 μ M of Tamra-GTP bound proteins were used with the excitation, wavelength of 543 nm (slit width: 8 micron) and emission wavelength of 580 nm (slit width: 10 micron), in a buffer containing 30 mM Tris/HCl (pH 7.5), 150 mM NaCl, 5 mM MgCl₂, 3 mM dithiothreitol and a total volume of 200 μ l at 25 °C. The observed rate constants (k_{obs}) were calculated by fitting the data as single exponential decay using GraFit software v.5.0.13¹⁵⁰.

RT-PCR prolife of endogenous *arf3a* and *arf3b* mRNAs in zebrafish embryos

To evaluate gene expression of *arf3a* and *arf3b* paralogs throughout zebrafish embryogenesis, total RNA was isolated from whole embryonic tissue samples at different stages of development (1–18 hpf) using TRIzol reagent (Invitrogen, 15596026). The first-strand cDNA was synthesized from total RNA using the SuperScript™ IV First-Strand Synthesis System (Thermo-Fisher, 18091050) according to the manufacturer's protocol and DNase treatment was performed to avoid genomic DNA contamination. RT-PCR was performed with specific primer sets annealing on conserved regions of *arf3a* and *arf3b* zebrafish paralogs (ENSART00000103639.5 and ENSART00000053775.3, respectively) using GoTaq® G2 Green Master Mix (Promega, M7822) (Supplementary Table 11). Amplification of the elongation factor 1 α (*ef1a*) was used as a housekeeping control gene. Alliance Mini HD9 with Q9 Mini 18.02-SN software (Uvitec) was used for signal detection. Uncropped gels are provided in the Supplementary information.

RT-PCR of myc-tagged ARF3 in COS-1 cells

To verify the expression of myc-tagged ARF3^{K12V/D67V} and ARF3^{K127E} after transient transfection in COS-1 cells, RNA from transfected cells was extracted using RNeasy Mini Kit (Qiagen, 74104) and the cDNA was retrotranscribed using oligo-dT SuperScript IV System kit (Thermo-Fisher, 18091050) according to manufacturer's protocols. The RT-PCR assay was designed to map the boundaries between the C-terminal coding region of ARF3 and the myc-tag sequence (Supplementary Table 11), low number of cycle (i.e. $n = 15$) were used in the PCR reaction to avoid PCR plateau phase and signal saturation. RT-PCR on GAPDH gene was used as internal housekeeping control. KAPA2G Fast ReadyMix (Sigma Aldrich, KK5603) was used to amplify the target sequence, according to protocol instructions. Alliance Mini HD9 with Q9 Mini 18.02-SN software (Uvitec) was used for signal detection. Uncropped gels are provided in the Supplementary information.

ARF3 overexpression and *arf3a* and *arf3b* downregulation in zebrafish embryos

Injection of in vitro synthesized capped mRNAs encoding myc- and mCherry-tagged ARF3 (15 pg, ARF3^{WT}, and mutant ARF3), mKOPF-CAAX (15 pg), H2A-mCherry (15 pg), EGFP-GalT (15 pg), EGFP-CAAX (15 pg) and EGFP-GalT (50 pg) was performed in one-cell stage zebrafish embryos using FemtoJet 4x microinjection system (Eppendorf). mRNA was produced using mMESSAGE mMACHINE[™] SP6 Transcription Kit Poly A Tailing Kit (ThermoFisher, AML340, and AML350). Injected embryos were cultured under standard conditions at 28 °C in fresh E3 medium and for each batch, not-injected fish were used as controls together with fish injected with the WT form of ARF3 mRNA. To perform *arf3a* and *arf3b* knockdown experiments in zebrafish embryos, 0.3 mM of each antisense morpholino oligonucleotides (MO, Gene Tools LLC) targeted specifically to the translational initiation site of *arf3a* and *arf3b* (resulting in 0.6 mM of MO in total) were co-injected into one cell stage embryos (Supplementary Table 11). All the injected fish were monitored every day, and survival rate and phenotype were scored at 24 and 48 hpf.

ARF3 protein localization and Trans-Golgi morphology analysis in fixed COS-1 cells

COS-1 cells (20×10^3) were seeded in 24-well cluster plates onto 12-mm cover glasses and transfected with WT or mutant mCherry-tagged ARF3 expression constructs for 48 h. Cells were then fixed with 4% paraformaldehyde for 10 min at room temperature, followed by permeabilization with 0.025% Triton X-100 for 5 min at room temperature. Cells were stained with mouse monoclonal anti-Golgin-97 antibody (1:50, Invitrogen, A21270) for 1 h at room temperature, rinsed twice with PBS and incubated with Alexa Fluor 488 goat anti-mouse secondary antibody (1:200, Invitrogen, A11017) for 1 h at room temperature. After staining, coverslips were mounted on slides by using Vectashield Antifade mounting medium containing 1.5 µg/ml DAPI (Vector Laboratories, H-1200-10). Images were acquired using a Leica TCS SP8X laser-scanning confocal microscope (Leica Microsystems) using LAS X software v.3.5 equipped with a pulsed and tunable white light laser source, 405 nm diode laser and 2 Internal Spectral Detector Channels (HyD) GaAsP, and an acousto-optical beam splitter (AOBS) allowing separation of multiple fluorescence spectra. Sequential confocal images were acquired using excitation laser lines at 405 nm (for DAPI, emission range 410–480 nm), 488 nm (for Alexa Fluor 488, emission range 500–550 nm) and 594 nm (for mCherry, emission range 600–650 nm), with a HC PL APO CS2 ×63 (numerical aperture, NA, 1.40) oil immersion objective (Leica Microsystems), a 1024 × 1024 format image, 0.38 µm pixel size and 400 Hz scan speed. Z-reconstructions were obtained from a z-step size of 0.5 µm, with an electronic zoom of 1.8x. Maximum intensity projection (MIP) of z-series was obtained by LAS X software v.3.5. Deconvolution analysis (HyVolution v.2 software, Leica Microsystems) using 'best resolution' algorithm of Golgin-97⁺ cisternae and vesicles was applied to z-stacks with an electronic zoom of 4x, to

improve contrast and resolution of confocal raw images; then surface 3D rendering was generated from the deconvoluted images using LASX 3D Analysis tool (LAS X software v.3.5). Evaluation of different Golgi morphologies was performed by creating different masks with Fiji¹⁵¹ to determine the Golgi area (Golgin-97⁺) and identify the cell boundaries (Arf3-mCherry⁺) in transfected cells. Total cell area, Golgi area and mean intensity (MI) for Golgin-97 were calculated for each cell. Whole-cell area was determined using mCherry fluorescence as a mask. Golgi mean intensity (MI of Golgin-97⁺ area, arbitrary units) vs. Golgi area [(Golgin-97⁺ area/total cell area) × 100] were plotted for ARF3^{WT}, ARF3^{K127E} and ARF3^{K127N} and the parameters giving the best separation between the chosen populations were manually selected, as reported in Fig. 3.

Time-lapse imaging of Golgi dynamics in COS-1 cells

For live imaging, COS-1 cells (10×10^4) were seeded into µ-dishes 35 mm (Ibidi) 24 h before transfection. The day after, cells were co-transfected with WT or mutant mCherry-tagged ARF3 and EGFP-GalT constructs. Four hours post-transfection, time-lapse acquisitions were performed with a Leica TCS-SP8X confocal microscope (Leica Microsystems) with a PL Apo CS2 ×20/0.75 objective, using excitation lines at 488 nm (for EGFP, emission range 500–550 nm) and 594 nm (for mCherry, emission range 600–650 nm). Parallel live imaging of control and mutant samples was performed simultaneously using the Mark & Find mode of the LAS X software v.3.5. Cells were monitored every 15 min and imaging was carried out with a 1024 × 1024 format, 0.38 µm pixel size, scan speed of 600 Hz, a zoom magnification up to 1.5 and z-step size of 0.7 µm, time-lapse microscopy was performed with a stage incubator (OkoLab) allowing to maintain stable conditions of temperature at 37 °C, with 5% of CO₂ and humidity during live cell imaging.

Trans-Golgi analysis in live zebrafish embryos

Trans-Golgi morphology was assessed from single confocal images of the animal pole of late gastrulae injected with ARF3^{WT} and ARF3 mutants as well as EGFP-GalT and mKOPF-CAAX mRNA. Images were acquired using a Leica TCS SP8X or Stellaris 5 confocal microscope (Leica Microsystems) equipped with LAS X software v.4.5, a pulsed and tunable white light laser source, 405 nm diode laser, hybrid detectors, and an acousto-optical beam splitter (AOBS) allowing separation of multiple fluorescence spectra, HC FLUOTAR L VISIR ×25/0.95 water-immersion objective, a 1024 × 1024 format at 400 Hz and z-step of 0.75 µm using laser line and emission filters as above. Trans-Golgi morphology (EGFP-GalT⁺) in each cell was scored independently by two researchers and two different categories of the EGFP-GalT⁺ signal were identified: cells showing a "ribbon-like" displayed a recognizable EGFP-GalT⁺ ribbon-like or a circular or semi-circular compact structure, while if no circular nor ribbon-like structure could be recognized and instead the pattern was more dotted, either with a single large and small dots recognizable or with spread dots distributed randomly inside the cytoplasm, cells were classified as harboring a "non-ribbon/puncta-like" EGFP-GalT⁺ staining, as indicated in the main text and in Supplementary Fig. 10.

Transmission electron microscopy analysis of Golgi morphology

COS-1 cells were seeded at 2×10^5 in six-well plates and transfected with ARF3 WT, K127E and D93N for 48 h. Cells were then fixed with 2.5% glutaraldehyde in 0.1 M sodium cacodylate buffer (pH 7.2) 1 h at RT, washed in buffer and post-fixed in 1% OsO₄ in 0.1 M sodium cacodylate buffer for 1 h at RT. Post-fixed specimens were washed in buffer, dehydrated through a graded series of ethanol solutions (30–100% ethanol) and embedded in Agar Resin Kit (Agar Scientific, RI031). Ultrathin sections, obtained by a UC6 ultramicrotome (Leica), were stained with uranyl acetate and Reynolds' lead citrate and examined at 100 kV by a Philips EM 208S transmission electron microscope (FEI-Thermo Fisher) equipped with acquisition system Megaview III SIS camera (Olympus-SIS Milan, Italy) and ITEM3 software.

Assessment of COP-I vesicles assembly, Tfn accumulation, and recycling in COS-1 cells expressing WT and mutant ARF3

COS-1 cells (20×10^3) were seeded in 24-well cluster plates onto 12-mm cover glasses and transfected with WT or mutant mCherry-tagged ARF3 expression constructs. After 48 h of transfection, COS-1 cells were washed and serum starved for 45 minutes at 37 °C and was then incubated with 50 µg/ml Alexa Fluor 488 or Alexa Fluor 647 conjugated transferrin (Invitrogen, T13342 and T23366, respectively) in serum-free medium for the indicated time (5 or 30 min). At the end of the 37 °C incubation period used to follow intracellular trafficking, the cells were cooled to 4 °C, washed twice with ice-cold PBS to remove unbound transferrin, and then incubated twice for 2 min at 4 °C with ice-cold stripping buffer (150 mM NaCl, 20 mM HEPES, 5 mM KCl, 1 mM CaCl₂, 1 mM MgCl₂, pH 5.5) to remove the excess of transferrin bound to the cell surface. To follow the formation of COP-I vesicles and the levels of Tfn present in early endosomes (EE), and lysosomes after 30 min of incubation, cells were fixed with 4% paraformaldehyde for 10 min at room temperature, followed by permeabilization with 0.025% Triton X-100 for 5 min at room temperature and were then stained with antibodies recognizing COP-I, EE and lysosomal markers overnight for 1 h at 4 °C. These antibodies were used: rabbit polyclonal anti-β COP (1:2000, Abcam, ab2899), rabbit monoclonal anti-Rab5 (1:200, Cell Signaling, 35475) and mouse monoclonal anti-LAMP-2 (1:200, Santa Cruz, sc-18822), respectively. Cells were then rinsed twice with PBS and incubated with Alexa Fluor 633 goat anti-mouse secondary antibody (1:200, Invitrogen, A21050) or Alexa Fluor 488 goat anti-rabbit secondary antibody (1:200, Invitrogen, A11070) for 1 h at room temperature. To assess the levels of Tfn present in recycling endosomes (RE) after 30 min of incubation, cells were co-transfected with the plasmid encoding the GFP-tagged RE marker Rab11. All the slides were mounted using Vectashield Antifade mounting medium containing 1.5 µg/ml DAPI (Vector Laboratories, H-1200-10). Confocal z-stacks of the cells incubated 5 min with Tfn and of those stained for βCOP or the cells expressing GFP-Rab11 and incubated 30 min with Tfn were obtained using TCS-SP8X confocal microscope (Leica Microsystems) with an HC PL APO CS2 ×63 (NA 1.40) oil immersion, using excitation lines at 488 nm (for GFP, emission range 500–550 nm), 594 nm (for mCherry, emission range 600–650 nm), 640 (for Alexa Fluor 647, emission range 650–700 nm) and 630 nm (for Alexa Fluor 633, emission range 640–690 nm), a 1024 × 1024 format at 400 Hz, 0.14 µm pixel size, a zoom magnification of ×2.5 and z-step size of 0.7 µm. Confocal z-stacks of the cells stained for Rab5 and Lamp2 at 30 min upon Tfn treatment were obtained using Stellaris 5 (Leica Microsystems), A HC PL APO CS2 ×63/1.40 oil objective was used. Confocal acquisitions were performed using 405, 488, 594, 633 nm laser excitation lines for the different fluorophores used and emission spectra as above. Sequential acquisitions were performed and with a 1024 × 1024 format at 400 (Rab 5) or 200 Hz (Lamp 2), and a z-step of 0.7 µm. For all the experiments, laser intensity and detector parameters and offsets were unchanged per each condition of a single experiment. Phenotype categories for cells expressing WT and mutant ARF3 were independently inspected by two researchers and classified as reported in the main text. Briefly, for COP-I vesicles assembly, the number of cells (%) showing “assembled”, “disassembled” or “extended” COP-I compartment at the PN was estimated by the occurrence of clustered, absent /highly scattered or increased β-COP⁺ area, respectively. The β-COP⁺ area was measured using a manual ROI selection, ROI manager, and measurement tool in Fiji. For each cell, the β-COP⁺ area was normalized by the total area of the nucleus and cells with an extended COP-I compartment were estimated by a ratio β-COP⁺ area/nucleus area. The distribution patterns of the Tfn inside the cytoplasm were scored in replicate for the different incubation times. The Tfn signal distribution inside the cell and its relative clustering at the perinuclear compartment (PN) were inspected and the number of cells (%) showing different classes of Tfn phenotype was calculated. Three

different categories of Tfn distributions were identified (accumulation at the PN = “clustered”, presence of a Tfn⁺ clusters and sparse dotted signal throughout the cell = “semidispersed”, no Tfn⁺ clusters visible = “dispersed”). Co-occurrence of Tfn with Rab5, Rab11 or Lamp2 at the PN was quantified using the colocalization algorithm of IMARIS software v.9.5 (Bitplane) and the built-in thresholding method, which was equally applied to all conditions within each experiment. Manders overlap coefficients were calculated for the fraction of Tfn overlapping the respective fluorophores in a manually selected ROI corresponding to the visible Tfn⁺ PN cluster and viceversa¹⁵².

Zebrafish body axis, notochord, and head phenotyping

Embryos were screened for gross phenotype penetrance and classified as class I (“normal”), class II (“developmental delay”), class III (“mild” microcephaly, with/without microphthalmia and/or mild shortening and lateral bending of body axis) and class IV (“severe” microcephaly/anencephaly with/without microphthalmia and marked trunk deformity, defective body elongation, and severe lateral bending) at 24 and 48 hpf, as reported in the main text. For detailed analysis, not injected controls and injected fish at 12 and 15 hpf (for body axis), 30 hpf (for notochord), and 48 hpf (for head size) were embedded in 2% low melting agarose (Sigma-Aldrich) dissolved in E3 medium. Bright-field images were acquired at Leica M205FA microscope (Leica Microsystems) equipped with LAS X software v.3.0, ×0.63 magnification (for body axis and head size) and Leica Thunder Imager microscope (Leica Microsystems) with N PLAN 5X/0.12 PHO objective (for notochord) equipped with LAS X software v.3.7. These parameters were assessed: (i) head size measured by the area surface between the rostral most part of the head and the optic vesicle; (ii) degree of the notochord angles (plotted in a Rose diagram using Oriana software v.4¹⁵³) and incidence of embryos showing mild and severe notochord curvatures (calculated on the average degree of all the curvatures per embryo); (iii) number of notochord curvatures and (iv) antero-posterior (AP) embryo extension, measured as length from the most anterior region of *Krox20* domain (R3) to the posterior region of *MyoD* domain (paraxial mesoderm) and (v) convergence-extension index, calculated as the ratio of AP and medio-lateral axes (ML, calculated as the length of the visible first somite); (vi) angle between the antero-posterior ends.

Zebrafish live imaging of brain volume and 3D rendering from *Tg(NBT:dsRed)* fish

Live *Tg(NBT:dsRed)* fish injected with WT and mutant ARF3-encoding mRNAs at 48 hpf were embedded in 2% low melting agarose/E3 medium and imaged using Leica Stellaris 5 confocal microscope (Leica Microsystems) equipped with LAS X software v. 4.5 using a sensitive hybrid detector and keeping minimal laser power (579 nm wavelength). Live z-stacks were performed using HC FLUOTAR L VISIR water immersion ×25/0.95 objective, and with an excitation lines at 594 nm (emission range 600–650 nm), a 512 × 512 format at 400 and 600 Hz and a z-step size of 2.5 µm. Volumetric brain reconstructions and quantifications were obtained using 3D Volume (Blend model) and Surfaces rendering reconstruction algorithm of IMARIS v.9.5 (Bitplane), employing the same parameters for the different individuals.

Whole-mount immunofluorescence in 48 hpf zebrafish embryos

Zebrafish embryos were fixed in 4% PFA/PBS (Thermo Fisher, 28908) for 3 h at room temperature (RT), dehydrated through methanol washes from 25% (in PBS) to 100% and stored at –20 °C. Fixed samples were rehydrated back to PBS through serial washes and incubated with 150 mM Tris-HCl pH 9.0 for 5 min at RT and 15 min at 70 °C for antigen retrieval. The samples were then permeabilized with 0.8% PBST (Triton, Sigma-Aldrich, X-100) and 1 µg/ml proteinase K (Sigma-Aldrich, P2308) for 40 min at RT (for acetylated α-tubulin and HuC/Elav) or with cold Acetone for 20 min (for PCNA and Phospho-Histone H3, pH3). The

samples were post-fixed in 4% PFA/PBS for 20 min at RT and incubated 4 h in a solution containing 10% of normal goat serum (NGS) and 2% of BSA in 0.8% PBST for 4 h at 4 °C. These primary antibodies were used: mouse anti-acetylated tubulin (1:250, Sigma Aldrich, T7451), rabbit anti-Elav3 + 4 (1:100, GeneTex, GTX128365), rabbit anti-PCNA at (1:250, GeneTex, GTX12449), mouse anti-pH3 (1:250, Abcam, ab14955) overnight at 4 °C with gentle shaking. These secondary antibodies were used: goat anti-mouse Alexa Fluor 488 (1:1000, Thermo Fisher, A11001), goat anti-rabbit Alexa Fluor 633 (1:1000, Thermo Fisher, A21070), goat anti-rabbit DyLight 594 (1:1000, GeneTex, GTX213110-05). The Stellaris 5 confocal microscope (Leica Microsystems) equipped with LAS X software v. 4.5 and an HC FLUOTAR L VISIR water immersion 25x/0.95 objective were used for z-stack image acquisition. Ventral z-stacks of embryos stained for acetylated α -tubulin, mounted in 2% low melting agarose/PBS (Sigma-Aldrich, A9414), were acquired with: 499 nm laser line (emission range 510–600 nm), 1024 × 1024 format at 400 Hz, and 1.5 μ m z-step size. Z-stacks of embryos stained for PCNA and pH3, mounted in 90% glycerol/PBS, were acquired sequentially with 591 nm and 631 nm laser lines and emission range 596–636 and 644–700 nm, respectively. Volumetric brain acquisitions were obtained by scanning with a 1024 × 1024 format at 200 Hz and 0.5 or 0.7 μ m z-step size and with a digital zoom of 2.5 (ventral brain) or by scanning with a 512 × 512 format at 400 Hz and 2 μ m z-step size (dorsal brain). Embryos stained for HuC/Elav were imaged using the confocal microscopes Leica TCS-SP8 or Olympus FV1000 equipped with FV10-ASW version 4.1, 20x/0.75 objective, using laser line 543 (for HuC/Elav, emission range 560–620 nm) and 635 nm (for acetylated tubulin, emission range 655–755 nm) scanning with a 1024 × 1024 format, a speed of 400 Hz and z-step size of 2 μ m.

Analysis of the forebrain anterior commissure

For morphological analyzes of the forebrain anterior commissure and its lateral bundles, the medial and lateral width was calculated using the “line selection” tool in Fiji¹⁵¹ as indicated in Supplementary Fig. 17.

Analysis of the number of mitotic cells and the pH3 distribution in precursor cells of the developing anterior brain

The number of pH3⁺ precursors cells (mitotic) was quantified in both ventral and dorsal anterior brain z-stacks of the stained 48 hpf embryos. The number of cells was quantified manually or using the “spot analysis” algorithm of IMARIS software 9.5 (Bitplane) throughout the 3D volume of the confocal acquisitions, applying the same parameters to all the scans. The automatic analysis was manually inspected and corrected. Superficial staining corresponding to large epidermal cells was excluded from the analysis. A 3D rendering in the whole dorsal anterior brain was also performed using the same software and showing the pH3⁺ cells. For the ventral scans, the pH3 signal positivity and distribution pattern was assessed in precursor cells found within the defined ROI corresponding to the proliferative zone of a ventral portion of the forebrain, clearly discernible in the confocal acquisitions. The total number of pH3⁺ cells (mitotic) were counted along the full z-stack of the ROI. Following Tang et al.¹⁵⁴, cells at different mitotic phases corresponding to early (prophase + prometaphase), metaphase, and late (anaphase + telophase) were scored based on the pH3 signal distribution, indicative of the cell's chromatin topological status. For the dorsal scans, to assess possible alterations of the normal spatial distribution of pH3⁺ cells within the optic tectum, the number of mitotic cells in different regions (left and right neuropil vs. medial proliferative zone and cerebellum), was manually quantified.

Staining and analysis of apoptotic cells in the anterior brain

To assess apoptotic cells in the anterior brain of developing fish expressing WT and mutant ARF3, live staining with acridine orange (AO) was performed. Briefly, microinjected larvae at 48 hpf were

incubated with 100 μ g acridine orange (Sigma-Aldrich, A6014) in E3 medium for 1 h in the dark at 28 °C then washed extensively with E3 and mounted for microscopy in multi-well dishes using 1.5% low melting agarose/E3 (Sigma-Aldrich, A9414). Live z-stacks of the anterior forebrain in x, y, z were acquired at the Thunder Imager microscope (Leica Microsystems), using HC PL Fluotar \times 10/0.32 DRY objective, 2048 × 2048 format, 475-nm excitation line and with a z-step of 5 μ m. AO⁺ spots were counted using the “multi-points” tool of Fiji¹⁵¹ after adjusting brightness and contrast equally across all the conditions of a single experiment.

Live imaging and analysis of mitotic spindles in precursor cells of the anterior brain

To examine spindle morphology of dividing progenitor cells in zebrafish forebrain, transgenic *Tg(XlEef1a1:dclk2DeltaK-GFP)* fish marking microtubules were injected with mRNA encoding myc-tagged ARF3^{WT}, ARF3^{K127E} and ARF3^{D93N} together with the mRNA encoding H2AmCherry marking the chromatin. Fish at 1 dpf (~30 hpf) were embedded in 1.5% low melting agarose in E3 medium and live confocal x, y, z, t acquisitions of the forebrain region were obtained at the Stellaris 5 confocal microscope (Leica Microsystems), with an HC Fluotar VISIR L \times 25/0.95 water immersion objective, 488 nm laser line (for GFP, emission range 504–600 nm), and 594 nm (for mCherry, emission range 625–700 nm) in sequential model and with a format of 512 × 512 at 400 Hz and with a z-step of 1.5 μ m. A time interval (TI) of 4 minutes was set between consecutive scans for ~1 h (ARF3^{WT} and ARF3^{D93N}, acquired with a digital zoom of 1.7) and >5 h (ARF3^{WT} and ARF3^{K127E}, acquired with a digital zoom of 1). The mitotic spindle's length and width were analyzed using the selection and measurement tools in Fiji¹⁵¹.

Whole-mount in situ hybridization of *Krox20* and *MyoD* mRNA

The fragments of *Krox-20* and *MyoD* cDNA used for riboprobe synthesis were amplified from a zebrafish cDNA preparation by PCR using One Taq DNA polymerase (NEB New England Biolabs, BM0509S) and the primers listed in Supplementary Table 11. The PCR fragments were cloned into pGEM-T Easy vector (Promega, A1380) and sequences were confirmed by DNA sequencing. The digoxigenin-labeled antisense riboprobes were synthesized by in vitro transcription with DIG RNA labeling kit SP6/T7 (Roche, 11277073910). In situ hybridization analysis in whole-mount zebrafish embryos at 15 hpf was performed as described in Thisse et al.¹⁵⁵. Briefly, samples were permeabilized with proteinase K treatment (1 μ g/ml, Sigma-Aldrich, P2308-25MG) for 2 min, pre-incubated in 2% blocking reagent (Roche, 11096176001) and incubated with the transcribed riboprobes (2 ng/ μ l) in hybridization mix: 50% formamide (Sigma-Aldrich, F9037-100ML), 1.3× SSC 20X (175.3 g NaCl, 88.2 g Na Citrate 300 mM, PH 7), 100 g/ml heparin, (Sigma-Aldrich, H3149-25KU), 50 μ g/ml yeast RNA (Sigma-Aldrich, 10109223001), 0.2% Tween-20.0 (Sigma-Aldrich, P2287), 5% CHAPS (Merck, 850500P-1G), 5 mM EDTA pH 8 (Sigma-Aldrich, E7889-100ML) at 65 °C for at least 15 h. Afterward, samples were rinsed with scalar dilutions of SSC solutions (25%, 50%, 75%) and incubated with anti-alkaline phosphatase (AP)-conjugated antibody (1:5000, Roche, 11093274-910) for 2 h at room temperature. Chromogenic staining was developed via BM Purple substrate (Sigma-Aldrich, 11442074001) according to the manufacturer's instructions. Specimens were mounted in 90% glycerol and dorsal images were acquired at the Olympus TH4-200 microscope (Olympus) equipped with Olympus cellSens Standard software v.1.14, with C Plan 10X/0.25 RC1 objective or Thunder Imager (Leica Microsystems) with N PLAN \times 5/0.12 PHO objective.

Embryo extension analysis at 13 hpf and confocal live imaging of zebrafish embryos during late gastrulation

Overall extension of embryos expressing myc-tagged ARF3 WT and mutants at 13 hpf was estimated by calculating the angle amplitude

between A-P ends (head and tail bud, respectively) from bright-field images acquired at Leica M205FA microscope (Leica Microsystems), using the “angle measurement” tool of Fiji⁵¹. For in vivo gastrulae imaging, embryos at the mid-gastrula stage were embedded in 2% low melting agarose (Sigma-Aldrich, A9414) in E3 medium. 4D (*x, y, z, t*) fluorescent data were acquired using Leica TCS-SP8 confocal microscope (Leica Microsystems) with hybrid detectors and keeping minimal laser power. Time-lapses were acquired with a PI Apo CS2 ×20/0.75 objective using a 488 nm laser line (for GFP, emission range 495–550 nm) and 594 nm (for mCherry, emission range 605–680 nm). Z-stacks were obtained with a TI of 30 min, a 1024 × 1024 format at 400 Hz and a z-step size of 3 μm. Fluorochromes unmixing was performed by the acquisition of an automated-sequential collection of multi-channel images, to reduce spectral crosstalk between channels, and the same setting parameters were used for all examined samples. Embryo live imaging was performed simultaneously using the Mark & Find the mode of the LAS X software.

Statistics and reproducibility

Data were analyzed independently by at least two researchers and statistical assessments were performed using GraphPad software v.9 (Prism). Log-rank (Mantel-Cox) test was used to assess survival in zebrafish mutants and morphants. For phenotypes penetrance assessment Chi-squared test in a 2 × 2 contingency table was used, performed as pairwise statistical comparisons across experimental conditions as indicated in the text and figures. Normality tests (Anderson–Darling, D’Agostino and Pearson, Shapiro–Wilk and Kolmogorov–Smirnov tests) were run to assess normal distribution of the data. Parametric data with more experimental groups were analyzed with ANOVA test, non-parametric data with Kruskal–Wallis test and specific *post hoc* tests were always used as indicated in the figure legends and Statistical Table 12. All the analyses were two-tailed.

Image processing

Raw images were analyzed with Fiji⁵¹, LAS X Life Science imaging software (Leica Microsystems, v.3, 3.5, 3.7, 4.5), FV10-ASW software v.4.1, Olympus cellSens Standard imaging software v.1.14 (Olympus Life Science) and IMARIS v.9.5 (Bitplane) and processed using Photoshop or Illustrator (Adobe Systems Incorporated) for figure assembly. Image acquisition parameters (laser lines and power, detector settings, objective used) were maintained equally within each experiment. Brightness and contrast were adjusted equally across whole images and between images belonging to the same experiment. Exceptions are explained here. In Fig. 10, due to possible background differences within each imaged well, each brightfield image showing the notochord was individually adjusted for brightness and contrast to allow the best notochord visualization. Given the high signal intensity that would shadow the Golgi staining, in Supplementary Fig. 10 the brightness of the mKOPF signal (blue) used only for membrane rendering was reduced in post-processing for ARF3^{K127E} as compared to ARF3^{WT}. All the schematic illustrations were generated by researchers using Illustrator 2021–2022 (Adobe) except for the human brain illustration item in Fig. 8 which was created with BioRender.com and modified in Illustrator 2021–2022 (Adobe).

Reporting summary

Further information on research design is available in the Nature Research Reporting Summary linked to this article.

Data availability

The clinical data were collected after signed consent forms. The entire dataset is included within the manuscript. Given the progressive nature of the disease, additional information eventually collected after this publication will be made available upon request to the corresponding authors (antonella.lauri@opbg.net, marco.tartaglia@opbg.net) and

referring clinicians. The sequencing data are available under restricted access for privacy/ethical reasons, access can be obtained by contacting the corresponding authors. The ARF3 variants identified in this study have been deposited in the ClinVar database under the following accession codes: SCV002549683 (c.34C>G, p.Leu12Val) [(ARF3):c.34C>3EG%20(p.Leu12Val)], SCV002549684 (c.95C>A, p.Thr32Asn) [(ARF3):c.95C>3EA%20(p.Thr32Asn)], SCV002549685 (c.139C>T, p.Pro47Ser) [(ARF3):c.139C>3ET%20(p.Pro47Ser)], SCV002549686 (c.200A>T, p.Asp67Val) [(ARF3):c.200A>3ET%20(p.Asp67Val)], SCV002549687 (c.277G>A, p.Asp93Asn) [(ARF3):c.277G>3EA%20(p.Asp93Asn)], and SCV002549688 (c.379A>G, p.Lys127Glu) [(ARF3):c.379A>3EG%20(p.Lys127Glu)]. The UCSC GRCh37/hg19 human genome assembly used as a reference for reads alignment is available at <https://www.ensembl.org/info/website/tutorials/grch37.html>. The dbSNP150, gnomAD V.2.1.1, ClinVar, and COSMIC v.96 databases used in this paper are available at <https://gnomad.broadinstitute.org/>, <https://genome.ucsc.edu/cgi-bin/hgTrackUi?db=hg38&g=snp150Common> and (<https://www.ncbi.nlm.nih.gov/clinvar/>), <https://cancer.sanger.ac.uk/cosmic>, respectively. The raw blots and raw data for the different measures of this study are provided in the Supplementary Information/Source data file. Due to the large size of each dataset, all the raw imaging data, supporting the findings of the work are available from the corresponding authors upon request. All the constructs generated in this study will be shared upon request to the corresponding authors. Source data are provided with this paper.

References

1. D’Souza-Schorey, C. & Chavrier, P. ARF proteins: roles in membrane traffic and beyond. *Nat. Rev. Mol. Cell Biol.* **7**, 347–358 (2006).
2. Cockcroft, S. et al. Phospholipase D: a downstream effector of ARF in granulocytes. *Science* **263**, 523–526 (1994).
3. Guo, Y., Sirkis, D. W. & Schekman, R. Protein sorting at the trans-Golgi network. *Annu. Rev. Cell Dev. Biol.* **30**, 169–206 (2014).
4. Makhoul, C., Gosavi, P. & Gleeson, P. A. Golgi dynamics: the morphology of the mammalian Golgi apparatus in health and disease. *Front. Cell Dev. Biol.* **7**, 112 (2019).
5. Makhoul, C., Gosavi, P. & Gleeson, P. A. The Golgi architecture and cell sensing. *Biochem. Soc. Trans.* **46**, 1063–1072 (2018).
6. Gosavi, P. & Gleeson, P. A. The function of the Golgi ribbon structure—an enduring mystery unfolds! *BioEssays* **39**, 1700063 (2017).
7. Wei, J.-H. & Seemann, J. Golgi ribbon disassembly during mitosis, differentiation and disease progression. *Curr. Opin. Cell Biol.* **47**, 43–51 (2017).
8. Xie, Z., Hur, S. K., Zhao, L., Abrams, C. S. & Bankaitis, V. A. A Golgi lipid signaling pathway controls apical Golgi distribution and cell polarity during neurogenesis. *Dev. Cell* **44**, 725–740.e4 (2018).
9. De Matteis, M. A. & Luini, A. Mendelian disorders of membrane trafficking. *N. Engl. J. Med.* **365**, 927–938 (2011).
10. Seifert, W. et al. Cohen syndrome-associated protein, COH1, is a novel, giant Golgi matrix protein required for Golgi integrity. *J. Biol. Chem.* **286**, 37665–37675 (2011).
11. Shamseldin, H. E., Bennett, A. H., Alfadhel, M., Gupta, V. & Alkur-aya, F. S. GOLGA2, encoding a master regulator of Golgi apparatus, is mutated in a patient with a neuromuscular disorder. *Hum. Genet.* **135**, 245–251 (2016).
12. Rasika, S., Passemard, S., Verloes, A., Gressens, P. & El Ghouzzi, V. Golgiopathies in neurodevelopment: a new view of old defects. *Dev. Neurosci.* **40**, 396–416 (2018).
13. Dupuis, N. et al. Dymeclin deficiency causes postnatal microcephaly, hypomyelination and reticulum-to-Golgi trafficking defects in mice and humans. *Hum. Mol. Genet.* **24**, 2771–2783 (2015).
14. Izumi, K. et al. ARCN1 mutations cause a recognizable craniofacial syndrome due to COPI-mediated transport defects. *Am. J. Hum. Genet.* **99**, 451–459 (2016).

15. Halperin, D. et al. SEC31A mutation affects ER homeostasis, causing a neurological syndrome. *J. Med. Genet.* **56**, 139–148 (2019).
16. Sheen, V. L. et al. Mutations in ARFGEF2 implicate vesicle trafficking in neural progenitor proliferation and migration in the human cerebral cortex. *Nat. Genet.* **36**, 69–76 (2004).
17. Cui, Y., Yang, Z. & Teasdale, R. D. The functional roles of retromer in Parkinson's disease. *FEBS Lett.* **592**, 1096–1112 (2018).
18. Ebanks, K., Lewis, P. A. & Bandopadhyay, R. Vesicular dysfunction and the pathogenesis of Parkinson's disease: clues from genetic studies. *Front. Neurosci.* **13**, 1381 (2019).
19. Liang, J. O. & Kornfeld, S. Comparative activity of ADP-ribosylation factor family members in the early steps of coated vesicle formation on rat liver Golgi membranes. *J. Biol. Chem.* **272**, 4141–4148 (1997).
20. Volpicelli-Daley, L. A., Li, Y., Zhang, C.-J. & Kahn, R. A. Isoform-selective effects of the depletion of ADP-ribosylation factors 1–5 on membrane traffic. *Mol. Biol. Cell* **16**, 4495–4508 (2005).
21. Chavrier, P. & Goud, B. The role of ARF and Rab GTPases in membrane transport. *Curr. Opin. Cell Biol.* **11**, 466–475 (1999).
22. Donaldson, J. G. & Jackson, C. L. ARF family G proteins and their regulators: roles in membrane transport, development and disease. *Nat. Rev. Mol. Cell Biol.* **12**, 362–375 (2011).
23. Zhang, C. J. et al. Expression of a dominant allele of human ARF1 inhibits membrane traffic in vivo. *J. Cell Biol.* **124**, 289–300 (1994).
24. Khan, A. R. & Ménétrey, J. Structural biology of Arf and Rab GTPases' effector recruitment and specificity. *Struct. Lond. Engl.* **1993** **21**, 1284–1297 (2013).
25. Gillingham, A. K. & Munro, S. The small G proteins of the Arf family and their regulators. *Annu. Rev. Cell Dev. Biol.* **23**, 579–611 (2007).
26. Donaldson, J. G., Finazzi, D. & Klausner, R. D. Brefeldin A inhibits Golgi membrane-catalysed exchange of guanine nucleotide onto ARF protein. *Nature* **360**, 350–352 (1992).
27. Helms, J. B. & Rothman, J. E. Inhibition by brefeldin A of a Golgi membrane enzyme that catalyses exchange of guanine nucleotide bound to ARF. *Nature* **360**, 352–354 (1992).
28. Randazzo, P. A., Yang, Y. C., Rulka, C. & Kahn, R. A. Activation of ADP-ribosylation factor by Golgi membranes. Evidence for a brefeldin A- and protease-sensitive activating factor on Golgi membranes. *J. Biol. Chem.* **268**, 9555–9563 (1993).
29. Antonny, B., Huber, I., Paris, S., Chabre, M. & Cassel, D. Activation of ADP-ribosylation factor 1 GTPase-activating protein by phosphatidylcholine-derived diacylglycerols. *J. Biol. Chem.* **272**, 30848–30851 (1997).
30. Goldberg, J. Structural basis for activation of ARF GTPase: mechanisms of guanine nucleotide exchange and GTP-myristoyl switching. *Cell* **95**, 237–248 (1998).
31. Amor, J. C., Harrison, D. H., Kahn, R. A. & Ringe, D. Structure of the human ADP-ribosylation factor 1 complexed with GDP. *Nature* **372**, 704–708 (1994).
32. Kjeldgaard, M., Nyborg, J. & Clark, B. F. The GTP binding motif: variations on a theme. *FASEB J.* **10**, 1347–1368 (1996).
33. Randazzo, P. A. Resolution of two ADP-ribosylation factor 1 GTPase-activating proteins from rat liver. *Biochem. J.* **324**, 413–419 (1997).
34. Reinhard, C., Schweikert, M., Wieland, F. T. & Nickel, W. Functional reconstitution of COPI coat assembly and disassembly using chemically defined components. *Proc. Natl Acad. Sci. USA* **100**, 8253–8257 (2003).
35. Rothman, J. E. Mechanisms of intracellular protein transport. *Nature* **372**, 55–63 (1994).
36. Popoff, V. et al. Several ADP-ribosylation factor (Arf) isoforms support COPI vesicle formation. *J. Biol. Chem.* **286**, 35634–35642 (2011).
37. Gilbert, C. E., Sztul, E. & Machamer, C. E. Commonly used trafficking blocks disrupt ARF1 activation and the localization and function of specific Golgi proteins. *Mol. Biol. Cell* **29**, 937–947 (2018).
38. Munro, S. The golgin coiled-coil proteins of the Golgi apparatus. *Cold Spring Harb. Perspect. Biol.* **3**, a005256 (2011).
39. Kulkarni-Gosavi, P., Makhoul, C. & Gleeson, P. A. Form and function of the Golgi apparatus: scaffolds, cytoskeleton and signalling. *FEBS Lett.* **593**, 2289–2305 (2019).
40. Kondo, Y. et al. ARF1 and ARF3 are required for the integrity of recycling endosomes and the recycling pathway. *Cell Struct. Funct.* **37**, 141–154 (2012).
41. Dascher, C. & Balch, W. E. Dominant inhibitory mutants of ARF1 block endoplasmic reticulum to Golgi transport and trigger disassembly of the Golgi apparatus. *J. Biol. Chem.* **269**, 1437–1448 (1994).
42. Robineau, S., Chabre, M. & Antonny, B. Binding site of brefeldin A at the interface between the small G protein ADP-ribosylation factor 1 (ARF1) and the nucleotide-exchange factor Sec7 domain. *Proc. Natl Acad. Sci. USA* **97**, 9913–9918 (2000).
43. Altan-Bonnet, N., Phair, R. D., Polishchuk, R. S., Weigert, R. & Lipincott-Schwartz, J. A role for Arf1 in mitotic Golgi disassembly, chromosome segregation, and cytokinesis. *Proc. Natl Acad. Sci. USA* **100**, 13314–13319 (2003).
44. Hanai, A. et al. Class I Arfs (Arf1 and Arf3) and Arf6 are localized to the Flemming body and play important roles in cytokinesis. *J. Biochem.* **159**, 201–208 (2016).
45. Nakayama, K. Regulation of cytokinesis by membrane trafficking involving small GTPases and the ESCRT machinery. *Crit. Rev. Biochem. Mol. Biol.* **51**, 1–6 (2016).
46. Rodrigues, F. F. & Harris, T. J. C. Key roles of Arf small G proteins and biosynthetic trafficking for animal development. *Small GTPases* **10**, 403–410 (2019).
47. Carvajal-Gonzalez, J. M. et al. The clathrin adaptor AP-1 complex and Arf1 regulate planar cell polarity in vivo. *Nat. Commun.* **6**, 6751 (2015).
48. Petko, J. A. et al. Proteomic and functional analysis of NCS-1 binding proteins reveals novel signaling pathways required for inner ear development in zebrafish. *BMC Neurosci.* **10**, 27 (2009).
49. Ge, X. et al. Missense-depleted regions in population exomes implicate ras superfamily nucleotide-binding protein alteration in patients with brain malformation. *NPJ Genom. Med.* **1**, 16036 (2016).
50. Sakamoto, M. et al. De novo ARF3 variants cause neurodevelopmental disorder with brain abnormality. *Hum. Mol. Genet.* **31**, 69–81 (2021).
51. Sobreira, N., Schiettecatte, F., Valle, D. & Hamosh, A. Gene-Matcher: a matching tool for connecting investigators with an interest in the same gene. *Hum. Mutat.* **36**, 928–930 (2015).
52. Lee, Y. et al. Makes caterpillars floppy-like effector-containing MARTX toxins require host ADP-ribosylation factor (ARF) proteins for systemic pathogenicity. *Proc. Natl Acad. Sci. USA* **116**, 18031–18040 (2019).
53. Pasqualato, S., Renault, L. & Cherfils, J. Arf, Arl, Arp and Sar proteins: a family of GTP-binding proteins with a structural device for 'front-back' communication. *EMBO Rep.* **3**, 1035–1041 (2002).
54. Carta, C. et al. Germline missense mutations affecting KRAS Isoform B are associated with a severe Noonan syndrome phenotype. *Am. J. Hum. Genet.* **79**, 129–135 (2006).
55. Zampino, G. et al. Diversity, parental germline origin, and phenotypic spectrum of de novo HRAS missense changes in Costello syndrome. *Hum. Mutat.* **28**, 265–272 (2007).
56. Click, E. S., Stearns, T. & Botstein, D. Systematic structure-function analysis of the small GTPase Arf1 in yeast. *Mol. Biol. Cell* **13**, 1652–1664 (2002).

57. Amor, J. C. et al. Structures of yeast ARF2 and ARL1: distinct roles for the N terminus in the structure and function of ARF family GTPases. *J. Biol. Chem.* **276**, 42477–42484 (2001).
58. Ménétrey, J. et al. Structural basis for ARF1-mediated recruitment of ARHGAP21 to Golgi membranes. *EMBO J.* **26**, 1953–1962 (2007).
59. Yu, X., Breitman, M. & Goldberg, J. A structure-based mechanism for Arf1-dependent recruitment of coatamer to membranes. *Cell* **148**, 530–542 (2012).
60. Ratcliffe, C. D. H., Sahgal, P., Parachoniak, C. A., Ivaska, J. & Park, M. Regulation of cell migration and $\beta 1$ integrin trafficking by the endosomal adaptor GGA3. *Traffic Cph. Den.* **17**, 670–688 (2016).
61. Xiang, Y., Seemann, J., Bisel, B., Punthambaker, S. & Wang, Y. Active ADP-ribosylation factor-1 (ARF1) is required for mitotic Golgi fragmentation. *J. Biol. Chem.* **282**, 21829–21837 (2007).
62. Lu, L., Tai, G. & Hong, W. Autoantigen Golgin-97, an effector of Arl1 GTPase, participates in traffic from the endosome to the trans-Golgi network. *Mol. Biol. Cell* **15**, 4426–4443 (2004).
63. Lu, L., Horstmann, H., Ng, C. & Hong, W. Regulation of Golgi structure and function by ARF-like protein 1 (Arl1). *J. Cell Sci.* **114**, 4543–4555 (2001).
64. Joshi, G., Chi, Y., Huang, Z. & Wang, Y. A β -induced Golgi fragmentation in Alzheimer's disease enhances A β production. *Proc. Natl Acad. Sci. USA* **111**, E1230–E1239 (2014).
65. Manolea, F. et al. Arf3 is activated uniquely at the trans-Golgi network by brefeldin A-inhibited guanine nucleotide exchange factors. *Mol. Biol. Cell* **21**, 1836–1849 (2010).
66. Hsu, V. W., Bai, M. & Li, J. Getting active: protein sorting in endocytic recycling. *Nat. Rev. Mol. Cell Biol.* **13**, 323–328 (2012).
67. Sheff, D., Pelletier, L., O'Connell, C. B., Warren, G. & Mellman, I. Transferrin receptor recycling in the absence of perinuclear recycling endosomes. *J. Cell Biol.* **156**, 797–804 (2002).
68. Mani, M. et al. Developmentally regulated GTP-binding protein 2 coordinates Rab5 activity and transferrin recycling. *Mol. Biol. Cell* **27**, 334–348 (2016).
69. Rink, J., Ghigo, E., Kalaidzidis, Y. & Zerial, M. Rab conversion as a mechanism of progression from early to late endosomes. *Cell* **122**, 735–749 (2005).
70. Ren, M. et al. Hydrolysis of GTP on rab11 is required for the direct delivery of transferrin from the pericentriolar recycling compartment to the cell surface but not from sorting endosomes. *Proc. Natl Acad. Sci. USA* **95**, 6187–6192 (1998).
71. Takahashi, S. et al. Rab11 regulates exocytosis of recycling vesicles at the plasma membrane. *J. Cell Sci.* **125**, 4049–4057 (2012).
72. Maxfield, F. R. & McGraw, T. E. Endocytic recycling. *Nat. Rev. Mol. Cell Biol.* **5**, 121–132 (2004).
73. Cullen, P. J. & Steinberg, F. To degrade or not to degrade: mechanisms and significance of endocytic recycling. *Nat. Rev. Mol. Cell Biol.* **19**, 679–696 (2018).
74. Gammella, E. et al. Unconventional endocytosis and trafficking of transferrin receptor induced by iron. *Mol. Biol. Cell* **32**, 98–108 (2021).
75. Johnson, M. B., Chen, J., Murchison, N., Green, F. A. & Enns, C. A. Transferrin receptor 2: evidence for ligand-induced stabilization and redirection to a recycling pathway. *Mol. Biol. Cell* **18**, 743–754 (2007).
76. Kimmel, C. B., Ballard, W. W., Kimmel, S. R., Ullmann, B. & Schilling, T. F. Stages of embryonic development of the zebrafish. *Dev. Dyn.* **203**, 253–310 (1995).
77. Zaghloul, N. A. et al. Functional analyses of variants reveal a significant role for dominant negative and common alleles in oligogenic Bardet-Biedl syndrome. *Proc. Natl Acad. Sci. USA* **107**, 10602–10607 (2010).
78. Suárez, R., Gobius, I. & Richards, L. J. Evolution and development of interhemispheric connections in the vertebrate forebrain. *Front. Hum. Neurosci.* **8**, 497 (2014).
79. Zaqout, S. & Kaundl, A. M. Autosomal Recessive Primary Microcephaly: Not Just a Small Brain. *Front. Cell Dev. Biol.* **9**, 784700 (2022).
80. Phan, T. P. & Holland, A. J. Time is of the essence: the molecular mechanisms of primary microcephaly. *Genes Dev.* **35**, 1551–1578 (2021).
81. Fasano, G., Compagnucci, C., Dallapiccola, B., Tartaglia, M. & Lauri, A. Teleost fish and organoids: alternative windows into the development of healthy and diseased brains. *Front. Mol. Neurosci.* <https://doi.org/10.3389/fnmol.2022.855786>. (2021).
82. Gebhardt, C. et al. An interhemispheric neural circuit allowing binocular integration in the optic tectum. *Nat. Commun.* **10**, 5471 (2019).
83. Ito, Y., Tanaka, H., Okamoto, H. & Ohshima, T. Characterization of neural stem cells and their progeny in the adult zebrafish optic tectum. *Dev. Biol.* **342**, 26–38 (2010).
84. Chippalkatti, R. & Suter, B. 5-Ethynyl-2'-deoxyuridine/phosphohistone H3 dual-labeling Protocol for cell cycle progression analysis in *Drosophila* neural stem cells. *J. Vis. Exp.* e62642 (2021) <https://doi.org/10.3791/62642>.
85. Phan, T. P. et al. Centrosome defects cause microcephaly by activating the 53BP1-USP28-TP53 mitotic surveillance pathway. *EMBO J.* **40**, e106118 (2021).
86. Barkovich, A. J., Dobyns, W. B. & Guerrini, R. Malformations of cortical development and epilepsy. *Cold Spring Harb. Perspect. Med.* **5**, a022392 (2015).
87. Chen, J.-F. et al. Microcephaly disease gene Wdr62 regulates mitotic progression of embryonic neural stem cells and brain size. *Nat. Commun.* **5**, 3885 (2014).
88. Kodani, A. & Sütterlin, C. The Golgi protein GM130 regulates centrosome morphology and function. *Mol. Biol. Cell* **19**, 745–753 (2008).
89. Wei, J.-H., Zhang, Z. C., Wynn, R. M. & Seemann, J. GM130 regulates golgi-derived spindle assembly by activating TPX2 and capturing microtubules. *Cell* **162**, 287–299 (2015).
90. Zhang, C.-H. et al. GM130, a cis-Golgi protein, regulates meiotic spindle assembly and asymmetric division in mouse oocyte. *Cell Cycle Georget. Tex.* **10**, 1861–1870 (2011).
91. Ansar, M. et al. Bi-allelic variants in DYNC112 cause syndromic microcephaly with intellectual disability, cerebral malformations, and dysmorphic facial features. *Am. J. Hum. Genet.* **104**, 1073–1087 (2019).
92. Farag, H. G. et al. Abnormal centrosome and spindle morphology in a patient with autosomal recessive primary microcephaly type 2 due to compound heterozygous WDR62 gene mutation. *Orphanet J. Rare Dis.* **8**, 178 (2013).
93. Novorol, C. et al. Microcephaly models in the developing zebrafish retinal neuroepithelium point to an underlying defect in metaphase progression. *Open Biol.* **3**, 130065 (2013).
94. Bagwell, J. et al. Notochord vacuoles absorb compressive bone growth during zebrafish spine formation. *eLife* **9**, e51221 (2020).
95. Ravichandran, Y., Goud, B. & Manneville, J.-B. The Golgi apparatus and cell polarity: roles of the cytoskeleton and Golgi matrix, and Golgi membranes. *Curr. Opin. Cell Biol.* **62**, 104–113 (2020).
96. Tate, J. G. et al. COSMIC: the Catalogue Of Somatic Mutations In Cancer. *Nucleic Acids Res.* **47**, D941–D947 (2019).
97. Tartaglia, M. & Gelb, B. D. Disorders of dysregulated signal traffic through the RAS-MAPK pathway: phenotypic spectrum and molecular mechanisms. *Ann. N. Y. Acad. Sci.* **1214**, 99–121 (2010).
98. Motta, M. et al. Activating MRAS mutations cause Noonan syndrome associated with hypertrophic cardiomyopathy. *Hum. Mol. Genet.* **29**, 1772–1783 (2020).
99. Flex, E. et al. Activating mutations in RRAS underlie a phenotype within the RASopathy spectrum and contribute to leukaemogenesis. *Hum. Mol. Genet.* **23**, 4315–4327 (2014).

100. Niihori, T. et al. Germline-Activating RRAS2 Mutations Cause Noonan Syndrome. *Am. J. Hum. Genet.* **104**, 1233–1240 (2019).
101. Capri, Y. et al. Activating mutations of RRAS2 are a rare cause of Noonan syndrome. *Am. J. Hum. Genet.* **104**, 1223–1232 (2019).
102. Denayer, E. et al. Mutation analysis in Costello syndrome: functional and structural characterization of the HRAS p.Lys117Arg mutation. *Hum. Mutat.* **29**, 232–239 (2008).
103. Lim, Y. H. et al. Somatic activating RAS mutations cause vascular tumors including pyogenic granuloma. *J. Investig. Dermatol.* **135**, 1698–1700 (2015).
104. Schubbert, S. et al. Germline KRAS mutations cause Noonan syndrome. *Nat. Genet.* **38**, 331–336 (2006).
105. Zenker, M. et al. Expansion of the genotypic and phenotypic spectrum in patients with KRAS germline mutations. *J. Med. Genet.* **44**, 131–135 (2007).
106. Landrum, M. J. et al. ClinVar: improving access to variant interpretations and supporting evidence. *Nucleic Acids Res.* **46**, D1062–D1067 (2018).
107. Nava, C. et al. Cardio-facio-cutaneous and Noonan syndromes due to mutations in the RAS/MAPK signalling pathway: genotype-phenotype relationships and overlap with Costello syndrome. *J. Med. Genet.* **44**, 763–771 (2007).
108. Gripp, K. W. & Lin, A. E. Costello syndrome: a Ras/mitogen activated protein kinase pathway syndrome (rasopathy) resulting from HRAS germline mutations. *Genet. Med.* **14**, 285–292 (2012).
109. Merithew, E. et al. Structural plasticity of an invariant hydrophobic triad in the switch regions of Rab GTPases is a determinant of effector recognition*. *J. Biol. Chem.* **276**, 13982–13988 (2001).
110. Denayer, E., de Ravel, T. & Legius, E. Clinical and molecular aspects of RAS related disorders. *J. Med. Genet.* **45**, 695–703 (2008).
111. Northup, J. K., Jian, X. & Randazzo, P. A. Nucleotide exchange factors. *Cell. Logist.* **2**, 140–146 (2012).
112. Pennauer, M., Buczak, K., Prescianotto-Baschong, C. & Spiess, M. Shared and specific functions of Arfs 1–5 at the Golgi revealed by systematic knockouts. *J. Cell Biol.* **221**, e202106100 (2022).
113. Burd, C. & Cullen, P. J. Retromer: a master conductor of endosome sorting. *Cold Spring Harb. Perspect. Biol.* **6**, a016774 (2014).
114. Carpentieri, J. A. et al. Endosomal trafficking defects alter neural progenitor proliferation and cause microcephaly. *Nat. Commun.* **13**, 16 (2022).
115. García-Cazorla, A., Oyarzábal, A., Saudubray, J.-M., Martinelli, D. & Dionisi-Vici, C. Genetic disorders of cellular trafficking. *Trends Genet.* **38**, 724–751 (2022).
116. Ayala, I. & Colanzi, A. Structural organization and function of the Golgi ribbon during cell division. *Front. Cell Dev. Biol.* **10**, 925228 (2022).
117. Kim, O.-H. et al. Zebrafish knockout of Down syndrome gene, DYRK1A, shows social impairments relevant to autism. *Mol. Autism* **8**, 50 (2017).
118. Liu, J. et al. ARF3 inhibits proliferation and promotes apoptosis in gastric cancer by regulating AKT and ERK pathway. *Acta. Biochim. Pol.* **68**, 223–229 (2021).
119. Boulay, P.-L. et al. ARF1 controls proliferation of breast cancer cells by regulating the retinoblastoma protein. *Oncogene* **30**, 3846–3861 (2011).
120. Jessen, J. R. et al. Zebrafish trilobite identifies new roles for Strabismus in gastrulation and neuronal movements. *Nat. Cell Biol.* **4**, 610–615 (2002).
121. Roszko, I., Sawada, A. & Solnica-Krezel, L. Regulation of convergence and extension movements during vertebrate gastrulation by the Wnt/PCP pathway. *Semin. Cell Dev. Biol.* **20**, 986–997 (2009).
122. Wallingford, J. B., Fraser, S. E. & Harland, R. M. Convergent extension: the molecular control of polarized cell movement during embryonic development. *Dev. Cell* **2**, 695–706 (2002).
123. Lauri, A., Fasano, G., Venditti, M., Dallapiccola, B. & Tartaglia, M. In vivo functional genomics for undiagnosed patients: the impact of small GTPases signaling dysregulation at pan-embryo developmental scale. *Front. Cell Dev. Biol.* **9**, 642235 (2021).
124. Prigozhina, N. L. & Waterman-Storer, C. M. Decreased polarity and increased random motility in Ptk1 epithelial cells correlate with inhibition of endosomal recycling. *J. Cell Sci.* **119**, 3571–3582 (2006).
125. Winter, J. F. et al. *Caenorhabditis elegans* screen reveals role of PAR-5 in RAB-11-recycling endosome positioning and apicobasal cell polarity. *Nat. Cell Biol.* **14**, 666–676 (2012).
126. Ulrich, F. et al. Wnt11 functions in gastrulation by controlling cell cohesion through Rab5c and E-cadherin. *Dev. Cell* **9**, 555–564 (2005).
127. Sarmah, S. et al. Sec24D-dependent transport of extracellular matrix proteins is required for zebrafish skeletal morphogenesis. *PLoS ONE* **5**, e10367 (2010).
128. Coutinho, P. et al. Differential requirements for COPI transport during vertebrate early development. *Dev. Cell* **7**, 547–558 (2004).
129. Horton, A. C. et al. Polarized secretory trafficking directs cargo for asymmetric dendrite growth and morphogenesis. *Neuron* **48**, 757–771 (2005).
130. Pezzani, L. et al. Atypical presentation of pediatric BRAF RASopathy with acute encephalopathy. *Am. J. Med. Genet. A* **176**, 2867–2871 (2018).
131. Ziegler, A. et al. Confirmation that variants in TT12 are responsible for autosomal recessive intellectual disability. *Clin. Genet.* **96**, 354–358 (2019).
132. Radio, F. C. et al. SPEN haploinsufficiency causes a neurodevelopmental disorder overlapping proximal 1p36 deletion syndrome with an epismutation of X chromosomes in females. *Am. J. Hum. Genet.* **108**, 502–516 (2021).
133. Lin, Y.-C. et al. SCUBE3 loss-of-function causes a recognizable recessive developmental disorder due to defective bone morphogenetic protein signaling. *Am. J. Hum. Genet.* **108**, 115–133 (2021).
134. Vetro, A. et al. ATP1A2- and ATP1A3-associated early profound epileptic encephalopathy and polymicrogyria. *Brain J. Neurol.* <https://doi.org/10.1093/brain/awab052> (2021).
135. Humphrey, W., Dalke, A. & Schulten, K. VMD: visual molecular dynamics. *J. Mol. Graph.* **14**, 27–28 (1996). 33–38.
136. Waterhouse, A. et al. SWISS-MODEL: homology modelling of protein structures and complexes. *Nucleic Acids Res.* **46**, W296–W303 (2018).
137. Pettersen, E. F. et al. UCSF Chimera—a visualization system for exploratory research and analysis. *J. Comput. Chem.* **25**, 1605–1612 (2004).
138. Dunbrack, R. L. Rotamer libraries in the 21st century. *Curr. Opin. Struct. Biol.* **12**, 431–440 (2002).
139. Páll, S. et al. Heterogeneous parallelization and acceleration of molecular dynamics simulations in GROMACS. *J. Chem. Phys.* **153**, 134110 (2020).
140. Huang, J. & MacKerell, A. D. CHARMM36 all-atom additive protein force field: validation based on comparison to NMR data. *J. Comput. Chem.* **34**, 2135–2145 (2013).
141. Mark, P. & Nilsson, L. Structure and dynamics of the TIP3P, SPC, and SPC/E water models at 298 K. *J. Phys. Chem. A* **105**, 9954–9960 (2001).

142. Bussi, G., Donadio, D. & Parrinello, M. Canonical sampling through velocity rescaling. *J. Chem. Phys.* **126**, 014101 (2007).
143. Darden, T., York, D. & Pedersen, L. Particle mesh Ewald: an $N\text{-log}(N)$ method for Ewald sums in large systems. *J. Chem. Phys.* **98**, 10089–10092 (1993).
144. Villefranc, J. A., Amigo, J. & Lawson, N. D. Gateway compatible vectors for analysis of gene function in the zebrafish. *Dev. Dyn.* **236**, 3077–3087 (2007).
145. Don, E. K. et al. A Tol2 gateway-compatible toolbox for the study of the nervous system and neurodegenerative disease. *Zebrafish* **14**, 69–72 (2017).
146. Cole, N. B. et al. Diffusional mobility of Golgi proteins in membranes of living cells. *Science* **273**, 797–801 (1996).
147. Choudhury, A. et al. Rab proteins mediate Golgi transport of caveola-internalized glycosphingolipids and correct lipid trafficking in Niemann–Pick C cells. *J. Clin. Invest.* **109**, 1541–1550 (2002).
148. Peri, F. & Nüsslein-Volhard, C. Live imaging of neuronal degradation by microglia reveals a role for v0-ATPase a1 in phagosomal fusion in vivo. *Cell* **133**, 916–927 (2008).
149. Tran, L. D. et al. Dynamic microtubules at the vegetal cortex predict the embryonic axis in zebrafish. *Development* **139**, 3644–3652 (2012).
150. Leatherbarrow, R. J. GraFit Version 7 (Erithacus Software Ltd., Horley, U.K., 2010).
151. Schindelin, J. et al. Fiji: an open-source platform for biological-image analysis. *Nat. Methods* **9**, 676–682 (2012).
152. Dunn, K. W., Kamocka, M. M. & McDonald, J. H. A practical guide to evaluating colocalization in biological microscopy. *Am. J. Physiol. Cell Physiol.* **300**, C723–C742 (2011).
153. Kovach, W. L. *Oriana—Circular Statistics for Windows* (Kovach Computing Service, 2011).
154. Tang, D., Yuan, H., Vilemeyer, O., Perez, F. & Wang, Y. Sequential phosphorylation of GRASP65 during mitotic Golgi disassembly. *Biol. Open* **1**, 1204–1214 (2012).
155. Thisse, C. & Thisse, B. High-resolution in situ hybridization to whole-mount zebrafish embryos. *Nat. Protoc.* **3**, 59–69 (2008).

Acknowledgements

H2A-mCherry:pDest and GFP-CAAX:pDest plasmids were kindly provided by Dr. Mette Handberg-Thorsager (Max Planck Institute of Molecular Cell Biology and Genetics, Dresden, MPI-CBG, Germany), pcDNA3/hArl3(WT)-mCherry was a gift from Kazuhisa Nakayama (Addgene plasmid # 79420; <http://n2t.net/addgene:79420>; RRI-D:Addgene_79420), EGFP-GalT was a gift from Jennifer Lippincott-Schwartz (Addgene plasmid # 11929; <http://n2t.net/addgene:11929>; RRID:Addgene_11929), GFP-rab11 WT was a gift from Richard Pagano (Addgene plasmid # 12674; <http://n2t.net/addgene:12674>; RRID:Addgene_12674). *Tg(XlEef1a1:clck2DeltaK-GFP)* was a kind gift from Prof. M. Mione (Laboratory of Experimental Cancer Biology—CIBIO, Trieste, Italy). We acknowledge Cineca ELIXIR-IIB for computing resources and thank Dr. Giovanna Zambruno for providing support and technical advice on TEM. This work was supported, in part, by Fondazione Bambino Gesù (Vite Coraggiose to M.T.), Italian Ministry of Health (CCR-2017-23669081, RCR-2020-23670068_001 and RCR-2021-23671215 to M.T.; RF-2018-12366931 to F.C.R., G.C., and B.D.; Ricerca Corrente 2021, Ricerca Corrente 2022 to A.L., S.C., and M.T., and RF-2013-02355240 to R.G.), Ministero della Salute (Ricerca 5x1000) to A.L. and M.T., Italian Ministry of Research (FOE 2019 to M.T.), the Tuscany Region Call for Health 2018 (DECODE EE, to R.G.), and the European Union Seventh Framework Program (DESIRE [602531] to R.G.), Istituto Superiore di Sanità (Bando Ricerca Indipendente ISS 2020-2022-ISS20-39c812dd2b3c to S.C.).

Author contributions

G.F. designed and performed the in vivo experiments and contributed to analyzing in vitro cell experiments and writing the manuscript. V.M. designed and performed the in vitro experiments and contributed to writing the manuscript. F.C.R. coordinated the clinical data collection and phenotyping, analyzed the clinical data, and contributed to writing the manuscript; M.V. performed the in situ hybridization assay, contributed to constructs preparation and to the analysis of cells experiments; N.M. performed the cell-free biochemical experiments with F.B.; S.C. designed and performed the Golgi morphological experiments in cells and contributed to the recycling and pull-down experiments with E.Z.; G.P. performed the cell proliferation and death assays in zebrafish; L.A.C. and S.Pe. contributed to the confocal scanning experiments. A.Z., A.V., F.P., S.Pi., A.B., and M.I. generated and analyzed the genomic data; G.C. performed the structural analyses and molecular dynamics simulations with I.G.P. and B.C.; L.B. e A.T. performed the TEM experiments; C.M. performed the ARF3 RT-PCR experiment in COS-1 cells; R.M. contributed to TEM sections preparations; M.B., C.B., D.M., A.Se., M.M., M.V.G., A.B., C.J.C., R.G., A.SL and B.D. identified the patients, and collected and analyzed the clinical data; M.R.A. supervised the cell-free biochemical experiments and analyzed the data; A.L. and M.T. conceived, designed, and supervised the project, analyzed the data, wrote and revised the manuscript. G.F., V.M., and F.C.R. equally contributed to the work, M.V. and N.M. equally contributed to the work. A.L. and M.T. jointly coordinated the study.

Competing interests

The authors declare no competing interests.

Additional information

Supplementary information The online version contains supplementary material available at <https://doi.org/10.1038/s41467-022-34354-x>.

Correspondence and requests for materials should be addressed to Antonella Lauri or Marco Tartaglia.

Peer review information *Nature Communications* thanks Vincent El Ghouzzi and the other, anonymous, reviewer(s) for their contribution to the peer review of this work. Peer reviewer reports are available.

Reprints and permissions information is available at <http://www.nature.com/reprints>

Publisher's note Springer Nature remains neutral with regard to jurisdictional claims in published maps and institutional affiliations.

Open Access This article is licensed under a Creative Commons Attribution 4.0 International License, which permits use, sharing, adaptation, distribution and reproduction in any medium or format, as long as you give appropriate credit to the original author(s) and the source, provide a link to the Creative Commons license, and indicate if changes were made. The images or other third party material in this article are included in the article's Creative Commons license, unless indicated otherwise in a credit line to the material. If material is not included in the article's Creative Commons license and your intended use is not permitted by statutory regulation or exceeds the permitted use, you will need to obtain permission directly from the copyright holder. To view a copy of this license, visit <http://creativecommons.org/licenses/by/4.0/>.

© The Author(s) 2022

Article

¹Genetics and Rare Diseases Research Division, Ospedale Pediatrico Bambino Gesù, IRCCS, 00146 Rome, Italy. ²Institute of Biochemistry and Molecular Biology II, Medical Faculty and University Hospital Düsseldorf, Heinrich Heine University Düsseldorf, Düsseldorf, Germany. ³National Center for Rare Diseases, Istituto Superiore di Sanità, 00161 Rome, Italy. ⁴Department for Innovation in Biological Agro-food and Forest systems (DIBAF), University of Tuscia, 01100 Viterbo, Italy. ⁵Department of Biology and Biotechnology “Charles Darwin”, Università “Sapienza”, Rome 00185, Italy. ⁶UFR Santé de l’Université d’Angers, INSERM U1083, CNRS UMR6015, MITOVASC, SFR ICAT, F-49000 Angers, France. ⁷Département de Génétique, CHU d’Angers, 49000 Angers, France. ⁸Institute of Biomembranes, Bioenergetics and Molecular Biotechnologies, Centro Nazionale delle Ricerche, 70126 Bari, Italy. ⁹Servizio grandi strumentazioni e core facilities, Istituto Superiore di Sanità, 00161 Rome, Italy. ¹⁰Centro di riferimento per la medicina di genere, Istituto Superiore di Sanità, 00161 Rome, Italy. ¹¹Pediatric Neurology, Neurogenetics and Neurobiology Unit and Laboratories, Meyer Children’s Hospital, University of Florence, 50139 Florence, Italy. ¹²Confocal Microscopy Core Facility, Ospedale Pediatrico Bambino Gesù, IRCCS, 00146 Rome, Italy. ¹³Department of Oncology and Molecular Medicine, Istituto Superiore di Sanità, 00161 Rome, Italy. ¹⁴Super Computing Applications and Innovation, CINECA, 40033 Casalecchio di Reno, Italy. ¹⁵Fondazione IRCCS Ca’ Granda Ospedale Maggiore Policlinico, 20122 Milan, Italy. ¹⁶Mariani Center for Fragile Children Pediatric Unit, Azienda Socio Sanitaria Territoriale Lariana, 22100 Como, Italy. ¹⁷Department of Laboratories Ospedale Pediatrico Bambino Gesù, IRCCS, 00146 Rome, Italy. ¹⁸Genetic Medicine, Dept of Pediatrics, University of California San Francisco, Ca, Fresno, Ca, San Francisco, CA 94143, USA. ¹⁹Medical Genetics, ASST Papa Giovanni XXIII, 24127 Bergamo, Italy. ²⁰These authors contributed equally: Giulia Fasano, Valentina Muto, Francesca Clementina Radio. ✉ e-mail: antonella.lauri@opbg.net; marco.tartaglia@opbg.net

Chapter 10

General discussion

Discussion

Nearly all cellular activities include members of the RAS superfamily and their downstream effectors. The GTPases' general purpose is to govern the readout of their effectors by mediating incoming signals and controlling them. To carry out this extremely complex activity, the signaling components must be organized spatially and temporally. Therefore, the emergence of many human disorders are commonly linked to the dysregulation of these components (Hebron *et al.*, 2022; Simanshu *et al.*, 2017). Between active GTP-bound and inactive GDP-bound states, RAS GTPases function as molecular switches. A network of nuclear and cytoplasmic signaling pathways are activated when RAS GTPases connect with a wide variety of effector proteins (Lowy and Willumsen, 1993).

RASopathies and cancer have both been linked to mutations in the genes encoding for the RAS/MAPK pathway. About three decades ago, somatic, gain-of-function mutations in the RAS genes were discovered to be the first distinct genetic changes linked to human cancer. RAS proteins have been identified as crucial elements of signaling networks regulating cellular proliferation, differentiation, or survival in studies conducted over the past years. It is recognized that the oncogenic mutations of the H-RAS, N-RAS, or K-RAS genes typically identified in human malignancies tip the balance of those signaling pathways, resulting in the formation of tumors. More recently, oncogenic mutations in a number of different RAS signaling pathway upstream or downstream elements (such as membrane RTKs or cytosolic kinases) have been found in connection with a number of malignancies. (Rauen, 2013; Fernández-Medarde and Santos, 2011; Baines *et al.*, 2011).

We have been successful in illuminating and characterizing various RAS-related signaling pathway members, among them RAF1, HRAS, and RIT1, in a variety of disorders primarily linked to germline gain of function mutation associated RASopathies, including Noonan syndrome and Costello syndrome in association with the development of hypertrophic cardiomyopathy and cutaneous disorders.

iPSC modeling of the RAF1-associated Noonan syndrome's altered myocardial structure and function

One aspect of this dissertation was a disease modeling approach to study the molecular mechanisms involved in development of hypertrophic cardiomyopathy with high incidence rate among Noonan syndrome patients harboring a germline mutation in RAF at Serine 257 residue. Development of HCM is linked to severe morbidity and a risk of cardiac mortality in Noonan syndrome (NS), the most common disease entity among the RASopathies. Notably, whereas HCM only occurs in roughly 20% of NS generally, it affects more than 90% of NS people with an RAF1 variation (Pandit *et al.*, 2007; Razzaque *et al.*, 2007).

To examine the molecular processes causing cardiac dysfunction in RAF1-related Noonan syndrome, patient-derived tissues were used to create CBs and BCTs using in

vitro cellular reprogramming of iPSC clones, differentiation, and tissue engineering. Beyond 2D systems and animal models, human 3D cardiac models provide in-depth molecular and functional insight into cardiac dysfunctions. A better understanding of the relationships between particular genetic mutations and pathologies is made possible by the advantages of creating patient-specific disease models and the potential use of gene editing techniques like CRISPR/Cas9. These techniques also offer a variety of options for therapeutic testing on these patient-specific disease models.

By using super-resolution and EM imaging, we were able to describe the cytoskeletal and sarcomeric ultra-structures of the CBs and BCTs as well as their calcium handling, contractility, and intracellular signal transduction. Collectively these complementary methods distinguished RAF1^{S257L} CMs from the gene-corrected isogenic control and wild-type CMs by their reduced MYH6 abundance over MYH7, elevated NPPB expression and pro-BNP secretion, decreased SERCA2/PLN ratio, reduced force generation coupled with a reduced rate of intracellular calcium transients, elevated levels of p-ERK1/2 and p-p38, and attenuated p-YAP.

Most interestingly, RAF1^{S257L} CBs, BCTs, and cardiac biopsy samples from affected patient showed an abnormal ultrastructural characteristic, including condensed I-bands while treatment with the MEK inhibitor PD0325901 inhibited the N2BA-to-N2B shift (shift in expression of titin isoforms from the longer variant to the shorter variant), restoring the shortening of the I-bands observed in RAF1^{S257L} CBs/BCTs. Different doses of MEK inhibitors have been utilized therapeutically as a therapy option for individuals with Noonan Syndrome, and these patients' heart health has significantly improved, cardiac hypertrophy has been suppressed, and their pro-BNP levels have returned to normal (Andelfinger *et al.*, 2019; Mussa *et al.*, 2021).

Based on the observations in coordination with earlier studies, CMs with heterozygous RAF1^{S257L} showed a 50% decreased inhibitory phosphorylation of RAF1 at S259 (Razzaque *et al.*, 2007; Jaffré *et al.*, 2019). Accordingly, and in line with other research (Dhandapany *et al.*, 2011), greater p-ERK1/2 levels were found in RAF1^{S257L} CMs compared to control CMs, and after MEKi treatment, p-ERK1/2 levels were noticeably decreased in CBs. In contrast to WT and MEKi-treated CBs, RAF1^{S257L} CBs showed differential expression of a fetal-like gene program, proteins of the contractile machinery, MYH7, and calcium transient regulators. According to earlier research, transcriptional activation of the hypertrophic-responsive gene promoters by GATA4, AP1, MEF2, NFAT, and NFB is likely what causes the observed alterations in the expression of these genes (Dirkx *et al.*, 2013; Ho *et al.*, 2001), most likely via variable activation states of ERK, p38 and YAP in RAF1^{S257L} CBs.

Additionally, we noticed that RAF1^{S257L} CBs expressed higher levels of YAP targets such as MYH7 and NPPB. Pro-BNP levels that were significantly above the clinical markers established for the possibility of a heart failure condition in patients (Strunk *et al.*, 2006) were secreted by the differentiated cardiomyocytes and detected in the supernatant of RAF1^{S257L} CBs, indicating the presence of highly increased quantities of the NPPB gene product. This supports the signaling effect of hyperactive RAF1^{S257L} signaling on the fetal

gene expression programs, which leads the cells towards a heart failure condition. We significantly suppressed the MEK-MAPK axis in cardiac cells without directly targeting RAF1, therefore we anticipated that only the MAPK-dependent phenotype is recovered after MEKi therapy. But as a result of MEKi treatment like MST2/YAP, parallel pathways downstream of RAF1 were also detected to be reversed.

We detected downregulation of two key regulators of intracellular calcium transients, SERCA2a and LTCC, as well as alterations in the SERCA2/PLN ratio in RAF1^{S257L} CMs. The SERCA2/PLN ratio was restored in RAF1^{S257L} CMs after MEKi therapy, while NPPB was markedly downregulated to levels comparable to WT CMs. This implies that ERK1/2 may directly or indirectly regulate the transcription of NPPB and the SERCA2A/PLN ratio. As a result of SERCA being inhibited by PLN, a decreased SERCA2/PLN ratio in RAF1^{S257L} CMs can alter the kinetics of calcium transients, which in turn reduces the ability of the heart to contract. As a result, it is possible to consider a reduced SERCA2a/PLN ratio as the stressor that drives towards the HCM phenotype (Huang *et al.*, 2014; Periasamy *et al.*, 2008).

Sarcomere structure was disrupted as seen in RAF1^{S257L} CMs. The atypical I-bands in both the RAF1^{S257L} CMs and the cardiac biopsy samples from the patient with harboring the heterozygous RAF1^{S257L} were a stunning and novel discovery. This phenotype was noted in a number of various experiments and techniques, and MEK inhibition entirely restored it.

In RAF1^{S257L} BCTs, two neighboring PEVK areas on the Z-line overlapped, but in WT, the Z-line was clearly encircled by two distinct and well-separated PEVK regions. This was shown by immunohistochemistry of the chosen region of the I-band, the PEVK domains of titin, and the Z-line. These abnormalities were corrected in BCTs after treatment with 0.1 M MEKi. When sarcomeres are stretched, the I-band of titin serves as a molecular spring that builds tension, simulating a regulatory node that integrates and perhaps coordinates several signaling events (Krüger and Linke, 2011). It has been demonstrated that the four-and-a-half LIM domain 1 protein (FHL-1) interacts directly as a scaffold protein with RAF1, MEK2, and ERK2 to boost cardiac MAPK signaling and bind to titin at the elastic N2B area (Sheikh *et al.*, 2008). In our studies, RAF1^{S257L} CMs had increased FHL1 mRNA expression. Furthermore, we noticed that in RAF1^{S257L} CMs, RAF1 was mostly observed in close proximity and/or at the sarcomeres. It's interesting to note that ERK2 has been shown to phosphorylate the N2B region of titin, which makes titin less stiff (Perkin *et al.*, 2015). Considering the observed higher expression levels of FHL1 in RAF1^{S257L} CBs, we suggest that RAF1^{S257L} promotes titin phosphorylation at its N2B region by hyperactivating the MEK1/2-ERK1/2 pathway, which is scaffolded alongside the sarcomeres, via FHL1. It is unknown how much these events may affect sarcomere distensibility and contribute to the cardiac defects linked to RAF1^{S257L}.

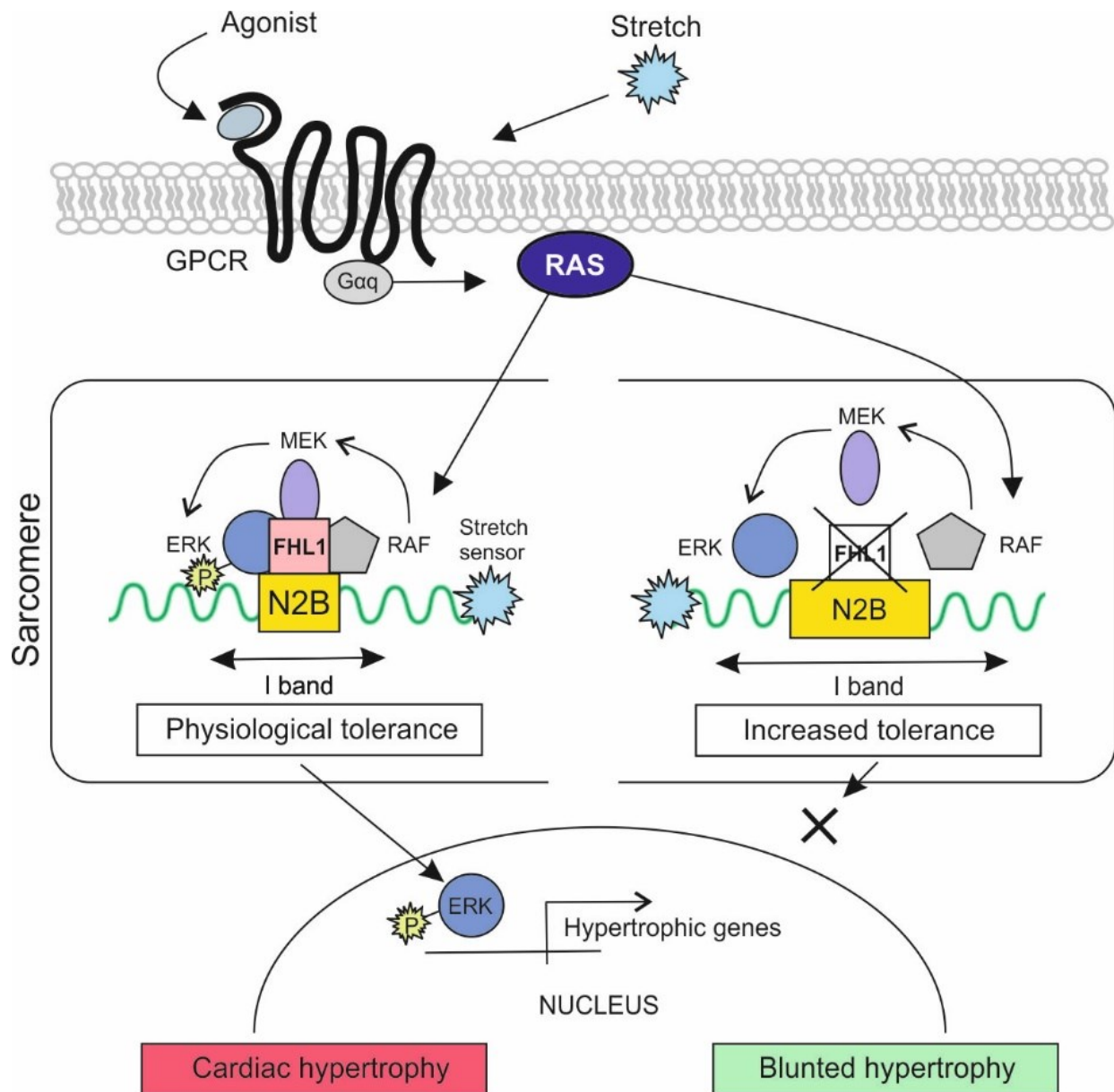


Figure 4. At the sarcomere of the muscle cells, FHL1 scaffolds RAF/MEK/ERK on the N2B domain of the massive protein titin. FHL1 limits the range at which sarcomere length may extend by acting as a stretch sensor at the I band sensing stretch or agonists induced GPCR (Gq) signaling. MAPK subunits RAF1, MEK, and ERK are all capable of direct interaction with FHL1. This highlights a MAPK scaffolding function for FHL1 at the titin N2B area of the sarcomere. The FHL1/RAF1/MEK/ERK complex all localized to the sarcomeric I band. An increase in ERK signaling brought on by a gain-of-function mutation in the gene for FHL1 contributes to the development of cardiac hypertrophy. In both mice and humans, FHL1 becomes significantly elevated in hypertrophic conditions, whereas FHL1 knockout hearts show a reduced response to development of cardiac hypertrophy.

It is unknown how the RAF1-MAPK signaling pathway affects the myocardium's ability to contract. One reason for the abnormal contractile activity of RAF1^{S257L} CMs could possibly

be the MYH6-to-MYH7 transition which has been perturbed as a result of the aberrantly active MAPK signaling. The cardiac-specific transcription factor GATA4 is known to be phosphorylated by ERK1/2 at S105, increasing its transcription regulating capacity. A number of structural and cardiac hypertrophy response genes, including NPPB, MYH7, TNNI3 (troponin I), and ACTA1 (-skeletal Actin) are known to be transcriptionally regulated by GATA4 (Dirkx *et al.*, 2013; Charron *et al.*, 1999; Liu *et al.*, 2015). We believe that the elevation of myosin heavy chain isoforms by RAF-MAPK is mediated by transcription factors unique to the heart. The SERCA2/PLN ratio, titin's phosphorylation by ERK1/2, the disorganized sarcomeric structures, and changes in the length and shape of titin's flexible I-band region may all have an impact on the myocardium's ability to generate force and maintain its elastic properties in addition to the MYH6-to-MYH7 switch.

HRAS p.Gly12Ser affects RIN1-mediated integrin trafficking in epidermal keratinocytes

The epidermal manifestation in individuals with Costello syndrome raises concerns about the functional impact of HRAS mutations linked to Costello syndrome in keratinocytes, which make up the majority of skin cells. The experiments demonstrated that the HRAS effector RIN1, which had previously received less attention compared to RAF kinases, is robustly expressed in both permanent and primary keratinocytes and is significantly enriched in HRASGly12Ser precipitates. RIN1 specifically and affinitively binds to active HRAS (Han and Colicelli, 1995). Similar to this, we discovered that RIN1 has a strong affinity for HRASGly12Ser. It has been shown that RIN1 as a high affinity binder effectively competes with RAF1 for binding to activated RAS (Wang *et al.*, 2002).

However, modest levels of RAF1 expression in HaCaT keratinocytes show that RAF1 is only a minor RIN1 rival in these cells. Accordingly, expression of active HRASGly12Ser in HaCaT cells had a negligible impact on RAF-MAPK signaling. In contrast, previous studies had shown that RAS-RAF kinase signaling is dramatically affected by CS-associated HRAS mutations in neuronal cells or fibroblasts (Niihori *et al.*, 2011; Krencik *et al.*, 2015b).

Additionally, the activation of RAB5 GTPases is modulated by the binding of active HRAS to RIN1. We revealed that RIN1 and HRAS regulate RAB5 signaling in HaCaT cells, which is consistent with the literature (Tall *et al.*, 2001). Since RIN1 is known to enhance ligand-induced receptor internalization in fibroblasts, epithelial cells, and cancer cells in addition to having a significant influence on endosome shape and endosome fusion, a role for RIN1 in the control of endocytic trafficking is well established (Tall *et al.*, 2001; Balaji and Colicelli, 2013; Barbieri *et al.*, 2003; Hunker *et al.*, 2006). We demonstrated that HRAS-RIN1 signaling regulates integrin trafficking and, consequently, the availability of integrins on the cell surface of epidermal HaCaT keratinocytes. Activation of HRAS-RIN1 signaling also increases the intracellular 1 integrin fraction at the expense of surface 1 integrin.

We emphasize the HRAS-RIN1 signaling axis, which controls integrin receptor expression and/or distribution. The capacity of keratinocytes to adhere to the ECM is mediated by integrins, and the HRASGly12Ser variation further disturbs these mechanisms by altering the cellular distribution of integrin. Costello syndrome patients have impacted cell adhesion defects. These findings are consistent with how individuals with Costello syndrome present with epidermal and cell adhesion defects clinically. In conclusion, abnormal endosomal sorting of cell surface receptors may explain certain epidermal symptoms in different RASopathies and connected diseases.

Characterization of RIT1 indels in Arteriovenous Malformations Enables Targeted Therapy

Numerous investigations employing various cell lines have shown that RIT1 is expressed in numerous tissues at various phases of development and also confers functional roles in neuronal morphogenesis, neural differentiation, and cellular stress tolerance (Shi *et al.*, 2006; Lein *et al.*, 2007; Cai *et al.*, 2011; Spencer *et al.*, 2002). Along with the initial reports of several somatic cancer mutations (Gomez-Segui *et al.*, 2013; Berger *et al.*, 2014), the discovery of germline mutations in Noonan syndrome individuals (Aoki *et al.*, 2013; Kouz *et al.*, 2016; Yaoita *et al.*, 2016) brought attention to the significance of RIT1 mechanistic studies and targeted therapies.

In patients with peripheral AVMs, three previously unreported somatic activating RIT1 indel mutations were described. All three variants are found near the RIT1 Switch 2 domain, which also contains RIT1 germline mutations frequently linked to Noonan syndrome. It's interesting to note that vascular malformations have been linked to indel variations of RAS GTPases in KRAS and HRAS, while in both cases located around the Switch 2 region as well (Eijkelenboom *et al.*, 2019). Biochemically, ERK hyperactivation was far more prominent in the indel mutations in comparison to the Noonan-associated RIT1 mutations.

We reasoned that since SHP2 works upstream of RAS proteins while MEK and ERK work downstream in the RAS-MAPK pathway, RIT1-induced ERK hyperactivation may respond differently to SHP2 and MEK inhibition. MEK inhibition with PD0325901 demonstrated to be a very promising approach towards rescuing the hyperactivated ERK profile and indicated a massive reduction in the readout of the MAPK pathway for all three indel variants. Given RIT1's readout towards ERK activation and its position as a member of the RAS family of GTPases, it was hypothesized that treatment with a SHP2 inhibitor (SHP099) may also exert an impact on the phosphorylation state of ERK in cells transfected with the novel indel variants. However, there was no significant impact from the SHP2 inhibitor observed on any of the three indel variants, suggesting that RIT1's upstream regulation may follow a different axis from that of classical RAS GTPases (H-K-N-RAS).

References

- Alison, M. R., Poulson, R., Forbes, S. & Wright, N. A. (2002). An introduction to stem cells. *The Journal of Pathology: A Journal of the Pathological Society of Great Britain and Ireland* 197(4): 419-423.
- Andelfinger, G., Marquis, C., Raboisson, M. J., Théoret, Y., Waldmüller, S., Wiegand, G., Gelb, B. D., Zenker, M., Delrue, M. A. & Hofbeck, M. (2019). Hypertrophic Cardiomyopathy in Noonan Syndrome Treated by MEK-Inhibition. *J Am Coll Cardiol* 73(17): 2237-2239.
- Aoki, Y., Niihori, T., Banjo, T., Okamoto, N., Mizuno, S., Kurosawa, K., Ogata, T., Takada, F., Yano, M. & Ando, T. (2013). Gain-of-function mutations in RIT1 cause Noonan syndrome, a RAS/MAPK pathway syndrome. *The American Journal of Human Genetics* 93(1): 173-180.
- Aoki, Y., Niihori, T., Kawame, H., Kurosawa, K., Ohashi, H., Tanaka, Y., Filocamo, M., Kato, K., Suzuki, Y. & Kure, S. (2005). Germline mutations in HRAS proto-oncogene cause Costello syndrome. *Nature genetics* 37(10): 1038-1040.
- Baines, A. T., Xu, D. & Der, C. J. (2011). Inhibition of Ras for cancer treatment: the search continues. *Future medicinal chemistry* 3(14): 1787-1808.
- Balaji, K. & Colicelli, J. (2013). RIN1 regulates cell migration through RAB5 GTPases and ABL tyrosine kinases. *Communicative & integrative biology* 6(5): e25421.
- Bar-Sagi, D. & Hall, A. (2000). Ras and Rho GTPases: a family reunion. *Cell* 103(2): 227-238.
- Barbieri, M. A., Kong, C., Chen, P.-I., Horazdovsky, B. F. & Stahl, P. D. (2003). The SRC homology 2 domain of Rin1 mediates its binding to the epidermal growth factor receptor and regulates receptor endocytosis. *Journal of Biological Chemistry* 278(34): 32027-32036.
- Bentires-Alj, M., Paez, J. G., David, F. S., Keilhack, H., Halmos, B., Naoki, K., Maris, J. M., Richardson, A., Bardelli, A. & Sugarbaker, D. J. (2004). Activating mutations of the noonan syndrome-associated SHP2/PTPN11 gene in human solid tumors and adult acute myelogenous leukemia. *Cancer research* 64(24): 8816-8820.
- Berger, A., Imielinski, M., Duke, F., Wala, J., Kaplan, N., Shi, G., Andres, D. & Meyerson, M. (2014). Oncogenic RIT1 mutations in lung adenocarcinoma. *Oncogene* 33(35): 4418-4423.
- Bernards, A. & Settleman, J. (2004). GAP control: regulating the regulators of small GTPases. *Trends in cell biology* 14(7): 377-385.
- Bishop, A. L. & Hall, A. (2000). Rho GTPases and their effector proteins. *Biochemical Journal* 348(2): 241-255.
- Bliss, J. M., Venkatesh, B. & Colicelli, J. (2006). The RIN family of Ras effectors. *Methods in enzymology* 407: 335-344.
- Bonner, T., Kerby, S., Suttrave, P., Gunnell, M., Mark, G. & Rapp, U. (1985). Structure and biological activity of human homologs of the raf/mil oncogene. *Molecular and cellular biology* 5(6): 1400-1407.
- Bos, J. L. (1989). Ras oncogenes in human cancer: a review. *Cancer research* 49(17): 4682-4689.
- Cai, W., Rudolph, J. L., Harrison, S. M., Jin, L., Frantz, A. L., Harrison, D. A. & Andres, D. A. (2011). An evolutionarily conserved Rit GTPase-p38 MAPK signaling pathway mediates oxidative stress resistance. *Molecular biology of the cell* 22(17): 3231-3241.
- Calcagni, G., Baban, A., Lepri, F. R., Marino, B., Tartaglia, M. & Digilio, M. C. (2016). Congenital heart defects in Noonan syndrome and RIT1 mutation. *Genetics in Medicine* 18(12): 1320-1320.
- Castel, P., Cheng, A., Cuevas-Navarro, A., Everman, D. B., Papageorge, A. G., Simanshu, D. K., Tankka, A., Galeas, J., Urisman, A. & McCormick, F. (2019). RIT1 oncoproteins escape LZTR1-mediated proteolysis. *Science* 363(6432): 1226-1230.
- Cavé, H., Caye, A., Ghedira, N., Capri, Y., Pouvreau, N., Fillot, N., Trimouille, A., Vignal, C., Fenneteau, O. & Alembik, Y. (2016). Mutations in RIT1 cause Noonan syndrome with possible juvenile

- myelomonocytic leukemia but are not involved in acute lymphoblastic leukemia. *European journal of human genetics* 24(8): 1124-1131.
- Charron, F., Paradis, P., Bronchain, O., Nemer, G. & Nemer, M. (1999). Cooperative interaction between GATA-4 and GATA-6 regulates myocardial gene expression. *Mol Cell Biol* 19(6): 4355-4365.
- Cherfils, J. (2014). Arf GTPases and their effectors: assembling multivalent membrane-binding platforms. *Current opinion in structural biology* 29: 67-76.
- Cherfils, J. & Zeghouf, M. (2013). Regulation of small gtpases by gefs, gaps, and gdis. *Physiological reviews* 93(1): 269-309.
- Chin, M. H., Mason, M. J., Xie, W., Volinia, S., Singer, M., Peterson, C., Ambartsumyan, G., Aimiwu, O., Richter, L. & Zhang, J. (2009). Induced pluripotent stem cells and embryonic stem cells are distinguished by gene expression signatures. *Cell stem cell* 5(1): 111-123.
- Cirstea, I. C., Kutsche, K., Dvorsky, R., Gremer, L., Carta, C., Horn, D., Roberts, A. E., Lepri, F., Merbitz-Zahradnik, T. & König, R. (2010). A restricted spectrum of NRAS mutations causes Noonan syndrome. *Nature genetics* 42(1): 27-29.
- Colicelli, J. (2004). Human RAS superfamily proteins and related GTPases. *Science's STKE* 2004(250): re13-re13.
- Colicelli, J., Nicolette, C., Birchmeier, C., Rodgers, L., Riggs, M. & Wigler, M. (1991). Expression of three mammalian cDNAs that interfere with RAS function in *Saccharomyces cerevisiae*. *Proceedings of the National Academy of Sciences* 88(7): 2913-2917.
- Cseh, B., Doma, E. & Baccarini, M. (2014). "RAF" neighborhood: Protein–protein interaction in the Raf/Mek/Erk pathway. *FEBS letters* 588(15): 2398-2406.
- De Franceschi, N., Hamidi, H., Alanko, J., Sahgal, P. & Ivaska, J. (2015). Integrin traffic—the update. *Journal of cell science* 128(5): 839-852.
- Desideri, E., Cavallo, A. L. & Baccarini, M. (2015). Alike but different: RAF paralogs and their signaling outputs. *Cell* 161(5): 967-970.
- Dhandapany, P. S., Fabris, F., Tonk, R., Illaste, A., Karakikes, I., Sorourian, M., Sheng, J., Hajjar, R. J., Tartaglia, M., Sobie, E. A., Lebeche, D. & Gelb, B. D. (2011). Cyclosporine attenuates cardiomyocyte hypertrophy induced by RAF1 mutants in Noonan and LEOPARD syndromes. *J Mol Cell Cardiol* 51(1): 4-15.
- Dirkx, E., da Costa Martins, P. A. & De Windt, L. J. (2013). Regulation of fetal gene expression in heart failure. *Biochim Biophys Acta* 1832(12): 2414-2424.
- Donaldson, J. G. & Jackson, C. L. (2011). ARF family G proteins and their regulators: roles in membrane transport, development and disease. *Nature Reviews Molecular Cell Biology* 12(6): 362-375.
- Dougherty, M. K., Müller, J., Ritt, D. A., Zhou, M., Zhou, X. Z., Copeland, T. D., Conrads, T. P., Veenstra, T. D., Lu, K. P. & Morrison, D. K. (2005). Regulation of Raf-1 by direct feedback phosphorylation. *Molecular cell* 17(2): 215-224.
- Drosten, M., Lechuga, C. & Barbacid, M. (2014). Ras signaling is essential for skin development. *Oncogene* 33(22): 2857-2865.
- Drosten, M., Lechuga, C. G. & Barbacid, M. (2013). Genetic analysis of Ras genes in epidermal development and tumorigenesis. *Small GTPases* 4(4): 236-241.
- Dvorsky, R. & Ahmadian, M. R. (2004). Always look on the bright site of Rho: structural implications for a conserved intermolecular interface. *EMBO reports* 5(12): 1130-1136.
- Dvorsky, R., Blumenstein, L., Vetter, I. R. & Ahmadian, M. R. (2004). Structural insights into the interaction of ROCK1 with the switch regions of RhoA. *Journal of Biological Chemistry* 279(8): 7098-7104.
- Eijkelenboom, A., van Schaik, F. M. A., van Es, R. M., Ten Broek, R. W., Rinne, T., van der Vleuten, C., Flucke, U., Ligtenberg, M. J. L. & Rehmann, H. (2019). Functional characterisation of a novel class of in-frame insertion variants of KRAS and HRAS. *Scientific Reports* 9(1): 8239.

- Etienne-Manneville, S. & Hall, A. (2002). Rho GTPases in cell biology. *Nature* 420(6916): 629-635.
- Fernández-Medarde, A. & Santos, E. (2011). Ras in cancer and developmental diseases. *Genes & cancer* 2(3): 344-358.
- Fischer, A., Baljuls, A., Reinders, J., Nekhoroshkova, E., Sibilski, C., Metz, R., Albert, S., Rajalingam, K., Hekman, M. & Rapp, U. R. (2009). Regulation of RAF activity by 14-3-3 proteins: RAF kinases associate functionally with both homo- and heterodimeric forms of 14-3-3 proteins. *Journal of Biological Chemistry* 284(5): 3183-3194.
- Freed, E., Symons, M., Macdonald, S. G., McCormick, F. & Ruggieri, R. (1994). Binding of 14-3-3 proteins to the protein kinase Raf and effects on its activation. *Science* 265(5179): 1713-1716.
- Gelb, B. D., Roberts, A. E. & Tartaglia, M. (2015). Cardiomyopathies in Noonan syndrome and the other RASopathies. *Progress in pediatric cardiology* 39(1): 13-19.
- Ghosh, S., Xie, W. Q., Quest, A., Mabrouk, G. M., Strum, J. C. & Bell, R. M. (1994). The cysteine-rich region of raf-1 kinase contains zinc, translocates to liposomes, and is adjacent to a segment that binds GTP-ras. *Journal of Biological Chemistry* 269(13): 10000-10007.
- Gomez-Segui, I., Makishima, H., Jerez, A., Yoshida, K., Przychodzen, B., Miyano, S., Shiraishi, Y., Husseinzadeh, H., Guinta, K. & Clemente, M. (2013). Novel recurrent mutations in the RAS-like GTP-binding gene RIT1 in myeloid malignancies. *Leukemia* 27(9): 1943-1946.
- Grskovic, M., Javaherian, A., Strulovici, B. & Daley, G. Q. (2011). Induced pluripotent stem cells—opportunities for disease modelling and drug discovery. *Nature reviews Drug discovery* 10(12): 915-929.
- Han, L. & Colicelli, J. (1995). A human protein selected for interference with Ras function interacts directly with Ras and competes with Raf1. *Mol Cell Biol* 15(3): 1318-1323.
- Hanai, A., Ohgi, M., Yagi, C., Ueda, T., Shin, H.-W. & Nakayama, K. (2016). Class I Arfs (Arf1 and Arf3) and Arf6 are localized to the Flemming body and play important roles in cytokinesis. *The journal of biochemistry* 159(2): 201-208.
- Hebron, K. E., Hernandez, E. R. & Yohe, M. E. (2022). The RASopathies: from pathogenetics to therapeutics. *Disease Models & Mechanisms* 15(2): dmm049107.
- Hegde, S. & Raghavan, S. (2013). A skin-depth analysis of integrins: role of the integrin network in health and disease. *Cell communication & adhesion* 20(6): 155-169.
- Helms, J. B. & Rothman, J. E. (1992). Inhibition by brefeldin A of a Golgi membrane enzyme that catalyses exchange of guanine nucleotide bound to ARF. *Nature* 360(6402): 352-354.
- Hinek, A., Teitell, M. A., Schoyer, L., Allen, W., Gripp, K. W., Hamilton, R., Weksberg, R., Klüppel, M. & Lin, A. E. (2005). Myocardial storage of chondroitin sulfate-containing moieties in Costello syndrome patients with severe hypertrophic cardiomyopathy. *American journal of medical genetics Part A* 133(1): 1-12.
- Ho, P. D., Fan, J. S., Hayes, N. L., Saada, N., Palade, P. T., Glembotski, C. C. & McDonough, P. M. (2001). Ras reduces L-type calcium channel current in cardiac myocytes. Corrective effects of L-channels and SERCA2 on [Ca(2+)](i) regulation and cell morphology. *Circ Res* 88(1): 63-69.
- Hu, H., Bliss, J. M., Wang, Y. & Colicelli, J. (2005). RIN1 is an ABL tyrosine kinase activator and a regulator of epithelial-cell adhesion and migration. *Current Biology* 15(9): 815-823.
- Huang, H., Joseph, L. C., Gurin, M. I., Thorp, E. B. & Morrow, J. P. (2014). Extracellular signal-regulated kinase activation during cardiac hypertrophy reduces sarcoplasmic/endoplasmic reticulum calcium ATPase 2 (SERCA2) transcription. *J Mol Cell Cardiol* 75: 58-63.
- Huleihel, M., Goldsborough, M., Cleveland, J., Gunnell, M., Bonner, T. & Rapp, U. (1986). Characterization of murine A-raf, a new oncogene related to the v-raf oncogene. *Molecular and cellular biology* 6(7): 2655-2662.
- Hunker, C. M., Giambini, H., Galvis, A., Hall, J., Kruk, I., Veisaga, M. L. & Barbieri, M. A. (2006). Rin1 regulates insulin receptor signal transduction pathways. *Exp Cell Res* 312(7): 1106-1118.

- Ikawa, S., Fukui, M., Ueyama, Y., Tamaoki, N., Yamamoto, T. & Toyoshima, K. (1988). B-raf, a new member of the raf family, is activated by DNA rearrangement. *Molecular and cellular biology* 8(6): 2651-2654.
- Jaffré, F., Miller, C. L., Schänzer, A., Evans, T., Roberts, A. E., Hahn, A. & Kontaridis, M. I. (2019). Inducible Pluripotent Stem Cell-Derived Cardiomyocytes Reveal Aberrant Extracellular Regulated Kinase 5 and Mitogen-Activated Protein Kinase Kinase 1/2 Signaling Concomitantly Promote Hypertrophic Cardiomyopathy in RAF1-Associated Noonan Syndrome. *Circulation* 140(3): 207-224.
- Jafry, M. & Sidbury, R. (2020). RASopathies. *Clinics in Dermatology* 38(4): 455-461.
- Jalink, K., Van Corven, E. J., Hengeveld, T., Morii, N., Narumiya, S. & Moolenaar, W. H. (1994). Inhibition of lysophosphatide- and thrombin-induced neurite retraction and neuronal cell rounding by ADP ribosylation of the small GTP-binding protein Rho. *The Journal of cell biology* 126(3): 801-810.
- Khan, A. R. & Ménétrey, J. (2013). Structural biology of Arf and Rab GTPases' effector recruitment and specificity. *Structure* 21(8): 1284-1297.
- Khatri, A., Wang, J. & Pendergast, A. M. (2016). Multifunctional Abl kinases in health and disease. *Journal of cell science* 129(1): 9-16.
- Kouz, K., Lissewski, C., Spranger, S., Mitter, D., Riess, A., Lopez-Gonzalez, V., Lüttgen, S., Aydin, H., Von Deimling, F. & Evers, C. (2016). Genotype and phenotype in patients with Noonan syndrome and a RIT1 mutation. *Genetics in Medicine* 18(12): 1226-1234.
- Krencik, R., Hokanson, K. C., Narayan, A. R., Dvornik, J., Rooney, G. E., Rauen, K. A., Weiss, L. A., Rowitch, D. H. & Ullian, E. M. (2015a). Dysregulation of astrocyte extracellular signaling in Costello syndrome. *Science translational medicine* 7(286): 286ra266-286ra266.
- Krencik, R., Hokanson, K. C., Narayan, A. R., Dvornik, J., Rooney, G. E., Rauen, K. A., Weiss, L. A., Rowitch, D. H. & Ullian, E. M. (2015b). Dysregulation of astrocyte extracellular signaling in Costello syndrome. *Sci Transl Med* 7(286): 286ra266.
- Krüger, M. & Linke, W. A. (2011). The giant protein titin: a regulatory node that integrates myocyte signaling pathways. *J Biol Chem* 286(12): 9905-9912.
- Kubicek, M., Pacher, M., Abraham, D., Podar, K., Eulitz, M. & Baccarini, M. (2002). Dephosphorylation of Ser-259 regulates Raf-1 membrane association. *Journal of Biological Chemistry* 277(10): 7913-7919.
- Land, H., Parada, L. F. & Weinberg, R. A. (1983). Cellular oncogenes and multistep carcinogenesis. *Science* 222(4625): 771-778.
- Lein, P. J., Guo, X., Shi, G.-X., Moholt-Siebert, M., Bruun, D. & Andres, D. A. (2007). The novel GTPase Rit differentially regulates axonal and dendritic growth. *Journal of Neuroscience* 27(17): 4725-4736.
- Litviňuková, M., Talavera-López, C., Maatz, H., Reichart, D., Worth, C. L., Lindberg, E. L., Kanda, M., Polanski, K., Heinig, M. & Lee, M. (2020). Cells of the adult human heart. *Nature* 588(7838): 466-472.
- Liu, Y. L., Huang, C. C., Chang, C. C., Chou, C. Y., Lin, S. Y., Wang, I. K., Hsieh, D. J., Jong, G. P., Huang, C. Y. & Wang, C. M. (2015). Hyperphosphate-Induced Myocardial Hypertrophy through the GATA-4/NFAT-3 Signaling Pathway Is Attenuated by ERK Inhibitor Treatment. *Cardiorenal Med* 5(2): 79-88.
- Lowy, D. R. & Willumsen, B. M. (1993). Function and regulation of ras. *Annual review of biochemistry* 62(1): 851-891.
- Maron, B. J. & Maron, M. S. (2013). Hypertrophic cardiomyopathy. *The Lancet* 381(9862): 242-255.
- Meilhac, S. M. & Buckingham, M. E. (2018). The deployment of cell lineages that form the mammalian heart. *Nature Reviews Cardiology* 15(11): 705-724.

- Mendez, H. M., Opitz, J. M. & Reynolds, J. F. (1985). Noonan syndrome: a review. *American journal of medical genetics* 21(3): 493-506.
- Moreno-Layseca, P., Icha, J., Hamidi, H. & Ivaska, J. (2019). Integrin trafficking in cells and tissues. *Nature cell biology* 21(2): 122-132.
- Morii, N., Teru-Uchi, T., Tominaga, T., Kumagai, N., Kozaki, S., Ushikubi, F. & Narumiya, S. (1992). A rho gene product in human blood platelets. II. Effects of the ADP-ribosylation by botulinum C3 ADP-ribosyltransferase on platelet aggregation. *Journal of Biological Chemistry* 267(29): 20921-20926.
- Morreale, A., Venkatesan, M., Mott, H. R., Owen, D., Nietlispach, D., Lowe, P. N. & Laue, E. D. (2000). Structure of Cdc42 bound to the GTPase binding domain of PAK. *Nature structural biology* 7(5): 384-388.
- Mott, H. R. & Owen, D. (2015). Structures of Ras superfamily effector complexes: What have we learnt in two decades? *Critical reviews in biochemistry and molecular biology* 50(2): 85-133.
- Mott, H. R., Owen, D., Nietlispach, D., Lowe, P. N., Manser, E., Lim, L. & Laue, E. D. (1999). Structure of the small G protein Cdc42 bound to the GTPase-binding domain of ACK. *Nature* 399(6734): 384-388.
- Mussa, A., Carli, D., Giorgio, E., Villar, A. M., Cardaropoli, S., Carbonara, C., Campagnoli, M. F., Galletto, P., Palumbo, M., Olivieri, S., Isella, C., Andelfinger, G., Tartaglia, M., Botta, G., Brusco, A., Medico, E. & Ferrero, G. B. (2021). MEK Inhibition in a Newborn with RAF1-Associated Noonan Syndrome Ameliorates Hypertrophic Cardiomyopathy but Is Insufficient to Revert Pulmonary Vascular Disease. *Genes (Basel)* 13(1).
- Nakayama, K. (2016). Regulation of cytokinesis by membrane trafficking involving small GTPases and the ESCRT machinery. *Critical reviews in biochemistry and molecular biology* 51(1): 1-6.
- Nakhaei-Rad, S., Haghighi, F., Nouri, P., Rezaei Adariani, S., Lissy, J., Kazeminejad, N. S., Dvorsky, R. & Ahmadian, M. R. (2018). Structural fingerprints, interactions, and signaling networks of RAS family proteins beyond RAS isoforms. *Critical reviews in biochemistry and molecular biology* 53(2): 130-156.
- Narumiya, S. & Thumke, D. (2018). Rho signaling research: history, current status and future directions. *FEBS letters* 592(11): 1763-1776.
- Niihori, T., Aoki, Y., Okamoto, N., Kurosawa, K., Ohashi, H., Mizuno, S., Kawame, H., Inazawa, J., Ohura, T., Arai, H., Nabatame, S., Kikuchi, K., Kuroki, Y., Miura, M., Tanaka, T., Ohtake, A., Otori, I., Ihara, K., Mabe, H., Watanabe, K., Nijima, S., Okano, E., Numabe, H. & Matsubara, Y. (2011). HRAS mutants identified in Costello syndrome patients can induce cellular senescence: possible implications for the pathogenesis of Costello syndrome. *J Hum Genet* 56(10): 707-715.
- Noonan, J. A. (1963). Associated noncardiac malformations in children with congenital heart disease. *Midwest Soc Pediat Res* 63: 468-470.
- Nouri, K., Timson, D. J. & Ahmadian, M. R. (2020). New model for the interaction of IQGAP1 with CDC42 and RAC1. *Small GTPases* 11(1): 16-22.
- Pandit, B., Sarkozy, A., Pennacchio, L. A., Carta, C., Oishi, K., Martinelli, S., Pogna, E. A., Schackwitz, W., Ustaszewska, A. & Landstrom, A. (2007). Gain-of-function RAF1 mutations cause Noonan and LEOPARD syndromes with hypertrophic cardiomyopathy. *Nature genetics* 39(8): 1007-1012.
- Paterson, H. F., Self, A. J., Garrett, M. D., Just, I., Aktories, K. & Hall, A. (1990). Microinjection of recombinant p21rho induces rapid changes in cell morphology. *The Journal of cell biology* 111(3): 1001-1007.
- Periasamy, M., Bhupathy, P. & Babu, G. J. (2008). Regulation of sarcoplasmic reticulum Ca²⁺ ATPase pump expression and its relevance to cardiac muscle physiology and pathology. *Cardiovasc Res* 77(2): 265-273.

- Perkin, J., Slater, R., Del Favero, G., Lanzicher, T., Hidalgo, C., Anderson, B., Smith, J. E., 3rd, Sbaizero, O., Labeit, S. & Granzier, H. (2015). Phosphorylating Titin's Cardiac N2B Element by ERK2 or CaMKII δ Lowers the Single Molecule and Cardiac Muscle Force. *Biophys J* 109(12): 2592-2601.
- Rapp, U., Goldsborough, M., Mark, G., Bonner, T., Groffen, J., Reynolds Jr, F. & Stephenson, J. (1983). Structure and biological activity of v-raf, a unique oncogene transduced by a retrovirus. *Proceedings of the National Academy of Sciences* 80(14): 4218-4222.
- Rauen, K. A. (2013). The rasopathies. *Annual review of genomics and human genetics* 14: 355-369.
- Razzaque, M. A., Nishizawa, T., Komoike, Y., Yagi, H., Furutani, M., Amo, R., Kamisago, M., Momma, K., Katayama, H. & Nakagawa, M. (2007). Germline gain-of-function mutations in RAF1 cause Noonan syndrome. *Nature genetics* 39(8): 1013-1017.
- Rippa, A., Vorotelyak, E., Vasiliev, A. & Terskikh, V. (2013). The role of integrins in the development and homeostasis of the epidermis and skin appendages. *Acta Naturae (англоязычная версия)* 5(4 (19)): 22-33.
- Roberts, A. E., Allanson, J. E., Tartaglia, M. & Gelb, B. D. (2013). Noonan syndrome. *The Lancet* 381(9863): 333-342.
- Roberts, A. E., Araki, T., Swanson, K. D., Montgomery, K. T., Schiripo, T. A., Joshi, V. A., Li, L., Yassin, Y., Tamburino, A. M. & Neel, B. G. (2007). Germline gain-of-function mutations in SOS1 cause Noonan syndrome. *Nature genetics* 39(1): 70-74.
- Robinton, D. A. & Daley, G. Q. (2012). The promise of induced pluripotent stem cells in research and therapy. *Nature* 481(7381): 295-305.
- Rodrigues, F. F. & Harris, T. J. C. (2019). Key roles of Arf small G proteins and biosynthetic trafficking for animal development. *Small GTPases* 10(6): 403-410.
- Rosenberger, G., Meien, S. & Kutsche, K. (2009). Oncogenic HRAS mutations cause prolonged PI3K signaling in response to epidermal growth factor in fibroblasts of patients with Costello syndrome. *Human Mutation* 30(3): 352-362.
- Schmidt, A. & Hall, A. (2002). Guanine nucleotide exchange factors for Rho GTPases: turning on the switch. *Genes & development* 16(13): 1587-1609.
- Schubbert, S., Zenker, M., Rowe, S. L., Böll, S., Klein, C., Bollag, G., Van Der Burgt, I., Musante, L., Kalscheuer, V. & Wehner, L.-E. (2006). Germline KRAS mutations cause Noonan syndrome. *Nature genetics* 38(3): 331-336.
- Semsarian, C., Ingles, J., Maron, M. S. & Maron, B. J. (2015). New perspectives on the prevalence of hypertrophic cardiomyopathy. *Journal of the American College of Cardiology* 65(12): 1249-1254.
- Shao, H. & Andres, D. A. (2000). A novel RalGEF-like protein, RGL3, as a candidate effector for rit and Ras. *Journal of Biological Chemistry* 275(35): 26914-26924.
- Sheikh, F., Raskin, A., Chu, P. H., Lange, S., Domenighetti, A. A., Zheng, M., Liang, X., Zhang, T., Yajima, T., Gu, Y., Dalton, N. D., Mahata, S. K., Dorn, G. W., 2nd, Brown, J. H., Peterson, K. L., Omens, J. H., McCulloch, A. D. & Chen, J. (2008). An FHL1-containing complex within the cardiomyocyte sarcomere mediates hypertrophic biomechanical stress responses in mice. *J Clin Invest* 118(12): 3870-3880.
- Shi, G.-X. & Andres, D. A. (2005). Rit contributes to nerve growth factor-induced neuronal differentiation via activation of B-Raf-extracellular signal-regulated kinase and p38 mitogen-activated protein kinase cascades. *Molecular and cellular biology* 25(2): 830-846.
- Shi, G.-X., Cai, W. & Andres, D. A. (2013). Rit subfamily small GTPases: regulators in neuronal differentiation and survival. *Cellular signalling* 25(10): 2060-2068.
- Shi, G.-X., Rehmann, H. & Andres, D. A. (2006). A novel cyclic AMP-dependent Epac-Rit signaling pathway contributes to PACAP38-mediated neuronal differentiation. *Molecular and cellular biology* 26(23): 9136-9147.

- Simanshu, D. K., Nissley, D. V. & McCormick, F. (2017). RAS proteins and their regulators in human disease. *Cell* 170(1): 17-33.
- Simpson, C. L., Patel, D. M. & Green, K. J. (2011). Deconstructing the skin: cytoarchitectural determinants of epidermal morphogenesis. *Nature Reviews Molecular Cell Biology* 12(9): 565-580.
- Soldner, F. & Jaenisch, R. (2012). iPSC disease modeling. *Science* 338(6111): 1155-1156.
- Spencer, M. L., Shao, H. & Andres, D. A. (2002). Induction of neurite extension and survival in pheochromocytoma cells by the Rit GTPase. *Journal of Biological Chemistry* 277(23): 20160-20168.
- Strunk, A., Bhalla, V., Clopton, P., Nowak, R. M., McCord, J., Hollander, J. E., Duc, P., Storrow, A. B., Abraham, W. T., Wu, A. H., Steg, G., Perez, A., Kazanegra, R., Herrmann, H. C., Aumont, M. C., McCullough, P. A. & Maisel, A. (2006). Impact of the history of congestive heart failure on the utility of B-type natriuretic peptide in the emergency diagnosis of heart failure: results from the Breathing Not Properly Multinational Study. *Am J Med* 119(1): 69.e61-11.
- Takahashi, K., Tanabe, K., Ohnuki, M., Narita, M., Ichisaka, T., Tomoda, K. & Yamanaka, S. (2007). Induction of pluripotent stem cells from adult human fibroblasts by defined factors. *Cell* 131(5): 861-872.
- Takahashi, K. & Yamanaka, S. (2006). Induction of pluripotent stem cells from mouse embryonic and adult fibroblast cultures by defined factors. *Cell* 126(4): 663-676.
- Tall, G. G., Barbieri, M. A., Stahl, P. D. & Horazdovsky, B. F. (2001). Ras-activated endocytosis is mediated by the Rab5 guanine nucleotide exchange activity of RIN1. *Developmental cell* 1(1): 73-82.
- Thapar, R., Karnoub, A. E. & Campbell, S. L. (2002). Structural and biophysical insights into the role of the insert region in Rac1 function. *Biochemistry* 41(12): 3875-3883.
- Tidyman, W. E. & Rauen, K. A. (2016). Pathogenetics of the RASopathies. *Human molecular genetics* 25(R2): R123-R132.
- Volpicelli-Daley, L. A., Li, Y., Zhang, C.-J. & Kahn, R. A. (2005). Isoform-selective effects of the depletion of ADP-ribosylation factors 1–5 on membrane traffic. *Molecular biology of the cell* 16(10): 4495-4508.
- Wang, Y., Waldron, R. T., Dhaka, A., Patel, A., Riley, M. M., Rozengurt, E. & Colicelli, J. (2002). The RAS effector RIN1 directly competes with RAF and is regulated by 14-3-3 proteins. *Molecular and cellular biology* 22(3): 916-926.
- Wennerberg, K., Rossman, K. L. & Der, C. J. (2005). The Ras superfamily at a glance. *Journal of cell science* 118(5): 843-846.
- Woodring, P. J., Hunter, T. & Wang, J. Y. (2003). Regulation of F-actin-dependent processes by the Abl family of tyrosine kinases. *Journal of cell science* 116(13): 2613-2626.
- Yamamoto, G. L., Aguen, M., Gos, M., Hung, C., Pilch, J., Fahiminiya, S., Abramowicz, A., Cristian, I., Buscarilli, M. & Naslavsky, M. S. (2015). Rare variants in SOS2 and LZTR1 are associated with Noonan syndrome. *Journal of medical genetics* 52(6): 413-421.
- Yaoita, M., Niihori, T., Mizuno, S., Okamoto, N., Hayashi, S., Watanabe, A., Yokozawa, M., Suzumura, H., Nakahara, A. & Nakano, Y. (2016). Spectrum of mutations and genotype–phenotype analysis in Noonan syndrome patients with RIT1 mutations. *Human genetics* 135(2): 209-222.
- Yoon, S. & Seger, R. (2006). The extracellular signal-regulated kinase: multiple substrates regulate diverse cellular functions. *Growth factors* 24(1): 21-44.
- Young, L. C., Hartig, N., Boned del Río, I., Sari, S., Ringham-Terry, B., Wainwright, J. R., Jones, G. G., McCormick, F. & Rodriguez-Vician, P. (2018). SHOC2–MRAS–PP1 complex positively regulates RAF activity and contributes to Noonan syndrome pathogenesis. *Proceedings of the National Academy of Sciences* 115(45): E10576-E10585.

Yuan, W. & Song, C. (2020). The emerging role of Rab5 in membrane receptor trafficking and signaling pathways. *Biochemistry Research International* 2020.

Zakrzewski, W., Dobrzyński, M., Szymonowicz, M. & Rybak, Z. (2019). Stem cells: past, present, and future. *Stem cell research & therapy* 10(1): 1-22.

ACKNOWLEDGEMENTS

I would like to thank my advisor Prof. Reza Ahmadian for his unwavering support throughout my Ph.D. program, for helping me develop as a researcher with his mentoring advice, inspiration, knowledge, and expertise, and for giving me the chance to in addition to cell and molecular biology, gain extensive exposure to the fields of protein biochemistry, biophysics, and cell signaling .

My sincere gratitude is extended to Prof. Axel Gödecke, the director and spokesperson of our graduate school, from whom I learned a great deal about the fundamentals of molecular cardiology research, as well as the scientific coordinators of the IRTG graduate program, especially Dr. Sandra Berger, who made it possible for me to take advantage of all the wonderful benefits of being a student here.

I want to express my gratitude to Prof. Vlada Urlacher, Prof. Jürgen Scheller, and Dr. Roland Piekorz for their inspiring discussions and advice throughout my PhD studies.

I also would like to express my thankfulness and share this feeling being at the ending stage of my doctoral studies towards my family; my mom, dad and sister as well as my partner Anna Rita Minafra for their continuous support and wise advices helping me to stablish myself in a new country and focus better on my aims to pursue and achieve my scientific goals. I would also like to thank my colleagues and friends Ehsan Amin and Puyan Rafii for their helpfull advices along the way.

EIDESSTATTLICHE ERKLÄRUNG

Ich versichere an Eides Statt, dass die Dissertation von mir selbständig und ohne unzulässige fremde Hilfe unter Beachtung der „Grundsätze zur Sicherung guter wissenschaftlicher Praxis an der Heinrich-Heine-Universität Düsseldorf“ erstellt worden ist. Diese Dissertation wurde in der vorgelegten oder einer ähnlichen Form noch bei keiner anderen Institution eingereicht und es wurden bisher keine erfolglosen Promotionsversuche von mir unternommen.

Düsseldorf

A handwritten signature in black ink, appearing to read 'Farhad', written in a cursive style.

Farhad Bazgir